Robust linear and non-linear control of magnetically levitated systems

Thesis Submitted to The University of Wales
for The Degree of Doctor of Philosophy

Alexandre Nikolov Pechev

Institute of Magnetics, Electronics and Electrical Systems
School of Engineering
Cardiff University

September, 2004

ProQuest LLC
789 East Eisenhower Parkway
P.O. Box 1346
Ann Arbor, MI 48106-1346

Acknowledgements

I would like to express my gratitude to Professor P.K. Sinha, Emeritus Professor at the University of Reading, for his financial and academic support during the course of this work. No doubt that without his support this project would not have been possible.

I would like also to thank Professor H. Bolton for giving me the opportunity to be a part of Cardiff University and to both him and Dr. A. Haddad for their constructive comments and suggestions on the thesis.

I am greatly indebted to Elena for her love, patience and understanding.

Last but not least I would like to express my gratitude to my parents in Bulgaria for their love.

To my son Dennis,
my family and my parents

Abstract

The two most advanced applications of contactless magnetic levitation are high-speed magnetic bearings and magnetically levitated vehicles (Maglev) for ground transportation using superconducting magnets and controlled d.c. electromagnets. The repulsion force from superconducting magnets provide stable levitation with low damping, while the suspension force generated by electromagnets is inherently unstable. This instability, due to the inverse force-distance relationship, requires the addition of feedback controllers to sustain stable suspension.

The problem of controlling magnetically levitated systems using d.c. electromagnets under different operating conditions has been studied in this thesis with a design process primarily driven by experimental results from a representative single-magnet test rig and a multi-magnet vehicle. The controller-design stages are presented in detail and close relationships have been constructed between selection of performance criteria for the derivation process and desired suspension characteristics. Both linear and nonlinear stabilising compensators have been developed. Simulation and experimental results have been studied in parallel to assess operational stability and the main emphasis has been given to assessing performance under different operational conditions. For the experimental work, a new digital signal processor-based hardware platform has been designed, built with interface to Matlab/Simulink.

The controller design methods and algorithmic work presented in this thesis can be divided into: non-adaptive, adaptive, optimal linear and nonlinear. Adaptive algorithms based on model reference control have been developed to improve the performance of the suspension system in the presence of considerable variations in external payload and force disturbances. New design methods for Maglev suspension have been developed using robust control theory ($\mathcal{H}_\infty$ and $\mu-$synthesis). Single- and multi-magnet control problems have been treated using the same framework. A solution to the $\mathcal{H}_\infty$ controller-optimisation problem has been derived and applied to Maglev control. The sensitivity to robustness has been discussed and tools for assessing the robustness of the closed-loop system in terms of sustaining stability and performance in the presence of uncertainties in the suspension model have been presented. Multivariable controllers based on $\mathcal{H}_\infty$ and $\mu-$synthesis have been developed for a laboratory scale experimental vehicle weighing 88 kg with four suspension magnets, and experimental results have been derived to show superiority of the proposed design methods in terms of ability to deal with external disturbances. The concept of $\mathcal{H}_\infty$ control has been extended to the nonlinear setting using the concepts of energy and dissipativity, and nonlinear state-feedback and output-feedback controllers for Maglev have been developed and reported. Simulation and experimental results have been presented to show the improved performance of these controllers to attenuate guideway-induced disturbances while maintaining acceptable suspension qualities and larger operational bandwidth.

Contents

Chapter 1

Introduction

1.1 Background

Defying gravity by suspending a body freely in space and controlling it in all six degrees of freedom to perform some useful functions has been a focus of attention and research for many years [1, 2]. Without a doubt, this technology has a considerable industrial potential since it offers absence of friction, wear and other dynamic effects in moving bodies. The two most advanced applications of contactless magnetic levitation are high-speed magnetic bearings and magnetically levitated vehicles (Maglev) for ground transportation using superconducting magnets and controlled d.c. electromagnets [1, 2, 3]. The repulsion force from superconducting magnets provide stable levitation with low damping, while the suspension force generated by electromagnets is inherently unstable. This instability, due to the inverse force-distance relationship, requires the addition of feedback control systems to sustain stable suspension.

Suspension based on electromagnetic methods for passenger carrying vehicles has been known and researched since the early 1900. These technologies, known as magnetically levitated vehicles or *Maglev*, are proposed as an alternative to air, automotive and rail transportation. Various experimental and research work has been done, with main participants Germany, Japan and UK [1, 2, 3, 4, 5, 6]. High-speed Maglev systems have been design and tested with speeds of up to 581 km/h (Yamanashi Prefecture, Japan, 2004), which is almost twice the maximum speed of commercial rails currently in operation [5, 7]. The first commercial transportation system based on magnetic suspension was implemented for the Birmingham International Airport and has operated with high reliability from 1985 to 1995 [6]. Test tracks with a total length of 100 miles are under active research in Germany and Japan. Recently China in collaboration with Germany has built the first high-speed commercial Maglev system to connect Shanghai with Pudong In-

ternational Airport [8, 9, 4, 10, 7] and to reach operational speeds beyond 450 km/h. This high-speed link, now in full operation, has shown that Maglev can be a practical transportation system which can be superior to the commercial transportation systems in terms of operational cost and reliability, safety, aesthetics and environmental acceptability [11, 12].

1.2 Control work motivation

Earnshaw's theorem (1842) states that a pole placed in a static field of force does not have a position of stable equilibrium [2]. The repulsion forces between magnets of fixed strength are therefore unstable and impractical for suspending a body in space. This inevitably requires some form of an active control to manipulate one or both fields of force to achieve a stable suspension.

A full review on the known principles of electromagnetic methods for supporting masses known at present time can be found in [1, 2]. Current research on advanced ground transportation is mostly based on the following two forms: (1) electrodynamic (superconducting) repulsion systems and (2) electromagnetic suspension systems with controlled DC electromagnets. Each has proved to have potential for industrial applications [4, 5, 10, 7].

Electrodynamic suspension uses superconductors to produce magnets with very high flux densities. Motion between such magnets and conducing sheets produces repulsive forces leading to suspension effects. This method is inherently stable above some critical speed ($\approx$80 km/h) and thus does not require active control systems for levitation and guidance. The first full-scale system with superconducting magnets was built in Japan to support work for applications for ground transportation. Test vehicles based on superconducting magnets are under constant research and development with test lines near Tokyo [5]. The first commercial Maglev link in Japan is planned to connect Osaka and Tokyo and to reduce the 500 km route to a one-hour-journey (currently the Shinkansen train takes 2h and 30 minutes).

Suspension with controlled DC electromagnets is by far the most advanced in terms of research and development for alternative ground transportation and contactless magnetic bearings [1, 2, 13, 4, 3]. The advantage of this principle, in contrast to electrodynamic suspension, is its ability to provide suspension at zero-speed. The system, however, is inherently unstable and requires a feedback control system to manipulate the forces of attraction and hence the suspension airgap (gap between the magnet and the track, typically less than 10 millimetres). The nonlinear nature of the dynamics due to the square rela-

tionship between the excitation current and the magnetic force, the open-loop instability and the necessary operational bandwidths, require a considerable analytical effort in the derivation of the control algorithms and the design of the digital hardware and supporting circuits. A quick glance of the control problem is given below.

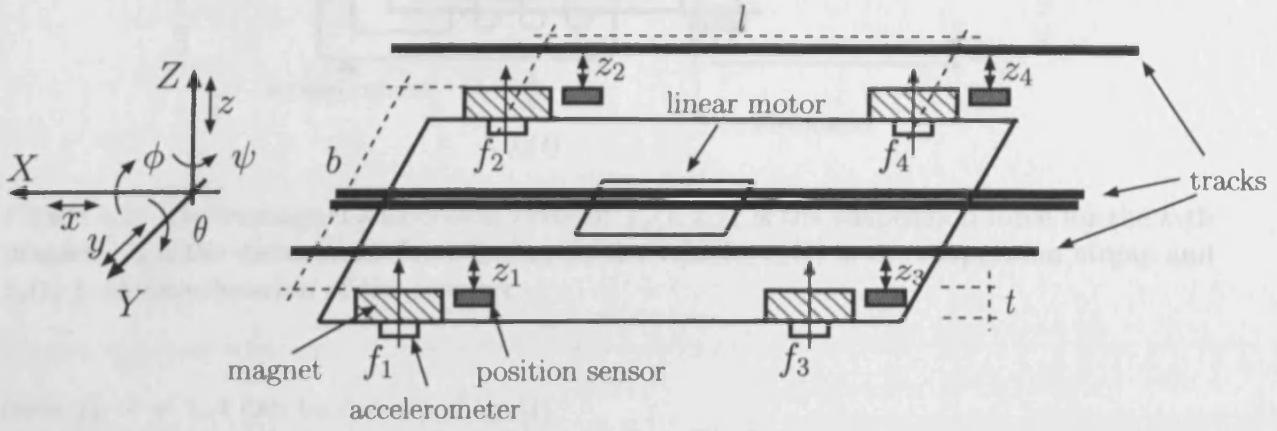

Figure 1.1: Block diagram of a magnetically levitated vehicle (suspension only). Four magnets, one in each corner, provide four suspension forces f_1 to f_4, which give three degree in freedom in the chassis: pitch θ, roll ϕ and heave z. A linear motor provides the fourth degree of freedom, propulsion along x.

A typical Maglev suspension vehicle system is assumed to behave as a rigid body in free space, Fig. 1.1, which is capable of linear and rotational motions along three orthogonal axes: (X, Y, Z). The main requirement from the suspension control system is to decouple the body from the guideway by suspending it freely in space and following the track-profile. Additionally, external disturbance forces, track and load irregularities have to be accommodated. To achieve this, the suspension forces have to be actively controlled. The linear motion along the X axis is typically controlled by the propulsion system and therefore five modes are controlled by the vehicle's control system. Although the minimal requirements to control these five modes require five independent magnets, for practical reasons four electromagnets are used to provide suspension forces along Z and rotational modes along X, Y, while other four electromagnets (not shown in the figure) provide guidance support.

Taking only one corner, a simplified schematically representation of each magnet is given in Fig. 1.2. Excitation current $i_k(t)$ flowing through the magnet's winding produces magnetic flux and thus electromagnetic suspension force $f_k(i, z, t)$ which suspends the the magnet and the body toward the guideway. Under certain assumptions, the suspension

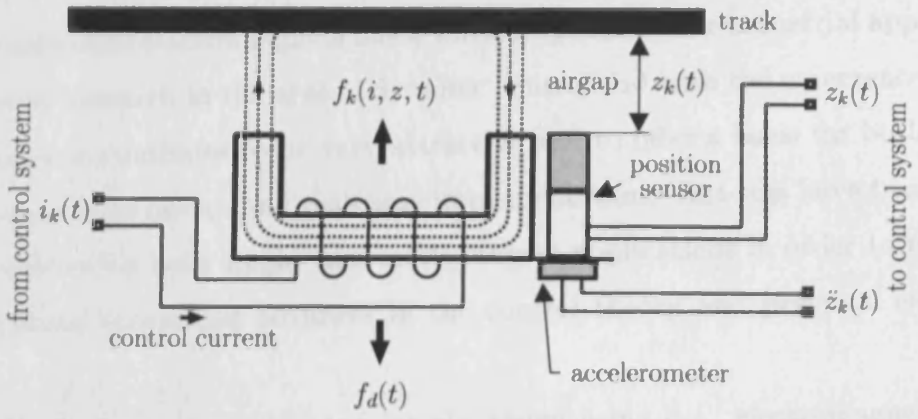

Figure 1.2: Electromagnet suspension system: $f_k(i,z,t)$ is the suspension force for the k-th magnet, f_d is the disturbance force acting on the vehicle, $z_k(t)$ is the suspension airgap and $\ddot{z}_k(t)$ is the acceleration of the magnet.

force f_k, $k = 1..4$ can be described by [1]

$$f_k(i,z,t) = \frac{B_k^2(t)A}{\mu_0} = \frac{\mu_0 N^2 A}{4}\left[\frac{i_k(t)}{z_k(t)}\right]^2 \qquad k = 1..n$$

where $B_k(t)$ is the magnetic flux density in the airgap, A is the magnetic pole-face area, μ_0 is the vacuum permeability, N is the number of coil turns, and $z_k(t)$ is the k-th airgap length. By controlling the excitation current, a balance can be reached where the suspension force will be equal to the gravitational and disturbance forces $f_d(t)$ and then the body will be suspended in air in equilibrium. The suspension force, however, is proportional to the square of the the control current and inversely proportional to the square of the airgap and thus the system is highly nonlinear. In addition, the multi-magnet configuration and the cross-coupling effects in the rigid body (Maglev vehicle in Fig. 1.1) would require a special control design to account for the multivariable nature of the system and to reduce undesirable dynamic effects from disturbances in the suspended rigid body.

1.3 Control work background

The first registered attempt to control DC-electromagnets dates back in the early 1900's, when Graeminger patented a feedback system for stable suspension [1]. The first known prototype, which was able to levitate a mass of 156 kg at 15 mm airgap, was demonstrated in the late 1930s. With advances in solid-state devices in the mid-1960s and the use of the linear motors, actively developed and promoted by Professor Eric Laithwaite, the potential of magnetic suspension for transportation became a reality. In the past few decades, a considerable research effort has been undertaken worldwide to prove that magnetic levita-

tion based on controlled electromagnets has a valuable potential for industrial applications. With the constant research in the area of dynamic control and with the emergence of faster processors, this area continues to be very attractive and to offer a basis for both applications of control-systems design and real-time implementation. Test-rigs have been built in different universities for both single- and multi-magnet applications in order to reduce the time delay between theoretical advances in the control theory and practical engineering applications.

Some of the earlier work on Maglev vehicle design using d.c. electromagnets was pioneered in the UK by the University of Sussex and several important results had been reported [14, 13, 15, 16]. A 1-ton research vehicle was built to study the dynamics of coupled magnets and control of the multivariable system [15]. A detailed analysis of the analytical and engineering aspects of of the design of controllers for multi-magnet vehicle suspension systems has been presented in [1, 13]. It has been established that the due to the multiple-degree of freedom in the vehicle, interaction of the various control loops through the dynamics of the vehicle is an important factor in the formulation of the overall control strategies [13]. Two fundamental control designs were developed: (a) integrated control which uses coordinate transformations and independent controllers for the heave, pitch and roll components and (b) local control that stabilises each magnet independently. Results showed that integrated control poses less overshoot in the response and faster transient responses. The analysis of the ride and track-clearance characteristics of an electromagnetic suspension system travelling along a guideway with random roughness has been analysed in [1, 16] to show that low-speed magnetically suspended vehicles (70 km/h) can travel without the aid of a secondary suspension. The track roughness and disturbances, however, have a considerable influence on the ride and stability characteristics of attraction-type of suspension systems due to the track-clearance requirements. Special attention has to be thus paid on the control-design aspects to attenuate these undesired effects on the suspended body.

The problem of designing magnetic suspension systems for higher speeds (500 km/h) and the modelling of their dynamics is discussed in [17]. Together with external disturbances such as wind force and track tolerances, early work at MBB paid some attention to uncertainties in the model (referred as system disturbances) such as instrumentation errors, accelerometer biases and gap and current measurements errors. An estimator for the track-disturbance is included in the control system design but the uncertainties in the

model are not accounted for. The Linear Optimal Control synthesis technique has been used to design a multivariable compensator for the vehicle. Some preliminary results from digital implementation of the controllers have been presented. This work was extended in [18] and a new model using finite-element methods has been designed to account for elasticity in the chassis, which is difficult to deal with using rigid-body modelling techniques. These results showed that several resonance frequencies are presented due to the elasticity in the body. The controllers have observer-based structures and use inputs from either current and position or acceleration and position to generate a feedback. It has been noted that the observers are, however, sensitive to uncertainty in the model and thus a careful account for the selection of their parameters has to be taken to avoid instability in the system. An important conclusion has been drawn that eddy current losses are produced due to the high velocity in the vehicle and this degrades the performance [1]. The digital control work in [18] has been carried out on a Honeywell digital computer with a maximum control-sampling frequency of 100Hz. The sampling frequency has been increased to 18 KHz in [19] to implement a digital state-feedback control system for a single-magnet electromagnetic suspension system. Comparison is made with an analogue controller to show the benefits from a flexibility and quality prospective to emulate the real-time performance of the classical op-amp based controller. Digital controllers provide a basis for implementing different controllers in software without a hardware rework.

A one-dimensional Maglev model which considers only the heave response has been presented in [20]. A secondary suspension is included and modelled as a spring-damper system. A set of inequalities are solved to get a compensator with two inputs (position and acceleration) and one output (control voltage) to maintain the position error, the acceleration and the drive output within pre-defined limits. Simulation results are presented to show airgap response due to guideway irregularities.

A small test vehicle (88 kg) running along a 5 m track using a linear motor was designed in [21]. The vehicle chassis is equipped with four magnets for suspension, while the guidance is provided from the inherent lateral stiffness. Transputer-based hardware was designed with appropriate inputs for magnet transducers. Four switched-mode current controllers were implemented to drive the magnets providing up-to 10 A of current. Each magnet was equipped with a position and an acceleration sensors. Using this configuration, a new force control configuration was proposed and designed in [21] which employed a detailed electromagnetic model to provide a linear force actuation. In [21] the control strategy was

firstly implemented on a single-magnet test-rig and then grouped to three independent controllers for the three modes (heave, pitch and roll) to control the suspension forces of the vehicle. The linear force actuation of this method is considered as an advantage, but low accuracy in the air-gap measurement at small airgaps was observed [21]. The control work was implemented in the digital domain using the on-board floating-point transputers and sampling frequencies of 500Hz. The mechanical chassis, sensors and power amplifiers from [21] are used in this thesis.

$\mu-$Synthesis of a single-magnet electromagnetic suspension system has been reported in [22]. A *pool* of uncertainty where the system is assumed to reside has been modelled by a complex uncertainty model. The controller synthesised using a mechanism which iterates between $\mathcal{H}_\infty$ design and μ-synthesis (DK-iteration) provides robust stability and performance for the selected range of model perturbations. This work has been extended in [23] by adding robust analysis in terms of linearision errors, parametric uncertainties and neglected dynamics. A mixed sensitivity problem is solved combining real and complex uncertainties. The system performance is analysed using experimental results from a single-magnet system and step responses in the force disturbance.

A frequency-shaping linear quadratic (LQ) controller for a single-magnet suspension system has been reported in [24]. Stochastic and deterministic disturbance inputs are targeted with the aim of frequency-domain weightings used in the performance criterion integral for the LQ optimisation. Results from a single-magnet suspension system are presented to show that the frequency-shaping LQ method is better than the classical LQ method for deterministic inputs. The design constraints are chosen to accommodate good ride qualities by limiting acceleration and position variation levels.

Linearising control for a single-magnet electromagnetic suspension system using observer-based structure was reported in [25]. Using a suitable coordinate transformation, the non-linear dynamics is linearised to get a system with three state variables: position, velocity and acceleration. Two weakly coupled Riccati equations are solved to derive the feed-back and the observation gains. The stability is analysed using Lyapunov techniques. The simulation results presented in [25] show that the linearising controller has a superior performance in terms of coping with parameter variations compared to the linear observer-based controller. Similar work on the design of a nonlinear feedback linearising controller for a single-magnet suspension system is presented in [26]. Experimental results are presented from a test rig to show that the proposed nonlinear controller is robust against perturba-

tion in the suspended mass and external force disturbance compared to the classical linear state-feedback controller. The control work in [26] was implemented on a TMS320C31 DSP with 3 kHz sampling rate. Feedback signals are the magnet's current, the position and the acceleration levels. Experimental results from a single-magnet system using a linearising controller are also reported in [27]. Special attention is given to the fact that although excellent results are obtained from the design process, a very accurate model is required to implement the coordinate transformation and hence the controller. Robust properties in the design of linearising nonlinear controllers for a single-magnet system was also presented in [28]. Parametric uncertainties are incorporated into the design to guarantee robustness. Experimental results are included to show that the nonlinear robust controller manages to track better large variations in the desired airgap compared to a nominal linear controller. This work has been extended in [29] by adding adaptive features to the linearising controller to cope with parametric uncertainty in the design. A single-magnet system is used for the experimental analysis.

An $\mathcal{H}_\infty$ loop-shaping design for a single magnet system with a secondary suspension is presented in [30]. A mixed sensitivity problem is solved numerically using an *evolutionary* algorithm. Simulation responses were presented to show the air-gap response and the acceleration levels for a chosen reference input. A detailed account was given of the numerical solution and a comparison is made with other genetic algorithms. The advantage in the developed approach was considered to be the ability to use a mixture of discrete and continuous parameters in the problem formulation. The design of an $\mathcal{H}_\infty$ controller for a magnetically suspended vehicle with four magnets is also reported in [31]. The authors had chosen to neglect the cross-coupling in the rigid body and to design four $\mathcal{H}_\infty$ compensators stabilising each corner independently. Experimental results from a 100kg vehicle were included to show that the $\mathcal{H}_\infty$ controllers give better dynamic responses to disturbances applied to one of the corners of the vehicle. Simulation results from a switched-mode $\mathcal{H}_\infty$ controller-design with gain scheduling is presented in [32]. A single-magnet system is considered where the authors assume a scenario with a very large variation in the operating airgap. To cope with this, a gain-scheduling mechanism was used in combination with an $\mathcal{H}_\infty$ design. Two compensators are alternated with a threshold monitor point on the operating airgap. The simulation results were compared with the linearising controller developed in [26] to show that the gain-scheduling controller achieved better tracking performance in the presence of parameter perturbation.

Sine recently more exotic applications of magnetic levitation have been reported such as the Magnetic Launch Assist, which is a magnetically levitated vehicle with propulsion to provide an initial velocity by using electrical power from ground source for launching space shuttles into space [33, 34]. Maglev is proposed as a suitable concept in reducing costs for future space explorations [33].

1.4 Scope of this thesis

Although several results for the control of single-magnet suspension systems have been reported, little account has been given to the development of a detailed design framework for the control of Maglev vehicles since the results presented in [17, 18, 15, 1, 21]. In this respect, the research work presented in this thesis has aimed to reduce the gap between recent advances in control theory and their engineering applications to Maglev. The problem of controlling magnetically levitated systems using DC electromagnets under different operating conditions has been studied with a design process primarily driven by experimental results. In previous research work, independent suspension controllers for each mode of the vehicle (heave, pitch and roll) have been designed using force control algorithms employing a detailed model of the electromagnet in conjunction with current and airgap feedbacks [21]. It was noted in [21] that the quality of the proposed control strategy depends on the accuracy of the model and the airgap measurements at small air-gaps. The research work undertaken in this thesis has aimed to continue the developments in [21] by employing optimal control theory to the design of Maglev controllers. New tools for the vehicle control have been developed to provide a basis for deriving feedback compensators by minimising cost functions using optimisation. With this approach, single- and multi-magnet control problems have been treated using the same framework. The design process has aimed to provide convenient tools for assessing the robustness of the closed-loop system in terms of sustaining stability and performance in the presence of uncertainty in the suspension model. The research work has been primarily driven from experimental results from a single magnet test rig and a small multi-magnet vehicle (88 kg) equipped with position and acceleration sensors and power amplifiers [21]. The controller-design stages are presented in detail and close relationships have been constructed between selection of performance criteria for the derivation process and desired suspension characteristics. Both linear and nonlinear compensators have been developed. Simulation and experimental results have been studied in parallel to assess operational stability and the main emphasis

has been given to assessing performance under different operational conditions. To support the experimental work, a new digital signal processor-based hardware platform has been developed to meet constraints from the computational and operational bandwidths. Some of the main areas of work undertaken during this research project are listed below.

- Adaptive algorithms based on model reference control have been developed to improve the performance of the suspension system in the presence of considerable variations in external payload and force disturbances [35].

- Design of custom-built DSP hardware and corresponding software libraries have been developed to control a three-degrees-of-freedom Maglev vehicle (88 kg with four magnets) and logging in real-time and delivering experimental data to a host computer for analysis (Matlab/Simulink). A software control framework for DSP has been developed which is fully customisable to provide the supporting experimental results presented in this thesis.

- Recent advances in robust control theory ($\mathcal{H}_\infty$ and $\mu-$synthesis) have been applied to both single- and multi-magnet suspension systems. An alternative solution to the $\mathcal{H}_\infty$ controller-optimisation problem has been derived and applied to Maglev control. Sensitivity to robustness has been discussed. Multivariable controllers based on $\mathcal{H}_\infty$ and $\mu-$synthesis have been developed for an 88 kg vehicle and experimental results are derived to show superiority in terms of ride qualities, acceleration levels and ability to deal with guidance- and track-induced disturbances.

- The concept of $\mathcal{H}_\infty$ has been extended to the nonlinear setting using the concepts of energy and dissipativity and nonlinear state-feedback and output-feedback controllers for Maglev have been developed for a first time [36]. Simulation and experimental results have been presented to show the superior performance of these controllers to attenuate guideway-induced disturbances while maintaining acceptable ride qualities and larger operational bandwidth.

1.5 Overview of the thesis

This thesis contains ten chapters and is organised as follows.

Chapter 2: Electromagnetic Suspension System: modelling, simulation and transputer-based control system

In this chapter, the electromagnetic suspension dynamic model of a single-magnet system is developed. The nonlinear relationship between the force of attraction, the control current and the distance, is linearised around a nominal operating point to derive a state-space model of the suspension system. Its parameters are matched with those of a single-magnet experimental test-rig. To modify the force-current relationship, a state-feedback controller is derived. The suspension characteristics are analysed experimentally using a network of three transputers (two 32-bit floating point units and one 16-bit integer unit) which was previously built in [21]. Experimental results in changing the desired reference airgap are compared with simulation results. Some implementation issues of the real-time control implementation are discussed.

Chapter 3: Adaptive pole-placement and model reference control of Maglev systems

For Maglev systems which are under the influence of external force and mass disturbances, a methodology of checking the stability properties of the closed-loop Maglev system is developed using real-time identification based on recurrent least-squares algorithms. An identification loop running in parallel with the main suspension controller is developed to monitor the location of the closed-loop poles of the experimental system and hence the force-airgap relationship. Analysis has shown that external force and mass disturbances can be modelled as a variation in the dynamic characteristics of the suspension system. To provide a framework for coping with external disturbances and uncertainties, two adaptive algorithms for Maglev control are developed: (a) adaptive-pole placement control and (b) adaptive model reference control. The adaptive pole-placement controller is derived using a recurrent least-square error-minimisation algorithm. The *Diophantine equation*, which defines an error measure between the desired and current location of the closed-loop poles, is minimised to adapt in real-time the gains of the state-feedback controller. The adaptive model-reference controller is derived by minimising analytically a cost function constructed from the error between the theoretically derived (using the model from Chapter 2) and the experimentally obtained state-variables (position, velocity and acceleration) and their error rate. The result is a mechanism for modifying the controller's gains in real-time to maintain the cost-function defined above minimal. Experimental responses in coping with external mass and force disturbances are presented to show the benefits of this controller compared

to the ordinary state-feedback. Some constraints from the real-time implementation of the adaptive pole-placement controller on the transputer hardware are discussed.

Chapter 4: DSP environment for Maglev control

The event-driven nature of the transputer architecture does not allow running real-time applications with a fixed sampling time and some jitter in the clock was observed during the controller implementation. Additionally, advanced control algorithms for Maglev put additional constraint on the signal-processing bandwidth. Because in the middle 1995's transputers were discontinued from manufacture, a new processor for the control work was needed. A suitable choice for real-time Maglev control was found to be the Analog Devices SHARC family of DSPs offering 40 MIPS and 80 MFLOPS sustained processing power and an interrupt driven architecture capable of delivering fixed sampling time. To explore compatibility of these DSPs for real-time Maglev control, this chapter develops a single-magnet DSP control hardware using a commercial EZ-KIT Light DSP hardware and a custom-build ADC/DAC interface for magnets. The state-feedback controller developed in Chapter 2 was firstly ported to the new hardware, followed by the adaptive pole-placement controller and the adaptive model-reference controller from Chapter 3. The sampling of the computationally intensive adaptive pole-placement controller was considerably reduced from 950 μs on the transputers to 200 μs on the DSP hardware and successful experimental results are obtained in attenuating 120N force disturbance. The adaptive model-reference controller was also ported to the DSP hardware and new experimental responses with 200 μs sampling time were analysed in attenuating external force and mass disturbances. An account is also given of selecting tuning parameters for the adaptation rate versus transient response in the disturbance attenuation. Applications of Fuzzy-Logic control for electromagnetic suspension systems are also discussed and three different Fuzzy controllers are derived using position, acceleration and velocity feedback from the suspended magnet. Experimental results in dealing with reference demand change are analysed and some of the key aspects of implementing Fuzzy-Logic controllers using DSP are discussed.

Chapter 5: Design of DSP hardware for Maglev control

The preliminary control work carried out in Chapter 4 using the SHARC family of DSPs has shown that this processor provides enough processing bandwidth to implement computationally intensive control tasks. The multiprocessing capabilities, Super Harvard Architecture with embedded program and data memory on-the-chip and 80 MFLOPS sustained

processing bandwidth made the SHARC DSP a suitable candidate for the multi-magnet control work. Also (mid 1999) no commercial hardware was capable of fulfilling the requirements for the multi-magnet control work. A new DSP board hence was built to offer: a direct interface to four magnets (inputs from eight transducer and four outputs to current controllers), a fast and reliable Ethernet interface, a customisable digital interface, up-to 32 Mbit SRAM memory on-board and facilities for multiprocessing. Hardware design aspects and design of software libraries, such as kernel, TCP/IP interface, interfaces to Matlab and Simulink, are addressed in this chapter. This hardware is used for all experimental work described in the remaining chapters of this thesis.

Chapter 6: $\mathcal{H}_\infty$ controllers for Maglev systems

In this chapter a detailed account of the derivation and implementation of $\mathcal{H}_\infty$ state-feedback and output-feedback controllers for Maglev systems is given. The mixed-sensitivity optimisation setting is introduced and details of the selection of performance weights for single-magnet electromagnetic suspension systems to satisfy pre-defined ride and performance qualities are given. Although algorithms for deriving $\mathcal{H}_\infty$ controllers are readily available, in this chapter an alternative analytical solution is developed using Lagrange multiplier methods and differential game theories. The motivation for this work is based on its analogy with the classical LQG solution which is well understood. Despite the fundamental difference in the derivation steps, the analytical solution for the $\mathcal{H}_\infty$ control problem produces identical results as reported in [37]. A full account of the derivation of $\mathcal{H}_\infty$ controllers for Maglev is given and the correspondence between performance weights and desired suspension characteristics. Simulation and experimental results are presented to highlight the fact that the suspension stiffness and the damping are well controlled with the new $\mathcal{H}_\infty$ controllers.

Chapter 7: Robust analysis and control for Maglev systems

Uncertainties in the linearised Maglev model used for the controller design arise from changes in operating conditions due to the nonlinear force-current relationship and external force and payload disturbances. Up to some degree, the electrical parameters of the magnet are also considered as uncertain. For a given bounded variation in the Maglev's parameters, it has been established that the $\mathcal{H}_\infty$ controller developed in Chapter 6 for the nominal model fails to provide robust stability and performance for variations in the parameters above 10% from the nominal values. A measure based on singular values has been derived

to test Maglev controllers against uncertainty in the model. The test for robustness has been extended by employing the definition of the structured singular value μ. It has been established analytically that the robustness (both stability and performance) is more sensitive to variations in the operation condition and external payload and less sensitive to variations in the electrical parameters. To provide a framework for robust Maglev design, the concepts of $\mu-$synthesis based on DK-iteration are used to derive robust controllers using the performance requirements derived in Chapter 6. A selection of simulation and experimental results are presented to show the robust properties of the new controller in terms of sustaining performance in the presence of large variations in the model.

Chapter 8: Multivariable Maglev control

This chapter develops a design framework for the multi-magnet vehicle controller using the developments of $\mathcal{H}_\infty$ and $\mu-$synthesis from Chapters 6 and 7. A three degree of freedom (3-DOF) state-space model of a representative suspension vehicle (four magnets) is developed, which is compatible for $\mathcal{H}_\infty$ design. Experimental results from a 88 kg test rig are used to validate the model. A robust multivariable controller with seven inputs (four airgap measurements from each magnet and reference pitch, roll and heave) and four outputs (control signals to magnet amplifiers) is derived using the $\mu-$synthesis algorithms from Chapter 7. An account of the selection of performance weights for achieving predefined ride qualities is given and a large selection of simulation and experimental results are given. These results show that the new multivariable controller is capable of sustaining good suspension qualities and, contrary to ordinary state-feedback controllers stabilising each corner independently, is also capable of maintaining robust stability in attenuating guidance induced disturbances. The design framework is extended to a 6-DOF model of a vehicle with facilities for active guidance control. Simulation results are used in the 6-DOF analysis of the suspension and guidance qualities.

Chapter 9: Nonlinear $\mathcal{H}_\infty$ control for Maglev

The concept of local dissipativity and supply power are used in this chapter to develop a design framework for the derivation of nonlinear $\mathcal{H}_\infty$ controllers. Using the values supplied and stored energy as criteria, the controller is designed to keep the energy of a penalty vector bounded and smaller than the energy of the disturbance input. The controller derivation requires finding a solution to Hamiltonian-Jacobi-Isaacs inequalities. While the analytical solution to these inequalities is not readily available, an approximate solution is

found by deriving sequential terms in its Taylor series expansion. Thus instead of deriving one single nonlinear controller, the algorithm developed in this chapter derives a whole class of Maglev controllers by collecting the appropriate terms in the series expansion. This methodology is used in both the derivation of a nonlinear state-feedback controller and a nonlinear estimator in conjunction with the nonlinear state-feedback controller. The derivations of the controller are performed analytically. The performance of the suspension system with the nonlinear $\mathcal{H}_\infty$ controller is analysed by studying the attenuation properties of the closed-loop system in attenuating track disturbances. The nonlinear output-feedback controller has been observed to provide a significant improvement in terms of dealing with track irregularities over the linear state-feedback controller.

Chapter 10: Concluding comments

Concluding comments with future research recommendations are included in this chapter.

Chapter 2

Electromagnetic Suspension System: modelling, simulation and transputer-based control

2.1 Electromagnetic suspension model

Electromagnets with d.c excitation have the ability to attract ferromagnetic materials with the force of attraction being controllable. As a device, an electromagnet consists of two poles and a magnetisation winding. Excitation current $i(t)$ flowing through the magnet's winding produces magnetic flux ($\phi_m(t)$) and thus electromagnetic suspension force $F(t)$ which suspends the the magnet and the body toward the guideway as shown in Fig. 2.1. There also a leakage flux $\phi_l, (t)$ which flows from one magnet pole to other and entirely depends on the magnet's shape, material and design. Usually it is desirable to minimise this by suitable magnet design [1].

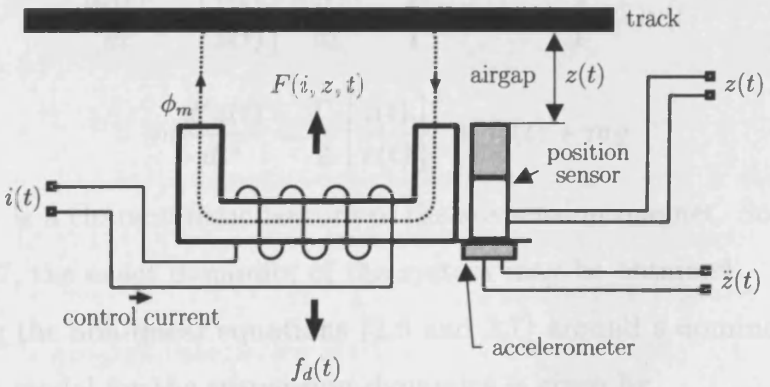

Figure 2.1: Electromagnet configuration [1]

With the assumption that for the iron track $\mu_r = \infty$, then the following equation

describes the force of attraction [1]

$$F(i,z,t) = \frac{B^2 A}{\mu_0} = \frac{\mu_0 N^2 A}{4}\left[\frac{i(t)}{z(t)}\right]^2 \tag{2.1}$$

where: B is the airgap flux density, A is the pole face area, μ_0 is the permeability of free space ($4e10^{-7}$ h/m), N is the number of the coil turns, $i(t)$ is the coil current, and $z(t)$ is the airgap. This force of attraction is a non-linear function of the current $i(t)$ and the airgap $z(t)$. If R is the total resistance of the circuit, for an instantaneous voltage $v(t)$ across the magnet winding

$$v(t) = Ri(t) + \frac{d}{dt}[L(i,z)] \tag{2.2}$$

where $L(i,z)$ is the inductance of the magnet winding, given by [1]

$$L(i,z) = \frac{\mu_0 N^2 A}{2}\left[\frac{i(t)}{z(t)}\right] \tag{2.3}$$

For vertical force balance of the system in Fig. 2.1

$$m\frac{d^2 z(t)}{dt^2} = -F(i,z) + f_d(t) + mg \tag{2.4}$$

where f_d is a disturbance force input. For the equilibrium point (i_0, z_0)

$$mg = F_0(i_0, z_0) = -\frac{\mu_0 N^2 A}{4}\left[\frac{i_0}{z_0}\right]^2 \tag{2.5}$$

Substituting Eqn.2.3 into 2.2 gives the following equations for the electrical and mechanical characteristics for suspension dynamics

$$\frac{di(t)}{dt} = \left[\frac{i(t)}{z(t)}\right]\frac{dz(t)}{dt} - \frac{R}{\Gamma}i(t)z(t) + \frac{1}{\Gamma}z(t)v(t) \tag{2.6}$$

$$m\frac{d^2 z(t)}{dt^2} = \frac{\Gamma}{2}\left[\frac{i(t)}{z(t)}\right]^2 + f_d(t) + mg \tag{2.7}$$

where $\Gamma = \frac{\mu_0 N^2 A}{2}$ is a characteristic feature of the suspension magnet. Solving numerically Eqns. 2.6 and 2.7, the exact dynamics of the system may be obtained.

By linearising the non-linear equations (2.6 and 2.7) around a nominal operating point (i_0, z_0) the linear model for the suspension dynamics is given by

$$\frac{d\Delta i(t)}{dt} = \left[\frac{i_0}{z_0}\right]\frac{d\Delta z(t)}{dt} - \left[\frac{R}{L_0}\right]\Delta i(t) + \left[\frac{1}{L_0}\right]\Delta v(t) \tag{2.8}$$

$$m\frac{d^2\Delta z(t)}{dt} = \frac{\partial F(i,z)}{\partial z}\Big|_{(i_0,z_0)}\Delta z(t) - \frac{\partial F(i,z)}{\partial i}\Big|_{(i_0,z_0)}\Delta i(t) + \Delta f_d(t) \tag{2.9}$$

$$m\frac{d^2\Delta z(t)}{dt} = k_z\Delta z(t) - k_i\Delta i(t) + \Delta f_d(t) \tag{2.10}$$

where

$$k_z = \Gamma\frac{i_0^2}{z_0^3}; k_i = \Gamma\frac{i_0}{z_0^2}; L_0 = \frac{\Gamma}{z_0}; k_i^2 = k_z L_0 \text{ and } mg = -\frac{\Gamma}{2}\left[\frac{i_0}{z_0}\right]^2 \text{ at } (i_0, z_0)$$

By constructing a vector using $\Delta z(t)$, $\Delta \dot{z}(t)$, and $\Delta i(t)$ and using Eqns. 2.9 and 2.10, the state-space model of the suspension system can be derived

$$\begin{bmatrix} \Delta\dot{z}(t) \\ \Delta\ddot{z}(t) \\ \Delta\dot{i}(t) \end{bmatrix} = \begin{bmatrix} 0 & 1 & 0 \\ \frac{k_z}{m} & 0 & -\frac{k_i}{m} \\ 0 & \frac{k_z}{k_i} & -\frac{R}{L_O} \end{bmatrix} \begin{bmatrix} \Delta z(t) \\ \Delta\dot{z}(t) \\ \Delta i(t) \end{bmatrix} + \begin{bmatrix} 0 & 0 \\ 0 & \frac{1}{m} \\ \frac{1}{L_O} & 0 \end{bmatrix} \begin{bmatrix} \Delta v(t) \\ f_d(t) \end{bmatrix} \tag{2.11}$$

Choosing the voltage signal $\Delta v(t)$ as the input and the air-gap between the magnet and the track $z(t)$ as the output, the block diagram of the system in time-domain is as shown in Fig. 2.2. The corresponding transfer function becomes

$$G(s) = \frac{\Delta z(s)}{\Delta v(t)} = \frac{-\frac{k_i}{mL_O}}{s^3 + \frac{R}{L_O}s^2 - \frac{k_z}{m}\frac{R}{L_O}} \tag{2.12}$$

Eqn. 2.12 is the linearised single-input-single-output model of the non-linear magnetic suspension system in Fig. 2.1. Since k_i and k_z depend on the linearisation of the system around the nominal operating point, the dynamics of the system are dependent on the choice of this point. If a considerable variation in the choice of (i_0, z_0) is expected, the controller has to compensate for this. This is analysed in subsequent chapters. Eqn. 2.12 is used for all designs in the following chapters. In Chapter 8, this model is extended to describe force and torque relationships in multi-magnet vehicles.

Due to the lack of damping in the mechanical dynamics (Eqn. 2.10), the closed-loop system has one positive pole and hence the system is inherently unstable in open loop. A feedback compensator is therefore required to stabilise the magnet underneath the track at a specified airgap. In this respect, the main emphasis in this thesis is the development of control algorithms for electromagnetic suspension systems working under different operating conditions. The experimental work is carried out on single magnet representative rig and a multi-magnet vehicle. The single-magnet rig is described in the following section. Details of the multi-magnet vehicle are given in In Chapter 8, page 165.

2.2 Experimental system

The experimental system consists of an electromagnet, an accelerometer, and an airgap sensor (Fig. 2.3). The cantilever magnet and the track are supported by a base. The mechanical components are designed to enable the magnet to move freely in the vertical

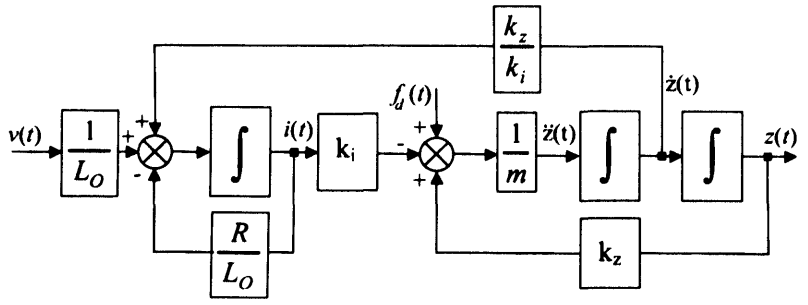

Figure 2.2: Block diagram based on the linearised state equations.

direction (closer to the track and away from the track). The mechanical dimensions have been worked out such that at the nominal operating point, the magnet is parallel to the track.

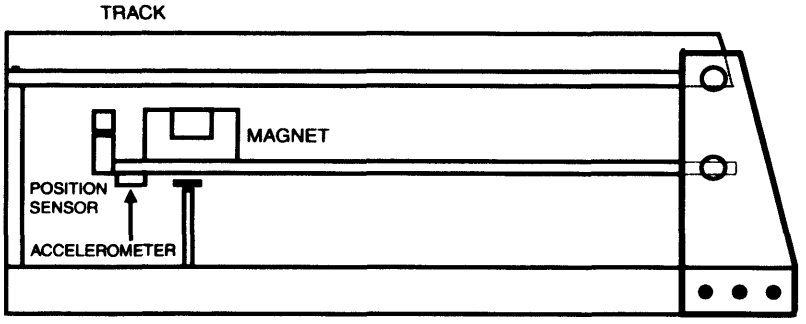

Figure 2.3: Experimental single-magnet system. Photographic image of the test rig is shown in Fig. 2.4.

The magnet used in this experimental system is an E-shaped magnet with laminated core with dimensions shown in Fig. 2.5 [1]. It is designed to work around the equilibrium point (i_0=2 A, z_0=2.5 mm), and can be used with current up to 10 Amps. The constants of the magnet at the nominal operating point are:

$R = 1.1\Omega$

$L_0 = 3.0$ mH

$k_i = 12.61$ N/A

$k_z = 6305.3$ N/m

$m = 1.8$ kg

The experimental system is designed to work with airgap distances between 0.5 and 9 mm. The transducer used to measure the airgap ($\Delta z(t)$) is an inductive non-contacting transducer manufactured by Pepperl & Fuchs model IA8-M1K-I3. The output is a current signal linearly proportional to the distance (0-20mA, 3% error). The measurement accuracy

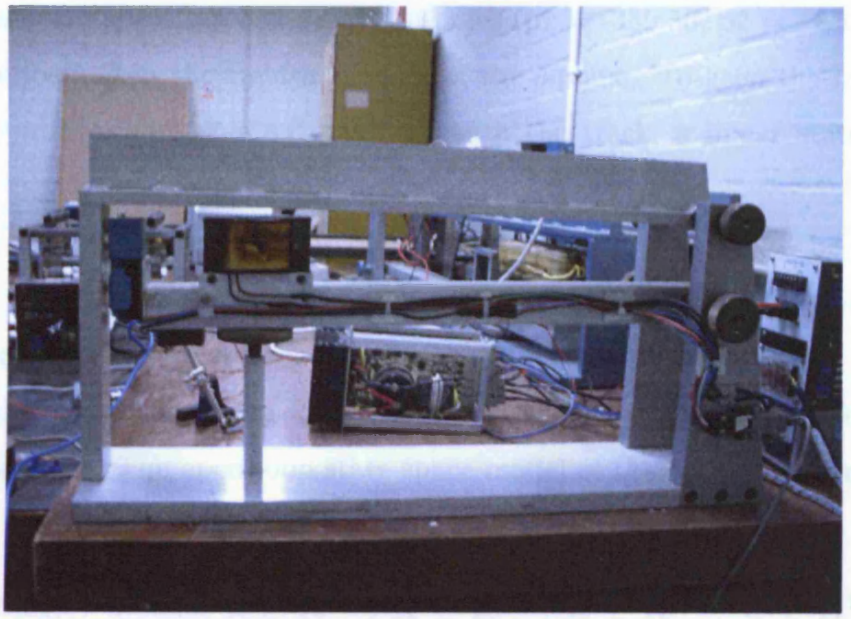

Figure 2.4: Photographic image of the magnet-track configuration.

of this sensor is given to be less than 30mm in the full $+10^0$ to $+40^0$ C temperature range.

To construct the full state-space model, the acceleration of the magnet is required. For this purpose an accelerometer is used with voltage output proportional to accelerations in the range of ± 5 g ($\pm 50 m/s^2$) (ICSensors, type 3110-005). The full-scale voltage output is ± 2 volts, with a 2.5 volt offset. The accelerometer generates internally a 2.5 volts reference for the conversion circuits. The accuracy is $\pm 1\%$ over the full -10^0 to $+40^0$ C temperature range.

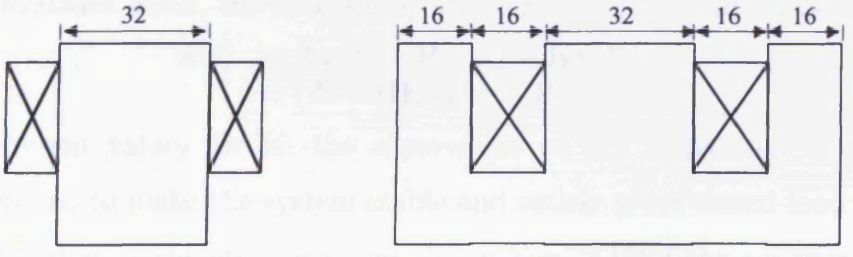

Figure 2.5: The E-core magnet dimensions [mm]. left: side view; right: front view [1]

2.3 State-feedback control for Maglev

Substituting the parameters for the experimental magnet shown in Fig. 2.3, the numerical form of Eqn. 2.12 becomes

$$G(s) = \frac{\Delta z(s)}{\Delta v(s)} = -\frac{2335.3}{s^3 + 366.67s^2 - 1.284 \times 10^6}$$

As discussed earlier, the system has three real poles (p1 = -356.56, p2 = - 65.28 and p3 = 55.17) with one located in the right-hand-side of the s-plane. To keep the magnet stable and close to a pre-specified nominal point beneath the track, a linear state-feedback is derived below.

To stabilise the Maglev system, all right-hand s-plane poles have to be relocated on the left-half of the s-plane, the precise locations being related to the given set of closed-loop requirements. The linear state feedback control law is aimed at deriving the feedback gains of the three state variables such that the closed-loop poles are moved to a set of pre-specified locations. The open-loop state-space model of the system is given by

$$\begin{aligned} \dot{\mathbf{x}}(t) &= \mathbf{A}\mathbf{x}(t) + \mathbf{B}\mathbf{u}(t) \\ y(t) &= \mathbf{C}\mathbf{x}(t) \end{aligned} \tag{2.13}$$

where for the Maglev system, $\mathbf{x} \in \mathbf{R^{3\times 1}}$, $\mathbf{A} \in \mathbf{R^{3\times 3}}$, $\mathbf{B} \in \mathbf{R^{3\times 1}}$, $\mathbf{C} \in \mathbf{R^{1\times 3}}$, u is the input to the system and y is the output . The state variable $\mathbf{x}$ here has three elements corresponding to the airgap, velocity and acceleration (current being related to force or acceleration). The dynamics of the system in state space form is fully determined by the eigenvalues of the matrix $\mathbf{A}$, or the roots of the characteristic equation [38]

$$\det(\mathrm{sI} - \mathrm{A}) = 0 \tag{2.14}$$

Introducing a control signal in the form:

$$\mathrm{u(t)} = \mathrm{v(t)} - \mathrm{Kx(t)} \tag{2.15}$$

where $v \equiv \Delta z_R(t)$ is the desired output (position) from the system, and $\mathbf{K}$ is a vector containing the feedback gains, the closed-loop state space representation becomes

$$\begin{aligned} \dot{\mathbf{x}}(t) &= \mathbf{A}\mathbf{x}(t) + \mathbf{B}(\mathbf{v}(t) - \mathbf{K}\mathbf{x}(t)) \\ &= (\mathbf{A} - \mathbf{B}\mathbf{K})\mathbf{x}(t) + \mathbf{B}\mathbf{v}(t) \end{aligned} \tag{2.16}$$

By choosing different values for $\mathbf{K}$, the eigenvalues of this closed-loop system may be explicitly determined to make the system stable and satisfy given closed-loop performance requirements. Combining the state-space model in Eqn. 2.12 of the experimental system with the state feedback controller (for the linear model in Fig. 2.2):

$$\begin{aligned} \Delta v(t) &= [k_P \; k_V \; k_A] \begin{bmatrix} \Delta z_R(t) - \Delta z(t) \\ \Delta \dot{z}(t) \\ \Delta i(t) \end{bmatrix} \\ &= k_P \Delta z_R(t) - k_P \Delta z(t) + k_V \Delta \dot{z}(t) + k_A \Delta i(t) \end{aligned} \tag{2.17}$$

the closed-loop suspension system is transformed to

$$\begin{bmatrix} \Delta \dot{z}(t) \\ \Delta \ddot{z}(t) \\ \Delta \dot{i}(t) \end{bmatrix} = \begin{bmatrix} 0 & 1 & 0 \\ \frac{k_z}{m} & 0 & -\frac{k_i}{m} \\ \left(\frac{k_P}{L_O} + \frac{k_A k_z}{m L_O}\right) & \left(\frac{k_V}{L_O} + \frac{k_z}{k_i}\right) & -\left(\frac{R}{L_O} + \frac{k_i k_A}{m L_O}\right) \end{bmatrix} \begin{bmatrix} \Delta z(t) \\ \Delta \dot{z}(t) \\ \Delta i(t) \end{bmatrix} + \begin{bmatrix} 0 \\ 0 \\ -\frac{k_P}{L_O} \end{bmatrix} \Delta z_R(t) \tag{2.18}$$

The input to the system is the desired position value (distance between the magnet and the track $v \equiv z_{ref} \equiv \Delta z_R(t)$) with the state variables being the position, the velocity and the acceleration signals. The block diagram of the closed-loop system (Eqn. 2.17 added to Fig. 2.2) is shown in Fig. 2.6. The characteristic polynomial of the closed-loop is [1]

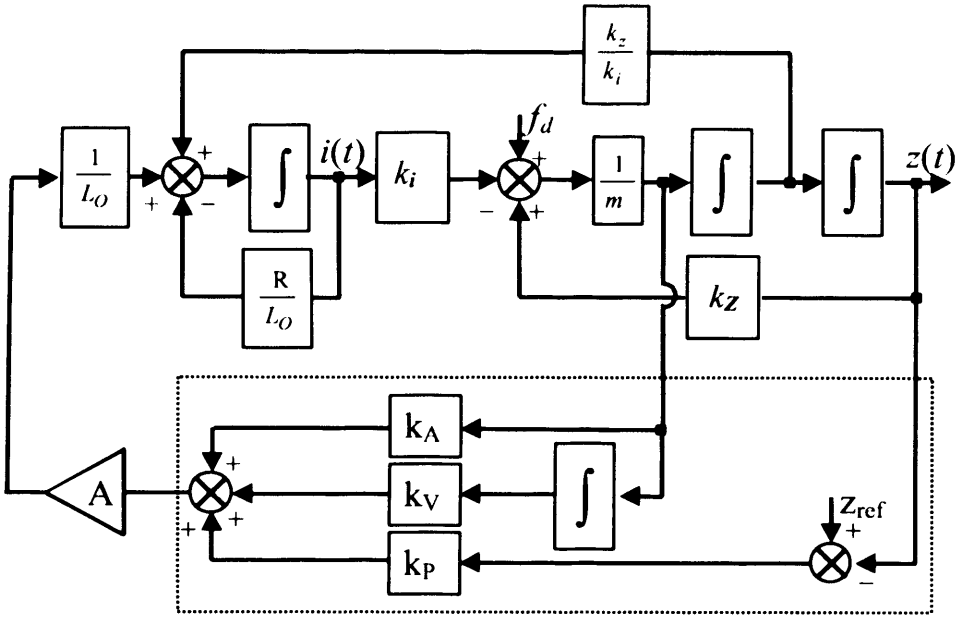

Figure 2.6: Linearised model with linear state feedback controller.

$$\det(s\mathbf{I} - (\mathbf{A} - \mathbf{BK})) = s^3 + \left(\frac{R}{L_O} + \frac{k_i k_A}{mL_O}\right) s^2 + \frac{k_i k_V}{mL_O} s + \frac{1}{mL_O}(k_i k_P - k_Z R) \qquad (2.19)$$

Using the magnet's parameters from Section 2.2, and feedback controller's gains specified by experimentally derived values: k_P=20833.0, k_V=250.0, and $k_A = 4.0$, the closed-loop system is successfully stabilised. A simulation of the magnet system with a state feedback controller was implemented in MATLAB. Two step inputs in changing the desired airgap $\Delta z_{ref}(t)$ were applied at times shown as arrows in Fig. 2.7. The responses of the simulated magnet indicate a rise time in the order of 40ms.

A key feature in the design is the choice of the nominal operating point such that the parameters (k_i, k_z and L_0) remain unchanged for the whole of the operating ranges for the current and the airgap. An analysis of robustness and the effects of variations in the operating conditions is analysed in Chapter 7. If $\left(\frac{R}{L_O} + \frac{k_i k_A}{mL_O}\right) >> 1$, the closed-loop system can be modelled as a second-order system with k_p controlling the steady-state error, the natural frequency and the stiffness (Fig. 2.6, page 22), k_v controlling the damping ration and k_a controlling the overall stability. Although the well established PID method is able to provide the basic suspension performance, acceleration-velocity feedback adds more

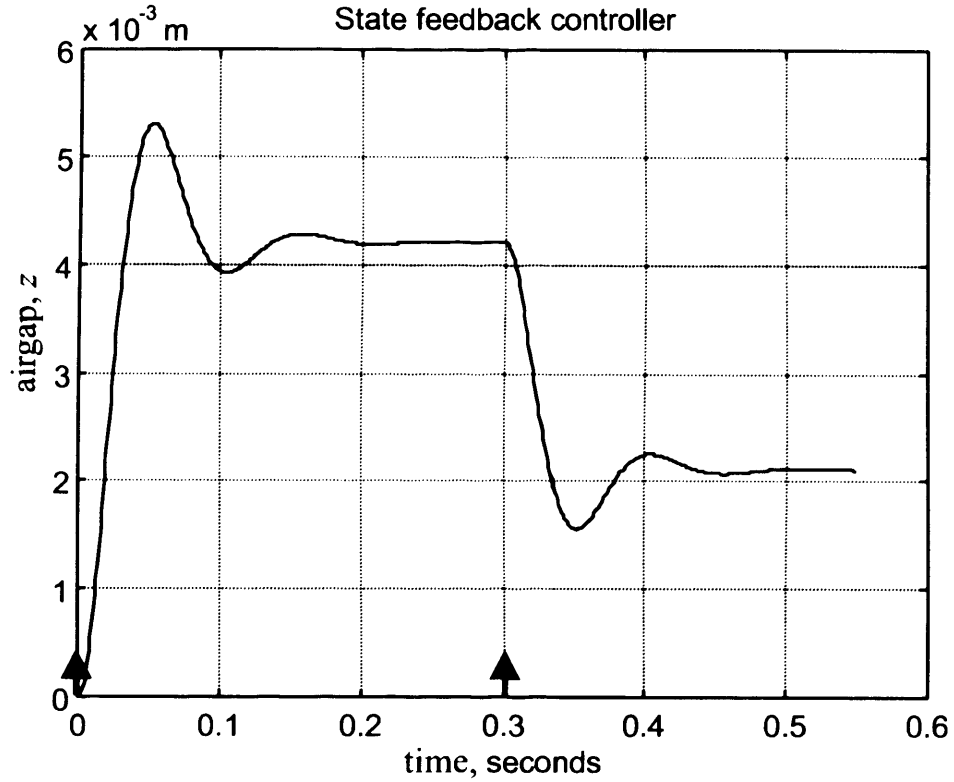

Figure 2.7: Closed-loop response with desired air-gap change.

flexibility in the choice of suspension damping. Use of state-feedback, however, requires additional transducer to measure the vertical acceleration. Although the cost of this is negligible compared to the overall cost of the vehicle/control system, additional algorithms are required for full-scale fault-tolerant applications. The lack of dc-integration in the loop frequency response leads to steady-state errors. These can be compensated with pre-filter on the reference input or adaptive algorithms. Experimental results with the state-feedback controller are described below.

2.4 Transputer-based platform for control

Because of instability of the system without any feedback and the relatively small time constants inherent in the system, the stabilising controller requires a high bandwidth and hence a fast processor. Some of the early Maglev work used transputers [21]. These 32-bit devices were specifically designed for multiprocessing with the ability to link up several processors through asynchronous links to increase the total processing bandwidth [39]. A specific feature of the transputer is that it can execute several separately defined tasks (processes), sharing data as necessary, within a single device (processor). Those tasks may be run as higher or lower priority tasks. The ability of the transputer/software to map these

processes on to several processors (separate devices) communicating through their links, made transputers well suited for multi-loop control systems. Within a transputer many tasks may be run in parallel with common data. Along with this internal multiprocessing, the transputers may be connected in a point-to-point network through links to pass data with a bandwidth of up to 20Mbit/s [39].

The early part of the experimental work was undertaken with existing and updated transputer hardware [21] with the specific aim of gaining practical experience in the design of Maglev systems in general and in the implementation of real-time control algorithms for the experimental system specifically. A brief review of transputer elements and the associated control hardware used in the experimental work described here is given in Fig. 2.8.

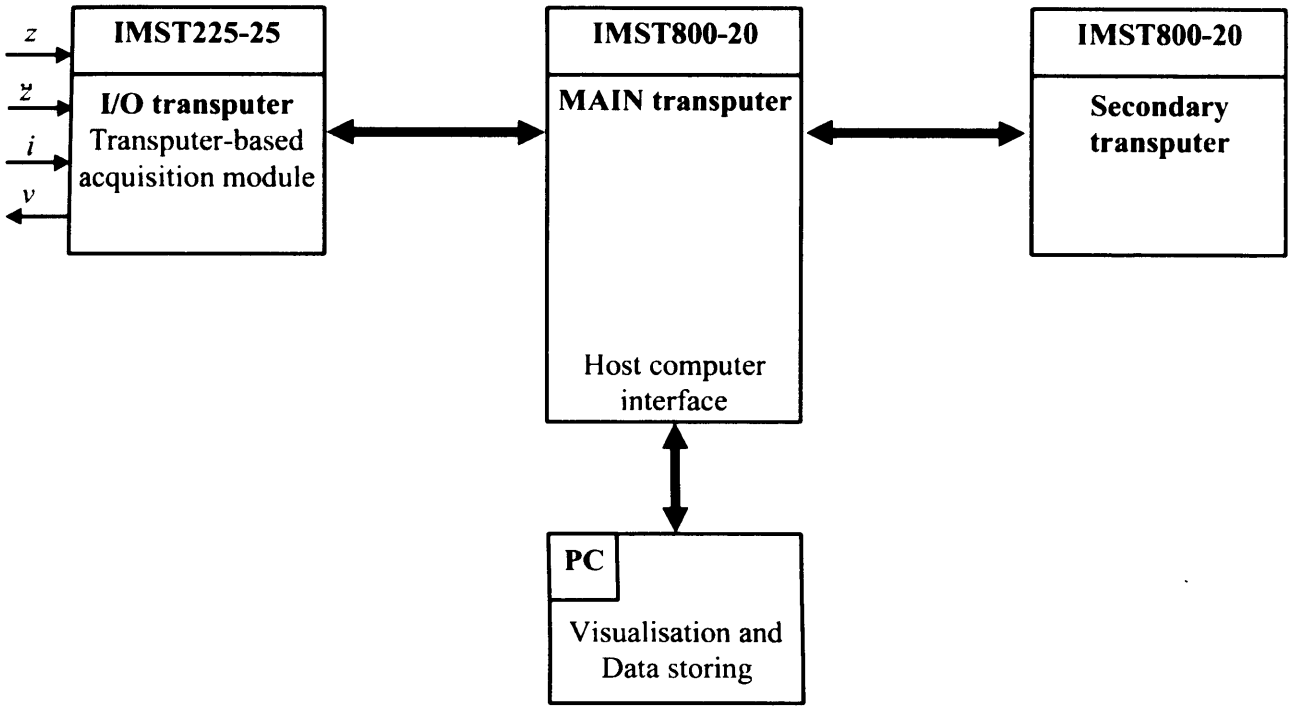

Figure 2.8: Hardware configuration of the processor modules.

The custom-built system consists of three interconnected processors. The first processor, IMST225-25 (I/O transputer), is a 16-bit transputer running at 25 MHz. The task of this processor is to control the analogue I/O modules, to pre-process the analogue data and to pass magnet signals over to the next unit in the network. IMST800-20 (referred as the MAIN transputer) is a 32-bit floating-point unit used to implement the controller algorithmic tasks. It runs at 20MHz and is connected through link to the next processor in the network, and to a supervisory (host) computer (PC). The third processor, IMST800-20 (secondary transputer) acts as a secondary processor and is used to increase the processing bandwidth for computationally demanding control algorithms. The complete networked

hardware is housed on an Inmos full length B-008 AT plug-in board [40], which is memory mapped to the PC's address space. The host computer contains a *software server* which is responsible for data passing between the applications executed on the PC and the transputer-network. Details related to the software environment of the networked processors are given in the following section.

For the measurement of the feedback signals, an 8-channel 12-bit analogue to digital converter has been used. Each input of the ADC accepts a voltage signal (±2.5 V) with a maximum sampling frequency of 500 kHz (MAX-180ACQH). As the transducers have different output ranges, the analogue signals are pre-processed before the ADC. This includes noise filtering, antialiasing, amplification and dc-biasing. For this purpose, an external Input/Output board was designed with a functional block diagram as shown in Fig. 2.9. The current signal output from the airgap sensor is firstly converted into a voltage signal,

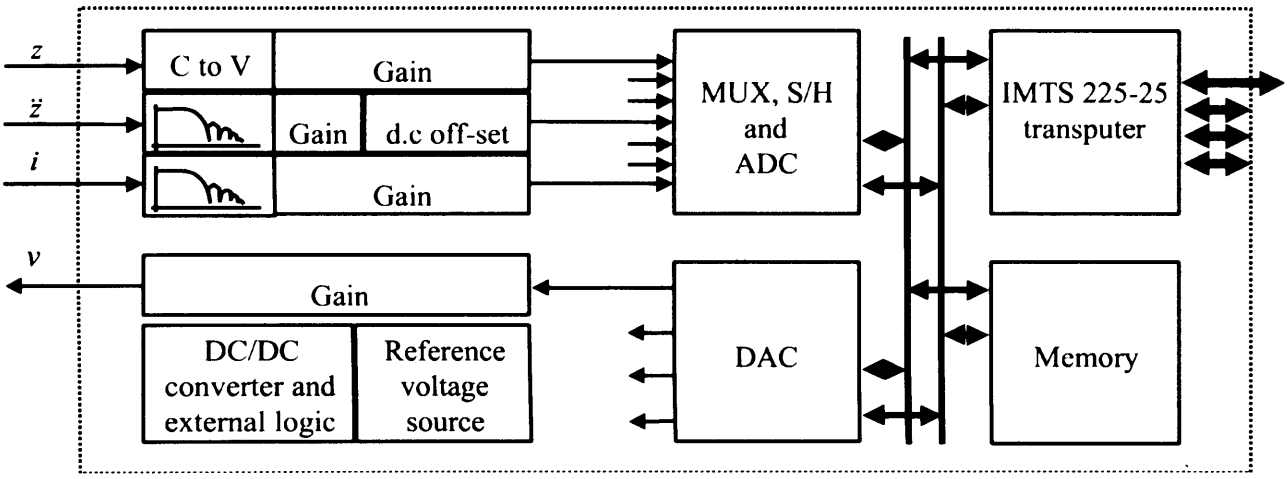

Figure 2.9: Block diagram of the input/output module, the analogue and the digital part.

using a current-to-voltage converter. Because of its sensitivity to vibrations, the output of the accelerometer is a high frequency signal with a significant noise content and a 2.5 V offset. In order to remove a high frequency noise beyond the bandwidth of the control signal, the voltage signal is filtered using a 2nd order Chebyshev low-pass analogue filter with cut-off frequency specified at 500 Hz The output of the filter is further amplified and the dc-offset-removed to satisfy the ADC's input requirements of ±2.5V full scale. The current through the magnet winding is also measured. This signal is filtered (2nd order Chebyshev analogue low-pass filter with cut-off frequency specified at 500 Hz) and amplified before connecting to the ADC's input. At this stage of developing control algorithms the current signal is used only for monitoring.

For the control output, a digital to analogue converter is used (MAX527DCWG) to

generate the feedback signal for the magnet power amplifier. A four-channel, 12-bit DAC is used, memory mapped on the processor's bus. The device gives an output range of ± 2.5 volts with an analogue output update interval of $12\mu s$. This is considered as sufficient to meet the bandwidth requirements of the closed-loop suspension system.

A current amplifier is used to generate a power output from the DAC's signal to drive the magnet. This high-power current controller was especially developed by earlier researchers [21] for use in experimental vehicles. It consists of a standard pulse-width modulator that drives an optically isolated H-bridge with a switching frequency of 40 kHz and a continuous rating of up to 20 Amps at 24 Volts. The efficiency of the amplifier was estimated to be around 80% [21].

2.5 Software environment for transputers-based control

For the control work, a custom-designed software environment was built. The core of this environment is a network of three transputers and the necessary data communications facilities to the host computer (486/DX4 PC). A brief description of the data communication environment developed for this application is given below.

(a) Analogue/digital data: The analogue to digital and digital to analogue converters are connected to the data bus of the 16-bit IMST225-25 transputer (the I/O transputer, Figs. 2.8 and 2.9) with both devices being accessed as memory devices. This I/O transputer performs the following tasks.

- Reads the three signals, position, acceleration and the current, from the ADC.
- Transforms the three numerical values read above to integer data in the $\pm\ 2^{11}$ bits ($\pm$ 2048 units) range.
- Passes those values to the main transputer via link#1. The main transputer integrates the acceleration to get velocity, and implements the control law (for example Eqn. 2.17). The feedback signal is communicated to the I/O transputer (Fig. 2.8 and 2.10).
- The I/O transputer reads the above control signal from the main transputer via link#1 and prepares the numerical form into a format compatible for input to the DAC.

- The signal is loaded to the registers of the DAC. After the conversion time (in the order of $10\mu s$), the analogue output is generated for the power amplifier.

The PC hosts an interface software within the Windows environment to provide facilities for changing operational conditions for the magnet (desired airgap, parameters of the feedback controller, etc.). The software hosts also data collection mechanism and facilities for graphical visualisation of different signals with a basic form of mimic diagram (Figs. A.1 and A.2, page 260). A server has been developed to handle all data passing, booting and configuration demand. A description of this software is given in Section 2.6. On the MAIN transputer (Fig. 2.10), a group of tasks are executed to handle the communication with the host server. Those tasks are as follows:

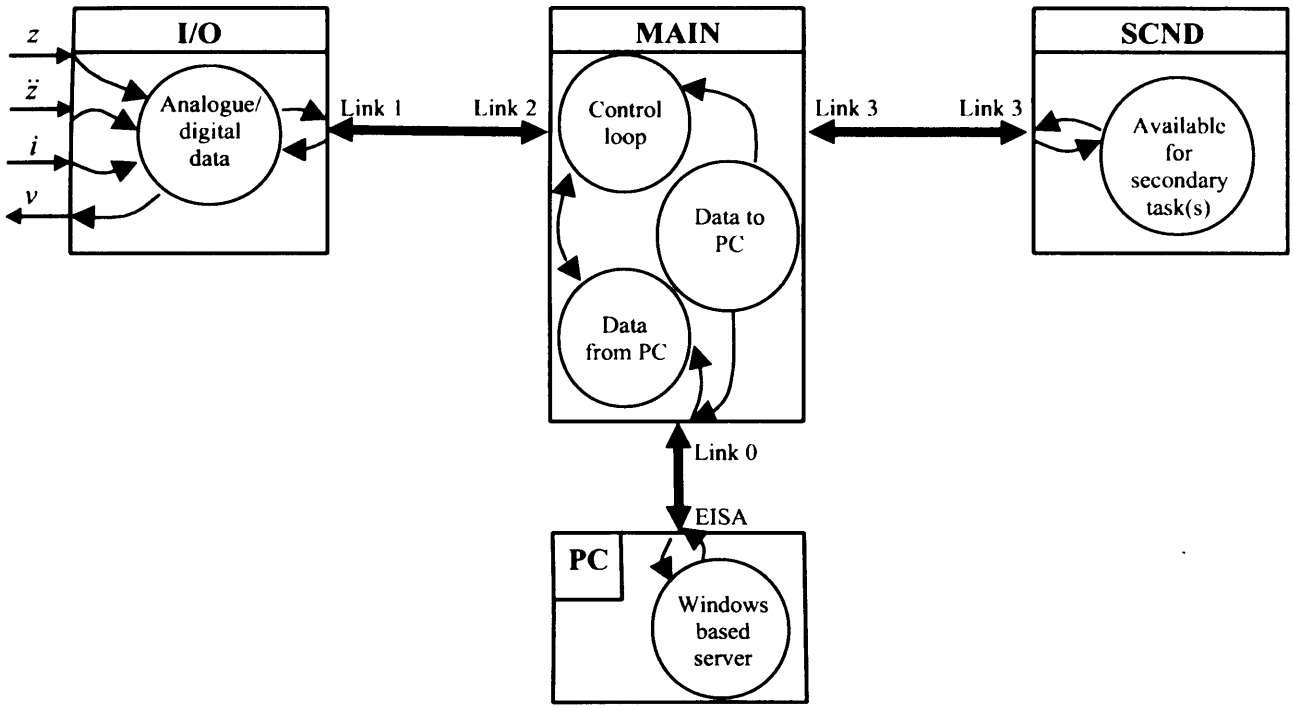

Figure 2.10: Configuration of the different software tasks within the transputer hardware. The arrows show the data path.

Communication with the host: This low-priority task is executed at a pre-defined time (default interval: 10ms). It connects to the server on the host computer to receive a buffer of data which contains parameters as required by the control law. For the state feedback controller these are the desired airgap value, the feedback gains, and the saturation limits in the output current. At a predefined time (default interval 50 ms), another task passes data buffers to the server; for the Maglev these are the suspension airgap, the current acceleration signal, the velocity of the magnet and the operational current. Data

related to the controller are also communicated.

Control loop: In this task, the control output is calculated according to the mathematical control law (Eqn. 2.17 for example). The feedback signals are received from the I/O transputer. The sequence of execution of the tasks and processes described above is shown in Fig. 2.11. Sampling time here is dictated by the execution time of the individual tasks, and thus depends on data availability, the asynchronous nature of individual subtasks as well as the actual operation performed within the controller algorithm. To establish a practical limit with the given hardware, the sampling time in the experimental set up was varied. This was observed to require a minimum of $400\mu s$. The execution time calculated and indicated in the last subtask above is used for ensuring a constant sampling interval in the experimental system. This is achieved by executing a delay loop, specified at $400\mu s$ minus the execution time. Because of the event nature of the transputers, however, it is not possible to achieve a strict sampling interval and some jitter (in the order of $\pm 30\mu s$) was observed around the specified $400\mu s$ [39].

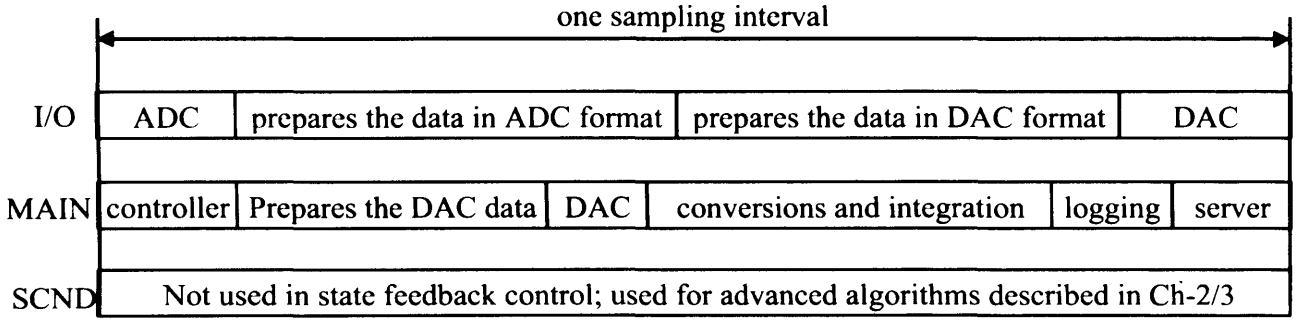

Figure 2.11: Process timing of the transputer hardware.

For more computationally demanding algorithms (such as adaptive control) the secondary transputer is used to increase the total processing power within the network. Implementation issues for this are described in Chapters 3 and 4.

2.6 Host interface

The host computer executes a collection of tasks; these include, booting the root transputers (MAIN transputer in Fig. 2.8) communicating with other transputers in the network; visualising the three sensor outputs, changing operational conditions (state feedback gains and set-point) and logging data for further processing. This server application also generates the user-interface mimic shown in Fig. A.1, A.2 (Appendix). This application is

written in C using National Instruments LabWindows/CVI package [41] for WindowsTM environment. A brief discussion of these tasks is given below.

The overall application interface is shown in Fig. A.1. Current magnet data can be monitored on the left panel (Magnet-1). These are updated every 200ms (this interval was observed to be adequate for near enough real-time display). The desired position may be changed from the interface. A history window is implemented to visualise the operating conditions of the magnet. The feedback controller can be updated using numerical inputs (Fig. A.1 (right top)).

2.7 Transputer implementation of the state feedback controller

Using the above hardware setup, experimental results are obtained to validate the theoretical basis of the state-feedback design. A step response in the reference airgap position was generated and the corresponded experimental response is given in Fig. 2.12(top) from 4 mm to 3 mm at $t = 0$ sec. and from 3mm to 4mm at t=300 ms. Fig. 2.12(bottom) shows the expanded response over the 0-50 ms time interval to provide a better indication of the initial part of the transient. The airgap responses are stable and well damped with a low overshoot (< 1 mm) and a settling time of approximately 200 ms. A close comparison is observed between the experimental and the simulated responses giving some confidence in the theoretical design. The limitation in the design is that the linear control law is related to the three gains being strictly suited for a particular operating point (specified by the nominal values of the position and the magnet current, Section 2.3, constant matrix $\mathbf{A}$). Choice of the three feedback gains (row matrix $\mathbf{K}$ in Eqn. 2.17) is based on the desired locations of the closed-loop poles to meet stability and transient response specifications [38]. Selection of feedback gains is directly related to the closed-loop poles and hence the ride qualities. As the system dynamics change, the closed-loop matrix ($\mathbf{A} - \mathbf{BK}$) changes and the closed-loop poles change. Depending on parameter variations, the closed-loop poles may move significantly from the original designated values leading to instability. To overcome this limitation of the feedback compensator, further improvements of the state feedback controller have been considered. The mathematical details and implementation issues related these control techniques are developed in the next chapter.

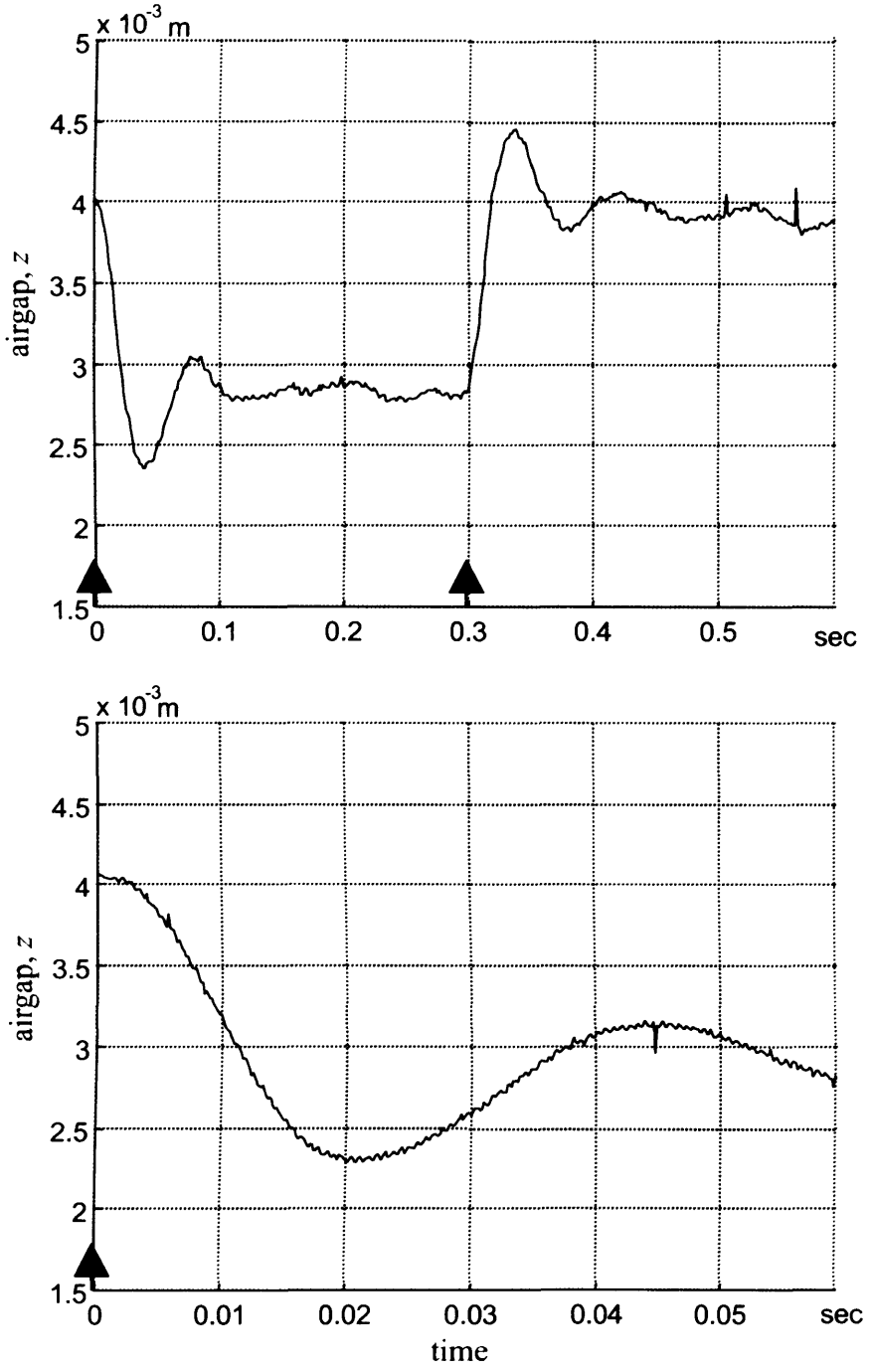

Figure 2.12: Step change of the desired air-gap (top) using state feedback controller, and expanded version of the first step over the first 50ms (bottom). Feedback gains: k_P =20833; k_V =250; k_A=4;

Chapter 3

Adaptive pole placement and model reference control of Maglev systems

Adaptive state-feedback controllers for Maglev are developed below for applications where significant changes in the operating conditions are expected. The exposition begins with identification of closed-loop systems to analyse suspension characteristics with state-feedback controllers.

3.1 On-line identification of Maglev model

The identification process described here aims to derive a mathematical model of the suspension system around the nominal operating point. This is accomplishment by comparing the output from the system with the output from the model and minimising the error between them by adjusting parameters of the model; the input to both systems is same (see Fig. 3.1). The mathematical model is used in adaptive model-reference design for suspension systems with a considerable variation in the operating conditions. This is typically contributed from internal and external disturbances.

3.1.1 Problem formulation and background information

As the Maglev system is unstable in open-loop, the identification has to be performed with the closed-loop system operating at a chosen airgap. The aim here is to find a model, which correlates the position of the magnet with respect to the track and the reference position demand z_{ref}. For this, the state feedback controller is used. The identification process uses the structure of the model derived in Chapter 2. For the digital work, this is represented in the $Z-$domain to get the general form

$$\tilde{G}_{cl}(z) = \frac{B(z)}{A(z)} = \frac{z_m(k)}{z_{ref}(k)} = \frac{b_1 z^{-1} + b_2 z^{-2} + b_3 z^{-3}}{1 + a_1 z^{-1} + a_2 z^{-2} + a_3 z^{-3}} \tag{3.1}$$

or

$$\begin{aligned} z_m(k) &= b_1 z_{ref}(k-1) + b_2 z_{ref}(k-2) + b_3 z_{ref}(k-3) \\ &\quad -a_1 z_m(k-1) - a_2 z_m(k-2) - a_3 z_m(k-3) \end{aligned} \tag{3.2}$$

This system is assumed to be a third order system [1]. If the unknown coefficients a_i and b_i are organised as a vector

$$\theta = [b_1, b_2, b_3, a_1, a_2, a_3]^T \tag{3.3}$$

and the system's inputs and outputs organised as a vector

$$\varphi(k)^T = [z_{ref}(k-1), z_{ref}(k-2), z_{ref}(k-3), -z_m(k-1), -z_m(k-2), -z_m(k-3)] \tag{3.4}$$

the difference equation model may be re-written in vector form as

$$z_m(k) = \varphi(k)^T \theta \tag{3.5}$$

Representation of the parameter estimation mechanism is shown in Fig. 3.1. Using a

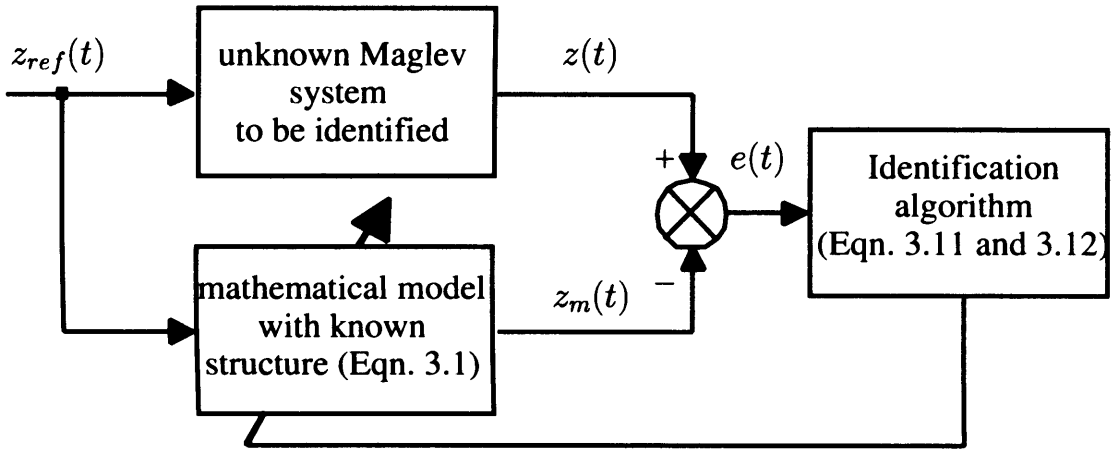

Figure 3.1: The identification algorithm

reference input $z_{ref}(k)$ to both real system and mathematical model, the error $e(k)$ signal may be produced by subtracting the output of the system $z(k)$ from the output of the model $z_m(k)$

$$e(k) = z(k) - z_m(k) = z(k) - \varphi(k)^{\mathrm{T}} \theta \tag{3.6}$$

The aim of the identification is to minimise this error by the definition of a cost function as [42, 43]

$$J(\theta) = \frac{1}{2} E^T E \tag{3.7}$$

where the vector E consists of N samples of the error $e(k)$

$$E = [e(k),\ e(k-1),\ \cdots,\ e(k-N)]^T = \begin{bmatrix} z(k) - z_m(k) \\ z(k-1) - z_m(k-1) \\ \cdots \\ z(k-N) - z_m(k-N) \end{bmatrix} \tag{3.8}$$

It is shown in [43] that the least-squares algorithm minimises the loss function by adjusting the unknown model's parameters θ according to

$$\theta = (\mathbf{F^T F})^{-1}\mathbf{F^T z} \tag{3.9}$$

In this equation $z = [z(k),\ z(k-1)\ \cdots,\ z(k-N)]^T$ is a vector that consists of N outputs $z(k)$ from the system; θ is the vector of the unknown model's coefficients, and F is a matrix with dimension $(n+m)$xN, where n is the order of the numerator and m is the order of the denominator in the assumed system model. Each row of this matrix F is the vector $\varphi(k)$ at the given sample k, where the number of columns is equal to the number of collected samples N and is given in the form

$$\mathbf{F} = \begin{bmatrix} \varphi(k)^T \\ \varphi(k-1)^T \\ \vdots \\ \varphi(k-N)^T \end{bmatrix} \tag{3.10}$$

F usually has more than two rows and columns. The off-line approach for identification uses pre-stored data (φ) for the identification. Often the size of this data or the dimension of the matrix F is not appropriate for intensive matrix calculations (transpose, inversion and multiplication). In application, where the control algorithm entirely depends from an updated model of the system, a recursive on-line version of LS may be used (recursive least squares or RLS). At every sample the algorithm receives the input ($z_{ref}(k)$), the output ($z(k)$), and produces the new estimation ($\theta(k)$). If the system's parameters do not change, after certain time the estimated parameters approach to stable values. The coefficients of the closed-loop model using RLS algorithm are updated at every sample using the rule below [43]

$$\theta(k) = \theta(k-1) - K(k)[z(k) - \varphi(k)^T\theta(k-1)] \tag{3.11}$$

In this equation:

$$\theta = [b_1, b_2, b_3, a_1, a_2, a_3]^T$$

and

$$\varphi(k)^T = [z_{ref}(k-1), z_{ref}(k-2), z_{ref}(k-3), -z(k-1), -z(k-2), -z(k-3)]$$

The covariance matrix $\mathbf{P}$ is updated by the following rule

$$\begin{aligned} K(k) &= \mathbf{P}(k-1)\varphi(k)[\lambda I + \varphi(k)^T\mathbf{P}(k-1)\varphi(k)]^{-1} \\ \mathbf{P}(k) &= \tfrac{[I-K(k)\varphi(k)^T]\mathbf{P}(k-1)}{\lambda} \end{aligned} \tag{3.12}$$

Eqns 3.3 and 3.4 form the basis of the recursive-least squares technique [43]. The forgetting factor $\lambda \in [0 : 1]$ determines the importance of the data φ. Values of λ close to one give higher importance on the recent samples ($\varphi(k-1)$ over $\varphi(k-10)$). This mechanism is used to control the adaptation rate. The system's dynamics have to be also used in the selection of λ to avoid unstable estimations.

3.1.2 Implementation and results

To identify the closed-loop Maglev with the state feedback controller derived in Chapter 2, recursive identification was implemented on the transputer-based real time control software. The identification task was distributed among three transputers, interconnected as shown in Fig. 2.8 (Section 2.4, Chapter 2). The velocity signal is generated from the acceleration signal using the digital filter below

$$\dot{z}(k) = c_f \dot{z}(k-1) + d_f \ddot{z}(k), \tag{3.13}$$

where for 400μs sampling time the coefficients are: $c_f = 0.992063$, $d_f = 396.8253 \times 10^{-6}$ (equal to a pole at $(-20 \pm j0)$). As shown in Fig. 3.2, the identification of the closed loop Maglev system is executed in parallel with state feedback control. Inputs are the reference demand $z_{ref}(k))$ and $z(k))$. The solution to the problem is the set of coefficients of the dynamical model in Eqn. 3.1. The current values for a_i and b_i are correct for a given nominal operating point. The identification process is run on the secondary transputer to run in parallel with the state-feedback controller run on the main transputer (Fig. 2.10). For identification, the transputer routine receives current feedback signals via the link ports to update $\varphi(k)$ (Eqn. 3.4). Using this vector and the current estimation $\theta(k)$, the output from the model $z_m(k)$ is generated (Eqn. 3.5) to produce the estimation error $e(k) = z(k) - z_m(k)$ (Eqn. 3.6). The initial values for $\mathbf{P}(k)$ are fixed at $1 \times 10^{+4} \times \mathbf{I}$. Eqn. 3.11 is used in the construction of the model in the k-th sample.

For the purpose of the analysis, the algorithm on the secondary transputers calculates the roots of the denominator in Eqn. 3.1 to find the location of the poles. The result is a vector of real and complex numbers which is transferred to the MAIN transputer via link#3. The purpose of this was to build a mechanism for automatically tuning the state-feedback controller using this information. Design of an adaptive pole-placement controller using RLS is discussed in the following section. A root locus plot is also designed for real-time visualisation (Fig. 3.5). The sampling time of the identification is fixed at 10 ms due to the intensive calculations involved. To be independent from the sampling time, the

$z-$domain values for the closed-loop poles are transferred to the s-domain for the analysis. For a realistic comparison with the experimental response being controlled with a sampling time of $400\mu s$ the identified model is converted to a z-domain representation with 400 μs. The above sequence of operations is shown in Fig. 3.3. Fixing $\lambda = 0.99913$ and applying

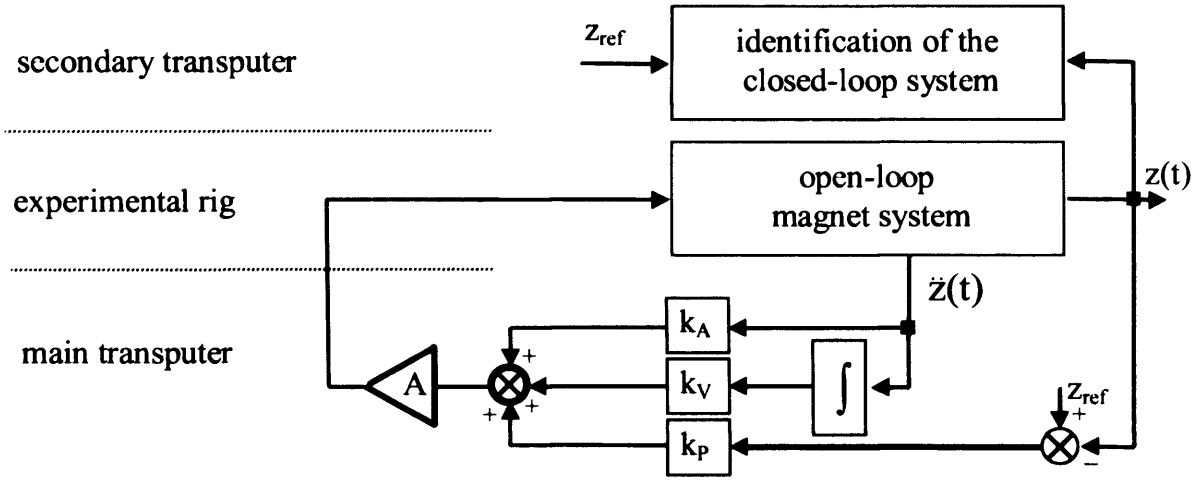

Figure 3.2: Identification of the closed-loop magnet system.

an identification signal, after 1.3 sec. the following model was generated to represent the closed-loop Maglev system

$$\tilde{G}_{cl}(z) = \frac{z_m(k)}{z_{ref}(k)} = \frac{0.3261z^{-1} + 0.0685z^{-2} - 0.1480z^{-3}}{1 - 1.1607z^{-1} + 0.1122z^{-2} + 0.2861z^{-3}}$$

This transfer function was simulated in Matlab and the comparison with the experimental

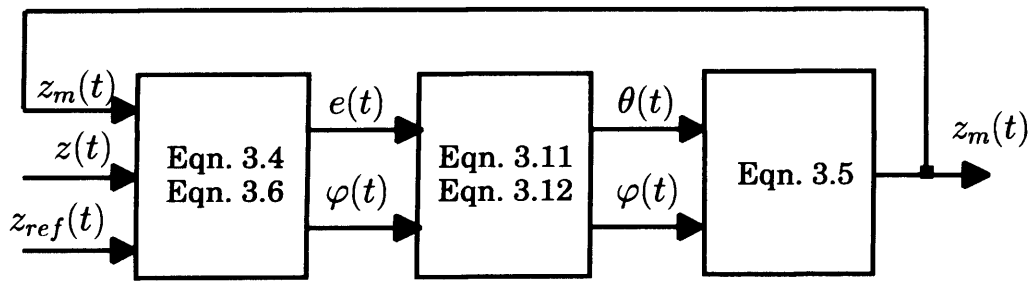

Figure 3.3: The sequence of operations on the real-time software for identification of the closed-loop system.

responses shown in Fig. 3.4. These results react adequately in both steady state and transient, and this model may be used as a basis for other model-based design methods.

The application window used to visualise the location of the poles numerically and graphically on the host computer is shown in Fig. 3.5. This analysis was used as a basis for the development of the adaptation algorithms described below.

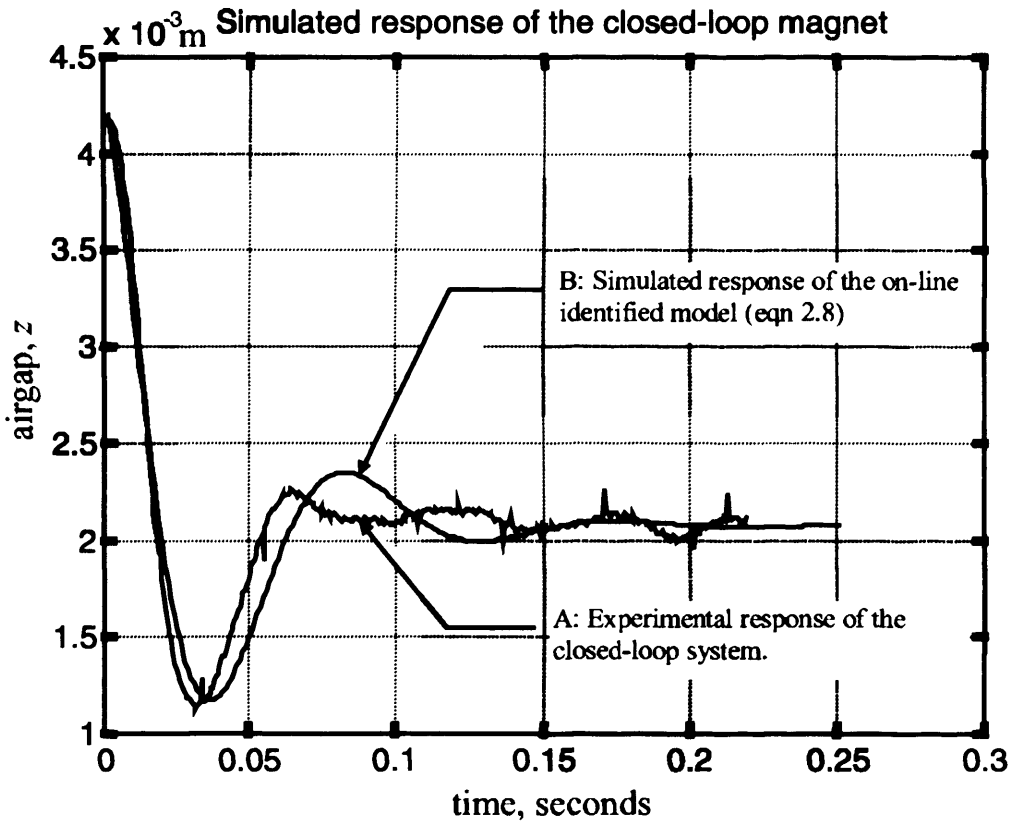

Figure 3.4: Comparison between responses from the experimental system and the model obtained from on-line identification. The input to both is a step change in air-gap from 4mm to 2 mm

3.2 Adaptive pole-placement control

In traditional adaptive techniques, the adaptation algorithm collects information on-line about a working system without a controller and then derives an optimised controller. This approach is not suitable here because Maglev is unstable in open loop. As shown earlier, poles of the closed-loop system are controlled by the feedback gain vector K. If K is constant, suspension dynamics may change with parameter variations or due to disturbance inputs. As a consequence, the closed-loop stability and performance degrades leading to undesired suspension qualities. The algorithm explored in this section is based on the requirement that a set of pre-specified closed loop poles are always maintained by the controller to make the system invariant to disturbances.

The open-loop transfer function of a Maglev system may be symbolically expressed as

$$G(s) = \frac{z(s)}{v(s)} = \frac{b_{m_0}}{s^3 + a_{m_1}s^2 + a_{m_2}s + a_{m_3}} = \frac{B(s)}{A(s)}, \tag{3.14}$$

where b_{m_0}, a_{m_1}, a_{m_2} and a_{m_3} are related to the internal parameters of the magnetic circuit

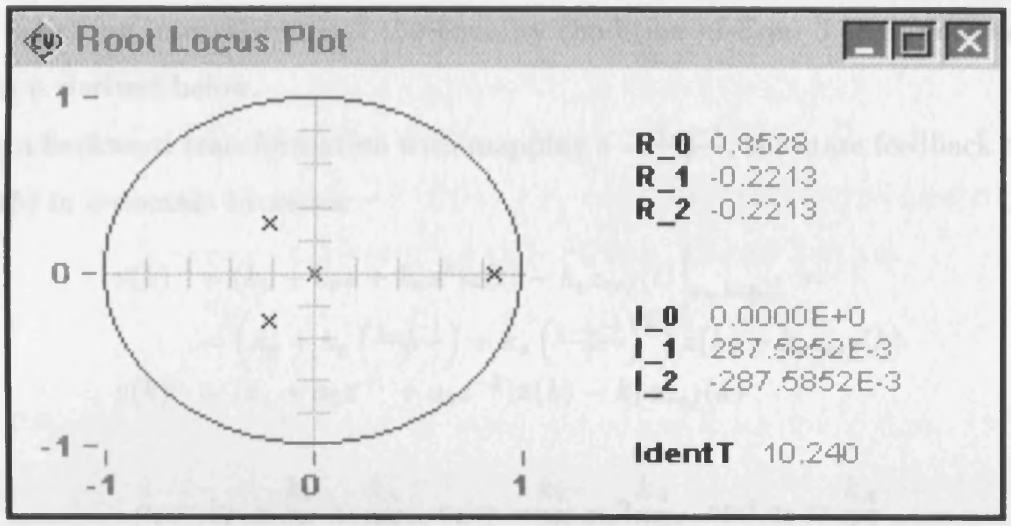

Figure 3.5: Root-locus plot as seen on the host screen. The closed-loop poles are generated on the transputer at every sample k using the identified model and then transferred to the host computer for plotting and analysis.

(Chapter 2, Eqn. 2.12).

The s-domain representation of the state feedback control law (Fig. 2.6) may be expressed as

$$v(s) = (k_P + k_V s + k_A s^2)z(s) - k_P z_{ref}(s) = G_C(s)z(s) - k_P z_{ref}(s) \tag{3.15}$$

where $G_C(s)$ is the transfer function of the feedback compensator.

Substituting Eqn. 3.15 in Eqn. 3.14, the closed-loop transfer function becomes

$$G_{CL}(s) = \frac{z(s)}{z_{ref}(s)} = \frac{-k_P G(s)}{1 - G(s)G_C(s)} = \frac{-k_P B(s)}{A(s) - B(s)G_C(s)} \tag{3.16}$$

By specifying a characteristic polynomial $T(s)$ for the closed-loop system, with pre-specified roots, the above equation becomes

$$G_{CL}(s) = \frac{z(s)}{z_{ref}(s)} = \frac{-k_P B(s)}{A(s) - B(s)G_C(s)} = \frac{-k_P B(s)}{T(s)} \tag{3.17}$$

The aim is to produce a feedback compensator ($G_C(s)$) which guarantees that the denominator polynomial of the closed-loop system converges to $T(s)$, If the system $A(s)$ and $B(s)$ (open-loop model) are known then $G_C(s)$ represents the conventional feedback compensator which satisfies

$$A(s) - B(s)G_C(s) = T(s) \tag{3.18}$$

If, however, the open-loop model of the system varies due to changes in operational conditions, (= parameters changes in $A(s)$ and $B(s)$), an adaptive algorithm to adjust $G_C(s)$

at every sampling interval to meet the equality condition of Eqn. 3.18 is necessary. This algorithm is derived below.

Using a backward transformation with mapping $s = \frac{1-z^{-1}}{T}$, the state feedback controller (Eqn. 3.15) in z-domain becomes:

$$\begin{aligned} v(k) &= (k_p + k_v s + k_a s^2) z(t) - k_p z_{ref}(t) \Big|_{s=\frac{1-z^{-1}}{T}} = \\ &= \left(k_p + k_v \left(\tfrac{1-z^{-1}}{T}\right) + k_a \left(\tfrac{1-z^{-1}}{T}\right)^2\right) z(k) - k_p z_{ref}(k) \\ v(k) &= (a_1 + a_2 z^{-1} + a_3 z^{-2})\mathbf{z}(k) - k_P \mathbf{z}_{ref}(k) \end{aligned} \tag{3.19}$$

where

$$a_1 = k_P + \frac{k_V}{T} + \frac{k_A}{T^2}, \quad a_2 = -\frac{k_V}{T} - 2\frac{k_A}{T^2}, \quad \text{and } a_3 = \frac{k_A}{T^2} \tag{3.20}$$

If $B(z^{-1})$ and $A(z^{-1})$ are the open-loop Maglev numerator and denominator respectively, the closed-loop transfer function using Eqn. 3.19 becomes

$$G_C(z^{-1}) = \frac{\mathbf{z}(k)}{\mathbf{z}_{ref}(k)} = \frac{-k_P B(z^{-1})}{A(z^{-1}) - B(z^{-1})(a_1 + a_2 z^{-1} + a_3 z^{-2})} \tag{3.21}$$

The Diophantine equation in z-domain can be then constructed as

$$A(z^{-1}) - B(z^{-1})(a_1 + a_2 z^{-1} + a_3 z^{-2}) = T(z^{-1}) \tag{3.22}$$

Locating the roots of $T(z^{-1})$ within the unit circle guarantees stable response of the system with typical values beeing determined by the identification procedure developed in the previous section.

$$G_C(z^{-1}) = \frac{\mathbf{z}(k)}{\mathbf{z}_{ref}(k)} = \frac{-k_P B(z^{-1})}{A(z^{-1}) - B(z^{-1})(a_1 + a_2 z^{-1} + a_3 z^{-2})} = \frac{-k_P B(z^{-1})}{T(z^{-1})} \tag{3.23}$$

Multiplying both sides the denominator of Eqn. 3.22 by the system's output $z(k)$ gives

$$A(z^{-1})\mathbf{z}(k) - B(z^{-1})(a_1 + a_2 z^{-1} + a_3 z^{-2})\mathbf{z}(k) = T(z^{-1})\mathbf{z}(k) \tag{3.24}$$

Using the equivalent transformation $A(z^{-1})z(k) = B(z^{-1})v(k)$, the above equation may be rewritten as

$$B(z^{-1})v(k) - B(z^{-1})(a_1 + a_2 z^{-1} + a_3 z^{-2})\mathbf{z}(k) = T(z^{-1})\mathbf{z}(k) \tag{3.25}$$

The unknowns in this equation are the controller coefficients a_i, and the open-loop system's numerator $B(z^{-1})$. If the open-loop system $G_C(s)$ (Eqn. 2.12, Chapter 2) is transformed into z-domain using back-wards mapping, the numerator $B(z^{-1})$ consists of a single value b_0. The following error signal can be then constructed

$$\begin{aligned} e(k) &= T(z^{-1})\mathbf{z}(k) - B(z^{-1})v(k) + B(z^{-1})(a_1 + a_2 z^{-1} + a_3 z^{-2})\mathbf{z}(k) \\ &= T(z^{-1})\mathbf{z}(k) - \tilde{\varphi}^T \tilde{\theta}. \end{aligned} \tag{3.26}$$

which is expanded in difference form as below

$$\begin{aligned} e(k) &= T(z^{-1})\mathbf{z}(k) - b_0 v(k) + b_0 a_1 \mathbf{z}(k) + b_0 a_2 \mathbf{z}(k-1) + b_0 a_3 \mathbf{z}(k-2) = \\ &= T(z^{-1})\mathbf{z}(k) - b_0 v(k) + \tilde{a}_1 \mathbf{z}(k) + \tilde{a}_2 \mathbf{z}(k-1) + \tilde{a}_3 \mathbf{z}(k-2), \end{aligned} \tag{3.27}$$

The recursive least squares technique (Eqns. 3.11 and 3.12) may now be used to minimise this error, where the appropriate vectors θ and φ (Eqns. 3.3 and 3.4) are

$$\begin{aligned} \tilde{\varphi} &= [v(k), -\mathbf{z}(k), -\mathbf{z}(k-1), -\mathbf{z}(k-2)]^T \\ \tilde{\theta} &= [b_0, \tilde{a}_1, \tilde{a}_2, \tilde{a}_3] \end{aligned} \tag{3.28}$$

The identification is now performed by using the output from the system $z(k)$ and the input to the system $v(k)$ (Fig. 3.2). When the coefficients converges to constant values, the gains of the state feedback controller may be calculated to give closed-loop poles specified by $T(z^{-1})$. The equations for the recursive least squares algorithm which generates these coefficients are

$$\begin{aligned} \tilde{\theta}(k) &= \tilde{\theta}(k-1) - K(k)[T(z^{-1})\mathbf{z}(k) - \tilde{\varphi}(k)^T \tilde{\theta}(k-1)] \\ K(k) &= \mathbf{P}(k-1)\tilde{\varphi}(k)[\lambda I + \tilde{\varphi}(k)^T \mathbf{P}(k-1)\tilde{\varphi}(k)]^{-1} \\ \mathbf{P}(k) &= \frac{[I - K(k)\tilde{\varphi}(k)^T]\mathbf{P}(k-1)}{\lambda} \end{aligned} \tag{3.29}$$

The new coefficients $\tilde{a}_n$ a related to the model's coefficients a_i as

$$a_i = \frac{\tilde{a}_i}{b_0}, \tag{3.30}$$

with $i = 1..3$. Using Eqn. 3.20, the feedback gains k_P, k_V, and k_A are derived below

$$\begin{bmatrix} \frac{1}{T^2} & \frac{1}{T} & 1 \\ -\frac{2}{T^2} & -\frac{1}{T} & 0 \\ \frac{1}{T^2} & 0 & 0 \end{bmatrix} \begin{bmatrix} k_A \\ k_V \\ k_P \end{bmatrix} = \begin{bmatrix} a_1 \\ a_2 \\ a_3 \end{bmatrix} \tag{3.31}$$

3.2.1 Outline of implementation issues

The adaptive pole-placement technique was implemented on the transputer-based real-time control software, described in Chapter 2 using the three transputers in the network (Fig. 2.10, Chapter 2). As discussed earlier, the MAIN transputer receives the two state variables (position $z(k)$, and acceleration $\ddot{z}(k)$) from the I/O transputer. Further it generates the third state variable , the velocity $\dot{z}(k)$. The state feedback controller uses these signals to generate the control output (Eqn. 3.15). At every sample (950 μs), a software sub-task located on the MAIN transputer sends the current position $z(k)$ and the current control signal $v(k)$ to the secondary transputer (Fig. 2.10, Chapter 2) vial link port 3. These values, and two past values for the position ($z(k-1)$, $z(k-2)$) are used for updating the vector $\tilde{\varphi}$ (Eqn. 3.28). This vector is used as an input for the least squares algorithm (Eqn. 3.29). In order to solve Eqn. 3.29, firstly the vector $K(k)$ is updated,

using an initial value of the matrix $P(0)$ equal to $1 \times 10^{+4} \times \mathbf{I}$. The new coefficients at the current sample $\tilde{\theta}(k)$ are generated by Eqn. 3.29. The following values are used to specify the desired closed-loop suspension damping and settling time

$$T(z^{-1}) = (z - 0.19077)(z - [0.8951 + 0.0850\text{j}])(z - [0.8951 - 0.0850\text{j}]) \tag{3.32}$$

The corresponding s-domain poles are located at (-1840.8, -118+j105, -118-j105). These values are generated by analysis of identification results for various operating conditions. The final stage in the adaptation rule requires calculating the feedback gains using Eqns. 3.30 and 3.31. It was observed that when the feedback gains converge to stable values (closed-loop poles converge to the poles specified by $T(z^{-1})$) the trace of the covariance matrix P increases. This incremental variation in P was used in a decision-making mechanism to derive an operational threshold for switching from fixed to adaptive state-feedback gains (Eqn. 3.31).

The parameter $\lambda \in [0 : 1]$ in Eqn. 3.29, determines the adaptation rate and the sensitivity of the adaptive pole-placement algorithm to disturbances. For this purpose an algorithm for varying λ was constructed. To calculate $\lambda(k)$, the difference between the position gain at sample $k_P(k)$ and at sample $k_P(k-1)$ is calculated. This error is a rough estimation of the amplitude of the external disturbance, and based on this error (≡disturbance), a linear function f is used $\lambda = f(k_P(k) - k_P(k-1))$ for determining the new value for λ. f is typically a constant or an exponential function.

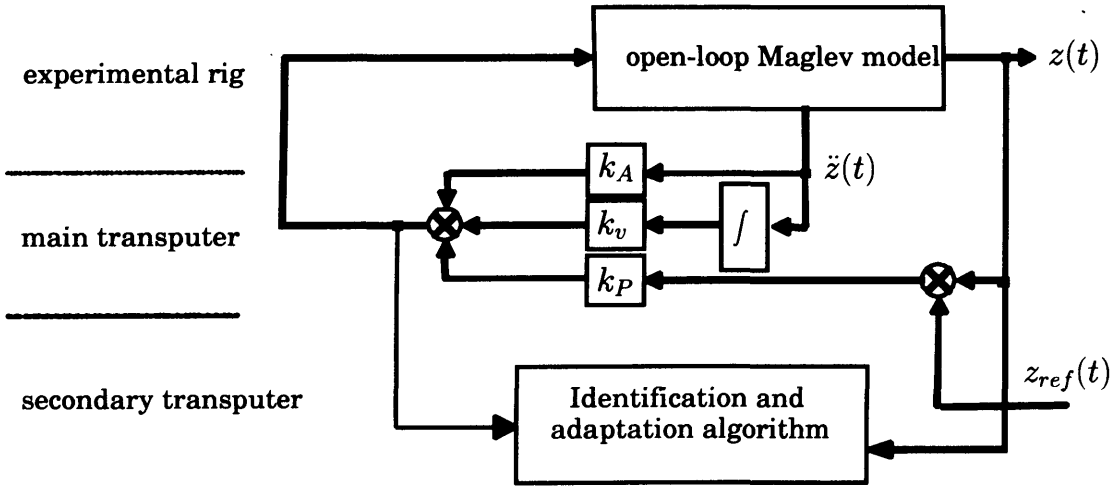

Figure 3.6: Configuration of the adaptive pole-placement controller.

A schematic representation of the adaptive pole-placement algorithm is shown in Fig. 3.6. It was observed that the execution of the algorithm takes around 900μs on the transputers, leading to a choice of sampling time equal to 950μs. After a series of experimental

tests, two problems were identified during the development of this adaptive pole placement algorithm on the transputer hardware.

1. The characteristic polynomial $T(z^{-1})$ determines the overall quality of the adaptation algorithm and the closed-loop stability and suspension damping. The poles used in the construction of $T(z^{-1})$, however, differ from the closed-loop system poles after the adaptation. This is due to the assumptions made in the derivations, i.e. linear representation of a non-linear system, conversion from the s-domain to the z-domain, numerical errors generated during the computation.

2. At the time of writing this chapter, the algorithm described above is not fully functional. This is due partly to the fact that the sampling time necessary for one cycle of computation on the transputer network is around 900μs. Although some stable responses have been obtained, the suspended system does not appear to be capable of accepting disturbance inputs. However, this algorithm has been successfully implemented with DSPs with a sampling time of 400μs. This is described in Chapter 4, Section 4.4.2.

3.3 Model reference adaptive control of a Maglev system

The general configuration of the model-reference control environment derived in this section is shown in Fig. 3.7, where the reference model is derived from the identification of the closed-loop system described in Section 3.1 operating at its nominal airgap and current levels. This is considered to be a realistic basis for adaptive control as (a) magnets are designed to offer optimum performance (lift to weight ratio) over a preferred range of airgaps and currents, and (b) the operating airgap (set-point) of the system is normally set at a prescribed value to meet various (somewhat conflicting) requirements, including magnet efficiency, passenger ride comfort, and probability of contact between the moving magnet and the guideway [1].

In the model-reference control the closed-loop system is compared with that of a given reference model and the algorithm attempts to minimise the difference between the two systems by adjusting the feedback gains. Compared to the pole-placement algorithm, the adaptation rate is specified by a reference model instead of locations of the closed-loop poles.

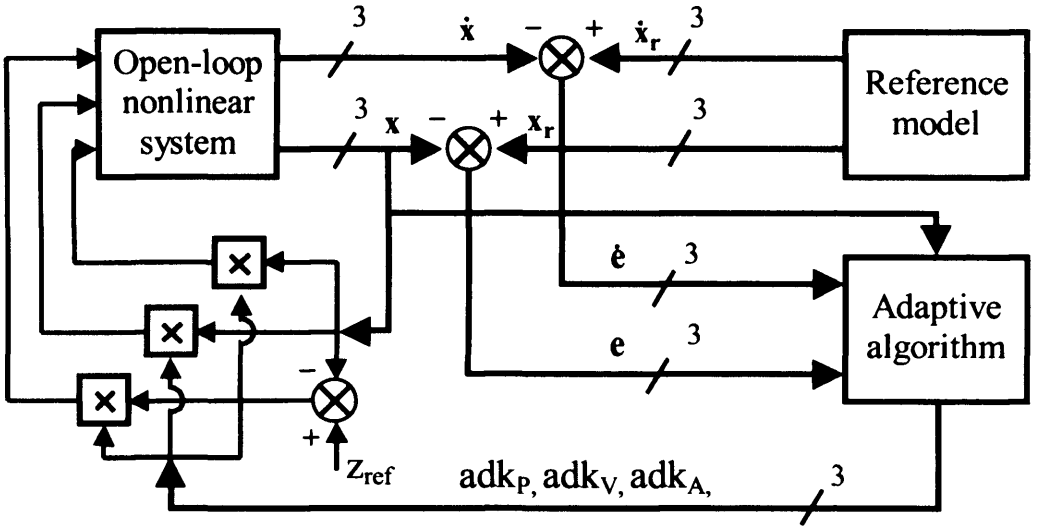

Figure 3.7: Configuration of the model-reference controller set-up.

Combining the dynamical representation of the Maglev system (Eqn. 2.13, Chapter 2) and the feedback controller, the closed-loop system is represented by (**A** corresponds to the closed-loop system)

$$\dot{\mathbf{x}} = \mathbf{A}\mathbf{x} + \mathbf{B}\mathbf{r}, \tag{3.33}$$

and the dynamics of the reference model specified by

$$\dot{\mathbf{x}}_r = \mathbf{A}_r\mathbf{x}_r + \mathbf{B}_r\mathbf{r} \tag{3.34}$$

The general requirement is to keep $\mathbf{A}$ close to $\mathbf{A}_r$ by minimising the error

$$\dot{\mathbf{e}} = \dot{\mathbf{x}}_r - \dot{\mathbf{x}} = \mathbf{A}_r\mathbf{x}_r + \mathbf{B}_r\mathbf{u} - \mathbf{A}\mathbf{x} - \mathbf{B}\mathbf{u} + \mathbf{A}_r\mathbf{x} - \mathbf{A}_r\mathbf{x} \tag{3.35}$$

This error has its own dynamics given by

$$\dot{\mathbf{e}} = \mathbf{A}_r\mathbf{e} + \mathbf{G}\mathbf{x}, \tag{3.36}$$

where $\mathbf{G} = \mathbf{A}_r - \mathbf{A}$. Selecting a performance function in the form

$$J(\mathbf{e}) = \mathbf{e}^{\mathbf{T}}\mathbf{P}\mathbf{e} + \dot{\mathbf{e}}^{\mathbf{T}}\mathbf{Q}\dot{\mathbf{e}} \tag{3.37}$$

where $\mathbf{P}$ and $\mathbf{Q}$ are n-squared weighting matrices it can be proved that

$$\frac{d\alpha}{dt} = +\gamma\frac{\partial J(\mathbf{e})}{\partial \alpha}, \gamma > 0 \tag{3.38}$$

where α is a controller parameter to be adjusted for model following (a feedback gain), and $J(\mathbf{e})$ is the performance function, given by Eqn. 3.37. This equation minimises analytically the error between the system and the model by adjusting the feedback gain α. In general

for any n-error vector, the first derivative of the performance criterion in Eqn. 3.37 with respect to the controller parameters α is

$$\frac{\partial J(\mathbf{e})}{\partial \alpha} = \frac{\partial(\mathbf{e^T P e} + \dot{\mathbf{e}}^{\mathbf{T}}\mathbf{Q}\dot{\mathbf{e}})}{\partial \alpha} = \mathbf{e^T M}\frac{\partial \mathbf{e}}{\partial \alpha} + \dot{\mathbf{e}}^{\mathbf{T}}\mathbf{N}\frac{\partial \dot{\mathbf{e}}}{\partial \alpha} \tag{3.39}$$

where P, Q, M, N are n-square matrices related by: $\mathbf{M} = \mathbf{P} + \mathbf{P}^{\mathrm{T}}$ and $\mathbf{N} = \mathbf{Q} + \mathbf{Q^T}$. Combination of equations 3.36 and 3.38 gives:

$$\begin{aligned} \tfrac{\partial J(\mathbf{e})}{\partial \alpha} &= \mathbf{e^T M}\tfrac{\partial \mathbf{e}}{\partial \alpha} + \dot{\mathbf{e}}^{\mathbf{T}}\mathbf{N}\left(\mathbf{A_r}\tfrac{\partial \mathbf{e}}{\partial \alpha} + \tfrac{\partial \mathbf{G}}{\partial \alpha}\mathbf{x}\right) \\ &= \mathbf{e^T M}\tfrac{\partial \mathbf{e}}{\partial \alpha} + \dot{\mathbf{e}}^{\mathbf{T}}\mathbf{N}\mathbf{A_r}\tfrac{\partial \mathbf{e}}{\partial \alpha} + \dot{\mathbf{e}}^{\mathbf{T}}\mathbf{N}\tfrac{\partial \mathbf{G}}{\partial \alpha}\mathbf{x} \end{aligned} \tag{3.40}$$

For mathematical convenience **M** and **N** are replaced with

$$\mathbf{M} = \mathbf{W\dot{e}I_r A_r} \text{ and } \mathbf{N} = -\mathbf{WeI_r}, \tag{3.41}$$

and then the gradient optimisation equation becomes:

$$\frac{d\alpha}{dt} = \gamma\frac{\partial J(\mathbf{e})}{\partial \alpha} = -\gamma\dot{\mathbf{e}}^{\mathbf{T}}\mathbf{We}\frac{\partial \mathbf{G}}{\partial \alpha}\mathbf{x} \tag{3.42}$$

where $\mathbf{I_r} = [\mathbf{1\ 1\ 1}]$ and **W** is a diagonal normalisation matrix. **W** is derived from the maximum amplitudes of the errors in the adaptation channels. For the single degree-of-freedom suspension system, α assumes three adaptive gains adk_P, adk_V, and adk_A, and **W** (with an additional scaling parameter w) being given by

$$\mathbf{W} = \begin{bmatrix} w\frac{1}{max(e_1)} & 0 & 0 \\ 0 & w\frac{max(e_1)}{max(e_2)} & 0 \\ 0 & 0 & w\frac{max(e_1)}{max(e_3)} \end{bmatrix} \tag{3.43}$$

Substitution of the values of **G** from Eqn. 3.36 and its partial derivatives with respect to the three feedback gains k_P, k_V and k_A in Eqn. 3.42 generates the following three first order differential equations for adaptive feedback parameters

$$\begin{aligned} \tfrac{d}{\mathrm{dt}}(adk_P) &= -\gamma\dot{\mathbf{e}}^{\mathbf{T}}\mathbf{We}\tfrac{g_P}{L_O}x_1 \\ \tfrac{d}{\mathrm{dt}}(adk_V) &= -\gamma\dot{\mathbf{e}}^{\mathbf{T}}\mathbf{We}\tfrac{g_V}{L_O}x_2 \\ \tfrac{d}{\mathrm{dt}}(adk_A) &= -\gamma\dot{\mathbf{e}}^{\mathbf{T}}\mathbf{We}\left(\tfrac{g_A k_z}{mL_O}x_1 - \tfrac{g_A k_i}{mL_O}x_3\right) \end{aligned} \tag{3.44}$$

where g_P, g_V and g_A are the gains to the corresponding sensors (voltage/physical unit). Integration of Eqn. 3.44 produces the adaptive gains required to minimise the performance criterion in Eqn. 3.37.

3.3.1 Implementation of the adaptive algorithm

The above adaptive control algorithm was implemented on the software control environment for transputers according to the interconnection diagram in Fig. 3.7. The open-loop

model represents the magnet which produces the two state variables (position $z(k)$ and acceleration $\ddot{z}(k)$). These signals are converted to digital values via the ADC/DAC module (Chapter 2, Fig. 2.9), where the I/O transputer pre-process and passes them via link port#1 to the MAIN transputer. The software on the MAIN transputer receives current state-variables, generates the velocity by integrating the acceleration, and produces the state vectors $x(k)$ and $\dot{x}(k)$. Using the three state variables it generates a control signal based on the state feedback controller law with feedback gains as given in Chapter 2, Section 2.7. Simultaneously, the secondary transputer (Fig. 2.10) using the current reference position $z_{ref}(k)$ generates the three state variables corresponding to the reference system $\mathbf{x_r(k)}$. This reference model is the discrete transformation of the state space model derived in Eqn. 2.18, Chapter 2

$$\begin{array}{ll} \mathbf{x}(k+1) & = \Phi\mathbf{x}(k) + \Gamma z_{ref}(k) \\ \mathbf{y}(k) & = \mathbf{C}\mathbf{x}(k), \end{array} \tag{3.45}$$

where the matrices Φ, Γ, and $\mathbf{C}$ are

$$\begin{aligned} \Phi &= \begin{bmatrix} 1.000 & 3.99 \times 10^{-4} & -8.4192 \times 10^{-7} \\ -1.1177 \times 10^{-2} & 9.9192 \times 10^{-1} & -3.7032 \times 10^{-3} \\ 2.6275 \times 10^{2} & 2.3687 & 4.3548 \end{bmatrix}, \\ \Gamma &= \begin{bmatrix} 8.3015 \times 10^{-5} \\ 5.8466 \times 10^{-1} \\ -1.8908 \times 10^{2} \end{bmatrix}, \text{and } \mathbf{C} = \begin{bmatrix} 1 & 0 & 0 \\ 0 & 1 & 0 \\ 2000 & 0 & -13.6 \end{bmatrix} \end{aligned} \tag{3.46}$$

The reference state variables are transferred back to the MAIN transputer to calculate the error signals $\mathbf{e}(k)$, and $\dot{\mathbf{e}}(k)$ (Eqn. 3.35). Eqn. 3.44 is then used to derive the adapted feedback gains adk_P, adk_V, and adk_A using

$$\mathbf{W} = \begin{bmatrix} \frac{1}{4\times10^{-6}} & 0 & 0 \\ 0 & \frac{1}{1\times10^{-2}} & 0 \\ 0 & 0 & \frac{1}{50} \end{bmatrix}. \tag{3.47}$$

These adapted gains are further integrated and used as feedback gains (k_P, k_V, and k_A) to the system as shown in Fig. 3.7.

3.3.2 Results

From operational viewpoints, a Maglev system should ideally possess infinite suspension stiffness, that is the airgap error should be zero for any changes in operating conditions or any external disturbance. For example, a change in suspended mass will induce a change in the model, consequently with a non-adaptive controller the steady-state error in airgap will change from its nominal design value. Although the Maglev system is designed with

a rated suspended mass at the nominal operating point, changes in passenger loading (in full-scale vehicles) are to be expected. The suspension magnet may be moved from its ideal linear design range to the non-linear parts of its magnetising curve. To compensate for this, the adaptive technique was designed to keep the system's state variables close to those reference model, regardless of disturbance inputs. The algorithm was tested for two classes of disturbance: additional force disturbance applied to the magnet and additional mass applied and removed from the magnet. The results are shown in Figs. 3.8, and 3.9. Fig. 3.8 shows the response of the magnet in terms of air-gap due to a step change of 5kg mass applied. On the top is the non-adaptive response, where only state feedback controller is presented, and at the bottom is the system's response when a model reference adaptive technique is activated. As a consequence of the error appearing between the system's state variables and those coming from the reference model, the algorithm changes the feedback gains in order to minimise the error. This error reduces to zero two seconds after the disturbance input has been applied.

The same experiment was performed for force disturbances. The variation of airgap due to a step change of 50N force applied to the magnet is shown in Fig. 3.9. The top response corresponds to variation in the suspension airgap using the ordinary state-feedback controller. The bottom response corresponds to airgap change corresponding to the adaptive controller. Due to the minimisation in the error criteria, the feedback gains are adapted to control the suspension airgap to the reference level.

In the adaptation rule, the parameter γ (Eqn. 3.44) determines the rate of adaptation of the feedback gains. For large values of γ the system adapts faster and reacts quicker to external disturbances. For very large values of γ, however, the overall behaviour might become sensitive to disturbances and the value has to be derived in accordance to the operating conditions. Due to the considerable number of floating point calculations involved in the calculation of the above adaptation rule, the minimal sampling time achieved on the transputer-based hardware is 400 microseconds. For multi-magnet applications, either more transputers have to be added to the multiprocessing environment or new computational units delivering better processing power have to be chosen. The latter is followed up in Chapter 4.

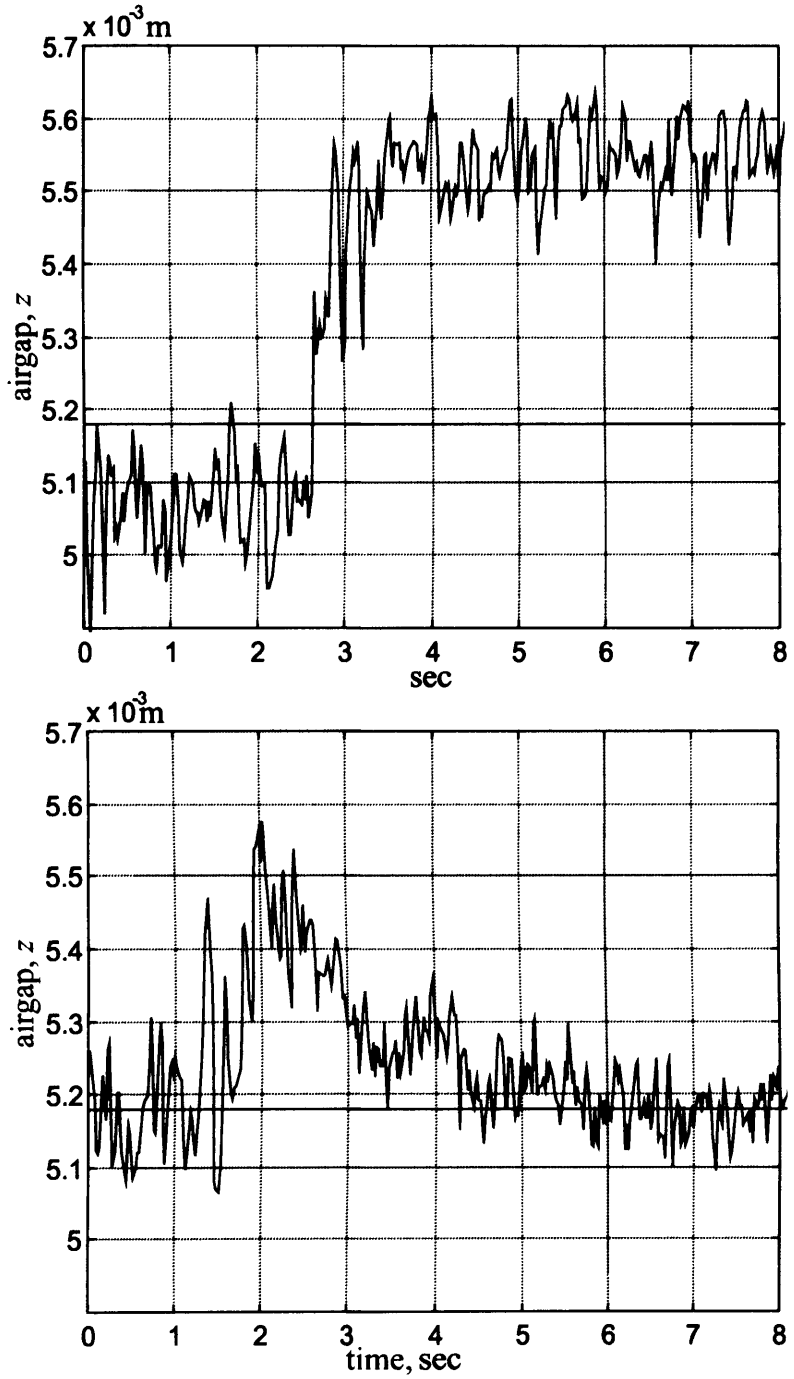

Figure 3.8: Transient responses of airgap due to a step change of 5kg mass (300% mass change) with 400μs sampling time (nominal operating point set at 5.1 mm and 1.8A), and transputer-based system: top non-adaptive system (linear state feedback control law); bottom: adaptive system.

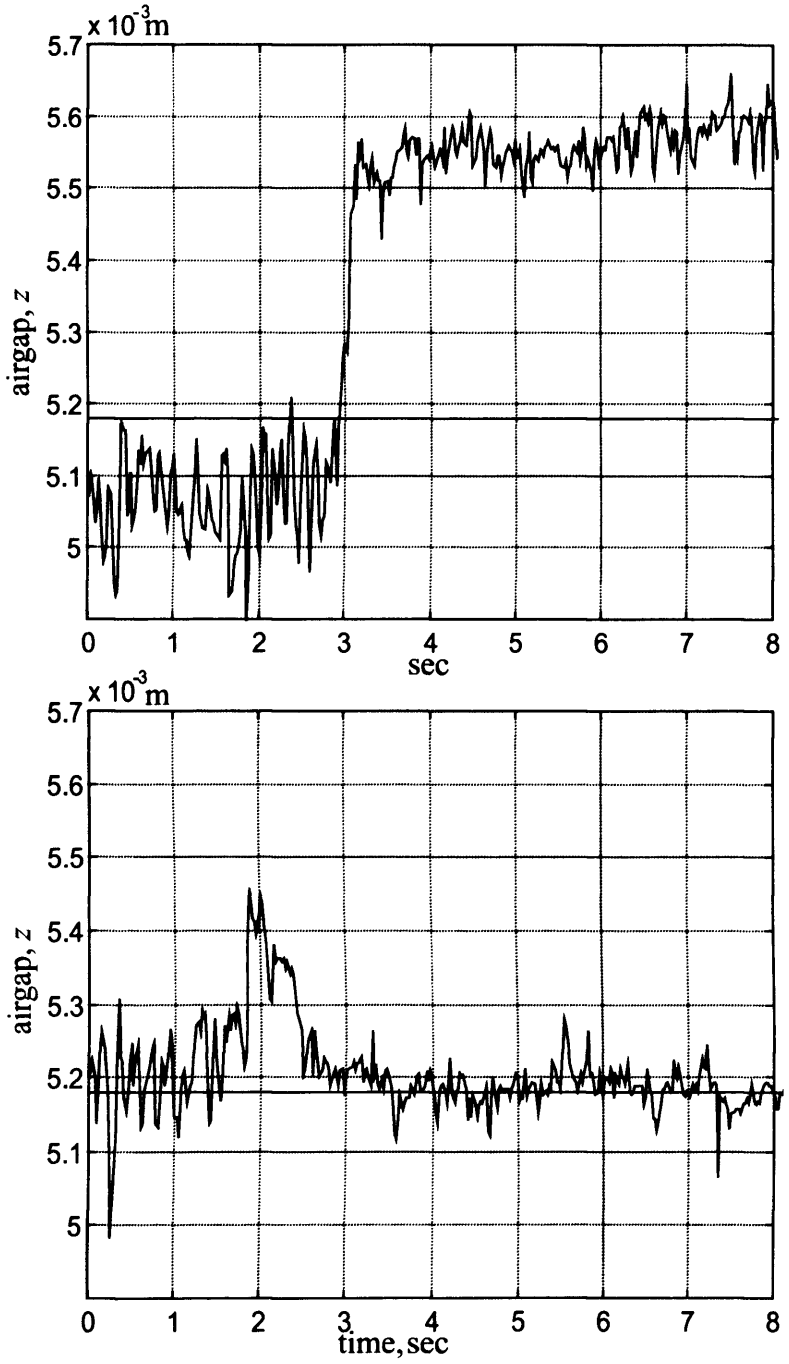

Figure 3.9: Transient responses of airgap due to a step change of force with (nominal operating point set at 5.1 mm and 1.8A) 50N force and transputer-based controller with 400μs sampling time. Top: linear state feedback controller (non-adaptive); bottom: adaptive controller.

Chapter 4

DSP environment for Maglev control

4.1 Digital signal processors

Since the introduction of the transputer, several semiconductor manufacturers have developed more advanced processors under the generic name of digital signal processors (DSP). Although some of these are comparable in performance with the new T-9000 from Inmos/SGS Thomson, the decision of SGS not to volume manufacture (and more recently to discontinue) the T-9000 processor left the whole field of multiprocessor DSPs to manufacturers such as Texas Instruments, Analog Devices, Motorola and other US/Japanese companies. As discussed in earlier chapters, because of instability of the Maglev system without any feedback and the relatively small time constants inherent in the system, the control technique requires a high signal processing bandwidth and hence a fast processor. After assessing the performance of different processors to substitute the transputers as the computational unit in the control framework, the ADSP-2106x family of SHARC DSPs from Analog Devices was chosen in early 1998 for the new generation of control hardware for Maglev.

Model	Memory	Links	Performance	Frequency	Supply	Package
ADSP-21060	4 MBit	6/4bit	40MIPS, 120MFLOPS	33, 40MHz	3.3, 5V	240-LEAD PQFP
ADSP-21061[1]	1 MBit	0	40MIPS, 120MFLOPS	33 -50MHz	3.3, 5V	240-LEAD PQFP
ADSP-21062	2 MBit	6/4bit	40MIPS, 120MFLOPS	33, 40MHz	3.3, 5V	240-LEAD PQFP
ADSP-21065[2]	0.5 MBit	0	60MIPS, 180MFLOPS	50, 60MHz	3.3V	208-LEAD PQFP
ADSP-21160[3]	4 MBit	6	600 MFLOPS	100MHz	2.5, 3.3V	400-BALL PBGA

Table 4.1: Summary of main features of SHARC-DSP devices.
NOTES:
1: This is the processor used in the DSP-based control hardware.
2: This DSP is not code-compatible with the SHARC family and has some functional differences as glue-less connection to an external SDRAM memory.
3: This DSP is the latest version of the family. It is still at the sampling stage(when this chapter was written) and is not fully code-compatible with the other members.

The SHARC family of DSPs consists of four members (mid 1999): ADSP-2106-0, 1, 2, 5 [44, 45](Table 4.1). The first three are code-and function-compatible differing only in internal memory size, where the latest version ADSP-21065 is a low cost version of the family having few functional differences. The SHARC DSPs are 32-bit floating-point devices, where SHARC stands for Super Harvard ARChitecture [44]. Together with their high performance, 40 MIPS and 120 MFLOPS, these DSPs have the ability to be connected in a multiprocessor configuration (120MFLOPS peak performance and 80MFLOPS is sustained performance). Two schemes for multiprocessing are integrated within the SHARC architecture: clustering multiprocessing and point-to-point multiprocessing via links. The first scheme allows up to six signal processors and a host processor to share a common address space, where the distributed bus arbitration logic is included on-chip. At any instant of time one of the processors acts as a bus-master and owns the bus. The maximum throughput for data transfer is 240 Mbytes/sec. In the second scheme, the SHARC DSP features six four-bit wide serial link ports for point-to-point (device to device or processor to processor) communication. These links pass code and data (in a manner similar to the transputer links) and can operate independently and simultaneously from the DSP's processor unit with a maximum data throughput of 240 Mbytes/sec (40 Mbytes/sec per link). Factors such as high processing power and multiprocessing ability influenced the choice of this family of DSPs as an alternative to transputers for the new Maglev control environment.

4.2 DSP based hardware

Due to the transfer to the new processing platform for Maglev, new hardware had to be developed, the three main modules of this hardware are identified in Fig. 4.1: DSP-based processing module, an interface module, and an I/O module. The DSP-based processing module carries a digital signal processor, and a communication link with a host computer. The interface module integrates analogue I/Os as well as digital I/Os, and interface different transducers. A brief description is given below.

At this early stage of developing a DSP-based control framework for Maglev, a commercial processing module EZ-KIT Light is being used [46]. The board carries one ADSP-21061 32-bit floating-point signal processor, which is the link-less member of the family and performs cluster-type of multiprocessing (Table 4.1). The DSP contains 1Mbits dual-ported internal SRAM memory, featuring single cycle access (25ns at 40MHz clock-rate). The

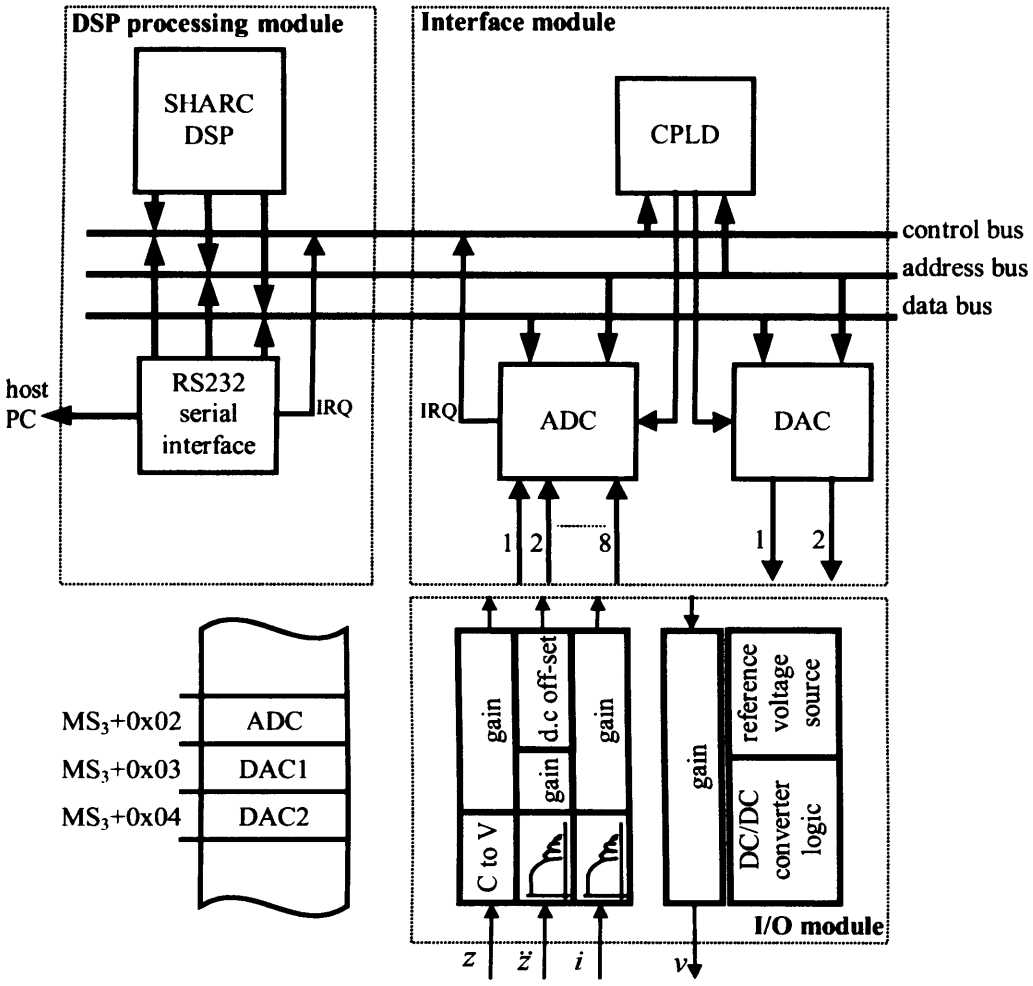

Figure 4.1: DSP-based control hardware for Maglev. The main blocks are: DSP processing module, interface module, and I/O module. The memory map is also shown with address location of the converters.

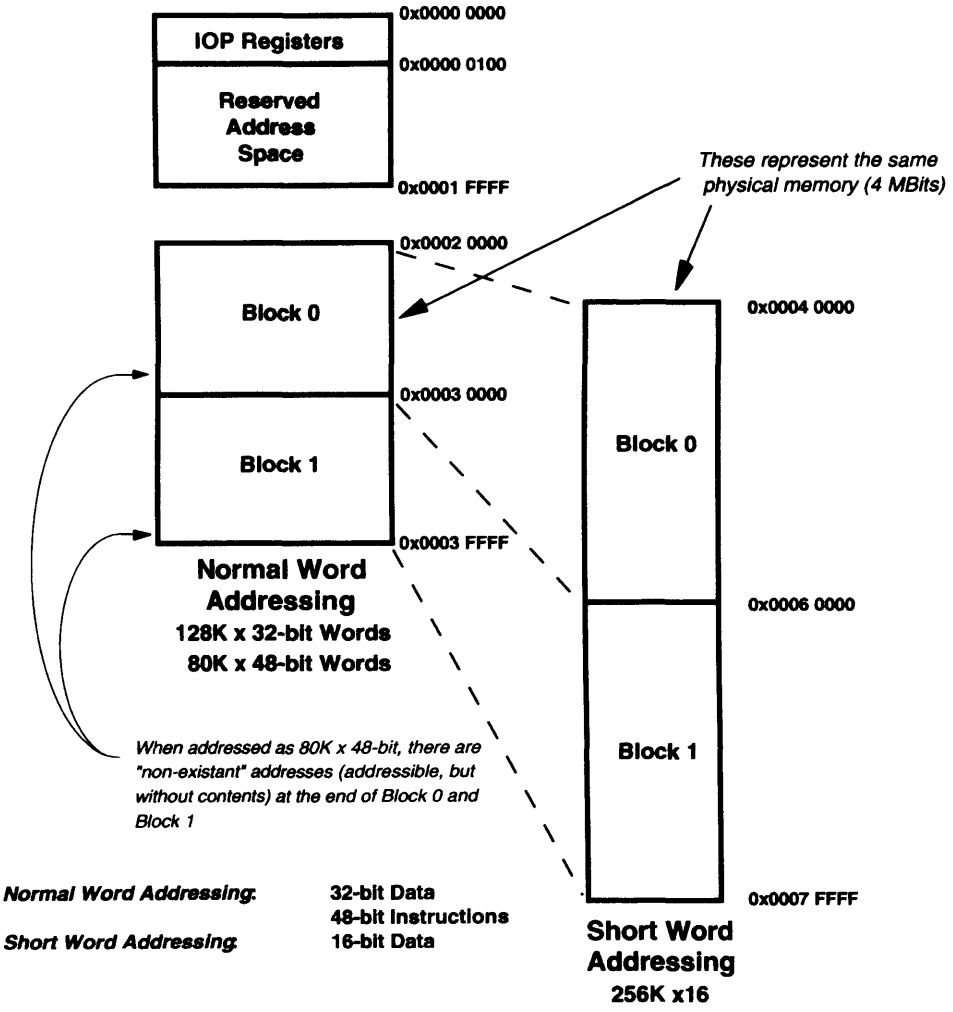

Figure 4.2: DSP's internal memory space (figure taken from [44]).

real-time control software is located within this memory which is organised as two blocks configured for program and/or data (Fig. 4.2). The board communicates with a host computer (PC) through a serial (RS-232) channel with speed up to 115200b/sec. A software kernel, located on an EPROM populated on the board, is responsible for the data communication with the host as well as booting the DSP (to download program from the host to the DSP's internal memory) and to pass data to and from the host [46]. Fig. 4.2 shows the organisation of the DSP's internal memory.

An interface board was especially designed and developed to facilitate interfacing to different transducers required for the Maglev control model (see Section 2.2, Chapter 2). This module connects to the EZ-KIT module, and carries an analogue-to-digital converter (ADC), a digital-to-analogue converter (DAC), digital input/outputs, glue logic, and a DC-DC converter (Fig. 4.1). These devices are memory mapped to the DSP's address space and pass data via the processor's data bus. A programmable logic chip (Lattice ispLSI1016-80 complex programmable logic device CPLD [47]) was especially programmed to synchronise the converters with the signal processor. The converters are memory mapped into the processor's external memory space and the CPLD control logic manages the memory access. The external memory space is shown in Fig. 4.1, where the ADC is located on address MS3+0x02, and the DAC on MS3+0x03 and MS3+0x04. The base memory address MS3 is chosen from the initialisation software ([44, 45] describes in details the memory configuration).

The analogue-to-digital converter is an 8-channel 12-bit data acquisition system (AD7891AP-1, [48]) from Analog Devices. This high-performance converter accepts ± 5 V and ± 10 Volts on its channels and converts this data to its digital equivalence with a maximum sampling rate up to 454 kSPS (kilo samples per second). This allows running the control algorithm at a maximum sampling frequency of 50 kHz. The conversion takes 2.2μs and the device is interrupt driven. At every interrupt, the DSP triggers a software routine which reads the transducers' data and initialises the ADC for the next sample. In the work described here, three channels are used for measuring the position, the acceleration and the magnet current.

Two 12-bit parallel-loading digital-to-analogue converters (AD667JN [49]) were integrated on the module to produce unipolar or bipolar control signals (+5, +10, ± 2.5, ± 5, ± 10 volts) with an output settling time of 3μs (conversion time). The conversion is scheduled by the DSP by writing to the registers of the DAC at every control sample.

4.3 DSP software for Maglev control

In contrast to the event-driven architecture of the transputers, the DSP control work is interrupt driven with a pre-specified interval arrangement. The software serves two interrupts: from the internal DSP timer and from the ADC. The internal timer is used to generate the sampling time for the controller. The resolution is 25ns and is adjusted according to the controller's bandwidth. Once the ADC is configured, it will generate interrupts at a pre-defined interval which will be served by the DSP. Typical values are from $200\mu s$ to $1ms$ for the magnet used in this chapter. The minimal configuration for state-feedback control requires inputs for the position and acceleration signals. The DSP integrates digitally the acceleration to produce the velocity of the magnet. A first order filter is used

$$\dot{z}(k) = a_0\dot{z}(k-1) + b_0\ddot{z}(k). \tag{4.1}$$

For 200 μs sampling time, the coefficients are: $a_0 = 0.992063$, $b_0 = 198.4123 \times 10^{-6}$ to give a pole at $(-20 \pm j0)$.

The communication between the host computer and the DSP is accomplished by the kernel on the DSP board [46]. The host provides a buffer of data and a pointer to the DSP memory used for reading or writing. This mechanism is also used for booting during program loading. For the analysis of experimental Maglev data, the DSP would update two data buffers: experimental data such as position, velocity, current, acceleration, force estimation, control output, etc. and controller coefficient vectors updated from the host such as desired position value, sampling time and feedback gains. These two buffers are updated at every sampling interval (200 μs). On the host side, the software environment for Maglev developed in Section 2.6, Chapter 2 was further extended to work with the DSP-based control framework.

4.4 Control algorithms ported to DSP-based control framework

When porting control algorithms from the transputer environment to the DSP, the primary concern was that the software distributed on the three transputers had to be organised as a single-processor environment. Although there are several tasks which need to be executed concurrently within one single DSP to make the control software multitasking, the task switching was implemented using interrupts.

4.4.1 State-feedback control

The initial control work on the DSP uses the state-feedback controller from Chapter 2, Section 2.3. Using the same feedback gains, the response in changing the desired reference airgap is shown in Fig. 4.3. The sampling time of the controller was set to 100 μs. The response offers good suspension damping and is seen to be comparable with that of the transputer-based control, giving some assurance about the satisfactory operation of the new DSP hardware for Maglev control. The main benefits of the DSP-implementation vs. transputer-implementation are: (a) the whole framework is implemented on a single processor which reduces the development effort, and (b) the sampling time is fixed by the timer interrupt and hence very low jitter ($< 25ns$) is expected. Various experimental studies indicated that the absolute minimum time required for the implementation of the state feedback control law is around 10μs. The dynamic characteristics of the single-magnet system described here allow sampling time of 1ms to include an additional time-slot for the more computationally-demanded control algorithms described in the following chapters.

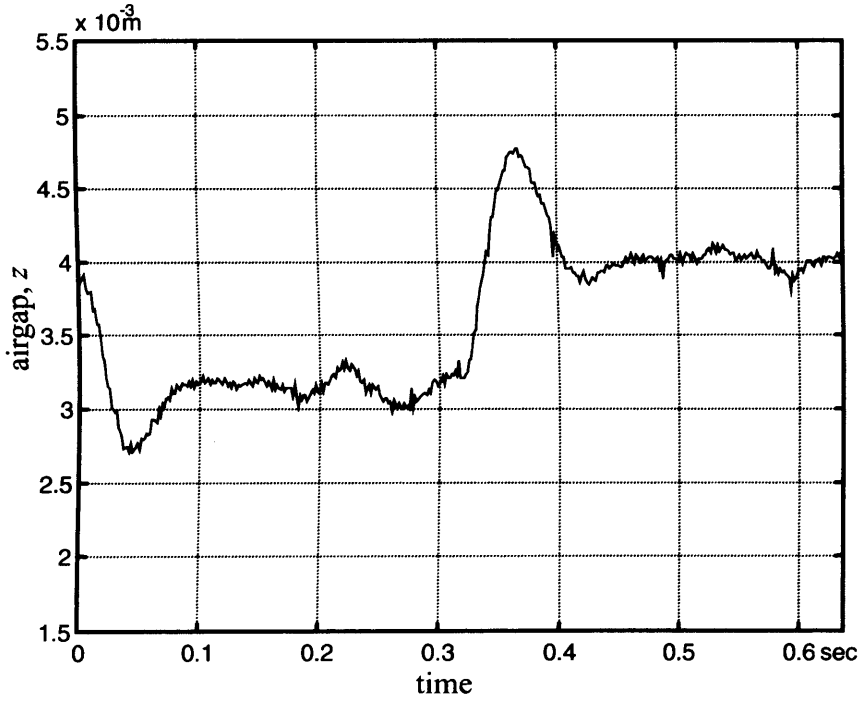

Figure 4.3: State feedback controller implemented on the DSP-based hardware. At time $t = 0$ sec a step in the desired position $z_{ref} = 3.0$mm is applied and at time t=0.3 sec a second step of $z_{ref} = 4.0$mm is applied. Similar response from the transputer-based control is shown in Fig. 2.12. The feed-back gains are $k_P = 20833$; $k_V = 250$; $k_A = 4$, as in Fig. 2.12, Chapter 2.

4.4.2 Adaptive pole-placement control

As mentioned in the transputer section (Chapter 3, Section 3.2), because of the relatively intensive computations needed in the adaptation algorithm, satisfactory results with transputer-based hardware were not obtained. By increasing the processing power with the DSP, the sampling time was reduced to 200 μs (vs. 950μs required for the transputer algorithm, Section 3.2). The general configuration of the adaptive pole-placement controller is shown in Fig. 3.6, page 40. On the DSP, all tasks are executed on a single processor. The algorithm initially uses the state feedback gains derived in Section 4.4.1. In parallel with the controller, the adaptive pole-placement algorithm is executed. At every sample, the control signal $v(k)$ and the airgap position $z(k)$ are used in the procedure developed in Chapter 3, Section 3.2. The characteristic function $T(z^{-1})$ used in the specification of the Diophantine equation are: $z_1 = 0.08850$, $z_2 = 0.9715 + j0.0850$, and $z_3 = 0.9715 - j0.0850$. The corresponding s-domain poles are located at -12326, -126+j436, and -126-j436. The response of the suspension airgap using the adaptive pole-placement technique is shown in Fig. 4.4. As the main emphasis in the algorithm is to attenuate undesired disturbance effects in the suspension system, two step inputs in force disturbances were applied (marked with the two arrows on the time axis). The first input added a disturbance with amplitude of 120N to the suspended system, and the second one removed this force disturbance from the suspended system. Based on the adaptation rule, the algorithm modifies the feedback gains in the controller to minimise the error in the airgap position. With a desired position value of z_{ref} = 3mm, a 120N force input changes the airgap to nearly $z(k)$=5.0 mm. As a consequence of the adaptation loop, this error is decreased to zero within one second, equal to 5000 identification cycles. Within these cycles, the least square algorithm identifies the system (Eqn. 3.29, Chapter 3) and updates the feedback gains. For comparison, similar responses are explored in the next section, where the DSP-based system with a model reference control technique is given for force disturbance equal to 100 N. Although the compensator is able to reduce the error to zero after the disturbance is applied to the suspension system, for some applications this might lead to instability due to outputs saturating the airgap transducers. This can be overcome by using controllers with better stiffness. The corresponding minimum sampling time for overall stability has to be carefully chosen in relationship with λ and the location of the closed-loop poles. Limitation is also considered so that there is no a direct mapping between the desired and the actual poles of the system due to linearisation errors and approximations in the design.

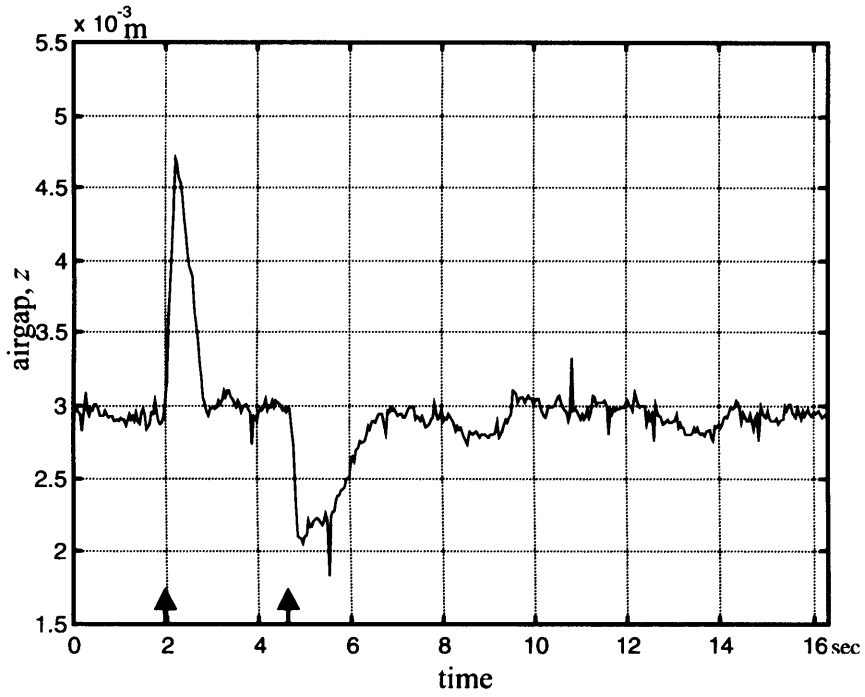

Figure 4.4: DSP-based system with an adaptive pole-placement controller. The sampling time is equal to 200μs. The first arrow shows when a step disturbance of 120N force is applied. The next arrow shows when this disturbance is removed.

4.4.3 Model reference control

Model reference control was also implemented on the new DSP control hardware. The various tasks distributed on three transputers had to be reorganised and run on a single DSP. These tasks are shown graphically in Fig. 3.7 (Chapter 2) and are generalised as follows. Generate the model states $\mathbf{x_r(k)}$; using the error signal (Eqn. 3.35) calculate the adaptive gains *adkx* (Eqn. 3.44), and update an existing state feedback controller using these gains. At every sample (generated from a timer interrupt) the DSP calculated the mathematical reference model to generate the state variables: $\mathbf{x_r(k)}$. In addition, the state variables from the system $x(k)$ are prepared. The vector of error signals is produced using Eqn. 3.35, and Eqn. 3.44 is used to calculate the adapted state-feedback gains.

To check the reaction of the system to disturbance inputs applied to the suspended magnet, two sets of experiments are used: additional mass disturbance input and additional force disturbance. The response of the magnet in terms of air-gap due to a step change of 5-kg mass (300%) is shown in Fig. 4.5. The non-adaptive response using ordinary state feedback is shown on the top. On the bottom is shown the system's response when a model reference adaptive technique is activated. As a consequent of the difference between the system's states and the reference model, the algorithm adapts the feedback gains to

minimise this error. The system approaches the reference model within two seconds after the mass disturbance is applied. The transient responses in airgap due to a step change

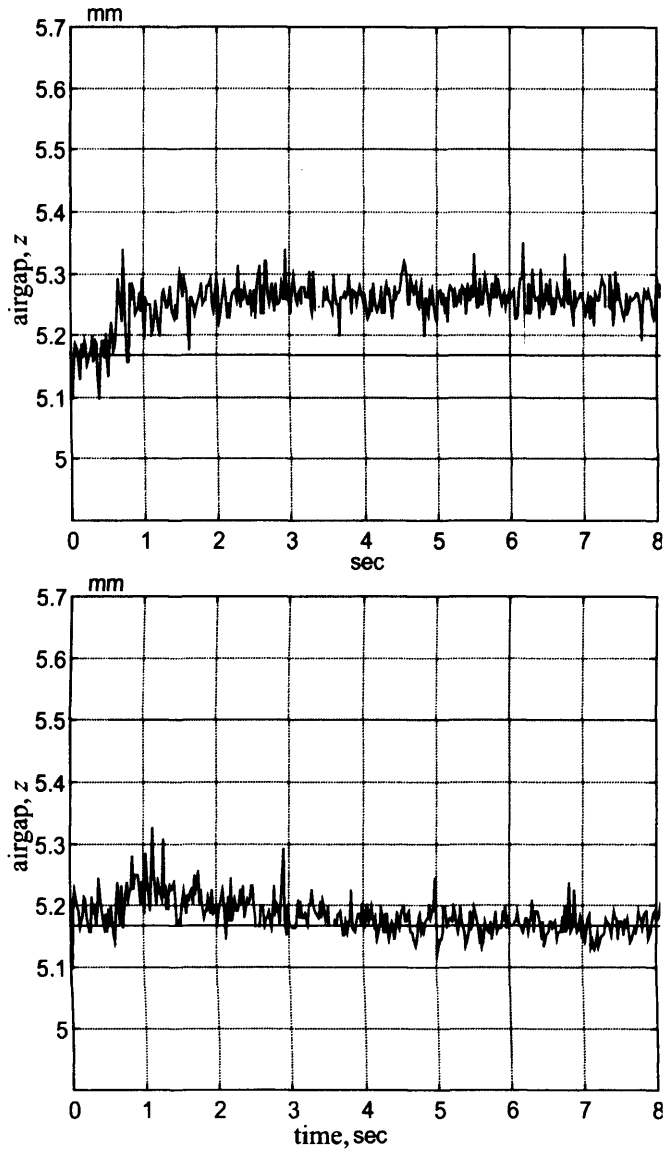

Figure 4.5: Transient responses in airgap due to a step change of 5kg mass (300% mass change) with 400μs sampling time (nominal operating point set at 5.2mm and 1.8A). DSP-based system, where the top is a non-adaptive system and bottom is an adaptive system.

of 50 N force disturbance with nominal operating points z_0=5.2 mm and i_0=1.8 is shown in Fig. 4.6. The top response uses an adaptive controller with 400 μs sampling time. To compare the effect of the sampling time, the bottom figure shows the response of the same controller with 200 μs sampling time for 100 N force disturbance. The first experiment was performed to compare the response of the system with those from the transputers (Fig. 3.9). The second experiments show how the increased processing power when the DSP is used, reducing the sampling time (200μs), gives an improvement in the overall behaviour that is capable of taking two times larger disturbances due to the increased stiffness of the overall

system.

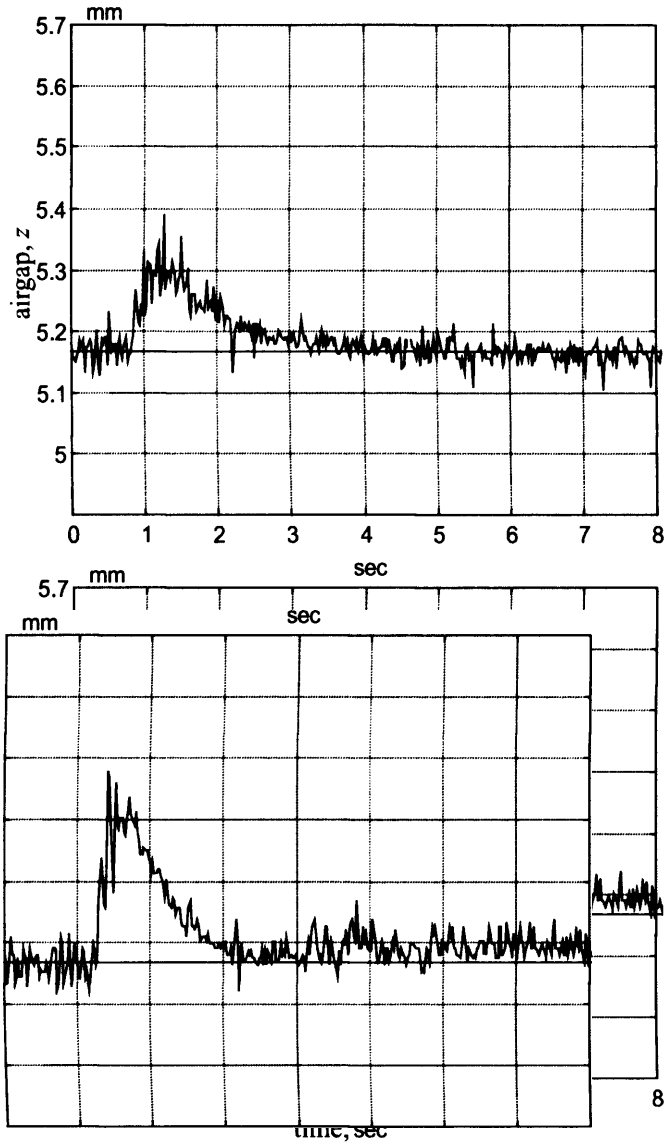

Figure 4.6: Transient responses in airgap due to a step change of force with (nominal operating point as in Fig. 4.5). DSP-based adaptive controller, where the top is an adaptive controller with $400\mu s$ sampling time for 50N step force disturbance, and bottom is an adaptive controller with $200\mu s$ sampling time for 100N step force disturbance.

The parameter γ (Eqn. 3.42) determines the adaptation rate. To demonstrate the effect of this parameter, a set of experiments was performed as demonstrated in Fig. 4.7. In Fig. 4.7(a) the transient response of airgap is shown with a step change of 10 kg extra-added mass to the suspended system. The top figure shows a non-adaptive system, where the top-down responses are shown with different values for γ: 19.25, 38.5, 77.0 and 144.0. In Fig. 4.7(b) the same experiment is performed where the disturbance applied to the system is a step change of 100 N force. Again the top figure shows a non-adaptive system, and top-down adaptive system with different values for γ (as Fig. 4.7(a)). Large values of γ con-

siderably reduce the adaptation time. Large values of γ, however, effect the sensitivity in the adaptation to disturbances and the value has to be chosen for a given boundary of disturbances. Compared to the transputers, the DSP-based control system was observed to be capable of managing disturbances of two times higher amplitude (Fig. 4.6 vs. Fig. 3.9) compared with the transputer-based system. This attribute comes from the reduced sampling time(200μs for the DSP vs. 400μs for the transputer) which effects the rate of adaptation. As in the case of the state-feedback controller, various experiments indicated that the 200 μs sampling time is not the absolute minimum. Experiments with sampling times down to 150 μs were performed and the value of 200 μs was chosen based on the factors as indicated in the state feedback section. Analysis of the various experimental responses indicates that the responses from the adaptive pole placement controller demonstrate less stiffness than those from the model-reference control. In the first case the force disturbance with 100 N amplitude introduces 1.75 mm of static error (see Fig. 4.6, the first response) while with the latter controller the error was only <0.5 mm.

Since the suspension balance is driven by a force balance, the vertical acceleration signal is most sensitive to external disturbances with acceleration gain being the most responsive during adaptation (from 25% to 250% change from its initial value). k_v has varied within $\pm$25%, while k_p has varied only 5% from its initial value. Several factors may influence the choice of the reference model including the amount of energy available for the adaptation by the magnet's lift-force rating and the available current supply from the power amplifier. The operating conditions for the reference model have been chosen in the linear part of the force-current characteristics. The adaptation rule thus can return the airgap of the suspended system to that of the reference model for large variations in the operating conditions. For large variation within the nonlinear part of the force-airgap characteristics, a family of pre-stored models or a nonlinear model can be used.

4.5 Fuzzy logic control

This section develops a fuzzy controller design framework for Maglev. A range of experimental results are presented to compare the transient performance of three types of fuzzy controller: (i) position error and velocity inputs fuzzified with a single control rule table plus constant gain acceleration feedback, (ii) all three state feedback signals fuzzified but position error and velocity having one control rule table and position error and acceleration having a separate control rule table, and (iii) a single control rule table for all three fuzzified

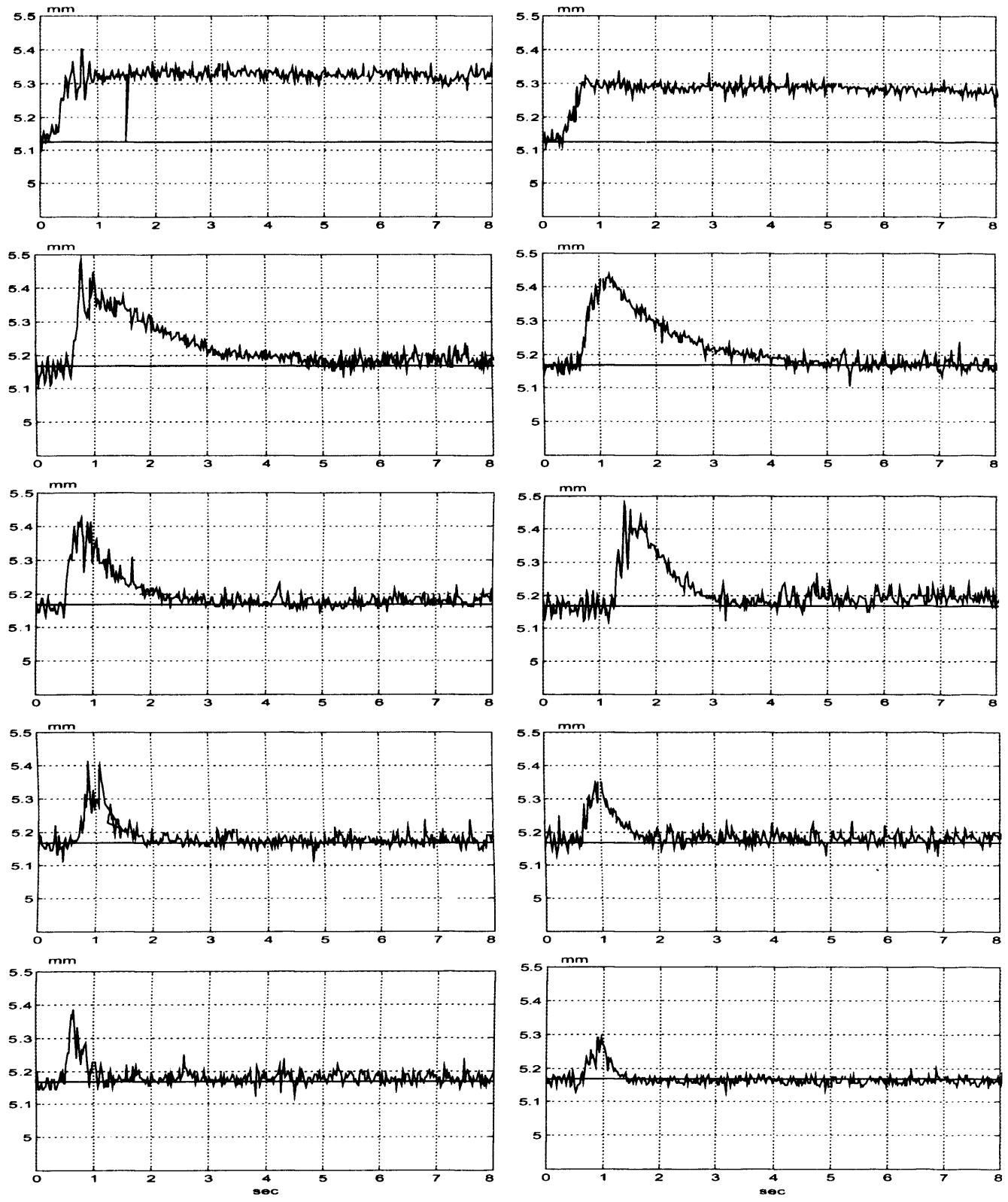

Figure 4.7: Transient responses of airgap with DSP-based controller for four different values of γ. Top: state feedback controller without any adaptation, then top-down adaptive loop where the values of γ are: 19.25, 38.5, 77.0 and 144.0. Nominal operating parameters are z_0=5.2; i_0=1.8A; step changes in mass and force are as indicated in (a) and (b). Sampling time was set at 200μs for all experiments.

input signals.

The three stages of fuzzy controller design are fuzzification, inference and defuzzification (Fig. 4.8) [50, 51, 52, 53, 54, 55]. Fuzzification is a process of converting each signed real-valued input signals into one or more degrees of linguistically defined membership functions defined over each *fuzzy set*. This is done by dividing the full scale range of each input (feedback) signal into several (typically five or seven) quantised levels identifiable by linguistic descriptions of like small, very small, etc, and then superimposing one or more (typically, two) membership functions on each quantised level as in Fig. 4.9. The choice of these membership functions is arbitrary. L-functions (triangular shapes) are widely used in the literature [50, 54, 51].

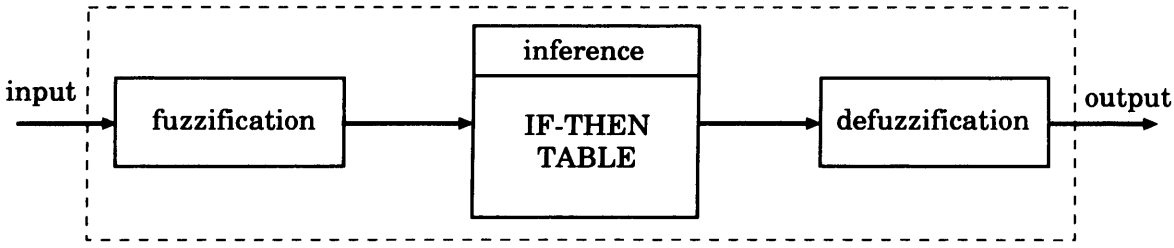

Figure 4.8: Internal structure of a fuzzy controller. The sequence of operations are: fuzzification of the numerical inputs (*input*) for producing fuzzy outputs; inferring a *fuzzy Output* from a list of IF-THEN rules; producing a numerical output (*output*) from this *fuzzy Output.*

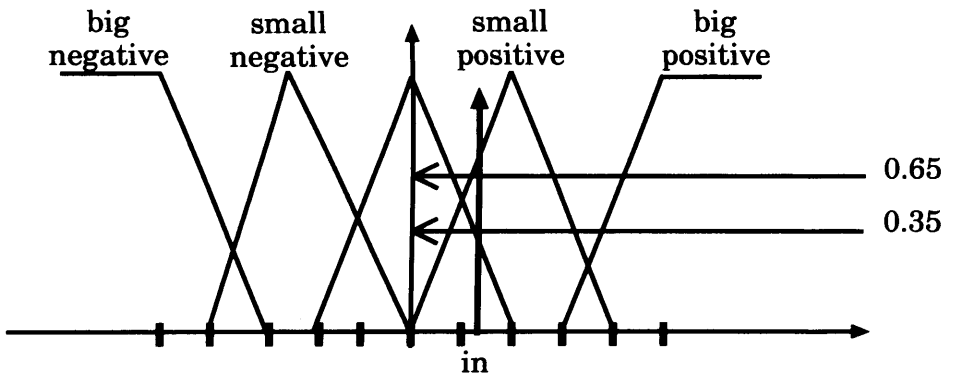

Figure 4.9: Membership functions of the input. Numerical input (in) is converted to two fuzzy sets (*zero* with degree of membership 0.35 and *small positive* with 0.65 degree of membership).

Fuzzy inference consists of one or more fuzzy control rule tables (also known as control tables) and a collection of fuzzy inference rules. A control table describes the cause-effect (IF-THEN) relationship of the system's inputs and outputs. These are linguistic description of desired control input into the system for all possible combinations of the fuzzified

Operation	Notation	
NOT	$\mu_{\overline{A}}(u)$	$\mu_{\overline{A}}(u) = 1 - \mu_A(u)$
AND	$\mu_{A_1 \cap A_2}(u)$	$\mu_{A_1 \cap A_2}(u) = min\{\mu_{A_1}(u), \mu_{A_2}(u)\}$
OR	$\mu_{A_1 \cup A_2}(u)$	$\mu_{A_1 \cup A_2}(u) = max\{\mu_{A_1}(u), \mu_{A_2}(u)\}$

Table 4.2: Operations over fuzzy sets

feedback. For a Maglev controller, a typical set of IF-THEN rules is given below (from Section 4.6.1).

```
    IF the airgap error is zero AND the the airgap velocity is negative
    small THEN the output is small
OR  IF the airgap error is negative small AND the airgap velocity is
    zero THEN the the output is big
OR  . . .
```

Logical operations (AND,OR and NOT) are also performed with fuzzy sets. These combine inputs in the antecedent part of the IF-THEN rules, and outputs in the consequent part. Since fuzzy sets are defined by their membership functions, the logical operations are performed over the membership functions. There are a few different ways to represent fuzzy operations [54], where the most commonly used are listed in Table 4.2 (A, A_1, and A_2 are fuzzy sets). The notation $\mu_A(u)$ describes the membership function and takes values in the interval [0,1].

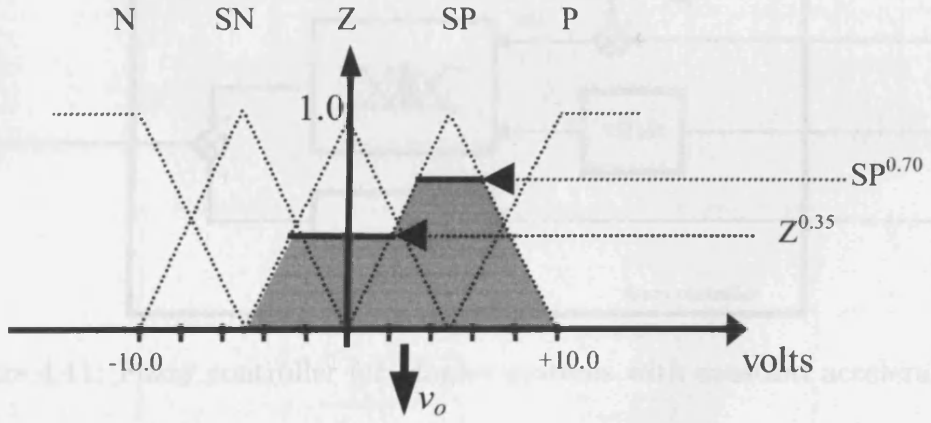

Figure 4.10: Membership functions of the output.

As with the input signals, the full scale range of the control output is also quantised with superimposed membership functions as in Fig. 4.10. The fuzzy inference operations (IF-THEN rules) identify one or more degrees of membership of the output fuzzy sets. Defuzzification is a process of converting these into a signed real-valued signals (control

signal) for use as the control input into the system. Commonly used method is the centre-of-area defuzzification equation

$$v_0 = \frac{\sum_{i=1}^{N} \mu_B(v_i) v_i}{\sum_{i=1}^{N} \mu_B(v_i)}, \tag{4.2}$$

4.6 Fuzzy logic control for Maglev

In the context of the above, the input space of an ideal fuzzy controller should contain all three state variables, with output space containing the voltage into the magnet's power amplifier. The availability of all three feedback signals leads to three types of fuzzy controllers according to the number of control rule tables employed: (a) position error and velocity inputs fuzzified with one control rule table plus constant acceleration (Fig. 4.11), (b) all three feedback signals fuzzified but position error and velocity having one control rule table and acceleration having a separate control rule table (Fig. 4.12), and (c) a single control rule table for all three fuzzified input signals (Fig. 4.13).

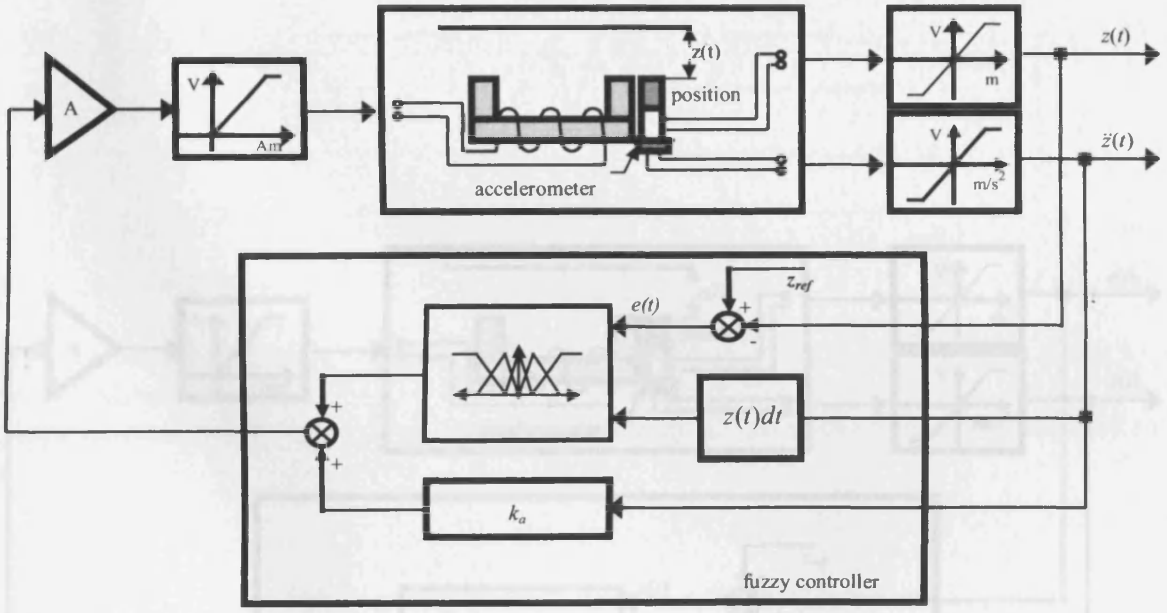

Figure 4.11: Fuzzy controller for Maglev systems with constant acceleration.

4.6.1 Fuzzy control with constant acceleration

The three state variables of the Maglev system are the position, the velocity and the acceleration. The error signal $e(t)$ is generated as the difference between the current position of the Maglev $z(t)$ and the desired position z_{ref}. The error signal $e(t)$ is classified linguistically as: negative big(NB), negative small(NS), zero(Z), positive small(PS), and positive

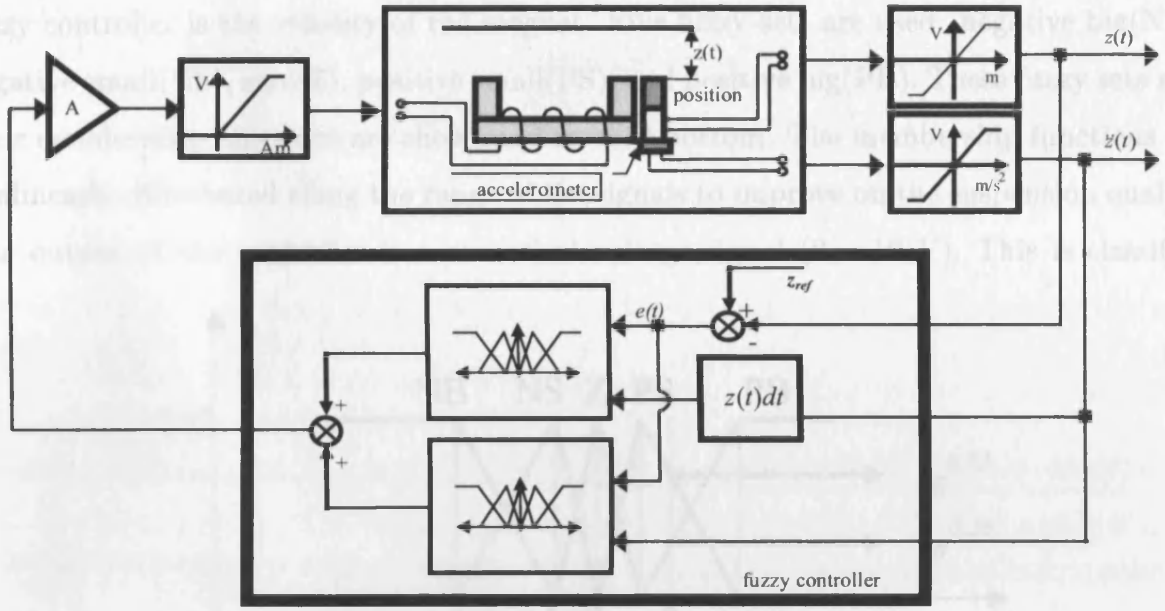

Figure 4.12: Fuzzy controller for Maglev systems with fuzzy acceleration.

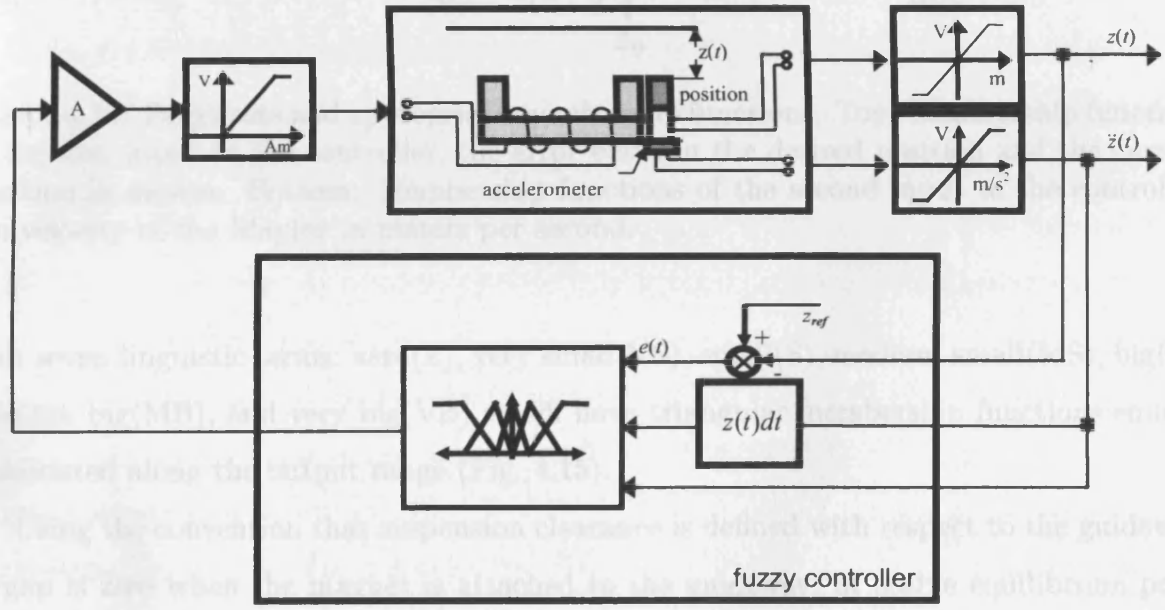

Figure 4.13: Fuzzy controller for Maglev systems using three state variables.

big(PB). These fuzzy sets are described with triangular membership functions, as shown in Fig. 4.14 top (the appropriate ranges as shown in the figure). The second input to the fuzzy controller is the velocity of the magnet. Five fuzzy sets are used: negative big(NB), negative small(NS), zero(Z), positive small(PS), and positive big(PB). These fuzzy sets and their membership functions are shown in Fig. 4.14 bottom. The membership functions are nonlinearly distributed along the range of the signals to improve on the suspension quality. The output of the controller is a numerical voltage signal (0 – 10 V). This is classified

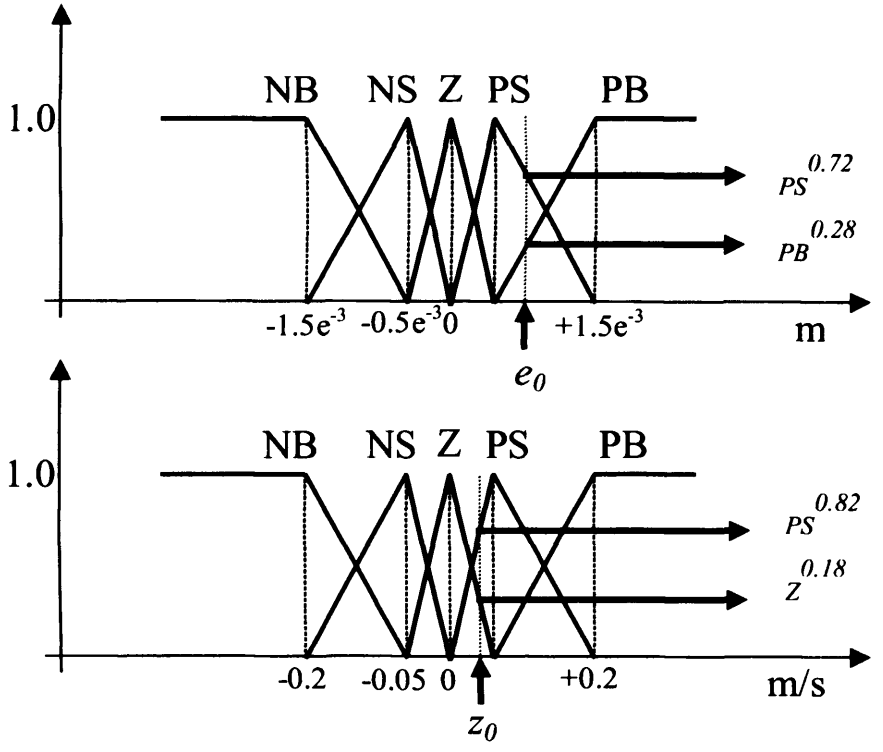

Figure 4.14: Fuzzy sets and appropriate membership functions. Top: Membership functions of the first input to the controller, the error between the desired position and the current position in meters. Bottom: Membership functions of the second input to the controller, the velocity of the Maglev in meters per second.

with seven linguistic terms: zero(Z), very small(VS), small(S), medium small(MS), big(B), medium big(MB), and very big(VB) which have triangular membership functions equally distributed along the output range (Fig. 4.15).

Using the convention that suspension clearance is defined with respect to the guideway, airgap is zero when the magnet is attached to the guideway; at stable equilibrium point (ideally, the set reference airgap, z_{ref}) the airgap error and the vertical acceleration are zero with the magnet current being what is necessary to generate a vertical attraction force equal to the weight of the suspended object. The current goes down as the airgap error becomes positive and vice versa. Likewise as the magnet moves away from the guideway,

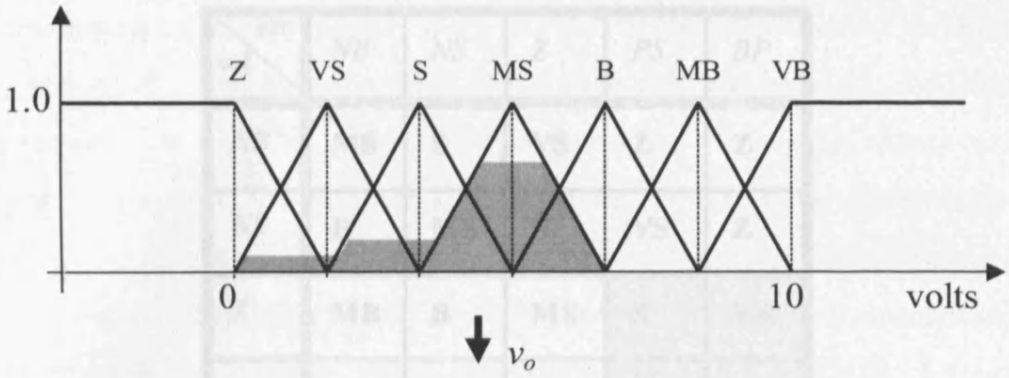

Figure 4.15: Output fuzzy sets and their membership functions. v_0 is produced by estimating the centre of the area.

the vertical acceleration and vertical velocity become positive and the magnet current needs to go up to sustain stability. These form the basis for the control rules (only a part of these are described below, the full set is given in a matrix form in Fig. 4.16)

```
    IF the airgap error is zero AND the airgap velocity is negative small THEN
    the output is small
OR  IF the airgap error is negative small AND the airgap velocity is zero THEN
    the the output is big
OR  . . .
```

The antecedent part consists of two fuzzy inputs(error and velocity), combined with and AND operator. The consequent consist of one output(the control signal). The full combination of inputs and outputs and IF-THEN rules is 25 (Although it is not necessary to have the full list of IF-THEN rules to implement a controller, in this experiment the full list of 25 rules is used). For easy mathematical operations, rules are combined in a *rule-matrix* as in Fig. 4.16. The columns of this matrix contains the fuzzy sets defined over the position error, where the rows are those sets defined over the velocity. The fuzzy matrix may be interpreted as follows: IF the velocity is negative small(NS, row 2) and the error is positive small(PS, column 4) THEN the control signal is very small(VS).

To generate a fuzzy output, the signals are firstly fuzzified. This is performed at every control sample. For illustration purposes, the two numerical inputs are denoted as e_0 and $\dot{z}_0$ (Fig. 4.14). These are classified as: positive small μ_{PS} and positive big μ_{PB} for the error, and zero μ_Z and positive small μ_{PS} for the velocity. These four fuzzy sets are combined in four IF-THEN rules:

```
IF the error is PS AND the velocity is Z THEN the output is S
```

vel \ err	*NB*	*NS*	*Z*	*PS*	*BP*
NB	**MS**	**S**	**VS**	**Z**	**Z**
NS	**B**	**MS**	**S**	**VS**	**Z**
Z	**MB**	**B**	**MS**	**S**	**VS**
PS	**VB**	**MB**	**B**	**MS**	**S**
PB	**VB**	**VB**	**MB**	**B**	**MS**

Figure 4.16: IF-THEN rules combined as a rule-matrix. Columns: fuzzy sets defined over the error signal; rows: fuzzy sets defined over the velocity signal.

```
OR  IF the error is PS AND the velocity is PS THEN the output is MS
OR  IF the error is PB AND the velocity is Z THEN the output is VS
OR  IF the error is PS AND the velocity is PS THEN the output is S
```

which are highlighted in the rule-matrix (Fig. 4.16). Using the min-operator to calculate the logical AND between fuzzy sets (membership functions), the following membership values for the output are estimated

$$\begin{aligned} \text{or} \quad & min\{\mu_{PS}^{0.72}, \mu_{PS}^{0.82}\} = \mu_{MS}^{0.72} \\ \text{or} \quad & min\{\mu_{PB}^{0.28}, \mu_{Z}^{0.18}\} = \mu_{VS}^{0.18} \\ \text{or} \quad & min\{\mu_{PB}^{0.28}, \mu_{Z}^{0.18}\} = \mu_{VS}^{0.18} \\ \text{or} \quad & min\{\mu_{PB}^{0.28}, \mu_{PS}^{0.82}\} = \mu_{S}^{0.28} \end{aligned} \tag{4.3}$$

The right parts of this equation gives the membership functions for the output (voltage in Fig. 4.15). The IF-THEN rules are combined by an OR operator and using the *max*-operator, the final shape of this function is shown in Fig. 4.15. This membership function is the *inferred* fuzzy result from the list of IF-THEN rules with inputs: e_0 and $\dot{z}_0$. The results stand for: the control output is very small with a degree of membership 0.18, small with a degree of 0.28 and medium small with a degree of membership 0.72. For the numerical control work, these membership functions are defuzzified by taking the centre-of-the-area to produce a numerical output (v_0). This is shown graphically in Fig. 4.15.

The above fuzzy controller was implemented on the DSP control hardware for Maglev. At every sample ($100\mu s$) the algorithm reads the airgap position and the acceleration,

which is integrated to get the velocity. The state variables are converted to physical units (m, m/s, and m/s^2). The position error and the velocity are fuzzified. The membership functions are shown in Fig. 4.14. The values that determine the location of each membership function are: (a)position:$[-1.5e^{-3}\ -0.5e^{-3}\ 0.0\ 0.5e^{-3}\ +1.5e^{-3}]$ m; (b)velocity: $[-0.2\ -0.05\ 0.0\ 0.05\ +0.2]$ m/s. The membership functions for the output are shown in Fig. 4.15. The fuzzification is constructed as a subroutine to receive the airgap position error and the airgap velocity and a vector to specify the fuzzy sets. The shape of the membership functions is fixed as triangular. Only two membership functions are overlapped. The result from the fuzzification is two vectors with the enabled fuzzy sets and the appropriate degree of membership. Using this output, a subroutine is executed that infers a fuzzy result. This task uses the the rule-matrix in Fig. 4.16 to produce a fuzzy output, as shown in Fig. 4.15(highlighted area). This subroutine also includes the defuzzification procedure to generate the numerical value for the control signal. This is finally added to the acceleration signal multiplied by a gain $k_A = 0.041\ m/s^2/V$. The result is loaded to the DAC.

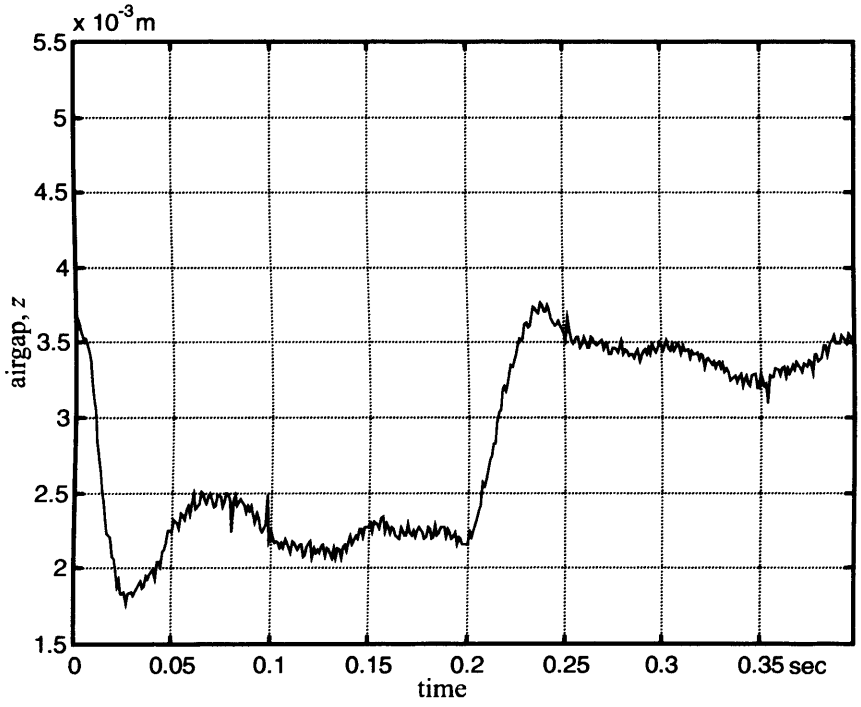

Figure 4.17: Response in airgap from the fuzzy logic control system as shown in Fig. 4.11.

The suspension quality is analysed by two step changes in desired airgap. The first step is from 3.7mm to 2.7mm and the second one is from 2.7mm to 3.7mm. The responses are shown in Fig. 4.17. The fuzzy controller is capable of producing stable responses. The tuning procedure is simplified, compared to the state-feedback controller and it does not require the model of the system. The location of the fuzzy sets for the position error were

specified at -1.5mm and +1.5mm. These are based on the maximum permissible error. The boundary limits for the velocity are set to ±0.2m/s, which is taken after analysis of pre-logged data from previous experiments. Initially, the membership functions were linearly distributed: ±1.5mm, and ±0.75mm for the position error, and ±0.2m/s, and ±0.1m/s for the velocity. After a sequence of several test runs, these ranges were updated to the values in Fig. 4.14 to improve on the suspension stiffness. The fuzzy logic produces suspension characteristics comparable with the state feedback controller. Since the operation of the controller is described linguistically without a detailed model, this reduces the development effort. The structure of the controller is relatively simple and is well suited for small laboratory-based systems where suspension stability and damping are primary design requirements.

4.6.2 Fuzzy controller for Maglev with fuzzy acceleration

Here the same approach as the one described in the previous section is used but this time the acceleration and the position error are used in a separate fuzzy controller as shown in Fig. 4.12. Five fuzzy sets with triangular membership functions are chosen to describe linguistically the acceleration: negative big, negative small, zero, positive small, and positive big. The location of the membership functions are chosen after analysis of logged data. These were fixed at: [-50.0, -20.0 , 0.0, 20.0, 50.0] m/s^2. The membership functions of the position error, velocity and output control voltage are kept unchanged as the in the previous experiment. The software implementation is similar to before. This time, however, the subroutines that perform the fuzzification are executed twice. The same list of IF-THEN rules was used, as the rules given in Section 4.6.1. This time instead of the velocity, the acceleration was combined with the position error and the output (Fig. 4.16) to form the rule matrix. Two step changes in the desired airgap were applied to the closed-system, and the results are shown in Fig. 4.18. The first one was from 3.7mm to 2.7mm and the second back from 2.7mm to 3.7mm. Although the results are similar to the previous fuzzy controller, the additional rule-table provides an adaptive gain for the acceleration and hence the controller is likely to be appropriate where the suspended object needs to operate with high stiffness such as in small laboratory-scale magnetic bearings. As acceleration gain influences suspension damping, this controller provides a reasonable combination of design simplicity and operational convenience in that the acceleration gain can be controlled independently to provide the required damped natural frequency. The

non-symmetry in the response is contributed from the nonlinearity in the suspension system and the compensator.

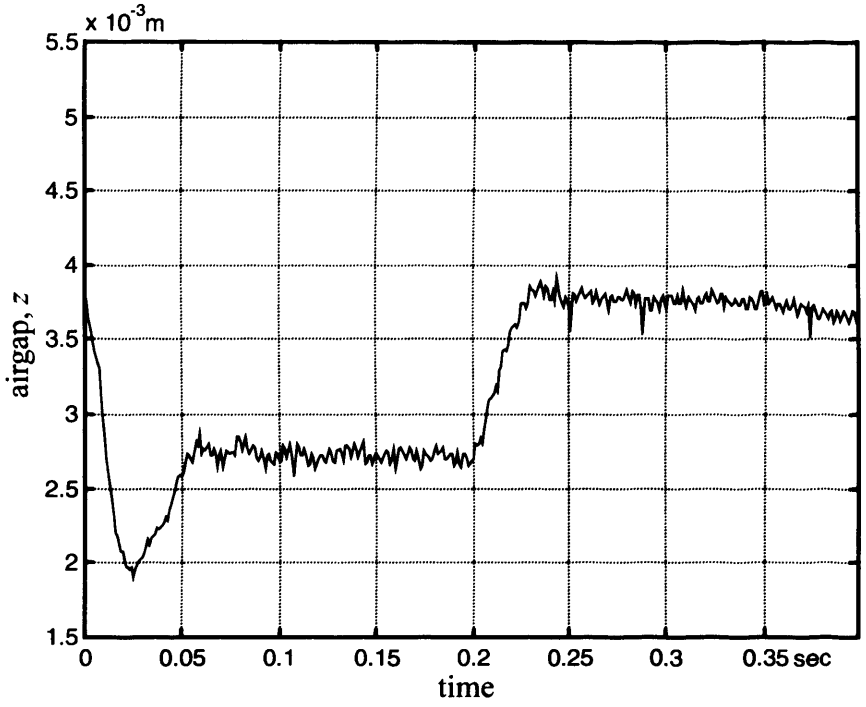

Figure 4.18: Response in airgap from the fuzzy logic control system as shown in Fig. 4.12.

4.6.3 Fuzzy controller using three state variables

Combining all the three state variables gives the controller in Fig. 4.13. The ranges of the three state variables are classified linguistically using five fuzzy sets with triangular shape. These are shown in Fig. 4.19. The output signal was classified using seven fuzzy sets. This time, the IF-THEN rules consists of three elements in their antecedent part, and given as

IF the error is e_0 AND the velocity is $\dot{z}_0$ AND the acceleration is $\ddot{z}_0$
THEN the output is v_0
OR $\cdots$

The total number of rules is equal to 125 rules. The IF-THEN rules were organised as a rule-matrix with 3-dimensions (Fig. 4.20), where each direction corresponds for an input: position error, velocity, and the acceleration. Fig. 4.19 shows the consequence of operations performed by the software on DSP in order to produce a control signal. The three signals are firstly fuzzified using the same subroutine as described in the previous sections. Because only two fuzzy sets are overlapped, the result from the fuzzification is two fuzzy sets with two degrees of membership per input signal. These are shown in Fig. 4.19. The results from the fuzzification are given as $NS^{e}_{(0.55)}$, where this notation stands for: the error signal

e is a *negative small* with degree of membership 0.55. In a similar manner all six results are produced. At the next step, the software determines the IF-THEN rules that combine these fuzzy sets. The IF-THEN rule-matrix is shown in Fig. 4.20. Five 5x5 matrices are necessary to capture the whole set of rules, where each matrix corresponds to a given fuzzy set defined for the acceleration. In each matrix, the fuzzy sets for the error is located as rows and the fuzzy sets for the velocity are located as columns. The fuzzification produces 2 fuzzy outputs per input signal(Fig. 4.19), hence a small 2x2x2 cube of rules is produced. These IF-THEN rules are highlighted in Fig. 4.20. Using a *min*-operator for a logical AND, and a *max*-operator for a logical OR, as shown in Fig. 4.19, the algorithm produces the membership functions of the output signal. This function is shown in Fig. 4.19 bottom. Using the centre of the area defuzzification (Eqn. 4.2), the software on the DSP produces the control output. This is shown as v in Fig. 4.19. This value is then loaded to the DAC to drive the magnet.

Similarly to the other two fuzzy controllers, two step changes in the desired airgap were applied to the closed-loop system. The results are shown in Fig. 4.21. By combining all three inputs in a rule matrix gives the flexibility to determine fully the operation of the controller by the construction of these rules. The suspension stiffness and the position error can be controlled by adjusting the ranges of the membership functions. It has been observed that superimposing two or more close to the origin improves on the stiffness as the response is more sensitive to small changes in the airgap. This controller is better suited to applications with more demanding design specifications such as vehicle suspension and large industrial magnetic bearings.

Considering the Fuzzy control environment above, a benefit is considered to be the fact that the linguistic description of the operation reduces the developing effort. In addition, there is no need to have a model of the system for the control work. For the Maglev control work, one major drawback of the fuzzy logic controller is considered to be the lack of a systematic theory for studying the stability and the robustness of the closed-loop system. Therefore for the multi-magnet vehicle control work, a different approach is considered based on robust optimal control. This is described in the following chapters.

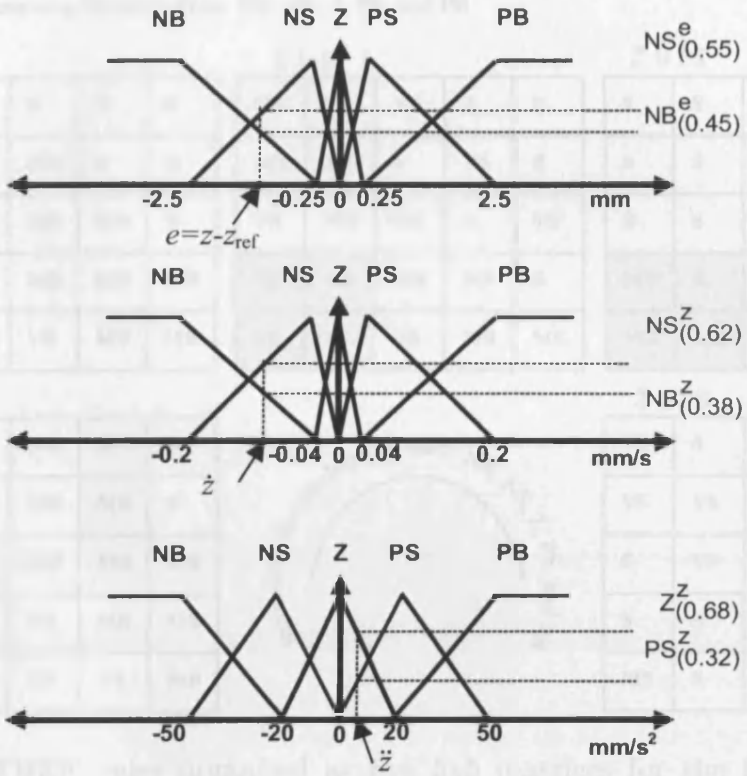

IF e is NB AND $\dot{z}$ = NB AND $\ddot{z}$ = Z THEN v is VB

...

IF e = NB AND $\dot{z}$ = NS AND $\ddot{z}$ = PS THEN v is MB

...

IF e = NS AND $\dot{z}$ = NS AND $\ddot{z}$ = PS THEN v is B

$$\min\{NB^{e}_{(0.45)}, NB^{\dot{z}}_{(0.38)}, Z^{\ddot{z}}_{(0.68)}\} \quad VB^{v}_{(0.38)}$$

$$\min\{NB^{e}_{(0.45)}, NS^{\dot{z}}_{(0.62)}, PS^{\ddot{z}}_{(0.32)}\} \quad MB^{v}_{(0.32)}$$

$$\min\{NS^{e}_{(0.55)}, NS^{\dot{z}}_{(0.62)}, PS^{\ddot{z}}_{(0.32)}\} \quad B^{v}_{(0.32)}$$

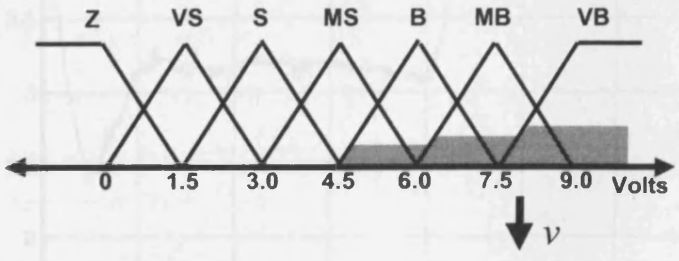

Figure 4.19: From top: membership functions; part of the list of IF-THEN rules; inferring an output membership function for defuzzification. A combination of the three input feedback signals is shown to illustrate the construction of the output (control voltage into the magnet) for the state-fuzzy controller.

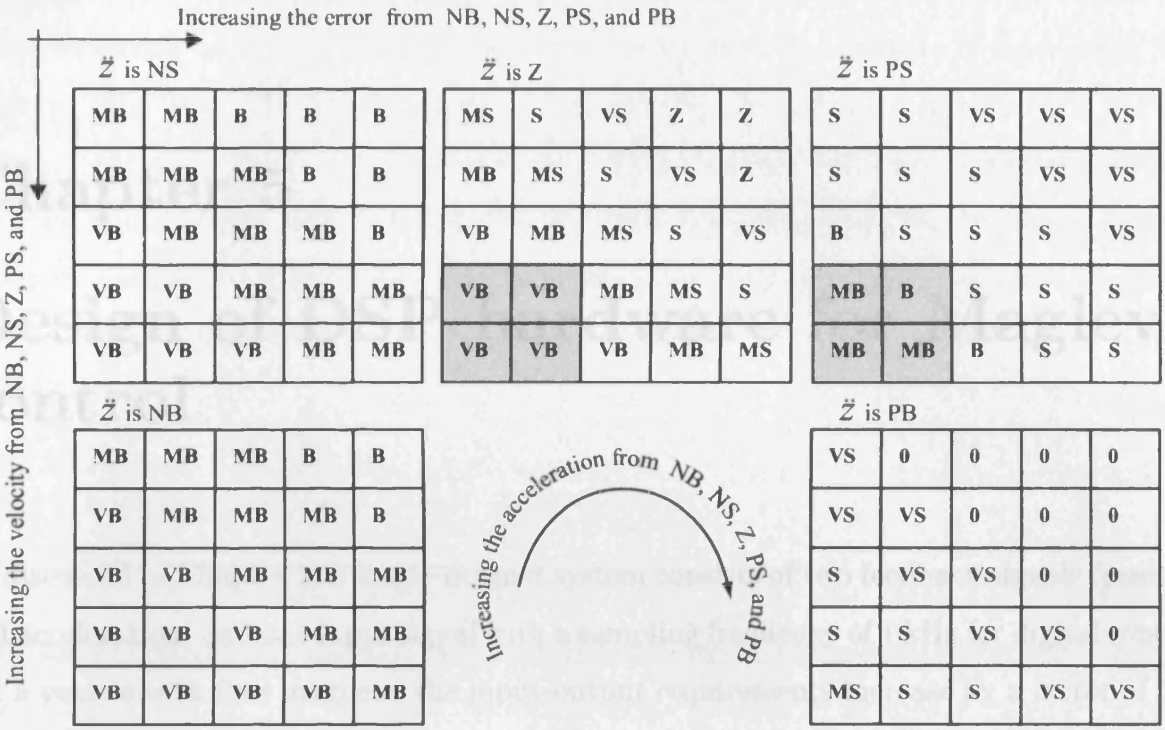

Figure 4.20: IF-THEN rules organised as five 5x5 matrices for the fuzzy controller in Fig. 4.13. The rows capture the fuzzy sets defined for the velocity signal, where the columns capture the fuzzy sets defined defined for the position error. Five of those matrices are then generated, for the different fuzzy sets defined for the acceleration.

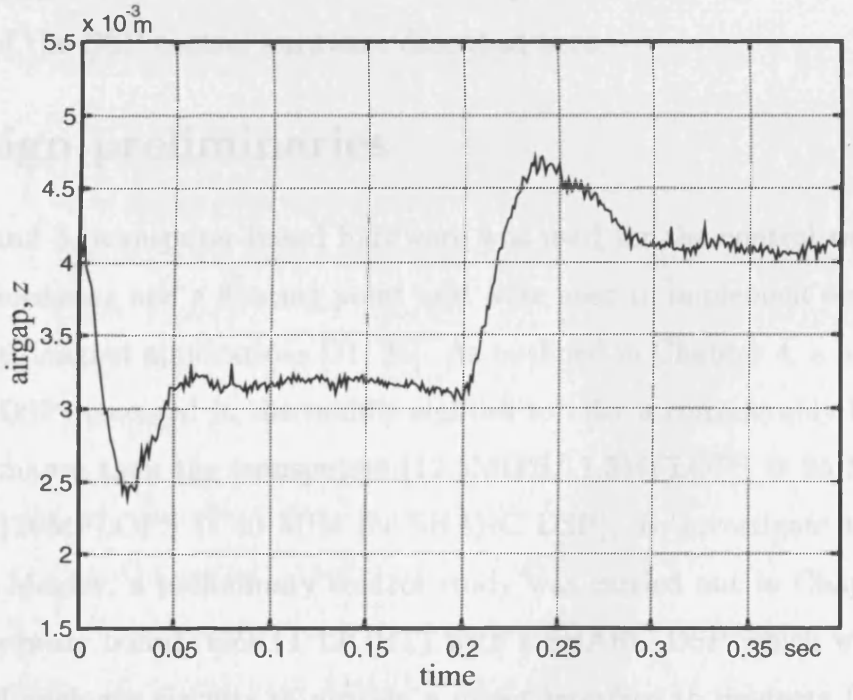

Figure 4.21: Response in airgap from the fuzzy logic control system as shown in Fig. 4.13.

Chapter 5

Design of DSP hardware for Maglev control

As discussed in Chapter 2, a single-magnet system consists of two feedback signals (position and acceleration) and one input signal with a sampling frequency of 1 kHz for digital control. For a vehicle with four magnets, the input-output requirements increase by a factor of four to give: eight analogue inputs for position and acceleration and four control outputs. Each control loop is sampled at 1 kHz which is calculated from the operating bandwidth (356.6 rad/s $\times 20 \approx$ 1135 Hz) to reduce sampling and phase effects in the control loop. After an extensive search of hardware manufacturers' data suitable for multi-magnet Maglev control (mid 1999), it was concluded that the required number of input-output channels and a suitable processor on board was beyond the spec of the available hardware. This led to the design of the DSP control hardware described here.

5.1 Design preliminaries

In Chapter 2 and 3, transputer-based hardware was used for the control work. Its facilities for multiprocessing and a floating point unit were used to implement control tasks for single and multi-magnet applications [21, 35]. As outlined in Chapter 4, a new generation of processors (DSP) emerged in the middle eighties to offer a considerably better computational performance than the transputers (12.5MIPS/ 1.5MFLOPS @ 25 MHz for T80x vs. 40MIPS/ 120MFLOPS @ 40 MHz for SHARC DSP). To investigate the applicability of DSP for Maglev, a preliminary control study was carried out in Chapter 4 using a commercial hardware board (EZKIT LIGHT) with a SHARC DSP which was customised with additional analogue circuits to provide a direct interface to magnets (Fig. 4.1) [35]. While the DSP offered enough processing power to implement demanding Maglev control tasks, the new hardware lacked a high-bandwidth communication link to a host computer

and facilities for interfacing four magnets simultaneously. This required constructing a list of requirements for a new Maglev control hardware with capabilities of interfacing four magnets (Fig. 5.1). The specifications of this are given in Table 5.1 (some of the fields in this table were finalised after the completion of the design). Although the requirement to interface four magnets puts additional constraints on the hardware design, this solution is believed to relax the complexity of implementing multi-Maglev control systems. A survey of the available commercial DSP hardware as an alternative to the proposed design is given below.

5.2 Commercial DSP hardware

Some of the major companies involved in the design of SHARC-based DSP hardware are (mid 1999): Spectrum Signal Processing Inc., Bittware Inc., Blue Wave Systems Inc., and D.SignT Gmbh. (all non-UK manufactures). Although there is a large number of general purpose DSP-based hardware, only two systems were found with specifications close to the required list. The first hardware that partly meets these constraints is designed by D.SignT Gmbh, and consists of two separate boards: (a) a main board (processing module) with a SHARC DSP (D.Module.21065), and (b) an analogue I/O interface module (ADS12-300). The specification of this system is given in Table 5.2. The second compatible hardware is offered by Bittware Inc. and two separate boards are needed to meet the specifications; these are: Blacktip-EX (processing module) and bitsi-DAQ (I/O module). The characteristics of this hardware are given in Table 5.3. The following conclusions can be drawn from this survey.

- Most of the available hardware systems are plug-in boards and use PCI, VME, or Compact-PCI bus interfaces. To operate the boards for control purposes, an additional host computer is required. This reduces the mobility of the system and increases the overall cost.

- From the list of available stand-alone hardware, all provide a limited number of analogue inputs and outputs (see Table 5.2 and 5.3). Increasing the number of analogue I/O channels requires combining two or more hardware boards together. This increases the overall cost and the complexity of the design and reduces the reliability.

- All commercial stand-alone hardware units offer only RS232 interface to a host com-

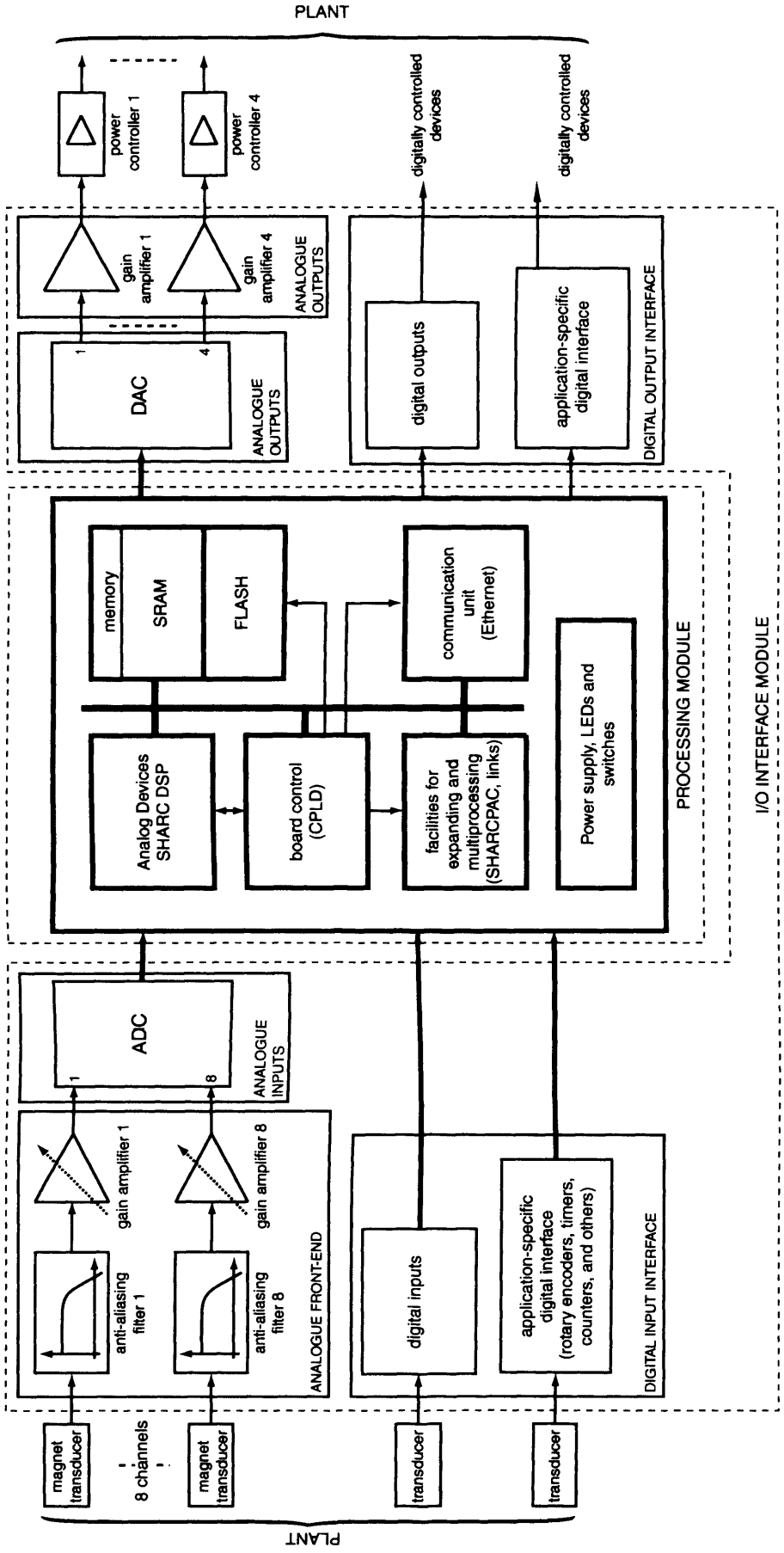

Figure 5.1: A block diagram of a typical digital control hardware system for Maglev.

Processor	One ADSP-21062 Analog Devices SHARC processor 40MHz, 25ns instruction rate, 120MFLOPS, 40MIPS 32/40-bit floating point, 32-bit integer 2Mbits dual-ported on-chip SRAM memory, organised x32 or x48 six 40MB/s link ports, and two 40Mbit/s serial ports
Interface	One SHARCPAC interface
External Memory	4Mbit FLASH memory Up to 32Mbit SRAM zero wait state memory
Connectivity	One 10Mbit/s Ethernet port 10Base-T unshielded twisted pair with RJ45 interface
Link Ports for multiprocessing	Four external link connectors Two are connected directly to the SHARC on the board Two are routed from the SHARCPAC module
Serial Ports	Four serial interfaces routed to the SHARCPAC connector
Analogue inputs	Eight 12-bit analogue inputs Maximum conversion rate 454 kHz four $\pm$5.0V input channels four 0-20mA input channels Eight independent anti-aliasing analogue filters (25KHz cut-off freq.) Four programmable gain amplifiers with 255 positions Four fixed gain amplifiers (1:1)
Analogue outputs	Four 12-bit analogue outputs 6μs settling time four $\pm$5.0V output channels Four fixed gain amplifiers (1:1)
Digital I/O	Eight programmable digital I/Os with TTL input/output levels
Encoder inputs	Two 12-bit inputs for rotary encoders with TTL input levels Direct interface to standard encoders
Programmable I/O	Gate-programmable digital I/Os (Lattice ispLSI1016-180 CPLD)
Debug Port	14-pin IDC header for IEEE JTAG 1149.1 boundary scan with extensions for in-circuit emulation Supports Analog Devices EZ-ICE emulator
Software support	Embedded kernel on board that supports TCP/IP and host booting Host interface tool for booting Support of the Analog Devices developing tools Matlab client/server module for direct interface to Matlab/Simulink
Power	650mA@5V typical (not including optional SHARCPAC module) optional 650mA@12V (not including optional SHARCPAC module)
Size	4.7"x6.4"

Table 5.1: Specifications of new DSP-based control hardware.

puter with a maximum bandwidth of 115200 bit/s. Based on previous experience for the amount of experimental data that is usually transfered, this speed is considered as insufficient.

- Due to the lack of a single embedded solution that integrates the DSP and the analogue I/O circuits on a single board, meeting the constraints in Table 5.1 requires combining two hardware systems: one with analogue I/O interface circuits and another with the DSP and its supporting circuits. This reduces the functionality of the system and increases the overall costs.

Processor	One Analog Devices SharcTM 21061 Floating Point DSP @ 40 MHz 120 MFLOPS peak performance 32 bit IEEE floating point, 32 bit integer arithmetic 128 kByte internal dual ported RAM Six High Speed Link Ports for array multiprocessing, each 40 MByte/sec JTAG Emulator Port
External memory	196 kByte (32k x 48) zero wait state SRAM 128 kByte non-volatile sector-architecture Flash Memory
Connectivity	UART RS232 line interface, up to 38400 baud
Interface	External Bus Interface (occupied by the I/O module)
Software support	Software controlled module configuration Service Utility for program uploads via RS232 port
Analogue inputs	4 Channel 12 Bit Successive Approximation A/D Converter Synchronous or alternating sampling, up to 300 kHz Programmable sampling frequency and filter cutoff 4 Inputs, differential, $\pm$ 2.5V to $\pm$ 10V, 4th order Butterworth filter
Analogue outputs	2 Channel 12 Bit D/A Converter 2 Outputs, single-ended, $\pm$ 2.5V, 2nd order Butterworth filter

Table 5.2: Specifications of D.Module.21065 (processing module) and ADS12-300 (I/O module) designed by D.SignT Gmbh..

These conclusions show that to support the development of control algorithms for multi-magnet systems, it is more convenient to design a new hardware by following the specifications in Table 5.1. The additional effort required for this design is expected to contribute the research work addressed in this thesis and to provide a hardware/software framework to support other academic and industrial work. A brief description of the hardware is given below and its photographic image is shown in Fig. 5.3.

Processor	One Analog Devices SharcTM 21061 Floating Point DSP @ 40 MHz 120 MFLOPS peak performance 32 bit IEEE floating point, 32 bit integer arithmetic 128 kByte internal dual ported RAM Six High Speed Link Ports for array multiprocessing, each 40 MByte/sec JTAG Emulator Port
External memory	up to 512K x 48 optional SRAM 2Mbit x8 bank FLASH Memory
Communication	two RS232 line interface
Interface	BITSI I/O mezzanine interface (occupied by the I/O module)
Software support	The DSP21k Toolkit for Windows Analog Devices ANSI C compiler, assembler, linker, simulator, and source code debugger
Analogue inputs	8 Channel 12 Bit analogue inputs up to 500 kHz sampling rate $\pm$ 5.0V input range
Analogue outputs	4 Channel 14 Bit D/A Converter, 100kHz $\pm$ 2.5V output range

Table 5.3: Specifications of Blacktip-EX (processing module) and bitsi-DAQ (I/O module) designed by Bittware Ltd..

5.3 Hardware description

From a functional point of view, the DSP hardware is divided into: an analogue I/O interface module and a processing module. A general overview of the data paths is shown in Fig. 5.2. A description of each block is given below.

- *Analogue I/O module*: To provide an interface to four magnets simultaneously, an eight channel, 12-bits analogue-to-digital converter (ADC) is used (AD7891AS-1 [48]). The minimum control sampling frequency is 1 K-samples per second per channel, for compatibility with the dynamic characteristics of the open-loop system. With a dominant pole of the single-magnet system located at 356.56 rad/s, the sampling time is chosen to be 20 times the open-loop bandwidth [43] to give an ADC conversion rate of 1 kHz per channel for good signal-to-noise ratio and minimal influence of the digitalising process. The chosen ADC offers up to 454 kHz conversion rate to give maximum of 50 kHz sampling rate per channel.

  To reduce the aliasing effects of the sampling process, the analogue signals are band limited to half the sampling frequency(=Nyquist frequency) before quantisation using eight independent second-order Chebishev filters. The cut-off frequency of the filter

is fixed at 25 kHz (-2.62 dB).

To provide a direct interface to magnet position transducers, four of the ADC inputs are designed to measure current inputs from 0 to 20mA. The other four channels measure voltage signals within ± 5V which is suitable for accelerometer outputs. The voltage input channels have programmable gain circuits that allow measuring input signals from 20mV using the full ADC resolution of 12-bits.

A digital to analogue converter (DAC) with four separate outputs and a 12-bits resolution is used to interface magnet power amplifiers (DAC8412FPC [56]). The settling time per channel is $6\mu s$. The unipolar analogue outputs (0-2.5V) from the DAC are converted to bipolar outputs (± 5V) using a set of external analogue amplifiers (MC33202D [57]). The outputs of the DACs can drive magnet current amplifiers directly without a pre-amplifier (the input gain of the current amplifier is adjusted to 2A/V to give maximum driving force).

A programmable logic device with 2000 gates, 96 registers and 32 ports (ispLSI1016E-125LT [47]) is used to provide digital inputs and outputs for application specific digital interfaces. Examples are digital encoders for motor control, timers, counters, PWM and PDM generators. This interface is on-the-board re-programmable.

- *Processor*: The main computational unit on the board is a 32-bit, floating-point SHARC DSP processor (ADSP-21062KS-160 [45, 44]). It runs at 40 MHz to give 40 MIPS and 80MFLOPS sustained DSP performance. The DSP provides 2 Mbit of internal memory for storing application programs and data. The DSP has a 32-bit data bus which is connected to all memory mapped devices (such as the ADC and the DAC). More details on this computational unit are discussed in Section 4.1.

- *Memory module*: The memory module of the board consists of a static RAM memory block (SRAM) and a non-volatile memory block (FLASH). FLASH memory with 4Mbits capacity (AM29F040-120JC [58]) is used to store the operating kernel on the board (more details on the kernel are given below). After reset, the DSP reads from the FLASH to transfer its content into the DSP's internal memory. The execution of the kernel then begins with initialising the hardware and preparing a communication link for Maglev control software download.

  External SRAM memory is provided by a dedicated plug-in 72-pin SIMM interface. The hardware is designed to operate with or without the static memory and to use

off-the-shelf SIMM SRAM modules (CYM1846PM-12C SRAM SIMM is used). Typically, 16Mbits (512Kx32bits) of SRAM is used to provide a storage capacity of 524288 floating point numbers which is approximately the capacity of storing 9 minutes of magnet data at 1 kHz sampling rate.

- *Ethernet*: The communication facility on the board is provided by an Ethernet communication block (CS8900A-CQ [59, 60]) with a capacity for transferring data at 10Mbits/s bandwidth over a local area network (LAN). Since the DSP hardware connects to the network, more than one host computer can read/write and operate with the board at a time. TCP and IP protocol layers are built on the top of the Ethernet to enhance the usability of the board. The communication device is memory mapped on the DSP board to achieve full communication performance. Isolation transformers are used to separate the hardware from the remaining LAN devices.

- *Expansion and board control*: Since all modules described above are memory mapped on the DSP's address and data busses, a programmable logic circuit is used to synchronise the operation of each device. This is the in-system-programmable chip, ispLSI2032-180LT44 [61], with 1000 user gates, 32 I/O pins, and 32 registers.

  Although the board provides all necessary circuits to build multi-magnet control systems, the industrial SHARCPAC interface [62] is integrated on the board to provide facilities for expansion. Typical commercial SHARCPAC modules are: SHARCPAC DSP modules with 1,2,4 or 8 SHARC DSPs, high bandwidth ADCs and DACs for image processing, optical interfaces, CAN interfaces, analogue inputs/outputs, field programmable gate arrays (FPGAs) and others. The dimensions of the SHARCPAC interface is 3.1 by 4.5 inches, and it has four 90-pin connectors with a total number of 360 pins. The DSP's data, address, and control busses are connected to the SHARCPAC interface to allow a direct memory mapped interface.

The hardware design actively undertaken during this project was challenging and required an extensive research on system design and testing. The total number of components is above 200 and required designing a printed circuit board (PCB). As a good compromise between board complexity and manufacturing price, a four layer PCB technology was considered. Two of the layers are signal layers referred as *top signal layer* and *bottom signal layer*, and the other two are the supply *power plane* and the *ground plane* layers. A four layer PCB with separate power and ground planes has a low electro-magnetic interference

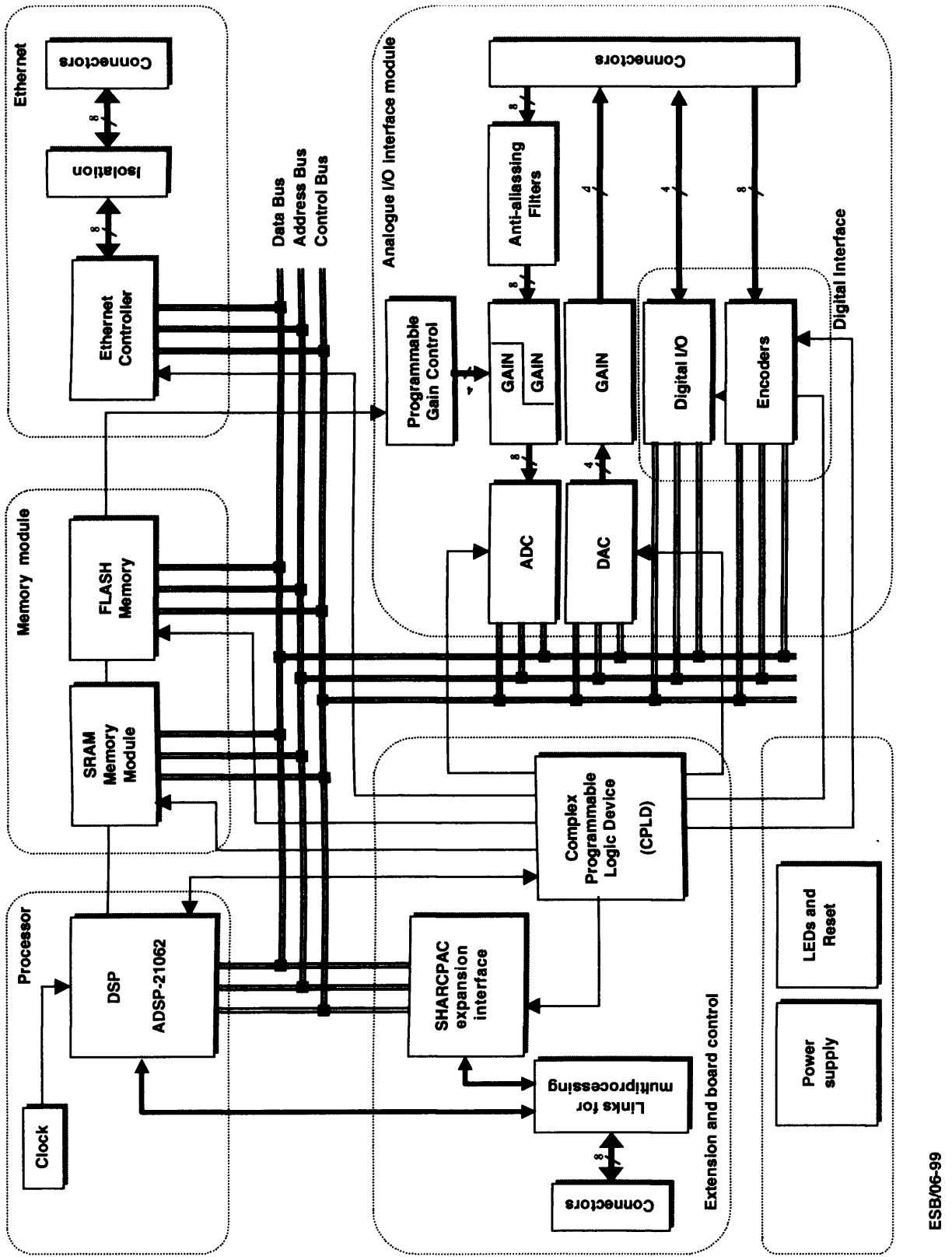

Figure 5.2: Functional blocks of the DSP hardware. The schematics are given in Appendix B, page 278.

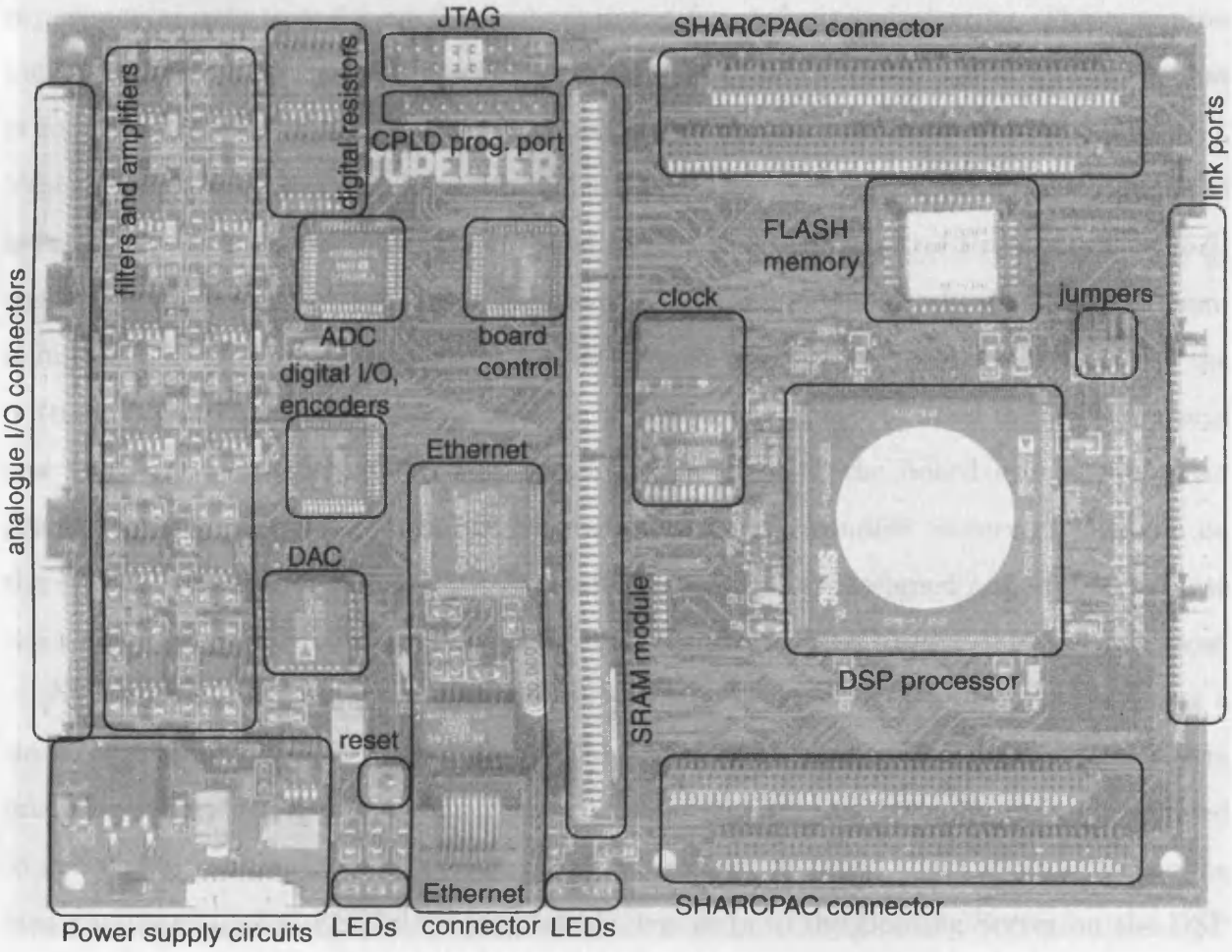

Figure 5.3: Functional blocks of the new DSP hardware.

(EMI) [63]. It also provides a basis for employing special routing techniques to help attenuating the effect of the digital noise on the analogue signals [64]. The final PCB with all components is shown in Fig. 5.2.

5.4 Software description

Two are the main requirements from the software: (a) to provide a communication link for downloading user-specific programs on the DSP and (b) to provide facilities for transferring experimental data to and from the host computer for analysis and plotting. These requirements are met by designing a specialised kernel (that portion of an operating system that is kept in main memory at all times [65]) resident on the DSP hardware (FLASH memory). When the board is reset, the kernel is loaded to the DSP and executed. A main part of the kernel is the Internet Protocol (IP [66]) and the Transmission Control Protocol (TCP [67]) routines that run on the top of the Ethernet [68] communication link. The network communication in the kernel uses packets for data transfer and has a layered structure. On the bottom is the Ethernet link and its packets, next is the IP protocol, then the TCP protocol and finally user-specific applications. Communication with the board uses client/server principles. Clients typically run on the host machine and connect to servers that run on the DSP. For operational flexibility, two software servers are designed and embedded into the kernel: Booting Server and Matlab Interface Server. A brief description is given below.

New control algorithms for Maglev are typically designed on a host computer using a simulation language such as Matlab and Simulink. These are then converted to software programs using C and/or Assembler languages for SHARC DSPs [69, 70, 71] and compiled to get an executable code suitable for DSP. A specially designed client application for the host computer (called ESBLd) reads this file, connects to the Booting Server on the DSP and transfers the new Maglev control program via the network. At the end of the transfer cycle, the DSP begins executing the new control program.

Matlab is typically used for analysis of experimental data. To provide a direct interface between the DSP and the Matlab environment, two tools are designed: a client application that runs within Matlab (called ESBtcp) and a Matlab Interface Server that runs on the DSP. Once the communication link is established between the client and the server, Matlab can read and write data to any memory location on the DSP. This mechanism allows supervisory control over the DSP software operation. Matlab can update controller coefficients while the DSP program is running, and can change operation modes as it uploads

experimental data from the DSP. This mechanism is used for obtaining the plots in the thesis.

5.5 Software framework for control applications

A software framework for control applications is designed to assist the development of new Maglev controllers. It provides essential functions and data structures for the DSP which are expandable with new algorithms. Main building blocks are: software routines to interface the analogue input and output circuits, modules that handle the communication with the host (Matlab), a set of data structures and initialisations routines, and a set of pre-tuned controllers for Maglev systems. A general overview of this environment is shown in Fig. 5.4. Bold boxes represent software functions and arrows are used to describe flow of the data between the modules. *ADCInit* and *ADCHandler* are software programs that initialise the ADC converter and read data from its registers. The number of analogue input channels to measure is user-selectable and reflects the sampling frequency for the ADC (50 kHz per channel generated from a hardware clock in the DSP). The ADC automatically generates an interrupt to the DSP at the end of the conversion cycle. Data is then read (from *ADCHandler*) and stored into two vectors iADCCh (in ADC units) and fADCCh (in voltage units). Both vectors consists of 8 elements with an index corresponding to the ADC input channel. The ADC data is logged into a data buffer which is available for transfer to Matlab.

To guarantee a fixed sampling frequency, the control algorithm is driven from a software interrupt generated from an internal timer in the DSP with a software programmable period. A software routine called *ControlLoop* (Fig. 5.4) is executed at every timer interrupt. As indicated earlier, a typical sampling frequency is 1 kHz (the DSP hardware described here has been successfully used for up to 44 kHz sampling period). The ADC units are suitably converted to physical units: positions in $[m]$ and acceleration in $[m/s^2]$. The acceleration is digitally integrated to get velocity in $[m/s]$. These three state variables are thus available for Maglev control and also logged into the data buffer for Matlab.

New control algorithms are implemented in the function *Control Algorithm*. The designer has an access to all inputs and outputs and hence only the new mathematical control algorithm has to be coded into DSP instructions. The control outputs are converted from volts to DAC-units and outputted to the current controllers. This control framework has proved to be flexible for implementing all control algorithms described in the following

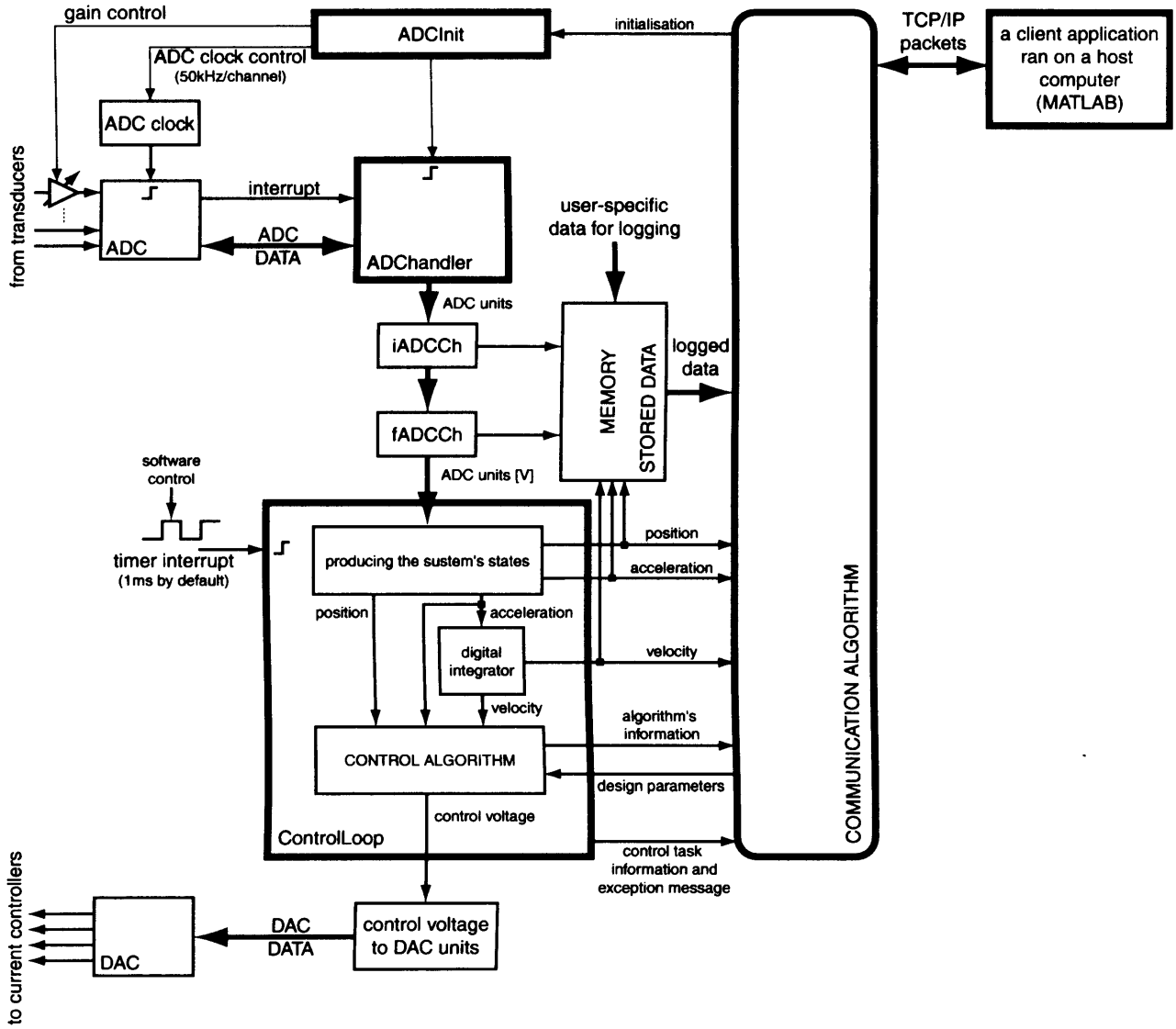

Figure 5.4: Typical configuration of the digital control system for Maglev and its data paths.

chapters.

5.6 Conclusions

A single magnet system consists of two feedback signals and one control output with a sampling frequency of 1 kHz. The input and output requirements increase by a factor of four for a Maglev vehicle with 4 magnets. A commercial interface hardware with eight analogue inputs, four analogue outputs with an embedded processor suitable for this project was not found. A new SHARC DSP hardware system was thus designed to provide an experimental platform. For operational flexibility, a suitable set of software programs for the DSP and for the host computer were designed to download application code to the DSP and to communicate between the hardware and Matlab. This platform is used in the development of Maglev control algorithms in the following chapters.

Chapter 6

$\mathcal{H}_\infty$ controllers for Maglev systems

6.1 The $\mathcal{H}_\infty$ control problem

In the previous control work, the effect of the disturbance input on the closed-loop system is not specifically used in the synthesis. Consequently, while satisfying the basic criteria of stability under nominal operating conditions, the controller parameters have no explicit relationship with (unknown) disturbance inputs. The theory of $\mathcal{H}_\infty$ control overcomes this limitation by using the generalised plant with disturbance input and a feedback controller shown in Fig. 6.1 [72, 37], where d is the disturbance input, r is the input reference with $w = \begin{bmatrix} d \\ r \end{bmatrix}$ and $q = Gu + d - r$ is a penalty output. By adding a feedback controller $K(s)$, the input-output transfer functions of the Fig. 6.1 are given by

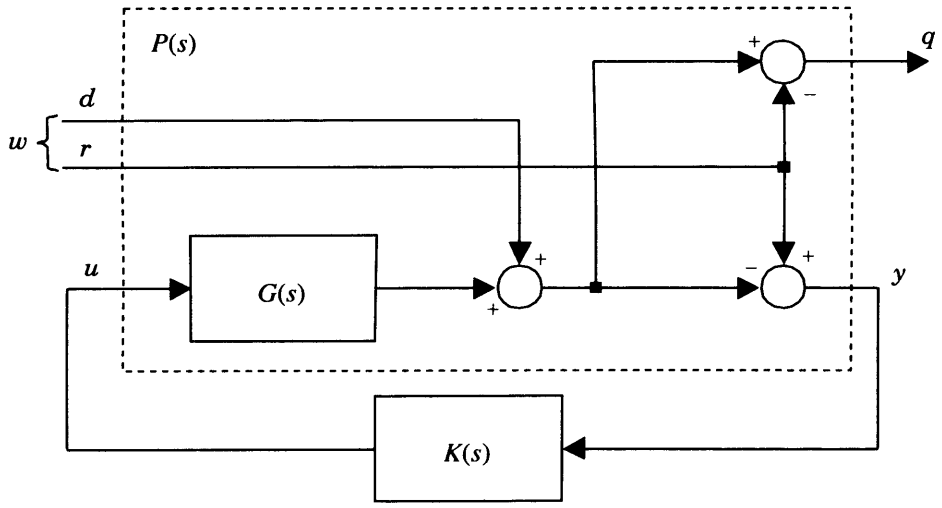

Figure 6.1: Closed-loop system representation used in the definition of the $\mathcal{H}_\infty$ control design problem. $P(s)$ is known as the *generalised open-loop system.*

$$q = \underbrace{(1 + GK)^{-1}}_{T_{qw}} w \tag{6.1}$$

$$y = \underbrace{-(1+GK)^{-1}}_{T_{yw}} w \tag{6.2}$$

The effect of disturbance input is suppressed by minimising the infinity norm of the transfer function from $w(t)$ to $q(t)$. The basic definition related the derivations of the $\mathcal{H}_\infty$ controllers is stated below. For a single input single output system, the ∞-norm of a transfer function is defined as the peak magnitude of $T_{qw}(j\omega)$, i.e. $\|T_{qw}\|_\infty = \max_{w\in\mathbf{R}} |T_{qw}(j\omega)|$. Based on this, the $\mathcal{H}_\infty$ control problem is formulated as: Find the real-rational proper controller K that minimises the $\infty-$norm of the transfer function from w to q, $T_{qw}(P,K)$, under the constraint that K stabilises G, i.e. [73]

$$\min_K \|T_{qw}(P,K)\|_\infty \tag{6.3}$$

In the $\mathcal{H}_\infty$ literature, this minimisation problem is treated as a constraint optimisation problem of finding the feedback controller $K(s)$. In this chapter, two analytical solution to this problem are derived. In the time domain, the $\infty-$norm is defined as

$$\|T_{qw}(P,K)\|_\infty = \max_w \frac{\|q(t)\|_2}{\|w(t)\|_2} \tag{6.4}$$

where the 2-norms or the energies of the signals $q(t)$ and $w(t)$ are defined as

$$\|w\|_2 = \sqrt{\int_{-\infty}^{\infty} w^T(t)w(t)dt}, \text{ and } \|q\|_2 = \sqrt{\int_{-\infty}^{\infty} q^T(t)q(t)dt} \tag{6.5}$$

Therefore the greatest increase in energy that can occur between the input w and the output q is given by Eqn. 6.4 and is equal to the infinity norm of the system [74]. Computing the ∞-norm usually requires a search. For a SISO system the computation requires calculating the Bode plot of T_{qw} and then finding the peak. A general purpose algorithm for the computation of ∞-norms of SISO and MIMO systems is described in Section 6.3 [37]. This algorithm is used in the procedure for deriving $\mathcal{H}_\infty$ controllers presented in the following section.

The primary aim of this chapter is to develop an analytical framework to derive feedback controllers for Maglev $K(s)$ that minimises T_{qw} as per Eqn. 6.3. The derivations are presented in a manner that both state and output feedback controllers maybe generated by using the same principles (Sections 6.4 and 6.5, respectively). Some of the essential derivations and the definitions of weighted sensitivity and mixed sensitivity functions for specification of suspension damping are given in the following section.

6.2 Derivations of transfer functions

6.2.1 Transfer function from w to q (T_{qw})

For Maglev systems, d represents the external force, pay-load and track disturbances and r represents the reference input. To derive T_{qw}, the following input-output relationships are constructed from Fig. 6.1

$$\begin{bmatrix} q \\ y \end{bmatrix} = P(s) \left[\begin{array}{c} d \\ r \\ \hline u \end{array}\right] = P(s) \begin{bmatrix} w \\ u \end{bmatrix} \tag{6.6}$$

where $P(s)$ is given below

$$P(s) = \left[\begin{array}{cc|c} 1 & -1 & G(s) \\ -1 & 1 & -G(s) \end{array}\right] = \left[\begin{array}{c|c} P_{11}(s) & P_{12}(s) \\ \hline P_{21}(s) & P_{22}(s) \end{array}\right] \tag{6.7}$$

In this notation, each $P_{i,j}(s)$ is a transfer function related as below

$$\begin{aligned} q &= P_{11}(s)w + P_{12}(s)u \\ y &= P_{21}(s)w + P_{22}(s)u \end{aligned} \tag{6.8}$$

With $u = Ky$, the output y in Eqn. 6.8 can be reduced to (in the following equations, the complex frequency s will be dropped for better readability)

$$\begin{aligned} y &= P_{21}w + P_{22}Ky \\ y(1 - P_{22}K) &= P_{21}w \\ y &= (1 - P_{22}K)^{-1}P_{21}w \end{aligned} \tag{6.9}$$

Substituting this equation back in 6.8, gives the following equation for q.

$$\begin{aligned} q &= P_{11}w + P_{12}Ky \\ q &= P_{11}w + P_{12}K(1 - P_{22}K)^{-1}P_{21}w \\ q &= \underbrace{\left(P_{11} + P_{12}K(1 - P_{22}K)^{-1}P_{21}\right)}_{T_{qw}(P,K)} w \end{aligned} \tag{6.10}$$

T_{qw} in Eqn. 6.10 is a function of the open-loop system P and the feedback controller K. Since $P(s)$ is the dynamics of the open-loop system, the only unknown in the equation above is the controller K. Based on Eqn. 6.10, the $\mathcal{H}_\infty$ control problem can be formulated as the following minimisation problem: find K such that the cost function J is minimised

$$J = \|T_{qw}(P,K)\|_\infty = \|P_{11} + P_{12}K(1 - P_{22}K)^{-1}P_{21}\|_\infty \;\rightarrow\; \min_K \tag{6.11}$$

6.2.2 Sensitivity minimisation

For the feedback system in Fig. 6.1, substituting Eqn. 6.7 in Eqn. 6.8 reduces T_{qw} to

$$\begin{aligned} q = T_{qw}(P,K)w &= [P_{11} + P_{12}K(1 - P_{22}K)^{-1}P_{21}]\,w \\ &= [1,\ -1] + GK(1 + GK)^{-1}[-1,\ 1]w \\ &= [1 - GK(1 + GK)^{-1},\ -1 + GK(1 + GK)^{-1}]w \\ &= [(1 + GK)^{-1},\ -(1 + GK)^{-1}]w \end{aligned} \tag{6.12}$$

Substituting w with its equivalent $w = [d,\ r]^T$ (Fig. 6.1) transforms T_{qw} to

$$q = \underbrace{(1 + GK)^{-1}}_{S=T_{qw}}(d - r) \tag{6.13}$$

$S = (1 + GK)^{-1}$ which maps w to q, determines the sensitivity of the system to external disturbances; S is known as the *sensitivity function* of the system. In the frequency domain, S has the characteristics of a high-pass filter (typical plot of $S(j\omega)$ is shown in Fig. 6.2(top)). Within the bandwidth of the system ($\omega < 10^{-1}$ rad/s in Fig. 6.2), S has a very low gain. This low gain minimises the influence of w on q. Above the bandwidth ($\omega > 10^{-1}$ rad/s in Fig. 6.2), $|S(j\omega)| \approx 0$ dB and hence all disturbance signals w are passed to the output q without attenuation.

Based on the above, the designer would require to make the sensitivity function $S(j\omega)$ small for good disturbance attenuation of the closed-loop system. For the sensitivity problem, $T_{qw} \equiv S$ and the design problem of minimising S becomes an $\mathcal{H}_\infty$ control problem (Eqn. 6.3) which can be reformulated as: find this stabilising controller K such that the ∞-norm of the sensitivity function is bounded from above, i.e.

$$\|S\|_\infty = \max_{w \in \mathbf{R}} |S(j\omega)| = \left\|(1 + GK)^{-1}\right\|_\infty < \gamma \tag{6.14}$$

γ defines the maximum gain of S and thus becomes a design parameter for the controller. The $\mathcal{H}_\infty$ design task becomes a task of minimising the *worst gain* of S by selecting K. The solution to the problem defined in Eqn. 6.14 is the controller $K(s)$ that makes $\|S\|_\infty < \gamma$. Typically, $\gamma = 1$.

6.2.3 Weighted sensitivity minimisation

Restricting $\|S\|_\infty < \gamma$ (γ is a small value) for the whole frequency range is restrictive as at high-frequency $|S(j\omega)| = 1$. A more practical approach is to introduce a design weighting function $W(j\omega)$ to achieve the desired shape of $S(j\omega)$ by defining a frequency dependent bound on the sensitivity function from above. For the single-magnet design the idea is graphically illustrated in Fig. 6.2(top). Multiplying $S(j\omega)$ by the *performance bound* $W(j\omega)$ gives a new function WS. The frequency response of the new function is shown in Fig. 6.2(bottom). This function has the following properties:

- $|WS(j\omega)|$ is > 0dB when $|S(j\omega)|$ is $> |W^{-1}(j\omega)|$ for some frequencies, and
- $|WS(j\omega)| < 0$ dB when the sensitivity function is bellow the bound $|W^{-1}(j\omega)|$.

Therefore instead of minimising $S(j\omega)$ in Eqn. 6.14, the $\mathcal{H}_\infty$ design problem can be reformulated as: find this controller $K(s)$ which minimises the norm of WS, i.e. ($\gamma \approx 1$)

$$\|WS\|_\infty = \|W(1+GK)^{-1}\|_\infty < \gamma \tag{6.15}$$

In this weighted sensitivity minimisation problem, $W(j\omega)$ in this equation gives the desired shape for $S(j\omega)$ and thus becomes a design parameter for the $\mathcal{H}_\infty$ control optimisation (Fig. 6.3). The shape of $S(j\omega)$ has a direct impact on the quality of the closed-loop system, i.e. phase margins, gain margins, maximum overshoot, settling time. More details on selecting $W(j\omega)$ to give user-defined closed-loop suspension requirements are given in Section 6.4.2.

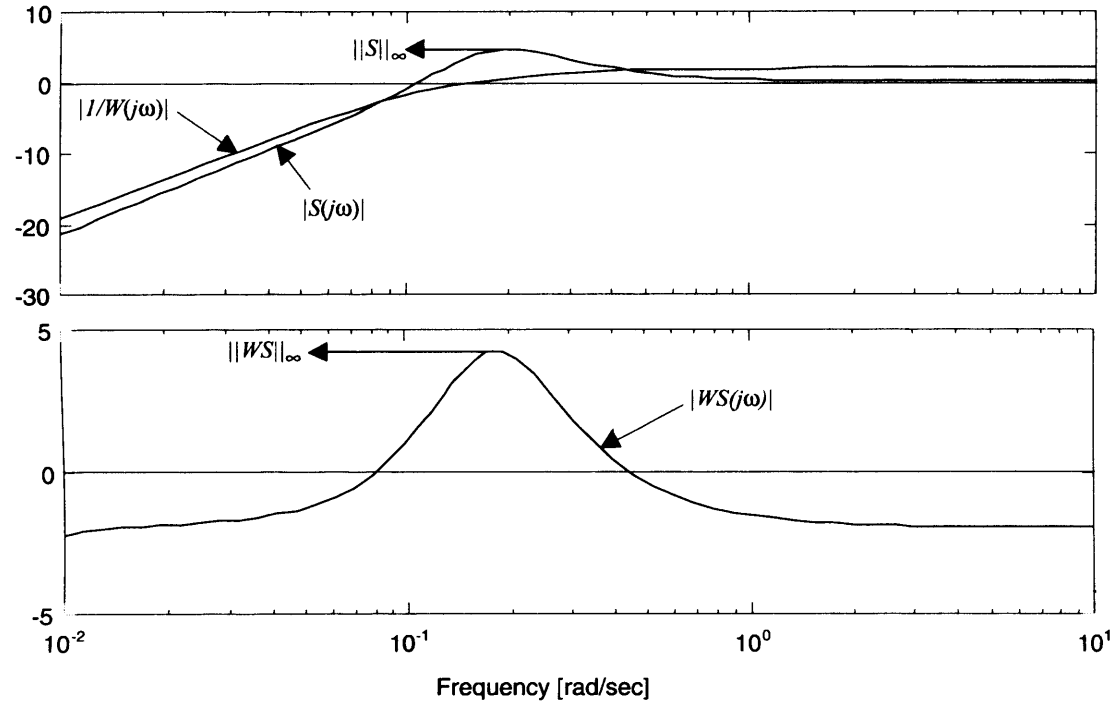

Figure 6.2: Top: sensitivity function $S(j\omega)$ and its performance weight $W^{-1}(j\omega)$; Bottom: magnitude response of $|WS(j\omega)|$. $W(j\omega)$ gives the desired shape for $S(j\omega)$; When $\|WS\|_\infty < 1$ (0dB), $|S(j\omega)|$ is located below $|W^{-1}(j\omega)|$.

6.2.4 Mixed sensitivity minimisation

To control the robust properties of the closed-loop system, it is also useful to limit the magnitude of the control action by specifying an upper bound on the control signal u. This is $\mathcal{H}_\infty$ problem defined as minimise the *worst* gain (i.e. the infinity norm) of this function. From Eqn. 6.8 and Fig. 6.3

$$y = P_{21}(s)w + P_{22}(s)u = [-1,\ \ 1]w - GKy$$

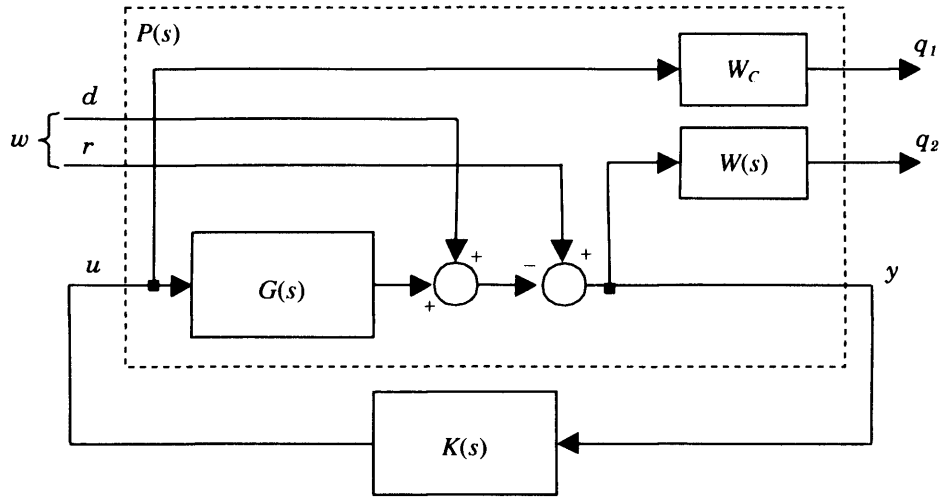

Figure 6.3: Mixed sensitivity $\mathcal{H}_\infty$ control problem. $W(s)$ and W_c are design parameters for the $\mathcal{H}_\infty$ optimisation procedure.

Substitute $u = Ky$, then after some transformations

$$\begin{aligned} u &= K(1+GK)^{-1}[-1,\ 1]w \\ &= K(1+GK)^{-1}[r-d] \\ &= KS(r-d) \end{aligned}$$

$KS = K(1+GK)^{-1}$ is the input sensitivity function and represents the closed-loop transfer function from w to u. When the gain of KS is large, small amplitudes of w produce large amplitudes in control action u. While the sensitivity and frequency responses may be satisfactory, the resulting robustness may not be satisfactory. This limitation is overcome by an additional weight $W_c(j\omega)$. For robustness, the magnitude of u can be controlled by defining a limiting transfer function $W_c(j\omega)$ (see Eqn. 6.15). This becomes an $\mathcal{H}_\infty$ optimisation problem of finding K such that

$$\|W_cKS\|_\infty = \left\|W_cK(1+GK)^{-1}\right\|_\infty < \gamma \tag{6.16}$$

$W_c(j\omega)$ defines the desired shape of KS and becomes a second design parameter in the $\mathcal{H}_\infty$ design problem. More details on selecting W_c to give certain closed-loop performance characteristics is are given in Section 6.4.1.

The two transfer functions WS and W_cKS are combined to form a column transfer function. The mixed sensitivity function is then defined as a column vector transfer function (Fig. 6.3)

$$q = \begin{bmatrix} q_1 \\ q_2 \end{bmatrix} = \begin{bmatrix} W(1+GK)^{-1} \\ W_cK(1+GK)^{-1} \end{bmatrix} w \tag{6.17}$$

Combining Eqn. 6.15 and 6.16 gives the definition of the the mixed sensitivity $\mathcal{H}_\infty$ design

problem: find K such that Eqn. 6.18 is satisfied.

$$\left\| \begin{array}{c} WS \\ W_cKS \end{array} \right\|_\infty = \left\| \begin{array}{c} W(1+GK)^{-1} \\ W_cK(1+GK)^{-1} \end{array} \right\|_\infty < \gamma \tag{6.18}$$

The optimal solution K is achieved when the upper bound for the above ∞-norm is $\gamma = 1$. A sub-optimal solution can also be sufficient as long as γ is the minimum. Optimal $\mathcal{H}_\infty$ controllers designed for the mixed sensitivity problem guarantee that: (a) the response of $|S(j\omega)|$ has an upper bounded specified by $|W(j\omega)|$ and (b) the control action (u) is limited by the upper bound $W_c(j\omega)$.

In many practical applications, the designer aim is to limit the norm of KS equally for the whole frequency range of interest and hence W_c becomes a constant which gives the maximum peak in $\|KS\|_\infty$. This approach is adopted here.

To summarise: the $\mathcal{H}_\infty$ design problem defined in Eqn. 6.3 is reformulated as a problem of determining $K(s)$ that satisfies the mixed sensitivity problem in Eqn. 6.18. The latter approach provides a design mechanism (via the design parameters $W(s)$, W_c) for achieving closed-loop stability and performance margins. The solution to this problem, i.e. finding $K(s)$, is the topic of Section 6.4 and 6.5.

6.3 Algorithms for computing the ∞ norm of a system

To compute the infinity norm of T_{qw} it is necessary to find the minimum value for γ that satisfies

$$\|T_{qw}\|_\infty < \gamma \tag{6.19}$$

The ∞-norm of T_{qw} is equal to the upper boundary of the magnitude response of $T_{qw}(j\omega)$ [74]

$$\|T_{qw}\|_\infty = \sup_\omega \bar{\sigma}\left(T_{qw}(j\omega)\right) \tag{6.20}$$

With $s = j\omega$, the singular values of $T_{qw}(j\omega)$, $\sigma[T_{qw}(j\omega)]$, are given by the square roots of the eigenvalues of the matrix $T_{qw}(-j\omega)^T T_{qw}(j\omega)$, and the maximum of these eigenvalues λ_{max} is equal to the maximum singular value $\bar{\sigma}$. The ∞-norm then becomes

$$\|T_{qw}\|_\infty = \bar{\sigma}\left(T_{qw}(j\omega)\right) = \max_i \sqrt{\lambda_i[T_{qw}(-j\omega)^T T_{qw}(j\omega)]} \tag{6.21}$$

where λ_i is the $i-th$ eigenvalue. Using this definition, Eqn. 6.19 is equivalent to

$$\lambda_i[T_{qw}(-j\omega)^T T_{qw}(j\omega)] < \gamma^2 \tag{6.22}$$

Since the eigenvalues of $T_{qw}(-j\omega)^T T_{qw}(j\omega)$ are strictly real, the singular values of $T_{qw}(j\omega)$ are the positive square roots of these eigenvalues (6.21). Further, the eigenvalues of $T_{qw}(-j\omega)^T T_{qw}(j\omega)$ are less than γ^2 if

$$\lambda_i \underbrace{[\gamma^2 I - T_{qw}(-j\omega)^T T_{qw}(j\omega)]}_{\Phi(j\omega)} > 0 \tag{6.23}$$

The function $\Phi(j\omega)$ is positively definite (i.e. $\lambda_i > 0$) if $\Phi(j\omega)$ has no zeros on the imaginary axis [37]. Equivalently, $\Phi(j\omega)$ is positively definite if $\Phi^{-1}(j\omega)$ has no poles on the imaginary axis. The problem of finding the infinity norm of $T_{qw}(j\omega)$ then becomes:
(a) chose a relatively large value for γ and compute the poles of $\Phi^{-1}(j\omega) = [\gamma^2 I - T_{qw}(-j\omega)^T T_{qw}(j\omega)]^{-1}$
(b) reduce γ and continue from (a) until for some value of γ there exist one or more poles which are pure imaginary. Stop the computation and take the last value of γ as the infinity norm of $T_{qw}(s)$.

6.3.1 State-space model of $P(s)$

To compute the infinity norm it is more convenient to use the state-space model of the suspension system in Fig. 6.3. This is derived below

Step 1 : $G(s)$, $W(s)$ and W_c are transformed from transfer functions to state space representations. This transformation results in the definition of the following state-space matrices:
(a) for the open-loop (Maglev) system $G(s) = \left[\begin{array}{c|c} A_G & B_G \\ \hline C_G & D_G \end{array}\right]$

$$\begin{aligned} \dot{x}_1 &= A_G x_1 + B_G u \\ y &= -C_G x_1 + Ir - Id - D_G u_1 \end{aligned} \tag{6.24}$$

where x_1 is the state-vector of G, u, y are defined in Fig. 6.3. In the notations above, the subscript denotes the transfer function (e.g. A_G is the A matrix of G).
(b) for the design weight $W(s) = \left[\begin{array}{c|c} A_W & B_W \\ \hline C_W & D_W \end{array}\right]$

$$\begin{aligned} \dot{x}_2 &= A_W x_2 + B_W[r - y - d] \\ q_2 &= C_W x_2 + D_W[r - y - d] \end{aligned} \tag{6.25}$$

where x_2 is the state-vector of the performance weight W, and r, d, y and q_2 are given in Fig. 6.3.
(b) since W_c is a constant, the equation for q_1 reduces to

$$q_1 = W_c u \tag{6.26}$$

where q_1 and u are given in Fig. 6.3.

Step 2 : y in Eqn. 6.24 is substituted in Eqn. 6.25. Rearranging the terms and combining all equations to one single state-space equation yields

$$\begin{bmatrix} \dot{x}_1 \\ \dot{x}_2 \end{bmatrix} = \underbrace{\begin{bmatrix} A_G & 0 \\ -B_W C_G & A_W \end{bmatrix}}_{A} \begin{bmatrix} x_1 \\ x_2 \end{bmatrix} + \underbrace{\begin{bmatrix} 0 & 0 \\ -B_W & B_W \end{bmatrix}}_{B_1} \begin{bmatrix} d \\ r \end{bmatrix} + \underbrace{\begin{bmatrix} B_G \\ -B_W D_G \end{bmatrix}}_{B_2} u$$

$$\begin{bmatrix} q_1 \\ q_2 \\ \hline y \end{bmatrix} = \underbrace{\overbrace{\left[\begin{array}{cc} 0 & 0 \\ -D_W C_G & C_W \\ \hline -C_G & 0 \end{array}\right]}^{C_1}}_{C_2} \begin{bmatrix} x_1 \\ x_2 \end{bmatrix} + \underbrace{\overbrace{\left[\begin{array}{cc} 0 & 0 \\ -D_W & D_W \\ \hline -I & I \end{array}\right]}^{D_{11}}}_{D_{21}} \begin{bmatrix} d \\ r \end{bmatrix} + \underbrace{\overbrace{\left[\begin{array}{c} W_c \\ -D_W D_G \\ \hline -D_G \end{array}\right]}^{D_{12}}}_{D_{22}} u \tag{6.27}$$

This equation can be transformed to its compact form

$$\begin{aligned} \dot{x} &= Ax + B_1 w + B_2 u \\ q &= C_1 x + D_{11} w + D_{12} u \\ y &= C_2 x + D_{21} w + D_{22} u \end{aligned} \tag{6.28}$$

where: $x = [x_1, x_2]^T$, $q = [q_1, q_2]^T$, $w = [d, r]^T$, and A, B_1, B_2, C_1, C_2, D_{11}, D_{12}, D_{21} and D_{22} are defined in Eqn. 6.27.

Using the above equation, T_{qw} becomes

$$T_{qw} = C_1(sI - A)^{-1}B_1 + D_{11} = \left[\begin{array}{c|c} A & B_1 \\ \hline C_1 & D_{11} \end{array}\right] \tag{6.29}$$

The right-hand side notation is a compact representation of transfer functions using state-space matrices. The order of the open-loop system in Eqn. 6.28 (=the dimension of A) is equal to the order of $G(s)$ plus the order of the performance weight W (W_c is a constant and does not add additional state variables).

6.3.2 Algorithm for computing the ∞ norm

To compute the poles of $\Phi^{-1}(s)$ in Eqn. 6.23, the transfer matrix $\Phi^{-1}(s) = [\gamma^2 I - T_{qw}(-s)^T T_{qw}(s)]$ has to be constructed. Example is given with T_{qw} in Eqn. 6.29

$$T_{qw}(s) = C_1(sI - A)^{-1}B_1 + D_{11}$$

The complex-conjugate transpose $T_{qw}(-s)^T$ is given by [74]

$$T_{qw}(-s)^T = -B_1^T(sI + A^T)^{-1}C_1^T + D_{11}^T$$

For simplicity and without changing the generality of the derivations, D_{11} is assumed to be $D_{11} = 0$ (this requires choosing a strictly proper weight $W(s)$ with $D_W = 0$).

Interconnecting in series $T_{qw}(-s)^T$ with $T_{qw}(s)$ after suitable rearrangements yields to

$$T_{qw}(-s)^T T_{qw}(s) = \left[\begin{array}{cc|c} A & 0 & B_1 \\ -C_1^T C_1 & -A^T & 0 \\ \hline 0 & B_1^T & 0 \end{array}\right]$$

Furthermore,

$$\gamma^2 I - T_{qw}(-s)^T T_{qw}(s) = \left[\begin{array}{cc|c} A & 0 & B_1 \\ -C_1^T C_1 & -A^T & 0 \\ \hline 0 & -B_1^T & \gamma^2 \end{array}\right] \tag{6.30}$$

Some transformations can show that the inverse of the left-hand side of Eqn. 6.30 is given by [74]

$$[\gamma^2 I - T_{qw}(-s)^T T_{qw}(s)]^{-1} = \left[\begin{array}{c|c} \begin{bmatrix} A & 0 \\ -C_1^T C_1 & -A^T \end{bmatrix} - \gamma^{-2} \begin{bmatrix} B_1 \\ 0 \end{bmatrix} \begin{bmatrix} 0 & -B_1^T \end{bmatrix} & \gamma^{-2} \begin{bmatrix} B_1 \\ 0 \end{bmatrix} \\ \hline -\gamma^{-2} \begin{bmatrix} 0 & -B_1^T \end{bmatrix} & \gamma^{-2} \end{array}\right]$$

which can be simplified to

$$\Phi^{-1}(s) = [\gamma^2 I - T_{qw}(-s)^T T_{qw}(s)]^{-1} = \left[\begin{array}{cc|c} A & \gamma^{-2} B_1 B_1^T & \gamma^{-2} B_1 \\ -C_1^T C_1 & -A^T & 0 \\ \hline 0 & \gamma^{-2} B_1^T & \gamma^{-2} \end{array}\right] \tag{6.31}$$

The poles of $\Phi^{-1}(s)$ in Eqn. 6.31 are uniquely determined from the following Hamiltonian matrix

$$\begin{bmatrix} A & \gamma^{-2} B_1 B_1^T \\ -C_1^T C_1 & -A^T \end{bmatrix} \tag{6.32}$$

The spectrum of this matrix is symmetrical with respect to the imaginary axis, i.e. it has n number of eigenvalues with Real(s) > 0 and n number of eigenvalues with Real(s) < 0. Using the above derivations, the algorithm for computing the ∞-norm of T_{qw} can be summarised as follows

1. For the open-loop Maglev model $G(s)$ and a performance weights $W(s)$, W_c, construct the state-space representation in Eqn. 6.27 to get A, B_1 and C_1.

2. Choose a relatively large value for γ, and construct the Hamiltonian matrix in Eqn. 6.32.

3. Compute the eigenvalue of this matrix.

4. Reduce γ and continue from 2 until for some value of γ there exist one or more pure imaginary eigenvalues.

5. Stop the computation and take the last value of γ as the ∞-norm of the system, $\|T_{qw}(s)\|_\infty = \gamma$.

```
% G(s):=[Ag,Bg,Cg,Dg]
Ag = [ -366.67    1   0
        1.72e-11  0   1
        1.28e6    0   0];
Bg = [  0  0 -1.68e6]';
Cg = [  1  0  0];
Dg = [0];
% W(s):=[Aw,Bw,Cw,Dw]
Aw = -0.04;
Bw = 8;
Cw = 5;
Dw = 0;
%Wc
Wc = 0.5;
% Tqw(s):=[A,B1,C1,D11tab1ta]
A  = [Ag, [0,0,0]'; -Bw*Cg, Aw];
B1 = [0,0; 0,0; 0,0; -Bw,Bw];
C1 = [0,0,0,0;-Dw*Cg, Cw];
D11= [0,0;-Dw,Dw];
for gama = 2000:-1:0.0,
     HAM = [ A         gama^-2*B1*B1';
             -C1'*C1             -A'];
      if(min(abs(real(eig(HAM))))<1e-8,
         fprintf('The infinity norm = %f',gama);
         break;
      end
end;
```

Table 6.1: MATLAB program for computing the ∞-norm of T_{qw}

To demonstrate the above results, Table 6.3.2 lists a Matlab script-program that computes the ∞-norm of T_{qw} for the state-space model of $P(s)$ in Eqn. 6.28. To construct $P(s)$, the following inputs are required:

1. the open-loop Maglev model $G(s)$

$$G(s) = \frac{\frac{5}{10\times10^{-3}} \times -3363.8278}{(s+356.6)(s+65.28)(s-55.18)} = \left[\begin{array}{ccc|c} -366.67 & 1 & 0 & 0 \\ 1.72\times10^{-11} & 0 & 1 & 0 \\ 1.28\times10^{6} & 0 & 0 & -1.68\times10^{6} \\ \hline 1.0 & 0 & 0 & 0 \end{array}\right]$$

2. the performance weight $W(s)$

$$W(s) = \frac{40}{s+0.04} = \left[\begin{array}{c|c} -0.04 & 8 \\ \hline 5 & 0 \end{array}\right]$$

3. the performance weight W_c

$$W_c = 0.5$$

(the above numerical values for $G(s)$, $W(s)$ and W_c are derived in Section 6.4(B)). For $\gamma \approx 1414.0$, two of the eigenvalues of the Hamiltonian matrix in Eqn. 6.32 are approximately zero and thus the infinity norm is $\|T_{qw}(s)\|_\infty = \gamma = 1414$. The same norm is computed with Matlab (*norm(ss(A,B1,C1,0),inf)*) to get 1414.2.

6.4 Deriving state-feedback $\mathcal{H}_\infty$ controllers for Maglev

Previously in Chapter 2, the state-feedback controller was derived by specifying a set of locations for the closed-loop poles which in turn has a close relationship with the closed-loop characteristics such as closed-loop stability margins, suspension damping and suspension stiffness [1, 35]. In the classical pole-placement design, disturbance inputs are not specifically analysed and the state-feedback gains do not have any relationships with these inputs (reference r and noise d in Fig. 6.4). The $\mathcal{H}_\infty$ state-feedback design deals with the disturbances in a systematic way by minimising the ∞-norm from the disturbance input w to the penalty output q (Eqn. 6.18). The aim is to find the state-feedback gain K by solving the following $\mathcal{H}_\infty$ optimisation problem

$$\min_K \left\| \begin{array}{c} W(I+GK)^{-1} \\ W_cK(I+GK)^{-1} \end{array} \right\|_\infty \quad \rightarrow \quad \min_K \|T_{qw}\|_\infty \tag{6.33}$$

where K uses $x = [x_1,\ x_2]^T$ (Fig. 6.4), i.e.

$$u = Kx \tag{6.34}$$

Deriving K by solving the above minimisation problem is a constraint optimisation task. There now exist a number of elegant solutions using a wide variety of mathematical techniques: from early operator-theoretic approaches [74] to the more recent state-space procedures [37] and linear matrix inequalities (LMI) techniques [75]. The state-space algorithm proposed in [37] is widely accepted as an efficient and numerically stable way for deriving $\mathcal{H}_\infty$ controllers. This algorithm is included in several software packages (for example Matlab [76], Octave [77], SciLab [78]).

Although the algorithm for deriving $\mathcal{H}_\infty$ controllers is readily available, in this thesis an alternative analytical solution is developed using Lagrange multipliers methods and differential games theory. Motivation for this work is its close analogies with the classical LQG solution which is well understood by control engineers and extensively analysed and studied in the literature (for example [79]). In addition, the analytical solution to the problem has provided a deeper understanding for the theory and a valuable basis for future

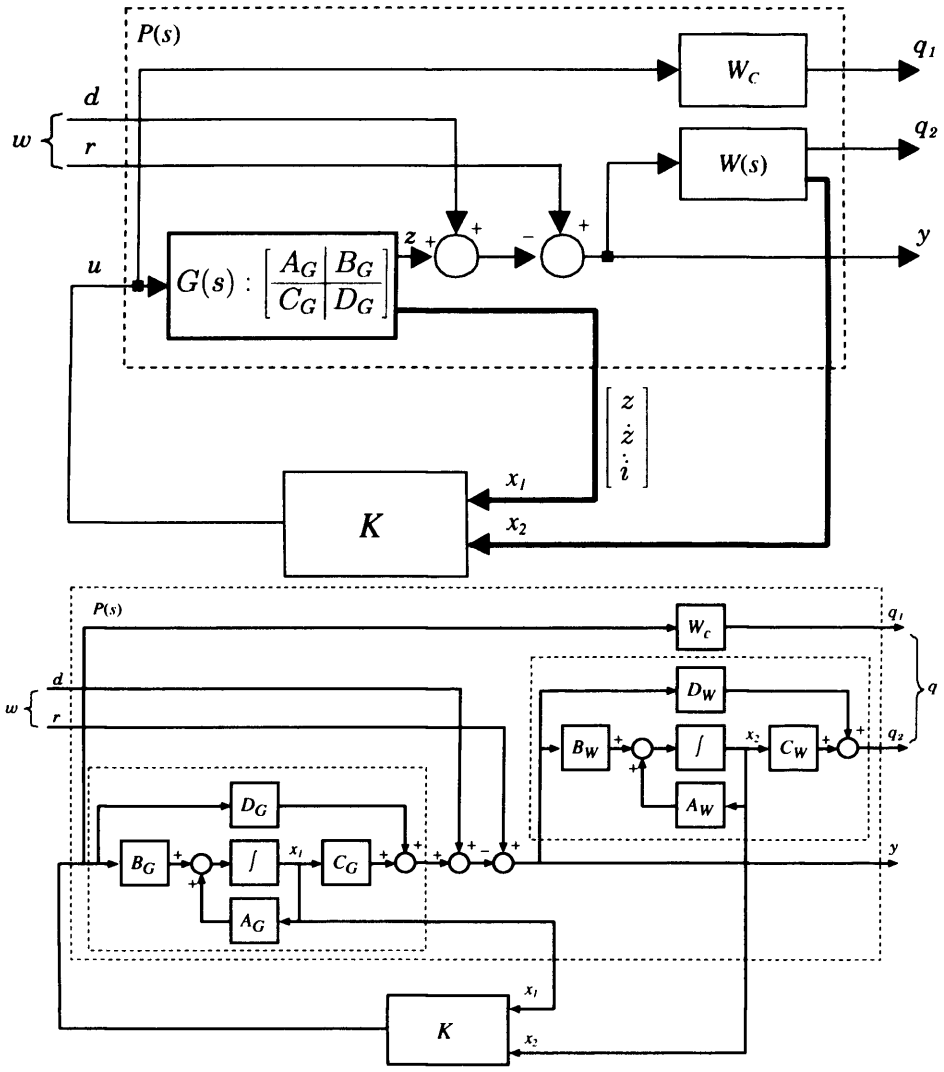

Figure 6.4: State-feedback $\mathcal{H}_\infty$ control. The feedback controller uses state variables x_1 from $G(s)$ and x_2 from $W(s)$ to construct the feedback law $u = K[x_1,\ x_2] = Kx$ (W_c is a constant).

research work on $\mathcal{H}_\infty$ Maglev control. Despite the fundamental difference in the derivations steps, the algorithm in this chapter produces identical results as in [37]. The mathematical derivations are fully described in Appendix C.1 [80, 81, 82, 83, 84, 85, 86, 87]. All simulation and experimental results in this chapter are derived from this algorithm.

The sequence of operation in the derivation of the state-feedback $\mathcal{H}_\infty$ controller as developed in Appendix C.1 is shown in Fig. 6.5. This is an optimisation loop for minimising γ which gives the upper bound on the ∞-norm in Eqn. 6.33. As γ approaches its minimum, the controller approaches the optimum controller (γ is embedded in $\mathbf{P}$).

Although the open-loop transfer function is known, the design procedure in Fig. 6.5 requires also W_c and $W(s)$ as inputs. Values and structure of these two weight transfer functions are related to the suspension characteristics. There is thus a need to first analyse

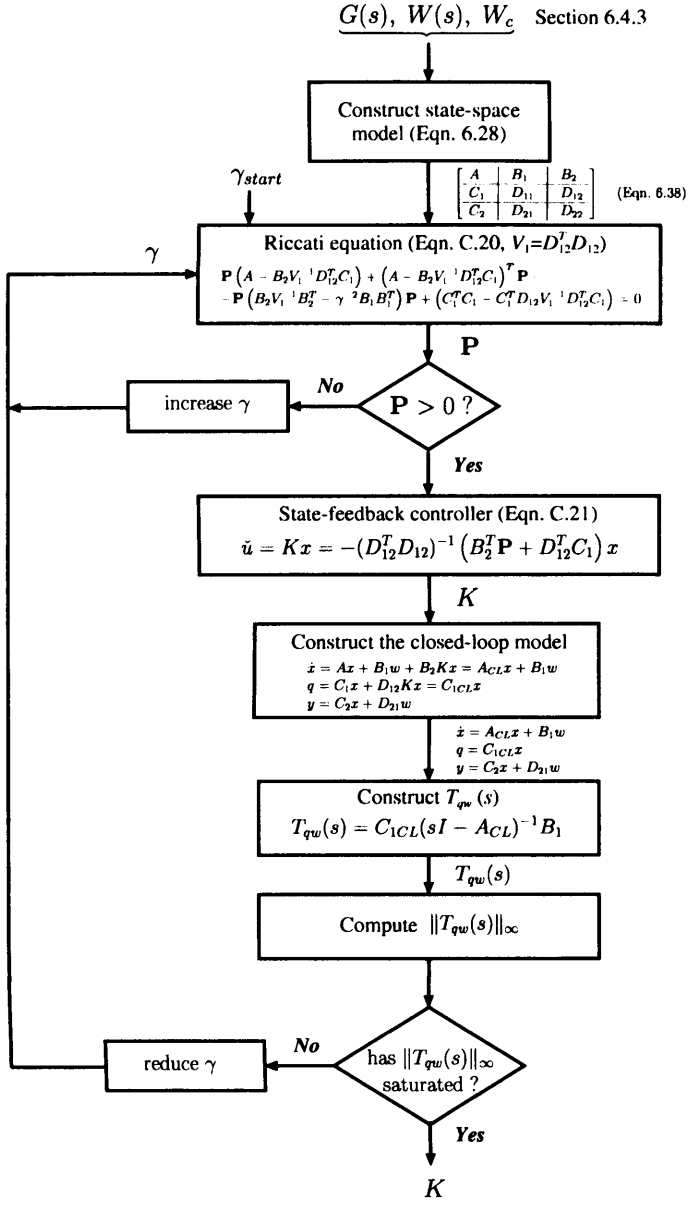

Figure 6.5: Sequence of operations used in the derivation of the state-feedback $\mathcal{H}_\infty$ controller. The full derivation steps are given in Appendix C.1.

the design requirements in the context of the closed-loop performance, and then select the appropriate forms of W_c and $W(s)$. An outline of the design requirements for the experimental Maglev system is given below. For the simulation work, a Matlab software has been developed to execute the complete flow-chart algorithm. Illustrative simulations are given in the following section.

6.4.1 Closed-loop requirements

1. The required closed-loop suspension bandwidth is 80-100 rad/s (≈15 Hz) to provide ≈ 150 msec settling time ($\approx 2\frac{1}{15}$) for the reference demand and the disturbance input.

This value is consistent with previous designs for the Maglev model (step response in Fig. 2.12, page 30) and provides a good separation between the closed-loop poles disturbance due to the track-guidance interaction [16, 17, 18].

2. The closed-loop system is required to have a good damping of step responses. There exist strong relationships between $\|S\|_\infty$ and the closed-loop stability margins [88]. For a single input single output system, the phase margin can be approximated to be $\textit{phase margin} \geq \frac{1}{\|S(j\omega)\|_\infty}$ rad. When the $\|S\|_\infty$ increases, the phase margin decreases and the overshoot, the oscillations and the settling time of the step response in the airgap also increase. The maximum gains of the sensitivity and complimentary functions are hence limited to +5dB (damping ration of 0.3 corresponds approximately to a phase margin > 32 degrees). The gain margin is required to be $> 6dB$ for robustness.

3. The control action in terms of upper bound on KS is chosen to be +6dB which is equal to two times amplification of control error to avoid saturation in the output circuits (the digital-to-analogue converter has $\pm$5V output range).

4. Small (ideally zero) steady state error in responses to step demands are required.

6.4.2 Selection of $W(s)$ and W_c

1. For good attenuation of low-frequency track disturbances, external pay-load and measurement noise disturbances the sensitivity function is required to have a low gain (i.e. -60dB) at the low-frequency range (1-20 rad/s). This will drive the gain of the complimentary function to unity at this range and hence provide zero steady-state error in the responses.

2. To provide the desired settling time of 150 msec, the sensitivity function is required to cross 0dB at around 40 rad/s. Since the closed-loop bandwidth is typically 3 to 5 times larger than the cross-over frequency of $S(j\omega)$, this will provide the desired closed-loop bandwidth of 100 rad/s.

3. For good damping, the peak of the sensitivity function, $\|S\|_\infty$, is limited to +5dB. Because of the close relationship between this parameter and the phase margins, a direct control is provided over the settling time, the overshoot and the oscillations in the response. Based on the above, the asymptotes for the sensitivity function are

drawn in Fig. 6.6 as the upper bound of $W(s)$. A suitable transfer function that meets this upper bound requirement can be implemented by a first-order model of the form

$$W(s) = \frac{40}{s + 0.04}$$

The gain plot of $W(s)^{-1}$ is given in Fig. 6.6, which provides the -60 dB bound at low frequencies and a 40 rad/s cross-over frequency. For illustration, $|W(j\omega)|$ is not bounded at higher frequencies and hence the design does not put any constraint on the high-frequency shape of $S(j\omega)$. As $\omega \to \infty$, however, $S = \frac{1}{1+K(j\omega)G(j\omega)} \to 1$ by the inherent characteristics of the open-loop system ($G(j\omega \to \infty) = 0$).

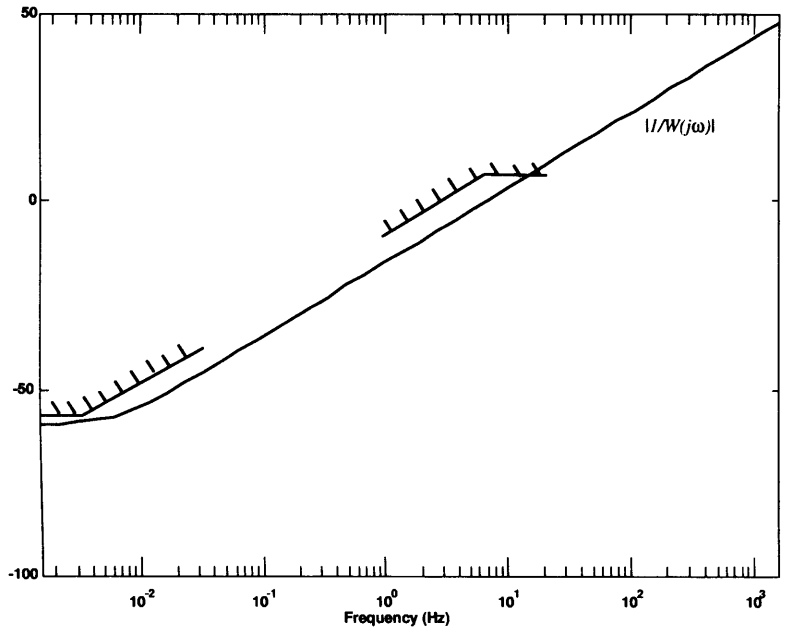

Figure 6.6: Asymptotes for the sensitivity function used to derive $W(s)$.

4. The second design parameter W_c limits the maximum control effort. Since this requirement is typically the same for the whole operating range, W_c is chosen to be a constant that provides an upper bound of +6dB

$$W_c = \frac{1}{2}$$

to guarantee that the maximum control effort would be a maximum of two-times the closed-loop error. This uses a normalised relationship between suspension airgap and position error.

$W(s)$ and W_c above provide a starting point for the synthesis. Typically, these are modified throughout the controller design until a satisfactory behaviour of the closed-loop system is achieved.

6.4.3 State-feedback design for Maglev

1. Input parameters are: open-loop transfer G(s)

$$G(s) = \frac{\frac{5}{10\times10^{-3}} \times -3363.8278}{(s+356.6)(s+65.28)(s-55.18)} = \left[\begin{array}{ccc|c} -366.67 & 1 & 0 & 0 \\ 1.72\times10^{-11} & 0 & 1 & 0 \\ 1.28\times10^{6} & 0 & 0 & -1.68\times10^{6} \\ \hline 1.0 & 0 & 0 & 0 \end{array}\right] = \left[\begin{array}{c|c} A_G & B_G \\ \hline C_G & D_G \end{array}\right] \tag{6.35}$$

$G(s)$ is inherently open-loop unstable with one positive pole at +55 rad/s, and two negative poles at [-356.56, -65.29] rad/s (Chapter 2). Since the airgap clearance is in the millimetre range, for the numerical work the steady-state gain of -51.6dB(= 2.63×10^{-3}) is normalised with a gain of $5/10 \times 10^{-3}$. The normalised transfer function has a gain of +2.34dB or +1.309.

2. performance weights $W(s)$ and W_c:

$$W(s) = \frac{40}{s+0.04} = \left[\begin{array}{c|c} -0.04 & 8 \\ \hline 5 & 0 \end{array}\right] = \left[\begin{array}{c|c} A_W & B_W \\ \hline C_W & D_W \end{array}\right] \tag{6.36}$$

$$W_c = \frac{1}{2} \tag{6.37}$$

3. The overall system contains the open-loop transfer function and the transfer functions $W(s)$ and W_c. For a single Maglev suspension with the above choice of $W(s)$ there are four state-variables: three for suspension and one for $W(s)$. The overall state-space model is given below (Fig. 6.4)

$$\left[\begin{array}{c|c|c} A & B_1 & B_2 \\ \hline C_1 & D_{11} & D_{12} \\ \hline C_2 & D_{21} & D_{22} \end{array}\right] = \left[\begin{array}{c|c|c} \begin{bmatrix} A_G & 0 \\ -B_W C_G & A_W \end{bmatrix} & \begin{bmatrix} 0 & 0 \\ -B_W & B_W \end{bmatrix} & \begin{bmatrix} B_G \\ -B_W D_G \end{bmatrix} \\ \hline \begin{bmatrix} 0 & 0 \\ -D_W C_G & C_W \end{bmatrix} & \begin{bmatrix} 0 & 0 \\ -D_W & D_W \end{bmatrix} & \begin{bmatrix} W_c \\ -D_W D_G \end{bmatrix} \\ \hline \begin{bmatrix} -C_G & 0 \end{bmatrix} & \begin{bmatrix} -I & I \end{bmatrix} & \begin{bmatrix} -D_G \end{bmatrix} \end{array}\right]$$

$$= \left[\begin{array}{cccc|cc|c} -3.6667\times10^{2} & 1 & 0 & 0 & 0.00 & 0.0 & 0.0 \\ +1.7280\times10^{-11} & 0 & 1 & 0 & 0.0 & 0.0 & 0.0 \\ +1.2844\times10^{6} & 0 & 0 & 0 & 0.00 & 0.0 & -1.6814\times10^{6} \\ -4.0000\times10^{1} & 0 & 0 & -4.0\times10^{-2} & -40.0 & 40.0 & 0.00 \\ \hline 0.00 & 0.00 & 0.00 & 0.00 & 0.00 & 0.00 & 0.50 \\ 0.00 & 0.00 & 0.00 & 1.00 & 0.00 & 0.00 & 0.00 \\ \hline -1.00 & 0.00 & 0.00 & 0.00 & -1.00 & 1.00 & 0.00 \end{array}\right] \tag{6.38}$$

Although the Maglev system has been instrumented to generate all three state-variables, K requires a state variable from $W(s)$ which is not available (measurable). Therefore, the state-feedback $\mathcal{H}_\infty$ controller is not suitable for practical implementation. By design, the order of the controller is equal to the order of the open-loop system plus the orders of the performance weights. Despite this fact, the mathematical tools developed here are essential part of the output-feedback controller which has an observer-based structure

(Section 6.5). The derivations below also provide an insight for the specification of the suspension performance via performance weights.

4. Derivation of K requires constructing the Riccati equation in Eqn. C.20. Using Eqn. 6.38 and the initial value for $\gamma = 100$, this equation is solved in Matlab to get

$$\mathbf{P} = \begin{bmatrix} 0.0006279 & 8.64 \times 10^{-6} & 7.401 \times 10^{-8} & -0.0041535 \\ 8.6401 \times 10^{-6} & 1.3269 \times 10^{-7} & 1.2362 \times 10^{-9} & -4.9673 \times 10^{-5} \\ 7.401 \times 10^{-8} & 1.2362 \times 10^{-9} & 1.4786 \times 10^{-11} & -2.9701 \times 10^{-7} \\ -0.0041535 & -4.9672 \times 10^{-5} & -2.9701 \times 10^{-7} & 0.034754 \end{bmatrix}$$

$\mathbf{P}$ above is a positive definite matrix and hence provides a stabilising solution to the control problem. The state-feedback controller for $\gamma = 100$ is constructed from Eqn. C.30

$$\breve{u} = Kx = -V_1^{-1}\left(B_2^T\mathbf{P} + D_{12}^T C_1\right)x = [0.4978,\ 0.0083,\ 0.0001,\ -1.9976]x$$

For $\gamma = 100$, the eigenvalues of the Hamiltonian matrix in Eqn. C.17 are

$$\lambda(\gamma = 100) = \left\{ \begin{array}{l} -356.23,\ 356.23,\ -136.48,\ 136.48,\ -64.387 - j98.428, \\ -64.387 + j98.428,\ 64.387 - j98.428i,\ 64.387 + j98.428 \end{array} \right\}$$

These eigenvalues are symmetrical and have non-zero real parts. The eigenvalues of the closed-loop matrix are computed from Eqn. C.31

$$eig(A_{CL}, \gamma = 100) = \{-356.55, -89.68, -43.845 + j47.81, -43.845 - j47.81\}$$

Since all eigenvalues have negative real parts, the closed-loop system is stable. In fact by taking γ to be a very large number, the state-feedback $\mathcal{H}_\infty$ problem reduces to a LQR control problem [80, 79]. As long as the Riccati equation in Eqn. C.20 has a positive definite solution $\mathbf{P}$, the closed-loop system is stable.

Since the real parts of the eigenvalues of the Hamiltonian matrix in Eqn. C.17 are away from the imaginary axis, γ can be reduced. For this purpose, an optimisation search loop was constructed. At every iteration, γ is reduced by a factor of δ from its previous value, i.e. $\gamma(k) = \gamma(k-1)/\delta$ where k is the loop iteration index and $\delta = 2$. When γ approaches its optimal value (i.e. it does not change so rapidly), the division factor is increased, i.e. $\delta = \delta \times 2$. Within this loop, the Riccati equation in Eqn. C.20 is solved for $\mathbf{P}$ and the feedback signal $\breve{u}$ is constructed. After 22 iterations, γ saturated to $\gamma = 1.657$ with the following optimal controller

$$\breve{u} = Kx = [1.0333,\ 0.0160,\ 0.0002,\ -5.8819]\ x \tag{6.39}$$

With this controller the eigenvalues of the closed-loop Maglev system in Eqn. C.31 are

$$eig(A_{CL}, \lambda = 1.657) = \{-356.37, -130.05, -66.51 + j64.19, -66.51 - j64.19\}$$

Since γ saturated to its minimal value and $\mathbf{P} > 0$, the closed-loop system is stable and the state-feedback $\mathcal{H}_\infty$ control problem is solved with K in Eqn. 6.39. This controller guarantees that the sensitivity function S and the input-sensitivity function KS are bounded by $W(s)$ and W_c. This completes the design loop in the algorithm.

5. Matlab simulation results: Since the state-feedback controller is not suitable for practical implementation, the validation of the result is performed in simulation. For this purpose, the following closed-loop transfer functions are constructed using the controller in Eqn. 6.39 and the closed-loop matrices in Eqn. C.31:

(a) T_{qw} between the disturbance input $w = [d,\ r]^T$ and the penalty output q

$$\begin{bmatrix} q_1 \\ q_2 \end{bmatrix} = \begin{bmatrix} W_cKS \\ WS \end{bmatrix} w = \left(C_{1CL}(sI - A_{CL})^{-1}B_1\right) w = \begin{bmatrix} \frac{117.6373(s+356.6)(s+65.28)(s-55.18)}{(s+356.4)(s+130.1)(s^2+133s+8544)} \\ \frac{-40(s+373)(s^2+246.4s+2.766e4)}{(s+356.4)(s+130.1)(s^2+133s+8544)} \end{bmatrix} \begin{bmatrix} d \\ r \end{bmatrix}$$

(b) The sensitivity function S between the input w and the output y

$$y = Sw = \left(C_2(sI - A_{CL})^{-1}B_1 + D_{21}\right) w = \frac{(s+373)(s+0.04)(s^2+246.4s+2.766e4)}{(s+356.4)(s+130.1)(s^2+133s+8544)} \begin{bmatrix} -d \\ r \end{bmatrix}$$

(c) The complementary function T between the disturbance input w and the air-gap clearance $z = [C_G,\ 0]$

$$z = Tw = \left(C_G(sI - A_{CL})^{-1}B_1\right) w = \frac{395.59 \times 10^6}{(s+356.4)(s+130.1)(s^2+133s+8544)} \begin{bmatrix} -d \\ r \end{bmatrix}$$

Without changing the generality of the results in the next series of analysis, r is assumed to be zero (i.e. $w = d$).

The mixed sensitivity problem in Eqn. 6.18 has two goals: (1) to shape the sensitivity function $S(s)$ using the performance weight $W(s)$ by selecting the feedback controller $u = Kx$, and (2) to limit the the magnitude of the control action by defining W_c and then minimising W_cKS by selecting K. These goals are achieved when $\left\| \begin{matrix} WS \\ W_cKS \end{matrix} \right\|_\infty \leq \gamma,\ \gamma \approx 1$. Fig. 6.7 shows the magnitude plots of WS and W_cKS. Since these are approximately below 0dB (i.e. the infinity norms are below $\gamma \approx 1$), K in Eqn. 6.39 solves the $\mathcal{H}_\infty$ optimisation problem. To check this further, $S(s)$ and Eqn. 6.36 are used to construct $W(s)S(s)$. The magnitude plots of $S(s)$ and $W(s)$ are shown in Fig. 6.8 (top). The magnitude plot of WS is shown in Fig. 6.8 (bottom). $|S(j\omega)|$ remains bounded by $|W^{-1}(j\omega)|$ and hence $|WS|$ is $\approx$ 0 dB for $0 < \omega < 10$ Hz and $|WS| < 0$ dB for $\omega > 10$ Hz (Fig. 6.8 (bottom)). Furthermore, the magnitude plot of $|S(j\omega)|$ crosses the -3 dB point at $\approx$5 Hz and hence the closed-loop bandwidth is expected to be ≥ 15 Hz. The peak of the sensitivity function is $\|S(j\omega)\|_\infty \approx 3.33$ dB and hence the closed-loop Maglev system is expected to have a

good damping to step responses and also good overshoot and stability margins. Although $W(s)$ does not limit the gain of $S(j\omega)$ at high frequency, this gain approaches unity from the inherent properties of the open-loop system at high frequencies, as suggested earlier.

To examine the suspension characteristics in the time-domain, a step response in the desired airgap r is generated using the complimentary function $T(s)$. The simulation result is shown in Fig. 6.9. As suggested from the frequency analysis, the closed-loop transfer function has a good damping ratio and a settling time of approximately 100 ms.

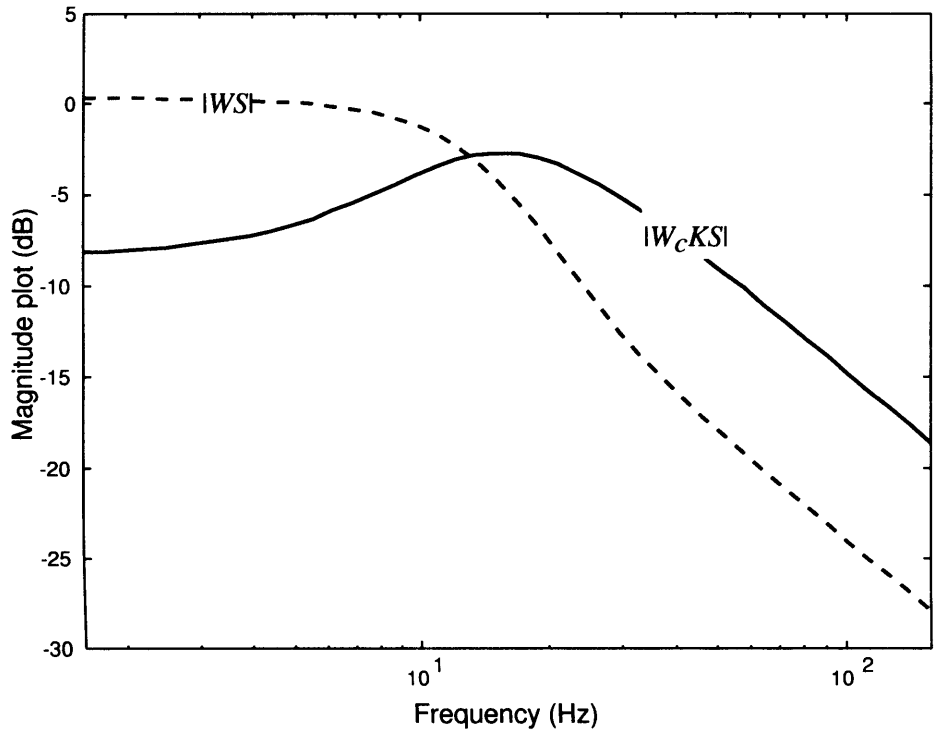

Figure 6.7: Magnitude plot of the performance weights W_cKS and WS.

To examine the effect of W_c on the controller design, four more experiments were carried out. For these, $W(s)$ is kept unchanged and W is reduced from 0.5 to [0.2, 0.1, 0.05]. These values correspond to maximum gains of [13.9, 20 and 26] dB for KS. Higher gains provide more aggressive control actions and hence an increase in the closed-loop bandwidth. This observation can be seen from the corresponding simulation results in Fig. 6.10. The effect of $W(s)$ on the control-system design is studied in Section 6.5.

In conclusion, the new $\mathcal{H}_\infty$ state-feedback controller provides better damping, settling time and bandwidth characteristics compared to the classical state-feedback controller (designed with pole-placement techniques). The designer has a systematic and well defined control over the closed-loop characteristics via the performance weights $W(s)$ and W_c. This controller, however, is impractical since a new state-variable is required from $W(s)$ for the

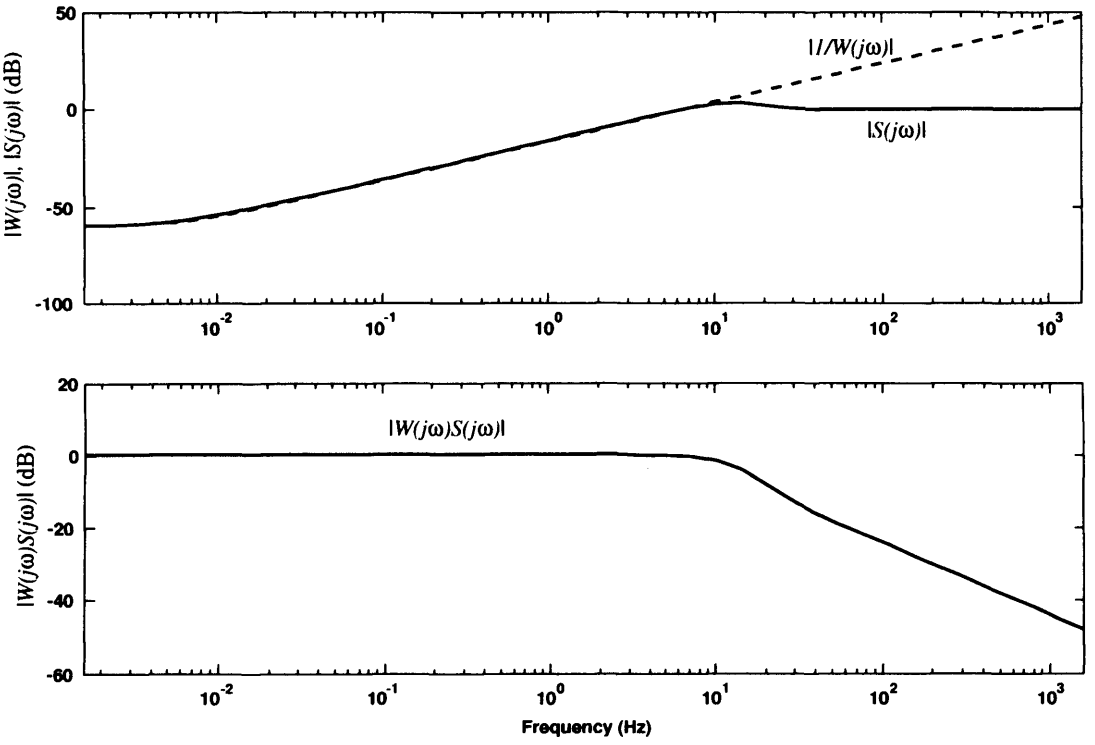

Figure 6.8: Top: Bode plot of the sensitivity function and the corresponding performance weight for this function. Bottom: Magnitude plot of WS. Optimal $\mathcal{H}_\infty$ controller guarantees that $|S(j\omega)|$ is bounded from above by $|W^{-1}(j\omega)|$ and hence $|WS| \leq 1$

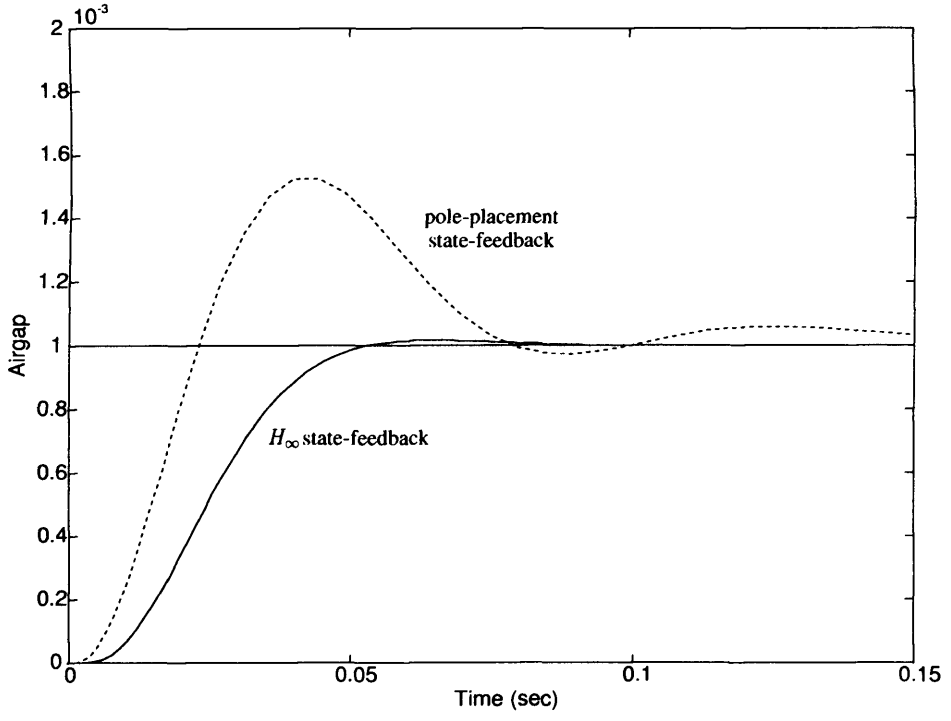

Figure 6.9: Step response of the closed-loop Maglev system with: (a) the new state-feedback $\mathcal{H}_\infty$ controller in Eqn. 6.39 and (b) the old state-feedback controller ($k_p = 2800$, $k_v = 18$; $k_a = 0.4$)

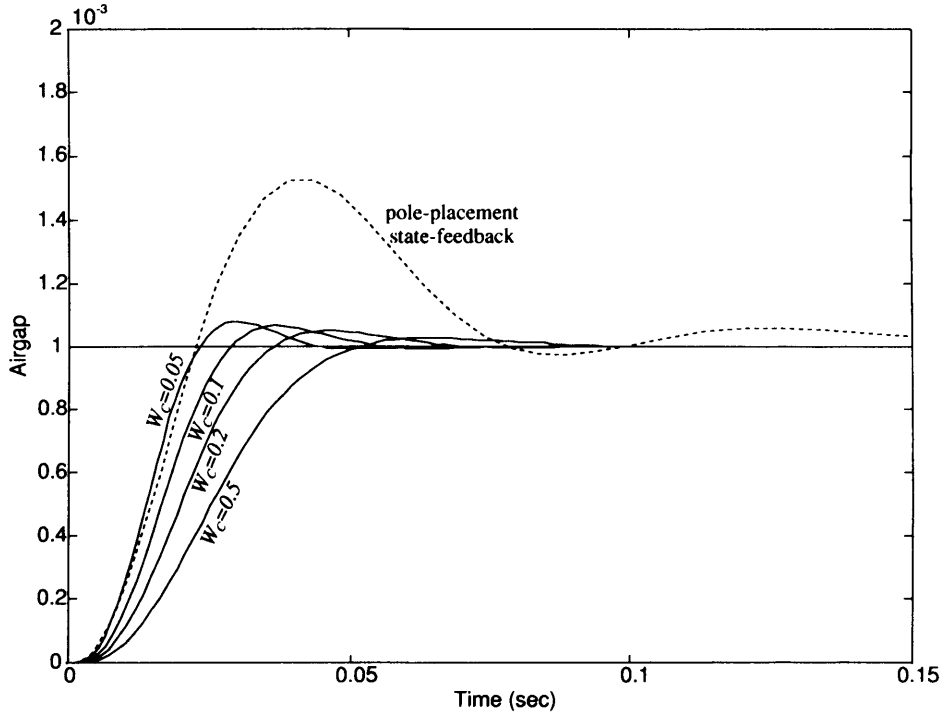

Figure 6.10: Step response of the closed-loop Maglev system with the state-feedback $\mathcal{H}_\infty$ controller in Eqn. 6.39 for four different values for the performance weight W_c.

construction of the feedback. Despite this fact, all tools developed here are used in the construction of the output-feedback controller which has an observer-based structure. Although the derivation procedure for the $\mathcal{H}_\infty$ controller is more involved compared to the classical pole-placement design, it will be shown that the design tools developed here are directly applicable to multi-magnet control problems (Chapter 8). In addition, the derivation steps can be extended with robustness analysis to provide a tool for designing robust controllers for multi-magnet systems. These applications are discussed in the following chapters. The exposition continuous with the derivation of the output-feedback controller.

6.5 Deriving output-feedback $\mathcal{H}_\infty$ controllers for Maglev

In the construction of the output-feedback compensator, only the position output is used for feedback stabilisation (Fig 6.11). This is considered as novel for this thesis since all previous approaches use state-feedback principles. This chapter demonstrates both in simulation and experiment that the output-feedback compensator provides comparable to the state-feedback controller suspension characteristics. Furthermore since only one output is used, a reduction in cost and a potential for other applications, e.g. magnetic bearings which

employ only a position version, is provided.

To derive the output-feedback $\mathcal{H}_\infty$ controller, the following mixed sensitivity problem (derived in Eqn. 6.18) has to be solved

$$\min_K \left\| \begin{array}{c} W(I+GK)^{-1} \\ W_c K(I+GK)^{-1} \end{array} \right\|_\infty \quad \rightarrow \quad \min_K \|T_{qw}\|_\infty \tag{6.40}$$

where the feedback controller K uses y (Fig 6.3), i.e.

$$u = Ky \tag{6.41}$$

Despite the fact that the solution to this problem is readily available (for example Matlab), for reasons outlined in Section 6.4 a new algorithm is developed for Maglev control. This uses Lagrange multipliers and differential game theories and is fully presented in Appendix C.2 [82, 83, 84, 89, 86, 90, 87]. The algorithm for deriving output-feedback $\mathcal{H}_\infty$ controllers is summarised in Fig. 6.12 (Appendix C.2). For validation purposes, this algorithm is compared with Matlab in Section 6.5.3.

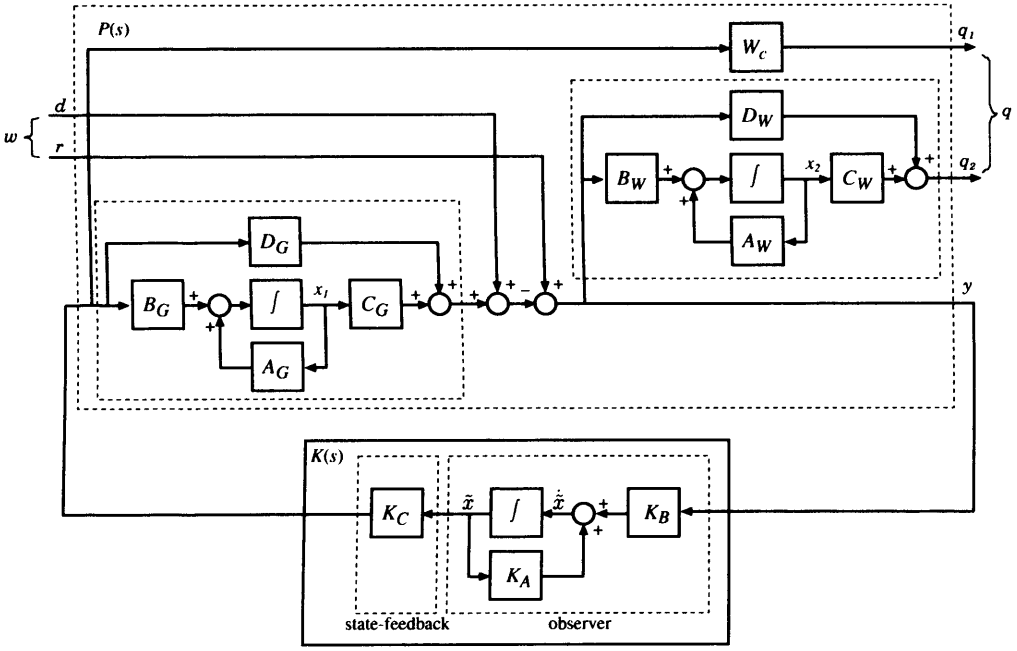

Figure 6.11: Output-feedback $\mathcal{H}_\infty$ control.

From a control point of view, the $\mathcal{H}_\infty$ output feedback controller has an observer-based structure and consists of an $\mathcal{H}_\infty$ state-estimator and the state-feedback $\mathcal{H}_\infty$ controller [37] (Fig. 6.11). In contrast to the classical optimal control (for example the LQR control [79, 91, 88] which uses a Kalman filter and a state-feedback controller) the new $\mathcal{H}_\infty$ design does not satisfy the separation properties. This requires the construction of a single design algorithm that derives the state-feedback controller (K_C) and the observer (K_A and

K_B) simultaneously within a single design loop (Fig. 6.12). Details on the mathematical developments are given in Section C.2.5. To solve the optimisation problem in Eqn. 6.40, the mathematical derivations in Appendix C.2 establish that two Riccati equations have to be solved: one for the state-feedback controller and another for the $\mathcal{H}_\infty$ observer. The sequence in the derivation steps is illustrated in Fig. 6.12. This is an optimisation loop for searching for the optimal γ which minimises the ∞-norm in Eqn. 6.40. As $\|T_{qw}\|_\infty$ approaches its minimum, the output-feedback controller approaches the optimal controller. γ is embedded in its coefficients via $\mathbf{P}$ and $\mathbf{Q_M}$. For the numerical work, a Matlab program is designed to follow the algorithm for deriving output-feedback controllers in Fig. 6.12. Illustrative examples for Maglev using this design tool are given below.

6.5.1 Closed-loop requirements

The closed-loop design requirements are fully derived in Section 6.4.1 (A and B).

6.5.2 Matlab design example

1. Input parameters for the design are: the open-loop Maglev model (Eqn. 6.35) and the performance weights $W(s)$ and W_c (Eqn. 6.36 and 6.37). The overall model $P(s)$ (Fig. 6.11) is derived in Eqn. 6.38 to get A, B_1, B_2, C_1, C_2, D_{11}, D_{12}, D_{21} and D_{22}.
2. Using the initial value $\gamma_{start} = 100$, the Riccati equation in Eqn. C.20 is solved for $\mathbf{P}$

$$\mathbf{P} = \begin{bmatrix} 6.2790 \times 10^{-4} & 8.6400 \times 10^{-6} & 7.4010 \times 10^{-8} & -4.1535 \times 10^{-3} \\ 8.6401 \times 10^{-6} & 1.3269 \times 10^{-7} & 1.2362 \times 10^{-9} & -4.9673 \times 10^{-5} \\ 7.4010 \times 10^{-8} & 1.2362 \times 10^{-9} & 1.4786 \times 10^{-11} & -2.9701 \times 10^{-7} \\ -4.1535 \times 10^{-3} & -4.9672 \times 10^{-5} & -2.9701 \times 10^{-7} & 3.4754 \times 10^{-2} \end{bmatrix}.$$

The eigenvalues of this matrix are computed and since they are all positive ($\mathbf{P}$ is positively definite), this matrix can be used in the construction of the modified estimator matrices (Eqn. C.56)

$$A_M = A + \gamma^{-2} B_1 B_1^T \mathbf{P} = \begin{bmatrix} -3.6667 \times 10^{2} & 1.0000 & 0 & 0 \\ 8.6402 \times 10^{-12} & 0 & 1.0000e+000 & 0 \\ 1.2844 \times 10^{6} & 0 & 0 & 0 \\ -4.0001 \times 10^{1} & -1.5895 \times 10^{-5} & -9.5044 \times 10^{-8} & -2.8879 \times 10^{-2} \end{bmatrix}$$

$$C_{1M} = (D_{12}^T D_{12})^{-1} \left(B_2^T \mathbf{P} + D_{12}^T C_1 \right) = [-4.98 \times 10^{-1},\ -8.31 \times 10^{-3},\ -9.94 \times 10^{-5},\ 1.997]$$

$$C_{2M} = C_2 + \gamma^{-2} D_{21} B_1^T \mathbf{P} = [-1.0000,\ -3.9738 \times 10^{-7},\ -2.3761 \times 10^{-9},\ 2.7803 \times 10^{-4}]$$

3. Using the matrices above, the observer Ricatti equation (Eqn. C.58) is constructed and

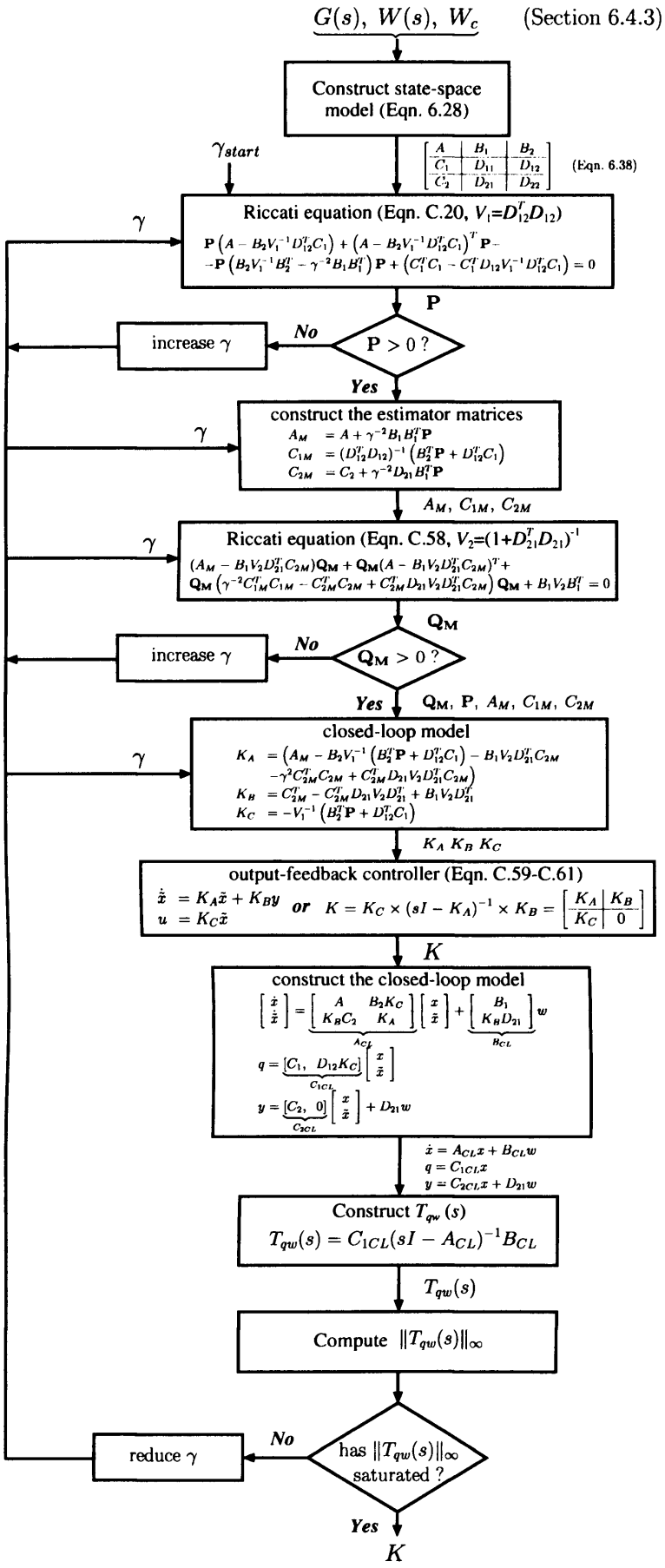

Figure 6.12: Sequence of operations used in the derivation of the output-feedback $\mathcal{H}_\infty$ controller. The full derivation steps are given in Appendix C.2.

solved to get

$$\mathbf{Q_M} = \begin{bmatrix} 3.3543 \times 10^2 & 1.4150 \times 10^5 & 7.8077 \times 10^6 & -6.9255 \times 10^1 \\ 1.4150 \times 10^5 & 5.9690 \times 10^7 & 3.2937 \times 10^9 & -2.9215 \times 10^4 \\ 7.8077 \times 10^6 & 3.2937 \times 10^9 & 1.8174 \times 10^{11} & -1.6120 \times 10^6 \\ -6.9255 \times 10^1 & -2.9215 \times 10^4 & -1.6120 \times 10^6 & -1.5323 \times 10^3 \end{bmatrix}$$

The eigenvalues of $\mathbf{Q_M}$ are positive and hence the matrix is positively definite.

4. $\mathbf{P}$ and $\mathbf{Q_M}$ above together with the open-loop model are used in Eqn. C.60 to derive the output-feedback controller

$$K_A = \begin{bmatrix} -4.7851 \times 10^2 & 9.9996 \times 10^{-1} & -2.6575 \times 10^{-7} & 3.1096 \times 10^{-2} \\ -4.7182 \times 10^4 & -1.8749 \times 10^{-2} & 9.9989 \times 10^{-1} & 1.3118 \times 10^1 \\ -2.1560 \times 10^6 & -1.3980 \times 10^4 & -1.6722 \times 10^2 & 3.3595 \times 10^6 \\ 9.6158 & 3.8210 \times 10^{-6} & 2.2847 \times 10^{-8} & -4.2673 \times 10^{-2} \end{bmatrix}$$

$$K_B = \begin{bmatrix} -1.1184 \times 10^2 \\ -4.7181 \times 10^4 \\ -2.6034 \times 10^6 \\ 4.9615 \times 10^1 \end{bmatrix}$$

$$K_C = [4.9777 \times 10^{-1},\ 8.3141 \times 10^{-3},\ 9.9446 \times 10^{-5},\ -1.9976]$$

In a transfer-function form the controller is given below

$$K(s) = K_C(sI - K_A)^{-1}K_B = \frac{-805.9465(s + 356.6)(s + 65.28)(s + 4.331)}{(s + 396.7)(s - 1.859)(s^2 + 250.9s + 4.287 \times 10^4)}$$

5. To assess the performance characteristics of this controller, the closed-loop system in Eqn. C.62 is constructed and used to derive the transfer function from w to q

$$\begin{bmatrix} q_1 \\ q_2 \end{bmatrix} = \begin{bmatrix} W_cKS \\ WS \end{bmatrix} = \begin{bmatrix} T_{qw}(1,1) & T_{qw}(1,2) \\ T_{qw}(2,1) & T_{qw}(2,2) \end{bmatrix} \begin{bmatrix} d \\ r \end{bmatrix}$$

where

$$T_{qw}(1,1) = -T_{qw}(2,1) = \frac{402.9732(s-55.18)(s+65.28)^2(s+356.6)^2(s+4.331)}{(s+356.6)(s+356.6)(s+89.8)(s+65.28)(s+56.46)(s^2+87.81s+4212)}$$

$$T_{qw}(1,2) = -T_{qw}(2,2) = \frac{-40(s+356.6)(s+396.7)(s+65.28)(s-55.18)(s-1.859)(s^2+250.9s+4.287e004)}{(s+0.04)(s+56.46)(s+65.28)(s+89.8)(s+356.6)(s+356.6)(s^2+87.81s+4212)}$$

The ∞-norm of $\|T_{qw}\|_\infty = 324.01$. Since this value is greater than one, this controller does not satisfy the closed-loop requirements. The phase margin of the closed-loop system is 11 degrees and the gain margin is below -2.1 dB (the design requirement is PM>40 degrees and GM>6dB).

6. To derive the optimal controller, an optimisation loop is constructed to search for the optimal γ that minimises $\|T_{qw}\|_\infty$. This algorithm works as follows. $\|T_{qw}\|_\infty$, is compared with the norm from the previous iteration for γ $(k-1)$ to produce the error in the norm

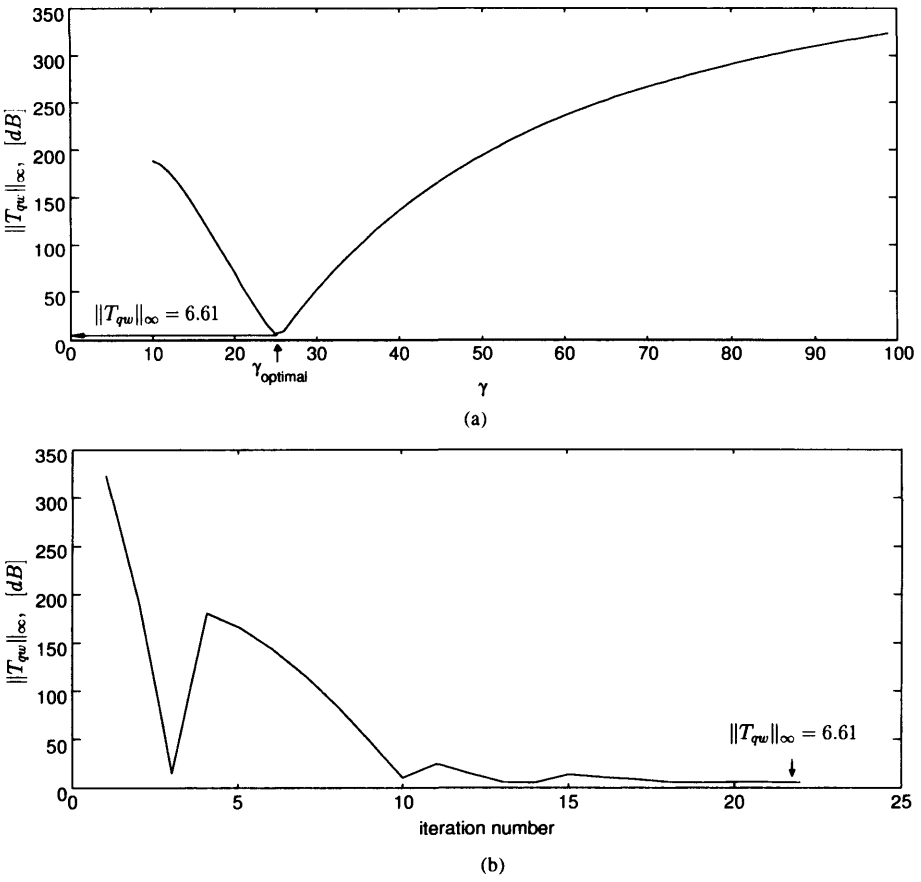

Figure 6.13: Convergence of $\|T_{qw}\|_\infty$ during the $\mathcal{H}_\infty$ output-feedback design procedure.

$(norm(k) - norm(k-1))$. If this error is below a certain threshold (e.g. 1×10^{-5}), the algorithms stops and the $\mathcal{H}_\infty$ controller from this iteration is considered to be the optimal. If, however, the error is higher than this threshold, γ is reduced by $\gamma(k) = \gamma(k-1) - \gamma(k-1)/\delta$ where δ is a division factor set initially to $\delta = 2$. When during the search procedure the error in the norm changes its sign, the δ factor is increased by four and its sign is alternated, i.e. $\delta = -\delta \times 4$. With the new value for $\gamma(k)$, the algorithm continues from Step 2. This is an optimisation loop that searches for the optimal γ that minimises $\|T_{qw}\|_\infty$. The response of $\|T_{qw}\|_\infty$ versus γ is shown in Fig. 6.13 (a) and the convergence of $\|T_{qw}\|_\infty$ during the controller optimisation procedure is shown in Fig. 6.13 (b). After 23 iterations for γ, $\|T_{qw}\|_\infty$ saturates to +6.62 dB for $\gamma = 25.2$. The corresponding output-feedback $\mathcal{H}_\infty$ controller is given below

$$K(s) = \frac{-938.7875(s+65.28)(s+356.6)(s+6.801)}{(s+403.6)(s+0.03934)(s^2+266.7s+4.795\times10^4)} \tag{6.42}$$

The complimentary function from the reference airgap r to the airgap output, $T(s) = GK(1+GK)^{-1}$ with K above is given below

$$T(s) = \frac{1577675559.0522 \times (s+356.6)(s+65.28)(s+6.796)}{(s+356.6)(s+356.5)(s+94.28)(s+74.88)(s+65.28)(s^2+89.31s+4244)}$$

The corresponded sensitivity function from disturbance input to system's output, $S(s) = (1 + GK)^{-1}$ is also derived

$$S(s) = \frac{(s + 403.5)(s + 356.6)(s + 65.28)(s - 55.18)(s + 0.03621)(s^2 + 266.6s + 4.793 \times 10^4)}{(s + 356.6)(s + 356.5)(s + 94.28)(s + 74.88)(s + 65.28)(s^2 + 89.31s + 4244)}$$

The poles of the closed-loop system are negative and the largest is located at -356.5 rad/s. This suggests that the desired closed-loop bandwidth of 15 Hz has been met. The magnitude response of $S(s)$ is shown in Fig. 6.14. The maximum gain is about +12 dB. This value is considered as rather high [88] and it suggests that the closed-loop system has a small phase margin and poor performance characteristics. A simulation step response in the airgap is shown in Fig. 6.18 (plot-1). The phase margin with K in Eqn. 6.42 is 12.774 degrees (computed with Matlab). This is rather low and justifies the poor performance characteristics of the system. 12 dB infinity norm is equal to a gain of approximately four and hence step responses in the airgap disturbance or in the position demand would be multiplied by a factor of four; this effect is shown in Fig. 6.18. From Fig. 6.14, the closed-loop bandwidth was calculated to be 166.83 rad/s or 26.55 Hz. This value is consistent with the design requirements. In addition to $|S(s)|$, Fig. 6.14 shows four more responses: (a) the performance bound $|W^{-1}(s)|$, (b) the optimisation product $|WS|$, (c) the performance bound $|W_c^{-1}|$, and (d) the optimisation product $|W_cKS|$. $|WS|$ and $|W_cKS|$ construct the $\mathcal{H}_\infty$ design criteria for the mixed sensitivity problem as per Eqn. 6.2.4; the design goal is to keep $\|T_{qw}\|_\infty = \left\| \begin{matrix} WS \\ W_cKS \end{matrix} \right\|_\infty \leq 1$ by deriving K. Since both $|WS|$ and $|W_cKS|$ are above 0 dB, K in Eqn. 6.42 is a sub-optimal solution to the problem. Although the performance weights are kept unchanged as in the state-feedback design, the optimisation procedure here saturates with higher γ values (6.62 dB vs. 1.66 dB). Empirical studies with the design algorithms suggest that the output-feedback design requires more effort since two Riccati equations have to be solved simultaneously. This completes one cycle of design.

The above results suggest that the bound on the control signal W_c is rather low. This limits the control reaction of the system and results in poor outputs from the $\mathcal{H}_\infty$ optimisation procedure. To prove that W_c constrains the optimisation result, in the next study W_c is kept unchanged ($W_c = 0.5$) but the performance weight on the sensitivity function is changed to

$$W_1(s) = \frac{0.66667(s + 60)}{(s + 0.04)} \tag{6.43}$$

to bound the sensitivity function to +3.52 dB from above at $\omega > 60$ rad/s (see $|W^{-1}|$ in Fig. 6.15). With this new weight, the optimisation procedure saturates with $\|T_{qw}\|_\infty =$

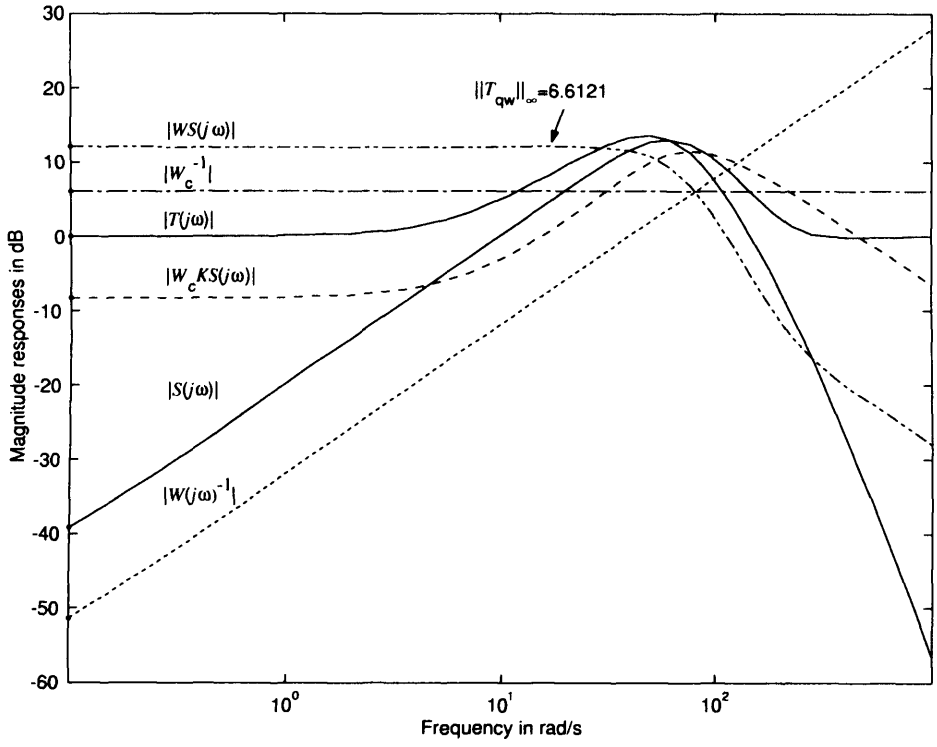

Figure 6.14: Closed-loop transfer functions and their performance weights for $K(s)$ in Eqn. 6.42 and Maglev model as per Eqn. 6.35.

6.9965 and the following feedback controller

$$K_1(s) = \frac{-1010.4289(s+356.6)(s+65.28)(s+6.319)}{(s+406.9)(s+0.039)(s^2+272s+5.078\times 10^4)}$$

Since $\|T_{qw}\|_\infty = 6.9965$ has remained almost unchanged, the result suggests that the new performance weight did not have any impact on the closed-loop system and the controller. The gains of the sensitivity and complimentary functions also remained unchanged and the phase margin was calculated to be 14.43 degrees. A set of frequency responses for this new controller is shown in Fig. 6.15.

The design cycles are repeated with different values for W_c and $W_1(s)$ unchanged as per Eqn. 6.43. The following results were obtained.

- For $W_{c1} = 0.25$ (=12.04 dB bound on KS), $\|T_{qw}\|_\infty$ was reduced to 4.9747 dB.
- For $W_{c2} = 0.1$ (20 dB), $\|T_{qw}\|_\infty$ was reduced to 3.5671 dB.
- For $W_{c3} = 0.075$ (22.5 dB), $\|T_{qw}\|_\infty$ was reduced to 3.28 dB.
- And finally for $W_{c4} = 0.005$ (46 dB), $\|T_{qw}\|_\infty$ was reduced to 2.1 dB.

The feedback $\mathcal{H}_\infty$ controller for $W_{c4} = 0.005$ and $\|T_{qw}\|_\infty = 2.1$ dB is given below

$$K_2(s) = \frac{-33423.4256(s+356.6)(s+65.28)(s+18.78)}{(s+811.9)(s+0.03477)(s^2+665.8s+4.825\times 10^5)} \tag{6.44}$$

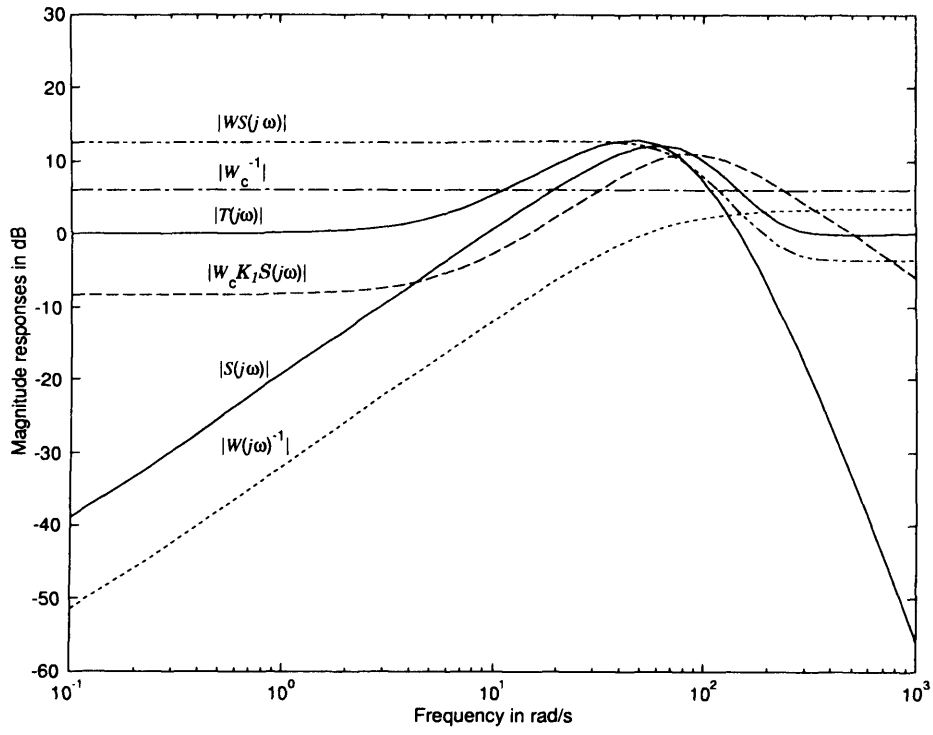

Figure 6.15: Closed-loop transfer functions with K_1. $W_1(s)$ is given in Eqn. 6.43 and $W_c = 0.5$ is unchanged.

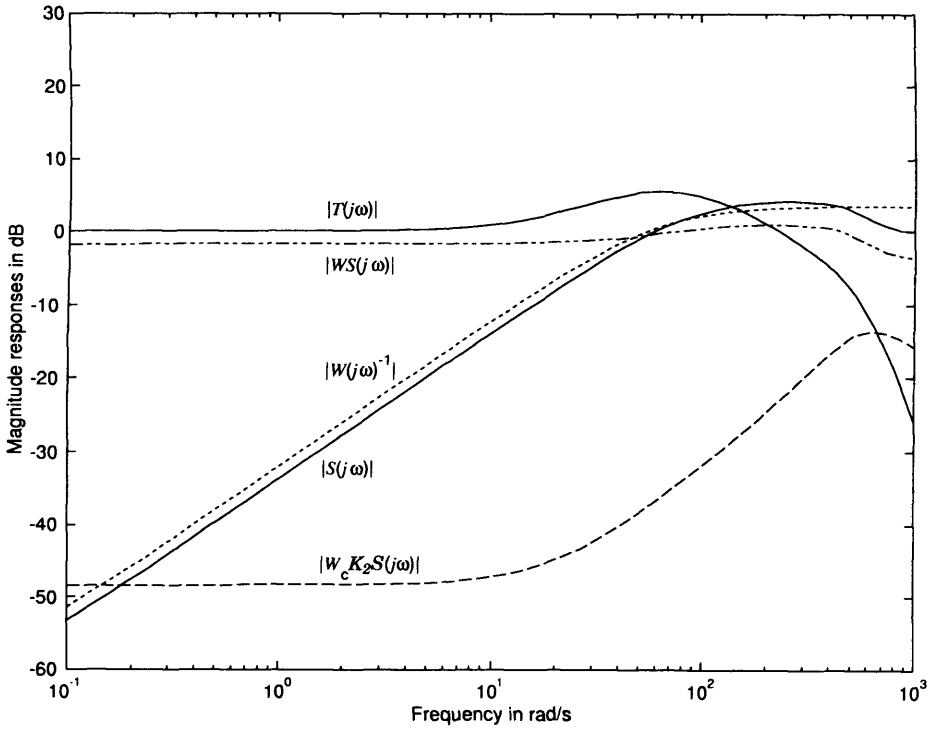

Figure 6.16: Closed-loop transfer functions with $W(s)$ in Eqn. 6.43 and $W_c = 0.005$ (46dB and hence the plot is outside the range in the figure).

The frequency responses in Fig. 6.16 show that this controller achieves a significant reduction in terms of peak of the sensitivity function. $\|S\|_\infty = 3.8$ dB suggests good damping to step responses. The phase margin of the closed-loop system with K_2 is 41.1 degree and the closed-loop bandwidth has increased to 52.2 Hz. The correspondent magnitude responses of the complimentary and the sensitivity functions are shown in Fig. 6.17(bottom). The magnitude response of $K_2(s)$ (Eqn. 6.44) is shown in Fig. 6.17(top) and suggests that the

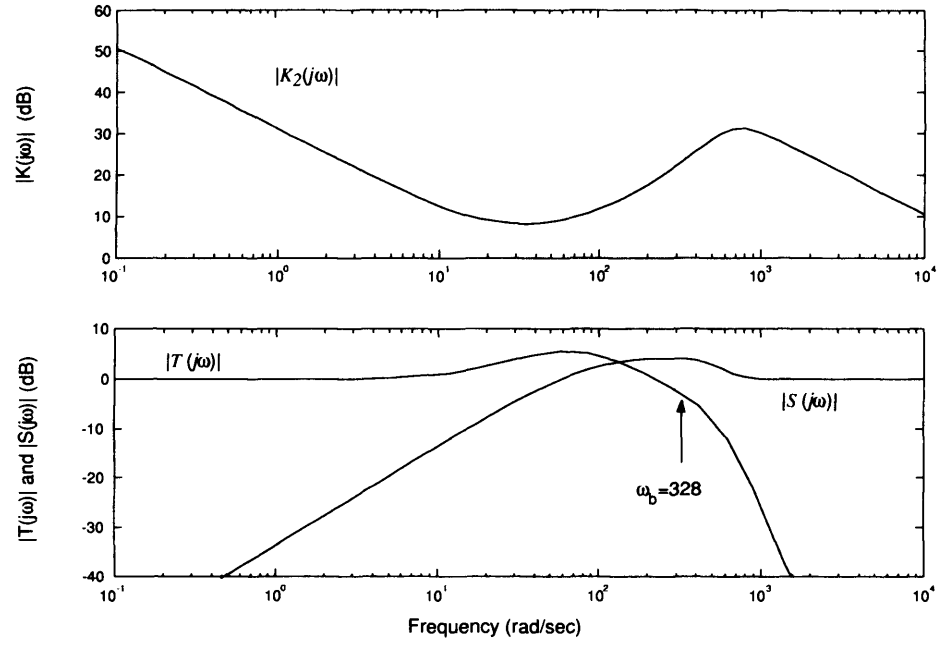

Figure 6.17: Top: magnitude response of $K_2(s)$ in Eqn. 6.44. Bottom: complimentary and sensitivity functions for this controller.

controller has a lag action in the low-frequency range to reduce steady-state errors, lead action in the middle frequency range around the bandwidth to improve gain and phase margins, and filtering properties in the high-frequency range to attenuate noise. The zero steady-state error property is also shown in Fig. 6.17 (bottom) where: (a) the complimentary function has 0 dB gain at the low frequency range and hence provides good tracking, and (b) the sensitivity function has a low gain at the low frequency range and hence provides good disturbance rejection. The figure also shows that the bandwidth of the system with this controller is $\omega_b = 328$ rad/s (52 Hz). Although large bandwidth provides some good qualities, for the single-magnet system this value approaches the practical limit and the dynamic characteristics of the amplifiers and sensors in this range might have a considerable effect on the system. A simulated step response in the airgap with K_2 is shown in Fig. 6.18 (plot-2). As suggested from the above frequency-domain results, this new compensator provides considerably better suspension characteristics. The settling time

is reduced to 100 milliseconds, and the overshoot and the oscillations are within typical Maglev design requirements.

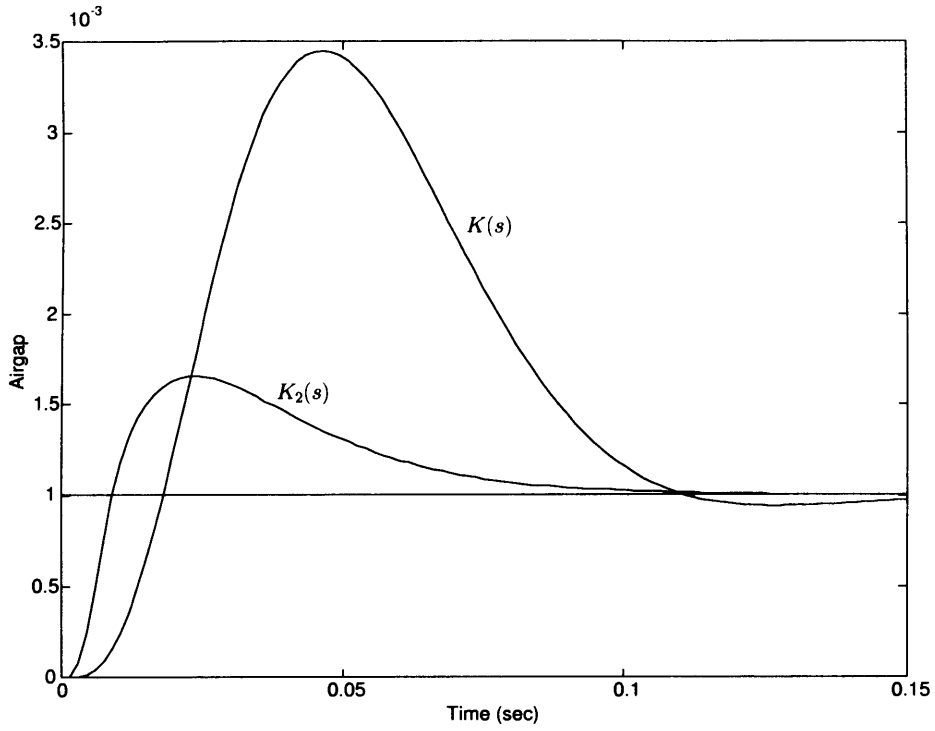

Figure 6.18: Simulated step responses with output-feedback controllers ($K(s)$ in Eqn. 6.42 and $K_2(s)$ in Eqn. 6.44).

6.5.3 Assessment of the $\mathcal{H}_\infty$ design

As indicated earlier (page 109), for validation purposes, a comparison is made between the $\mathcal{H}_\infty$ design developed here and the algorithm provided by Matlab as a part of the *μ-Analysis and Synthesis Toolbox* [76, 37]. The step response in the reference airgap of the closed-loop system and the Bode plot of the controllers are used as a benchmark. In the next discussion, *Algorithm I* refers to the algorithm developed here, and *Algorithm II* refers to the Matlab algorithm.

Using the performance weights in Eqn. 6.43 and Eqn. 6.37, *Algorithm II* has produced the following feedback controller

$$K_{MATLAB}(s) = \frac{-2766251.9565(s+356.6)(s+65.28)(s+17.37)}{(s+2.61\times10^4)(s+0.04)(s^2+1577s+1.193\times10^6)}$$

A simulated step response in the reference airgap from 3 mm to 4 mm with K_2 in Eqn. 6.44 (Algorithm I) and K_{MATLAB} above (Algorithm II) is shown in Fig. 6.19. Both controllers provide almost identical closed-loop bandwidth, settling time and overshot in the response.

The damping is unchanged with slightly higher values for K_{MATLAB}. The Bode plots of the controller are shown in Fig. 6.20. In the low-frequency range, the controllers are identical and provide integration effects for zero steady state error. In the mid-frequency range, both controllers have lead-lag characteristics to give the desired phase margin (40 degrees by design). Just after the bandwidth, Algorithm I starts decreasing in amplitude to provide high-frequency disturbance attenuation and low dissipation on the system. Algorithm II has all-pass characteristics from 10^2 to 10^3 Hz. Although this provides a slightly higher phase margin (50 degrees for Algorithm II), the high gain at high frequencies allows high-frequency disturbances to enter the system and hence more dissipation on the magnet. In conclusion, the $\mathcal{H}_\infty$ optimisation algorithm developed here compares closely with the Matlab algorithm and provide a convenient tool for Maglev control.

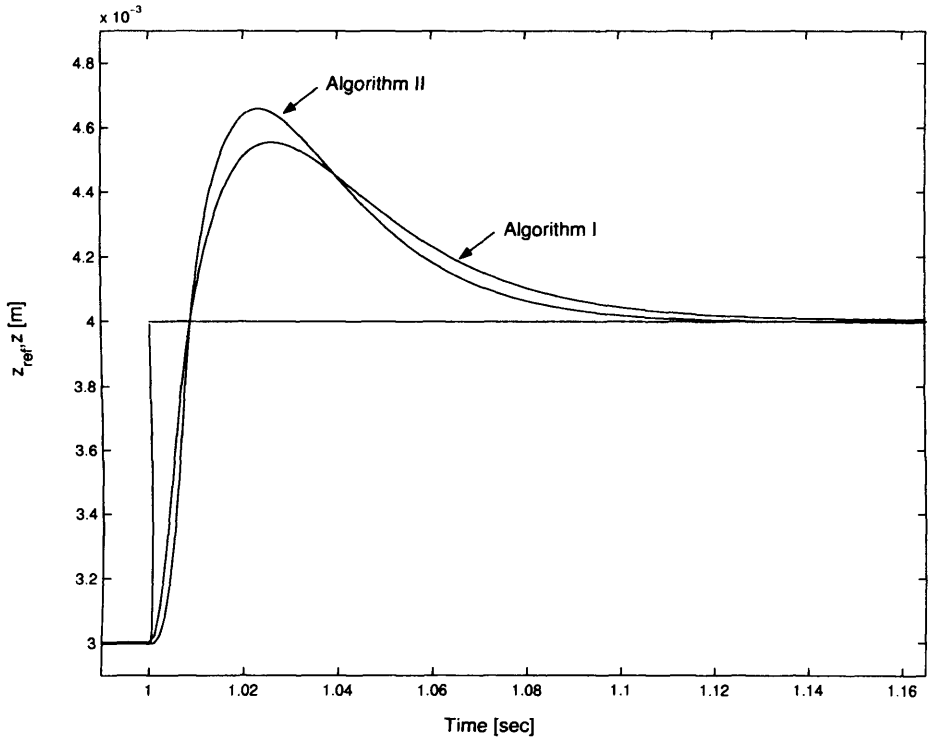

Figure 6.19: Simulated step responses with $K_2(s)$ (Algorithm I) and $K_{MATLAB}(s)$ (Algorithm II).

To conclude, the algorithm for deriving $\mathcal{H}_\infty$ controllers is able to solve the controller-design task and the closed-loop system closely follows the design requirements. W and W_c give a significant control over the suspension characteristics and by varying these, the designer can achieve desired suspension qualities and closed-loop bandwidth and phase margins. These design parameters can be derived intuitively by accessing the disturbance-attenuation requirements of the closed-loop system. Compared to the state-feedback con-

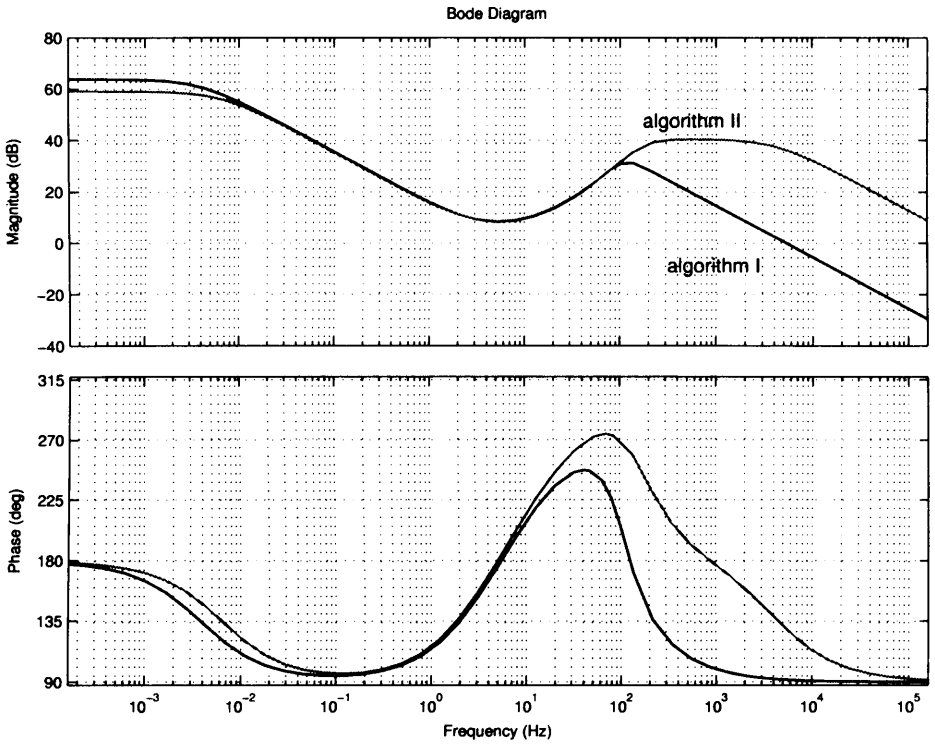

Figure 6.20: Bode plot of $K_2(s)$ (Algorithm I) and $K_{MATLAB}(s)$ (Algorithm II).

troller derived with pole-placement techniques (Fig. 6.9), the $\mathcal{H}_\infty$ controller provides a faster step response with less oscillations. A considerable advantage is considered also the fact that only one output is used for stabilisation and hence a reduction in cost can be achieved. The experimental studies with the new compensator are presented below.

6.6 Experimental studies

The experimental hardware (one magnet + DSP) discussed in Chapter 5 has been used for the $\mathcal{H}_\infty$ controller implementation. For the digital control work, a 32 bit floating point DSP processor and 16 Mbits of external memory for storing experimental results are provided. The sampling frequency is fixed at 1 kHz to be compatible with the bandwidth characteristics of the closed-loop system (20 times larger that the closed-loop bandwidth) and to reduce sampling effects. Although a much higher sampling frequency was used for previous Maglev designs, analysis has shown that 1 kHz provides a good compromise for the operational stability and available computational slot. Eight anti-aliasing analogue filters are integrated on the board with cut-off frequencies of 25 kHz(=half the sampling frequency of the ADC per channel). The control algorithms are written in C language for the SHARC family of DSPs. The continuous controllers designed in Matlab (Eqn. 6.44)

are converted to their digital equivalent using the Tustin algorithm. Since the sampling frequency (1 kHz) is considerably higher than the controller's bandwidth, the discretisation does not pose any phase delays. The $\mathcal{H}_\infty$ design environment in Section 6.5.2 automatically stores the controller's coefficients in a file. Before each DSP experiment, this file is transfered automatically to the DSP memory to update the controller. The DSP hardware integrates facilities for real-time communication with Matlab/Simulink (Section 5.4, 84). The experimental data is transferred from the DSP memory to Matlab without disturbing the control loop. This is used to derive the experimental plots in this chapter.

For validation purposes, the experimental results are compared with similar simulation results derived from the Simulink simulator in Fig. 6.21. There are two sources of disturbance entering this model: (a) disturbance due to changes in the desired reference airgap r, and (b) disturbances due to measurement noise d. For the purpose of the analysis, the airgap and the control outputs (y and u) are stored in Matlab at the end of the simulation cycle to be compared with similar experimental responses. For the validation, the controller in the Simulink model is identical to the controller implemented on the experimental system.

To assess the performance of the output-feedback controller derived in the previous section, two sets of experiments in terms of comparison between simulation and experiment were performed. The output-feedback controller $K(s)$ in Eqn. 6.42 derived with $W(s)$ and W_c (Eqns. 6.36 and 6.37) is compared with the output-feedback controller $K_2(s)$ in Eqn. 6.44 derived with $W_1(s)$ (Eqn. 6.43) and $W_{c4} = 0.005$. A step change in the reference position was applied and the corresponding simulation and experimental responses are shown in Fig. 6.22 for $K(s)$ and Fig. 6.23 for $K_2(s)$, respectively. The reference airgap was changed from 4×10^{-3}m to 3×10^{-3}m at t=0.5 sec. and then from 3×10^{-3}m back to 4×10^{-3}m at t=1 sec. The results in the figure suggest a good comparison between theory and experiment. The large gain of the sensitivity function with $K(s)$ in Eqn. 6.42 leads to large overshoots in the response. This causes saturation in the position sensor (Fig. 6.22) and the latter needs to recover which results in a modified transient response. The axes in Fig. 6.22 and Fig. 6.23 are deliberately kept unchanged to show the significant improvement in terms of stability and robustness offered by $K_2(s)$. As suggested earlier, this controller offers: (a) small peak in $|S(s)|$ and hence good suspension damping, (b) 52.2 Hz closed-loop bandwidth and hence a settling time of 0.1 sec. For a close comparison, Fig. 6.24 (airgap output) and Fig. 6.25 (control output) present the response in Fig. 6.23 in a different scale. These results show the good comparison between the theoretical model

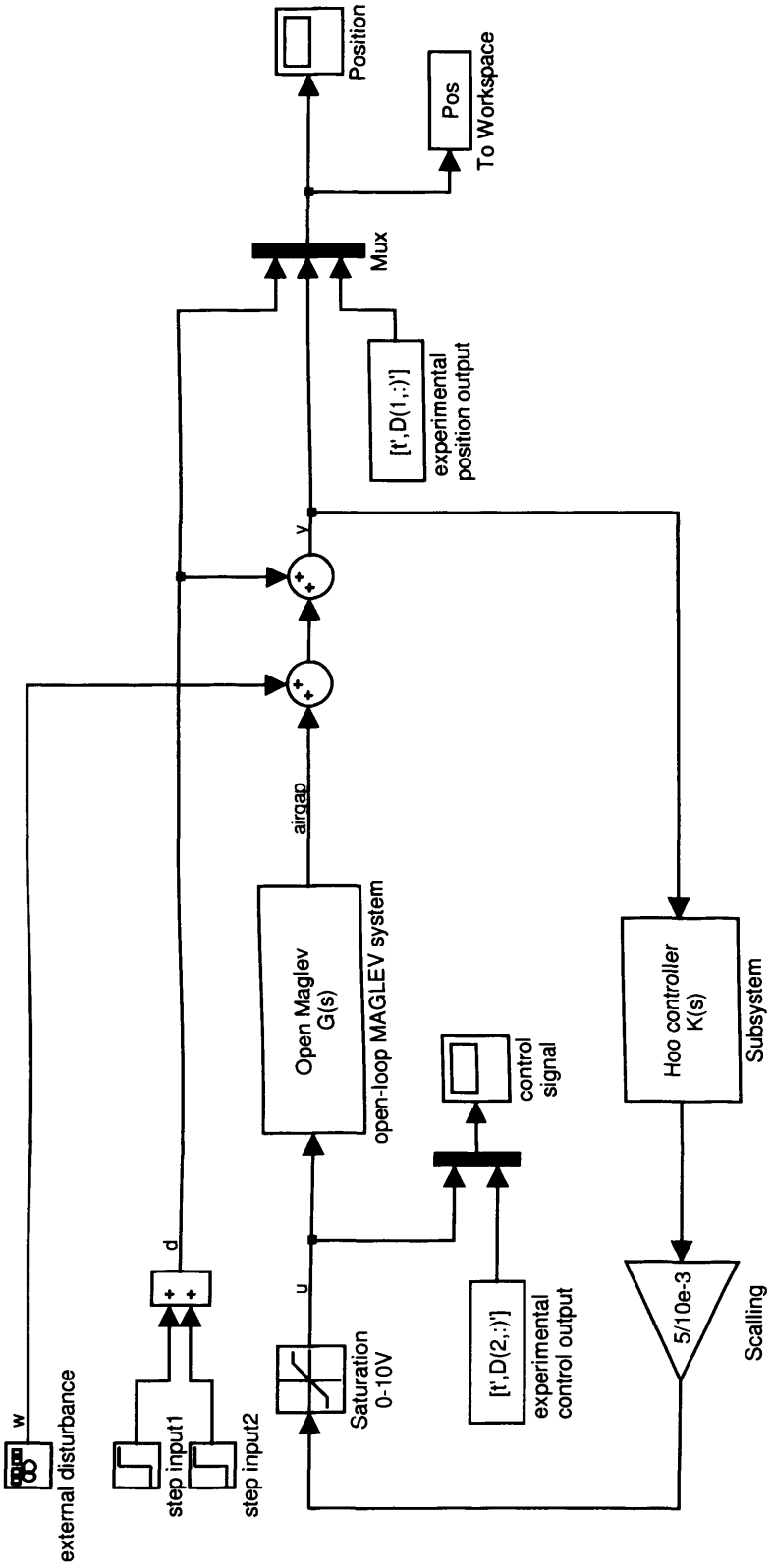

Figure 6.21: Simulink model used for the comparison of experimental and simulation results.

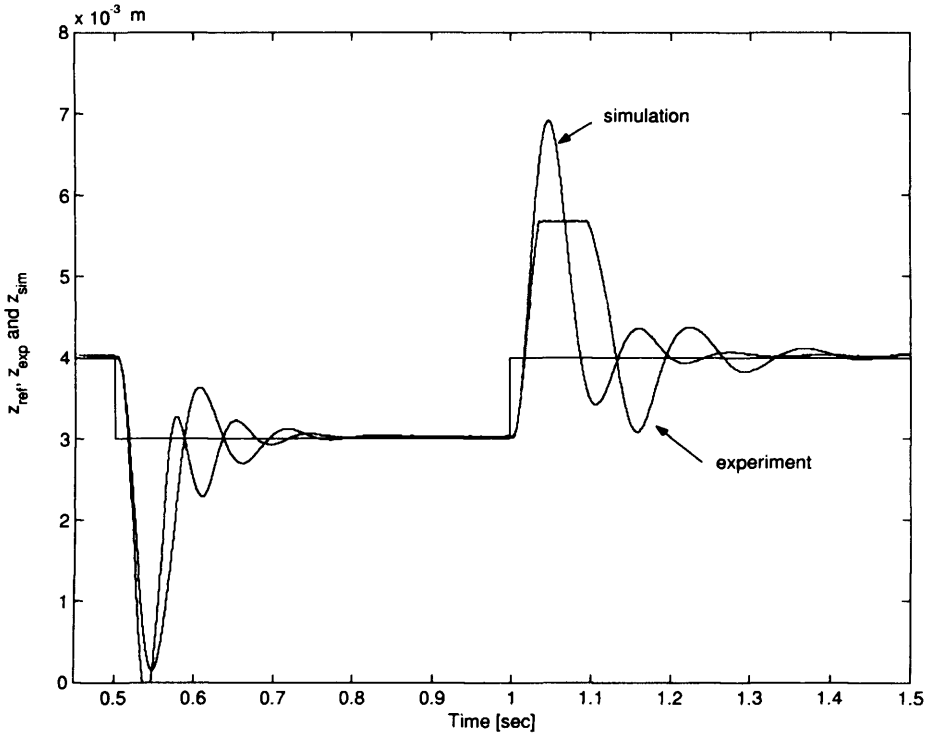

Figure 6.22: Output-feedback $\mathcal{H}_\infty$ control: simulation and experimental step responses in the reference airgap with $K(s)$ in Eqn. 6.42.

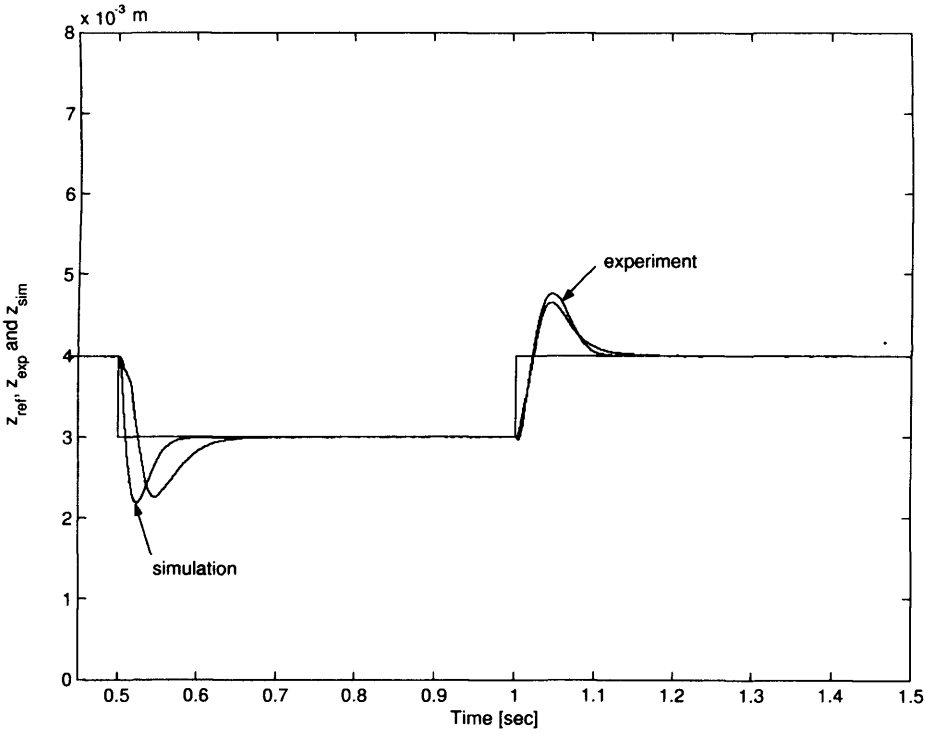

Figure 6.23: Output-feedback $\mathcal{H}_\infty$ control: simulation and experimental responses in the reference airgap with $K_2(s)$ in Eqn. 6.44.

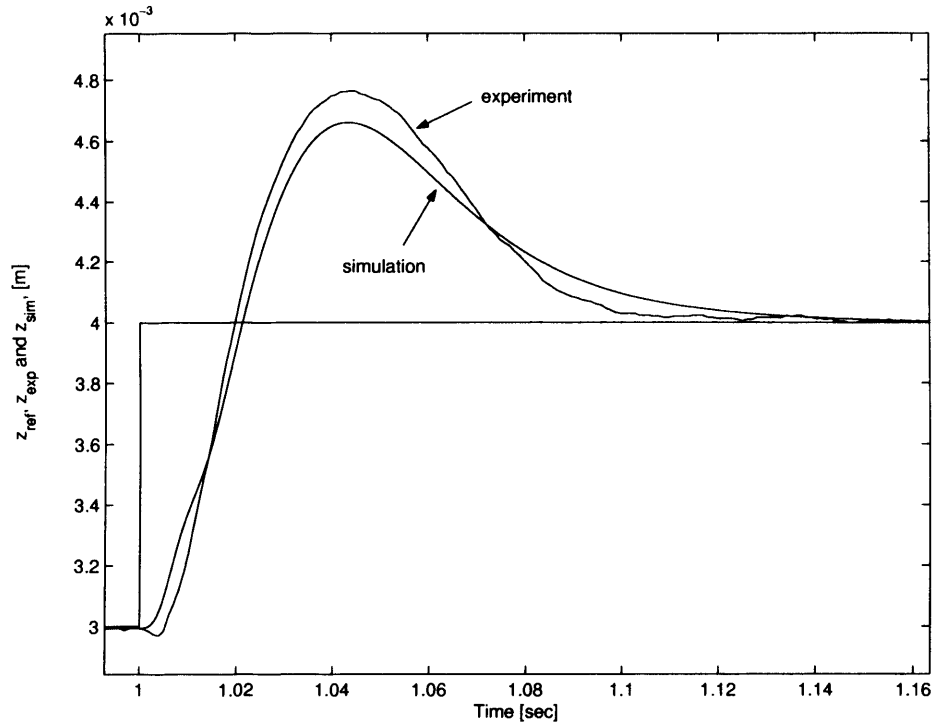

Figure 6.24: Output-feedback $\mathcal{H}_\infty$ control: simulation and experimental responses in the reference airgap with $K_2(s)$ in Eqn. 6.44.

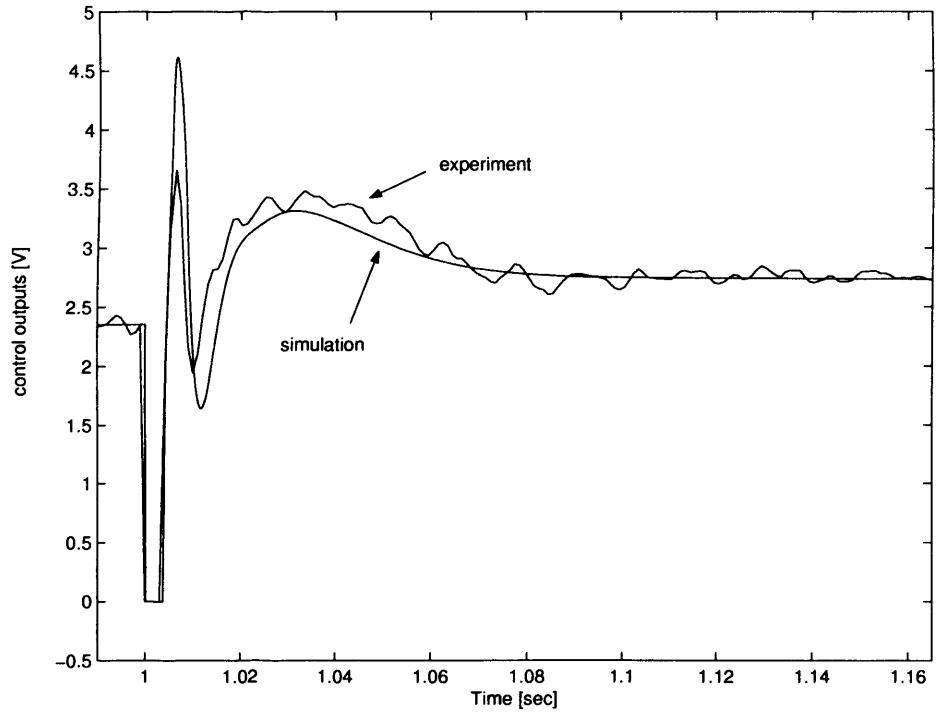

Figure 6.25: Output-feedback $\mathcal{H}_\infty$ control: control output for the responses in Fig. 6.24

and the experimental result.

For a further assessment of the controller, the sensitivity and the complimentary functions of the closed-loop system are derived experimentally for K_2 in Eqn. 6.44. For the analysis, the DSP software is modified such that a sine-wave disturbances is internally generated in the DSP software and added to the control signal. Varying the frequency of this signal and collecting data from: (a) signal before the additional identification source, and (b) control signal after the injected sine-wave source, allow the experimental derivation of the frequency response of the complimentary and the sensitivity functions. For this anal-

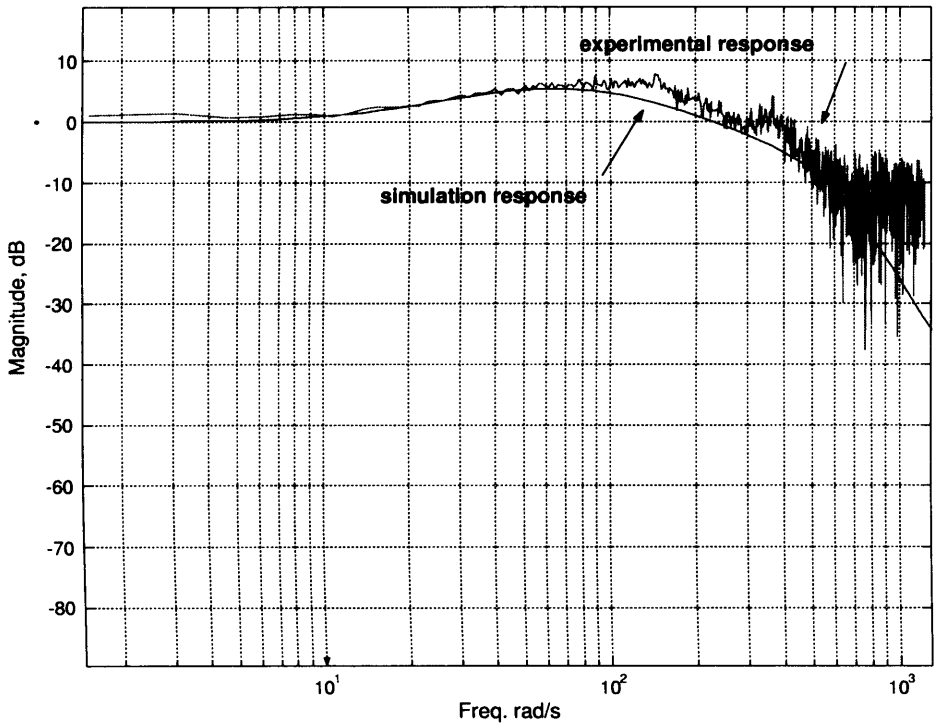

Figure 6.26: Simulation and experimental magnitude plot of the complimentary function of the closed-loop system with the feedback controller in Eqn. 6.44.

ysis, the chirp sine-wave source was varied from 0 Hz to 200 Hz for a period of 50 seconds. The input and the corresponding output signals: (a) before the identification sine-wave signal and (b) after the identification signal were collected and stored in the DSP memory. At the end of the experiment, the data was transfered to Matlab. For the frequency-domain assessment, a Matlab program was built for Dynamic Signal Analysis (DSA). This tool performs Fourier transformation over the input and the output data to produce the frequency responses in Figs. 6.26 for the complimentary function and in Fig. 6.27 for the sensitivity function.

The experimental responses in Figs. 6.26 and Fig. 6.27 show the good comparison between experiment and theory, especially in the low-frequency range ($\omega < 100$ rad/s).

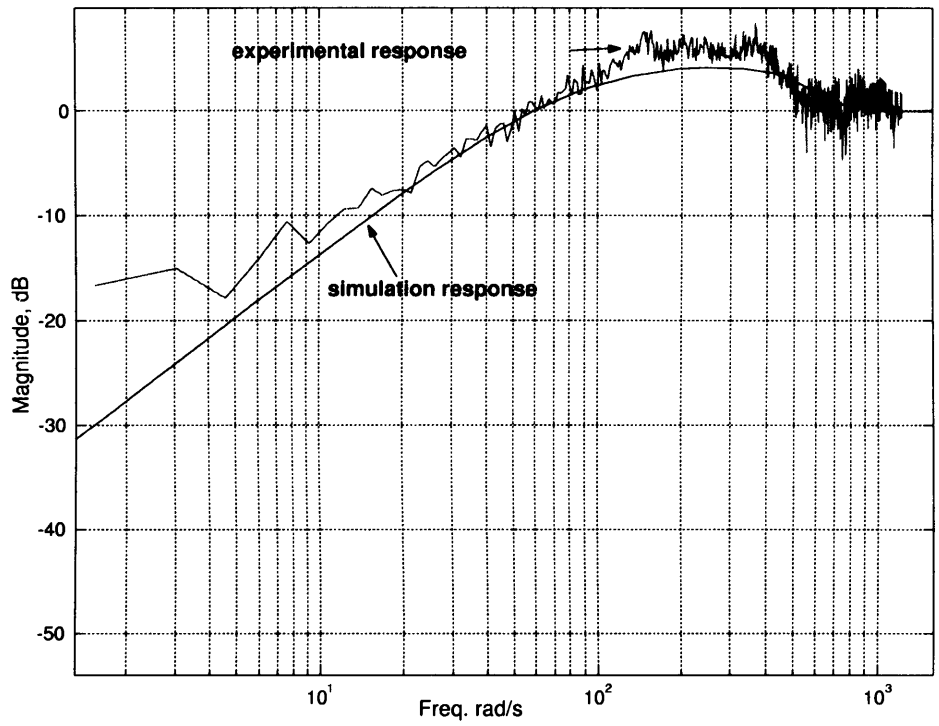

Figure 6.27: Simulation and experimental magnitude plot of the sensitivity function of the closed-loop system with the feedback controller in Eqn. 6.44.

Within the middle frequency range, $100 < \omega < 1000$ rad/s, the experimental responses have slightly larger gains than the theoretical response and hence the theoretical model used for the syntheses differs from the experimental. This is believed to be due to the dynamic characteristics of the remaining dynamical systems in the loop (the position sensor and the power amplifier are excluded from the overall model $G(s)$). Overall, there exists a good comparison between theory and experiment and the $\mathcal{H}_\infty$ algorithms developed in this chapter provide a convenient tool for Maglev design. The suspension characteristics are well within the Maglev system requirements and the responses compare with responses from classical design techniques. The designer has a control over the closed-loop requirements by varying the performance weights $W(s)$ and W_c. The design tool is deterministic and the results are systematic. Although the design procedure is more involved than a simple pole-placement, it will be shown that the $\mathcal{H}_\infty$ design tool provides a basis for multi-magnet control and for robust analysis and design. This is discussed in the following chapters.

For the analysis of the suspension properties of the system in attenuating force disturbance, only simulation studies are used due to the close-comparison between theoretical and experimental results as presented above. The response of the system's airgap in adding 100 N force disturbance to the suspension system at $t = 1$ sec is shown in Fig. 6.28. The suspension remains stable, with overshoot in the response approximately 1 mm. Although

the size of the overshot in the airgap position to this disturbance is two times larger than the response with the adaptive model-reference controller (Fig. 4.6:bottom), the settling time has been reduced from 3 sec. to 0.15 sec. resulting in low-levels of the suspension acceleration ($< 8m/s^2$). In addition, the non-adaptive nature of the compensator provides a basis for deriving stability and robustness conditions. This is described in the following chapter.

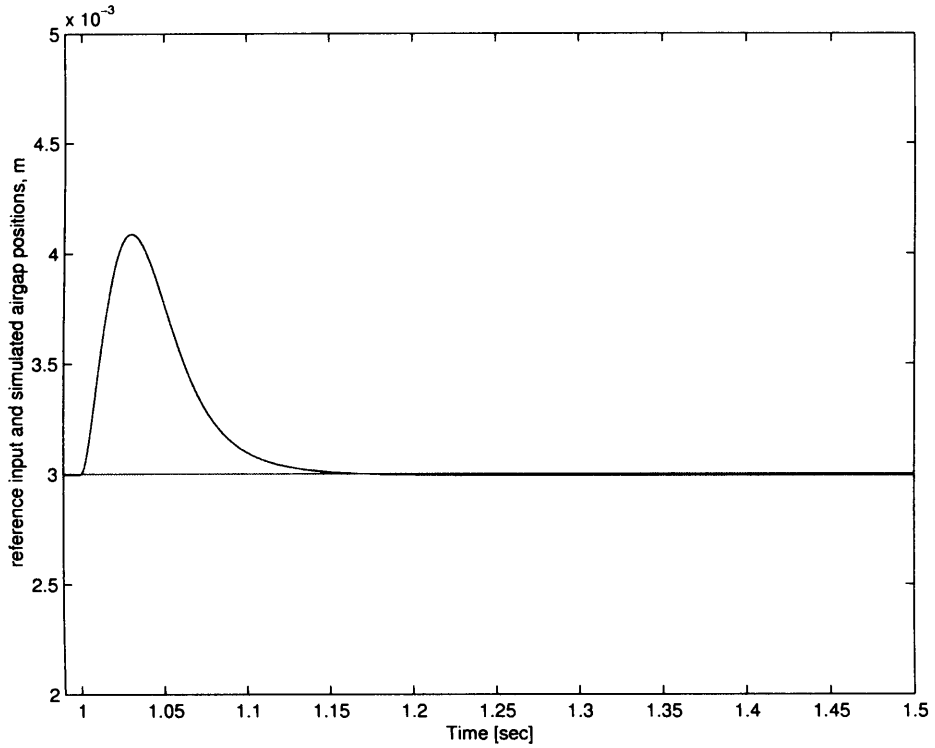

Figure 6.28: Output-feedback $\mathcal{H}_\infty$ control: attenuating force disturbance of 100 N with $K_2(s)$ in Eqn. 6.44.

6.7 Concluding comments

This chapter deals with the synthesis of output-feedback controllers for Maglev using $\mathcal{H}_\infty$ methods. This approach is considered as novel for this thesis since all previous approaches use state-feedback principles. It has been established through a series of simulation and experimental studies that the new controllers have characteristics which are comparable with previous designs. The suspension stiffness and the damping qualities are well within the Maglev system requirements. Furthermore since only one output is used for control, the new designs provides reduction in cost and provisions for dealing with faults in sensors for full-scale application.

To gain a better understanding for the $\mathcal{H}_\infty$ theory, the solution to the controller-optimisation problem has been derived. This is fully described in Appendix C.1. Despite the fundamental differences in the derivation steps which are based on Lagrange multipliers and differential game theories, the mathematical developments produce two Riccati equations which are identical to the well established solution in [37]. All controllers in this chapter are derived from this algorithm. For validation purposes a comparison is made to show that the controllers derived here are identical to the controllers derived from the Matlab algorithm.

The performance requirements of the $\mathcal{H}_\infty$ Maglev controller are specified by two performance weights. A relationship has been constructed between typical suspension requirements and the selection of these performance weights. It has been established through a series of designs that the $\mathcal{H}_\infty$ control environment offers convenient tools for systematic design of Maglev controllers with well defined suspension characteristics.

So far the open-loop Maglev model used for the controller design has been considered as ideal and there is no provision for dealing with uncertainties in its modelling characteristics. Although the experimental results show that there exists a close relationship between theory and experiment, the differences between the model and the real system might have a considerable effect for full-scale applications. In addition due to the nonlinear character of the Maglev system, changes in the operating conditions introduce additional modelling errors. It is important from a design point of view to be able to measure the robust properties of the closed-loop system. This analysis is presented in the following chapter.

Chapter 7

Robust analysis and control for Maglev systems

7.1 Problem definition

In the derivation of the $\mathcal{H}_\infty$ theory (Chapter 6), and the state-feedback designs in Chapters 2 to 4, the linear Maglev model is taken as a very accurate representation of the experimental system. In this respect, while dealing with the disturbance inputs, there are no provisions for dealing with uncertainties in the model during the controller-design process. Although the simulation and the experimental results show a good agreement between the theory and the experiment, uncertainty in the model might have a considerable effect on the closed-loop response for full-scale Maglev applications and hence it has to be included in the design. Classical feedback system-design deals with plant uncertainty by prescribing stability margins (phase and gain margins). This however is a crude model since the phase lag of the system may be underestimated by as much as 40^0 leading to instability [88]. Description of uncertainty via phase and gain margins does not trace the origin of the perturbations.

To define the robust properties of the Maglev system, the generalised control configuration in Chapter 6 (page 93) is redrawn in Fig. 7.1. $G(s)$ is substituted with each member of $\tilde{G}(s)$; $\tilde{G}(s)$ represents a set of plants with parametric uncertainties and unmodelled dynamics. The following two terms are used to define the robust properties of this system [88]

- **robust stability:** a closed-loop system is referred as a *robust stable* when it remains stable for all models in the set $\tilde{G}(s)$
- **robust performance:** a closed-loop system is said to have *robust performance properties* when the performance characteristics of the system (i.e. overshoot, closed-loop bandwidth, phase-margins) are satisfied for all members in the set $\tilde{G}(s)$

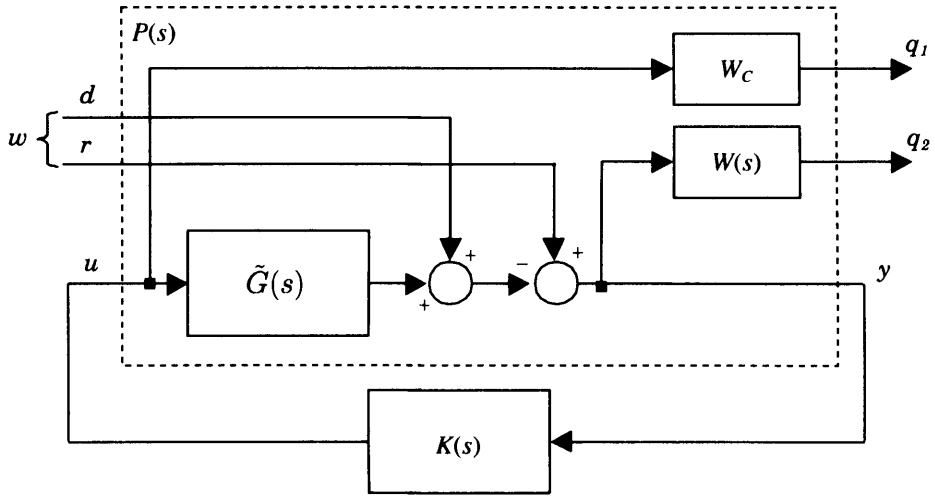

Figure 7.1: Block diagram of the uncertain closed-loop system. $\tilde{G}(s)$ represents a set of models constructed for different combination in the parameters and unmodelled dynamics.

An intuitive definition of these two terms can be derived using Fig. 7.2. $K(j\omega)G(j\omega)$ is the Nyquist plot of the system and $K(j\omega_*)G(j\omega_*)$ defines the response at a chosen frequency ω_*. Uncertainty in the model $G(j\omega)$ is defined with a circle (plot-1 with radius $w_A(j\omega_*)$) around the nominal Nyquist plot. $\hat{G}(j\omega_*)$ represents the worst plant in terms of uncertainty. Generally, the size of the uncertainty is a function of the frequency and this is specified by $w_A(j\omega)$. The distance from $K(j\omega_*)G(j\omega_*)$ to the critical point $-1+j0$ is equal to $|1-K(j\omega_*)G(j\omega_*)|$ and for robust stability, it is required that $|1 - K(j\omega_*)G(j\omega_*)| \geq |K(j\omega_*)w_A(j\omega_*)|$. In words, the circle marked as (1) in the figure should be away from the critical point and at most be tangential to it on the boundary condition for robust stability. For robust performance, a new circle is added (2) which defines the performance characteristics of the system. $W(j\omega)$ is the performance weight used in the $\mathcal{H}_\infty$ design definition and the condition for robust performance becomes $|1 - K(j\omega_*)G(j\omega_*)| \geq |K(j\omega_*)w_A(j\omega_*)| + |W(j\omega_*)|$.

The application of this method for checking robustness is restricted to single-input-output systems. To extend the results to the multivariable case, this chapter performs three tasks. The origins of the uncertainty in the Maglev system are identified and modelled (Section 7.2). These are then used to develop a tool for robust analysis of closed-loop Maglev systems when the controller is already known (Section 7.3) to provide a systematic condition for determining how far the circles are from the critical point. A mechanism is then derived for the design of robust $\mathcal{H}_\infty$ controllers (Section 7.5).

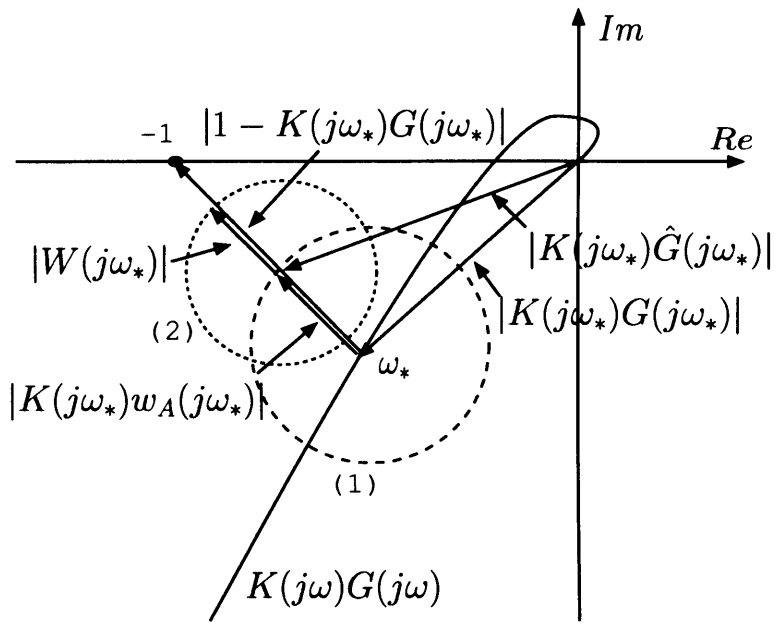

Figure 7.2: Definition of robustness using the Nyquist plot.

7.2 Maglev model with uncertainty, $\tilde{G}(s)$

7.2.1 Sources of uncertainty in the Maglev model

The uncertainty in the Maglev model is contributed by: (1) variations in the parameters in the model caused by changes in the working conditions; (2) estimated numerical values for the parameters in the model, and (3) unmodelled dynamics of sensors and power-amplifiers.

The open-loop Maglev model is a linearised approximation of the nonlinear system (Chapter 2) [1]. Two of the parameters k_i and k_z are nonlinear functions of the operating current i_0 and operating airgap z_0 ($k_i = \frac{\mu_0 N^2 A}{4}\frac{i_0}{z_0^2}$ and $k_z = \frac{\mu_0 N^2 A}{4}\frac{i_0^2}{z_0^3}$). Variations in ($i_0$, z_0) due to changes in the operating air-gap and disturbance forces cause variations in k_i and k_z. The open-loop model thus changes. For typical operating conditions (z_0, i_0) = ($4mm$, $3A$), $\pm 25\%$ variation in the operating airgap and current leads to $\approx \pm 30\%$ variation in k_i and k_z.

The mass of the system m depends on the suspended load. The nominal mass is equal to the mass of the magnet, the chassis and the supporting magnet brackets. Since Maglev systems are designed to carry loads, the suspended mass (nominal mass plus load mass) can vary as much as $+200\%$ from the nominal mass.

The resistance of the winding R and the inductance of the winding L are calculated from the physical parameters of the magnet's wire. To account for the approximation in these calculations, the values for R and L_0 are assumed to vary as much as $\pm 30\%$ from the

nominal values.

Uncertainty due to unmodelled dynamics is contributed by the dynamics of the power-amplifier and the sensors. These have been chosen to have a considerably larger bandwidth compared to the closed-loop bandwidth (1.5 kHz for the sensors and 44 kHz for the power amplifier). Therefore, each sensor has the characteristics of a gain over the frequency of interest (up to 150Hz $\approx$ 5 times the closed-loop bandwidth). To simplify the analysis, variations in this gain are represented by the uncertainty in the resistance R and the inductance L.

Based on the above, five parameters in the Maglev are considered as uncertain. k_i, k_z, R and L are assumed to vary by $\pm 30\%$ from the nominal values while the suspended mass is assumed to vary by up to +200% from the nominal mass. Although for the laboratory-scale experiments these variations are beyond the typical operating ranges, the analysis work presented here targets other Maglev aplications and aims to develop a reference design for robust control.

7.2.2 Performance of the closed-loop Maglev system in the presence of uncertainties in the parameters

The performance of the closed-loop system degrades when the feedback controller is designed for the nominal model $G(s)$ as this model changes due to uncertainty. To study this, a simulation experiment is carried out which uses the closed-loop configuration in Fig. 7.1. $K(s)$ is the $\mathcal{H}_\infty$ compensator in Eqn. 6.44, page 116 (designed for the nominal Maglev model). $\tilde{G}(s)$ is constructed by varying the parameters of the nominal system using ranges of variations as identified in the previous section. L, R, k_i and k_z are varied by $\pm 30\%$ from their nominal value in 3 discrete levels: -30%, 0% and +30%; the suspended mass is varied by +200% from the nominal value in three discrete levels: 0% 100% 200% (the nominal values are given in Chapter 2). In total, 81 simulations are carried out. For each combination, the loop transfer function $L(s) = K(s)\tilde{G}(s)$ is constructed and the phase and gain margins are computed. Parameters for phase margins below 10^0 are logged into a file for analysis.

From the set of 81 combinations (k_i and k_z move up or down together), 11 transfer functions with phase margins below 10^0 are selected and listed in Table 7.1. The Nyquist plot for each of these is shown in Fig. 7.3. Although some transfer functions are excluded from the plot in Fig. 7.3 for cleaner plots, these are still taken into account in the subsequent design process. For comparison purposes, plot-1 in the figure represents the response of

experiment number	k_i [%]	k_z [%]	m [%]	R [%]	L [%]	phase margin [^{0}]
1	0	0	0	0	0	39.46
2	-30	-30	100	30	0	9.04
3	-30	-30	100	30	30	7.99
4	-30	-30	200	0	-30	8.61
5	-30	-30	200	0	0	7.06
6	-30	-30	200	0	30	5.52
7	-30	-30	200	30	-30	-0.04
8	-30	-30	200	30	0	-0.86
9	-30	-30	200	30	30	-1.68
10	0	0	200	30	-30	8.80
11	0	0	200	30	0	7.79
12	0	0	200	30	30	6.77

Table 7.1: Variation in the Maglev parameters and corresponding phase margins. The nominal parameters are: k_i = N/A, k_z =, $R = 1.1\ \Omega$, $L_0 = 31$ mH, $m = 1.8$ kg

the nominal system ($K(s)G(s)$). The results in Fig. 7.3 show the considerable effect of the variation of the parameters on the quality of the closed-loop system. From the set of 81 combinations, 11 closed-loop systems have phase margins below 10^0 (the design requirement is 40 degrees as per Section 6.4.1) and hence highly degraded closed-loop performance. For three combinations (7,8 and 9), the closed-loop system is unstable.

In the linear Maglev model, the steady-state gain of the system is a function of k_i, k_z and R (Eqn. 2.12, page 18). Reduction in the operating currents and airgaps result in reduced values for k_i and k_z. This reduction, combined with low values for the resistance R, reduces considerably the gain of the open-loop model within the cross-over frequency. This in turn reduces the phase margin of the system. In addition, increasing the mass of the suspended system reduces the bandwidth of the open-loop model which additionally contributes to the reduction of the open-loop gain around the cross-over frequency (=21.47 Hz for the nominal model) and consequently the phase margin. The results show that the inductance L contributes to poles outside the closed-loop bandwidth and hence does not have as considerable an effect as the remaining parameters in the model.

7.2.3 Modelling parametric uncertainties

A straightforward and accurate representation of uncertainty in the model can be constructed in the frequency domain by varying the uncertain parameters and computing the frequency response for each combination. This leads to a set of Nyquist responses (see Fig. 7.3). The uncertainty is modelled by a circle with a radius which depends on the

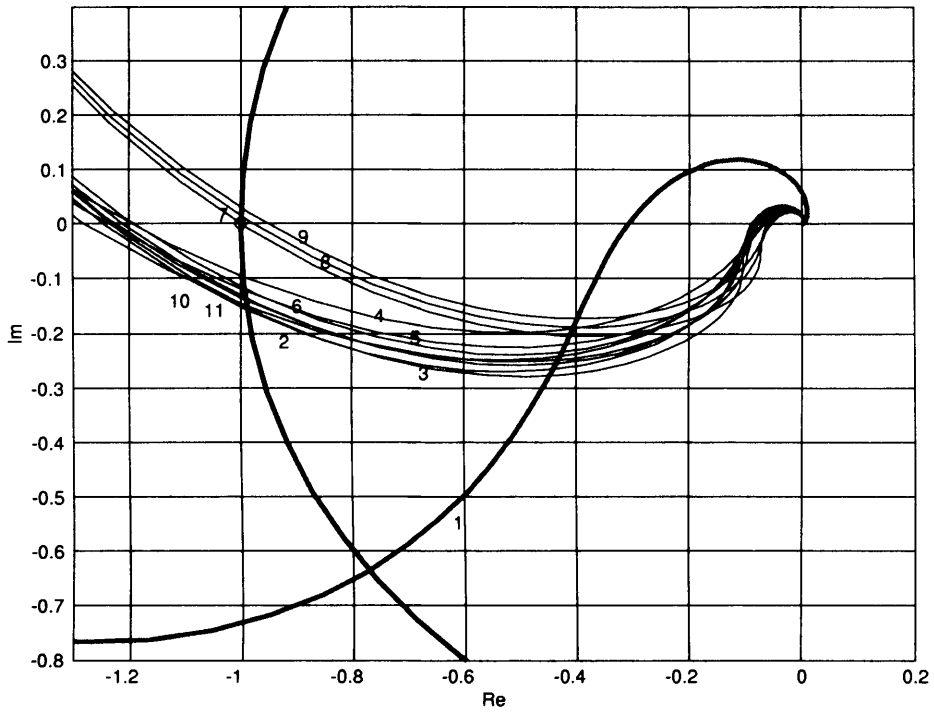

Figure 7.3: Nyquist plot of the closed-loop system with variation in the uncertain parameters as per Table 7.1.

difference between the nominal model and the uncertain model (Fig. 7.2). In this respect, two commonly used models for representing uncertainty are

$$\text{additive model}: \ \bar{G}(s) = G(s) + \Delta_A(s)$$

and

$$\text{multiplicative model}: \ \bar{G}(s) = G(s)[1 + \Delta_M(s)]$$

where $\Delta_A(s)$ and $\Delta_M(s)$ represents the perturbation in the model [73, 88]. For numerical convenience, it is suitable to scale the perturbations to $\Delta_A(s) = w_A(s)\Delta(s)$ and $\Delta_M(s) = w_M(s)\Delta(s)$, where $w_A(s)$ and $w_M(s)$ are frequency-dependent weights chosen by the designer to represent the uncertainty and $\Delta(s)$ is a complex perturbation restricted to $\|\Delta(s)\|_\infty \leq 1$. This leads to the representations in Fig. 7.4. $G(s)$ is the nominal plant and hence known; The procedure of selecting w_A and w_M for the Maglev model is described below.

1. Additive uncertainty: Using Fig. 7.4 (a), the extended open-loop model $\tilde{G}(s)$ is constructed below

$$\tilde{G}(s) = G(s) + w_A(s)\Delta(s), \quad \|\Delta(s)\|_\infty \leq 1 \tag{7.1}$$

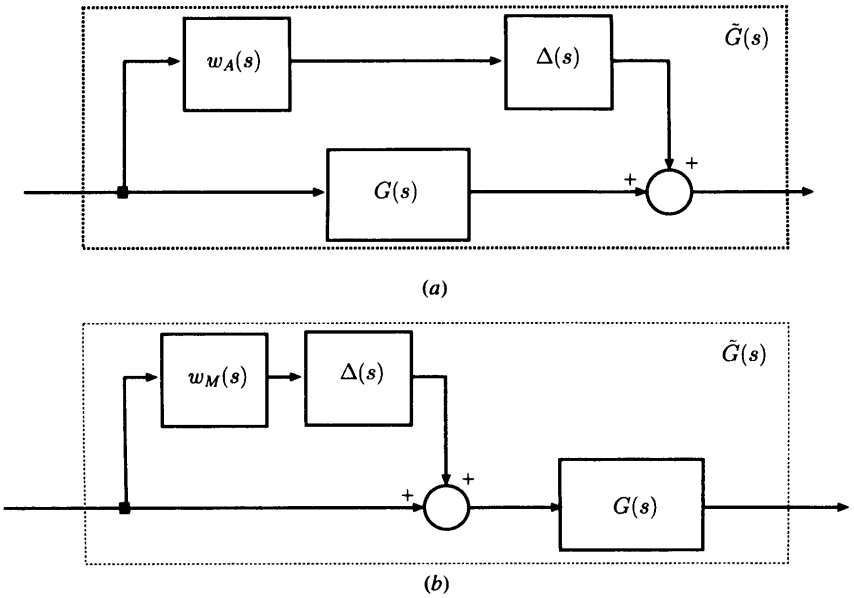

Figure 7.4: Representing uncertainty in the model using: (a) additive principle, and (b) multiplicative principle.

This provides a basis for selecting $w_A(s)$ such that $|\tilde{G}(s)-G(s)| \leq |w_A(s)|$ for all frequencies; $w_A(j\omega)$ thus becomes a frequency-dependent weight which captures uncertainty in the parameters and represents the worst difference between $|G(s)|$ and $|\tilde{G}(s)|$. The procedure for selecting $w_A(j\omega)$ for the Maglev model is described below. The parametric uncertainties k_i, k_z, m, R, and L_0 are varied in three discrete levels (Section 7.2.2). Using Matlab, 81 models are computed for each combination. These are marked as $\tilde{G}(s)[k]$, $k = 1..81$. The following difference is then computed

$$\left|\tilde{G}[k](j\omega) - G(j\omega)\right|, \quad k = 1 \; to \; 81 \quad \rightarrow w_A(j\omega) \tag{7.2}$$

and plotted in Fig. 7.5. The upper bound $|w_A(j(\omega)|$ on $\left|\tilde{G}[k](j\omega) - G(j\omega)\right|$ is a function of the frequency ω. For numerical convenience, this function is fitted to the following transfer function with an amplitude $|w_A(j\omega)|$ (the phase is not used in the μ synthesis analysis). Based on gain versus frequency matching, a suitable transfer function that satisfies Eqn. 7.2 is given by

$$w_A(s) = \frac{1400(s+1000)}{(s+200)(s+100)^2} \tag{7.3}$$

2. Multiplicative uncertainty: Fig. 7.4(b) is used to derive the following model

$$\tilde{G}(s) = G(s)[1 + w_M(s)\Delta(s)], \quad \|\Delta(s)\|_\infty \leq 1 \tag{7.4}$$

$w_M(s)$ is selected such that $\left|\frac{\tilde{G}(s)-G(s)}{G(s)}\right| \leq |w_M(s)|$. The uncertain parameters k_i, k_z, m, R, and L_0 are varied in three discrete levels (Section 7.2.2) and for each combination the

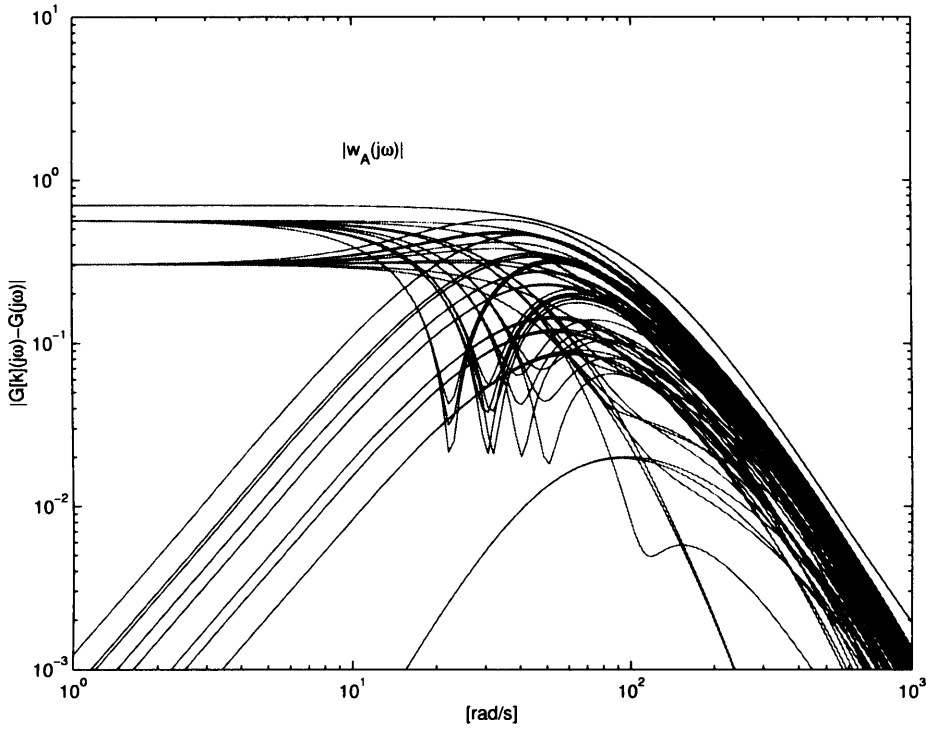

Figure 7.5: Frequency response of $w_A(j\omega)[k]$ in Eqn. 7.2 for 81 combinations of the uncertain parameters in the Maglev model.

following value is computed

$$\left|\frac{\tilde{G}[k](j\omega) - G(j\omega)}{G(j\omega)}\right|, \quad k = 1 \; to \; 81 \tag{7.5}$$

Graphically these are shown in Fig. 7.6. $w_M(s)$ is then selected to give an upper bound on these differences. As above, for a numerical convenience this function is fitted to a transfer function with an amplitude $|w_M(j\omega)|$. Based on gain versus frequency matching, a suitable transfer function that satisfies Eqn 7.5 is given by

$$w_M(s) = 0.9\frac{(s+25)}{(s+50)} \tag{7.6}$$

Once the numerical forms of $w_A(s)$ and $w_M(s)$ are determined, the uncertain Maglev model $\tilde{G}(s)$ can be constructed from Eqns. 7.1 or 7.4. The uncertain model is then fully determined and the robust analysis and synthesis procedure can be carried out.

7.3 Robustness of closed-loop Maglev systems

Robustness of single-input-output closed-loop Maglev systems can be analysed with the aid of Fig. 7.2. In this section these results are generalised to provide a procedure for single- and multi-input-output robustness analysis. In the following derivations, $K(s)$ is the $\mathcal{H}_\infty$

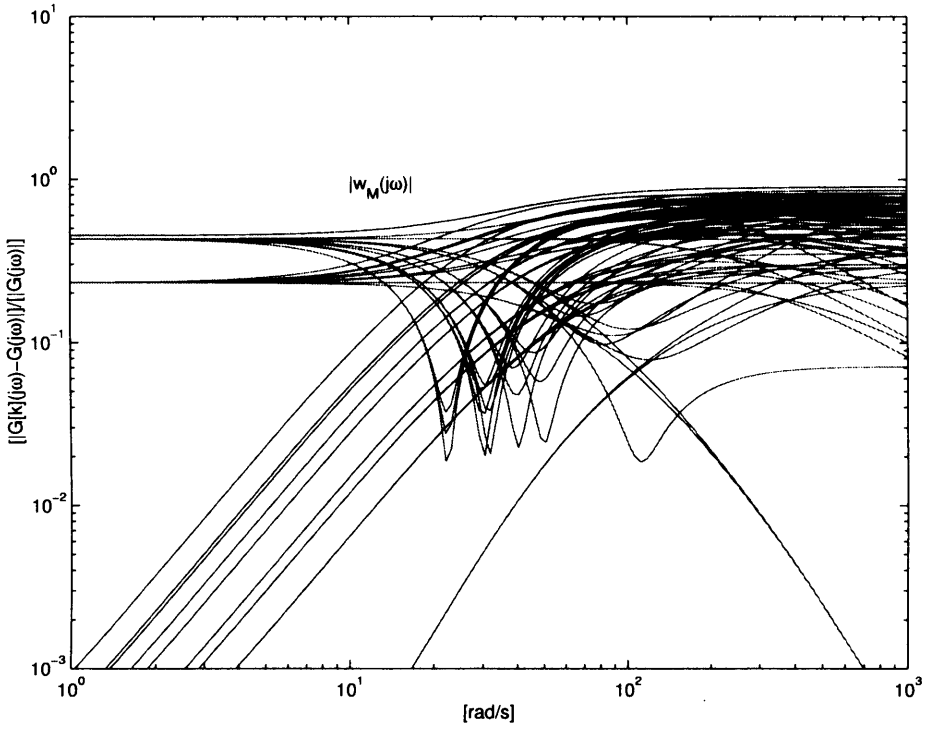

Figure 7.6: Frequency response of $w_M(j\omega)$ in Eqn. 7.5 for 81 combinations of the uncertain parameters in the Maglev model.

compensator in Eqn. 6.44, page 116 and $\tilde{G}(s)$ is the uncertain plant (described in Eqn. 7.1 or 7.4). Since a theoretical basis for selecting one of the two scheme for modelling the uncertainty in the Maglev model was not found, in the following derivations the additive and the multiplicative models are studied independently and the results are compared. $w_M(s)$ and $w_A(s)$ are derived above.

7.3.1 Maglev model with additive uncertainty

Using the developments in the previous section, the open-loop Maglev system in Fig. 7.1 is expanded with the additive uncertainty to get the generalised plant $P(s)$ in Fig. 7.7. In this figure, $K(s)$ is the $\mathcal{H}_\infty$ controller in Eqn. 6.44, $G(s)$ is the nominal open-loop model (Eqn. 6.35), $W_c(s)$ and $W(s)$ are the performance weights for the $\mathcal{H}_\infty$ design (Eqn. 6.36), and w_A is the additive uncertainty in Eqn. 7.3. The inputs to $P(s)$ are

$$[e,\ d,\ r,\ u]^{\mathrm{T}},$$

and the outputs are

$$[s,\ q_1,\ q_2,\ y]^{\mathrm{T}}.$$

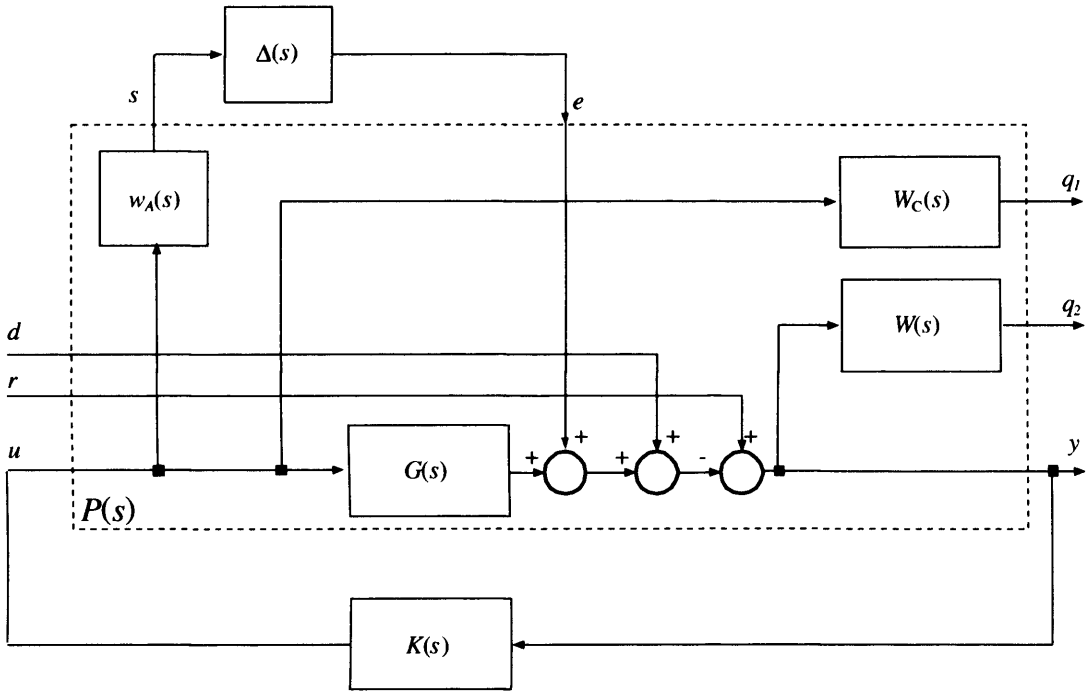

Figure 7.7: Maglev control configuration with performance weights $W_c(s)$ and $W(s)$ and an additive uncertainty $w_A(s)$.

Using Fig. 7.7, the following relationships have been constructed

$$\begin{aligned} s &= w_A(s)u \\ q_1 &= W_c(s)u \\ q_2 &= W(s)[r - G(s)u - e - d] \\ y &= r - G(s)u - e - d \end{aligned}$$

The transfer matrix P from the inputs to the outputs

$$\begin{bmatrix} s \\ q_1 \\ q_2 \\ y \end{bmatrix} = P \begin{bmatrix} e \\ d \\ r \\ u \end{bmatrix} \tag{7.7}$$

is derived from Fig. 7.7

$$P(s) = \left[\begin{array}{c|c} P_{11} & P_{12} \\ \hline P_{21} & P_{22} \end{array}\right] = \left[\begin{array}{ccc|c} 0 & 0 & 0 & w_A \\ 0 & 0 & 0 & W_c \\ -WG & -W & W & -WG \\ \hline -I & -I & I & -G \end{array}\right] \tag{7.8}$$

Substituting $u = Ky$ in Eqn. 7.7, after some transformations the closed-loop system in Fig. 7.7 can be simplified to a system with two inputs and two outputs (Fig. 7.8 with $q = [q_1 \ q_2]^T$ and $w = [d \ r]^T$)

$$\begin{bmatrix} s \\ q \end{bmatrix} = \left[\begin{array}{c|c} N_{11} & N_{12} \\ \hline N_{21} & N_{22} \end{array}\right] \begin{bmatrix} e \\ w \end{bmatrix}. \tag{7.9}$$

where the transfer matrix $N(s)$ is given below

$$N(s) = \left[\begin{array}{c|cc} -w_A K(I+GK)^{-1} & -w_A K(I+GK)^{-1} & w_A K(I+GK)^{-1} \\ \hline -W_c K(I+GK)^{-1} & -W_c K(I+GK)^{-1} & W_c K(I+GK)^{-1} \\ -W(I+GK)^{-1} & -W(I+GK)^{-1} & W(I+GK)^{-1} \end{array}\right]. \tag{7.10}$$

Using the definitions for: (a) complimentary function $T = GK(I+GK)^{-1}$ and sensitivity function $S = (I+GK)^{-1}$, Eqn. 7.10 can be rewritten to its simpler form

$$N(s) = \left[\begin{array}{c|cc} -w_A KS & -w_A KS & w_A KS \\ \hline -W_c KS & -W_c KS & W_c KS \\ -WS & -WS & WS \end{array}\right]. \tag{7.11}$$

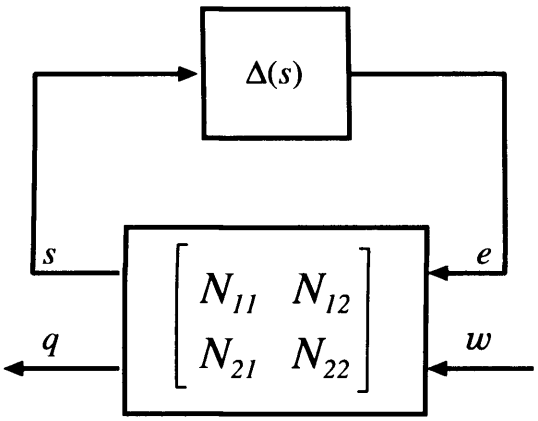

Figure 7.8: A simplified block diagram of the closed-loop system in Fig. 7.7.

Fig. 7.8 is a simplified form of the closed-loop system in Fig. 7.7. The $\mathcal{H}_\infty$ compensator $K(s)$ (part of $N(s)$) has been designed to stabilise the Maglev system and to attenuate the unknown (but bounded) disturbance effect w on the output q when $\|\Delta(s)\|_\infty = 0$. This controller, however, is not explicitly designed to perform these tasks for $\|\Delta(s)\|_\infty \neq 0$. These observations thus give rise to two questions: (1) the ability of the controller to stabilise the system for all perturbations $\Delta(s)$, $\|\Delta(s)\|_\infty \leq 1$ (robust stability) and (2) the ability of the closed-loop system to perform as required (settling time, overshoot, oscillations in the response) for all $\Delta(s)$, $\|\Delta(s)\|_\infty \leq 1$ (robust performance). A mathematical tool that provides an answer to those questions is described below.

In order to determine whether the closed-loop configuration in Fig. 7.8 remains stable for all perturbation Δ, the transfer function from w to q has to be constructed. From Eqn. 7.9 it follows that

$$\begin{aligned} s &= N_{11}e + N_{12}w \\ q &= N_{21}e + N_{22}w \end{aligned}$$

With $e = \Delta s$, the transfer function from w to q becomes

$$q = [N_{22} + N_{21}\Delta(I - N_{11}\Delta)^{-1}N_{12}]w \tag{7.12}$$

The closed-loop system $N(s)$ remains stable for all perturbations Δ only if the transfer function in Eqn. 7.12 remains stable for all Δ. Eqn. 7.12, on another hand, is stable as long as $(I - N_{11}\Delta)^{-1}$ is non-singular, or equivalently $\det[(I - N_{11}\Delta)] \neq 0$ [92, 93, 88]. Since the determinant of a matrix is equal to the product of the eigenvalues, i.e.

$$\det[(I - N_{11}\Delta)] = \prod_i \lambda_i(I - N_{11}\Delta)$$

the condition for stability can be reduced to satisfying the following inequality

$$\prod_i \lambda_i(I - N_{11}\Delta) \neq 0 \quad \Leftrightarrow I - \prod_i \lambda_i(N_{11}\Delta) \neq 0$$

which is equivalent to

$$\lambda_i(N_{11}\Delta) < 1$$

where λ_i is any of the eigenvalues of $(N_{11}\Delta)$. Using the fact that [93]

$$\lambda(N_{11}\Delta) < \bar{\sigma}(N_{11}\Delta)$$

the criteria for robust stability becomes

$$\bar{\sigma}(N_{11}\Delta) < 1 \tag{7.13}$$

or equivalently ($\|\Delta\|_\infty \leq 1$)

$$\|N_{11}\|_\infty < 1 \tag{7.14}$$

To summarise: the closed-loop Maglev system in Fig. 7.7 remains stable for all perturbations Δ as long as the $\infty-$norm of N_{11} in Eqn. 7.10 remains < 1 for all frequencies, i.e.

$$\|N_{11}\|_\infty = \| - w_A K(I + GK)^{-1}\|_\infty = \| - w_A KS\|_\infty < 1$$

This condition can be used for single- and multi-input-output systems and requires only the closed-loop transfer matrix $N(s)$. The graphical developments in Fig. 7.2 state that the system is robust stable as long as $|1 - K(j\omega_*)G(j\omega_*)| \geq |K(j\omega_*)w_A(j\omega_*)|$. Multiplying this on both side by $(1-K(j\omega_*)G(j\omega_*))^{-1}$ gives $|w_A KS| \leq 1$ which for the single-magnet model is same as the condition above. Using the additive uncertainty in Eqn. 7.3, the nominal Maglev model in Eqn. 6.35 and the $\mathcal{H}_\infty$ controller in Eqn. 6.44, $w_A KS$ is computed with Matlab

$$N_{11} = w_A KS = \frac{46787371.6908(s+1000)(s+356.6)(s+65.28)(s-55.18)(s+18.77)}{(s+200)(s+646.3)(s+100)^2(s+78.37)(s+60)(s^2+637.8s+3.469\times 10^5)}$$

and its frequency response is plotted in Fig. 7.9. Since $\|w_A KS\|_\infty = 4.23$ dB (> 1), the

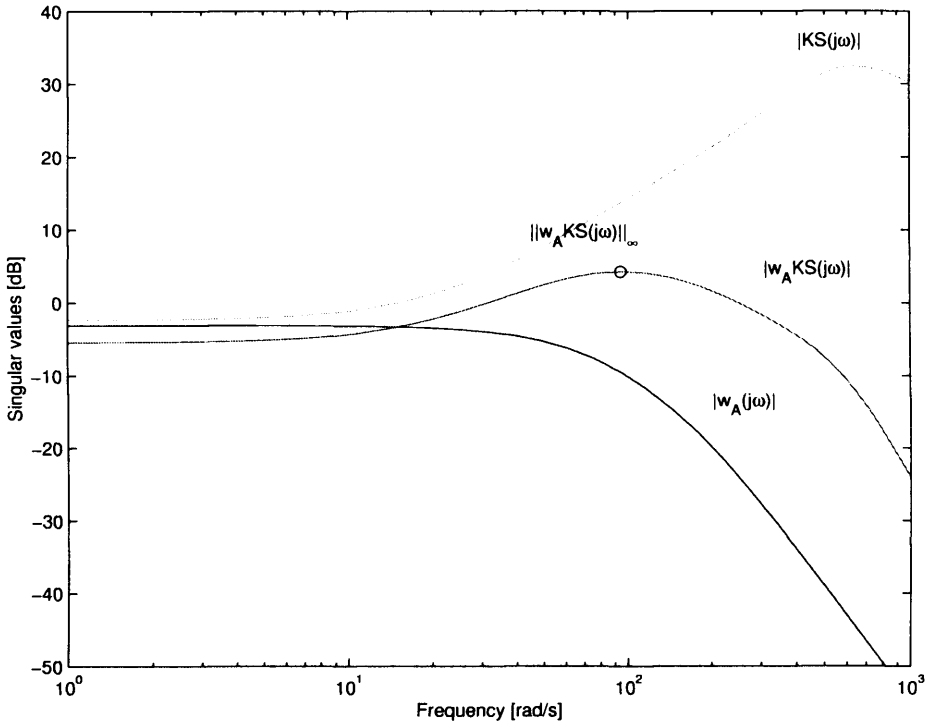

Figure 7.9: Test for robust stability for the system in Fig. 7.7

closed-loop system does not satisfy the condition for robust stability. Therefore, the $K(s)$ does not guarantee stability for 30% variation in k_i, k_z and m and 200% variation in m. This is consistent with the results in Fig. 7.3 where for experiment 7, 8 and 9 the closed-loop system is unstable. The test developed above estimates the robust stability of the system, but it does not directly calculate the robust stability margin beyond which the system fails to provide a stable suspension. To calculate this: (1) the uncertainty in the parameters are decreased (from 30% to 20% for example), (2) a new model $w_A(s)$ is estimated for the new uncertainty, and (3) the test for robust stability in Eqn. 7.14 is calculated for the new $w_A(s)$. If the conditions for robust stability are not satisfied, the procedure continues from (1). This process is carried out for the Maglev model in Section 7.4.

7.3.2 Nominal Maglev model with multiplicative uncertainty

To analyse the robust stability with the multiplicative model, the nominal open-loop Maglev system is expanded $\tilde{G}(s)$ as in Fig. 7.4(b); the resultant generalised system is given in Fig. 7.10. The inputs to this system are

$$[e,\ d,\ r,\ u]^{\mathrm{T}},$$

and the outputs are

$$[s,\ q_1,\ q_2,\ y]^{\mathrm{T}}.$$

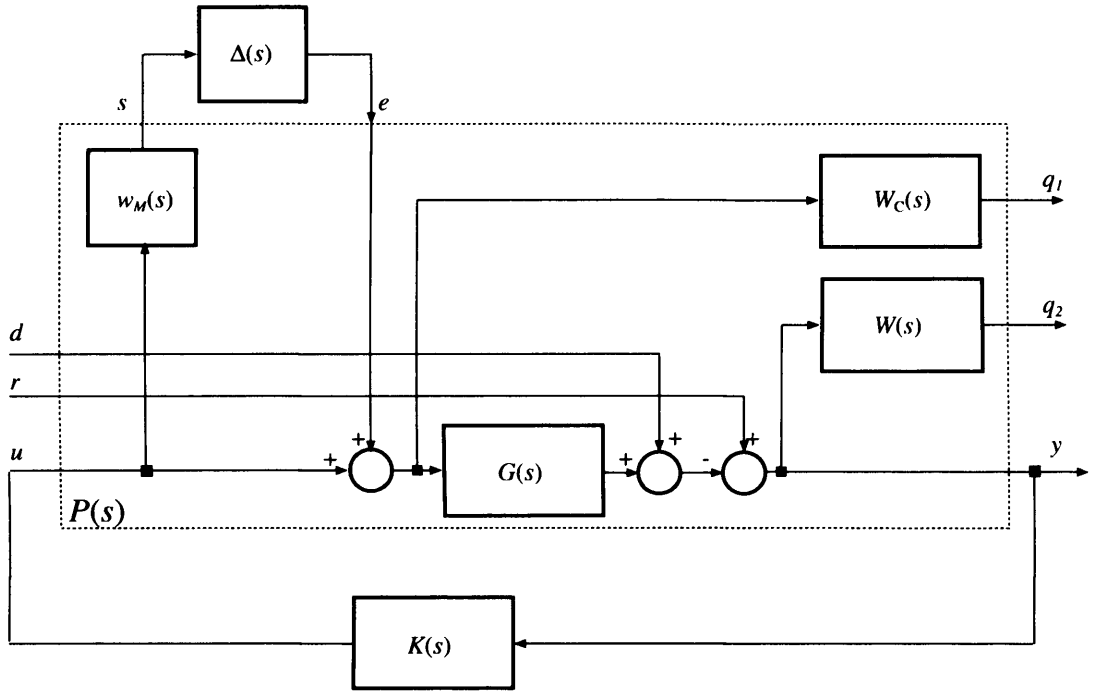

Figure 7.10: Maglev system with performance weights $W_c(s)$ and $W(s)$ and a multiplicative uncertainty $w_M(s)$.

The following relationships are constructed from Fig. 7.9

$$\begin{aligned} s &= w_M(s)u \\ q_1 &= W_c(s)(u+e) \\ q_2 &= W(s)[r - G(s)u - G(s)e - d] \\ y &= r - G(s)u - G(s)e - d \end{aligned}$$

These lead to the following transfer matrix $P(s)$

$$P(s) = \left[\begin{array}{c|c} P_{11} & P_{12} \\ \hline P_{21} & P_{22} \end{array}\right] = \left[\begin{array}{ccc|c} 0 & 0 & 0 & w_M \\ W_c & 0 & 0 & W_c \\ -WG & -W & W & -WG \\ \hline -G & -I & I & -G \end{array}\right]$$

Using $u = Ky$, after some simplifications the closed loop transfer matrix $N(s)$

$$\left[\begin{array}{c} s \\ q \end{array}\right] = \left[\begin{array}{c|c} N_{11} & N_{12} \\ \hline N_{21} & N_{22} \end{array}\right] \left[\begin{array}{c} e \\ w \end{array}\right],$$

is obtained

$$N(s) = \left[\begin{array}{c|cc} -w_M GK(I+GK)^{-1} & -w_M K(I+GK)^{-1} & w_M K(I+GK)^{-1} \\ \hline W_c(I+GK)^{-1} & -W_c K(I+GK)^{-1} & W_c K(I+GK)^{-1} \\ -WG(I+GK)^{-1} & -W(I+GK)^{-1} & W(I+GK)^{-1} \end{array}\right],$$

Employing the definitions for complementary and sensitivity functions, the latter reduces to

$$N(s) = \left[\begin{array}{c|cc} -w_M T & -w_M KS & w_M KS \\ \hline W_c S & -W_c KS & W_c KS \\ -WGS & -WS & WS \end{array}\right]. \tag{7.15}$$

Using the criteria developed in the previous section (Eqn. 7.13), the closed-loop system in Fig. 7.10 remains robust stable as long as

$$\|N_{11}\|_\infty = \| - w_M GK(I + GK)^{-1}\|_\infty = \| - w_M T\|_\infty < 1$$

Using the $\mathcal{H}_\infty$ controller in Eqn. 6.44 and the multiplicative uncertainty in Eqn. 7.6, N_{11}

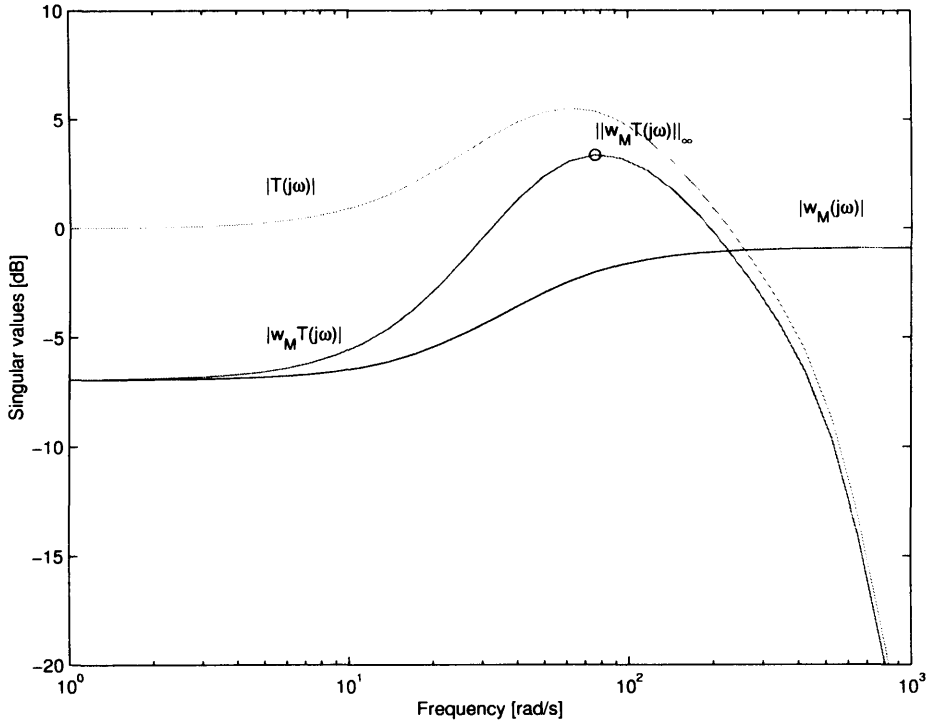

Figure 7.11: Testing robust stability for the system in Fig. 7.7

is computed

$$N_{11} = w_M T = \frac{50572888094.6999(s+25)(s+18.77)}{(s+50)(s+60)(s+78.37)(s+646.3)(s^2+637.8s+3.469\times 10^5)}$$

and its frequency response is shown in Fig. 7.11. Since $\| - w_M T\|_\infty = 3.34$dB, the $\mathcal{H}_\infty$ controller does not guarantee closed-loop stability for all perturbations Δ. This is consistent with the previous results for the robustness. Since $w_M(s)$ in Fig. 7.6 more tightly bounds the differences in the model than $w_A(j\omega)$ in Fig. 7.5, the norm $\| - w_A KS\|_\infty = 4.23$ is slightly higher than $\| - w_M T\|_\infty = 3.34$dB. A more detailed analysis on the stability robustness is presented in the following section.

For a mathematical convenience, the perturbation in the model $\Delta(j\omega)$ is typically structured as a block-diagonal matrix (this is considered later, Fig. 7.13). In this respect studying the robustness of multivariable problems using Eqn. 7.13 can, in some cases, be so conservative as to be useless [88]. Therefore it is more convenient to develop a modified test for

robust analysis which uses the structural information for $\Delta(j\omega)$. This is presented in the following section.

7.4 Robustness analysis using the structured singular value-μ

7.4.1 Robust stability

According to Fig. 7.4, $\tilde{G}(s)$ approaches the nominal model $G(s)$ as long as $\Delta(j\omega)$ approaches zero ($\|\Delta(j\omega)\| \rightarrow 0$). In this respect the condition for robust stability states that the generalised closed-loop system in Fig. 7.8 is robust stable as long as Eqn. 7.13 is satisfied for which

$$\det[I - N_{11}(j\omega)\Delta(j\omega)] \neq 0, \quad \|\Delta\|_\infty \leq 1 \tag{7.16}$$

If $\|\Delta(j\omega)\|$ =0, then the condition above is always satisfied and the system in Eqn. 7.12 is robust stable. If

$$\det[I - N_{11}(j\omega)\Delta(j\omega)] = 0, \quad \|\Delta\|_\infty \leq 1 \tag{7.17}$$

for some $\Delta(j\omega)$, then the transfer function does not exist and the robustness stability test is violated. Since $\Delta(j\omega)$ represents perturbations in the model (Fig. 7.4), its maximum singular value $[\bar{\sigma}(\Delta(j\omega))]$ can be used for the robustness analysis. With block-diagonal structure of Δ, the robustness index is quantified by [92]

$$\mu(N_{11}) = \frac{1}{\min\{\bar{\sigma}(\Delta(j\omega)) : \det(I - N_{11}\Delta(j\omega)) = 0, \ \Delta(j\omega) \text{ is structured}\}} \tag{7.18}$$

and equals the reciprocal of $\bar{\sigma}(\Delta(j\omega))$ when $\det(I - N_{11}\Delta(j\omega)) = 0$. If $\det(I - N_{11}\Delta(j\omega)) \neq 0$ for all ω, then $\mu(N_{11}) = 0$. In this respect μ is an indicator for robust stability: large values for μ stand for closed-loop system with poor stability margins since small perturbations Δ make $(I - N_{11}\Delta(j\omega))$ singular. Employing the definition of μ, the closed-loop system (Fig. 7.8) is robust stable as long as [92, 93]

$$\mu(N_{11}(j\omega)) \leq 1, \ \forall\omega. \tag{7.19}$$

As indicated earlier (Section 7.2.3), $\Delta(j\omega)$ represents perturbations of the internals of the system $G(s)$ and is not quantifiable in physical terms. For this reason $\mu(N_{11})$ is used to quantify the stability properties of the system in the presence of internal parameter variations (robustness stability). Algorithms to compute the exact value of $\mu(N_{11})$ are not yet available. For this reason the upper and lower bounds are estimated. Empirical

studies suggest that the differences between the upper and the lower bounds are within 5% (at maximum 15%) [88]. For design puposes the upper bound (worst-case scenario) is relevant and the its derivation is described in Appendix D. The equation uses the following optimisation condition

$$\mu(N_{11}) = \inf_{D} \bar{\sigma}(DN_{11}D^{-1}) \tag{7.20}$$

where the main task is finding the diagonal matrix D such that the maximum singular value $\bar{\sigma}(DN_{11}D^{-1})$ is minimal at each frequency. The algorithm usually starts with the identity matrix for D and then it searches for the optimal $\hat{D}$ that makes $\bar{\sigma}(\hat{D}N_{11}\hat{D}^{-1})$ minimal. μ is then equal to $\bar{\sigma}(\hat{D}N_{11}\hat{D}^{-1})$. It has been established that this optimisation task is convex in D [94]. A simplified version of this algorithm is developed in Appendix D. Applications of μ for the Maglev model are discussed below.

Using Matlab and the $\mu-$analysis and synthesis toolbox, the $\mu(N_{11})$ values are computed for $N(s)$ in Eqns. 7.15 and 7.11 (Figs. 7.7 and 7.10). The corresponding results are shown in Fig. 7.12. μ is larger than one for $30 \leq \omega \leq 300$ rad/s and hence Eqn. 7.19 states that the system is robust unstable for some combinations in the perturbations Δ. This is consistent with the results for robust stability based on Eqn. 7.14 (Fig. 7.9). In fact for one-dimensional perturbations Δ, $\mu(N_{11}) = \bar{\sigma}(N_{11})$ and the robust stability based on μ is identical to the analysis based on σ [92].

The above result does not define the robust stability margin in terms of parameter variation. To calculate the sensitivity of the robustness, the following analysis is carried out. From the list of parameter perturbations defined in Section 7.2, k_i and k_z are excluded. The remaining uncertain parameters are: 30% for R and L_0 and 200% for m. New uncertain models ($w_A(s)$ and $w_M(s)$) are derived using the procedure in Section 7.2.3 for the additive and the multiplicative representations. The numerical results are given in Figs. E.1 and E.2, Appendix E, page 306. The new models $w_A(s)$ and $w_M(s)$ are listed in Table 7.2 (row-2, columns 6 and 7). Row-3 in Table 7.2 is constructed by varying k_i, k_z, R and L_0 with 30% (the mass m is excluded). Similarly, data plots in Figs. E.1 and E.2 are used to derive $w_A(s)$ and $w_M(s)$ in rows 4 and 5. For comparison purposes, row-1 represents the worst-case scenario where all five parameters are varied. The conclusion from the above results is that none of the combinations in Table 7.2 (rows 1 to 5) produce $\mu < 1$ (plots of the μ values are included in Fig. E.3, page 308) and hence the system is not robust stable when one of the parameters is excluded from the uncertainty. The stability robustness is more sensitive to variations in k_i, k_z and m, and less sensitive to variations in R. L_0 has almost no effect

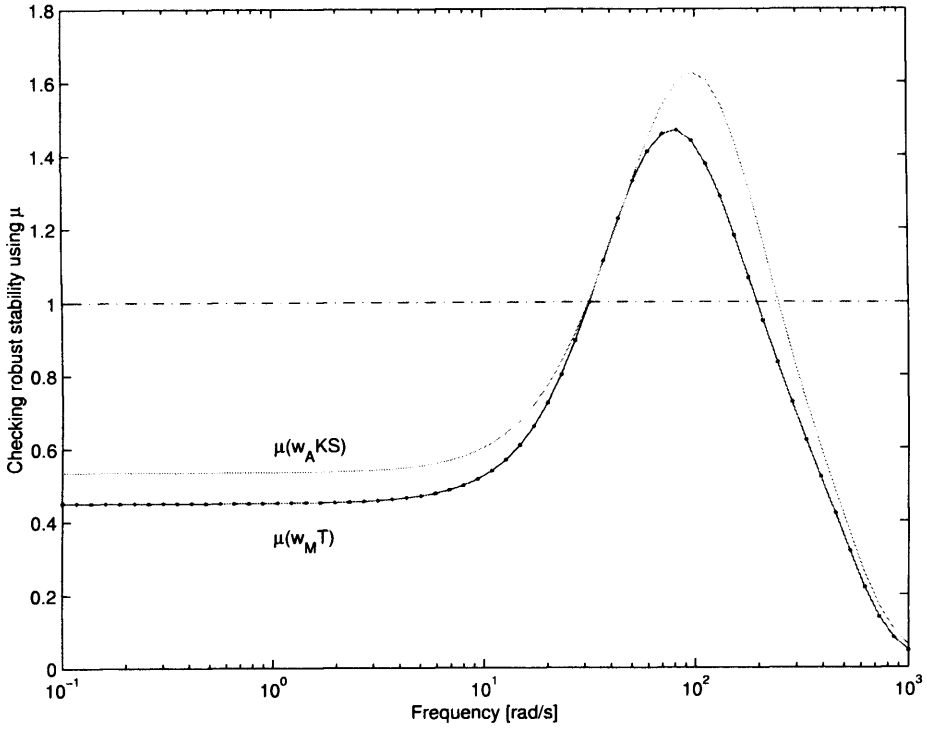

Figure 7.12: Testing robust stability for the system in Fig. 7.7 using the structured singular value μ.

experiment	k_i, k_z [%]	m [%]	R [%]	L_0 [%]	$w_A(s)$	$w_M(s)$	$\mu(N_{11})$ for $w_A(s)$	$\mu(N_{11})$ for $w_M(s)$
1	30	200	30	30	$\frac{1400(s+1000)}{(s+200)(s+100)^2}$	$\frac{0.90(s+25)}{(s+50)}$	1.63	1.47
2	–	200	30	30	$\frac{1160(s+1000)}{(s+200)(s+100)^2}$	$\frac{0.74(s+25)}{(s+42)}$	1.35	1.26
3	30	–	30	30	$\frac{1200(s+1000)}{(s+200)(s+100)^2}$	$\frac{0.86(s+25)}{(s+50)}$	1.39	1.40
4	30	200	–	30	$\frac{1240(s+1000)}{(s+200)(s+100)^2}$	$\frac{0.84(s+25)}{(s+48)}$	1.44	1.41
5	30	200	30	–	$\frac{1360(s+1000)}{(s+200)(s+100)^2}$	$\frac{0.88(s+25)}{(s+50)}$	1.58	1.44
6	15	100	15	15	$\frac{840(s+1000)}{(s+200)(s+100)^2}$	$\frac{0.37(s+25)}{(s+65)}$	0.976	0.962

Table 7.2: Sensitivity of the robust stability

on the robust stability and this is consistent with the results in Table 7.1. Since Maglev systems are nonlinear, variations in the operating conditions (i_0, z_0) contribute to variations in k_i and k_z and hence to the robustness. Although the operating airgap z_0 for Maglev is typically kept constant and unchanged, disturbance forces acting on the syspension system affect the operating current and hence the internals of the model. A resasonable degree of uncertainty in k_i, k_z has thus to be included in the controller-design process. Suspension systems are obviously designed to carry loads and since variations in m have an impact on the overall stability robustness this parameter has to be also included in the robust design. The resistance and the inductance have the least efect on the robustness stability and for mathematical convenience these can be excluded provided that a care is taken in the estimation of their values.

To calculate the stability margin, all five parameters are reduced simultaneously to get $\mu < 1$ for the values in row-6 (Table 7.2, Fig E.3). On the margin of the robust stability index, however, the system is expected to have a poor performance and this analysis is presented in the following section.

7.4.2 Robust performance

In addition to a stable suspension, Maglev systems are required to maintain an acceptable level of performance in the face of perturbations. The suspension characteristics (bandwidth, suspension damping and settling time) are required to remain unchanged for all bounded variations in the plant. The problem of checking robust performance can be transformed to a problem of checking robust stability by introducing a fictitious perturbation Δ_f that connects $q = [q_1,\ q_2]$ with $w = [d,\ r]$ as in Fig. 7.8. The resultant closed-loop configuration is shown in Fig. 7.13. For this closed-loop system

$$\begin{bmatrix} s \\ q \end{bmatrix} = N \begin{bmatrix} e \\ w \end{bmatrix}$$

and

$$\begin{bmatrix} e \\ w \end{bmatrix} = \mathbf{\Delta} \begin{bmatrix} s \\ q \end{bmatrix}$$

Combining these two equations gives

$$\begin{bmatrix} s \\ q \end{bmatrix} = N\mathbf{\Delta} \begin{bmatrix} s \\ q \end{bmatrix} \quad \Leftrightarrow \quad \begin{bmatrix} s \\ q \end{bmatrix} [I - N\mathbf{\Delta}] = 0$$

If $[I - N\mathbf{\Delta}]$ is non-singular ($\det[I - N\mathbf{\Delta}] \neq 0$) then the only solution to this equation is $[s, q] = [e, w] = 0$. If, however, $[I - N\mathbf{\Delta}]$ is singular then there exists infinite number

of solutions and the inputs and the outputs can be arbitrarily large [93]. Since $\mathbf{\Delta} = \begin{bmatrix} \Delta & 0 \\ 0 & \Delta_f \end{bmatrix}$, tests for robust analysis can be performed by employing the structured singular value [93]

$$\mu(N(s)) < 1, \quad \forall\omega \tag{7.21}$$

Eqn. 7.21 provides a basis for estimating the robust performance properties of the $\mathcal{H}_\infty$

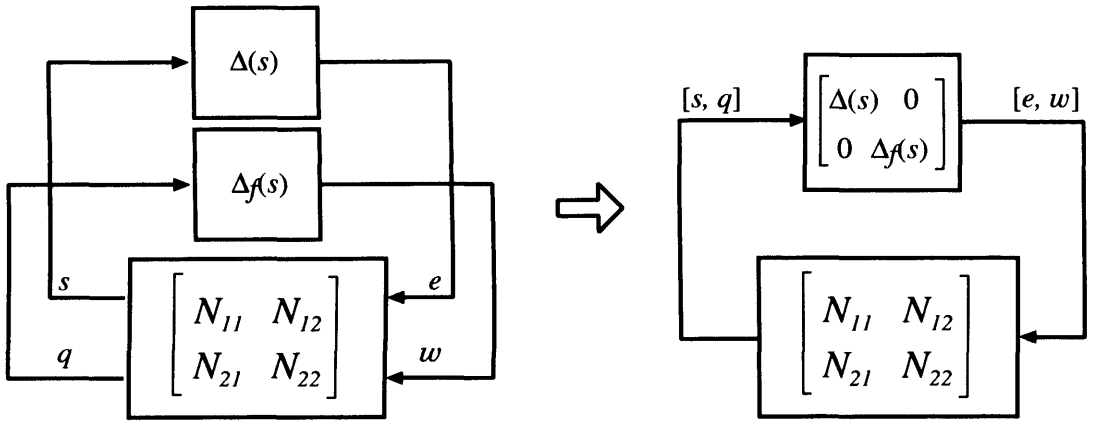

Figure 7.13: A feedback structure for testing robust performance for the system in Fig. 7.7 using the structured singular value μ.

compensator. Using the feedback transfer matrices $N(s)$ in Eqn. 7.11 and 7.15 and the μ-analysis toolbox for Matlab, $\mu(N(s))$ is computed and plotted in Fig. 7.12. Since for both uncertainty models, μ is larger than one for $20 < \omega < 200$ rad/s, the robust-performance properties of the system are not satisfied. The closed-loop system is thus expected to have a very poor phase margin leading to under-damped oscillatory responses. To justify these conclusions, the following time-domain experiment was carried-out. According to Table. 7.1, the closed-loop performance degrades when the mass of the system increases. In the frequency domain, this is given in Fig. 7.3. Five experiments are carried out in the time-domain by varying m in five discrete levels: 0%, 50%, 100%, 150%, 200%. The corresponding results are shown in Fig. 7.15 (top); plot-1 represents the nominal plant. The corresponded phase margins are: 39.46, 32.83, 26.11, 20.51 and 15.89 degrees (computed with Matlab). The increase in the mass of the system changes the phase characteristics of the open-loop model and this reduces the phase-margin. Oscilatory responses correspond to sensitivity functions with larger ∞-norms and therefore the closed-loop properties prescribed by the performance weight $W(s)$ (Figs. 7.7 and 7.10) are not longer guaranteed and the controller fails to meet the robust performance properties. This justifies the results in Fig. 7.14. To confirm the test for robust stability based on μ, k_i, k_z, R and L_0 were also

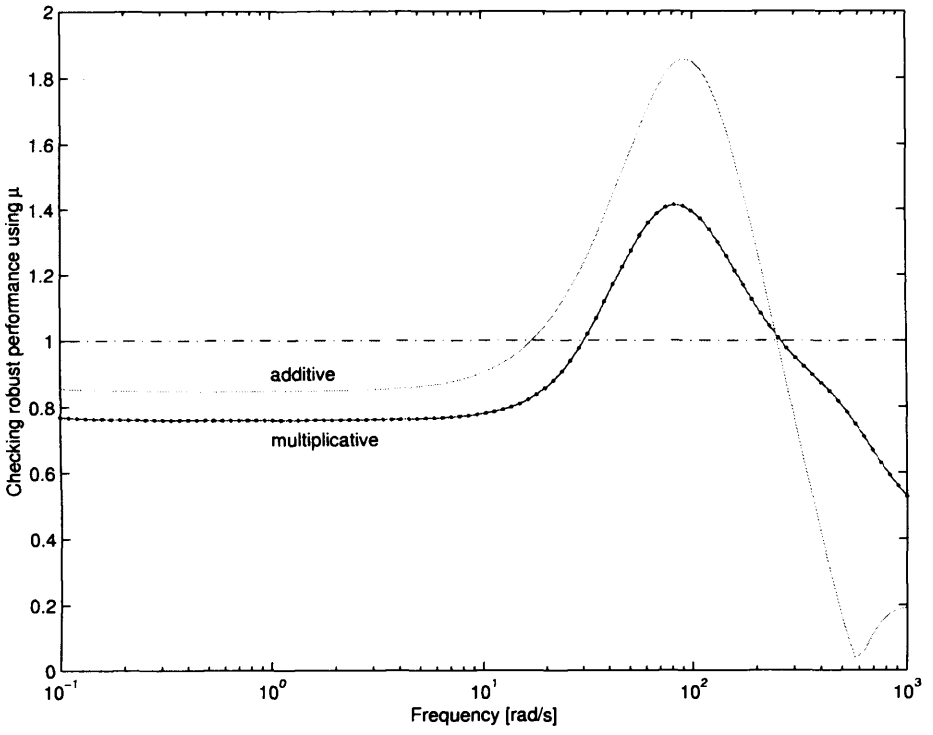

Figure 7.14: Checking robust performance for the system in Fig. 7.10 using the structured singular value μ.

varied together with the mass m in three discrete levels of 0%, -30% and 30%. The corresponding simulated step responses are shown in Fig. 7.15 (bottom). These results support the hypothesis that the $\mathcal{H}_\infty$ controller designed for the nominal model does not guarantee robust stability for variations in the parameters.

experiment	k_i, k_z [%]	m [%]	R [%]	L_0 [%]	$w_A(s)$	$w_M(s)$	$\mu(N)$ for $w_A(s)$	$\mu(N)$ for $w_M(s)$
1	30	200	30	30	$\frac{1400(s+1000)}{(s+200)(s+100)^2}$	$\frac{0.90(s+25)}{(s+50)}$	1.80	1.53
2	–	200	30	30	$\frac{1160(s+1000)}{(s+200)(s+100)^2}$	$\frac{0.74(s+25)}{(s+42)}$	1.53	1.33
3	30	–	30	30	$\frac{1200(s+1000)}{(s+200)(s+100)^2}$	$\frac{0.86(s+25)}{(s+50)}$	1.57	1.45
4	30	200	–	30	$\frac{1240(s+1000)}{(s+200)(s+100)^2}$	$\frac{0.84(s+25)}{(s+48)}$	1.62	1.46
5	30	200	30	–	$\frac{1360(s+1000)}{(s+200)(s+100)^2}$	$\frac{0.88(s+25)}{(s+50)}$	1.76	1.49
6	15	100	15	15	$\frac{840(s+1000)}{(s+200)(s+100)^2}$	$\frac{0.37(s+25)}{(s+65)}$	1.15	1.17
7	10	50	10	10	$\frac{700(s+1000)}{(s+200)(s+100)^2}$	$\frac{0.61(s+15)}{(s+65)}$	0.99	0.93

Table 7.3: Sensitivity of the robust performance

To calculate the sensitivity of the performance robustness versus variations in the parameters, the analysis in Table 7.2 is repeated. The corresponding results are shown in Table 7.3 with $w_A(s)$ and $w_M(s)$ as computed in Appendix E. The robust index μ is derived for $N(s)$ in Eqn. 7.11 and 7.15 for all $w_A(s)$ and $w_M(s)$ in the table. The results

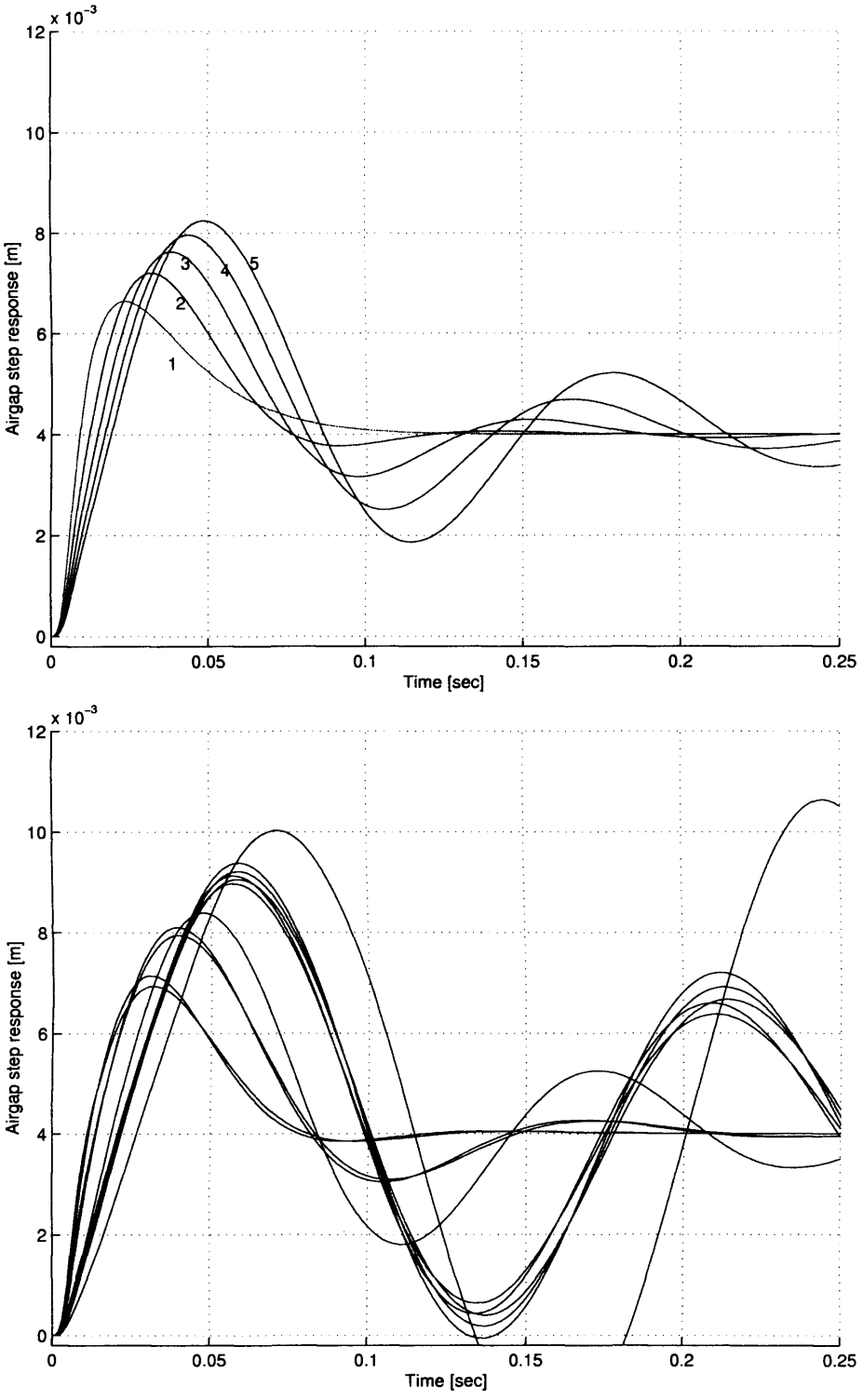

Figure 7.15: Step responses of the nominal system with K in Eqn. 6.44 and: (top) variation in m for $m = 0\%$ (plot-1), $m = 50\%$ (plot-2), $m = 100\%$ (plot-3), $m = 150\%$ (plot-4) and $m = 200\%$ (plot-5). (bottom) variation in m as above and k_i, k_z, R and L_0

(μ values are plotted in Fig. E.3, page E.4) show that the performance robustness is more sensitive to variations in k_i, k_z and m, and less sensitive to variations in R and L_0. This is consistent with the results for robust stability. As suggested earlier, on the margin of the stability robustness (15% variation in k_i, k_z, R and L_0 and 100% variations in m, row-6 in Table 7.2 and Fig. E.4), the robust performance in the suspension response in not satisfied ($\mu-$values in row-6 in Table 7.3 and Fig. E.4). It was estimated empirically that the $\mathcal{H}_\infty$ compensator provides robust performance, $\mu(N(s)) < 1$, for a maximum 10% variation in k_i, k_z, R and L_0 and 50% variation in m (row-7 in Table 7.3 and Fig. E.4). Therefore, robustness in terms for stability and performance can be achieved only by re-designing the feedback compensator $K(s)$ and embeddeding the perturbations in its parameters. This is presented in the following section.

7.5 Robust controller design for Maglev systems

In this section, new robust controllers (or μ-optimal controllers) are derived by embedding the uncertainty into the design process. The design task is to achieve $\mu(N(s)) < 1$ for $N(s)$ in Eqns. 7.11 or 7.15. The algorithm for μ-optimal controller-design, known as DK-iteration, combines $\mu-$analysis (described in the previous section) and $\mathcal{H}_\infty$-synthesis (described in the previous chapter) and aims to solve [73, 93]

$$\min_K \max_D \|DND^{-1}\|_\infty \tag{7.22}$$

where: N is given in Eqn. 7.11 or Eqn. 7.15, K is the unknown feedback controller and D is a diagonal scaling matrix used in the computation of μ. $\min_K \|DND^{-1}\|_\infty$ is an $\mathcal{H}_\infty$ controller-design optimisation problem whose solution was derived in Chapter 6. $\max_D \|DND^{-1}\|_\infty$ defines the optimisation problem for deriving μ (Eqn. 7.20). Combining these two in Eqn. 7.22 leads to the following procedure for deriving $K(s)$

Step 1 Select an initial stable transfer matrix $D(s)$; usually the identity matrix is a suitable first choice for $D(s)$.

Step 2 $K-$ *step*: Derive an $\mathcal{H}_\infty$ controller $K(s)$ following the algorithm in Chapter 6 using the following design criteria

$$\min_K \|DND^{-1}\|_\infty$$

Step 3 $D-$ *step*: Use K as derived above to construct $N(s)$ in Eqn. 7.15 (or 7.11). Calculate the upper bound $\mu(N)$ to determine the robust properties of the controller. This

process requires calculating an appropriate frequency-dependent weight $D(\omega)$ (see the algorithm for computing μ in Appendix D)

$$\mu(N) = \min_{D} \bar{\sigma}(DND^{-1})$$

Step 4 Fit the magnitude response of $D(\omega)$ computed at step-3 to a stable and a minimum phase transfer function $D(j\omega)$.

Step 5 Continue from step 2 by constructing (DND^{-1}) with D form Step 4.

Step 6 Stop the design iteration when $\mu(N) \leq 1$.

This optimisation procedure is a convex problem in determining D and K [94]. The above design steps are typically embedded in algorithms for deriving μ-optimal controllers such as the μ-analysis and synthesis toolbox for Matlab [76]. For the Maglev work, a set of customised Matlab programs were constructed that use the open-loop Maglev model and the design requirements to derive new optimal controllers for Maglev. Simulation and experimental results are discussed below. The overall order of the new μ-compensator is equal to the sum of the orders of the system $G(s)$, the performance weight $W(s)$, plus twice the order of $D(s)$. For implementation purposes, the order of the compensator is reduced to practical values with order-reduction algorithms which preserve the robust properties.

7.5.1 Design of μ-optimal controllers for Maglev systems

Two new controllers for Maglev were derived: (a) $K_{\mu 1}(s)$ for the multiplicative model in Fig. 7.10 and (b) $K_{\mu 2}(s)$ for the additive model in Fig. 7.7. Comparisons in terms of the robustness are made with the $\mathcal{H}_\infty$ controller in Eqn. 6.44, page 116. The numerical design work is carried out in Matlab. Customised software programs are written with the following inputs: (1) the open-loop Maglev model in Eqn. 6.35, (2) the performance weights $W(s)$ and W_c in Eqns. 6.36 and 6.37 (104), and (3) the uncertainty models $w_A(s)$ and $w_M(s)$ in Eqns. 7.3 and 7.6 (Section 7.2.3). Using these inputs and the Matlab programs, two new robust controllers are derived: $K_{\mu 1}(s)$ in Fig. 7.7 for the additive model of uncertainty, and (b) $K_{\mu 2}(s)$ in Fig. 7.10 for the multiplicative model of uncertainty (these are not included in a numerical form for the following purposes). The robust measures achieved after two D-K design iterations in the optimisation algorithm are given below

1. $\mu(N_{11}) = 0.98$ and $\mu(N) = 1.4$ for the additive scheme, and

2. $\mu(N_{11}) = 0.99$ and $\mu(N) = 1.5$ for the multiplicative scheme

$\mu(N_{11}) < 1$ for both compensators and hence in contrast to the $\mathcal{H}_\infty$ controller (Table 7.2, row-1), the new μ controllers provide robust stability for all variations in the uncertain parameters. Both measures for robust performance $\mu(N)$, however, are larger than one and hence the new controllers are only marginally better in terms of robust performance than the nominal $\mathcal{H}_\infty$ controller (Table 7.3, row-1). This requires constructing a new design cycle.

Design of robust controllers is an iterative procedure. A typical design cycle goes through three stages: (1) to identify and model the uncertainty in plant ($w_A(s)$ or $w_M(s)$, Section 7.2.3), (2) to specify the performance requirements for the closed-loop system (selection of $W(s)$ and W_c, Section 6.4.2, page 102), and (3) to design the $\mu-$optimal controller using $W(s)$, W_c, $w_A(s)$ or $w_M(s)$ and $G(s)$. If the μ values at the end of the DK-iteration are greater than one, then the design requirements are too tight and these should be relaxed. There are two possible approaches here: (1) to assess the uncertainty in the model by relaxing the variations and thus the models $w_A(s)$ and $w_M(s)$, or (2) to modify the performance requirements by changing $W(s)$ and W_c. Since the primary objective in this chapter is to design robust controllers for 30% variation in R, L_0, k_i, *and* k_z and 200% variations in m, $w_A(s)$ and $w_M(s)$ are kept unchanged. The performance weight $W(s)$ is however modified to

$$W(s) = \frac{0.13333(s + 60)}{(s + 0.008)},$$

Compared to the original weight in Eqn. 6.36, this new performance function provides larger gain at higher frequencies ($\approx$ 10 dB for $\omega > 60$ rad/s) which in turn allows larger peaks on the sensitivity function. Apart from relaxing the optimisation procedure, this modifications does not have any impact on the performance since the sensitivity function tends to have 0dB gain as $\omega \to 0$ from the inherent properties if the open-loop model. Using this new function and keeping $W_c = 0.005$ unchanged, two new μ controllers are designed with the following μ properties

1. $\mu(N_{11}) = 0.9$ and $\mu(N) = 0.99$ for the additive scheme, and

2. $\mu(N_{11}) = 0.98$ and $\mu(N) = 0.98$ for the multiplicative scheme

Since the μ-values are below one, these new controllers, as given below, provide robust stability and robust performance

$$K_{\mu 1}(s) = \frac{-210643.2402(s+354.3)(s+173.9)(s+65.08)(s+50)}{(s+14.09)(s+5.085)(s^2+520.4s+2.465\times10^5)} \times \frac{(s+1.056\times10^4)(s+196.7)(s+69.07)(s+12.29)(s+0.008)}{(s^2+520.8s+2.474\times10^5)(s^2+987.2s+5.674\times10^5)}$$

and

$$K_{\mu 2}(s) = \frac{-1825060.3396(s+2.901\times10^5)(s+356.6)(s+339.2)(s+200)}{(s+2.901\times10^5)(s+1.242\times10^4)(s+356.2)(s+79.12)(s+23.62)} \times \frac{(s+65.28)(s+24.94)(s+6.868)(s+3.904)(s^2+200s+1\times10^4)}{(s+3.268)(s+0.008)(s^2+365.9s+5.002\times10^4)(s^2+2643s+2.744\times10^6)}$$

For the practical implementation, the order of these controllers is reduced using the optimal Hankel norm approximation algorithm [95, 76] to improve for the phase delays in the digital representation. $K_{\mu 1}(s)$ is reduced from a controller with 9 state variables to five state variables

$$K_{\mu 1}(s) = \frac{-0.00734(s+2.866\times10^7)(s+326.9)(s+5.328)(s^2+88.92s+2304)}{(s+1.054\times10^4)(s+47.36)(s+0.008001)(s^2+979.5s+5.616\times10^5)} \quad (7.23)$$

and $K_{\mu 2}(s)$ is reduced from a controller with 11 state variables to five state variables

$$K_{\mu 2}(s) = \frac{0.066474(s-2.75\times10^7)(s+460.6)(s+9.628)(s^2+139.4s+4933)}{(s+1.246\times10^4)(s+221.6)(s+0.007997)(s^2+2653s+2.787\times10^6)} \quad (7.24)$$

The corresponding $\mu-$values of these reduced-order controllers were computed with Matlab and shown in Fig. 7.16 (top) for the additive scheme and Fig. 7.16 (bottom) for the multiplicative scheme. Since both controllers provide $\mu < 1$, the requirements for robust stability and robust performance are satisfied for all variations in the Maglev parameters.

7.5.2 Simulation results

In the following discussions, $K(s)$ refers to the nominal $\mathcal{H}_\infty$ controller designed in the previous chapter. A comparison plot between the Bode plot of the $K(s)$, and the Bode plot of the $\mu-$optimal controllers $K_{\mu 1}(s)$ and $K_{\mu 2}(s)$ is shown in Fig. 7.17. In the low-frequency range ($\omega < 100$ rad/s) apart from the small gain difference all three controllers have similar responses. The high roll off factor imposes good steady state characteristics and good attenuation to low-frequency disturbances. In the middle frequency range ($10 < \omega < 100$ Hz), however, the $\mu-$optimal controllers $K_{\mu 1}(s)$ and $K_{\mu 2}(s)$ have much wider lead-action compared to $K(s)$ which in turn gives better phase margins. To analyse this further, the loop transfer functions for the three controllers is calculated and plotted in Fig 7.18 where GK, $GK_{\mu 1}$, and $GK_{\mu 2}$ correspond to loop transfer function with $K(s)$, $K_{\mu 1}(s)$, $K_{\mu 2}(s)$, respectively. Superimposition of these functions shows that the $\mu-optimal$ controllers have

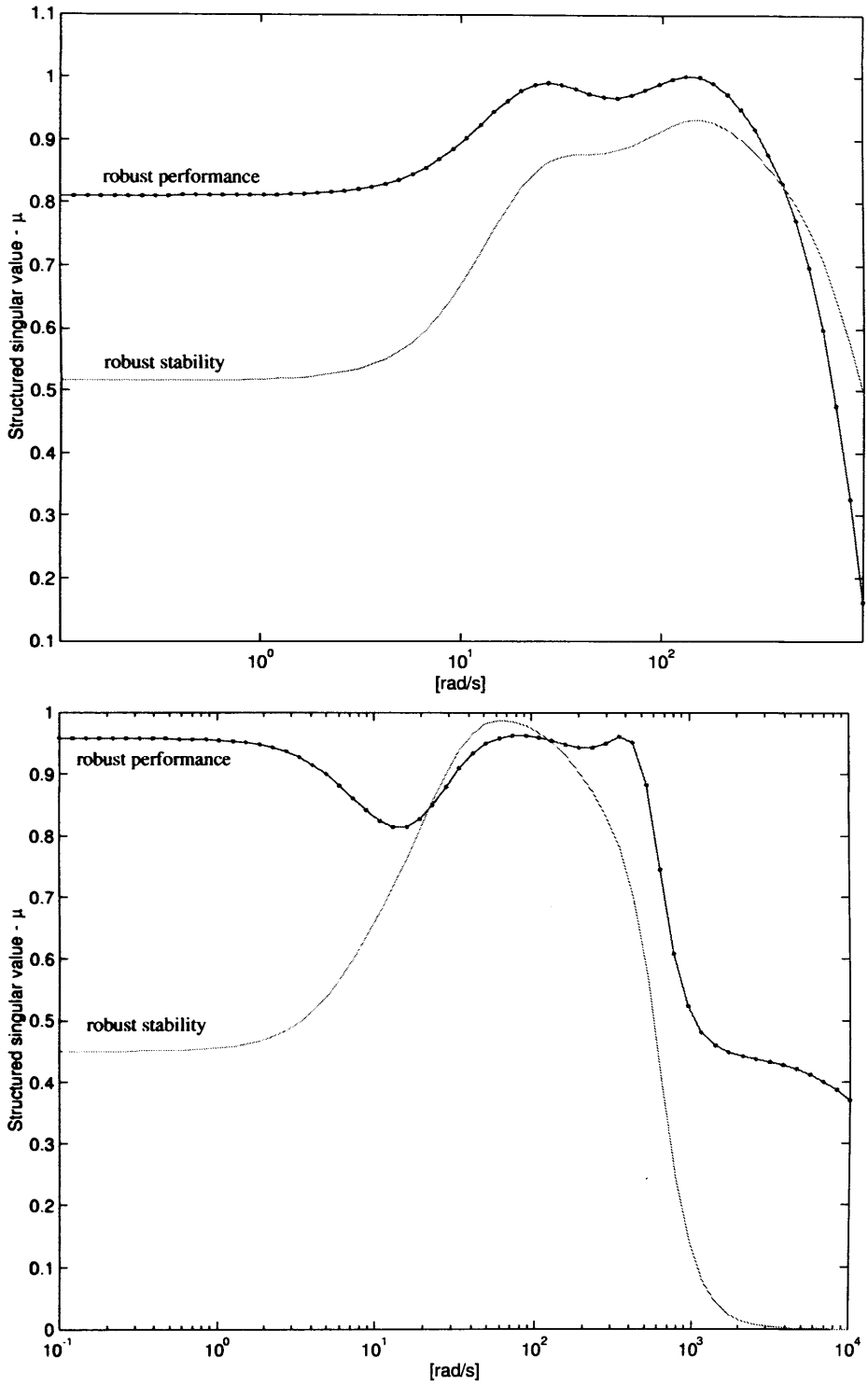

Figure 7.16: Robust stability and robust performance of the closed loop system. Top: system with $K_{\mu 1}$; Bottom: system with $K_{\mu 2}$

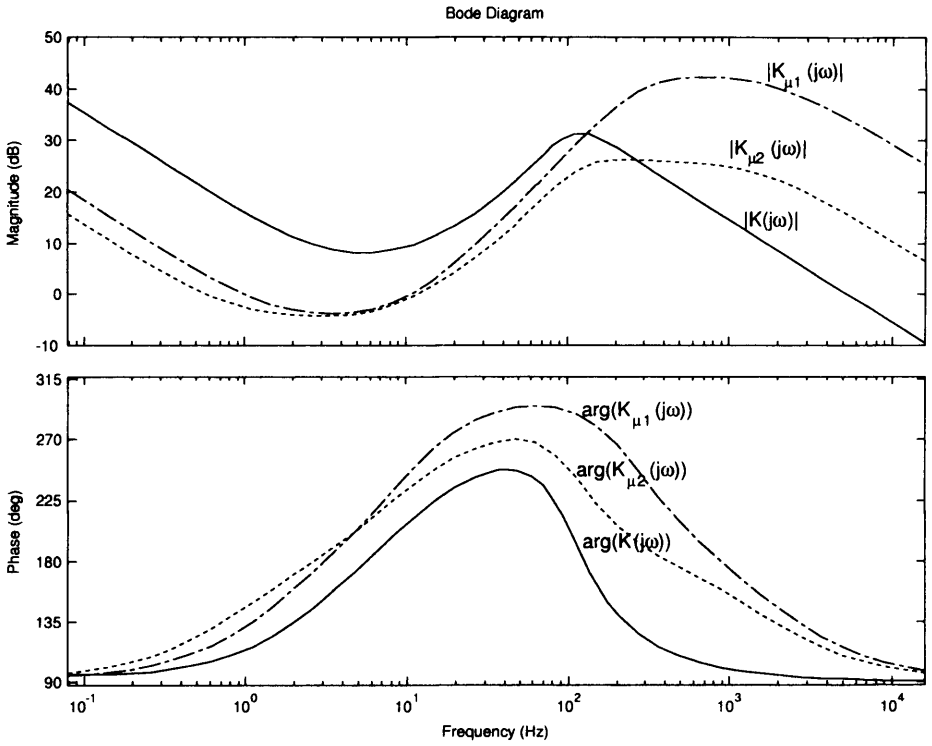

Figure 7.17: Bode plot of $K(s)$, $K_{\mu 1}(s)$ and $K_{\mu 2}(s)$

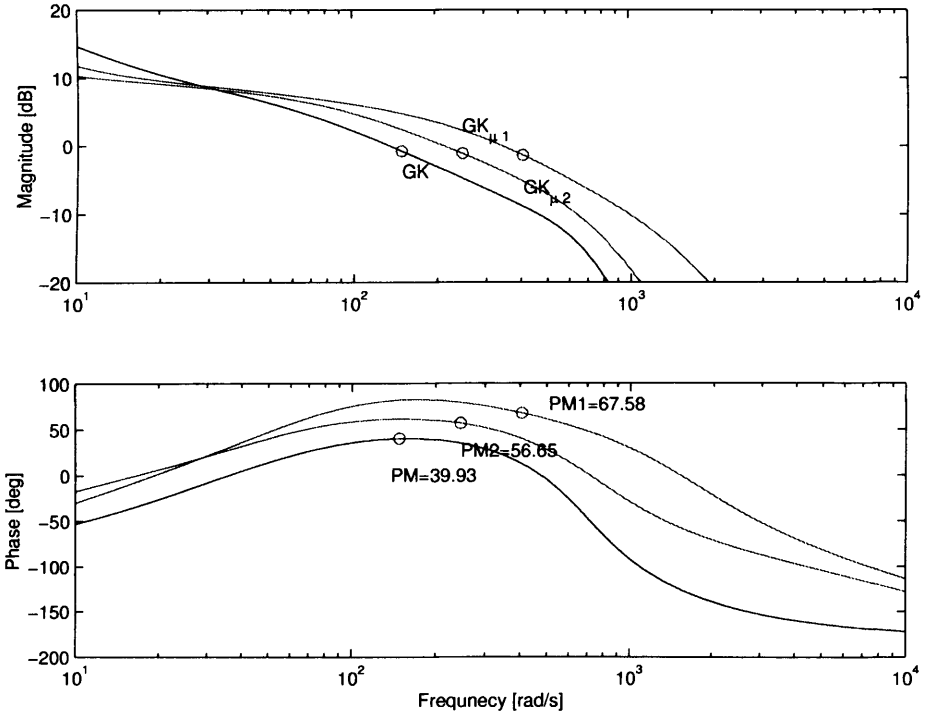

Figure 7.18: Phase margins of the closed-loop system for three different controllers: K, $K_{\mu 1}$ and $K_{\mu 2}$

nearly two-times higher phase margins compared to the nominal controller. It has been calculated that $PM(K) = 39.46$ at $\omega = 21.45$ Hz, $PM(K_{\mu 1}) = 59^0$ at $\omega = 33.76$ Hz and $PM(K_{\mu 2}) = 72^0$ at $\omega = 54.8$ Hz. Since these results are computed for the nominal model $G(s)$, variations in the Maglev's parameters would pose variations in the phase margins, but since the $\mu-$optimal controllers have very large phase margins, the robust properties of these controllers would be considerably better than those of the nominal controller. For the worst combination in the variation of the parameters, the phase margin is $> 30^0$. Taking $K_{\mu 1}$ as an example, reduction in the loop-gain of the system by a factor of two results in a reduction of the phase margin to 37^0 which is still within the design requirements of 35-40 degrees. Since $K_{\mu 1}(s)$ and $K_{\mu 2}(s)$ represent the same uncertainty and both have very closed properties and $\mu-$values, only $K_{\mu 1}(s)$ is used in the following studies. In addition, $K_{\mu 1}(s)$ has lower cross-over frequency (the bandwidth of $K_{\mu 2}(s)$ approaches the practical bandwidth for the experimental system) and hence is more suitable for the experimental work.

Initially, the robust properties of $K_{\mu 1}(s)$ were studied by repeating the experiments in Section 7.2.2. m, R and L_0 are varied as per Table 7.1 and the Nyquist plots of the closed-loop system is calculated for each combination. The responses of the nominal controller $K(s)$ are shown in Fig. 7.3. The corresponding Nyquist plots for the new $\mu-$optimal controller $K_{\mu 1}(s)$ are computed and shown in Fig. 7.19. These results show that for the worst set of variations in the Maglev parameters, the closed-loop system remains stable with good phase margins and hence suspension damping. Previously, for combinations 7, 8 and 9 the closed-loop system was unstable (Fig. 7.3) since the drop in phase margin was as much as 40^0. The comparison between plot 8 in Fig. 7.3 and plot 8 in Fig. 7.19 shows that for the worst combination, $K_{\mu 1}(s)$ offers a phase margin of 32^0, which is comparable with the phase margin of the nominal system (plot-1) in Fig. 7.19. Therefore, the closed-loop system remains robust stable and offers performance robustness for the whole set of variations. The simulated step responses of the system for the parameter variations in Table 7.1 are shown in Fig. 7.20. Robust controller design guarantees that all responses are within the envelop in the figure. This conclusion is further analysed by comparing the transient response of the closed-loop system with the $\mu-$optimal controller. This experiment, shown in Fig. 7.21, repeats the experiment in Fig. 7.15 (bottom). The mass is varied with +200% from the nominal value, and the inductance, the resistance and k_i and k_z are varied with $\pm 30\%$ from their nominal values. The results suggest that for all variations in the pa-

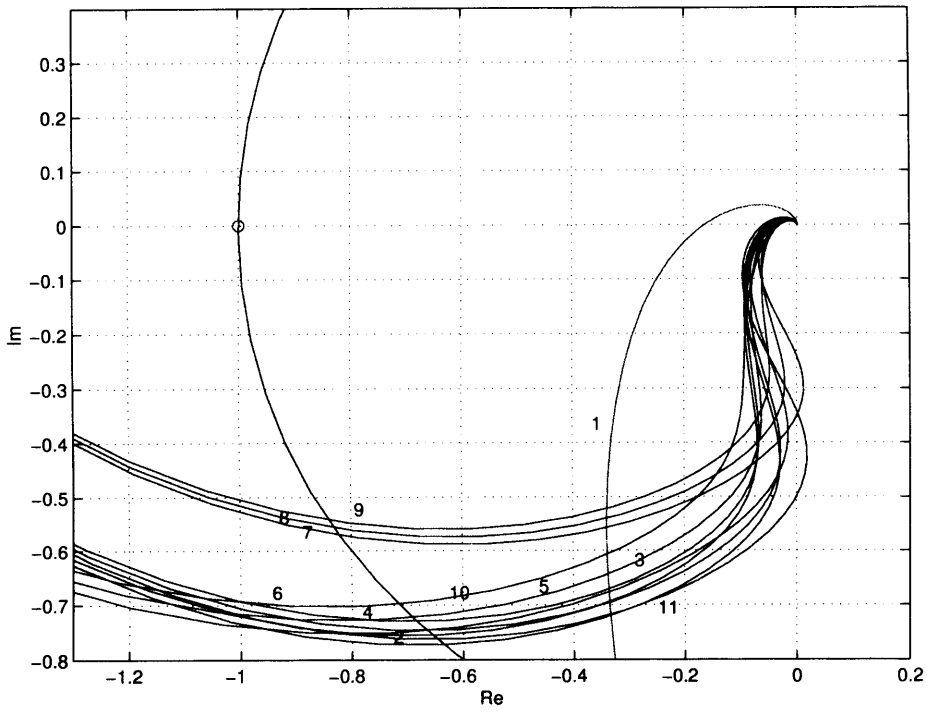

Figure 7.19: Nyquist plot of the closed-loop system with $K_{\mu 1}$ and parametric variation as per Table 7.1 (plot-numbers correspond to experiment number in the table)

rameters, the system remains stable with good settling time and zero steady-state error. The new $\mu-$optimal controller thus provides robust performance and stability. In terms of robustness, this feature makes it superior to the $\mathcal{H}_\infty$ controller. Experimental results are discussed below.

7.5.3 Experimental results

The experimental work was carried out on the DSP hardware for Maglev control, Chapter 5. For the DSP implementation, the $\mu - optimal$ controller (Eqn. 7.23) is discretized using the Tustin transformation. For the comparison, the simulation work was performed in Simulink using the block-diagram in Fig. 6.21, page 123 (with $K(s)$ replaced with $K_{\mu 1}(s)$). Each experiment was initiated from Matlab by sending a command to the control software on the DSP via the TCP/IP communication protocol. After receiving the command, the DSP software starts logging the control signal and the airgap as seen from the position sensor while changing the reference airgap. At the end of the experiment, the logged data is transfered to Matlab and superimposed with the simulation data. In the first experiment, the reference airgap is altered from 4.5mm to 3.5mm at $t = 0.5$ sec. and then back from 3.5mm to 4.5mm at $t = 1.0$ sec. The simulation and experimental transient responses are shown in Fig. 7.22 and show that the theoretical results compare well with the experimental

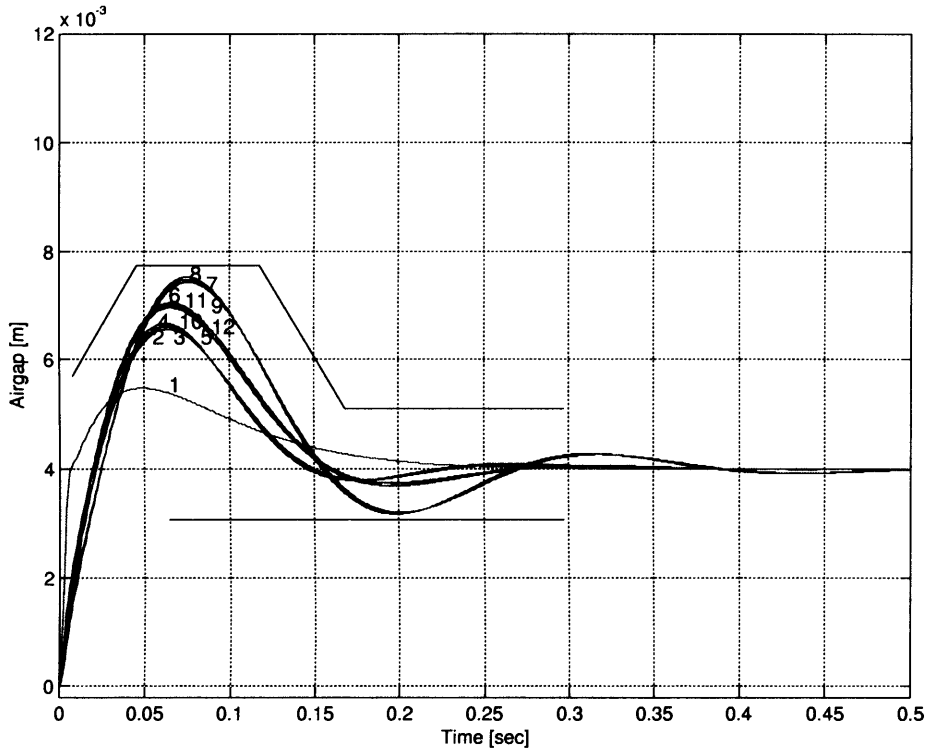

Figure 7.20: Step responses of the closed-loop system with $K_{\mu 1}(s)$ and parametric variation as in Table 7.1 (plot-numbers correspond to experiment number in the table). Robust controller design guarantees that all responses are within the envelop.

results in both airgap and control signal. The conclusions for the robust properties of the system which were based on simulation studies thus can be applied to the experimental systems. To justify this, one more experiment was performed in adding 200% (2.5kg) additional mass to the suspended system. With this mass, the reference airgap is changed from 3.5mm to 4.5mm. A comparison plot between the nominal $\mathcal{H}_\infty$ controller $K(s)$ and the new robust controller $K_{\mu 1}(s)$ is shown in Fig. 7.23. According to Fig. 7.15 (top), increasing the mass of the system decreases the gain of the open-loop system around the cross-over frequency and this leads to poor phase margins and thus oscillatory responses. This can be observed on the experimental plot in Fig. 7.23 which shows that the additional mass degrades the performance properties (oscillatory responses with the $\mathcal{H}_\infty$ controller). The $\mu-$optimal controller, however, manages to keep the closed-loop properties invariant to this perturbation. The response with the additional 200% (2.5kg) mass is comparable to the the response of the nominal system in Fig. 7.22. The $\mu-$optimal controller design thus provides robust stability and robust performance in the face of uncertainty in the model.

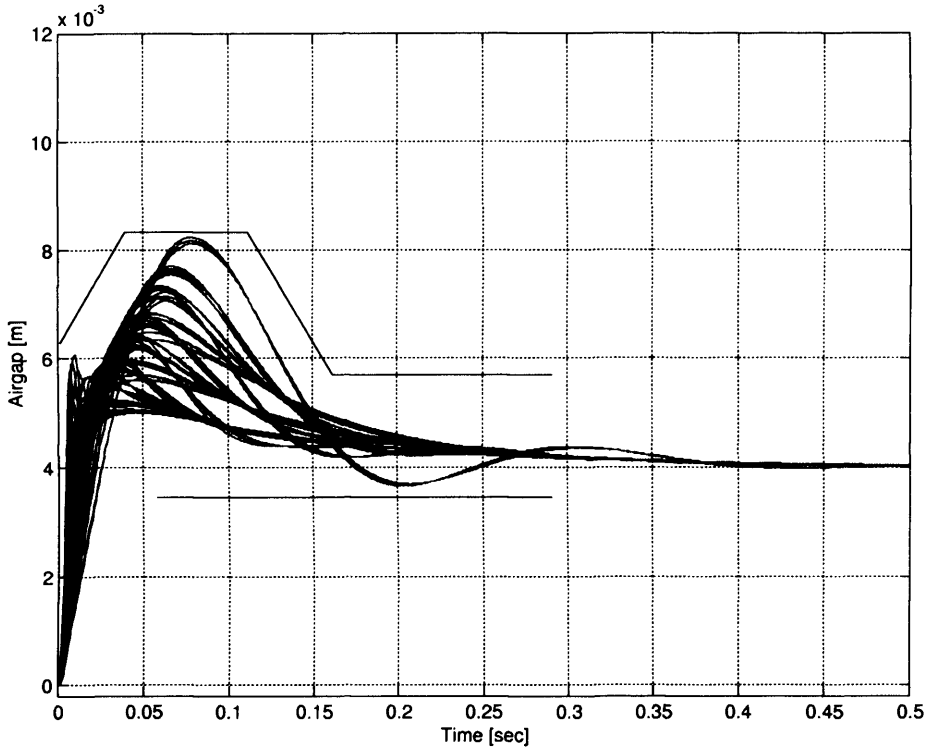

Figure 7.21: Step responses of the closed-loop system with $K_{\mu 1}$ and 81 variations in m, R, L_0, k_i and k_z (as per Section 7.2.3). The mass varies by 200% and the remaining parameters vary by $\pm 30\%$.

7.6 Conclusions

The notion of uncertainty is an important factor in the development of the feedback controllers for Maglev. This arises in two forms: (1) difference between the physical plant and the mathematical model used for design, and (2) unmeasured noises and disturbances that act on the suspension system. In Chapter 6, $\mathcal{H}_\infty$ theory was used to incorporate noise inputs into the controller design process. In the presence of variation in the Maglev parameters (30% variation in the values of R, L_0, k_i, *and* k_z and 200% variation in mass m), however, this controller fails to sustain stability and an acceptable level of performance. This necessitated developing a tool that: (a) is able to assess the robust properties of closed-loop Maglev systems, and (b) provides a basis for designing robust controllers for Maglev systems.

Two methods for modelling uncertainty are used in this chapter to represent the gap between the plant and its mathematical representation: the additive uncertainty model and the multiplicative uncertainty model. Both configurations are treated independently and the comparison results show that these are equally useful for robust analysis and design. Based on this development, a methodology is developed for assessing the robustness of

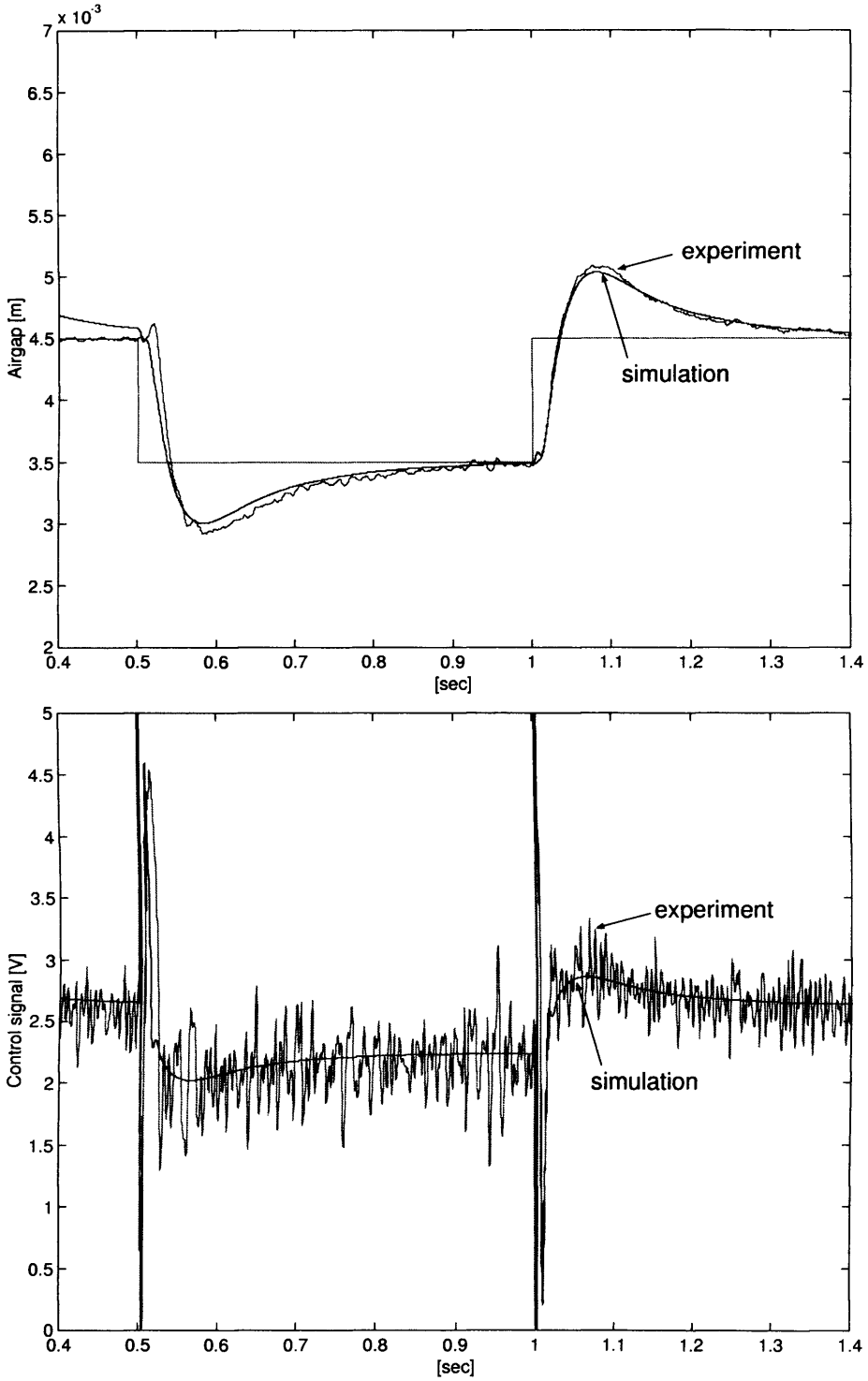

Figure 7.22: Superimposition of experimental and simulation results. Top: airgap response; Bottom: control signal. The feedback controller is $K_{\mu 1}(s)$.

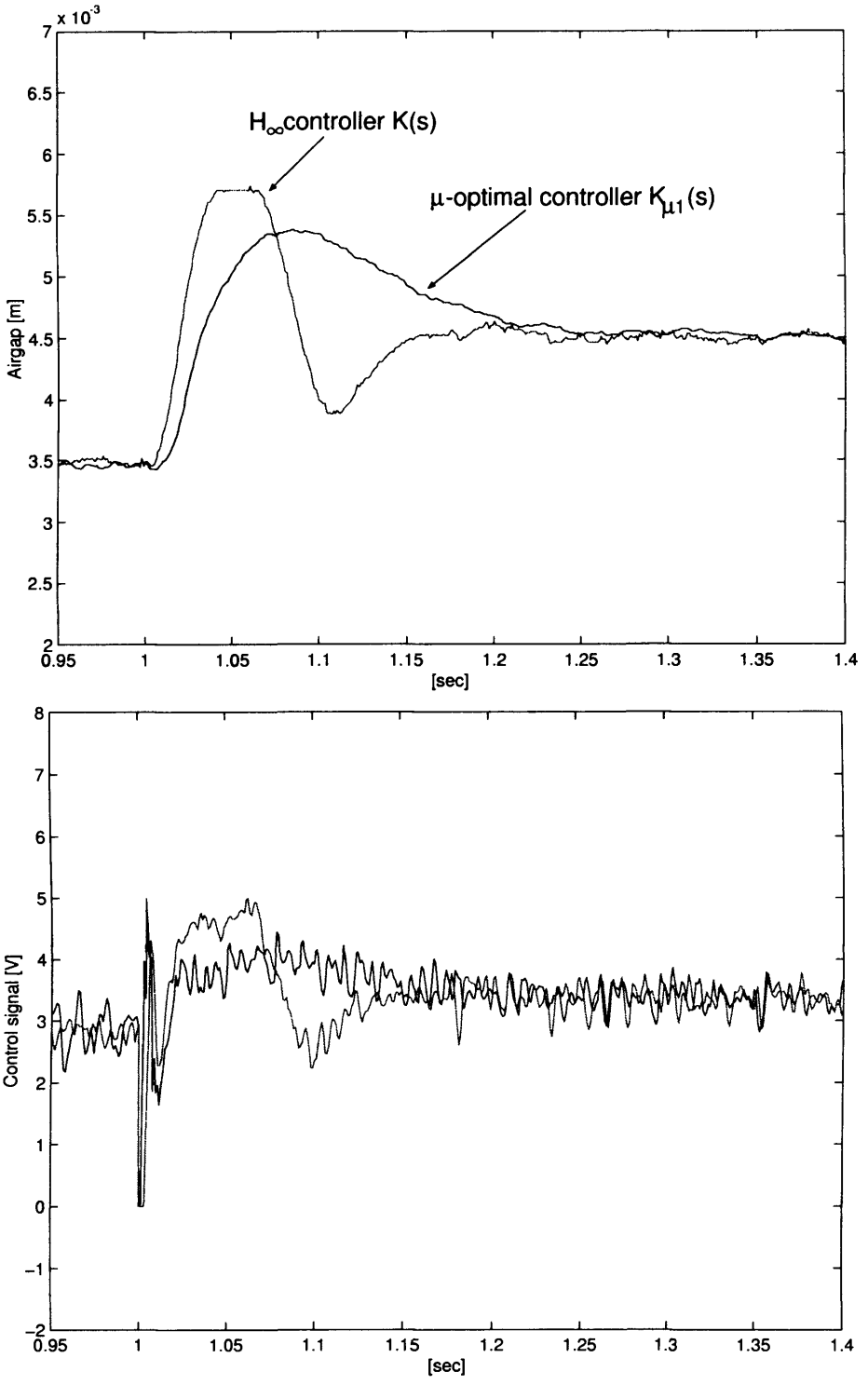

Figure 7.23: Experimental responses of the closed-loop system in the presence of 4.0kg mass added to the suspended object. The figure superimposed the results from the $\mathcal{H}_\infty$ controller and from the $\mu-$optimal controller. Top: airgap response; Bottom: control signal response.

closed-loop Maglev systems (when the feedback compensator is known) to derive a stability margin beyond which the system degrades in terms of performance. The concept of μ-analysis has proven to be a convenient instrument for assessing the robustness of closed-loop systems. A systematic methodology has been developed that requires the open-loop model, the feedback compensator and the model of uncertainty to determine the robust margin of the system. An advantage is considered to be the ability of this tool to assess robustness of multivariable systems.

Design for performance ($\mathcal{H}_\infty$ only) is unsuitable for applications with a considerable uncertainty about the mathematical representation of the plant. To provide a basis for robust controller design, the theory of $\mathcal{H}_\infty$ is combined with $\mu-$analysis in an algorithm for robust controller design (DK-iteration). It was established that the controllers derived from this new tool (called $\mu-$optimal) are markedly superior, compared to the $\mathcal{H}_\infty$ design, in terms of sustaining robust stability and performance for a large range of parameter variation. With the robust design technique, however, there exists a trade-off between the robust margin and the effort from the controller. A comparison between the Bode plots of the $\mathcal{H}_\infty$ controller and the $\mu-$optimal controllers shows that to achieve high phase margins and hence robustness, the controller needs a considerably larger gain at higher frequencies which is directly proportional to the power dissipation in the magnet. From an implementation point of view, care has to be taken during the modelling stage to account for uncertainties which are truly presented in the model. This will considerably reduce the effort of the controller and hence improve the overall results.

A large number of industrial systems that employ magnetic levitation principles consist of more than one degree of freedom. Examples are Maglev vehicles, magnetic bearings, magnetic tables, etc. where four or more magnets are controlled simultaneously to achieve the required forces and torques. To simplify the analysis and the synthesis, the designer reduces the complexity by neglecting a weak cross coupling in the system to deal with a single-input-single-output model. The stability theory and controller design techniques for these are well established. In the following chapter, the $\mathcal{H}_\infty$ and the μ-design methodologies developed here are generalised to design multivariable controllers to stabilise a Maglev vehicle suspended from four magnets simultaneously. The performance of these controllers is assessed with simulation and experimental results from a representative Maglev rig.

Chapter 8

Multivariable Maglev control

Four magnets permanently fixed on a rigid body provide suspension forces and contactless properties for Maglev vehicles. The unstable nature of the force-airgap relationship requires feedback stabilisation for each magnet. From a control point of view, four or more currents have to be driven simultaneously to achieve the required stable forces and torques. One approach is to neglect the cross-coupling and treat all loops as independent; this method has been previously reported [1, 21, 15, 31]. In this chapter, another approach based on multivariable control has been developed which takes into account angular rotations and vertical motions of the suspended body. This is considered to be better for Maglev control since it provides: (a) a systematic procedure for dealing with multivariable Maglev problems, and (b) tools for robust stability and analysis of multivariable systems. It has been also shown that these controllers have better stability properties for lateral disturbance reduction when no active guidance control is provided.

8.1 Multivariable Maglev control

A block diagram of a magnetically levitated vehicle is shown in Fig. 8.1. The contactless suspension of the body is provided by four suspension magnets denoted as M_1, M_2, M_3 and M_4. These provide four forces of attraction: f_1, f_2, f_3 and f_4 which in turn give three degree of freedom in the chassis: (a) rotation about the x-axis (roll ϕ), (b) rotation about the y-axis (pitch θ), and (c) translation along the z-axis (heave z). This configuration does not include lateral magnets and their force of attraction, and hence rotation about the $z-$axis (yaw ψ) is not presented. Lateral guidance is, however, provided by the inherent lateral stiffness which exists between the suspension magnet and the reaction railway [1, 21]. A linear motor (not shown in the figure) provides the fourth degree of freedom, propulsion along the x-axis.

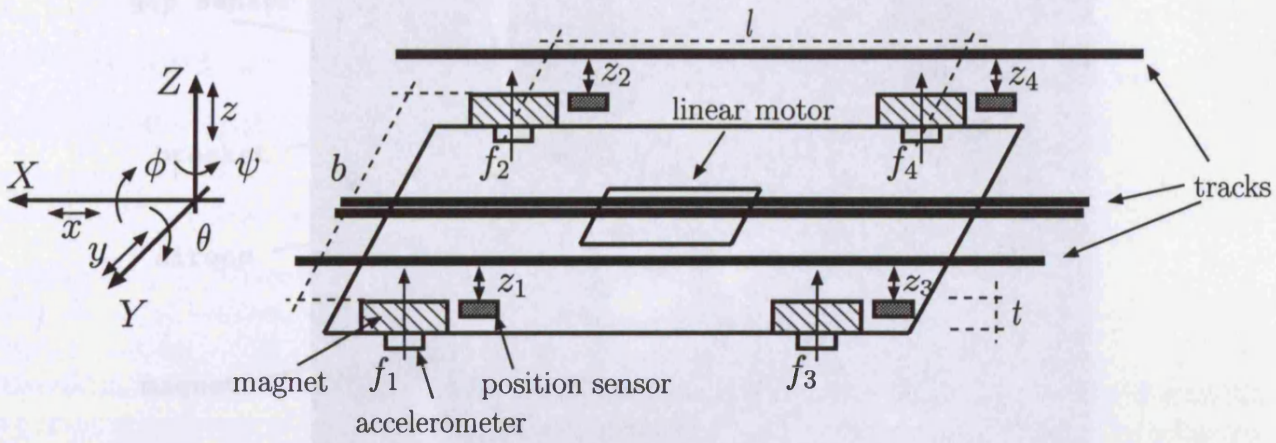

Figure 8.1: Block diagram of a magnetically levitated vehicle. Four magnets (M_1 to M_4) provide four suspension forces (f_1 to f_4) and hence three degree of freedom: pitch θ, roll ϕ and heave z. Photographic image of the vehicle is shown in Fig. 8.3. The magnet-track configuration is shown in Fig. 8.3

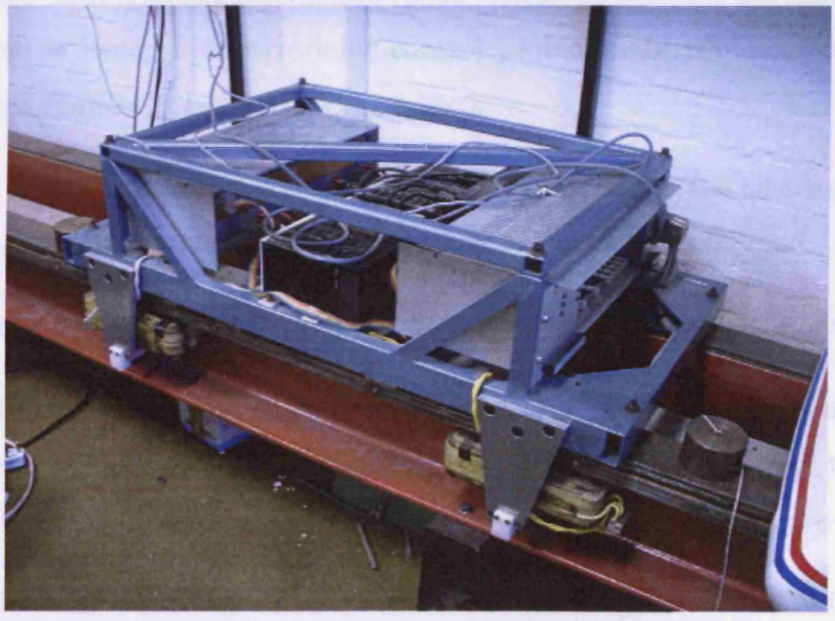

Figure 8.2: Photographic image of the Maglev vehicle.

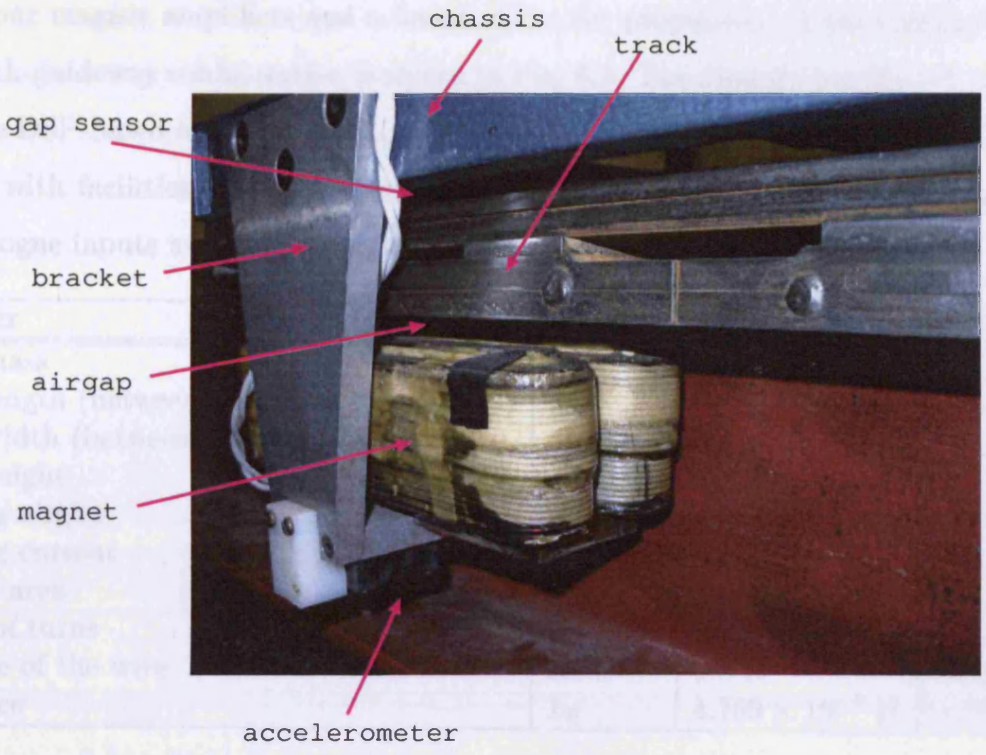

Figure 8.3: Magnet-track configuration (one corner).

The four lift suspension magnets on the vehicle control the three free-body motions, namely: heave z, pitch θ and roll ϕ. Since the magnets are permanently fixed on the rigid body, there exist a strong interaction (cross coupling) between the control loops. The control problem is hence a multivariable control problem. In this respect, the primary objective of this chapter is summarised as follows.

1. Develop a three degree of freedom state-space model for the suspension system in Fig. 8.1 and validate it using simulation and experimental studies.

2. Extend the developments in Chapters 6 and 7 to multivariable Maglev control.

3. Extend the multivariable model with provisions for guidance support and design new controllers for the six degree of freedom suspension model and assess the closed-loop system using simulation studies.

The experimental work was carried out on a multi-magnet vehicle built by previous researchers [1, 21]. The suspension characteristics are provided by four magnets as in the conceptional block-diagram in Fig. 8.1. A photographic image of the experimental rig is shown in Fig. 8.2. The mechanical and electrical parameters for the chassis and the magnets are listed in Table 8.1. The vehicle is equipped with four position sensors, four acceleration

sensors, four magnet amplifiers and a linear motor for propulsion. A photographic image of the track-guideway configuration is shown in Fig. 8.3. The digital control work is carried out on the DSP-based hardware with characteristics outlined in Chapter 5. This hardware was built with facilities for multi-magnet control (maximum four magnets) and provides eight analogue inputs and four analogue outputs.

parameter	notation	size	identified
chassis mass	M	88 kg	
chassis length (between electromagnet centres)	l	0.8 m	
chassis width (between electromagnet centres)	b	0.4 m	
chassis height	t	0.1 m	
operating airgap	z_0	4.0×10^{-3} m	
operating current	i_0	4.0 A	
pole face area	A	2.0×10^{-3} m^2	
number of turns	N	274	
resistance of the wire	R	0.8 Ω	0.32 Ω
inductance	L_0	4.769×10^{-3} H	1.764×10^{-3}H

Table 8.1: Parameters of the Maglev vehicle.

8.2 Multivariable model of the vehicle

8.2.1 Modelling the motion of the vehicle

Using the vehicle's configuration in Fig. 8.1, for small perturbation about the x and y axes, the heave z, pitch θ and roll ϕ movements can be derived from the four airgaps [1]

$$\begin{aligned} z &= \tfrac{1}{4}(z_1 + z_2 + z_3 + z_4) \\ \phi &= \tfrac{1}{2b}(-z_1 + z_2 - z_3 + z_4) \\ \theta &= \tfrac{1}{2l}(z_1 + z_2 - z_3 - z_4) \end{aligned} \tag{8.1}$$

b and l are the width and the length of the vehicle's chassis between the centres of the sensors and z_1 to z_4 correspond to the four airgaps produced by the sensors in Fig. 8.1.

For the free body in space, the force about the z axis F_z and the torque components: T_x about x and T_y about y, can be described using the following equations about the centre of the mass O [96, 1]

$$\begin{aligned} F_z &= M\ddot{z} \\ T_x &= I_{xx}\dot{\omega}_x + (I_{zz} - I_{yy})\omega_y\omega_x \\ T_y &= I_{yy}\dot{\omega}_y + (I_{xx} - I_{zz})\omega_z\omega_x \end{aligned} \tag{8.2}$$

In this equation:

1. M represents the total mass of the vehicle

2. I_{xx}, I_{yy} and I_{zz} are the moment of inertia tensor about x, y and z axes. Making the assumption that the vehicle's body is a solid rectangular parallelepiped, these moments of inertia can be calculated using the mass M and the dimensions of the vehicle [96] (t is the height of the vehicle)

$$\begin{array}{rcl} I_{xx} & = & \frac{M}{3}(b^2+t^2) \\ I_{yy} & = & \frac{M}{3}(l^2+t^2) \\ I_{zz} & = & \frac{M}{3}(b^2+l^2) \end{array} \tag{8.3}$$

3. ω_x, ω_y and ω_z are the angular velocities about the three axes associated with the Euler angles [96]

$$\begin{array}{rcl} \omega_x & = & \dot{\phi}+\dot{\psi}\sin(\theta) \\ \omega_y & = & \dot{\theta}\cos(\phi)-\dot{\psi}\sin(\phi)\cos(\theta) \\ \omega_z & = & \dot{\theta}\sin(\phi)+\dot{\psi}\cos(\phi)\cos(\theta) \end{array} \tag{8.4}$$

Using the fact that the vehicle does not have a provision for a controlled lateral force and hence $\psi = 0$, differentiating Eqn. 8.4 gives the following acceleration components about x and y axes [1, 21]

$$\begin{array}{rcl} \dot{\omega}_x & = & \ddot{\phi} \\ \dot{\omega}_y & = & \ddot{\theta}\cos(\phi)-\dot{\theta}\dot{\phi}\sin(\phi) \end{array} \tag{8.5}$$

Substituting this equation back in Eqn. 8.2 gives the following equation describing the 3DOF free body motion of the vehicle configuration in Fig. 8.1

$$\begin{array}{rcl} F_z & = & M\ddot{z} \\ T_x & = & I_{xx}\ddot{\phi}+(I_{zz}-I_{yy})\dot{\theta}\dot{\phi}\sin(\phi) \\ T_y & = & I_{yy}(\ddot{\theta}\cos(\phi)-\dot{\theta}\dot{\phi}\sin(\phi)) \end{array} \tag{8.6}$$

Furthermore, the total force of attraction about the x axis, F_z, and the torque components T_x and T_y can be derived from the four independent force of attractions f_1 to f_4

$$\begin{array}{rcl} F_z & = & (f_1+f_2+f_3+f_4) \\ T_x & = & B(-f_1+f_2-f_3+f_4) \\ T_y & = & L(f_1+f_2-f_3-f_4) \end{array} \tag{8.7}$$

where B and L are the distances between the centres of the magnets. Since the distance between the magnets and the airgap sensors are equivalent ($B = b$ and $L = l$), in the following derivations only b and l are used for both. To complete the model, the developments in Eqn. 2.2, page 17 are used to describe the relationship between the attraction force f_j, $j = 1..4$ of any jth electromagnet and the control current

$$f_j = k_z z_j(t) - k_i i_j(t) + f_{d_j}(t), \quad j = 1..4 \tag{8.8}$$

$$\frac{di_j(t)}{dt} = \frac{k_z}{k_i}\frac{dz_j(t)}{dt} - \frac{R}{L_0}i_j(t) + \frac{1}{L_0}u_j(t), \quad j = 1..4 \tag{8.9}$$

where: k_z and k_i are the operating-point dependant coefficients as given in Eqn. 2.2, $i_j(t)$ is the jth operating current; $f_{d_j}(t)$ is the disturbance force on the jth electromagnet; R and L are the resistance and the inductance of the magnets' wire; and $u_j(t)$ is the jth control signal. These equation assume that all magnets (M_1 to M_4) have identical electrodynamical characteristics.

Nonlinear model using differential equations: Model A

Combination of Eqns. 8.6 to 8.9 gives a full description of the motion of the vehicle's free-body at any moment of time. A conceptional block diagram of this multivariable 3DOF motion model based on differential equations is shown in Fig. 8.4. This model is built in Simulink and used for the analytical studies later in this chapter. The inputs to the model are four control signals, namely u_1 to u_4. These are transformed to excitation currents in the four magnets i_1 to i_4 via Eqn. 8.9. Furthermore, Eqn. 8.8 transforms these currents to four force of attractions f_1 to f_4 for each magnet. The independent forces of attraction produced by each magnet are transformed via Eqn. 8.7 to give the heave force F_z, the roll torque T_x and the pitch torque T_y. Applying these force and torque components to Eqn. 8.6 gives the three dynamic components of: (a) the heave acceleration $\ddot{z}$, (b) the roll acceleration $\ddot{\phi}$, and (c) the pitch acceleration $\ddot{\theta}$. Double integration of these three signals gives the heave, the pitch and the roll (z, θ, ϕ) in the chassis. Since the measurable outputs of the Maglev system are four airgap clearances, Eqn. 8.1 is used to transform these components to four airgaps z_1 to z_4. In a matrix form, Eqn. 8.1 is given below [1]

$$\begin{bmatrix} z \\ \phi \\ \theta \end{bmatrix} = \underbrace{\begin{bmatrix} \frac{1}{4} & 0 & 0 \\ 0 & \frac{1}{2b} & 0 \\ 0 & 0 & \frac{1}{2l} \end{bmatrix} \begin{bmatrix} 1 & 1 & 1 & 1 \\ -1 & 1 & -1 & 1 \\ 1 & 1 & -1 & -1 \end{bmatrix}}_{H} \begin{bmatrix} z_1 \\ z_2 \\ z_3 \\ z_4 \end{bmatrix} \tag{8.10}$$

This matrix is inverted using the transformation $H^+ = H^T(HH^T)^{-1}$ to get

$$\begin{bmatrix} z_1 \\ z_2 \\ z_3 \\ z_4 \end{bmatrix} = \underbrace{\begin{bmatrix} 1 & -\frac{b}{2} & \frac{l}{2} \\ 1 & \frac{b}{2} & \frac{l}{2} \\ 1 & -\frac{b}{2} & -\frac{l}{2} \\ 1 & \frac{b}{2} & -\frac{l}{2} \end{bmatrix}}_{H^+} \begin{bmatrix} z \\ \phi \\ \theta \end{bmatrix} \tag{8.11}$$

Linear model using differential equations: Model B

The vehicle's model of motion in Fig. 8.4 described with the Euler angles, is a nonlinear model due to the terms in Eqn. 8.6. For small perturbation angles around $(\theta, \phi) = (0, 0)$,

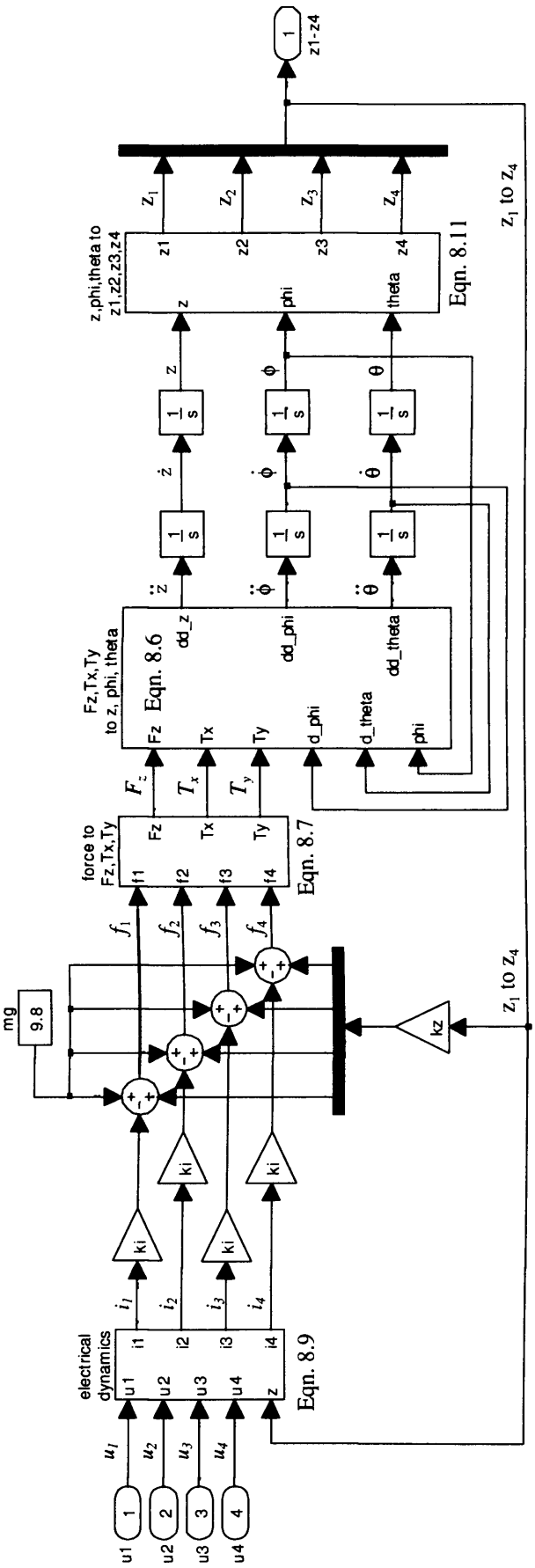

Figure 8.4: Simulation block diagram of the nonlinear model using Eqns. 8.6 to 8.9.

however, the Euler velocities about the x and y axes reduce to

$$\begin{aligned} \dot{\omega}_x &= \ddot{\phi} \\ \dot{\omega}_y &= \ddot{\theta} \end{aligned} \tag{8.12}$$

and consequently Eqn. 8.6 transforms to [1]

$$\begin{aligned} F_z &= M\ddot{z} \\ T_x &= I_{xx}\ddot{\phi} \\ T_y &= I_{yy}\ddot{\theta} \end{aligned} \tag{8.13}$$

These equations are used to develop the linear model of the vehicle's motion. A Simulink block diagram of this linear model is shown in Fig. 8.5. The interconnection block diagram in Fig. 8.5 has been constructed such that the three acceleration components $(\ddot{z}, \ddot{\theta}, \ddot{\phi})$ are converted to accelerations in the airgap clearances ($\ddot{z}_1$ to $\ddot{z}_4$) with the aim of Eqn. 8.11 before the integration. Although this model is overdetermined (it has two additional state variables), this representation is suitable for implementing classical state-feedback controllers that use position z_j, velocity $\dot{z}_j$ and acceleration $\ddot{z}_j$, $j = 1..4$ outputs to derive the feedback control law.

8.2.2 State-space model of the 3DOF Maglev: Model C

The mathematical models derived in Figs. 8.4 and 8.5 are in the form of second-order differential equations. The controller design proposed in this chapter requires a state-space model of the 3DOF equations of suspension motion. To describe the vehicle's motion, the following state-space representation is used

$$\begin{aligned} \dot{x} &= Ax + Bu \\ y &= Cx \end{aligned} \tag{8.14}$$

where: $u = [u_1,\ u_2,\ u_3,\ u_4]^T$ is a vector of four control inputs and $y = [z_1,\ z_2,\ z_3,\ z_4]^T$ is a vector of four airgap clearances. To construct the minimal realisation of the model, the equation of motion is described using (z, θ, ϕ) (Fig. 8.4). This leads to the selection of the following state variables

$$x = \left[z,\ \dot{z},\ \phi,\ \dot{\phi},\ \theta,\ \dot{\theta},\ i_1,\ i_2,\ i_3,\ i_4\right]^T \tag{8.15}$$

The relationship between the state-variables and the independent airgaps z_i, $i = 1..4$ are constructed below

$$\begin{bmatrix} \ddot{z} \\ \ddot{\phi} \\ \ddot{\theta} \end{bmatrix} = \begin{bmatrix} \frac{1}{M} & 0 & 0 \\ 0 & \frac{1}{Ixx} & 0 \\ 0 & 0 & \frac{1}{Iyy} \end{bmatrix} \begin{bmatrix} 1 & 1 & 1 & 1 \\ -b & b & -b & b \\ l & l & -l & -l \end{bmatrix} \begin{bmatrix} f_1 \\ f_2 \\ f_3 \\ f_4 \end{bmatrix}$$

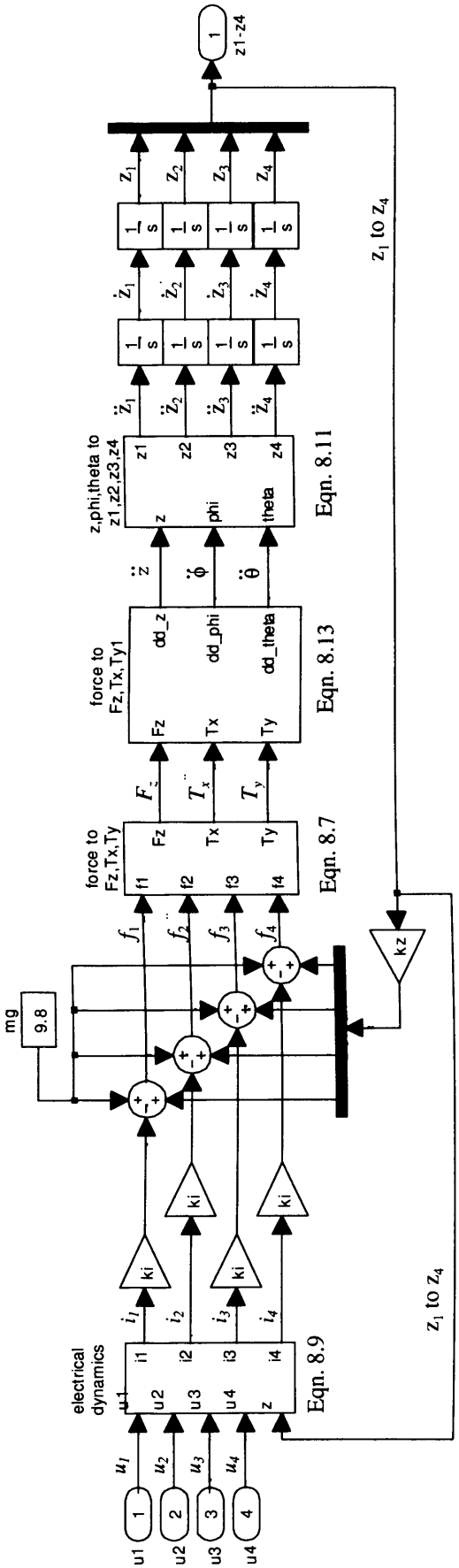

Figure 8.5: Simulation block diagram of the nonlinear model using Eqns. 8.6 to 8.9 with the assumption made in Eqns. 8.11 and 8.13.

with

$$\begin{bmatrix} f_1 \\ f_2 \\ f_3 \\ f_4 \end{bmatrix} = \begin{bmatrix} -k_i & 0 & 0 & 0 \\ 0 & -k_i & 0 & 0 \\ 0 & 0 & -k_i & 0 \\ 0 & 0 & 0 & -k_i \end{bmatrix} \begin{bmatrix} i_1 \\ i_2 \\ i_3 \\ i_4 \end{bmatrix} + \begin{bmatrix} k_z & 0 & 0 & 0 \\ 0 & k_z & 0 & 0 \\ 0 & 0 & k_z & 0 \\ 0 & 0 & 0 & k_z \end{bmatrix} \begin{bmatrix} 1 & -b/2 & l/2 \\ 1 & -b/2 & l/2 \\ 1 & b/2 & l/2 \\ 1 & b/2 & l/2 \end{bmatrix} \begin{bmatrix} z \\ \phi \\ \theta \end{bmatrix}$$

Combining these two equations and Eqn. 8.9 and after some transformations give the state-space matrix A as derived below

$$A = \begin{bmatrix} 0 & 1 & 0 & 0 & 0 & 0 & 0 & 0 & 0 & 0 \\ 4\frac{k_z}{M} & 0 & 0 & 0 & 0 & 0 & -\frac{k_i}{M} & -\frac{k_i}{M} & -\frac{k_i}{M} & -\frac{k_i}{M} \\ 0 & 0 & 0 & 1 & 0 & 0 & 0 & 0 & 0 & 0 \\ 0 & 0 & 2b^2\frac{k_z}{I_{xx}} & 0 & 0 & 0 & \frac{k_i b}{I_{xx}} & -\frac{k_i b}{I_{xx}} & \frac{k_i b}{I_{xx}} & -\frac{k_i b}{I_{xx}} \\ 0 & 0 & 0 & 0 & 0 & 1 & 0 & 0 & 0 & 0 \\ 0 & 0 & 0 & 0 & 2l^2\frac{k_z}{I_{yy}} & 0 & -\frac{k_i l}{I_{yy}} & -\frac{k_i l}{I_{yy}} & \frac{k_i l}{I_{yy}} & \frac{k_i l}{I_{yy}} \\ \frac{kz}{ki} & 0 & -\frac{b}{2}\frac{kz}{ki} & 0 & \frac{l}{2}\frac{kz}{ki} & 0 & -\frac{R}{L_0} & 0 & 0 & 0 \\ \frac{kz}{ki} & 0 & \frac{l}{2}\frac{kz}{ki} & 0 & \frac{l}{2}\frac{kz}{ki} & 0 & 0 & -\frac{R}{L_0} & 0 & 0 \\ \frac{kz}{ki} & 0 & -\frac{b}{2}\frac{kz}{ki} & 0 & -\frac{l}{2}\frac{kz}{ki} & 0 & 0 & 0 & -\frac{R}{L_0} & 0 \\ \frac{kz}{ki} & 0 & \frac{b}{2}\frac{kz}{ki} & 0 & -\frac{l}{2}\frac{kz}{ki} & 0 & 0 & 0 & 0 & -\frac{R}{L_0} \end{bmatrix} \tag{8.16}$$

Inputs to the model u_i, $i = 1..4$ are four control voltages; the B state matrix in Eqn. 8.14 is derived below

$$B = \begin{bmatrix} 0 & 0 & 0 & 0 \\ 0 & 0 & 0 & 0 \\ 0 & 0 & 0 & 0 \\ 0 & 0 & 0 & 0 \\ 0 & 0 & 0 & 0 \\ 0 & 0 & 0 & 0 \\ \frac{1}{L_0} & 0 & 0 & 0 \\ 0 & \frac{1}{L_0} & 0 & 0 \\ 0 & 0 & \frac{1}{L_0} & 0 \\ 0 & 0 & 0 & \frac{1}{L_0} \end{bmatrix} \tag{8.17}$$

The outputs from the state-space model are four airgap clearances. These are generated from the state variables using the following C matrix

$$C = \begin{bmatrix} 1 & 0 & -\frac{b}{2} & 0 & \frac{l}{2} & 0 & 0 & 0 & 0 & 0 \\ 1 & 0 & \frac{b}{2} & 0 & \frac{l}{2} & 0 & 0 & 0 & 0 & 0 \\ 1 & 0 & -\frac{b}{2} & 0 & -\frac{l}{2} & 0 & 0 & 0 & 0 & 0 \\ 1 & 0 & \frac{b}{2} & 0 & -\frac{l}{2} & 0 & 0 & 0 & 0 & 0 \end{bmatrix} \tag{8.18}$$

8.3 Validation of the electro-mechanical parameters in Table 8.1

The electro-mechanical parameters of the magnets in Table 8.1 are taken from [21]. Before the experimental work, these need to be validated. This is done by comparing experimental and simulation results. Closed-loop identification is chosen due to the unstable nature of the Maglev system in open-loop mode (similar work has been done in Section 3.1). Four independent feedback compensators are used to stabilise the vehicle; one magnet is then analysed independently. The stabilisation is done with a simple lead compensator with one pole and one zero. This simple structure has some advantages for the identification procedure because: (1) it uses only the position output from the system; (2) it has a simple structure and hence minimum poles and zeros are added to the closed-loop system; (3) a mathematical closed-loop model can be easily derived and compared with the experimental results. The identification process is described below.

1. Using the open-loop parameters in Table 8.1 and the open-loop model in Eqn. 2.12, page 18, a lead compensator is designed to provide $\approx 25^0$ phase margin at 13.241 Hz cross-over frequency. The design is performed in the frequency domain by iterating between the location of the pole and the zero of the compensator and the gain, until the requirements for the phase margin and bandwidth are met. The final structure and coefficients of the compensator are given below

$$K(s) = -8448\frac{3.2(s + 158.7)}{(s + 1752)} \tag{8.19}$$

2. For the identification purposes, the lead-lag compensator (Eqn. 8.19) was converted to its digital form using the Tustin transformation and 1 ms sampling time. The new digital structure was then implemented on the DSP control hardware (Chapter 5).

Initial test runs with this compensator, however, showed that the experimental system is unstable.

3. To make the system stable, the loop gain of the compensator was reduced from -2448.76 V/m to -1453.9 V/m. With the new gain, a marginally stable closed-loop system was obtained and the vehicle was suspended. The closed-loop transfer functions were then identified in the frequency domain with the dynamic signal analysis technique described in Chapter 6, page 127. An additional sine-wave identification signal with 0.5 V amplitude and frequency varied from 2Hz to 600Hz was injected in the control loop. Fourier analysis was performed over the input and the output to generate the experimental sensitivity and complimentary transfer functions (Fig. 8.6).

4. The comparison between the experimentally derived complimentary function and the simulated complimentary function is shown in Fig. 8.6. The identified and the

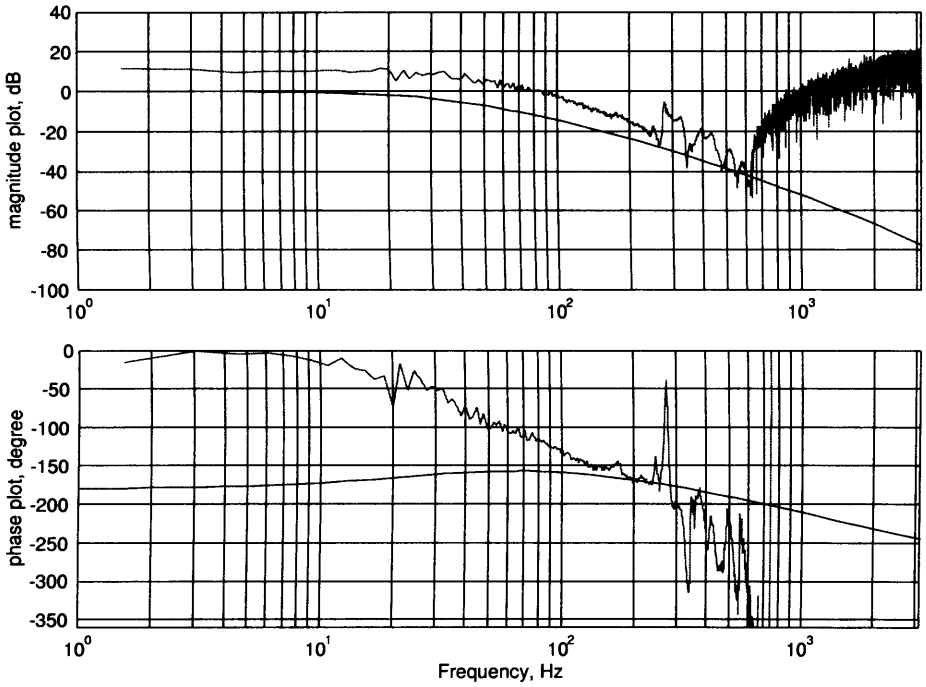

Figure 8.6: Comparison between the simulated complimentary function of the system with the lead compensator and with the experimentally derived complimentary function.

simulated models differ in both magnitude and phase responses. To compensate for the DC-gain, the resistance of the magnetic winding was reduced from 0.8 Ω to 0.32 Ω to match with the value measured with a digital multimeter. Furthermore, the phase response in Fig. 8.6 suggests that the inductance of the winding is rather low and this contributes to the lag in phase in the low frequency range. To compensate for this,

the value for the inductance is adjusted by 63% from the original value to get 1.764 mH and to shift the electrical dynamics of the magnet to higher frequencies. With the above modifications to the model, the simulated frequency-domain response was recalculated and the comparison between the experimentally derived complimentary function and the simulated complimentary function is shown in Fig. 8.7. Both the

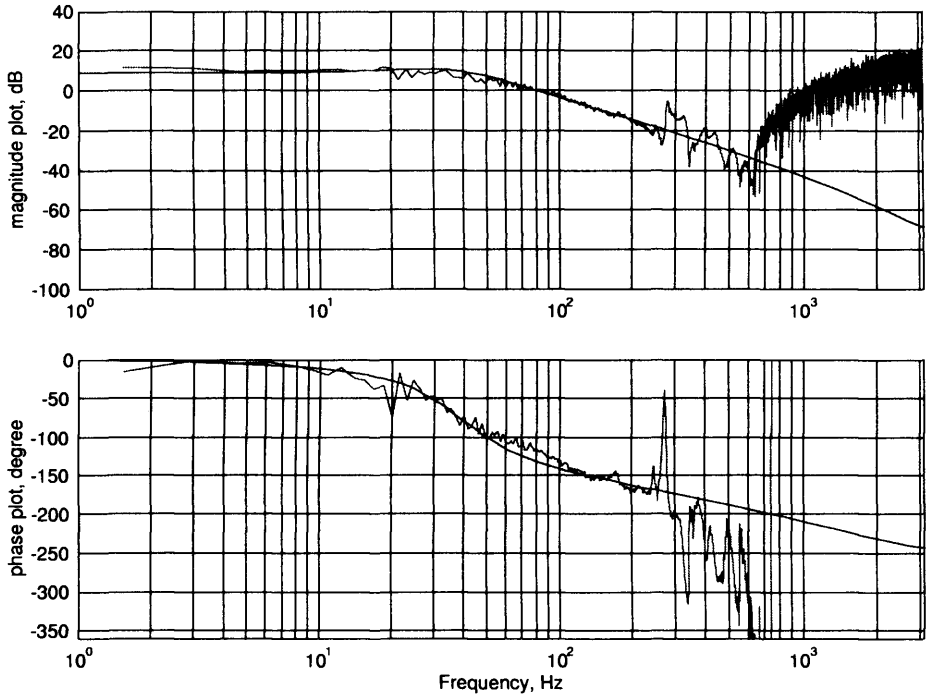

Figure 8.7: Comparison between the simulated complimentary function of the system with the lead compensator and with the experimentally derived complimentary function after some updates in the parameters of the model.

mathematical and the experimental responses match very well in both phase and amplitude within the operating frequency range and hence the new values for R and L_0 can be used for the controller synthesis work below. This completes the identification work.

8.4 Robust multivariable control for Maglev vehicles

For operational stability of Maglev vehicles, four magnets are controlled simultaneously to provide suspension forces. There are two possible approaches: (1) to neglect the cross-coupling in the rigid body and design independent controllers for each magnet (*integral* and *local control* in [1, 13, 21]), or (2) to design a multivariable controller with multiple inputs and outputs and internal cross-compensation structure. Approach-1 is popular since it reduces the complexity of the controller design to a single loop design (one cor-

ner at a time) [31]. For the Maglev vehicle, design of local control using state-feedback compensators (using design stages from Chapter 2) is shown in Appendix F.1. Although the suspension responses is stable, this controller has limitations in attenuating guidance induced disturbances. This is shown graphically in Fig. 8.8. At the moment marked in the figure a shock disturbance of 110 Newtons is applied in the lateral position of the vehicle. The phase delays in the control loops and the absence of decoupling in the state-feedback approach leads to critically damp oscillatory response in the vehicle. Furthermore, after 15 seconds this disturbance leads to instability in the vehicle due to oscillations which are outside the working range of the sensors. In comparison, the response of the multi-variable controller designed in this chapter to the same disturbance is shown in Fig. 8.26 and demonstrates superior abilities in the control characteristics. Although a criteria for assessing stability of multi-magnet systems can be derived analytically, this would require a detailed model of the suspension system including flux leakage which contributes to the lateral stiffness. This research is outside the scope of the work presented here. The design of the multivariable controller is described below.

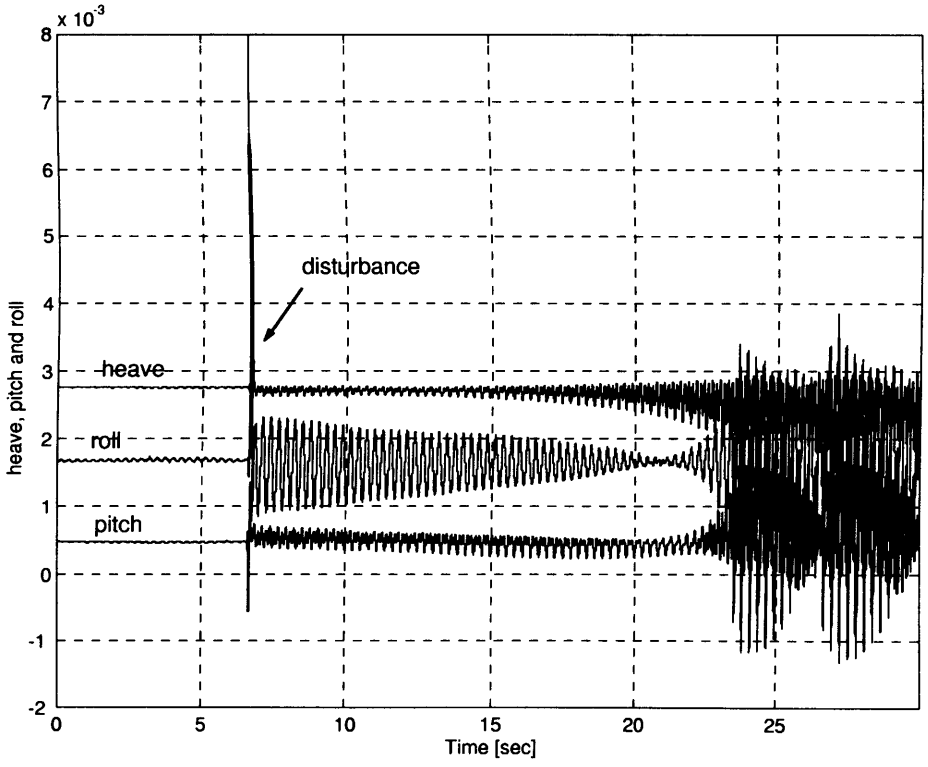

Figure 8.8: Shock disturbance of 110 N in the lateral position and four state-feedback controllers as per Appendix F.1.

8.4.1 Multivariable vehicle controller design using μ-synthesis

Initially, a $\mathcal{H}_\infty$ multivariable controller for the vehicle was designed using the theory from Chapter 6. This work is described in Appendix F.2. Although the suspension response is stable and the design process provides well-defined criteria for specifying desired suspension qualities, $\mu-$optimal design (Chapter 7) has been used for the main research work, because of its abilities to deal with uncertainty and thus to improve the robustness of the system. It is believed that for multi-magnet vehicles this is particularly necessary since the operational conditions (payload and operating airgap) vary, which results in non-fixed model parameters (k_i, k_z and mass M). Previous analysis (Section 7.4, page 145) has shown that the robustness of the system is particularly sensitive to variations in these parameters leading to unstable conditions.

The conceptional block diagram used for the multivariable design is shown in Fig. 8.9. The compensator is a *two-degree-of-freedom controller* with separate inputs for the reference vehicle modes and the suspension airgaps [97]. This controller is partitioned to $\mathbf{K} = [\mathbf{K_r},\ \mathbf{K_y}]$ and consists of $\mathbf{K_y}$ as the feedback part of the compensator and $\mathbf{K_r}$ as the prefilter on the reference input. In overall, $\mathbf{K}$ has seven inputs and four outputs as in Fig. 8.10. With the additional reference input and prefilter $\mathbf{K_r}$, the response of the desired transient response chassis can be specified explicitly using a performance weight. The results presented below will show that this controller, compared to the classical design, gives a well defined and overdamped response with low acceleration levels in the chassis and hence suitability for Maglev vehicle design. The performance requirements of the design are specified by four weighting functions (Fig. 8.9). A detailed account on choosing those is given below. The controller design uses the state-space multivariable model derived in Section 8.2.2.

8.4.2 Selection of performance weights

Four performance functions specify the performance requirements of the suspension vehicle control system in Fig. 8.9: (a) $\mathbf{W_d}$ is a prefilter on the disturbance signal; (b) $\mathbf{W_r}$ specifies the required closed-loop response of the system, $\mathbf{W_c}$ gives stability and robustness margins by limiting the control outputs and $\mathbf{W}$ defines the shape of the sensitivity function and hence the bandwidth of the system. H^+ is the static mapping from modes in the vehicle (heave, pitch and roll) to the corner airgaps (Eqn. 8.11). Although the electromagnetic characteristics of the model are identified with experimental data (Section. 8.3), uncertainty

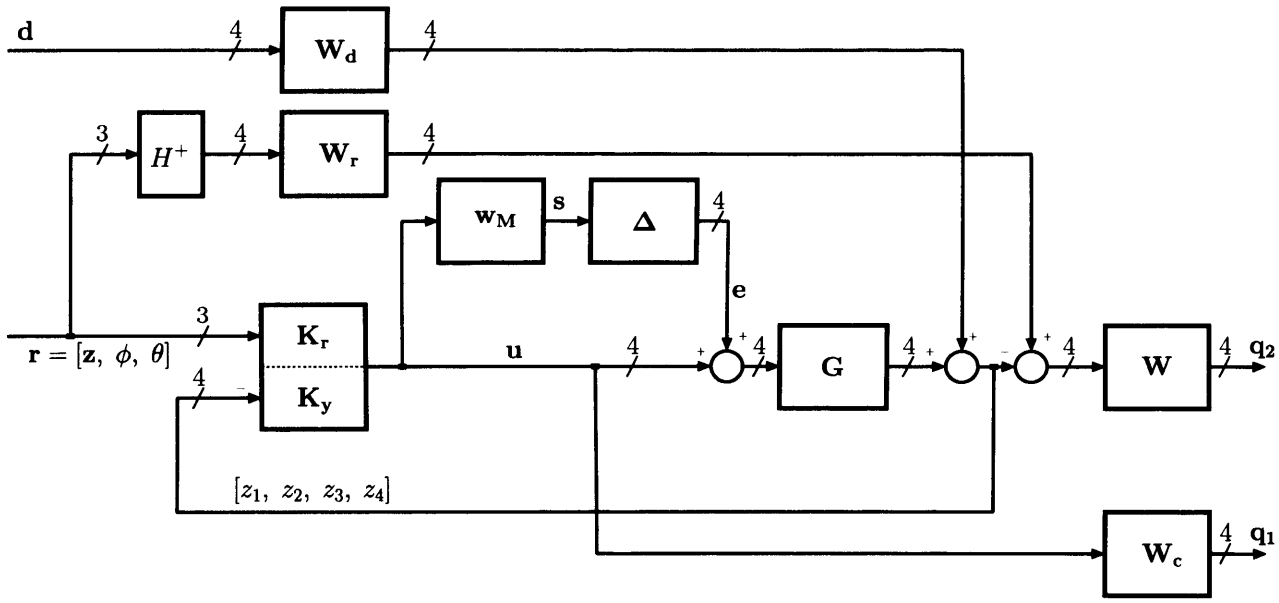

Figure 8.9: System configuration for the multivariable two-degree of freedom controller design.

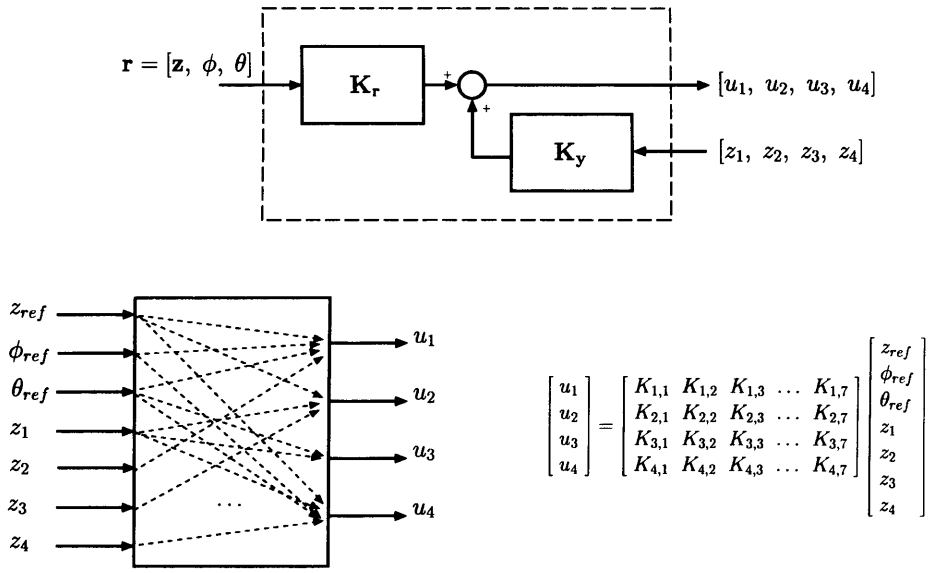

Figure 8.10: Multivariable feedback compensator in matrix form. The numerical form of the compensator is given in Appendix F.3, page 316.

is added to allow for variations in the operating track-magnet clearance and the operating mass. For this, the multiplicative model derived in Section 7.2.3, page 134 is used

$$\tilde{\mathbf{G}}(s) = \mathbf{G}(s)(I + \mathbf{w_M}(s)\boldsymbol{\Delta}), \quad \|\boldsymbol{\Delta}\|_\infty \leq 1$$

For the procedure of the selection of the performance weights, the closed-loop transfer-matrix is first derived with the help of Fig. 8.9. The input vector to the system is

$$[\mathbf{e},\ \mathbf{d},\ \mathbf{r}]^T$$

where $\mathbf{e} = [e_1, e_2, e_3, e_4]^T$ is the output from the perturbation matrix $\boldsymbol{\Delta}$; $\mathbf{d} = [d_1, d_2, d_3, d_4]^T$ is the disturbance vector; and $\mathbf{r} = [z, \phi, \theta]^T$ is the reference input. The output vector from the system is

$$[\mathbf{s},\ \mathbf{q_1},\ \mathbf{q_2}]^T$$

where $\mathbf{q_1} = [q_1, q_2, q_3, q_4]^T$ is the output from $\mathbf{W}$, $\mathbf{q_2} = [q_5, q_6, q_7, q_8]^T$ is the output from $\mathbf{W_c}$ and $\mathbf{s}$ is the output from the uncertainty weight $\mathbf{w_M}$. $\mathbf{q_1}$ and $\mathbf{q_2}$ are the penalty outputs which are to be minimised using the $\mathcal{H}_\infty$ algorithm. From Fig. 8.9 the following relationships are derived

$$\begin{aligned} \mathbf{s} &= \mathbf{w_M u} \\ \mathbf{q_1} &= \mathbf{W_c u} \\ \mathbf{q_2} &= \mathbf{W}\left(\mathbf{W_r r} - \mathbf{G(u+e)}\right) \end{aligned} \tag{8.20}$$

The control signal $\mathbf{u}$ is generated by the controller which is partitioned to

$$\mathbf{u} = [\mathbf{K_r} \quad \mathbf{K_y}] \times [\mathbf{r} \quad -\mathbf{W_d d} - \mathbf{G(u+e)}]^T$$

with $\mathbf{K_r}$ as a prefilter on the reference input $\mathbf{r}$ and $\mathbf{K_y}$ as the feedback part of the controller. Substitution of $\mathbf{u}$ above in Eqn. 8.20, after some transformations and simplifications gives the following closed-loop transfer matrix $\mathbf{N}$

$$\left[\begin{array}{c} \mathbf{s} \\ \hline \mathbf{q_1} \\ \mathbf{q_2} \end{array}\right] = \left[\begin{array}{c|c|c} -\mathbf{w_M K_y G}(I+\mathbf{K_y G})^{-1} & -\mathbf{w_M K_y}(I+\mathbf{K_y G})^{-1}\mathbf{W_d} & \mathbf{w_M K_r}(I+\mathbf{K_y G})^{-1} \\ \hline -\mathbf{W_c K_y G}(I+\mathbf{K_y G})^{-1} & -\mathbf{W_c K_y}(I+\mathbf{K_y G})^{-1}\mathbf{W_d} & \mathbf{W_c K_r}(I+\mathbf{K_y G})^{-1} \\ -\mathbf{WG}(I+\mathbf{K_y G})^{-1} & \mathbf{WK_y G}(I+\mathbf{K_y G})^{-1}\mathbf{W_d} & \mathbf{W}\left(\mathbf{W_r} - \mathbf{GK_r}(I+\mathbf{K_y G})^{-1}\right) \end{array}\right] \left[\begin{array}{c} \mathbf{e} \\ \hline \mathbf{d} \\ \mathbf{r} \end{array}\right] \tag{8.21}$$

Definitions of sensitivity function: $\mathbf{S} = (I + \mathbf{K_y G})^{-1}$ and complimentary function: $\mathbf{T} = \mathbf{K_y G}(I + \mathbf{K_y G})^{-1}$ transforms $\mathbf{N}$ to its more-compact form

$$\mathbf{N} = \left[\begin{array}{c|c} \mathbf{N}_{11} & \mathbf{N}_{12} \\ \hline \mathbf{N}_{21} & \mathbf{N}_{22} \end{array}\right] = \left[\begin{array}{c|c|c} -\mathbf{w_M T} & -\mathbf{w_M K_y S W_d} & \mathbf{w_M K_r S} \\ \hline -\mathbf{W_c T} & -\mathbf{W_c K_y S W_d} & \mathbf{W_c K_r S} \\ -\mathbf{WGS} & \mathbf{WTW_d} & \mathbf{W}\left(\mathbf{W_r} - \mathbf{GK_r S}\right) \end{array}\right] \tag{8.22}$$

$\mathbf{N}$ represents the closed-loop transfer matrix of the multi-magnet system. The equivalent matrix was derived in Chapter 7 for the single-magnet control work (Eqn. 7.15, page 143)

and used for the analysis of the robust properties of the $\mathcal{H}_\infty$ compensator. As described in Chapter 7, $\mathbf{N}_{11}$ is used to study the robust stability of the system with $\mu(\mathbf{N}_{11}(s)) \leq 1$ being the condition for robust stability. The optimal controller design aims to derive $\mathbf{K}$ such that $\|\mathbf{N}_{22}(s)\|_\infty \leq 1$. $\mathbf{N}_{22}(s)$ can be thus used in the specification of the design criteria and hence the performance weights. This is described below.

1. Selection of $\mathbf{W_r}$: The reference input to the system $\mathbf{r}$ is constructed from the reference heave, roll and pitch signals. $\mathbf{W_r}$ specifies the required closed-loop response of the vehicle independently for each of those signals. In this thesis, an assumption is made that the response of the vehicle is required to be same for all modes in the vehicle and thus $\mathbf{W_r}$ reduces to a 3×3 diagonal matrix

$$\mathbf{W_r} = \begin{bmatrix} W_r(s) & 0 & 0 \\ 0 & W_r(s) & 0 \\ 0 & 0 & W_r(s) \end{bmatrix}$$

   To allow some overshoot in the response, a second-order model is chosen for $W_r(i)(s)$, $i = 1..3$

$$W_r(s) = \frac{\omega_r^2}{s^2 + 2\zeta_r\omega_r + \omega_r^2} = \frac{(1/40)^2}{s^2 + 2 \times 0.9 \times (1/40)^2 + (1/40)^2} \tag{8.23}$$

   where ω_r defines the settling time of the closed-loop response and ζ_r determines the overshoot in the response. For operational quality, the ideal response in the pitch and the roll is required to behave as a overdamped second-order system with $\zeta = 0.9$ and $\omega_r = 40$ rad/s.

2. Selection of $\mathbf{W}$: The difference between the ideal response in the vehicle modes specified by $\mathbf{W_r}$ and the actual system response $(\mathbf{W_r} - \mathbf{GK_rS})$ is penalised by $\mathbf{W}$. Since the difference has the characteristics of the sensitivity function of the system, $\mathbf{W}$ is chosen in a similar fashion to W in Section 6.4.2, page 102. Typically for good disturbance attenuation and tracking, at lower frequencies the gain of the error $(\mathbf{W_r} - \mathbf{GK_rS})$ is made small. $\mathbf{W}^{-1}$ is thus selected to have a low gain at lower frequencies and as the frequency increases, the gain of $\mathbf{W}^{-1}$ should increase unit it approaches unity at the bandwidth frequency of the system. Above the bandwidth frequency, the gain of $\mathbf{W}^{-1}$ determines the peak on the sensitivity function. Since $\mathbf{W}$ penalises four outputs (the reference inputs $\mathbf{r}$ are converted to reference airgaps using H^+ in Fig. 8.9) $\mathbf{W}$ consists of four transfer functions $W(i)$, $i = 1..4$ located on

the main diagonal on a 4×4 identity matrix

$$\mathbf{W} = \begin{bmatrix} W(s) & 0 & 0 & 0 \\ 0 & W(s) & 0 & 0 \\ 0 & 0 & W(s) & 0 \\ 0 & 0 & 0 & W(s) \end{bmatrix}$$

Using the developments from Section 6.4.2, page 102, for the vehicle control work W is selected as a first-order filter with the following structure

$$W(s) = \frac{1}{\alpha_W} \frac{\tau s + \alpha_W}{\tau s + \beta_W}, \quad \alpha_W >> \beta_W$$

Based on the design in Chapter 6, the numerical form of this function is selected below

$$W(s) = \frac{1}{10^{(3/20)}} \frac{1/100s + 10^{(3/20)}}{1/100s + 10^{(-100/20)}}$$

such that in the low frequency range, the gain approaches -100 dB for good disturbance attenuation in track-airgap disturbances, and above the cross-over frequency of 100 rad/s, the gain is limited to +3 dB from above to reduce the overshot in the response to disturbances.

3. Selection of $\mathbf{W_c}$ and $\mathbf{W_d}$: $\mathbf{W_c}$ and $\mathbf{W_d}$ together penalise the input sensitivity function $\mathbf{K_yS}$ (Eqn. 8.22) and thus determine the robust properties of the closed-loop system. In practise, the peak of $\mathbf{K_yS}$ is located just above the bandwidth frequency (see the plot for KS in Fig. 7.9, page 142). Similarly to the single-magnet $\mathcal{H}_\infty$ design, $\mathbf{W}_c$ is chosen as a constant which limits the amplitude of the control actions and hence the accelerations in the vehicle. Since the penalty on $\mathbf{K_yS}$ is specified by two functions (Eqn. 8.22), the requirement for $\mathbf{W_d}$ is to provide a gain of unity at high frequencies where the peak of $\mathbf{K_yS}$ is presented. For the multivariable control problem, $\mathbf{W_c}$ and $\mathbf{W_d}$ are four-by-four diagonal matrices

$$\mathbf{W_c} = \begin{bmatrix} W_c & 0 & 0 & 0 \\ 0 & W_c & 0 & 0 \\ 0 & 0 & W_c & 0 \\ 0 & 0 & 0 & W_c \end{bmatrix}$$

$$\mathbf{W_d} = \begin{bmatrix} W_d(s) & 0 & 0 & 0 \\ 0 & W_d(s) & 0 & 0 \\ 0 & 0 & W_d(s) & 0 \\ 0 & 0 & 0 & W_d(s) \end{bmatrix}$$

As discussed in Section 6.4.2, page 102, W_c is selected to be a constant over the whole operating bandwidth for the suspension system

$$W_c = \frac{1}{20}$$

to specify an upper bound of +26 dB on $\mathbf{K_yS}$ to guarantee that the maximum control effort would be at maximum 20 times the closed-loop error.

4. Selection of $\mathbf{W_d}$: W_d has the following structure

$$W_d(s) = \frac{\tau s + \alpha_{Wd}}{\tau s + \beta_{Wd}}, \quad \alpha_{Wd} << \beta_{Wd}$$

$\mathbf{W_d}$ together with $\mathbf{W}$ penalise the response of the complimentary function $\mathbf{T}$. For good responses to tracking, the demand vehicle's modes $\mathbf{T}$ have to be unity at low frequencies up to the bandwidth of the system and steadily decreasing gain above it with an attenuation rate of > -40dB / decade. Since $\mathbf{W}^{-1}$ was previously selected in Step-2 above to have low-gain at low frequencies, to keep $\mathbf{T}$ unity at this range $\mathbf{W_d}^{-1}$ should be selected to have a large gain at low frequencies. It is also required that the order of $\mathbf{W_d}$ is same as the order of $\mathbf{W}$. This results in

$$W_d(s) = \frac{1/100s + 10^{(-100/20)}}{1/100s + 10^{(5/20)}}$$

The Bode plots (magnitude only) of the performance weights are given in Fig. 8.11. The numerical values for the performance weights have been selected after several iterations between the specification of the performance requirements and analysis of closed-loop suspension stability and performance series (as in Chapter 6). This work has been excluded from the presentation here for the sake of space, but important design considerations are given below.

A good starting point for $\mathbf{W}$ and $\mathbf{W_c}$ are the performance weights used for the single-magnet $\mathcal{H}_\infty$ design (Chapter 6, page 102). To avoid saturation effects in the output circuits and amplifiers, $\mathbf{W_c}$ has to be kept small. Small values for $\mathbf{W_c}$, however, limit the control actions and these lead to large γ values for the $\mathcal{H}_\infty$ optimisation results (see results and discussion in Figs. 6.15 and 6.16, page 117). Typically the designer would start with small values for $\mathbf{W_c}$ and then increase them until a good compromise between γ values and control actions for each magnet are achieved in simulation. $\mathbf{W}$ determines the properties of the sensitivity function (see results and discussion in Figs. 6.16, page 117). It also has an effect on the bandwidth of the system. Increasing the closed-loop bandwidth increases the bandwidth of the compensator and care has to be taken to keep it below a half of the Nyquist sampling frequency used for the digital control work ($\frac{1}{2}$ × 1 kHz for the design presented here). $\mathbf{W}$ and $\mathbf{W_d}$ determine the response of the complimentary function $\mathbf{T}$ at low frequencies and hence $\mathbf{W_d} \times \mathbf{W}$ has to be approximately 0dB in this range. $\mathbf{W_d}$ is typically selected to have magnitude response that is close to the inverse of $\mathbf{W}$.

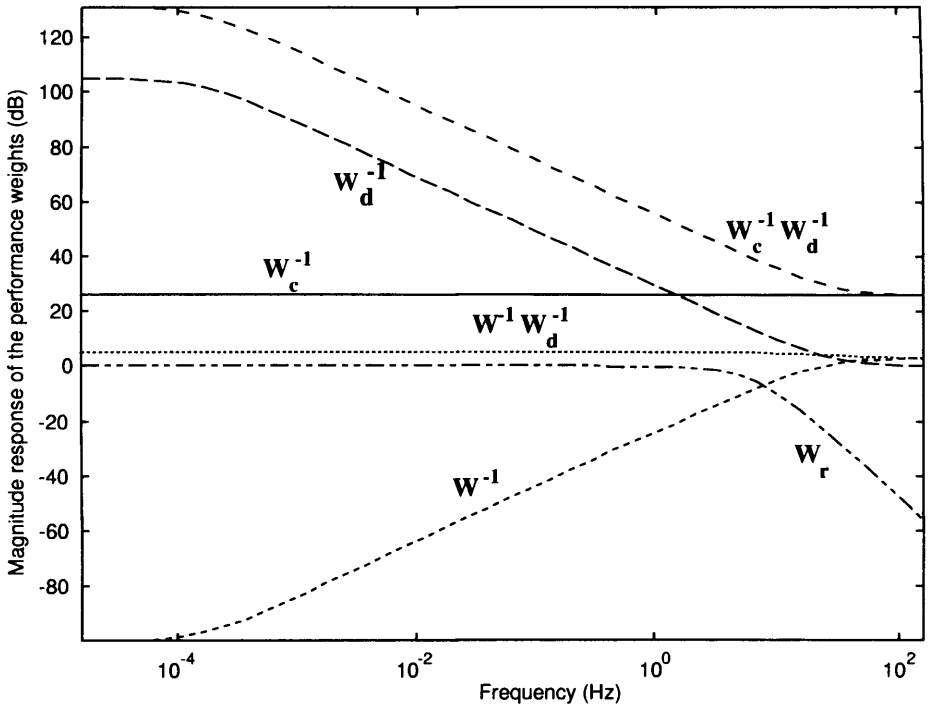

Figure 8.11: Magnitude response of the performance weights

8.4.3 Selection of the uncertainty bound

The procedure used for the selection of the uncertainty bound $\mathbf{w_M}$ uses the design steps developed for the single-magnet system in Section 7.2.3, page 134. With the assumption that the operating conditions are not constant, k_i, k_z are modelled to be uncertain with as much as $\pm 30\%$ from the nominal values and the total vehicle mass M being uncertain by as much as $+200\%$ from the nominal mass. Iterating these parameters provides a basis for modeling the uncertainty using Eqn. 7.5, page 137. These are shown in Fig. 8.12. Following the design steps in Section 7.2.3, page 134, the uncertainty bound w_M is selected as an upper bound to all responses; this function is shown graphically in Fig. 8.12 and numerically below

$$\mathbf{w_M} = 0.85\frac{s+21.08}{s+39.72} \times I_{4\times 4}$$

$\mathbf{w_M}$ is a four by four matrix with elements located along the main diagonal.

The remaining electrical parameters (R and L_0) have been excluded from the uncertainty model since these have been identified and also have least effect on the closed-loop robustness with the $\mathcal{H}_\infty$ compensator (Tables 7.2 and 7.3, pages 147 and 150).

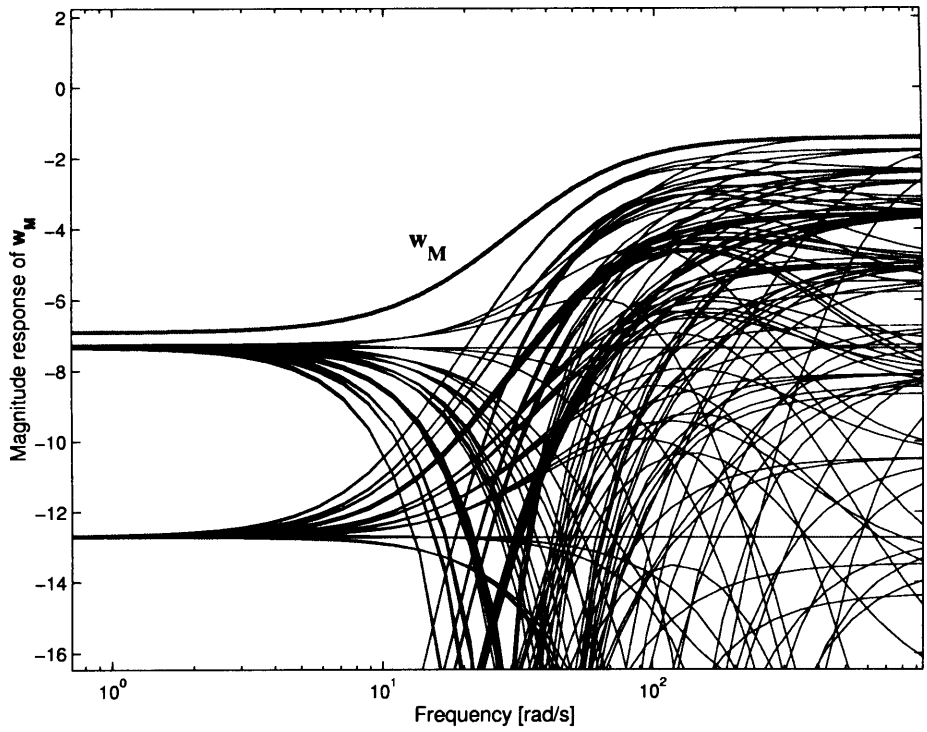

Figure 8.12: Selection of the uncertainty weight $\mathbf{w_M}$

8.4.4 μ−synthesis

The controller is numerically derived in Matlab using the μ−Analysis and Synthesis Toolbox and the design stages described in Chapter 7, page 152. The design aim is to derive $\mathbf{K}$ to give $\mu(\mathbf{N}) \leq 1$ for $\mathbf{N}$ Eqn. 8.22. The derivations steps are executed by a custom-build routines for Matlab. The inputs are: (a) the performance weights to specify desired suspension characteristics $\mathbf{W}$, $\mathbf{W_d}$, $\mathbf{W_c}$ and $\mathbf{W_r}$, (b) the uncertainty in the model to capture variations in operating conditions $\mathbf{w_M}$, and (c) the open-loop state-space model $\mathbf{G}$ of the 3-DOF system in Eqn. 8.16. The multi-magnet compensator $\mathbf{K}$ has seven inputs and four outputs (Fig. 8.10).

Applying the numerical form of $\mathbf{W}$, $\mathbf{W_d}$, $\mathbf{W_c}$ and $\mathbf{W_r}$ as derived in Section 8.4.2, the state-space model of the vehicle constructed in Section 8.2.2 with parameters in Table 8.1 and the uncertainty model $\mathbf{w_M}$, two iterations in the DK procedure were necessary to find $\mathbf{K}$ with 64 state variables, seven inputs and four outputs. The overall robust index with this compensator is $\mu(\mathbf{N}) = 1.1$. For practicality, the order of the controller is reduced to 14 state variables without affecting the robust index μ. This value has been determined by experimental analysis of results and a compromise between sampling frequency and operational bandwidth. For the digital control work, the compensator is conveniently transformed from linear state-space representation to a discrete state-space representation

with 1 ms sampling time. The numerical forms of the continuous and the discrete controllers are given in Appendix F.3, page 316. The total number of the controller's coefficients are 378 and these are stored into a coefficient *include*-file to be used during the DSP compilation stage. The numerical form of the controller is included in the Appendix (Eqn. F.1, page 316). Although a further reduction in the controller's order is possible by appropriate pole-zero cancellation (as shown in Eqn. F.1), for the digital work the state-space form is used and thus the minimal order for this realisation is 14th.

8.5 Simulation and experimental results

To assess the new controller in terms of providing acceptable ride qualities and suspension characteristics, the following four performance assessment stages are considered:
(a) Assessment of the responses of the system to the following changes: the reference heave, the reference roll and the reference pitch positions.
(b) Analysis and comparison of the simulated and experimentally derived frequency response functions.
(c) Assessment of the performance and the robustness properties of the closed-loop system in attenuating force and track disturbances.
(d) Analysis of the robust properties of the closed-loop system in attenuating track disturbance with extra mass added to the system.

A Simulink model has been constructed for the simulation work as in Fig. 8.13. This model retrieves automatically the coefficients for the digitalised controller from the coefficient-file generated during the synthesis procedure. At the end of the simulation cycle, the simulation results are automatically stored into a file for comparison with experimental results. In 8.13, both the linear and the discrete controllers are simulated. The open-loop multi-magnet model is based on the block-diagram in Fig. 8.4.

The experimental work is carried out on the experimental vehicle in Fig. 8.2 with parameters in Table 8.1. The digital control work uses the DSP hardware described in Chapter 5, page 74. $\mathbf{K}(s)$ is digitalised with 1 kHz sampling frequency for compatibility with the bandwidth requirements of the open-loop system and the controller. Analysis has shown that the state-space implementation in the digital domain gives considerably better results than implementation using independent controllers. The state-space controller is more compact and more convenient to code in comparison with implementing the 28 controllers

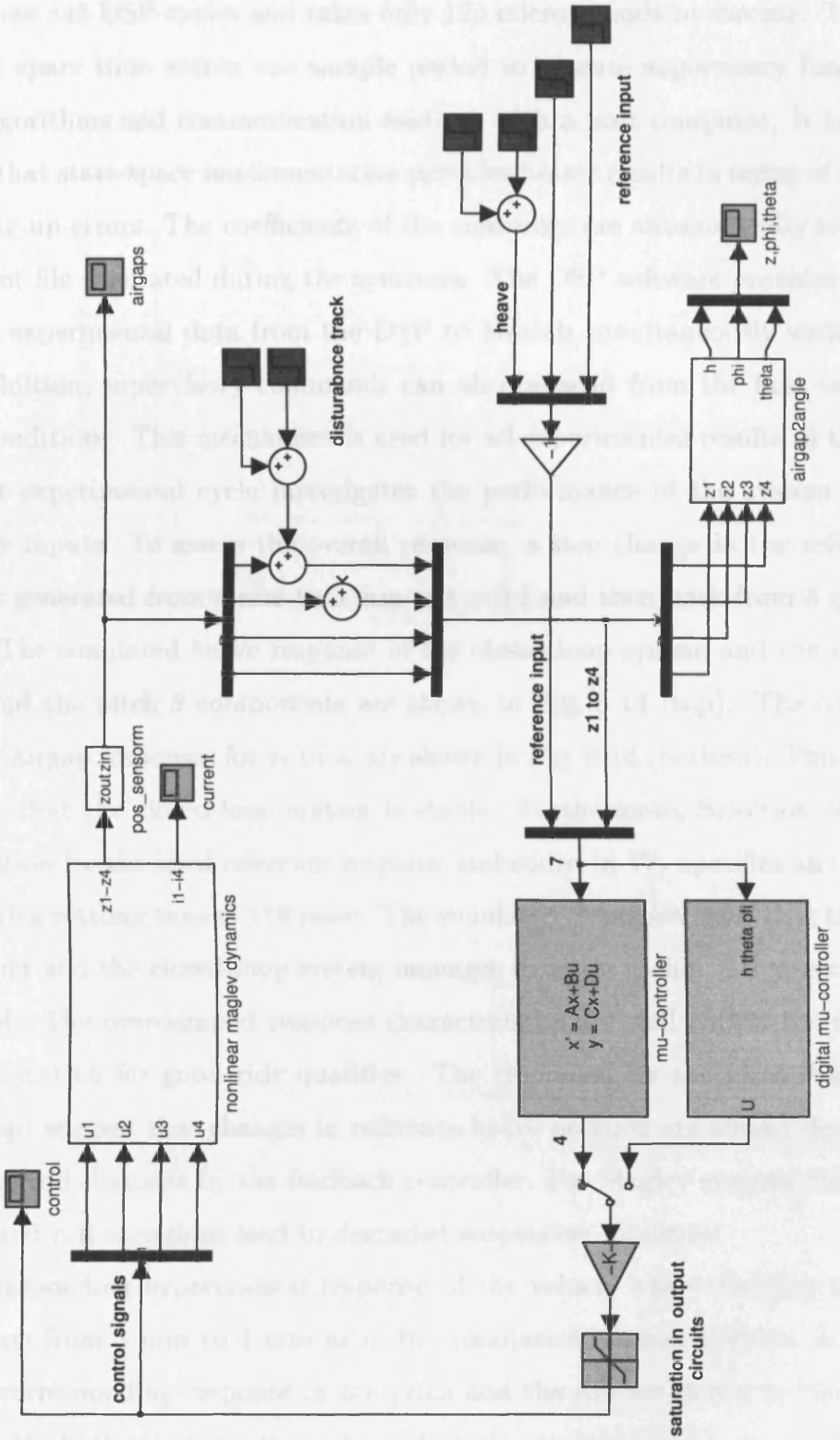

Figure 8.13: Simulation block diagram for the multivariable vehicle controller. Both the continuous and the discrete controllers are used in the comparison (the numerical forms of these controllers are listed in Appendix F.3, page 316). The Maglev dynamics uses the simulation model in Fig. 8.4 with parameters in Table 8.1.

required for the seven inputs and the four outputs. A 14-th order state-feedback controller requires 345 DSP cycles and takes only 125 microseconds to execute. This provides considerable spare time within one sample period to execute supervisory functions, fault detection algorithms and communication routines with a host computer. It has been also established that state-space implementation provides better results in terms of quantisation and rounding-up errors. The coefficients of the controller are automatically retrieved from the coefficient file generated during the synthesis. The DSP software provides facilities for transferring experimental data from the DSP to Matlab simultaneously with the control work. In addition, supervisory commands can also be send from the host to change the operating conditions. This mechanism is used for all experimental results in this section.

The first experimental cycle investigates the performance of the system in changing the reference inputs. To assess the overall response, a step change in the reference heave position z is generated from 4 mm to 3 mm at $t = 0.1$ and then back from 3 mm to 4 mm at $t = 1.6$. The simulated heave response of the closed-loop system and the responses for the roll ϕ and the pitch θ components are shown in Fig. 8.14 (top). The corresponding independent airgap responses for z_1 to z_4 are shown in Fig. 8.14 (bottom). This preliminary result shows that the closed-loop system is stable. Furthermore, Selection of $\zeta = 0.9$ in the specification for the ideal reference response embedded in $\mathbf{W_r}$ specifies an over-damped response with a settling time of 110 msec. The simulated responses show that these requirements are met and the closed-loop system manages to settle within 110 mseconds without an overshoot. The overdamped response characteristics are well within the requirements for Maglev systems for good ride qualities. The responses for the pitch θ and roll ϕ in Fig. 8.14 (top) suggest that changes in reference heave position are almost decoupled from the pitch and roll channels by the feedback controller. For Maglev systems this is required since pitch and roll variations lead to degraded suspension qualities.

The corresponding experimental response of the vehicle when changing the reference heave position from 3 mm to 4 mm as in the simulation studies is shown in Figure 8.15 (top). The corresponding response in the pitch and the roll are shown in the same figure while Fig. 8.15 (bottom) shows the independent air-gap responses z_1 to z_4. These results suggest a very close comparison between the theoretical results and the experimental results. Similarly to the simulated responses, the experimental responses provide a settling time of 110 milliseconds and over-damped response. The responses for the pitch and the roll show the ability of the multivariable controller to decouple these loops from the heave

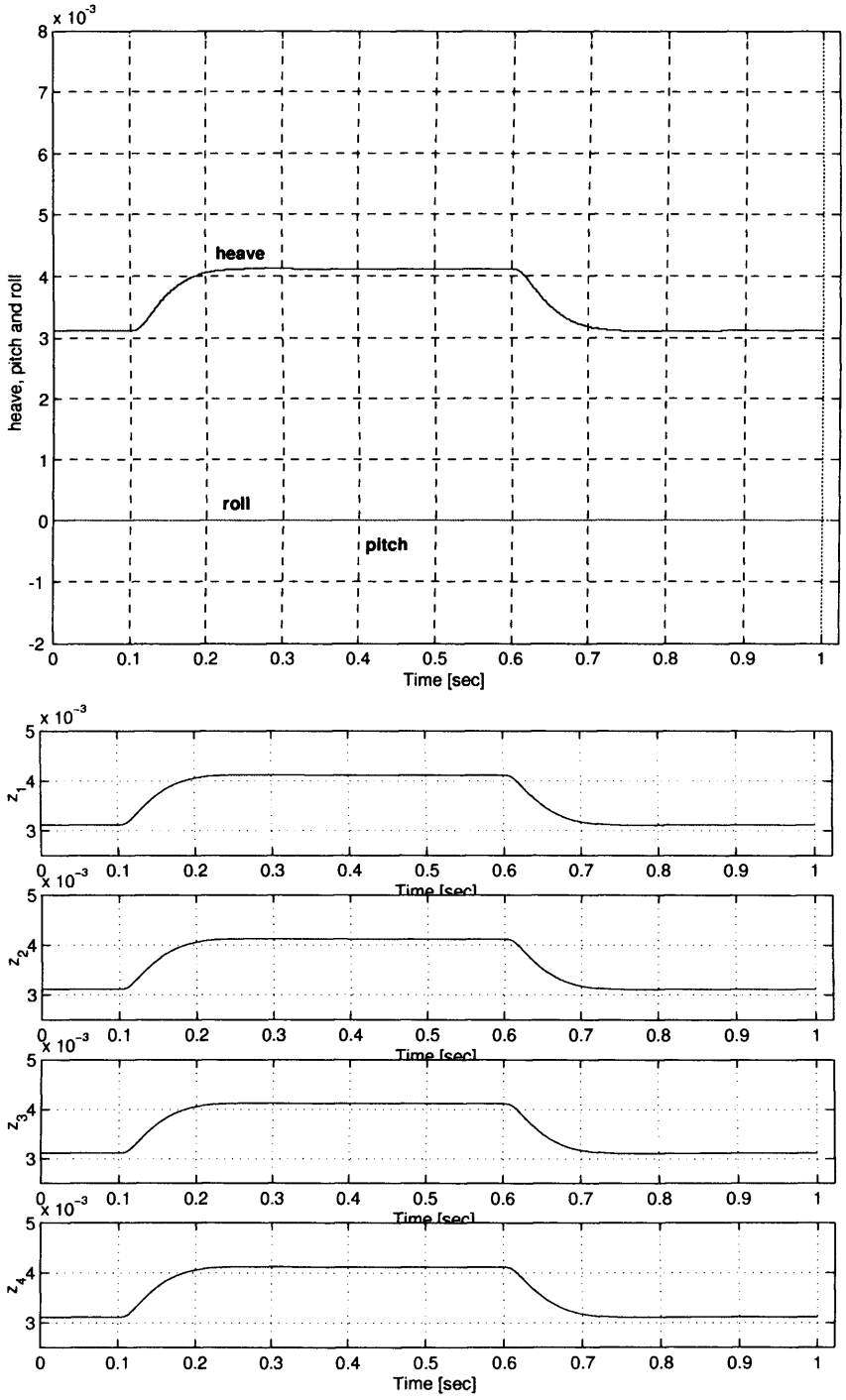

Figure 8.14: Simulated step responses to a 1 mm reference heave change. Top: heave, roll and pitch responses; Bottom: airgap responses.

response. As requested by the design specifications, a step change in heave position has almost no effect on the pitch and the roll components. The experimental acceleration levels in changing the reference heave produced by the vehicle's four accelerometers are given in Fig. F.4 (top), page 315. The steady-state values of $< 2.5m/s^2$ are within the ISO targets [16]. For high-speed application, further reduction in the acceleration in the cabin can be accommodated by using a second suspension to decouple the chassis from the magnet-guidance interaction. The independent response z_1 to z_4 in Fig. 8.15 (bottom) are almost identical and hence the four loops in the system pose similar characteristics.

A simulated step response in changing the roll and the pitch reference positions in the system are shown in Figs. 8.16 and 8.17. The corresponding experimental responses are shown in Figs. 8.18 and 8.19. Although changes in these reference demands are not required in Maglev applications, these experiments have been performed to assess the ability of the multivariable controller to decouple the vehicle modes. As depicted in the figures, changing one of the reference inputs has no effect on the behaviour of the remaining loops. The step response for all three demands: heave, pitch and roll is almost identical and hence, as required by the design, all three loops have identical closed-loop characteristics. The experimentally derived acceleration levels in changing the reference pitch and roll are shown in Fig. F.4 (middle and bottom). Again these changes have almost no effect on the acceleration level in the Maglev cabin and hence offer comfortable ride qualities.

In the second phase of experiments, the frequency characteristics of the closed-loop system is assessed. For this analysis, only one corner is studied independently. For the comparison, three different responses are obtained: (a) simulated frequency response of the closed-loop system using the mathematical model; (b) simulated frequency response of the system using the Simulink model in Fig. 8.13; and (c) experimentally derived frequency response of the system using the experimental vehicle. The last two experiments use the frequency-domain analysis technique developed in Section 6.6, page 121 and involve injecting a sine-wave identification signal into the loop and performing Fourier analysis. The analysis is performed for frequencies between 0 Hz to 100 Hz in 50 seconds. This allows an assessment of the system over a wide frequency range to identify parasitic elements having resonance characteristics. The results from the three experiments are shown in Figs. 8.20 and 8.21. A comparison plot between the analytical Bode plot and the experimentally derived Bode plot of the closed-loop system is shown in Fig. 8.20 (top). A comparison plot between the experimentally derived Bode plot from the Simulink model, the simulated

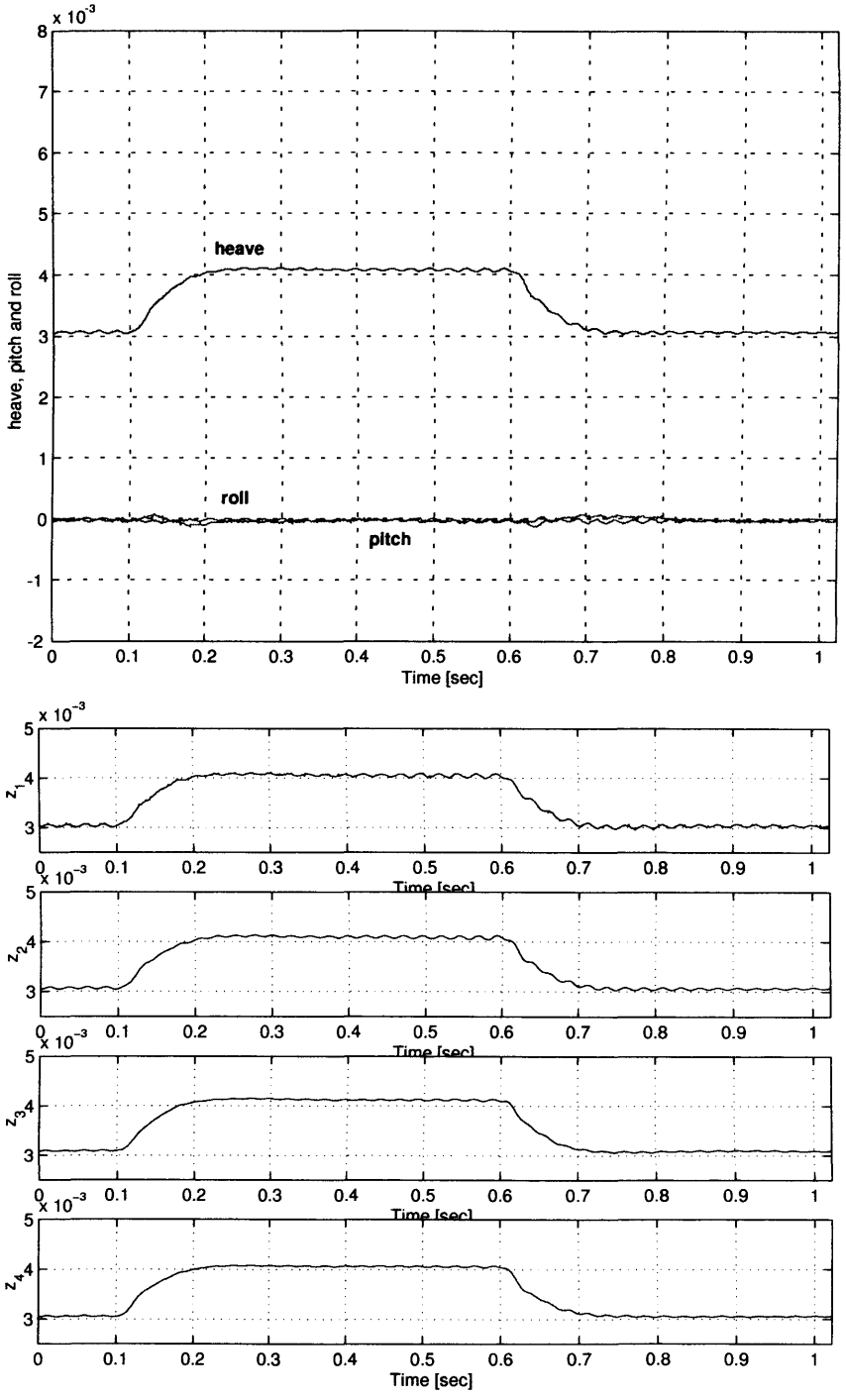

Figure 8.15: Experimentally derived step responses to a 1 mm reference heave change. Top: heave, roll and pitch responses; Bottom: airgap responses.

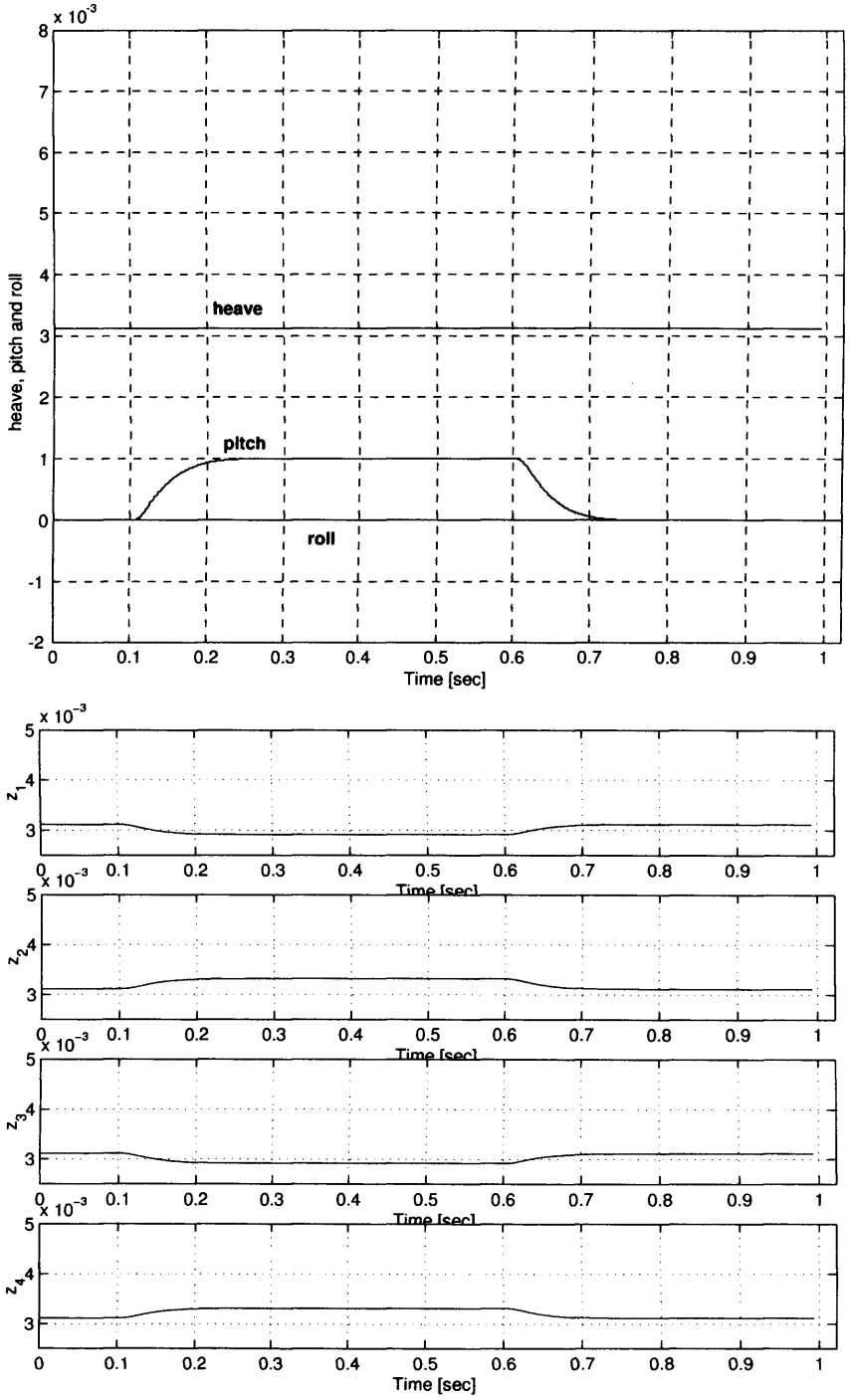

Figure 8.16: Simulated step responses to a 1 mm reference pitch change. Top: heave, roll and pitch responses; Bottom: airgap responses.

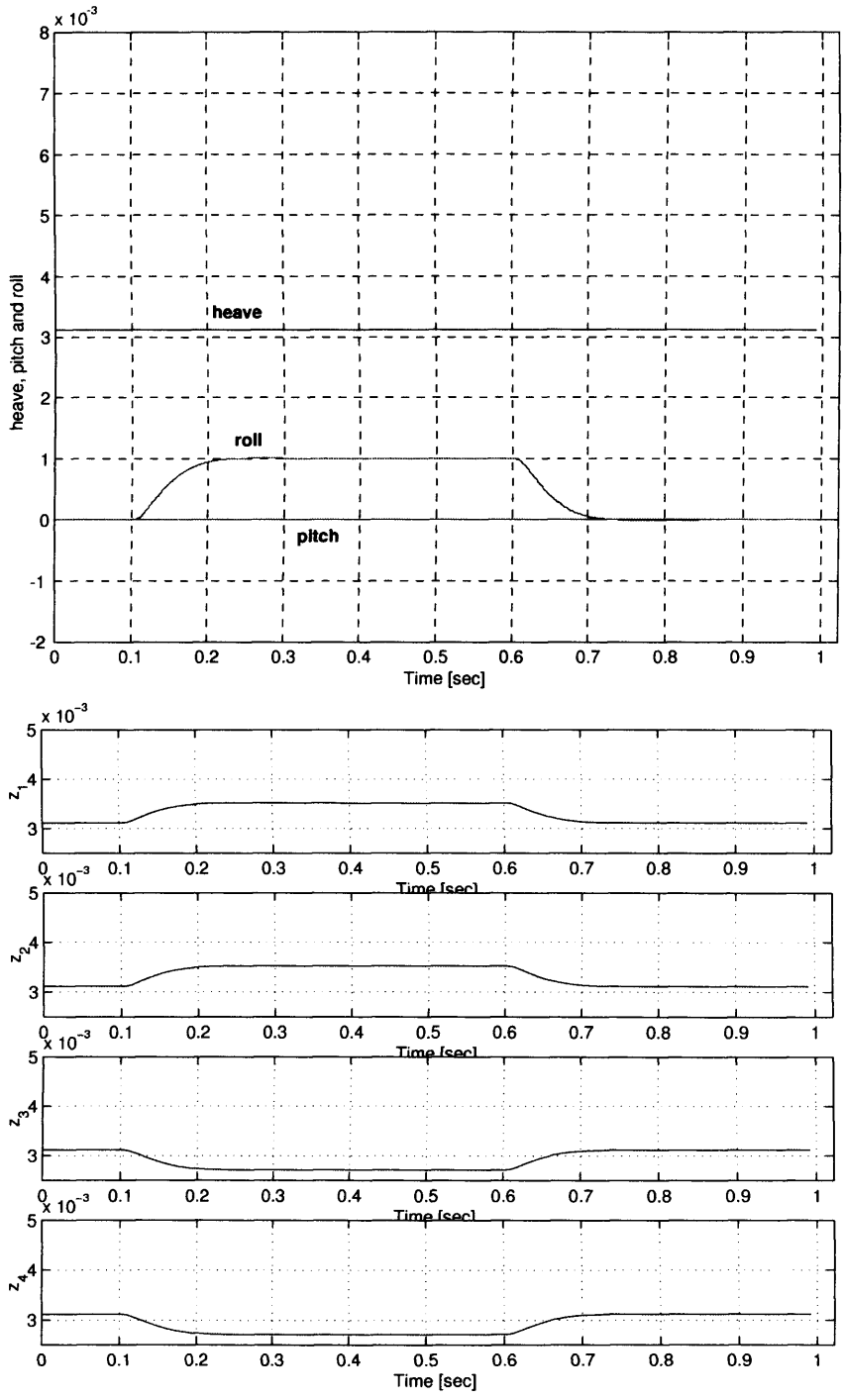

Figure 8.17: Simulated step responses to a 1 mm reference roll change. Top: heave, roll and pitch responses; Bottom: airgap responses.

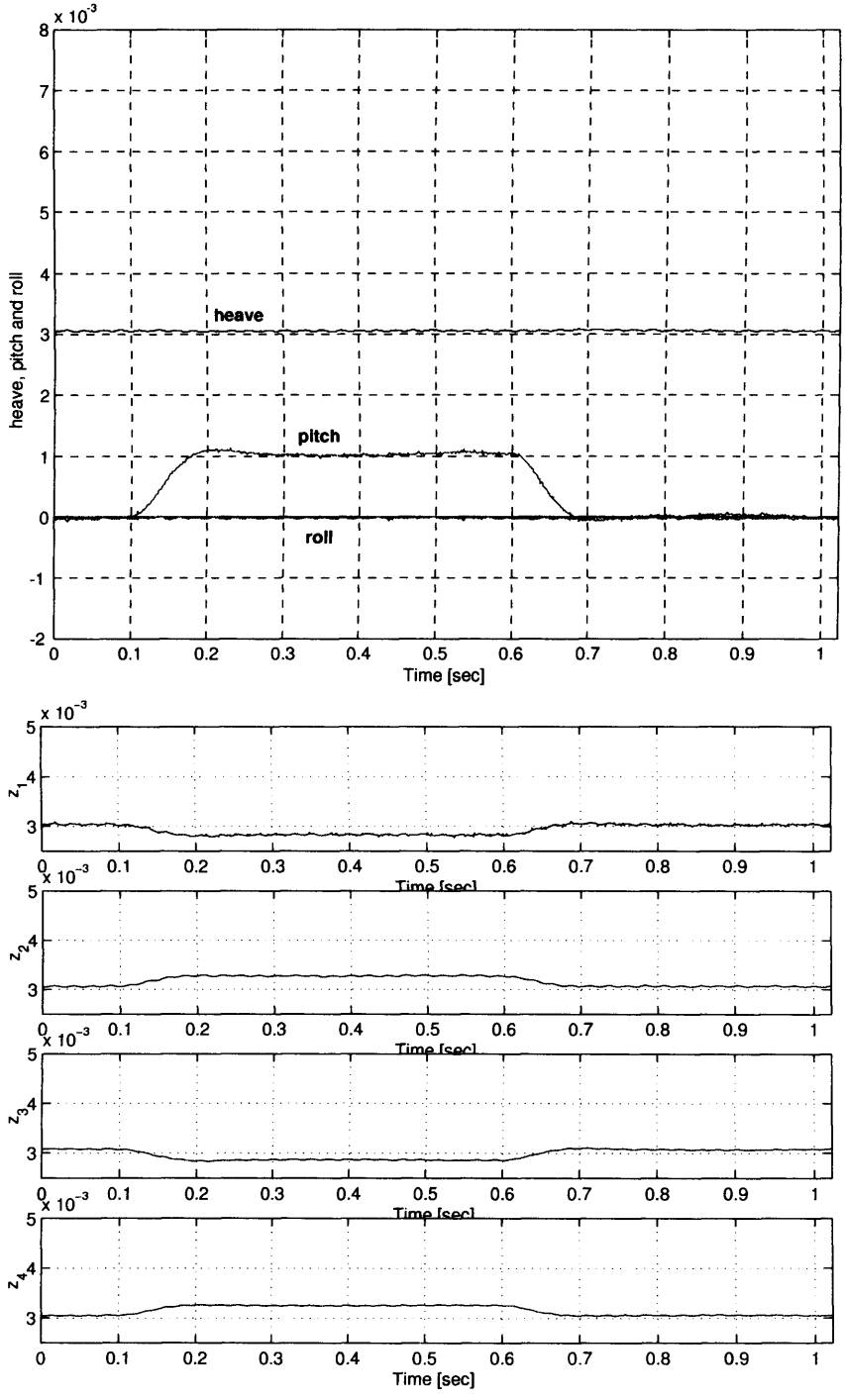

Figure 8.18: Experimentally derived step responses to a 1 mm reference pitch change. Top: heave, roll and pitch responses; Bottom: airgap responses.

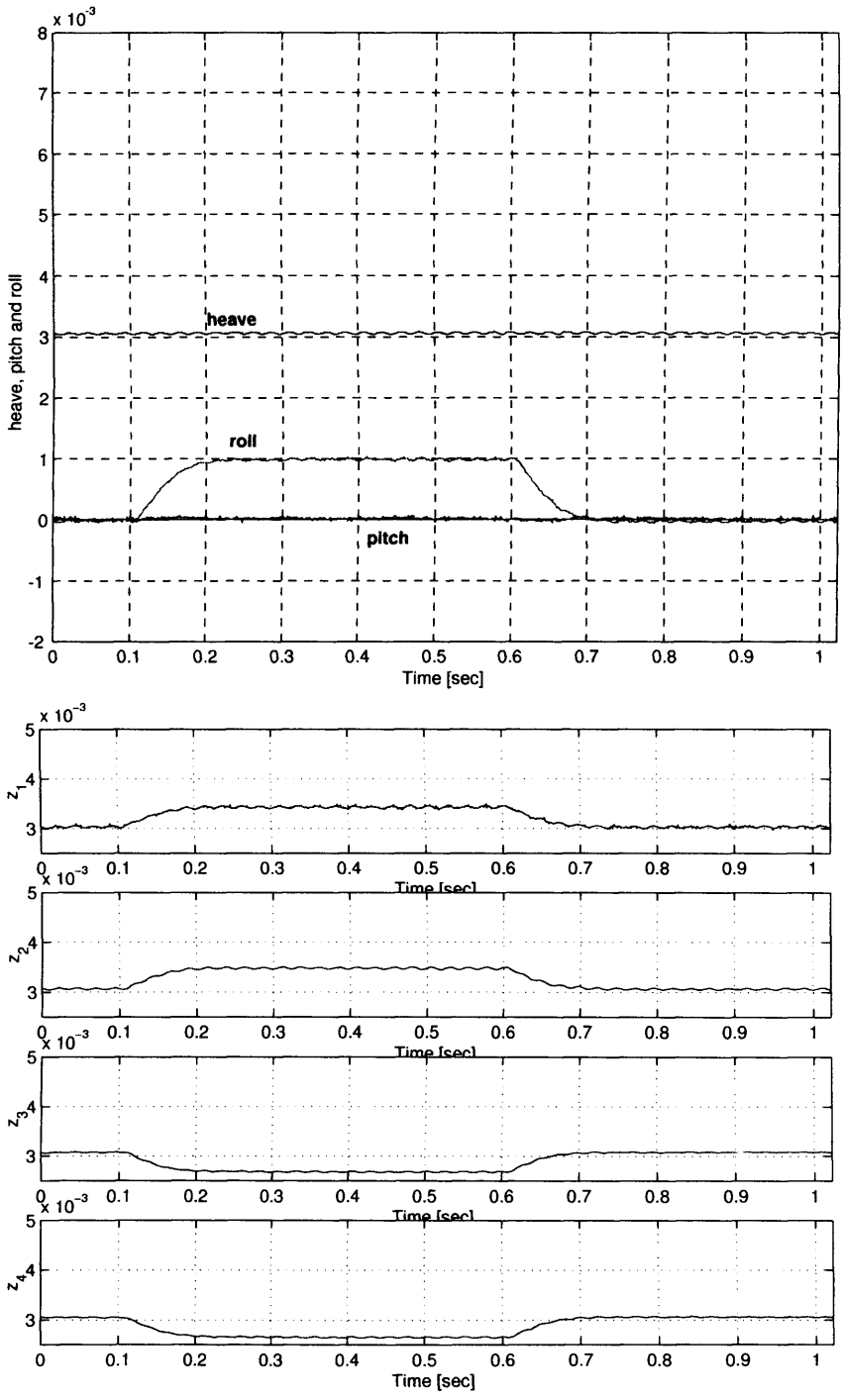

Figure 8.19: Experimentally derived step responses to a 1 mm reference roll change. Top: heave, roll and pitch responses; Bottom: airgap responses.

Bode plot and the experimentally derived Bode plot using the experimental vehicle is shown in Fig. 8.21 (top). A close comparison is observed between simulation and the experimental results in the frequency-domain. At low frequencies, the complimentary function has a 0 dB gain which leads to zero steady-state error in the response. As the frequency increases, the gain also increases to reach approximately 5 dB at 7.6Hz. Above the bandwidth frequency of 25 Hz (at -3 dB) the disturbances are attenuated by the reduced gain. It has to be noted that although the complimentary function has a gain >0dB, the step response in the reference position is still under-damped because of the pre-filtering characteristics of the compensator $\mathbf{K_r}$. A comparison plot between the experimentally derived sensitivity function from the Simulink model, the simulated sensitivity function and and the experimentally derived sensitivity function using the experimental vehicle is shown in Fig. 8.20 (bottom). This function has a low gain at low frequencies to attenuate the disturbances entering the system, reaching -3 dB cross-over frequency at 5 Hz. Its gain has a peak of 4 dB at 8 Hz and 0 dB above this frequency. From the experimental response in Fig. 8.20 (top) it was also observed that around 50 Hz there exists a parasitic resonance effect in the system. A close comparison between the frequency response plots here and the frequency response plot in Fig. 6.26, page 126 suggests that this effect is contributed by the magnet current amplifier and its filtering characteristics on the mains supply (both experiments use the same power-amplifier). In future Maglev designs, care has to be taken to attenuate these parasitic effects by employing more advanced filtering circuits on the supply.

In the third phase of experiments, the ability of the closed-loop system to suppress step disturbances in the track position has been analysed. This test is performed by injecting a parasitic step change in one pair of the position outputs to emulate the effects of misalignments in the guideway [21]. A step change of 1mm is applied to z_1 (Fig 8.9)at t=0.1 sec and then removed at t=0.6 sec.. The corresponding simulated responses are shown in Fig. 8.22 and the corresponding experimental responses are shown in Fig. 8.23. In both simulation and experiment, the closed-loop system needed approximately 100 milliseconds to attenuate the effects of the disturbances. The system also manages to drive the outputs z_1 and z_3 back to levels with zero steady-state errors in the heave responses. The heave position, which is of the greatest importance for Maglev applications, remains almost unchanged during and after the disturbance. Since the disturbance is applied to only one position output, it has a greater effect on the pitch and roll positions, which settle down after 200 milliseconds with larger peaks. Similarly to previous experiments, the experi-

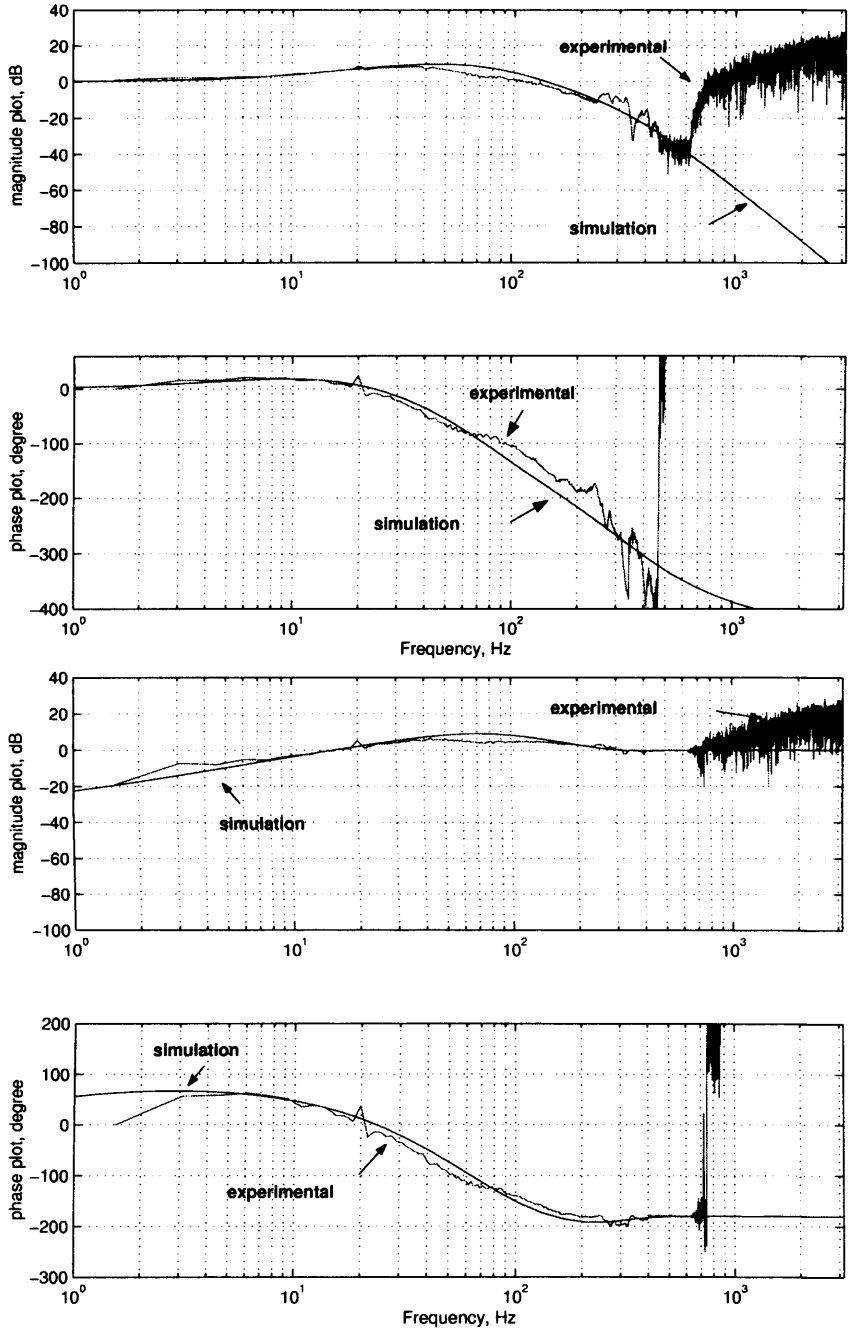

Figure 8.20: Comparison between simulated and experimentally derived frequency response functions. Top: Analytically derived complimentary function vs. experimentally derived complimentary function. Bottom: Analytically derived sensitivity function vs. experimentally derived sensitivity function.

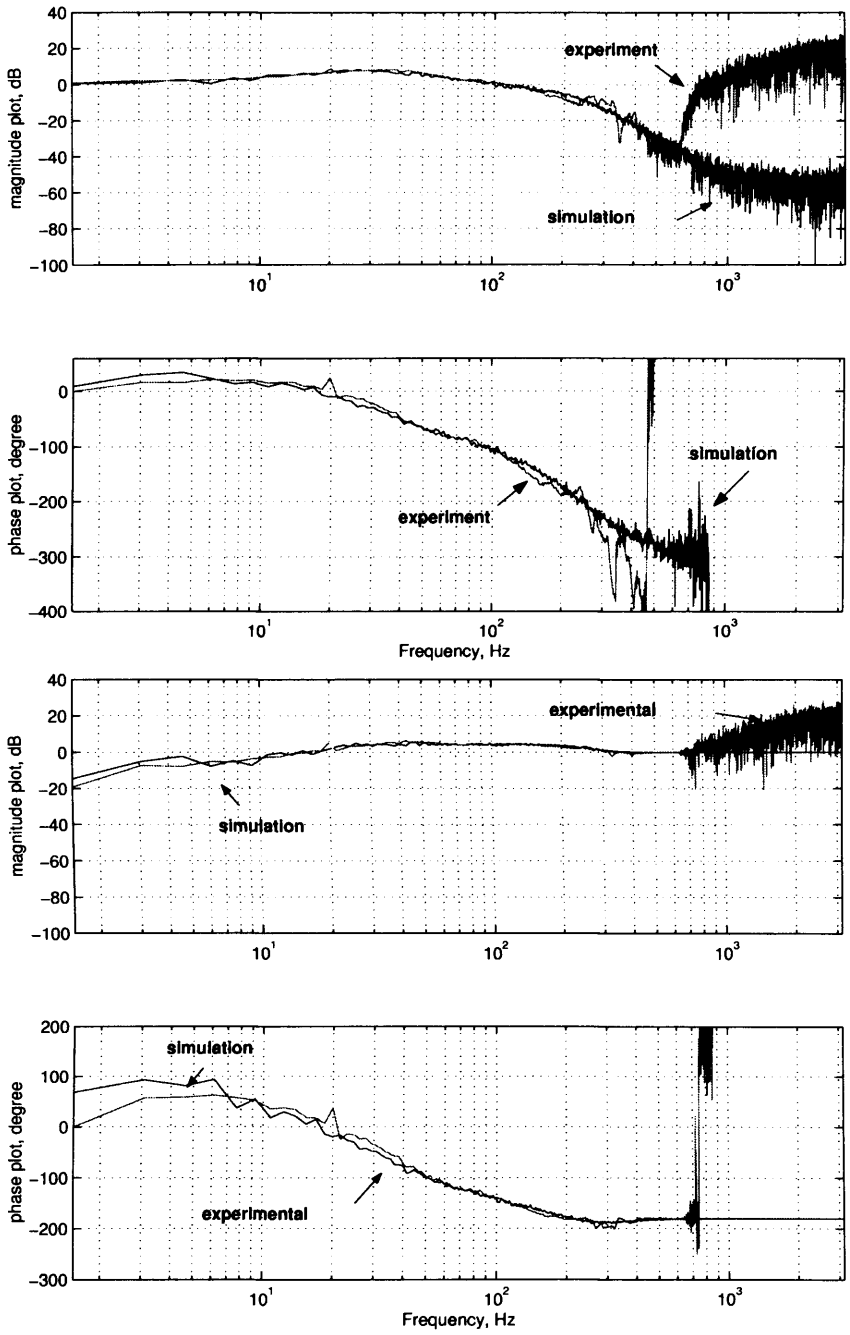

Figure 8.21: Comparison between simulated and experimentally derived frequency response functions. Top: Complimentary function derived from Simulink model vs. experimentally derived complimentary function. Bottom: sensitivity function derived from Simulink model vs. experimentally derived sensitivity function.

mental and simulated responses have very close dynamic characteristics. The larger peaks in the responses at t=0.6 sec when the step disturbance is removed, is contributed by the corresponding force disturbance added to the earth's gravitational force component.

The close comparison between the theoretical model and the experimental system gives some confidence in the simulation model and suggests that it can be used to emulate working conditions in the vehicle which are difficult to perform on the test rig. Based on this, two experiments have been carried out. The first experiment studies the disturbance attenuation characteristics of the controller by analysing the step response in adding 200 N force disturbance to the suspended system. The simulated heave, pitch and roll positions as well as the independent air-gap outputs are shown in Fig. 8.24. The closed-loop system requires 200 milliseconds to attenuate the effect of the 200 N force disturbance with an overshoot of 1 millimetre. Since for the simulation the force disturbance is equally distributed along the suspension vehicle, it has no effect on the roll and pitch components and hence these remain unchanged.

In the second experiment, the robust properties of the controller are analysed. For this, an additional component of 100 kg mass has been added to the suspended mass. A simulated step change in the track guideway has been generated with this additional load. The simulated response of the vehicle is shown in Fig. 8.25. The results show that the closed-loop system remains stable with closed-loop characteristics almost unchanged to the response in Fig. 8.22 for the nominal model. The controller manages to attenuate the disturbance within 200 milliseconds with low disturbance values for the heave component (below 0.4 millimetres peak to peak).

Overall, the experimental and simulation studies show that the new multivariable controller provides good ride qualities which are well within the requirements for Maglev applications. Furthermore, the compensator provides notably better robust stability properties for laterally induced disturbances compared to the state-feedback controller. At the instant marked in Fig. 8.26, a shock disturbance of 110 Newtons is applied in the lateral position of the vehicle. The multivariable controller manages to attenuate this within 11 seconds without any visible disturbance in the heave and the pitch positions. In contrast, the same disturbance leads to unstable response with the state-feedback controller (Fig. 8.8).

Some comments and considerations for the multivariable design are now given. To achieve low values for $\mu(\mathbf{N})$, i.e. to increase the robust properties of the system without changing the performance requirements, the controller and consequently the closed-loop

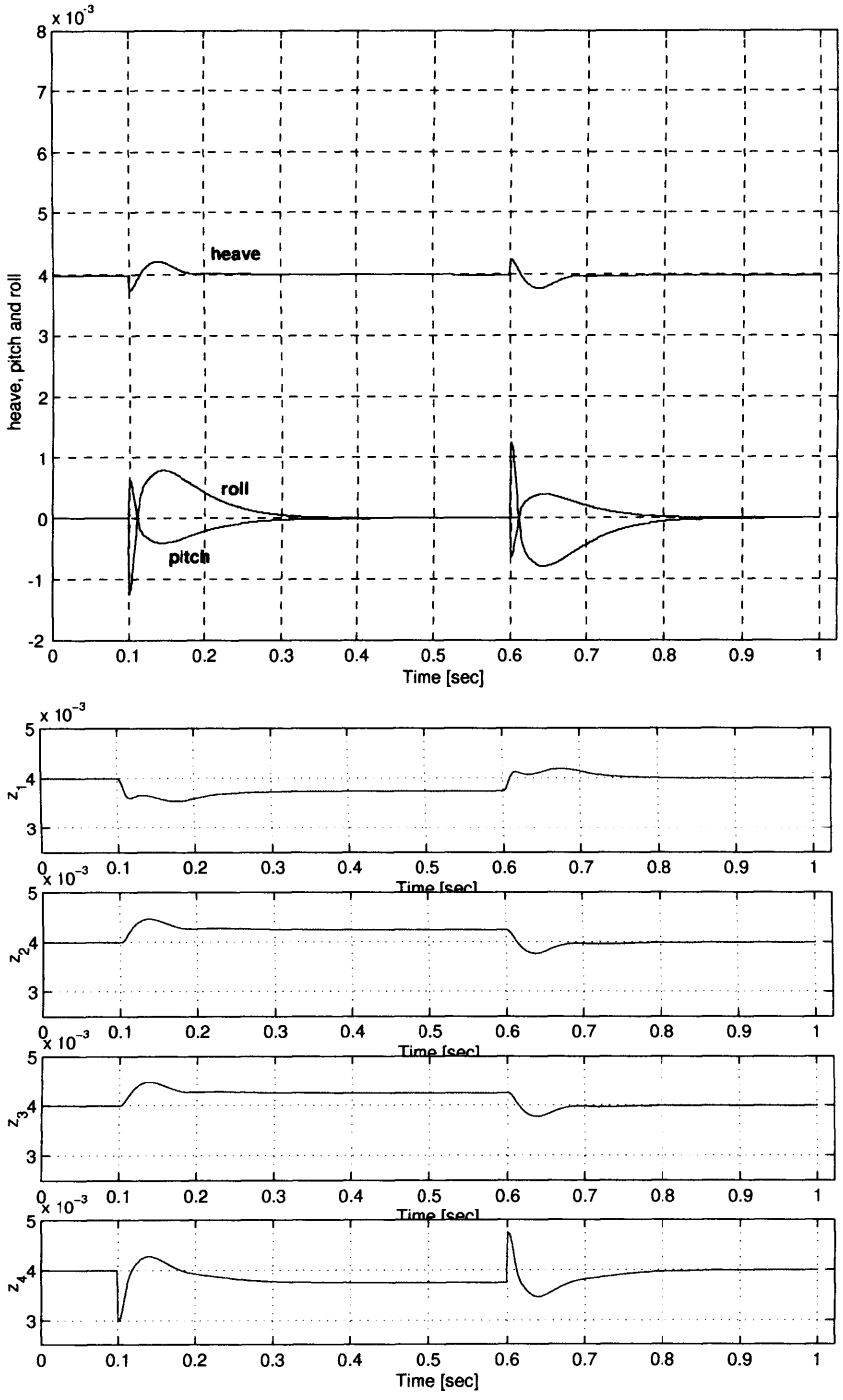

Figure 8.22: Simulated responses to a 1 mm track step change. Top: heave, roll and pitch responses; Bottom: airgap responses.

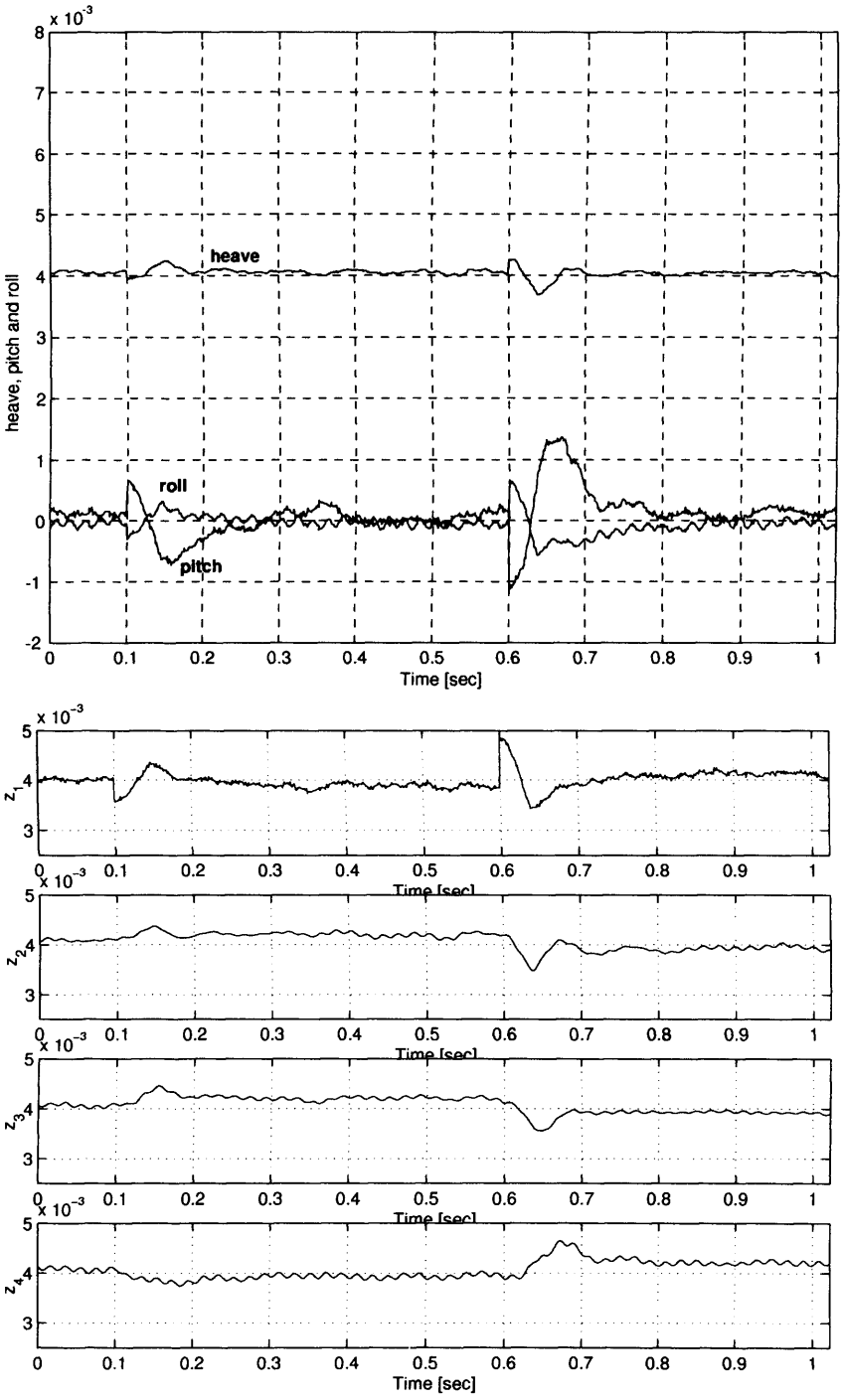

Figure 8.23: Experimental responses to a 1 mm track step change. Top: heave, roll and pitch responses; Bottom: airgap responses.

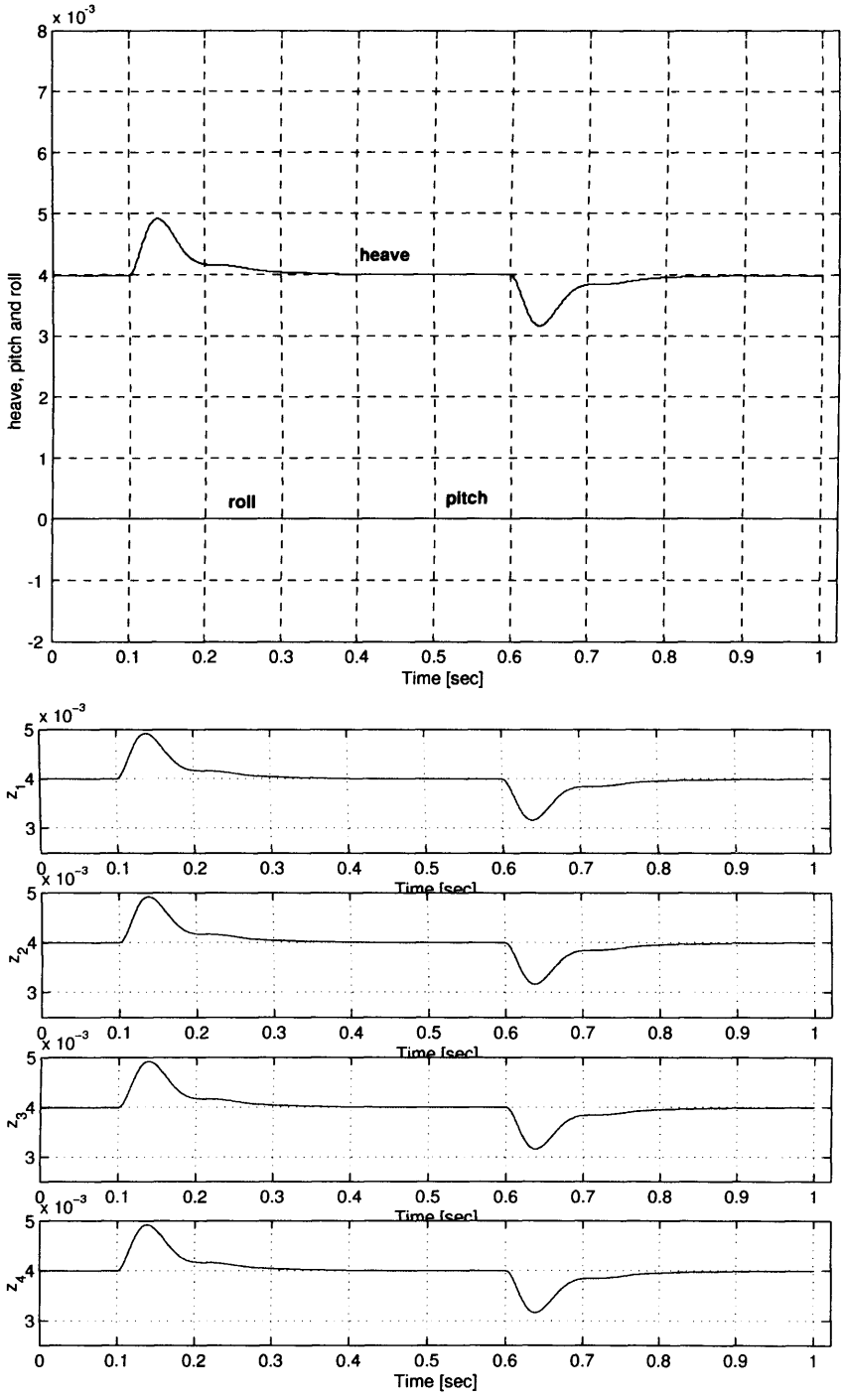

Figure 8.24: Simulated responses to a 200 N force disturbance. Top: heave, roll and pitch responses; Bottom: airgap responses.

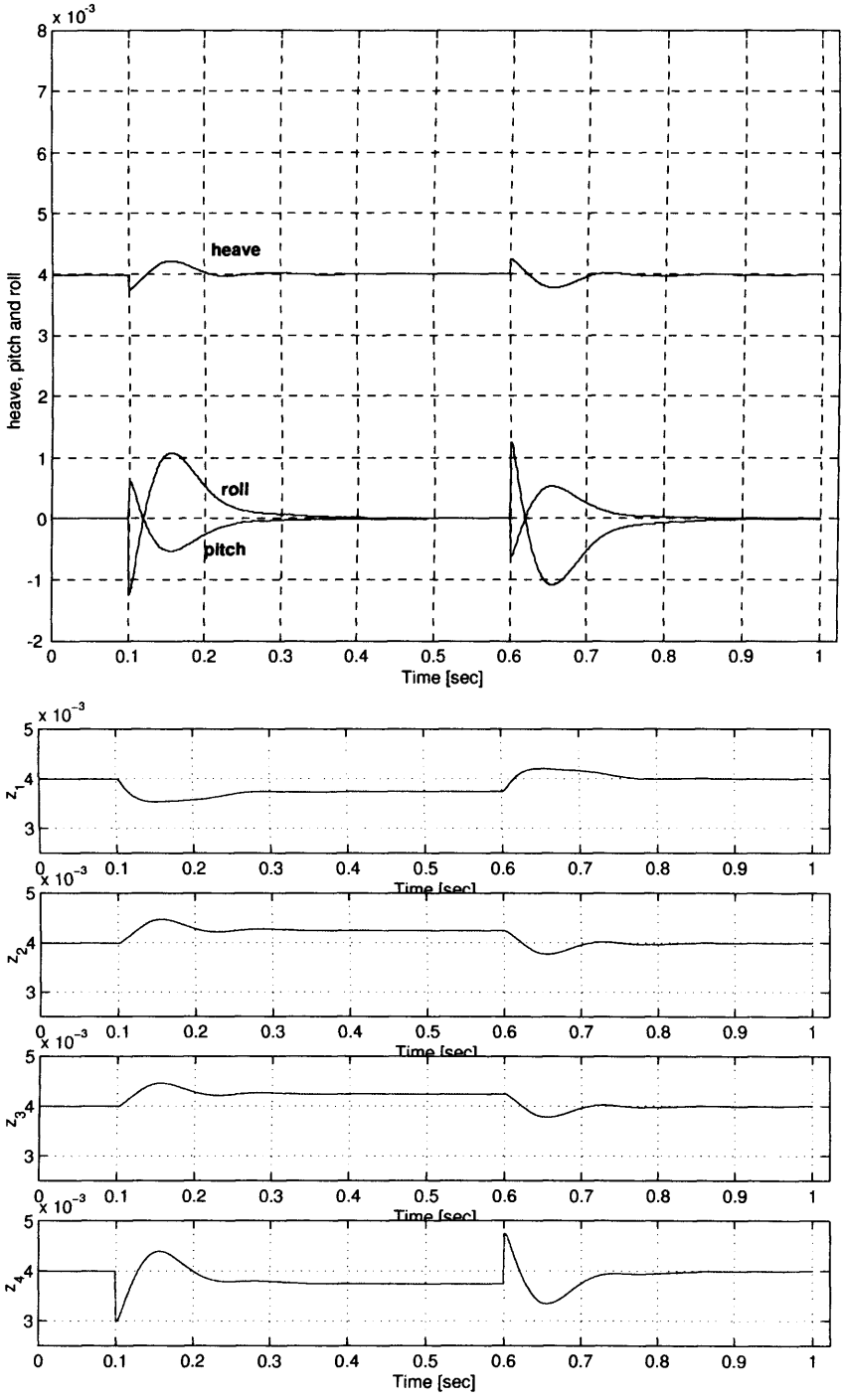

Figure 8.25: Simulated responses to a 1 mm track step change with 100kg additional mass added to the vehicle. Top: heave, roll and pitch responses; Bottom: airgap responses.

system have to work within wider operating bandwidth. This leads to faster control actions and hence better disturbance attenuation properties. It has been observed, however, that although in simulation the designer can increase the bandwidth nearly indefinitely, in practice some limitation are posed from the dynamic characteristics of the system, i.e. power amplifiers, transducers, Maglev vehicle. Large bandwidths allow high-frequency noise to enter the closed-loop system and this leads to resonance effects in the chassis causing oscillation with their natural frequencies. This, foe example, was observed with the coupling between the chassis and the brackets used to secure the magnets on the vehicle. Apart from the undesirable noises produced from suspended vehicles, the high frequency current inputs lead to higher peak-to-peak acceleration levels in the suspension modes and hence degraded ride qualities. For the experimental vehicle with parameters in Table 8.1, it has been observed that the acceptable operating range in terms of bandwidth is approximately 12-15 Hz with a 7 to 9 Hz cross-over frequency. In addition to the parasitic disturbances, increases in the system's bandwidth require reduction in the sampling time for the digital controller. This was also observed for the SISO μ-optimal controller in Section. 7.5.1, page 153, where the sampling time had to be reduced from 1 millisecond to 0.5 milliseconds to meet the requirements from the controller. In some applications, this might pose a practical limitation.

8.6 Multivariable Maglev control with guidance support

The experimental vehicle used in this thesis does not employ facilities for actively controlling the lateral movement in the chassis. Although such guidance is provided by inherent lateral stiffness from the suspension magnets, an industrial application of magnetically levitated vehicles would typically incorporate such abilities for controlling the movement along the y axis (Fig. 8.1) [1]. To address these applications this section develops a mathematical model and a control framework for multi-magnet control with guidance support using the design stages described above.

Multivariable Maglev model with guidance support

The multi-magnet system with support for active guidance control is shown schematically in Fig. 8.27. Together with the four suspension magnets (M_1 to M_4), four more magnets are used (M_5, M_6, M_7 and M_8) to control the guidance properties in the chassis. These

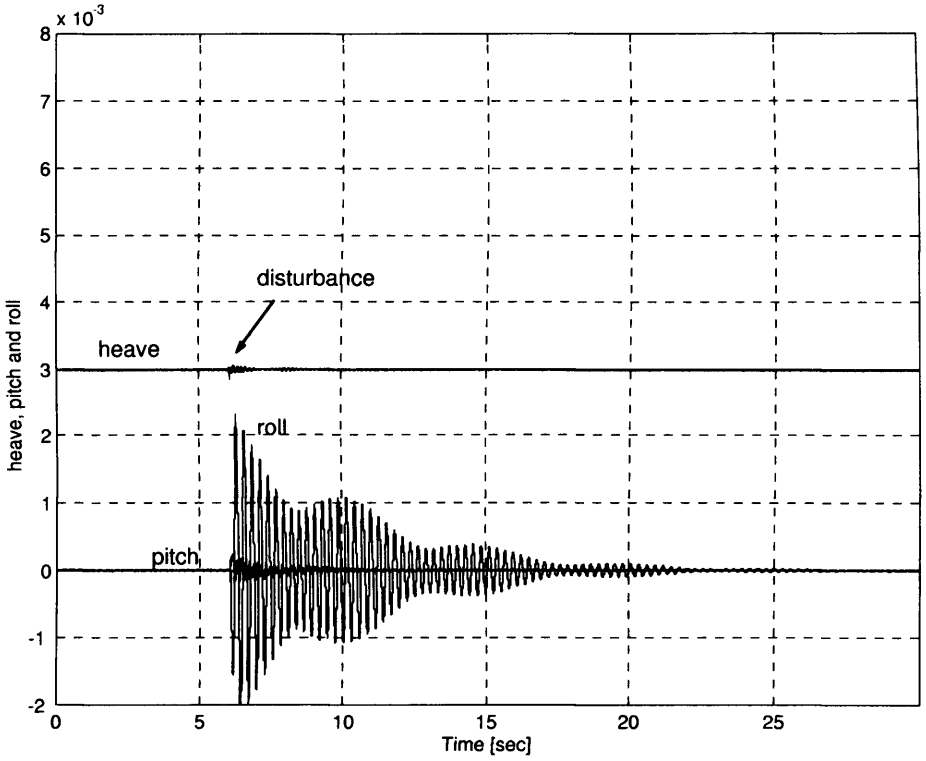

Figure 8.26: Shock disturbance of 110 N in the lateral position and the multivariable controller as in Fig. 8.9.

magnets produce four forces of attraction (f_5, f_6, f_7 and f_8) which in turn give the controlled lateral movement in the chassis along the y axis and the yaw movement ψ about the z axis. To construct the model for this configuration, two more components (torque T_z and force F_y) have been included to the equation of motion in Eqn. 8.2 to describe the mechanical dynamics [96]

$$\begin{aligned} F_z &= M\ddot{z} \\ F_y &= M\ddot{y} \\ T_x &= I_{xx}\dot{\omega}_x + (I_{zz} - I_{yy})\omega_y\omega_x \\ T_y &= I_{yy}\dot{\omega}_y + (I_{xx} - I_{zz})\omega_z\omega_x \\ T_z &= I_{zz}\dot{\omega}_z + (I_{yy} - I_{xx})\omega_x\omega_y \end{aligned} \tag{8.24}$$

where $\ddot{y}$ represents the acceleration of the translation component along the $y - axis$. The angular velocity ω_z is described by the Euler angles in Eqn. 8.4. Since now all three components, pitch θ, roll ϕ and yaw ψ are presented, the angular accelerations $\dot{\omega}$ used to describe the motion in the chassis are produced by differentiating Eqn. 8.4. Using the fact that for small angles $\sin(a) \approx a$ and $\cos(a) \approx 1$, the angular accelerations described with Euler angles are derived by differentiating Eqn. 8.4

$$\begin{aligned} \dot{\omega}_x &= \ddot{\phi} + \ddot{\psi}\theta + \dot{\psi}\dot{\theta} \\ \dot{\omega}_y &= \ddot{\theta} - \dot{\theta}\dot{\phi}\phi - \ddot{\psi}\phi - \dot{\psi}\dot{\phi} + \dot{\psi}\dot{\theta}\phi\theta \\ \dot{\omega}_z &= \ddot{\psi} + \ddot{\theta}\phi + \dot{\theta}\dot{\phi} - \dot{\psi}\dot{\phi}\phi - \dot{\psi}\dot{\theta}\theta \end{aligned} \tag{8.25}$$

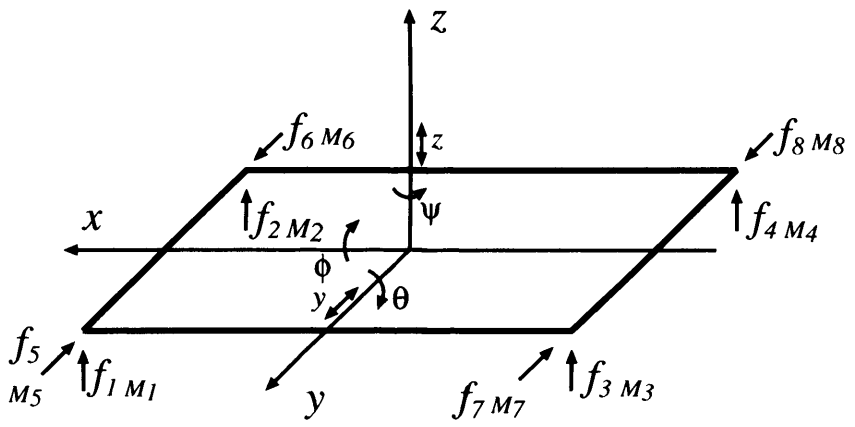

Figure 8.27: Block diagram of a magnetically levitated vehicle with active guidance control. M_1 to M_4 provide four suspension forces f_1 to f_4 which give pitch θ, roll ϕ and heave z; Another four magnets, M_5 to M_8 give another set of four forces f_5 to f_8 which provide translation along the $y-$axis and rotation along the $z-$axis ψ.

The Euler angles, θ, ϕ and ψ, can be uniquely determined from the eight airgaps. The heave z, the pitch θ and the roll ϕ are derived in Eqn. 8.1. The remaining components, the lateral translation y and the yaw ψ, are described by the remaining eight airgaps z_5 to z_8 using Fig. 8.27

$$\begin{aligned} y &= \tfrac{1}{4}(z_5 - z_6 + z_7 - z_8) \\ \psi &= \tfrac{1}{2\sqrt{l^2+b^2}}(z_5 - z_6 - z_7 + z_8) \end{aligned} \tag{8.26}$$

The transformation matrix from airgaps to heave, lateral movements and Euler angles is given below

$$\begin{bmatrix} z \\ y \\ \phi \\ \theta \\ \psi \end{bmatrix} = \underbrace{\begin{bmatrix} \frac{1}{4} & 0 & 0 & 0 & 0 \\ 0 & \frac{1}{4} & 0 & 0 & 0 \\ 0 & 0 & \frac{1}{2b} & 0 & 0 \\ 0 & 0 & 0 & \frac{1}{2l} & 0 \\ 0 & 0 & 0 & 0 & \frac{1}{2\sqrt{(l^2+b^2)}} \end{bmatrix} \begin{bmatrix} 1 & 1 & 1 & 1 & 0 & 0 & 0 & 0 \\ 0 & 0 & 0 & 0 & 1 & -1 & 1 & -1 \\ -1 & 1 & -1 & 1 & 0 & 0 & 0 & 0 \\ 1 & 1 & -1 & -1 & 0 & 0 & 0 & 0 \\ 0 & 0 & 0 & 0 & 1 & -1 & -1 & 1 \end{bmatrix}}_{H} \begin{bmatrix} z_1 \\ z_2 \\ z_3 \\ z_4 \\ z_5 \\ z_6 \\ z_7 \\ z_8 \end{bmatrix} \tag{8.27}$$

The force of attraction along the $z-axis$ F_z and the torque components along the x and y axes T_x and T_y have been described by the four forces f_1 to f_4 as in Eqn. 8.7. The remaining two components, the lateral force of attraction F_y and the torque along the z axis T_z are described by the remaining forces of attraction, f_5 to f_8, produced by the guidance magnets.

$$\begin{aligned} F_z &= (f_5 - f_6 + f_7 - f_8) \\ T_z &= \sqrt{l^2 + b^2}(f_5 - f_6 - f_7 + f_8) \end{aligned} \tag{8.28}$$

Combination of Eqns. 8.24, 8.25 8.8 and 8.9 gives the six-degree-of-freedom (6DOF)

multivariable model of the electromagnetically suspended vehicle. The block diagram of this nonlinear model is shown in Fig. 8.28. The inputs to this model are eight control signals, four for the suspension magnets and four for the guidance magnets. The outputs are the heave z, the lateral movement y, the pitch θ, the roll ϕ and the yaw ψ. These outputs are transformed to airgaps via the inverse mapping $H^+ = H^T(HH^T)^{-1}$ in Eqn. 8.27. The remaining degree of freedom is produced by the linear motor (not described here) which gives the propulsion motion along the $x-$axis.

8.6.1 State-space model of the 6DOF model

For the controller-design work, the multivariable model developed above has to be converted to its state-space representation

$$\begin{aligned} \dot{x} &= Ax + Bu \\ y &= Cx \end{aligned} \tag{8.29}$$

where: $u = [u_1,\ u_2,\ u_3,\ u_4,\ u_5,\ u_6,\ u_7,\ u_8]^T$ is a vector of eight control inputs and $y = [z_1,\ z_2,\ z_3,\ z_4,\ z_5,\ z_6,\ z_7,\ z_8]^T$ is the vector of eight airgap clearances. The multivariable model has 18 state-variables as given below

$$x = \left[z,\ \dot{z},\ y,\ \dot{y},\ \phi,\ \dot{\phi},\ \theta,\ \dot{\theta},\ \psi,\ \dot{\psi},\ i_1,\ i_2,\ i_3,\ i_4,\ i_5,\ i_6,\ i_7,\ i_8\right]^T \tag{8.30}$$

To construct the state-space model, Eqn. 8.24 and Eqn. 8.25 are linearised around $(\theta,\ \phi,\ \psi) = (0, 0, 0)$ to get

$$\begin{aligned} F_z &= M\ddot{z} \\ F_z &= M\ddot{y} \\ T_x &= I_{xx}\ddot{\phi} \\ T_y &= I_{yy}\ddot{\theta} \\ T_z &= I_{zz}\ddot{\psi} \end{aligned} \tag{8.31}$$

This simplification has been used in Section 8.2 to construct the 3DOF linear model. Typically, the linear state-space model is used for design purposes while the nonlinear model is used to analyse the behaviour of the closed-loop system in simulation. This approach has been previously adopted to assess the characteristics of the 3DOF controller.

Since the independent airgaps are not directly available as state-variables, to construct the state-space model these are generated using the the inverse H^+ of the mapping in Eqn. 8.27 as in Eqn. 8.16. After some transformations, the state-space matrices for the electromagnetic system with guidance provision are given below.

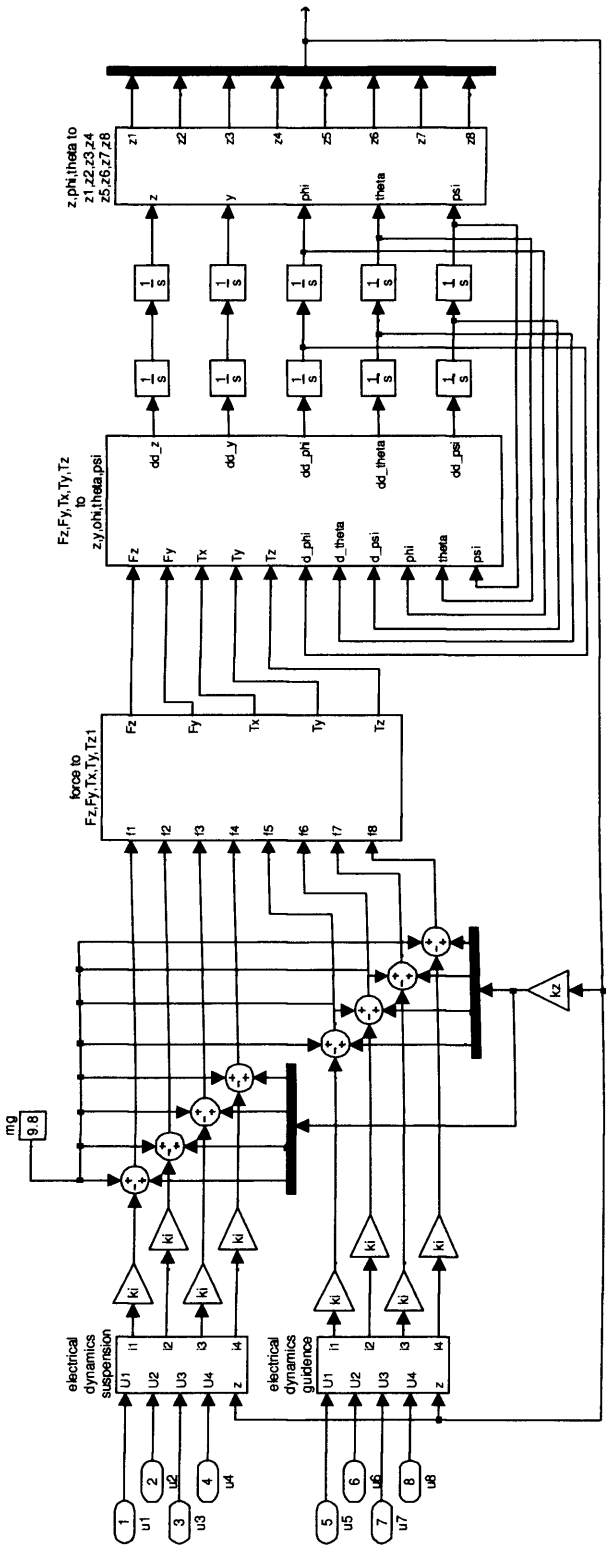

Figure 8.28: Block diagram of a magnetically levitated vehicle with guidance support. Eight magnets (M_1 to M_8) provide eight suspension forces (f_1 to f_8) and hence five degree of freedom: θ, ϕ, ψ, z and y.

$$
A = \begin{bmatrix}
0 & 1 & 0 & 0 & 0 & 0 & 0 & 0 & 0 & 0 & 0 & 0 & 0 & 0 & 0 & 0 & 0 & 0 \\
4\frac{k_z}{M} & 0 & 0 & 0 & 0 & 0 & 0 & 0 & 0 & 0 & -\frac{k_i}{M} & -\frac{k_i}{M} & -\frac{k_i}{M} & -\frac{k_i}{M} & 0 & 0 & 0 & 0 \\
0 & 0 & 0 & 1 & 0 & 0 & 0 & 0 & 0 & 0 & 0 & 0 & 0 & 0 & 0 & 0 & 0 & 0 \\
0 & 0 & 4\frac{k_z}{M} & 0 & 0 & 0 & 0 & 0 & 0 & 0 & 0 & 0 & 0 & 0 & -\frac{k_i}{M} & -\frac{k_i}{M} & -\frac{k_i}{M} & -\frac{k_i}{M} \\
0 & 0 & 0 & 0 & 0 & 1 & 0 & 0 & 0 & 0 & 0 & 0 & 0 & 0 & 0 & 0 & 0 & 0 \\
0 & 0 & 0 & 0 & 2b^2\frac{k_z}{I_{xx}} & 0 & 0 & 0 & 0 & 0 & \frac{k_i b}{I_{xx}} & -\frac{k_i b}{I_{xx}} & \frac{k_i b}{I_{xx}} & -\frac{k_i b}{I_{xx}} & 0 & 0 & 0 & 0 \\
0 & 0 & 0 & 0 & 0 & 0 & 0 & 1 & 0 & 0 & 0 & 0 & 0 & 0 & 0 & 0 & 0 & 0 \\
0 & 0 & 0 & 0 & 0 & 0 & 2l^2\frac{k_z}{I_{yy}} & 0 & 0 & 0 & -\frac{k_i l}{I_{yy}} & -\frac{k_i l}{I_{yy}} & \frac{k_i l}{I_{yy}} & \frac{k_i l}{I_{yy}} & 0 & 0 & 0 & 0 \\
0 & 0 & 0 & 0 & 0 & 0 & 0 & 0 & 0 & 1 & 0 & 0 & 0 & 0 & 0 & 0 & 0 & 0 \\
0 & 0 & 0 & 0 & 0 & 0 & 0 & 0 & 2\bar{l}\bar{b}^2\frac{k_z}{I_{zz}} & 0 & 0 & 0 & 0 & 0 & -\frac{k_i\bar{l}\bar{b}}{I_{zz}} & +\frac{k_i\bar{l}\bar{b}}{I_{zz}} & \frac{k_i\bar{l}\bar{b}}{I_{zz}} & -\frac{k_i\bar{l}\bar{b}}{I_{zz}} \\
\frac{kz}{ki} & 0 & 0 & 0 & -\frac{b}{2}\frac{kz}{ki} & 0 & \frac{l}{2}\frac{kz}{ki} & 0 & 0 & 0 & -\frac{R}{L_0} & 0 & 0 & 0 & 0 & 0 & 0 & 0 \\
\frac{kz}{ki} & 0 & 0 & 0 & \frac{b}{2}\frac{kz}{ki} & 0 & \frac{l}{2}\frac{kz}{ki} & 0 & 0 & 0 & 0 & -\frac{R}{L_0} & 0 & 0 & 0 & 0 & 0 & 0 \\
\frac{kz}{ki} & 0 & 0 & 0 & -\frac{b}{2}\frac{kz}{ki} & 0 & -\frac{l}{2}\frac{kz}{ki} & 0 & 0 & 0 & 0 & 0 & -\frac{R}{L_0} & 0 & 0 & 0 & 0 & 0 \\
\frac{kz}{ki} & 0 & 0 & 0 & \frac{b}{2}\frac{kz}{ki} & 0 & -\frac{l}{2}\frac{kz}{ki} & 0 & 0 & 0 & 0 & 0 & 0 & -\frac{R}{L_0} & 0 & 0 & 0 & 0 \\
0 & 0 & \frac{kz}{ki} & 0 & 0 & 0 & 0 & 0 & \frac{\bar{l}\bar{b}}{2}\frac{kz}{ki} & 0 & 0 & 0 & 0 & 0 & -\frac{R}{L_0} & 0 & 0 & 0 \\
0 & 0 & -\frac{kz}{ki} & 0 & 0 & 0 & 0 & 0 & -\frac{\bar{l}\bar{b}}{2}\frac{kz}{ki} & 0 & 0 & 0 & 0 & 0 & 0 & -\frac{R}{L_0} & 0 & 0 \\
0 & 0 & \frac{kz}{ki} & 0 & 0 & 0 & 0 & 0 & -\frac{\bar{l}\bar{b}}{2}\frac{kz}{ki} & 0 & 0 & 0 & 0 & 0 & 0 & 0 & -\frac{R}{L_0} & 0 \\
0 & 0 & -\frac{kz}{ki} & 0 & 0 & 0 & 0 & 0 & \frac{\bar{l}\bar{b}}{2}\frac{kz}{ki} & 0 & 0 & 0 & 0 & 0 & 0 & 0 & 0 & -\frac{R}{L_0}
\end{bmatrix} \tag{8.32}
$$

where $\bar{lb} = \sqrt{l^2 + b^2}$. Similarly, the B and C matrix for the state-space model are derived below

$$B = \begin{bmatrix} 0 & 0 & 0 & 0 & 0 & 0 & 0 & 0 \\ 0 & 0 & 0 & 0 & 0 & 0 & 0 & 0 \\ 0 & 0 & 0 & 0 & 0 & 0 & 0 & 0 \\ 0 & 0 & 0 & 0 & 0 & 0 & 0 & 0 \\ 0 & 0 & 0 & 0 & 0 & 0 & 0 & 0 \\ 0 & 0 & 0 & 0 & 0 & 0 & 0 & 0 \\ 0 & 0 & 0 & 0 & 0 & 0 & 0 & 0 \\ 0 & 0 & 0 & 0 & 0 & 0 & 0 & 0 \\ 0 & 0 & 0 & 0 & 0 & 0 & 0 & 0 \\ 0 & 0 & 0 & 0 & 0 & 0 & 0 & 0 \\ \frac{1}{L_0} & 0 & 0 & 0 & 0 & 0 & 0 & 0 \\ 0 & \frac{1}{L_0} & 0 & 0 & 0 & 0 & 0 & 0 \\ 0 & 0 & \frac{1}{L_0} & 0 & 0 & 0 & 0 & 0 \\ 0 & 0 & 0 & \frac{1}{L_0} & 0 & 0 & 0 & 0 \\ 0 & 0 & 0 & 0 & \frac{1}{L_0} & 0 & 0 & 0 \\ 0 & 0 & 0 & 0 & 0 & \frac{1}{L_0} & 0 & 0 \\ 0 & 0 & 0 & 0 & 0 & 0 & \frac{1}{L_0} & 0 \\ 0 & 0 & 0 & 0 & 0 & 0 & 0 & \frac{1}{L_0} \end{bmatrix} \tag{8.33}$$

$$C = \begin{bmatrix} 1 & 0 & 0 & 0 & -\frac{b}{2} & 0 & \frac{l}{2} & 0 & 0 & 0 & 0 & 0 & 0 & 0 & 0 & 0 & 0 & 0 \\ 1 & 0 & 0 & 0 & \frac{b}{2} & 0 & \frac{l}{2} & 0 & 0 & 0 & 0 & 0 & 0 & 0 & 0 & 0 & 0 & 0 \\ 1 & 0 & 0 & 0 & -\frac{b}{2} & 0 & -\frac{l}{2} & 0 & 0 & 0 & 0 & 0 & 0 & 0 & 0 & 0 & 0 & 0 \\ 1 & 0 & 0 & 0 & \frac{b}{2} & 0 & -\frac{l}{2} & 0 & 0 & 0 & 0 & 0 & 0 & 0 & 0 & 0 & 0 & 0 \\ 0 & 0 & 1 & 0 & 0 & 0 & 0 & 0 & \sqrt{l^2 + b^2}/2 & 0 & 0 & 0 & 0 & 0 & 0 & 0 & 0 & 0 \\ 0 & 0 & -1 & 0 & 0 & 0 & 0 & 0 & -\sqrt{l^2 + b^2}/2 & 0 & 0 & 0 & 0 & 0 & 0 & 0 & 0 & 0 \\ 0 & 0 & 1 & 0 & 0 & 0 & 0 & 0 & -\sqrt{l^2 + b^2}/2 & 0 & 0 & 0 & 0 & 0 & 0 & 0 & 0 & 0 \\ 0 & 0 & -1 & 0 & 0 & 0 & 0 & 0 & \sqrt{l^2 + b^2}/2 & 0 & 0 & 0 & 0 & 0 & 0 & 0 & 0 & 0 \end{bmatrix} \tag{8.34}$$

8.6.2 Controller design and simulation results

The closed-loop control configuration with guidance support is shown in Fig. 8.29. Similarly to the previous design, **K** is also a two-degree of freedom controller but this time with 13 inputs: five reference inputs z, y, θ, ϕ, ψ and eight airgap inputs z_1 to z_8. The compensator produces eight control outputs u_1 to u_8 to drive eight suspension and guidance magnets. This design configuration differs from the 3DOF configuration in Fig. 8.9 only in the number of control inputs and system outputs. This permits the use of the mathematical developments in Section 8.4.2 directly. The closed-loop transfer matrix **N** for Fig. 8.29 is given in Eqn 8.22. $\mathbf{N}_{12}$ can be used to specify the performance weights and to describe the closed-loop design requirements. Since the four guidance magnets are considered to have the same characteristics as the suspension magnets and the specifications from the closed-loop have remained unchanged, the performance matrices have been selected in the same manner as the performance matrices in Section. 8.4.2. $\mathbf{W}$, $\mathbf{W_r}$, $\mathbf{W_d}$ and $\mathbf{W_c}$ are

8×8 diagonal matrices. The individual diagonal elements are given in numerical form in Section. 8.4.2.

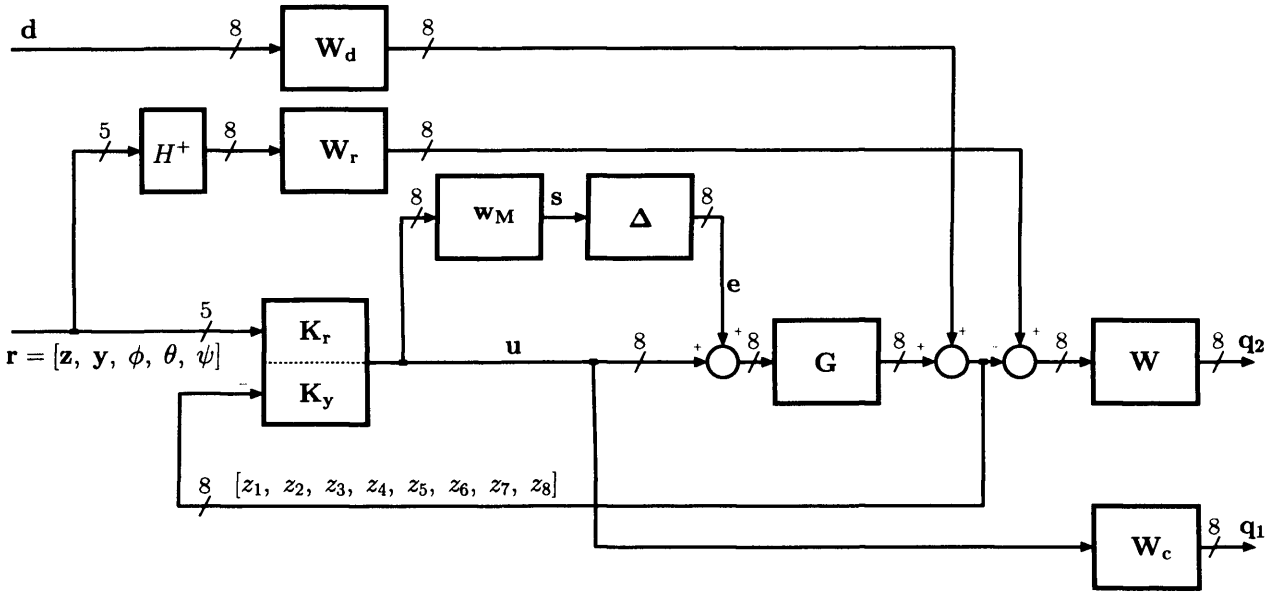

Figure 8.29: System configuration for the multivariable two-degree of freedom controller design.

For the synthesis work, Matlab and the μ−synthesis and Analysis Toolbox are used. Software routines are written to construct the open-loop state-space model in Eqn. 8.29. The parameters for the vehicle and the suspension magnets are listed in Table 8.1. The four guidance magnets M_5 to M_8 are assumed to have the same electro-mechanical characteristics as the suspension magnets. The Matlab routines accept as input the performance weights and the open-loop model to construct the generalised open-loop block diagram in Fig. 8.29. The μ-optimisation algorithm needs two iterations in the optimisation procedure to achieve a robust controller that achieves $\mu(N) = 1.09$. The two-degree-of-freedom controller has 106 state-variables. Since this order is considered as very high for simulation and practical implementation, the order of the controller is reduced to 20th order using the Hankel norm reduction algorithm [95].

Since the experimental vehicle does not have facilities for achieving guidance control, only simulation results are presented to validate the new multi-magnet controller. The close comparison between the theoretical and the experimental results presented in the previous section gives confidence in the model and motivates the simulation work in this section. The analysis is performed in Simulink with a custom built simulation model. This simulator uses the 6DOF nonlinear multivariable model and the two-degree of freedom μ−optimal controller and has facilities for assessing the behaviour of the system in adding

additional mass, force, track disturbance as well as changes in the reference demand. For reasons of space, only a selected set of responses are presented here. In overall terms, the simulation demonstrates that the new multivariable controller produces closed-loop Maglev suspension characteristics which are comparable with the 3DOF results. Since the design configuration for the controller and performance weights are same for the 3DOF and for the 6DOF designs, the responses in changing the reference heave, pitch, roll, track disturbance, force and mass disturbances are identical with the responses in Figs. 8.14 to Fig. 8.19.

The closed-loop response to changes in the reference heave position and the reference guidance position is shown in Fig. 8.30 (top). The independent airgap responses are shown in Fig. 8.30 (bottom). At t=0.1 sec. the reference airgap z is modified from 3 mm to 4 mm and at t=0.6 sec. the reference guidance position has been altered from 0 mm to 3 mm. The outputs from the system need 200 milliseconds to settle to the steady state values. Since the specification $\mathbf{W_r}$ for the ideal response from the system is identical for all reference inputs, the responses in the heave and the guidance position have identical characteristics. In addition, the multivariable controller decouples completely the heave and the guidance responses from the roll, the pitch and the yaw components which remain unchained in Fig. 8.30. In the second phase of simulations, the disturbance attenuation characteristics of the closed-loop system are studied. A step change of 1 mm in the track position is added to z_1 at t=0.1 sec. and then removed at t=0.6 sec. The corresponded simulated responses are shown in Fig. 8.31. The results confirm that the closed-loop system manages to attenuate these disturbances within 200 milliseconds and the heave position remains almost unchanged. In addition, the disturbance added to z_1 does not effect the guidance and the yaw positions. Fig. 8.32 shows similar responses in adding track disturbance to z_8. As with the previous responses, the closed-loop system manages to attenuate the disturbance within 200 milliseconds with almost undisturbed heave, roll, pitch and guidance positions.

8.7 Concluding comments

Control of multi-magnet systems is a challenging problem largely resulting from the open-loop instable nature of the magnetic suspension and the cross coupling between the magnets, fixed as they are to a common rigid body. Linear controllers independent for each magnet have been used in the past for multi-magnet stabilisation [1, 21]. For applications without actively controlled guidance, these controllers have some limitations in attenuat-

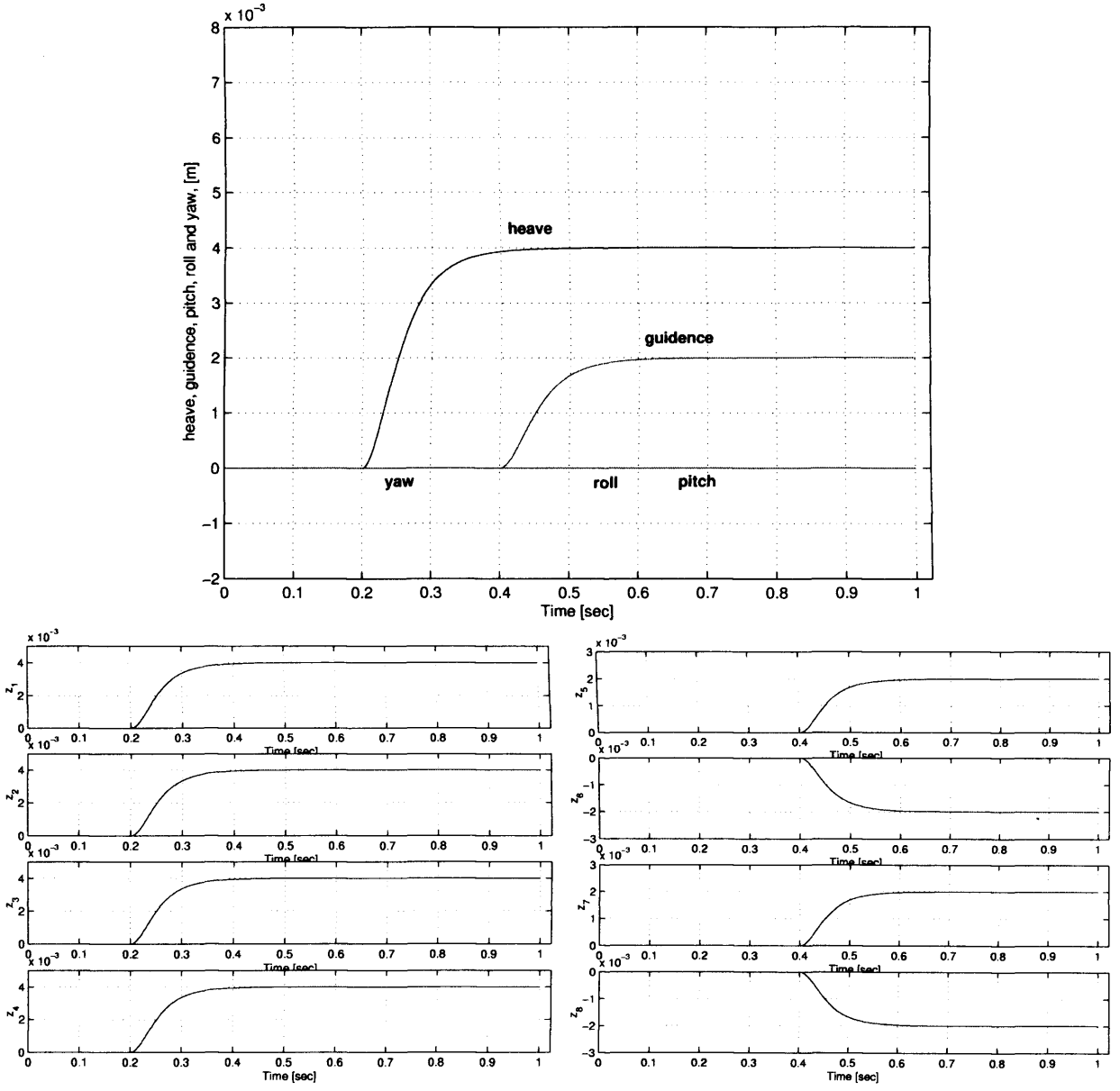

Figure 8.30: Simulated step responses to: (a) 4 mm change in the heave reference position at t=0.2 sec, and (b) 2mm change in the guidance reference position at t=0.4sec. Top: heave, guidance, roll, pitch and yaw responses; Bottom: airgap responses.

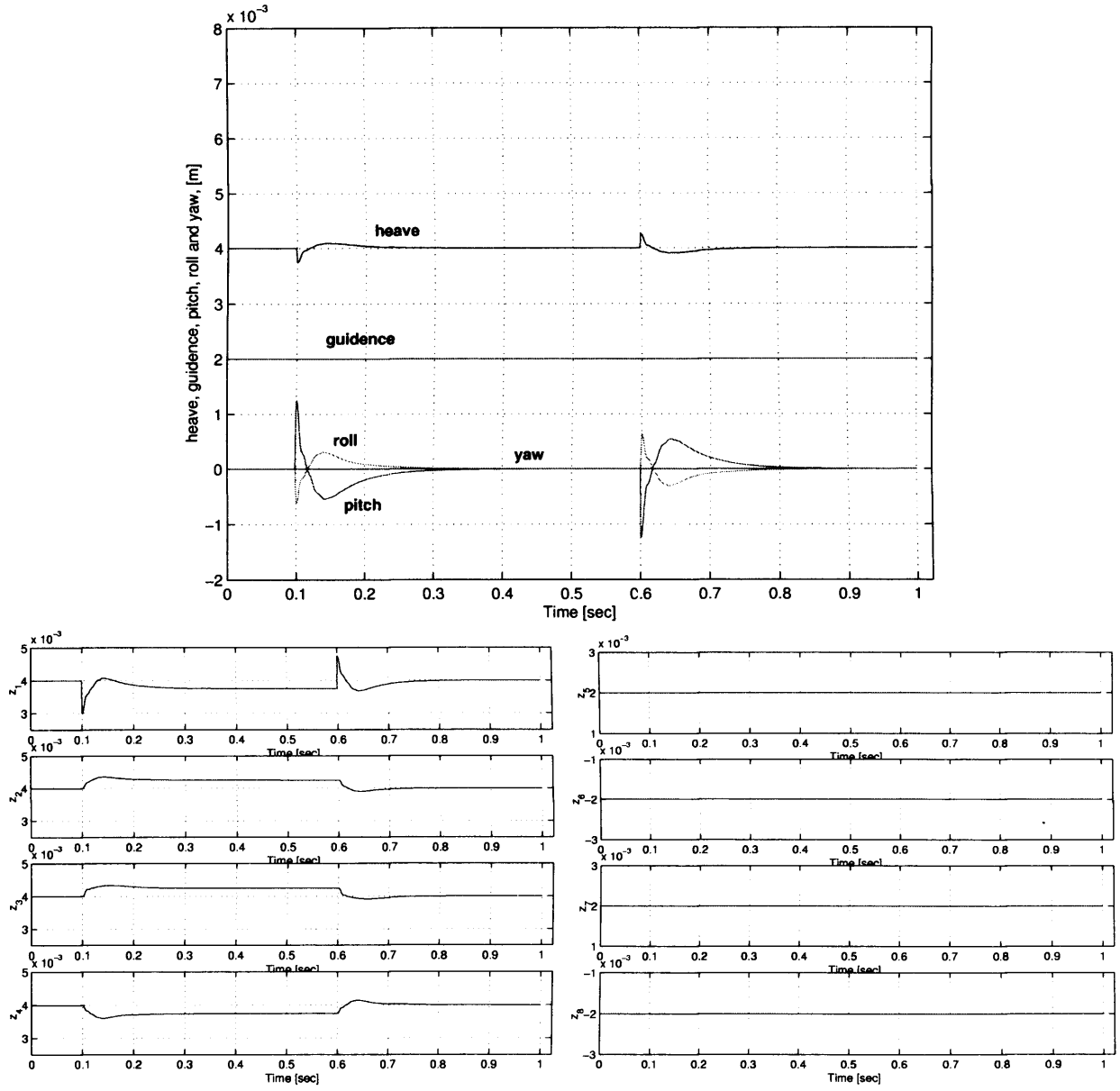

Figure 8.31: Simulated step responses to: (1) 1 mm track disturbance added to z_1 at t=0.1 sec., and (b) 1mm track disturbance removed from z_1 at t=0.6 sec. Top: heave, guidance, roll, pitch and yaw responses; Bottom: airgap responses.

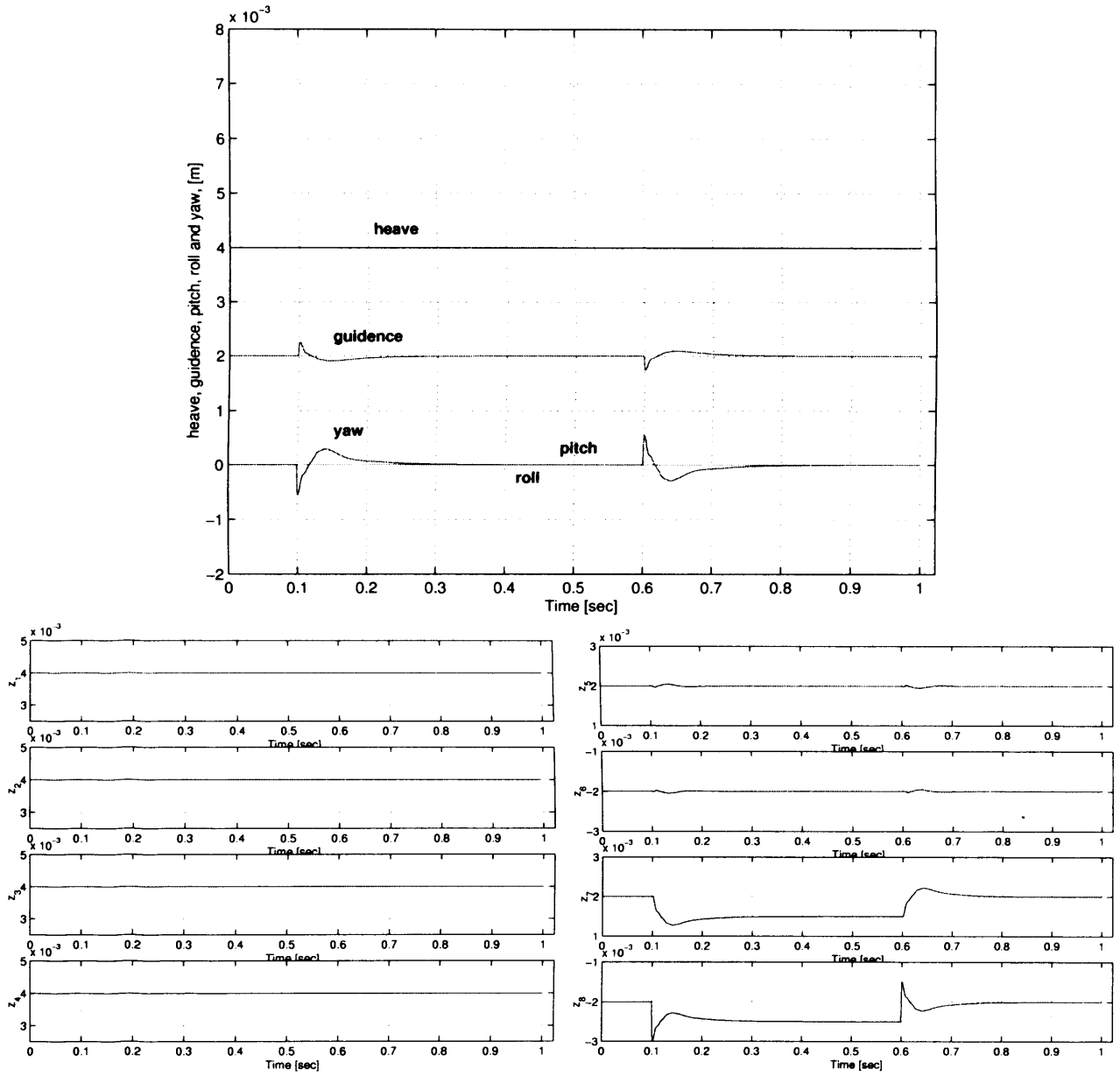

Figure 8.32: Simulated step responses to: (1) 1 mm track disturbance added to z_8 at t=0.1 sec., and (b) 1mm track disturbance removed from z_8 at t=0.6 sec. Top: heave, guidance, roll, pitch and yaw responses; Bottom: airgap responses.

ing guidance-induced disturbances. To improve the overall stability and robustness, this chapter has developed a design framework for multivariable Maglev control based on the developments on $\mathcal{H}_\infty$ and $\mu-$synthesis for Maglev presented in Chapters 6 to 7. For this purpose, a state-space model has been derived to model a 3DOF multivariable suspension system. This model was used in the derivation of $\mu-$optimal controllers. The suspension quality of the new control system has been assessed through an extensive range of simulation and experimental studies using a representative Maglev test rig. The results show that the new closed-loop system has the ability to maintain stable suspension characteristics well within the Maglev requirements and to suppress the effects of force, mass and track disturbances on the ride. To expand the design to feature Maglev control applications, in the second part of studies the 3DOF model is extended with provisions for active guidance control and a new multivariable controller with guidance support is derived using the same framework. Due to the lack of guidance magnets on the representative test rig, the behaviour of the controller is studied only in simulation. The results from the 3DOF controller implementation show that the developed here Maglev design environment provides a systematic and deterministic way of specifying and obtaining controllers for multi-magnet controller design.

During the controller-design process a trade off has to be made between the allowed uncertainty in the system, closed-loop bandwidth, sampling time and operational stability. Increasing the uncertainty in the system typically requires a relaxation of the upper-bound requirements on the control actions and hence an increase in closed-loop bandwidth. The controller is then required to operate over a larger bandwidth which puts an additional constraint on the sampling time. The increased number of state-variables in the multi-magnet controller tends to consume most of the available processing bandwidth. It was estimated that controlling multivariable system with guidance support would require approximately 350-400 microseconds. Reducing the sampling time for wider operational range and higher closed-loop bandwidth results in the computation approaching the available time-slot. For this applications, the multi-processing facilities provided by the DSP hardware have to be used. In addition, an increase in operational bandwidth leads to exciting components in the vehicle body which are excluded from the modelling work. Without additional account of this, undesirable resonance effects are generated leading to increased acceleration levels.

Maglev systems are nonlinear because of the nonlinear relationship between operating current and force of attraction. So far in this thesis, the nonlinearity is not explicitly

analysed and to deal with it, different design methodologies have been developed (adaptive control, robust control). In the following Chapter, a new design approach is considered which uses the nonlinear model of the suspension system to develop a design methodology for nonlinear $\mathcal{H}_\infty$ control for Maglev.

Chapter 9

Nonlinear $\mathcal{H}_\infty$ control for Maglev

The relationship between the excitation current, the operating airgap and the force of attraction in electromagnetic suspension systems is modelled by a set of nonlinear dynamic equations. In previous control work, these are linearised around the nominal operating point (i_0, z_0) to get a linear model. The nonlinearity is not explicitly analysed and to deal with it, different design methodologies have been developed (adaptive control, robust $\mu-$optimal control). In this chapter, a new design approach is considered which uses the nonlinear model of the suspension system to design two nonlinear $\mathcal{H}_\infty$ controllers for Maglev. A special emphasis is given on improving the suspension characteristics with reference to the track-guidance-induced interactions due to irregularities.

To extend the concept of the $\infty-$gain to nonlinear systems, the notations of local dissipativity and supply power are used to develop nonlinear $\mathcal{H}_\infty$ controllers. Since there exists a strong relationship between the ∞-norm and the energy of the system, these concepts have been embedded in the design process and a generalised framework for nonlinear controllers is developed with particular reference to Maglev applications. A set of Matlab routines is developed to derive the nonlinear controllers symbolically. The theoretical exposition is followed by a selected set of simulation and DSP experimental results.

9.1 The $\mathcal{H}_\infty$ gain of nonlinear systems

9.1.1 Nonlinear model of the electromagnetic system

As outlined in Chapter 2, an electromagnetic suspension system consists of a suspended magnet and a reaction surface (guideway). The vertical dynamics of the open-loop system is described by Eqn. 2.7. The magnet winding current (excitation) is related to the electrical parameters of the circuit and is satisfactorily represented by Eqn. 2.2. With a state-vector of the form $[x_1(t)\ x_2(t)\ x_3(t)]^T=[z(t)\ \dot{z}(t)\ i(t)]^T$, the following nonlinear state-space model

can be constructed to describe the dynamics of the electromagnetic suspension system

$$\begin{bmatrix} \dot{x}_1 \\ \dot{x}_2 \\ \dot{x}_3 \end{bmatrix} = \underbrace{\begin{bmatrix} x_2 \\ -\frac{\mu_0 N^2 A}{4m}\left(\frac{x_3}{x_1}\right)^2 \\ -\frac{2R}{\mu_0 N^2 A}x_3 x_1 + \frac{x_3 x_2}{x_1} \end{bmatrix}}_{A(x)} + \underbrace{\begin{bmatrix} 0 & 0 \\ \frac{1}{m}\alpha_1 & 0 \\ 0 & 0 \end{bmatrix}}_{B_1(x)} \begin{bmatrix} w_1 \\ w_2 \end{bmatrix} + \underbrace{\begin{bmatrix} 0 \\ 0 \\ \frac{2}{\mu_0 N^2 A}x_1 \end{bmatrix}}_{B_2(x)} u \qquad (9.1)$$

where $w_1 = f_d$ represents the external force disturbance, w_2 captures disturbances acting on the suspension airgap, m=mass of the electromagnet, R=magnet winding resistance, A=magnet's pole-face area, N=number of turns and $u(t)$=input control voltage to the magnet amplifier.

The block diagram of this nonlinear state equation is shown in Fig. 9.1. The corresponding general forms of the nonlinear state and output equations are

$$\begin{aligned} \dot{x} &= A(x) + B_1(x)w + B_2(x)u \\ y &= x_1 + \alpha_2 w_2 \equiv C_2(x) + D_{21}(x)w \end{aligned} \qquad (9.2)$$

where $w = [w_1, w_2]^T$, α_1 and α_2 are appropriate scaling parameters added for mathematical convenience, $x \in \mathbf{R}^n$, $w \in \mathbf{R}^r$, $u \in \mathbf{R}^m$ and $y \in \mathbf{R}^p$, where: $n = 3$, $r = 2$, $m = 1$ and $p = 1$.

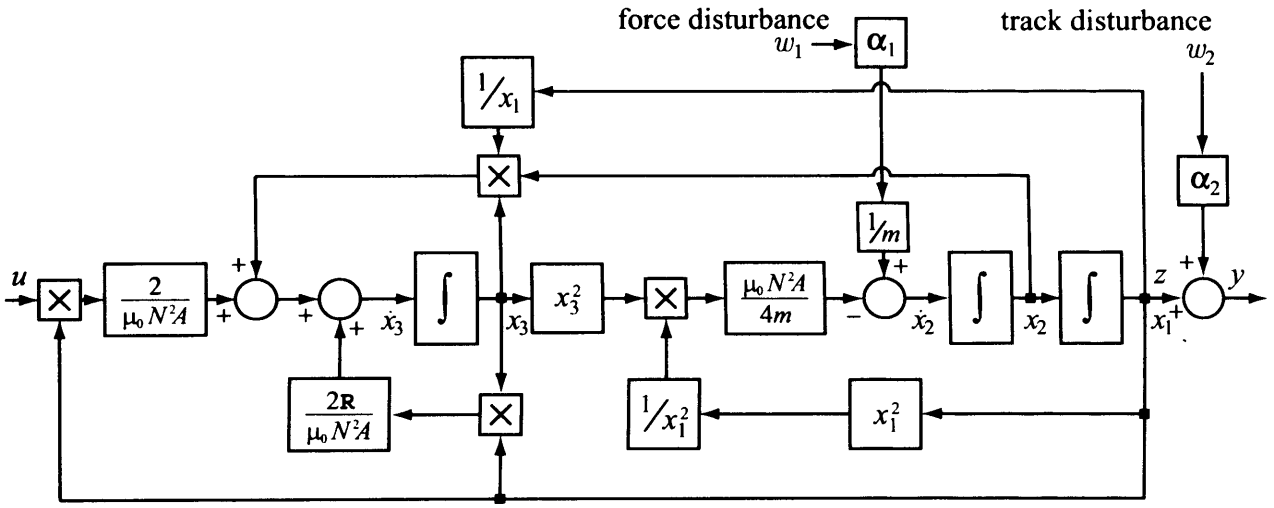

Figure 9.1: Nonlinear open-loop Maglev model.

The general control configuration used in the developments of the linear $\mathcal{H}_\infty$ controllers (Fig. 6.3) is conveniently redrawn for the nonlinear problem to get the representation in Fig. 9.2. With respect to this figure, the nonlinear $\mathcal{H}_\infty$ design methodology developed here aims to find a nonlinear feedback compensator $K(x)$ that minimises the effect of $w = [w_1, w_2]^T$ on a penalty vector $q \in \mathbf{R}^{(n+m)}$

$$q = \begin{bmatrix} \beta_1 & 0 & 0 \\ 0 & \beta_2 & 0 \\ 0 & 0 & \beta_3 \\ 0 & 0 & 0 \end{bmatrix} \begin{bmatrix} x_1 \\ x_2 \\ x_3 \end{bmatrix} + \begin{bmatrix} 0 \\ 0 \\ 0 \\ W_c \end{bmatrix} u = C_1(x) + D_{12}(x)u \qquad (9.3)$$

As in the linear $\mathcal{H}_\infty$ design, W_c is an upper bound on the control output. β_1, β_2 to β_3 are scaling weights on the state-variables, similar to the specification of $W(s)$ in the linear $\mathcal{H}_\infty$ design (Chapter 6). To extend the concept of the ∞-gain to nonlinear systems, the

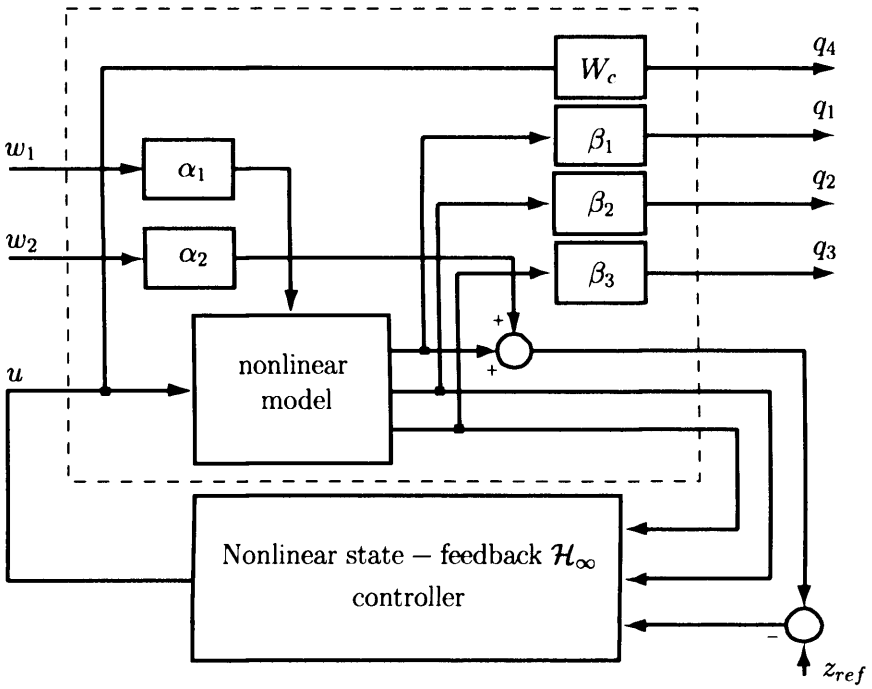

Figure 9.2: State-feedback control configuration.

notations of local dissipativity and supply power are used. This is described below.

9.1.2 Dissipative dynamical systems

While the exact nature of the disturbance inputs ($w = [w_1, w_2]$) to the suspended system are unknown, the assumption made here is that even in the worst-case their energy is bounded, i.e.

$$\|w\|_2^2 = \int_0^T \|w(t)\|^2 \, dt < \infty$$

for a finite T. This is consistent with design objectives of the $\mathcal{H}_\infty$ theory, i.e. to maintain the energy of the output signal within a finite limit. The nonlinear $\mathcal{H}_\infty$ design process developed here aims to identify a feedback controller that satisfies the L_2-gain inequality [98]

$$\int_0^T \|q(t)\|^2 \, dt \leq \gamma^2 \int_0^T \|w(t)\|^2 \, dt \tag{9.4}$$

by keeping the energy of the penalty vector q bounded and smaller than the energy of the disturbance input ($0 < \gamma \leq 1$). When $w = \hat{w}$ =worst-case disturbance input in Eqn. 9.4, the L_2-gain in this equation becomes the time-domain equivalent of the infinity-norm of

the system (Eqn 6.4, page 89). Because of this bounded energy notion, the core of the theoretical derivations in this chapter uses the notion of energy, *dissipativity* and *storage functions*. A system is called dissipative if the rate of increase in its stored energy is not greater than the supplied power. Typical examples of dissipative systems are electrical networks, where part of the electrical energy is dissipated in the resistors in the form of heat. Often the latter would be called passive systems [99]. The special interest in dissipative systems, from a control point of view, comes also from their implication on the stability investigated via Lyapunov methods. Under some assumptions about the storage functions, dissipative systems are stable systems [100].

Dissipative systems are typically associated with a supply rate(=input power) and a stored function(=stored energy). The supply rate is a function of the inputs and the outputs of the system and for the nonlinear Maglev system in Eqns. 9.2 and 9.3, the supply rate can be defined as [101, 102, 103, 104, 98]

$$s(w,z) = \gamma^2 \|w\|^2 - \|q\|^2 \tag{9.5}$$

A system is said to be locally dissipative with respect to this supply rate, if there exists a nonnegative smooth storage function $V(x)$ with $V(0) = 0$, such that

$$\begin{aligned} V(x(T)) - V(x(0)) &\leq \int_0^T s(w,q)dt \\ \text{or} \quad \underbrace{\frac{\partial V(x)}{\partial x}}_{V_x(x)} \dot{x}(t) &\leq \gamma^2 \|w\|^2 - \|q\|^2 \end{aligned} \tag{9.6}$$

This is the energy-balancing equation and in practical terms, this inequality may be interpreted as follows: a system is dissipative with respect to its supply rate if the rate of increase of stored energy is not higher than the supplied power. Substitution of $\dot{x}$ and q from Eqn. 9.2 and 9.3 transforms Eqn. 9.6 into the Hamilton-Jacobi-Isaacs (HJI) inequality [105]

$$\underbrace{V_x(x)^T [A(x) + B_1(x)w + B_2(x)u] + [C_1(x) + D_{12}(x)u]^T [C_1(x) + D_{12}(x)u] - \gamma^2 w^T w}_{\text{Hamiltonian function: } H[x,V_x(x),w,u]} \leq 0 \tag{9.7}$$

The premise of the design algorithms developed in the following sections is that any feedback control law u that satisfies the HJI inequality will lead to a closed-loop system that is locally dissipative with respect to its supply rate. As local dissipativity implies the existence of a storage function $V(x)$, the $\mathcal{H}_\infty$ design in this context may be recast as the problem of deriving the control law and the corresponding storage function which satisfy Eqn. 9.7. Two specific feedback structures are considered here: state feedback (Fig. 9.2) and output

feedback in conjunction with a state estimator (Fig. 9.5). The estimator parameters for the latter is also derived through a HJI inequality corresponding to the augmented system (= open-loop system plus the estimator) [106, 98, 104, 105].

9.2 Non-linear $\mathcal{H}_\infty$ state-feedback

The general control configuration of the closed-loop system with the nonlinear state-feedback is shown in Fig. 9.2. As the primary design objective is to suppress the effects of the unknown disturbance signal $w = [w_1, w_2]^T$, from an application view point it is sufficient to ensure that Eqn. 9.7 is satisfied under worst case disturbance. Since the $H[x, V_x(x), w, u]$ in Eqn. 9.7 is a quadratic function in terms of w and u, it has a unique local saddle point in (w, u) for each (x, V_x) and unique smooth functions $\hat{w}(x, V_x^T)$ and $\check{u}(x, V_x^T)$ exist in the neighbourhood of $(x, V_x(x), w, u) = (x_0, 0, 0, 0)$ [105]. These two functions are derived below.

9.2.1 Derivation of the controller

(*i*) *Derivation of the worst case disturbance signal*: Differentiating the Hamiltonian function $H(x, V_x(x), w, u)$ in Eqn. 9.7 with respect to w gives

$$\frac{\partial H[x, V_x(x), w, u]}{\partial w} = B_1^T(x)V_x(x) - 2\gamma^2 w = 0$$

Choosing $\gamma > 0$, the solution for the disturbance signal may be derived as

$$\hat{w}\{x, V_x(x)\} \quad = \tfrac{1}{2}\gamma^{-2}B_1(x)^T V_x(x) \tag{9.8}$$

Since

$$\left.\frac{\partial^2 H[x, V_x(x), w, u]}{\partial w^2}\right|_{w=\hat{w}} = -2\gamma^2 I$$

$\hat{w}(x, V_x)$ maximises $H[x, V_x(x), w, u]$ and represents the worst-case disturbance signal. The Hamiltonian function corresponding to this worst case disturbance input can be derived by substitution of $\hat{w}(x, V_x)$ in $H[x, V_x(x), w, u]$ to get $H[x, V_x(x), \hat{w}\{x, V_x(x)\}, u]$.

(*ii*) *Derivation of the control input under the worst case disturbance signal*:
To derive the optimal control law, $H[x, V_x(x)\hat{w}\{x, V_x(x)\}, u]$ is differentiated with respect to u.

$$\frac{\partial H[x, V_x(x), \hat{w}\{x, V_x(x)\}, u]}{\partial u} = B_2^T(x)V_x(x) + 2C_1^T(x)D_{12}(x) + 2D_{12}^T(x)D_{12}(x)u = 0$$

The solution to the right-hand side of the above equation gives

$$\check{u}\{x, V_x(x)\} = -\tfrac{1}{2}\left(D_{12}(x)^T D_{12}(x)\right)^{-1}\left(B_2(x)^T V_x(x) + C_1^T(x) D_{12}(x)\right) \tag{9.9}$$

Since

$$\left.\frac{\partial^2 H[x, V_x(x), \hat{w}\{x, V_x(x)\}, u]}{\partial u^2}\right|_{u=\check{u}} = 2D_{12}(x)^T D_{12}(x)$$

$\check{u}(x, V_x(x))$ minimises $H[x, V_x(x), \hat{w}\{x, V_x(x)\}, u]$ and may be taken as the optimal control signal ($D_{12}(x)$ is positively definite by selecting $W_c > 0$ in Eqn. 9.3). Substituting $\check{u}(x, V_x(x))$ in $H[x, V_x(x), \hat{w}\{x, V_x(x)\}, u]$ transforms the Hamiltonian function in Eqn. 9.7 to $H[x, V_x, \hat{w}\{x, V_x(x)\}, \check{u}\{x, V_x(x)\}]$.

As $\check{u}(x, V_x(x))$ minimises $H[x, V_x(x), \hat{w}\{x, V_x(x)\}, u]$ and $\hat{w}(x, V_x)$ maximises $H[x, V_x(x), w, u]$, these two optimal solutions identify a saddle point in $H[x, V_x(x), w, u]$ such that

$$H[x, V_x(x), w, u] \leq H[x, V_x(x), \hat{w}\{x, V_x(x)\}, \check{u}\{x, V_x(x)\}] \leq H[x, V_x(x), \hat{w}\{x, V_x(x)\}, u]$$

and therefore $\check{u}$ is the optimal control law that satisfies the HJI inequality. To derive the only remaining unknown, the storage function $V(x)$, $\hat{w}$ and $\check{u}$ are substituted in Eqn. 9.7. For numerical convenience, the state-space matrices for the Maglev model are constructed such that $C_1(x)^T D_{12}(x) = 0$ and the notation $D(x) = \left(D_{12}(x)^T D_{12}(x)\right)$ is used. Applying the optimal values for w and u gives the following form for the HJI inequality

$$\underbrace{V_x^T(x)A(x) - \check{u}^T D(x)\check{u} + \gamma^2 \hat{w}^T \hat{w} + C_1(x)^T C_1(x)}_{H_*[x, V_x(x)]} \leq 0 \tag{9.10}$$

9.2.2 Solution to the Hamilton-Jacobi-Isaacs inequality

While an analytical solution of the above equation is not readily available, for the numerical work the nonlinear form of Eqn. 9.10 may be transformed into an infinite sum by replacing the individual terms by their respective Taylor series. This approach was originally proposed by Al'brekht [107], adopted in [108] and subsequently used by various authors, eg. [109]. Thus if the storage function $V(x)$ and its derivative $V_x(x)$ are assumed to have the form

$$\begin{aligned} V(x) &= V^2(x) + V^3(x) + \cdots = \textstyle\sum_{k=1}^{\infty} V^{k+1}(x), \\ V_x(x) &= V_x^2(x) + V_x^3(x) + \cdots = \textstyle\sum_{k=1}^{\infty} V_x^{k+1}(x) \end{aligned} \tag{9.11}$$

then the corresponding feedback control signal $\check{u}(x)$ and the worst-case disturbance input $\hat{w}(x)$ may be expressed as

$$\begin{aligned} \check{u}(x) &= \check{u}^1 x + \check{u}^2(x) + \cdots = \textstyle\sum_{k=1}^{\infty} \check{u}^k(x), \\ \hat{w}(x) &= \hat{w}^1 x + \hat{w}^2(x) + \cdots = \textstyle\sum_{k=1}^{\infty} \hat{w}^k(x) \end{aligned} \tag{9.12}$$

where the superscript indicates the order of the expansion in the Taylor series. Thus, instead of deriving one single nonlinear storage function and a corresponding nonlinear controller, the algorithm developed here derives the individual terms in the expansion of $V(x)$, $\check{u}(x)$ and $\hat{w}(x)$, offering a unified framework for the derivation of a whole class of controllers by collecting the appropriate terms in the series expansion of $\check{u}(x)$. For example, the *first order controller* $\check{u} = \check{u}^1$ (= linear control law) is readily constructed from $V^2(x)$, and the *second order controller* $\check{u} = \check{u}^1 + \check{u}^2$ (= nonlinear control law) requires $V^2(x)$ and $V^3(x)$. The process continues in a similar manner for higher order nonlinear control laws. In the process of solving the HJI inequality, the parameters of the open-loop model in Eqns. 9.2 and 9.3 are also expanded in their Taylor series around the initial state vector x_0 (= nominal operating point) as

$$\begin{aligned} A(x) &= A^1(x_0) + A^2(x) + \cdots \\ B_1(x) &= B_1^1(x_0) + B_1^2(x) + \cdots \\ B_2(x) &= B_2^1(x_0) + B_2^2(x) + \cdots \\ C_1(x) &= C_1^1(x_0) + C_1^2(x) + \cdots \end{aligned} \tag{9.13}$$

The numerical forms of these equations are given on page 228. Substitution of these in Eqn. 9.10 gives the k-th power term in the infinite summation form of the HJI

$$V_x^2(x)^T A^k(x) + V_x^2(x)^T A^{(k-1)}(x) + \cdots + V_x^{k+1}(x)^T A^1 x - \check{u}^{1T} D \check{u}^k - \check{u}^{2T} D \check{u}^{k-1} - \cdots - \check{u}^{kT} D \check{u}^1 +$$

$$\gamma^2 \hat{w}^{1T} \hat{w}^k + \gamma^2 \hat{w}^{2T} \hat{w}^{k-1} + \cdots + \gamma^2 \hat{w}^{kT} \hat{w}^1 + C_1^{kT}(x) C_1^k(x) \leq 0 \tag{9.14}$$

where

$$\begin{aligned} \hat{w}^k &= \tfrac{1}{2}\gamma^{-2} \left[B_1^{1T} V_x^{k+1}(x) + B_1^{2T} V_x^k(x) + \cdots + B_1^{kT}(x) V_x^2(x) \right] \\ \check{u}^k &= -\tfrac{1}{2} D^{-1} \left[B_2^{1T} V_x^{k+1}(x) + B_2^{2T} V_x^k(x) + \cdots + B_2^{kT}(x) V_x^2(x) \right] \end{aligned} \tag{9.15}$$

First-order controller

To derive the first-order controller ($k = 1$), for convenience the first term in the expansion of the storage function is chosen to be have the quadratic form $V^2(x) = x^T \mathbf{P} x$, where the matrix $\mathbf{P} \in R^{n \times n}, \mathbf{P} > 0$, $\mathbf{P} = \mathbf{P}^T$ is unknown. With this storage function, the first order $\check{u}^1$ and $\hat{w}^1$ ($k = 1$ in Eqn. 9.15) become

$$\begin{aligned} \check{u}^1 &= -\tfrac{1}{2}(D_{12}^T D_{12})^{-1} B_2^{1T} \mathbf{P} x \\ \hat{w}^1 &= \tfrac{1}{2}\gamma^{-2} B_1^{1T} \mathbf{P} x \end{aligned} \tag{9.16}$$

These control laws are identical to the state-feedback control laws derived in Chapter 6 for the linear $\mathcal{H}_\infty$ problem (Eqn. C.21, page 284 with the assumption that $D_{12}^T C_1 = 0$). To find

the storage function $V(x)$, the first-order HJI equation (Eqn 9.14) reduces to the following Riccati equation

$$A^{1T}\mathbf{P} + \mathbf{P}A^1 + \mathbf{P}(\gamma^{-2}B_1^1 B_1^{1T} - B_2^1 D^{-1} B_2^{1T})\mathbf{P} + C_1^{1T}C_1^1 = 0 \tag{9.17}$$

This equation is also identical to the Riccati equation associated with the linear state-feedback $\mathcal{H}_\infty$ control law derived in Chapter 6 (Eqn. C.20). The solution of Eqn. 9.17 gives $\mathbf{P}$, and hence $\check{u}^1$ and $\hat{w}^1$.

Higher-order controllers

To derive the second-order controller, the procedure continuous with $k = 2$. The second-order HJI equation becomes

$$V_x^2(x)^T A^2(x) + V_x^3(x)^T A^1 x - \check{u}^{1T} D \check{u}^2 - \check{u}^{2T} D \check{u}^1 + \gamma^2 \hat{w}^{1T} \hat{w}^2 + \gamma^2 \hat{w}^{2T} \hat{w}^1 = 0 \tag{9.18}$$

where $V^3(x)$ is unknown, and $\hat{w}^2$ and $\check{u}^2$ being given by ($k = 2$ in Eqn. 9.15)

$$\begin{aligned} \check{u}^2 &= -\tfrac{1}{2}(D_{12}^T D_{12})^{-1} \left[B_2^{1T} V_x^3(x) + B_2^{2T}(x) V_x^2(x) \right] \\ \hat{w}^2 &= \tfrac{1}{2}\gamma^{-2} \left[B_1^{1T} V_x^3(x) + B_1^{2T}(x) V_x^2(x) \right] \end{aligned} \tag{9.19}$$

Substituting $\check{u}^2$ and $\hat{w}^2$ in the second-order HJI equation in Eqn. 9.18 and rearranging the terms lead to

$$V_x^3(x) A_* x = -V_x^2(x) \left[A^2(x) - B_2^{2T}(x) \check{u}^1 - B_1^{2T}(x) \hat{w}^1 \right] \tag{9.20}$$

where

$$A_* = (A^1 x + B_2^{1T} \check{u}^1 + B_1^{1T} \hat{w}^1) \tag{9.21}$$

To solve Eqn. 9.20, the unknown $V^3(x)$ is taken to be a cubic homogeneous function. For example, for a system with three state variables such as the Maglev model, it has the following form

$$V^3(x) = c_1 x_1^3 + c_2 x_1^2 x_2 + c_3 x_1^2 x_3 + \cdots + c_9 x_2 x_3^2 + c_{10} x_3^3 \tag{9.22}$$

Differentiating the above function versus x gives with

$$\frac{\partial V^3(x)}{\partial x} = V_x^3(x) = \begin{bmatrix} 3c_1 x_1^2 + 2c_2 x_1 x_2 + 2c_3 x_1 x_3 + c_4 x_2^2 + c_5 x_2 x_3 + c_6 x_3^2 \\ c_2 x_1^2 + 2c_4 x_1 x_2 + c_5 x_1 x_3 + 3c_7 x_2^2 + 2c_8 x_2 x_3 + c_9 x_3^2 \\ c_3 x_1^2 + c_5 x_1 x_2 + 2c_6 x_1 x_3 + c_8 x_2^2 + 2c_9 x_2 x_3 + 3c_{10} x_3^2 \end{bmatrix} \tag{9.23}$$

Substituting $V_x^3(x)$ in Eqn. 9.20 and equating similarly power terms on both sides leads to a set of simultaneous equations in terms of the unknown coefficients c_i. The solution to

this set of linear equations gives c_i. Substituting these coefficients in Eqn. 9.23 gives $V_x^3(x)$ and in turn the second order term in Eqn. 9.12

$$\check{u}^2(x) = -\frac{1}{2}(D_{12}^T D_{12})^{-1}\left[B_2^{1T}V_x^3(x) + B_2^{2T}(x)V_x^2(x)\right] \tag{9.24}$$

The second-order controller thus becomes

$$\check{u}(x) = \check{u}^1 + \check{u}^2 = -\frac{1}{2}(D_{12}^T D_{12})^{-1}\left[B_2^{1T}\mathbf{P}x + B_2^{1T}V_x^3(x) + B_2^{2T}(x)V_x^2(x)\right]$$

The above process may be continued with increasing values of k to derive $V^{k+1}(x)$ and $\check{u}^k$. For the sake of brevity, only first and second order controllers are considered here for the Maglev system. Simulation studies have shown that higher-order controllers (>2) have a moderate improvement over the suspension characteristics but are associated with computational and implementation difficulties.

9.2.3 Algorithm for deriving non-linear state-feedback $\mathcal{H}_\infty$ controllers

Using the derivation steps above, the algorithm for deriving non-linear state-feedback $\mathcal{H}_\infty$ controllers is summarised below

- **Step 1** Use the nonlinear model in Eqn. 9.1 and Eqn. 9.3 and a set of initial conditions (z_0, i_0) to derive the first-order and the second-order terms in the Taylor series expansion of the system (Eqn. 9.13). The results are: A^1, $A^2(x)$, B_1^1, $B_1^2(x)$, B_2^1, $B_2^2(x)$, C_1^1.

- **Step 2** Construct the first-order Riccati equation in Eqn. 9.17. Solve this equation to determine $\mathbf{P}$, $\mathbf{P} > 0$.

- **Step 3** Use $\mathbf{P}$ as computed above in Eqn. 9.16 to derive the first-order control output $\check{u}^1$ and the worst-case disturbance $\hat{w}^1$.

- **Step 4** Use $\mathbf{P}$ computed in Step 2 to derive $V^2(x) = x^T\mathbf{P}x$ and $V_x^2(x) = dV(x)/dx = 2\mathbf{P}x$. Use these two functions and the series expansions of the non-linear system to construct the right-hand-side in the second-order HJI equation in Eqn. 9.20.

- **Step 5** Construct the closed-loop system A_* in Eqn. 9.21 using A^1, $\hat{u}^1$ and $\check{w}^1$ as computed above.

- **Step 6** Construct the third-order storage function $V(x)^3$ using the polynomial form in Eqn. 9.22. In this equation c_i, $i = 1..10$ are unknown coefficients. Compute the gradient of this equation versus x to get $V_x^3(x)$ in Eqn. 9.23.

- **Step 7** Construct the second-order HJI equation in Eqn. 9.20. Use this equation to construct a system of ten equations by collecting terms with equal powers in x. Solve these ten equations to find the unknown coefficients c_i, $i = 1..10$ and consequently the third-order storage function $V^3(x)$ and its gradient $V_x^3(x)$ (Eqn. 9.23).

- **Step 8** Use $V_x^3(x)$ as computed above and $V_x^2(x)$ from Step 4 in Eqn. 9.19 to construct the second-order term $\breve{u}^2$ in the nonlinear controller. Use this solution and $\breve{u}^1$ from Step 3 to construct the nonlinear state-feedback $\mathcal{H}_\infty$ controller: $\breve{u} = \breve{u}^1 + \breve{u}^2$.

- **Step 9** End of the algorithm.

The application for this algorithm on Maglev is presented below.

9.2.4 Application to Maglev model

To derive the state-feedback controller, a set of Matlab Matlab routines have been developed. Because of the analytical nature of the derivations, the Symbolic Toolbox for Matlab has been used [95]. The software allows the design of controllers for a general class of nonlinear systems. The inputs to the program are the open-loop model of the system (Eqn. 9.2 and Eqn. 9.3) and the design parameters α, β and W_c. The individual terms in the series in Eqn. 9.13 are computed internally for a given set of initial conditions. The full listing of the source code is included in Appendix G.

For the experimental Maglev system in Eqn. 9.1 the first two terms in their corresponding Taylor's series expansion in Eqn. 9.13 with nominal operating point $x_0 = [z_0, \dot{z}_0, i_0]$ become:

First-order term in $A(x)$:

$$A^1 x = \begin{bmatrix} 0 & 1 & 0 \\ \frac{\mu_0 N^2 A}{2m}\frac{i_0^2}{z_0^3} & 0 & -\frac{\mu_0 N^2 A}{2m}\frac{i_0}{z_0^2} \\ (\frac{-2\mathrm{R}}{\mu_0 N^2 A} - \frac{\dot{z}_0}{z_0^2})i_0 & \frac{i_0}{z_0} & \frac{-2\mathrm{R}}{\mu_0 N^2 A} z_0 + \frac{\dot{z}_0}{z_0} \end{bmatrix} \begin{bmatrix} x_1 \\ x_2 \\ x_3 \end{bmatrix}$$

Second-order term in $A(x)$:

$$A^2(x) = \begin{bmatrix} 0 \\ -\frac{3\mu_0 N^2 A}{4m}\frac{i_0^2}{z_0^4}x_1^2 - \frac{\mu_0 N^2 A}{4m}\frac{1}{z_0^2}x_3^2 + \frac{\mu_0 N^2 A}{m}\frac{i_0}{z_0^3}x_1 x_3 \\ -\frac{i_0}{z_0^2}x_1 x_2 + (\frac{-2\mathrm{R}}{\mu_0 N^2 A} - \frac{\dot{z}_0}{z_0^2})x_1 x_3 + \frac{1}{z_0}x_2 x_3 + \frac{\dot{z}_0 i_0}{z_0^3}x_1^2 \end{bmatrix}$$

First-order term in $B_1(x)$ and $B_2(x)$

$$[B_1^1 \mid B_2^1] = \left[\begin{array}{cc|c} 0 & 0 & 0 \\ \frac{1}{m}\alpha_1 & 0 & 0 \\ 0 & 0 & \frac{2}{\mu_0 N^2 A} z_0 \end{array}\right]$$

Second-order term in $B_1(x)$ and $B_2(x)$

$$[B_1^2 \mid B_2^2] = \left[\begin{array}{c|c} 0 & 0 \\ 0 & 0 \\ 0 & \frac{2}{\mu_0 N^2 A}(x_1 - z_0) \end{array}\right]$$

First- and second-order terms in $C_1(x)$ and $C_2(x)$

$$C_1^1 = \begin{bmatrix} \beta_1 & 0 & 0 \\ 0 & \beta_2 & 0 \\ 0 & 0 & \beta_3 \\ 0 & 0 & 0 \end{bmatrix}, \quad C_1^2 = 0, \quad C_2^1 = [1 \;\; 0 \;\; 0]^T, \quad C_2^1 = 0$$

First- and second-order terms in $D_{12}(x)$ and $D_{21}(x)$

$$D_{12}^1 = [0 \;\; 0 \;\; 0 \;\; W_c]^T, \quad D_{21}^1 = [0 \;\; \alpha_2], \quad D_{12}^2 = 0, \quad D_{21}^2 = 0$$

First order controller

For the derivation of the first-order state-feedback controller, the nominal point is specified at

$$[z_0(t) \; \dot{z}_0(t) \; i_0(t)] = [4.0 \times 10^{-3} \;\; 0.0 \;\; 3.13].$$

Initially, the design parameters are chosen at $\alpha_1 = 1$, $\beta_1 = 1$, $W_c = 0.12$ and $\gamma = 1$. The nonlinear Maglev model in Eqn. 9.1 is derived using the parameters in Chapter 2

$$\begin{aligned} \dot{x}_1 &= x_2 \\ \dot{x}_2 &= -0.1681413334 \times 10^{-4} \frac{x_3^2}{x_1^2} + 0.6666666667 w_1 \\ \dot{x}_3 &= -136512.1406 x_1 x_3 + \frac{x_3 x_2}{x_1} + 19824.59201 x_1 u \end{aligned}$$

This model is linearised around the nominal operating point to get

$$A^1 = \begin{bmatrix} 0.0 & 1.0 & 0.0 \\ 10060.72443 & 0.0 & -6.952129418 \\ -1283745.024 & 1447.142858 & -955.5849842 \end{bmatrix}$$

$$B_1^1 = [0.0 \;\; 0.6666666667 \;\; 0.0]^T \quad B_2^1 = [0.0 \;\; 0.0 \;\; 138.7721441]^T$$

These matrices are substituted in Eqn. 9.17. The resultant Riccati equation is solved in Matlab to get

$$\mathbf{P} = \begin{bmatrix} 55198.07124 & 639.9428407 & -4.760108817 \\ 639.9428407 & 7.582268928 & -0.5293414249 \times 10^{-1} \\ -4.760108817 & -0.5293414249 \times 10^{-1} & 0.1084364426 \times 10^{-2} \end{bmatrix} \tag{9.25}$$

$\mathbf{P}$ is positive definite and hence a suitable candidate for the construction of the storage function. With $V_x^2(x) = 2\mathbf{P}x$, the first-order linear control law in Eqn. 9.16 is derived

$$\breve{u}^1(x) = 26213.11534 x_1 + 291.499383 x_2 - 5.9714118 x_3 \tag{9.26}$$

and the worst-case disturbance as (Eqn. 9.16)

$$\hat{w}^1(x) = [\hat{w}_1^1(x), \hat{w}_2^1(x)] = [426.62856 x_1 + 5.054846 x_2 - 0.352894283 \times 10^{-1} x_3, \;\; 0]^T$$

Second-order control law

To derive the second-order term in the feedback controller, the storage function V^3 is considered to take the following form

$$V^3(x) = c_1x_1^3 + c_2x_1^2x_2 + c_3x_1^2x_3 + c_4x_1x_2^2 + c_5x_1x_2x_3 + c_6x_1x_3^2 + c_7x_2^3 + c_8x_2^2x_3 + c_9x_2x_3^2 + c_{10}x_3^3$$

This function is differentiated with respect to x to get

$$V_x^3(x) = \begin{bmatrix} 3c_1x_1^2 + 2c_2x_1x_2 + 2c_3x_1x_3 + c_4x_2^2 + c_5x_2x_3 + c_6x_3^2 \\ c_2x_1^2 + 2c_4x_1x_2 + c_5x_1x_3 + 3c_7x_2^2 + 2c_8x_2x_3 + c_9x_3^2 \\ c_3x_1^2 + c_5x_1x_2 + 2c_6x_1x_3 + c_8x_2^2 + 2c_9x_2x_3 + 3c_{10}x_3^2 \end{bmatrix} \tag{9.27}$$

Using B_1^1 and B_2^1 as derived above, and the first-order solutions $\check{u}^1$ and $\hat{w}^1$, Eqn. 9.21 is used to derive the closed-loop state matrix of the first-order problem

$$A_* = (A^1x + B_2^{1T}\check{u}^1 + B_1^{1T}\hat{w}^1) = \begin{bmatrix} 0.0 & 1.0 & 0.0 \\ 5432.118506 & 3.369897302 & -6.602055955 \\ 1750497.228 & 23897.92535 & -1019.571770 \end{bmatrix}$$

Since the eigenvalues of this matrix are negative, the closed-loop Maglev system with the first-order state-feedback controller is stable. To continue with the derivations, this matrix and the gradient of the storage function, V_x^3 in Eqn. 9.27 are used to construct the left-hand-side in Eqn. 9.20. In this equation, $V_x^2 = 2x^T\mathbf{P}$, B_1^2 and B_2^2 are derived above and the numerical form of $A^2(x)$ is calculated below

$$A^2(x) = \begin{bmatrix} 0.0 \\ -1930387.3x_1^2 - 1.050883334x_3^2 + 3289.264835x_1x_3 \\ -195625.0x_2x_1 - 136512.1406x_1x_3 + 250.0x_2x_3 \end{bmatrix}$$

Substitution of the above terms in Eqn. 9.20 generates a homogeneous function of degree three in x_1, x_2 and x_3 on each side of Eqn. 9.20. Equating terms with equal powers lead to a set of ten simultaneous equations. A routine using the Gauss-Seidel elimination method for the solution of these equations (included with the symbolic program indicated earlier) generated the following coefficients for the Maglev system

$$\begin{array}{lll} c_1 = 1.2889 \times 10^7 & c_2 = 3.9820 \times 10^5 & c_3 = 1.7574 \times 10^2 \\ c_4 = 1.8152 \times 10^3 & c_5 = -2.0861 \times 10^1 & c_6 = -7.9762 \times 10^{-1} \\ c_7 = -1.2719 \times 10^1 & c_8 = -7.0574 \times 10^{-2} & c_9 = -5.7758 \times 10^{-3} \\ c_{10} = 4.8840 \times 10^{-5} & & \end{array}$$

With the above values of c_i, $V_x^3(x)$ in (Eqn. 9.23) and $\mathbf{P}$ derived earlier, Eqn. 9.24 generates the second order term in Eqn. 9.12 as

$$\begin{aligned} \check{u}^2(x) = \; & -483882.9537x_1^2 + 57438.22080x_1x_2 + 4392.370457x_1x_3 + \\ & 194.3201504x_2^2 + 31.80633378x_2x_3 - 0.4034296096x_3^2 \end{aligned}$$

Combining this equation with Eqn. 9.26 yields the second-order nonlinear state-feedback control law

$$\begin{aligned}\check{u}(x) = \check{u}^1(x) + \check{u}^2(x) = \; & 26213.11534x_1 + 291.4993829x_2 - 5.971411760x_3 - \\ & 483882.9537x_1^2 + 57438.22080x_1x_2 + 4392.370457x_1x_3 + \\ & 194.3201504x_2^2 + 31.80633378x_2x_3 - 0.4034296096x_3^2\end{aligned} \tag{9.28}$$

The expression for $\hat{w}^2$ is also generated at this stage but not included as it is required for the derivation of $V_x^4(x)$ and the third order controller.

9.2.5 Simulation results

To assess the behaviour of the closed-loop system with the state-feedback $\mathcal{H}_\infty$ controller, a simulation model for Simulink was constructed. This is shown in Fig. 9.3 and uses the nonlinear dynamic system in Fig. 9.1 and the nonlinear state-feedback controller in Eqn. 9.28 with the coefficients below

$$\begin{array}{lll} k(1) = 26213.11534 & k(2) = 291.4993829 & k(2) = -5.97141176 \\ k(4) = -483882.9619 & k(5) = 194.3201492 & k(6) = -0.403429607 \\ k(7) = 57438.21965 & k(8) = 4392.370468 & k(9) = 31.80633312 \end{array} \tag{9.29}$$

A step response of the closed-loop system to changes in the nominal operating airgap from 4 mm to 3 mm is shown in Fig. 9.4. This response indicates that the closed-loop system is dissipative around the operating point and hence stable. Furthermore, the new nonlinear $\mathcal{H}_\infty$ controller improves the settling time almost by a factor of two compared to the linear state-feedback controller (Fig. 2.7, page 23) and has lower damping than the linear $\mathcal{H}_\infty$ controller (Fig. 6.9, page 108). In contrast to the linear $\mathcal{H}_\infty$ controller, this compensator is suitable for practical implementation (results are presented in the following section). The reduction in overshoot suggests that within the definitions of linear systems, the infinity norm of the complimentary functions remain below the 0 dB boundary. The steady state error in the response is due to the absence of an integral action in the state-feedback controller. This can be compensated by an appropriate filter for the reference input.

The design parameters α_1 and α_2 are used to normalise the input disturbances. For the state-feedback design, α_1 is used to scale the force disturbances entering the system. For all experiments, $\alpha_1 = 1$. Similarly to the linear $\mathcal{H}_\infty$ control design (Chapter 6), the penalty on the control action is determined by W_c. Using the developments for the linear $\mathcal{H}_\infty$ design, this parameter was set to $W_c = 0.12$ for all experimental results to give an upper bound of +18.42 dB on the control signal. The design parameter γ determines the scale factor between the disturbance w and the penalty output q (Eqn 9.4). For all experiments in this chapter, γ is fixed at $\gamma = 1$ to give a dissipative closed-loop systems.

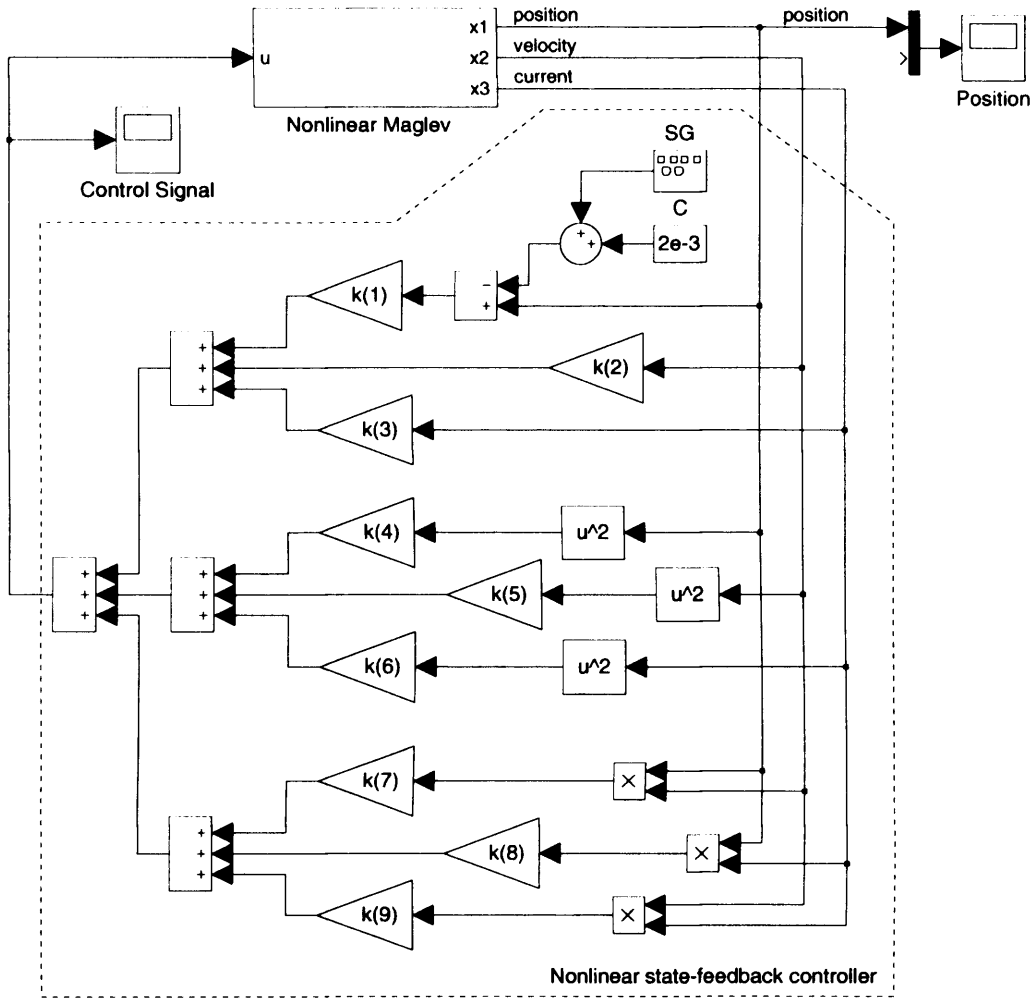

Figure 9.3: Simulink block-diagram used in the analysis of the nonlinear state-feedback $\mathcal{H}_\infty$ controller.

In contrast to the linear state-feedback $\mathcal{H}_\infty$ controller derived in Chapter 6, the nonlinear state-feedback controller does not use an additional transfer function as performance weights in the design ($W(s)$ for the linear $\mathcal{H}_\infty$ design). The developments and the numerical results are thus suitable for practical implementation. The corespondent experimental results are discussed in Section 9.4.2. In the next section, a design procedure for deriving nonlinear output-feedback controllers using the dissipation principles is derived. This controller can be used for Maglev applications (magnetic bearing for example) where only a position transducer is used for feedback.

9.3 Nonlinear output-feedback $\mathcal{H}_\infty$ controller

9.3.1 Derivation of the controller

Although all three state variables are available for feedback in a Maglev vehicle suspension system, the above results are extended to output feedback for two reasons: (a) use of $\mathcal{H}_\infty$

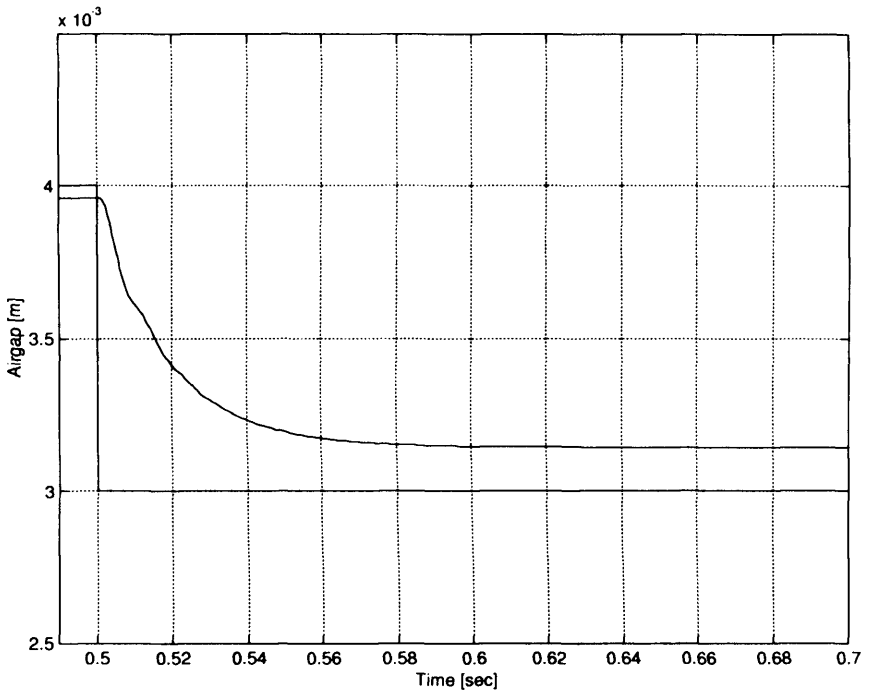

Figure 9.4: Simulated transient response due to a step change from 4 mm to 3 mm in the operational airgap and the nonlinear state-feedback controller.

controllers to other Maglev systems, such as a magnetic bearings which usually employ only position sensors, and (b) provide a basis for further work related to sensor fault accommodation in Maglev vehicles. The output feedback control law derived here uses a state estimator in conjunction with the same state feedback control laws from the previous section (Fig. 9.5). For compatibility with the numerical analysis, the nonlinear observer design method based on the concept of local dissipation has been adopted [105]. The full order state estimator used in this context has the following structure

$$\begin{aligned} \dot{\tilde{x}} &= A(\tilde{x}) + B_1(\tilde{x})w + B_2(\tilde{x})u + \mathbf{Q}(\tilde{x})(y - \tilde{y}) \\ \tilde{y} &= C_2(\tilde{x}) + D_{21}w \end{aligned} \tag{9.30}$$

where $\tilde{x}$ is the estimator state vector, $\tilde{y}$ is the estimator output and $\mathbf{Q}(\tilde{x})$ is a weight matrix (*output injection gain* [105]) to be determined. The design task is to derive $\mathbf{Q}(\tilde{x})$ such that the overall system is asymptotically stable. This methodology is outlined below.

The overall configuration of the closed-loop system with estimator state feedback is shown in Fig. 9.5; the corresponding state equations for the augmented system are given below

$$\underbrace{\begin{bmatrix} \dot{x} \\ \dot{\tilde{x}} \end{bmatrix}}_{\dot{x}_{cl}} = \underbrace{\begin{bmatrix} A(x) + B_1(x)w + B_2(x)u \\ A(\tilde{x}) + B_1(\tilde{x})w + B_2(\tilde{x})u + \mathbf{Q}(\tilde{x})(y - \tilde{y}) \end{bmatrix}}_{F_{cl}(x_{cl},w)}$$

Following the procedure developed earlier, derivation of $\mathbf{Q}(x)$ is constrained by the existence of a non-negative storage function $N(x_{cl}) = N(x, \tilde{x})$ and dissipativity of the closed-loop

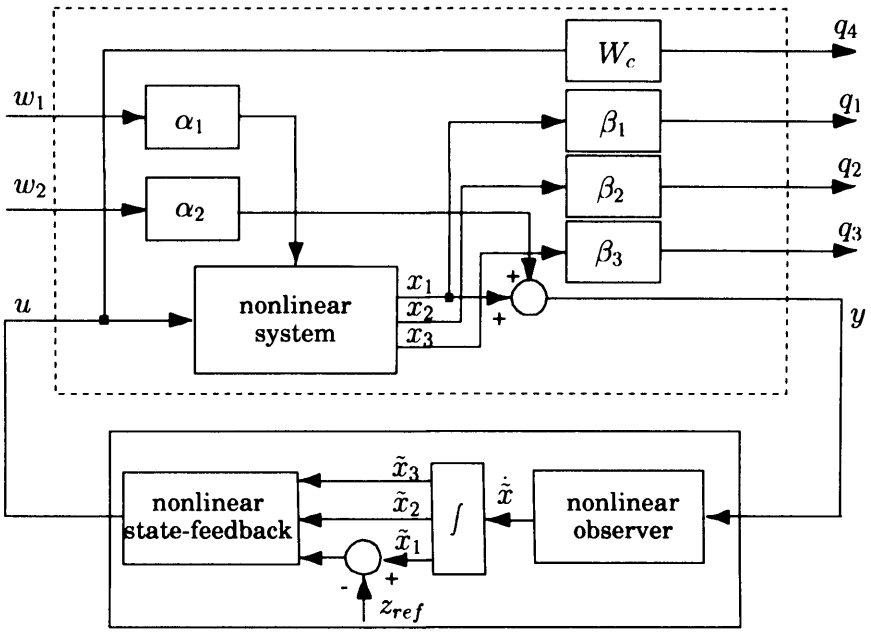

Figure 9.5: Output feedback control configuration.

system with respect to the supply rate in Eqn. 9.5. While the supply rate is dependent on the penalty vector and the disturbance, the structure of the supply rate does not change with the addition of the state estimator. Using Eqn. 9.7, existence of $N(x, \tilde{x})$ leads to to the HJI inequality [105]

$$\underbrace{\frac{\partial N(x,\tilde{x})}{\partial x}}_{N_x(x,\tilde{x})}\dot{x} + \underbrace{\frac{\partial N(x,\tilde{x})}{\partial \tilde{x}}}_{N_{\tilde{x}}(x,\tilde{x})}\dot{\tilde{x}} + q^T q - \gamma^2 w^T w \leq 0$$

The augmented system posses local dissipativity as long as the above inequality is satisfied. If the estimator is to have asymptotic stability in the locality of $\tilde{x} = 0$, [with $N_x(x,0) = N_x(x)$], then substituting for $\dot{x}$ from Eqn. 9.2 and $\dot{\tilde{x}}$ from Eqn. 9.30, with $N_{\tilde{x}}(x,0)\mathbf{Q}y = -Y^T(x,y)y$, the above inequality becomes [105]

$$\underbrace{N_x(x)[A(x) + B_1(x)w] - Y^T(x,y)y + q^T q - \gamma^2 w^T w}_{\text{Hamiltonian function: } M(x,N_x,w,Y)} \leq 0 \tag{9.31}$$

$Y^T(x,y)y$ is a vector of smooth functions that vanish at $y = 0$ [105]. To relate this inequality with the state feedback derivation, the following equivalent transformations are performed. First, $H(x, V_x, w, u = 0)$ in Eqn. 9.7 is added to and subtracted from to the right-hand-side of the above inequality

$$N_x(x)[A(x)+B_1(x)w]-Y^T(x,y)y+q^T q-\gamma^2 w^T w-H(x,V_x,w,0)+H(x,V_x,w,0) \leq 0 \tag{9.32}$$

Then using Eqns. 9.3 and Eqn. 9.7, Eqn. 9.32 simplifies to [with $u(\tilde{x}) = u(x) = 0$]

$$[N_x(x) - V_x(x)][A(x) + B_1(x)w] - Y^T(x,y)y + H(x,V_x,w,0) \leq 0$$

Since $H(x, V_x, w, 0) < H_*(x, V_x) \leq 0$, the above also implies the existence of the inequality below

$$\underbrace{[N_x(x) - V_x(x)][A(x) + B_1(x)w] - Y^T(x, y)y}_{M(x, N_x, w, Y) - H_*(x, V_x)} \leq 0 \tag{9.33}$$

and hence $M(x, N_x, w, Y) \leq 0$, i.e. the closed-loop system is dissipative at the equilibrium point. Since $e = x - \tilde{x} \rightarrow 0$ is the general requirement for the estimator design, combination of Eqns. 9.2 and 9.30 with $\tilde{x} = 0$ (equilibrium point) leads to the following identity

$$A(x) + B_1(x)w = \mathbf{Q}y$$

Substituting this equation in Eqn. 9.33 gives the following upper bound of Eqn. 9.33 [105]

$$[N_x(x) - V_x(x)]\mathbf{Q}(x) = Y^T(x, y) \tag{9.34}$$

This equation forms a basis for the derivation of $\mathbf{Q}(x)$.

Deriving $\mathbf{Q}(x)$

There are two stages in the estimator design: (a) derive $N(x)$ in Eqn. 9.34 and (b) use this storage function to compute $\mathbf{Q}(x)$. As w is the unknown disturbance, it is convenient first to estimate the value of w that maximises $M(x, N_x, w, Y)$ in Eqn. 9.31. Denoting the solution of

$$\frac{\partial M(x, N_x, w, Y)}{\partial w} = 0 \qquad \text{as} \quad w(x) = \hat{w}(x, N_x, Y) \tag{9.35}$$

Eqn. 9.31 indicates that

$$\partial^2 M(x, N_x, w, Y)/\partial w^2 < 0$$

Since $Y^T(x, y)$ in Eqn. 9.34 is also unknown, with the above value of $\hat{w}(x, N_x, Y)$, $M[x, N_x, \hat{w}(x, N_x, Y)), Y]$ is further differentiated versus Y

$$\frac{\partial M(x, N_x, w, Y)}{\partial Y} = 0 \tag{9.36}$$

to get the critical point $\check{Y}(x, N_x)$ where $M[x, N_x, \hat{w}(x, N_x, Y)), Y]$ is minimum. Denoting this minimum as $M[x, N_x, \hat{w}\{x, N_x, \check{Y}(x, N_x)\}, \check{Y}(x, N_x)]$, the following inequality can be established.

$$M[x, N_x, w, Y] \leq M[x, N_x, \hat{w}\{x, N_x, \check{Y}(x, N_x)\}, \check{Y}(x, N_x)] \leq M[x, N_x, \hat{w}\{x, N_x, Y\}, Y]$$

The above results corresponding to the critical points $\hat{w}(x, N_x, \check{Y}(x, N_x))$ and $\check{Y}(x, N_x)$ transforms Eqn. 9.33 into

$$M[x, N_x, \hat{w}\{x, N_x, \check{Y}(x, N_x)\}, \check{Y}(x, N_x)] - H_*(x, V_x) \leq 0 \tag{9.37}$$

This HJI inequality can be solved to derive $N_x(x)$. This $N(x)$ can be further used in

$$(N_x(x) - V_x(x))\,\mathbf{Q}(x) = \check{Y}^T(x, N_x(x)) \tag{9.38}$$

to compute the output injection gain $\mathbf{Q}(x)$. $V(x)$ is already known and corresponds to the storage function used in the derivation of the state feedback control law. The procedure for determining $N_x(x)$ is given below.

Solution to the HJI inequality

A possible numerical approach for the solution of Eqn. 9.37 is to expand $N(x)$ around the origin as

$$N(x) = N^2(x) + N^3(x) + \cdots$$

and then to substitute the individual terms in $M(x, N_x, w, Y)$ (Eqn. 9.31) along with the Taylor series expansions for the system's model (A_1, B_1, C_1, C_2 and D_{21}). Eqn. 9.37 may then be solved for $N^2(x), N^3(x)$, ..., individually, and the final solution of $N(x)$ obtained by adding all such individual solutions. This is then used to derive the complete value of $\mathbf{Q}$ which, in general, will have a nonlinear structure.

First order solution:

To derive the first order term $N^2(x)$, this function is assumed to have the following structure

$$N^2(x) = x^T\mathbf{R}x$$

where $\mathbf{R}$ is unknown and $N^2(x) = \partial N_x^2(x)/\partial x = 2x^T\mathbf{R}$. The problem reduces to solving Eqn. 9.37 for the unknown matrix $\mathbf{R}$ ($\mathbf{R} = \mathbf{R}^T$, $\mathbf{R} > 0$). To construct this equation, N_x^2 is substituted in Eqn. 9.31, together with the first-order expansion in the system's model, i.e. A^1, B_1^1, C_1^1 and C_2^1. The resultant Hamiltonian function $M(x, N_x, w, Y)$ is differentiated as per Eqn. 9.35 to get

$$\hat{w}\{x, N_x(x), Y\} = \tfrac{1}{2}\gamma^{-2}[2B_1^{1T}\mathbf{R}x - D_{21}^T Y(x, y)]$$

This signal is substituted back in Eqn. 9.31 and the new function $M(x, N_x, \hat{w}, Y)$ is differentiated in terms of $Y(x, y)$ to determine

$$\check{Y}\{x, N_x(x)\} = 2(D_{21}D_{21}^T)^{-1}(D_{21}B_1^{1T}\mathbf{R}x + \gamma^2 C_2^1 x)$$

The substitution of the above function in $M(x, N_x, \hat{w}, Y)$ together with $H_*(x, V_x)$ (Eqn. 9.10) are used to construct Eqn. 9.37. Since all terms in this equation are quadratic in x, after

rearrangements this first-order HJI inequality can be rewritten as a matrix Riccati equation of the form

$$A_R\mathbf{R} + \mathbf{R}A_R + \mathbf{R}B_R\mathbf{R} + C_R = 0 \tag{9.39}$$

where

$$\begin{aligned} A_R &= A^1 - B_1^1 D_{21}^T (D_{21} D_{21}^T)^{-1} C_2^1 \\ B_R &= \gamma^{-2}[B_1^1 B_1^{1T} - B_1^1 D_{21}^T (D_{21} D_{21}^T)^{-1} D_{21} B_1^{1T}] \\ C_R &= C_1^{1T} C_1^1 - H_* \end{aligned}$$

The solution $\mathbf{R}$ for this equation, and the solution for $\mathbf{P}$ in Eqn 9.17 provide a basis for computing the first-order $\mathbf{Q}$ in Eqn. 9.38

$$(\mathbf{R} - \mathbf{P})\mathbf{Q} = (D_{21} D_{21}^T)^{-1} (D_{21} B_1^{1T} \mathbf{R} + \gamma^2 C_2^1) \tag{9.40}$$

Although this $\mathbf{Q}$ is linear, the resulting observer is nonlinear due to the nonlinearities in the other terms in Eqn. 9.30. It has been observed that deriving higher-order terms in $\mathbf{Q}$ do not improve the general estimation quality of the observer and hence to simplify the complexity in the DSP implementation, only the first-order solution is considered for the Maglev work. This is demonstrated in the following section.

9.3.2 Algorithm for deriving non-linear output-feedback $\mathcal{H}_\infty$ controllers

Based on the mathematical developments in the previous section, the algorithm for deriving non-linear output-feedback $\mathcal{H}_\infty$ controllers is summarised below.

- **Step 1** Use the nonlinear model in Eqn. 9.1 and Eqn. 9.3 and a set of initial conditions (z_0, i_0) to derive the first-order and the second-order terms in the Taylor series expansion of the system as per Eqn. 9.13. The results are: $A^1, A^2(x), B_1^1, B_1^2(x), B_2^1, B_2^2(x), C_1^1$.

- **Step 2** Construct the first-order Riccati equation in Eqn. 9.17. Solve this equation to determine $\mathbf{P}$, $\mathbf{P} > 0$.

- **Step 3** Use $\mathbf{P}$ as computed above in Eqn. 9.16 to construct the first-order control output $\breve{u}^1$ and worst-case disturbance $\hat{w}^1$.

- **Step 4** Use $\mathbf{P}$ computed in Step 2 to construct $V^2(x) = x^T\mathbf{P}x$, $V_x^2(x) = 2\mathbf{P}x$ and H_* in Eqn. 9.17 (left-hand-side).

- **Step 5** Construct the Riccati equation for the estimation problem in Eqn. 9.39. Solve this equation to determine the unknown matrix $\mathbf{R}$, $\mathbf{R} > 0$.

- **Step 6** Use $\mathbf{R}$ as computed above and $\mathbf{P}$ as computed at Step 2 in Eqn. 9.40 to derive the output-injection gain $\mathbf{Q}$.
- **Step 7** Construct the nonlinear observer in Eqn. 9.30 using the nonlinear model of the system and $\mathbf{Q}$ as computed above.
- **Step 8** Combine the nonlinear observer and the nonlinear state-feedback controller as per Fig. 9.5 to construct the nonlinear $\mathcal{H}_\infty$ output-feedback controller.
- **Step 9** End of the algorithm.

Application of this algorithm to Maglev systems is described below.

9.3.3 Application to Maglev system

Computation of Q

To derive the output injection gain $\mathbf{Q}$ and the nonlinear observer in Fig. 9.5, the above design steps were coded in a set of symbolic routines for Matlab. These routines require the open-loop Maglev model and the design parameters α, β and W_c. The output is the nonlinear observer and the second-order nonlinear state-feedback controller. The full source code is given in Appendix G. Employing the parameters of the system A_1, B_1, C_2, D_{21} derived in Section 9.2.4 and H_* in Eqn. 9.10, the Riccati equation in Eqn. 9.39 is solved to get

$$\mathbf{R} = \begin{bmatrix} 9.6628 \times 10^{11} & -2.8380 \times 10^{7} & -9.3912 \times 10^{8} \\ -2.8379 \times 10^{7} & 2.4514 \times 10^{4} & -1.2372 \times 10^{5} \\ -9.3912 \times 10^{8} & -1.2372 \times 10^{5} & 2.4921 \times 10^{6} \end{bmatrix}$$

Using this value of $\mathbf{R}$, and $\mathbf{P}$ in Eqn. 9.25, $\mathbf{Q}$ is computed from Eqn. 9.40 to get

$$\mathbf{Q} = \begin{bmatrix} 8173.302 \\ 33.401 \times 10^{6} \\ 47.382 \times 10^{5} \end{bmatrix} \tag{9.41}$$

Nonlinear observer

To construct the observer in Eqn. 9.30, u and w are taken to be the first order terms ($\breve{u}^1$ and $\hat{w}^1$) as derived in Section 9.2.4 with $x = \tilde{x}$

$$\begin{aligned} \breve{u}^1(\tilde{x}) &= 26213.11534\tilde{x}_1 + 291.499383\tilde{x}_2 - 5.9714118\tilde{x}_3 \\ \hat{w}^1(\tilde{x}) &= [426.62856\tilde{x}_1 + 5.054846\tilde{x}_2 - 0.352894283 \times 10^{-1}\tilde{x}_3, \;\; 0]^T \end{aligned}$$

Substituting these equations in Eqn. 9.30, together with the Maglev model (Eqn. 9.1), yields the following observer dynamics

$$\begin{aligned} \dot{\hat{x}} &= A(\tilde{x}) + B_1(\tilde{x})\hat{w}^1(\tilde{x}) + B_2(\tilde{x})\breve{u}^1(\tilde{x}) + \mathbf{Q}(y - C_2(\tilde{x}) + D_{21}\hat{w}^1(\tilde{x})) \\ &= A(\tilde{x}) + \gamma^{-2}B_1B_1^{1T}\mathbf{P}\tilde{x} - D^{-1}B_2B_2^{1T}\mathbf{P}\tilde{x} - \mathbf{Q}C_2^1\tilde{x} + \gamma^{-2}\mathbf{Q}D_{21}B_1^{1T}\mathbf{P}\tilde{x} + \mathbf{Q}y \end{aligned}$$

Using the numerical form of **Q** derived in Eqn. 9.41 and the Maglev model in Eqn. 9.1, the following nonlinear state-observer is derived in a numerical form

$$\begin{aligned}
\dot{\tilde{x}}_1 &= -8173.303\tilde{x}_1 + \tilde{x}_2 + 8173.302y \\
\dot{\tilde{x}}_2 &= -33.4 \times 10^6\tilde{x}_1 + 7.992\tilde{x}_2 + 159 \times 10^{-3}\tilde{x}_3 + 0.168 \times 10^{-4}\frac{\tilde{x}_3^2}{\tilde{x}_1^2} + 33.401 \times 10^6 y \\
\dot{\tilde{x}}_3 &= -4738.236 \times 10^3\tilde{x}_1 + \frac{\tilde{x}_3\tilde{x}_2}{\tilde{x}_1} + 47.382 \times 10^5 y
\end{aligned} \tag{9.42}$$

Integration of these equations gives the estimator's output $\tilde{x} = [\tilde{x}_1, \tilde{x}_2, \tilde{x}_3]$ which can be used with the second order state-feedback controller (Eqn. 9.28) to construct the output-feedback control law $\breve{u}(\tilde{x})$ as in Fig. 9.5.

9.3.4 Simulation results

A Simulink block-diagram of the nonlinear observer in Eqn. 9.42 is shown in Fig. 9.6. The coefficients in this figure are given below

$$\begin{array}{lll}
\mathbf{Q}1 = 8173.3029 & \mathbf{Q}2 = 3340.0749 \times 10^4 & \mathbf{Q}3 = 4738236.7017 \\
G1 = 1.0 & G2 = 0.0 & G3 = 0.0 \\
G4 = -4.7382 \times 10^6 & G5 = -0.0159 & G6 = -1.6814 \times 10^{-5} \\
G7 = -3.3400 \times 10^7 & G8 = 7.9920 & G9 = 0.0 \\
G10 = 1.0 & G11 = -8.1733 \times 10^3 &
\end{array} \tag{9.43}$$

The nonlinear output-feedback controller is constructed from this observer and the nonlinear state-feedback controller in Eqn. 9.28. A Simulink block diagram of the closed-loop system is shown in Fig. 9.7. To compare to the previous results in this chapter, the oper-

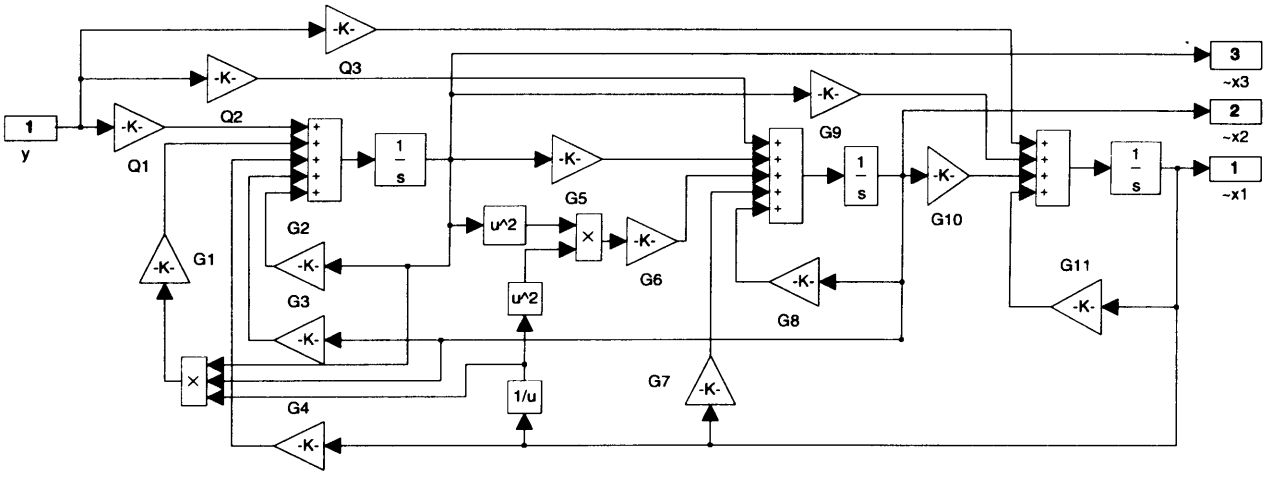

Figure 9.6: Simulink block diagram of the nonlinear observer; the input is the position between the magnet and the track, and outputs are the three states: position $\tilde{x}_1$, velocity $\tilde{x}_2$ and current $\tilde{x}_3$.

ating airgap is modified from 4 mm to 3 mm. The closed-loop response in the suspension airgap is shown in Fig. 9.8. As with the results obtained from the nonlinear state-feedback

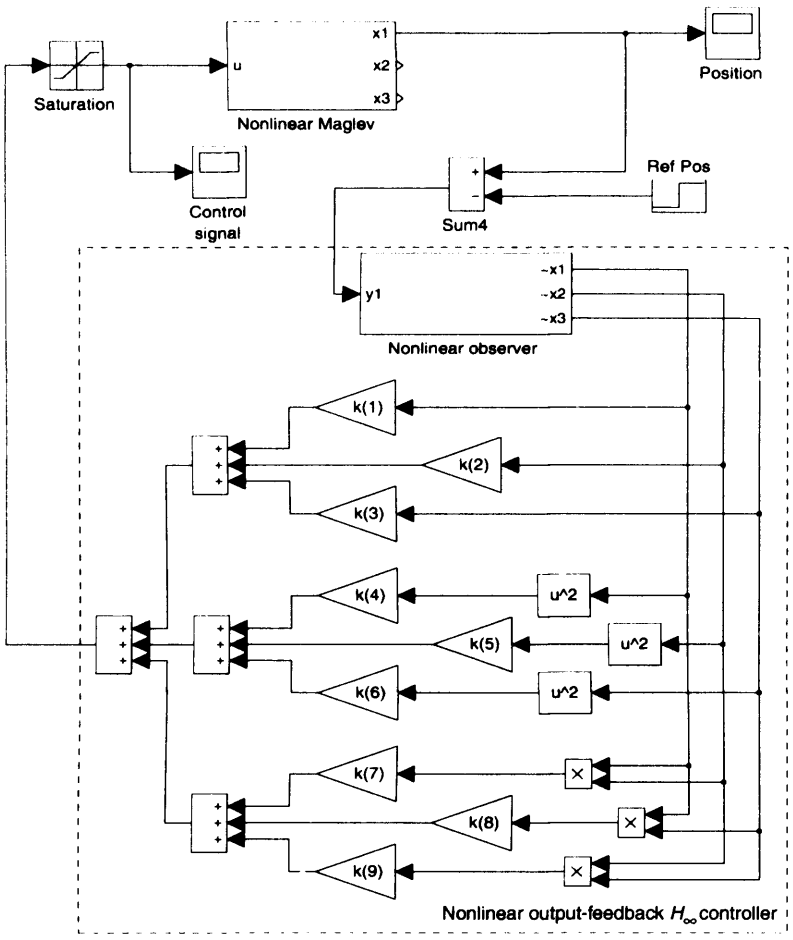

Figure 9.7: Simulink block diagram of the closed-loop Maglev system with the nonlinear $\mathcal{H}_\infty$ controller.

controller, the closed-loop system is stable and the response is over-damped. In comparison to the linear output-feedback $\mathcal{H}_\infty$ controller (Fig. 6.18, page 119), the settling time in the airgap is reduced by almost a factor of two, and the overshoot in the response has been reduced to 0 mm. This characteristic is well suited for Maglev applications since it gives good ride qualities with low acceleration levels in the cabin. Responses with similar characteristics were obtained by using two-degrees-of-freedom controllers ($\mu-$optimal design for multi-magnet vehicles in Chapter 8).

9.4 Experimental results

9.4.1 DSP implementation of the nonlinear controllers

To asses the suspension characteristics of the closed-loop system, the nonlinear state- and output-feedback controllers derived above are implemented on the DSP control hardware for Maglev (Chapter 5). For operational convenience, the Matlab function is constructed to transfer the coefficients of the nonlinear controllers directly to the control software on

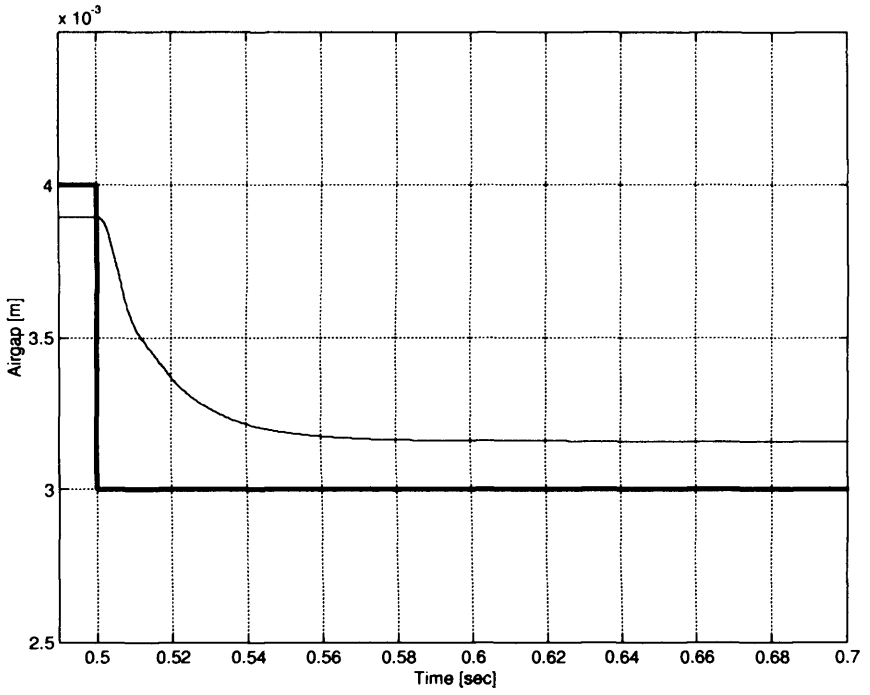

Figure 9.8: Simulated transient response due to a step change from 4 mm to 3.0mm in the reference airgap applied at $t = 0.5$ sec. and the nonlinear output-feedback $\mathcal{H}_\infty$ controller

the DSP via the provided Ethernet/TCP/IP communication channels. The DSP control software collects experimental data during the operational run and then transfers it to Matlab for visualisation and analysis. The sampling time for the control loop is fixed to 1 millisecond for compatibility with the electrical time constant of the experimental system (magnet winding inductance). The main tasks performed by the control software at each sample are: data capture and conversion (including integration of the acceleration signal to generate velocity), implementation of the control algorithms, outputting of the control signal and logging data for off-line analysis. Each sample is interrupt driven from the internal timer of the DSP. The control software was written in C and assembly languages for the SHARC family of DSPs [45, 69, 70]. The analogue processing tasks such as data conversion, integration and domain conversion, consume 5% to 8% of the sampling time. The nonlinear state-feedback controller (Eqn. 9.28) uses a further 5% to 10% of 1 ms. For the rest of the time the processor serves tasks requested from the host computer.

To implement the output-feedback controller (state estimator + state-feedback controller) on the embedded hardware, the classical linear control requires a transformation from the continuous time-domain to the discrete time-domain. Because of the nonlinear nature of the observer (Eqn. 9.42), this procedure is not directly applicable. A possible way of overcoming this limitation is to include a Runge-Kutta solver within the control loop.

At every sample (= 1ms) the software on the DSP receives the most recent output of the system (y) and multiplies it by the output injection gain $\mathbf{Q}$. The set of first-order differential equations (Eqn. 9.42) is then integrated numerically by a dedicated Runge-Kutta-4 integration routine. A typical control sample for the nonlinear output-feedback controller

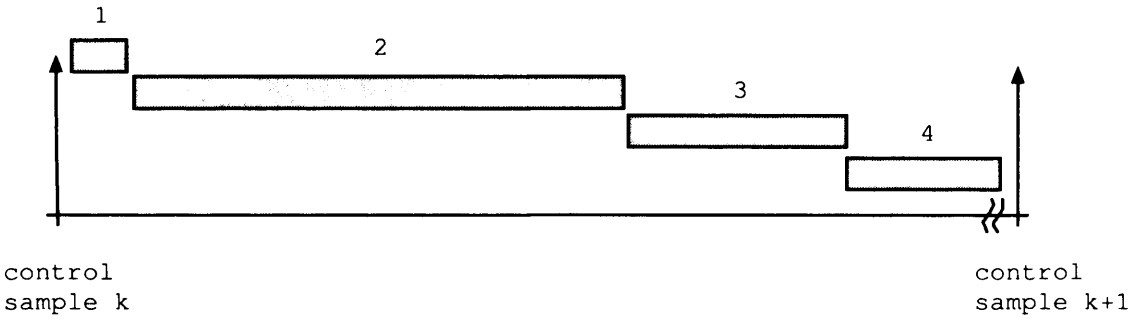

Figure 9.9: DSP tasks executed by the nonlinear $\mathcal{H}_\infty$ controller within one control sample (1 ms). (1) Read the position value from ADC and store data for analysis. (2) Solve the nonlinear Dynamics (Eqn. 9.42) with a Runge-Kutta solver to get $\tilde{x}$. (3) Calculate the nonlinear output-feedback $\mathcal{H}_\infty$ controller from Eqn. 9.28 and output the value to the output circuits. (4) Spare time.

is shown in Fig. 9.9. At the beginning of the sample, the software integrates the nonlinear dynamics of the observer (task-2). For satisfactory convergence of this integration process, experience suggests that around 50 steps, each of length $h = 10.0 \times 10^{-6}$, are needed to produce a representative estimation of the system's states $\tilde{x}$. At the end of the 50th step the final values of the three state variables , $\tilde{x}(50)$, are taken as the input to the nonlinear state-feedback controller in Eqn. 9.28 (task-3). The full collection of software tasks for nonlinear output-feedback control takes around 400μs per cycle; the remaining 600μs of the sampling time being taken up to serve the host. This is indicated as $spare - time$ in Fig. 9.9 (task-4).

9.4.2 Experimental results

One of the fundamental requirements of the attraction type suspension system is its capability for sustaining stable equilibrium under all operating conditions and disturbances. In addition to changes in suspended load, sources of disturbance on a moving vehicle include unsteady aerodynamic forces, guideway induced vibrations, and continuous excitation due to guideway roughness and misalignments. The guideway usually consists of beams supported at equal intervals which would introduce additional modes into the suspension system leading to dynamic interactions between the guideway and the suspension control

loops. Random or sinusoidal variations in the guideway profile would introduce undesirable resonance conditions. To avoid such interactions, an adequate separation between the guideway natural frequency and the suspension natural frequency needs to be maintained [1]. In order to emulate guideway movement with a view to assessing the effects

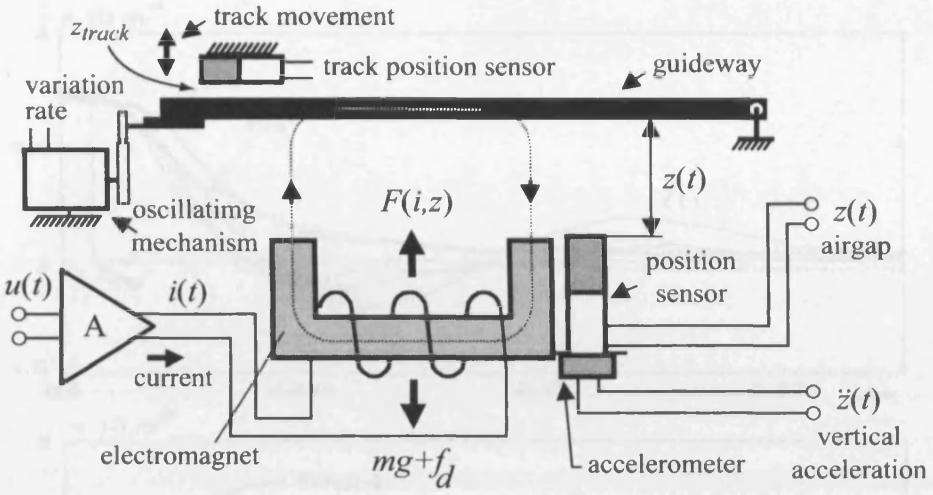

Figure 9.10: Magnet-guideway configuration of the experimental system. Disturbance to the guideway is introduced by the oscillating mechanism on the top left corner.

of the new generation of nonlinear control laws derived in the previous sections, an oscillating mechanism was added to the experimental system. This mechanism is shown in Fig. 9.10 and consists of a DC motor and an unbalanced disk. Facilities are provided for varying the rotational speed of the shaft and hence the variation rate in the guideway profile. Rotational movements in the shaft are translated to linear displacements via a bearing mechanism connected permanently to the track. A position sensor is employed to register the position of the track z_{track}. This signal is sampled by the control hardware for visualisation purposes. The oscillating mechanism is capable of introducing step changes as well as periodic motion in the guideway position with respect to the suspended magnet. The resulting configuration permits the analysis of the suspension system with track disturbance in both frequency- and time-domains.

In the first set of experiments, the step responses of the closed-loop system due to track disturbances in the reference position and the track were studied. Fig. 9.11(top) and 9.11 (bottom) show the responses of the suspension system to a step change in guideway position (z_{track}) and a step change in the reference airgap (z_{ref}) for three types of controllers:

(a) linear state-feedback as derived in Chapter 2, curve-1

(b) second order nonlinear state-feedback (Eqn. 9.28), curve-2 and

(c) the nonlinear output-feedback (Eqn. 9.42 with conjunction with Eqn. 9.28), curve-3.

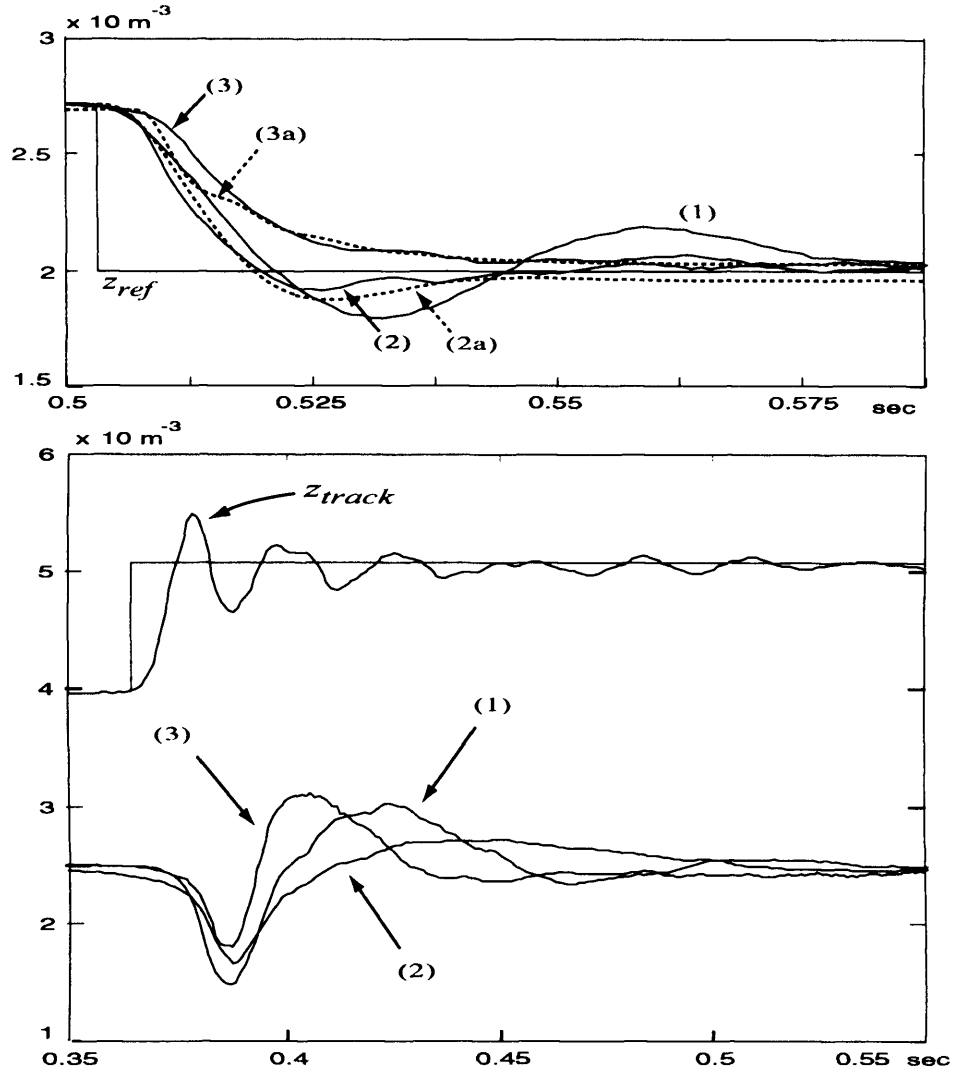

Figure 9.11: Experimental and simulation transient responses. Top: step change in airgap reference (clamped guideway); z_{ref} = 2.75mm to z_{ref} = 2.0mm. (1) Linear state-feedback controller with k_p =207.923, k_v = 1.5 and k_a = 0.00424. (2) Nonlinear state-feedback controller (Eqn. 9.28) with $\alpha_1 = \alpha_2 = \gamma = 1$, $\beta = diag\{1, 1, 1\}$ and W_c = 0.12, (2a) corresponding simulation response. (3) Nonlinear output-feedback controller(Eqn. 9.42 and Eqn. 9.28) with $\alpha, \beta, \gamma, W_c$ as in the nonlinear state-feedback, (3a) corresponding simulation response. Nominal operating conditions for all nonlinear controllers are i_0=3.13A and z_0=4.0mm. Bottom: Experimental responses due to a step change in guideway position (z_{ref} kept constant at 2.5mm); controller parameters as above.

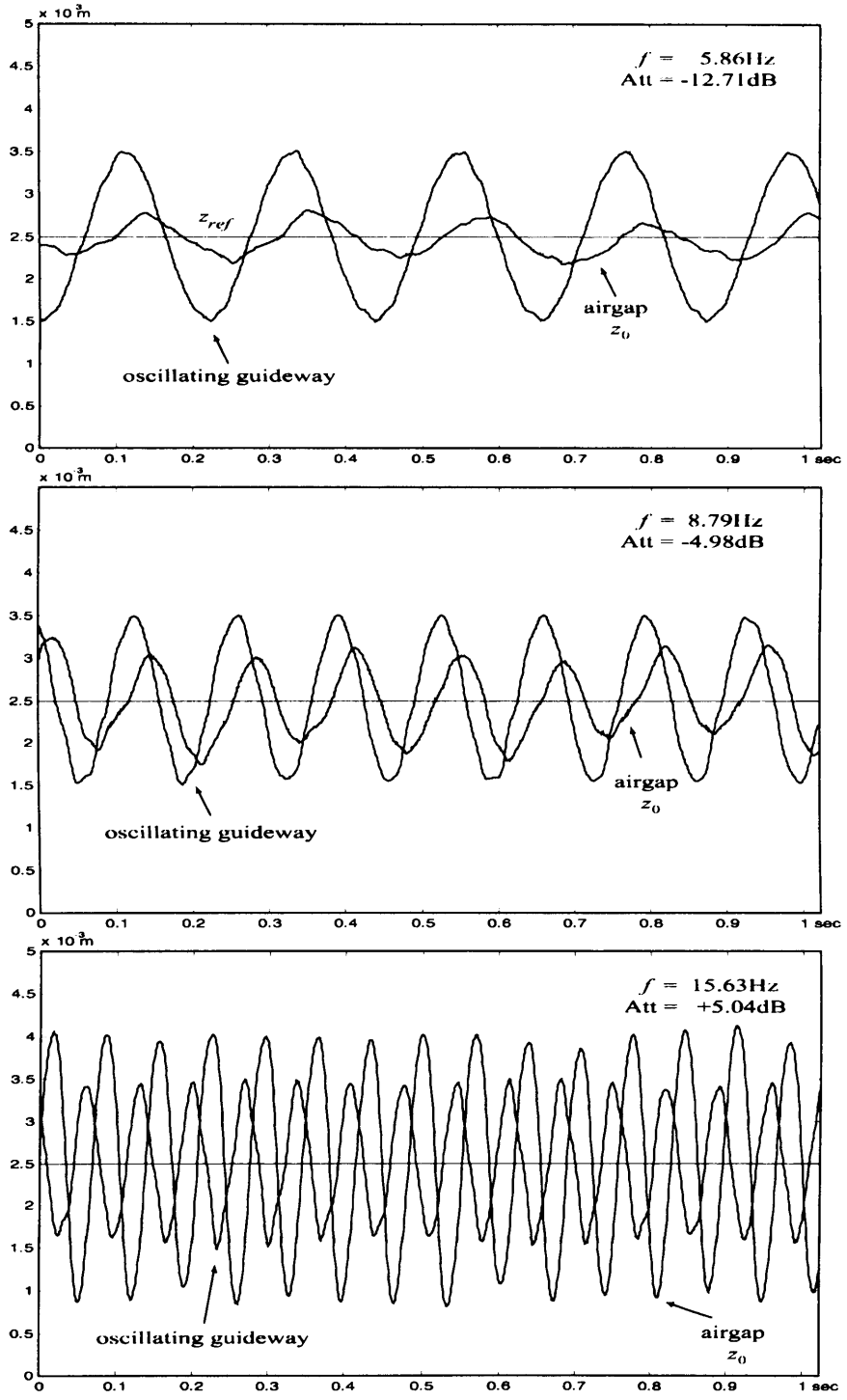

Figure 9.12: Experimental responses due to sinusoidally oscillating track for three different frequencies with linear state-feedback controller; k_p =207.923, k_v = 1.5 and k_a = 0.00424.

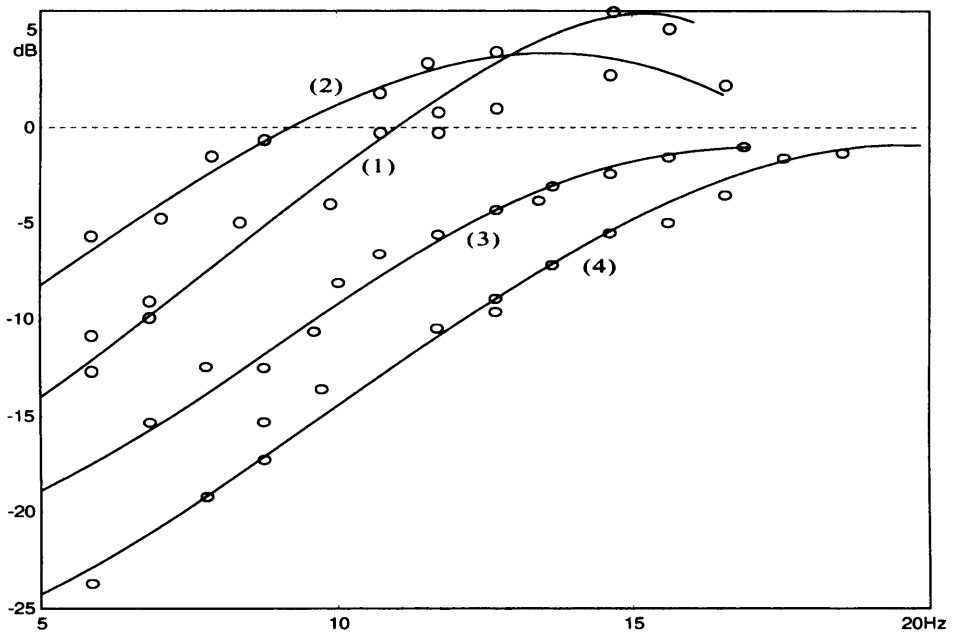

Figure 9.13: Experimental frequency responses (the sensitivity function) of the closed-loop system; (1) linear state-feedback controller, (2) first-order nonlinear state-feedback controller (Eqn. 9.26), (3) second-order nonlinear state-feedback controller (Eqn. 9.28), and (4) nonlinear output-feedback controller (Eqn. 9.42 and Eqn. 9.28). [γ specifies the peak value of the sensitivity function. The value of W_c puts a penalty on the control signal; small values of W_c lead to faster transient response and hence wider bandwidth. $\gamma = 1$ and $W_c = 0.12$ in all experimental responses contained in this paper.]

The first order nonlinear state-feedback control law in Eqn. 9.26 was also implemented. The corresponding step responses, however, are very close to the responses from the linear state-feedback control law and therefore are not included in Fig. 9.11.

The experimental responses in Fig. 9.11 indicate that the new nonlinear controllers improve the overall settling time almost by a factor of two, compared with the conventional linear state feedback controller. These observations are consistent with the simulation results in Figs. 9.4 and Fig. 9.8 (included in the figure with dotted lines). The reduction in overshoots in Fig. 9.11(curve-3) indicates that, within the definitions of linear systems, the peak amplitude in the sensitivity function will remain below the 0 dB boundary. The shapes of the complementary functions for different controllers provide a reasonable basis for the assessment of the disturbance attenuating properties of the suspension system (= track following capability) with sinusoidal variations in the guideway profile. To study this further, a series of experiments were carried out with sinusoidal variations in the guideway position. At each run, the system is suspended at a fixed z_{ref}, the track is oscillated, and the airgap and the guideway positions logged. Fourier analysis is then employed on the logged data to determine the fundamental frequency of the guideway profile and the

attenuation rate of the airgap error ($z_{ref} - z$). Initially, these experiments were performed with a linear state-feedback controller, and the corresponding responses for three different frequencies are shown in Fig. 9.12. The attenuation rate of the closed-loop system is given in the figure. These experiments were repeated over the whole of the frequency range for which the system maintained a stable suspension, and the corresponding sensitivity function (curve 1) is plotted in Fig. 9.13. The bandwidth of the closed-loop system from the track disturbance input to the airgap position with the linear state feedback controller was observed to be around 9.5 Hz. The peak value of this sensitivity function is 6 dB. Therefore, disturbances with frequencies above 9.5 Hz will be amplified nearly by a factor of two by the closed-loop system, leading to an unacceptable operation (airgap error rising up to two times the guideway variation). Although there was insignificant difference between the step responses of the linear state feedback and the nonlinear first order state feedback controllers (Figs. 9.11), the latter was seen to have a narrower bandwidth but a lower peak (curve 2 in Fig. 9.13).

The above sequence of operations were also performed with the nonlinear second-order state-feedback controller and the nonlinear output-feedback controller over the same range of frequencies. The corresponding responses are shown in Figs. 9.14 and 9.15. The experimentally derived sensitivity functions for these two controllers are given in Fig. 9.13 as curves 3 and 4, respectively. Two specific observations may be made from the shapes of these sensitivity function (Fig. 9.13):

(a) The closed-loop bandwidth with the nonlinear controllers increased. This results in better attenuation of track disturbances in the low-frequency range, and

(b) The peak of the sensitivity functions remains below 0 dB and hence the inequality in Eqn. 9.4 is satisfied. This observations stands that the increase in energy on the output remains bounded by $\gamma = 1$.

Consequently, at low frequencies (<10Hz), the magnet will follow the guideway profile satisfactorily (as in Figs. 9.14 and 9.15). While the airgap error goes up at higher frequencies, it would still remain below the amplitude of the guideway movement (measured from its datum line). As the permissible peak variation in the guideway is closely related to the mean operating airgap, this implies that the second order state-feedback and the output-feedback nonlinear controllers are capable of maintaining a stable suspension. Fig. 9.15 also shows that with the nonlinear controllers, the phase difference between the airgap and the guideway profile remains below 90° for variation above 10Hz, while the linear state-feedback

controller in Fig. 9.12 introduces a phase difference of up to 180° for this frequency range.

In comparison with the experimentally derived sensitivity functions for the linear $\mathcal{H}_\infty$ controller (Chapter 6, page 127), the nonlinear $\mathcal{H}_\infty$ controllers derived in this chapter improves the bandwidth by almost a factor of three (5.6 Hz vs. 17.5 Hz). The peak on the sensitivity function has been also reduced from +5 dB (Fig. 6.27) to -1 dB (Fig. 9.13). Although the the bandwidth for the linear design can be also controlled by the performance weights for the design (W_c and W), this would typically lead to an increase in the high-frequency noise within the operational bandwidth due to magnitude responses with gains above $0dB$ in the complimentary and the sensitivity transfer functions and the flat magnitude response with high gain within the lead part ($> 20Hz$ in Fig. 6.20) of the compensator. In contrast, the dissipation properties of the nonlinear $\mathcal{H}_\infty$ design lead to compensators with gains $< 0dB$ and hence a considerably better attenuation characteristics for the high-frequency noise. In addition, low-frequency noise generated from the supporting beams in the track (up to 10 Hz for a vehicle travelling with 500 km/h with track supports every 15 m [17]) is attenuated by -15 dB by the nonlinear $\mathcal{H}_\infty$ controllers. For multi-magnet design, however, the increased computational demands by the nonlinear controller might require employing multiprocessing to meet the computational requirements.

9.5 Conclusions

In this chapter, a unified framework for the derivation of nonlinear $\mathcal{H}_\infty$ controllers was presented with particular reference to its application to electromagnetic suspension systems. Two nonlinear controllers were derived: a nonlinear state-feedback $\mathcal{H}_\infty$ controller and a nonlinear output-feedback $\mathcal{H}_\infty$ controller. Simulation and experimental results were presented to demonstrate the stabilisation characteristics of the new controllers. The experimental results suggest that the second order state-feedback and the output-feedback controllers improve the disturbance rejection properties of the closed-loop system. While both nonlinear controllers lead to improved suspension characteristics, the output feedback controller (which subsumes a nonlinear state estimator) has been observed to provide significant improvement over the linear state-feedback controllers (Fig. 9.15).

One of the key differences between the nonlinear state and the output feedback controllers is the execution time of the control algorithms (Eqn. 9.28 and Eqn. 9.42): 4-5% of 1ms for the former and 400 μs for the latter. In multimagnets vehicles this may impose some operational constraints. To overcome this, the embedded DSP hardware has been

designed with communicating protocols between local control loops for individual magnets and supervisory control functions to co-ordinate the distribution of suspension force generated by the various magnets mounted on the vehicle chassis.

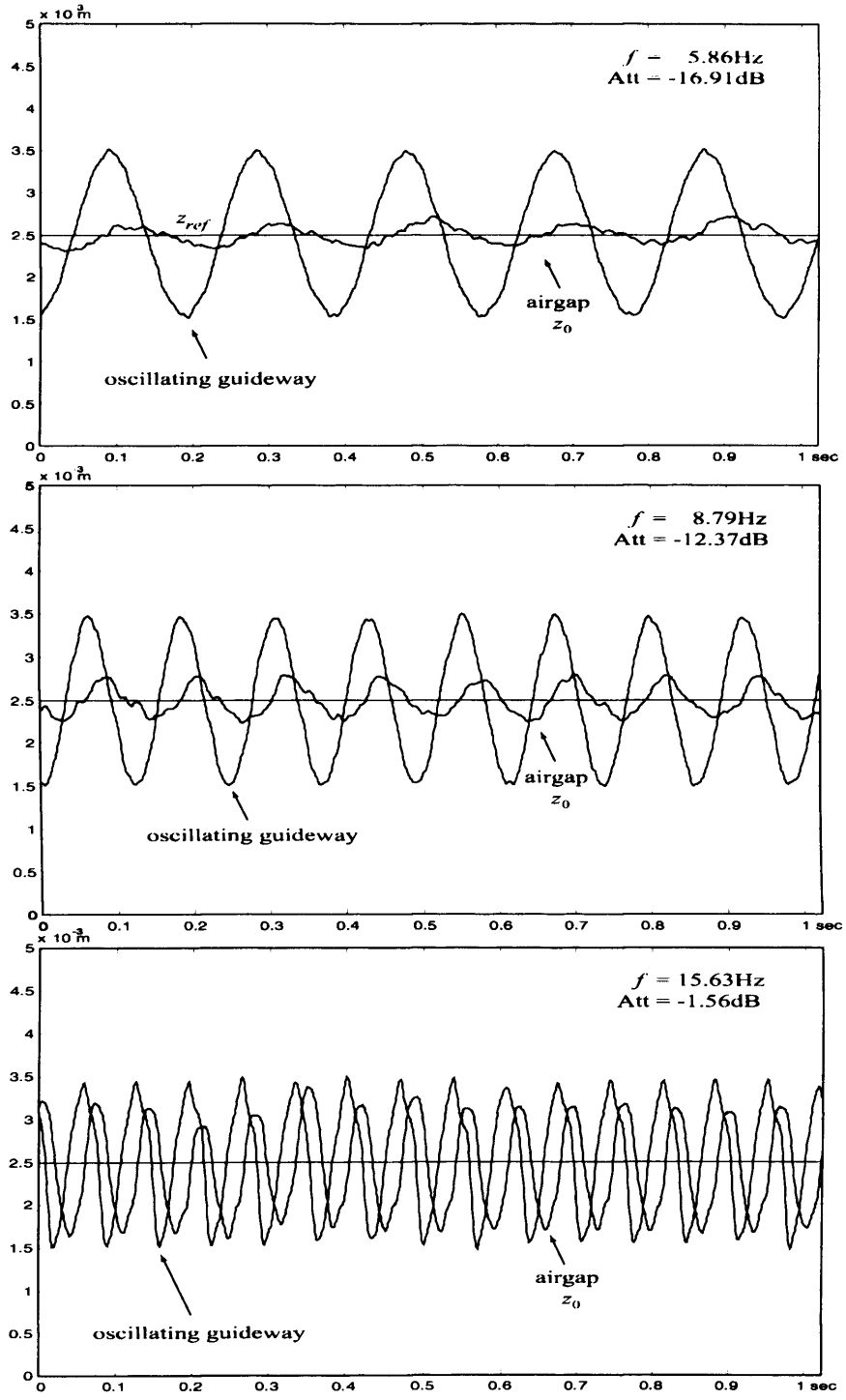

Figure 9.14: Experimental responses due to sinusoidally oscillating track for three different frequencies with nonlinear second-order state-feedback $\mathcal{H}_\infty$ controller (Eqn. 9.28).

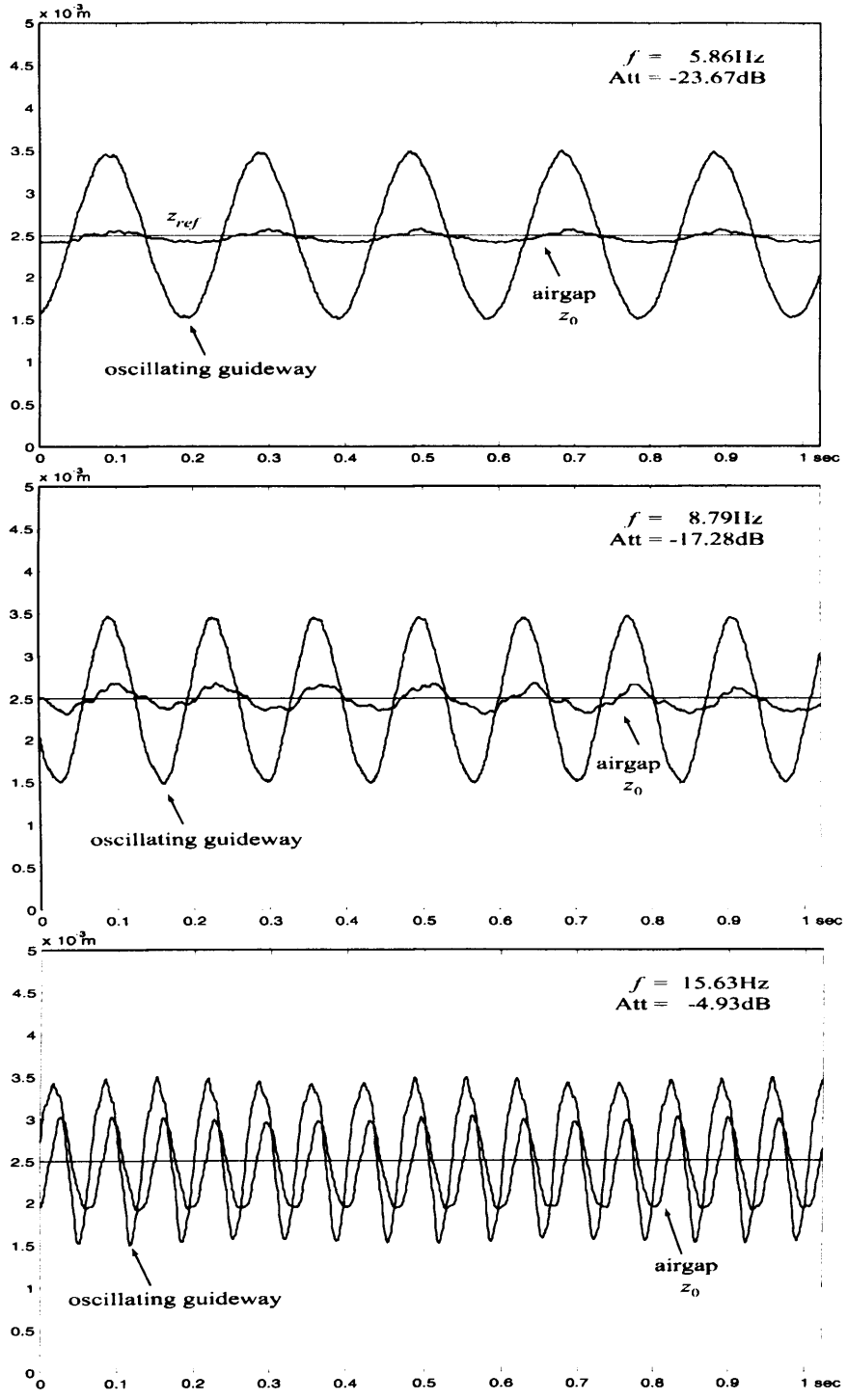

Figure 9.15: Experimental responses due to sinusoidally oscillating track for three different frequencies with nonlinear output-feedback $\mathcal{H}_\infty$ controller (Eqn. 9.42 and Eqn. 9.28).

Chapter 10

Conclusions and future work

10.1 Conclusions

In this thesis, the problem of controlling magnetically levitated systems using DC electromagnets under different operating conditions has been studied with a design process primarily driven by experimental results. With some generalisation, the controller design methods and algorithmic work presented in this thesis can be divided into: non-adaptive, adaptive, optimal linear and nonlinear.

State-feedback control using inputs from position, velocity and acceleration (Chapter 2), is by far the most widely studied control law for electromagnetic suspension systems [1, 13, 15, 16]. A key feature in the design is the choice of the nominal operating point such that the parameters (k_i, k_z and L_0) remain unchanged for the whole of the operating ranges for the current and the airgap. The closed-loop system can be modelled as a second-order system with k_p controlling the steady-state error, the natural frequency and the stiffness (Fig. 2.6, page 22), k_v controlling the damping ration and k_a controlling the overall stability [1]. Although the well established PID method is able to provide the basic suspension performance, acceleration-velocity feedback adds more flexibility in the choice of suspension damping. Use of state-feedback, however, requires additional transducers to measure the vertical acceleration. Although the cost of this is negligible compared to the overall cost of the vehicle/control system, additional algorithms are required for full-scale fault-tolerant applications. The lack of dc-integration in the loop frequency response, leads to steady-state errors and although these can be successfully accommodated for changes in the reference demand by using prefilters, response to unknown external force and mass disturbances lead to steady-state errors (Figs. 3.8 and 3.9, page 46). To account for this, the state-feedback controller needed to be enhanced and two adaptive mechanisms have been developed to improve the response by adapting the controller's parameters in real-time.

The adaptive pole-placement control law defines a cost function for a minimisation problem defined as the error between the desired and the current location of the closed-loop poles (Chapter 3). A minimisation algorithm based on a recursive least square algorithm has been implemented in real time to adapt the state-feedback parameters (k_p, k_v and k_a in Fig. 2.6, page 22) to minimise the above cost criteria (Fig. 3.6, page 40). The identification routine and the state-feedback controller have been implemented as software algorithms on the control hardware while the desired location of the closed-loop poles is defined as a characteristic polynomial from a host computer. The adaptation rate in this algorithm is determined by the parameter λ and choosing its value is crucial since it determines how fast the adaptation of the gains reacts to the external disturbances. A trade off in the selection of this parameter has to be made depending on the operational model. Analysis has shown that the locations of the closed-loop poles (derived from identification) slightly differ from the desired locations specified in the definition of the cost function. This is mainly due to errors from linearision, unmodelled dynamics and conversion from the linear $s-$domain to the discrete $z-$domain. The desired locations used for the experimental work were derived empirically to get high stiffness in the response. This might be adjusted depending on the application. The sampling time for the algorithm also influences the adaptation rate. Preliminary implementation results on the transputer hardware have shown that with $950\mu s$ sampling time, the suspension system did not appear to be capable of accepting disturbance inputs. This was improved on the DSP hardware by reducing the sampling time to $200\mu s$. To accommodate a disturbance force input of 120N, approximately 5000-6000 identification cycles ($\approx$1 second) were needed (Fig. 4.4, page 56) to reduce the steady-state error.

A model-reference adaptive controller, which minimises analytically the error between a reference system and the experimental system, was also derived (Fig. 3.7). The closed-loop reference model is run on the control hardware in real-time and at every control sample, the error is minimised by adapting the controller's gains. This configuration considerably improved the response of the system to external disturbances in force and payload (Fig. 4.1, page 4.1). Since the suspension balance is driven by a force balance, the vertical acceleration signal is most sensitive to external disturbances with acceleration gain being the most responsive during adaptation (from 25% to 250% change from its initial value). k_v has varied within $\pm$25%, while k_p has varied only 5% from its initial value. Several factors may influence the choice of the reference model including the amount of energy available for the adaptation by the magnet's lift-force raiting and available current supply from the power

amplifier. The operating conditions for the reference model have been chosen in the linear part of the force-current characteristics. The adaptation rule thus can return the airgap of the suspended system to that of the reference model for large variations in the operating conditions. For large variations within the nonlinear force-airgap characteristics, a family of pre-stored models or a nonlinear model can be used. Adaptive nonlinear control for electromagnetic system is proposed in [29]. These authors have studied the performance in response to changes in the desired airgap without explecitely analysing the performance to disturbance inputs. A mechanism is developed to analyse the stability of the closed-loop system using Lyapunov methods [29].

The notation of uncertainty, which arises in the form of discrepancies between the physical plant and the mathematical model used for controller design and unmeasured noises and disturbances that act on the physical plant, is an important factor in the design of the feedback controller. To cope with external force and payload noise, an adaptive mechanism for tuning the state-feedback controller in real time has been proposed [35]. The mechanism for the adaptation rate, however, is based on good knowledge of the mathematical model and although by using precise identification, this requirement can be fulfilled for small-scale applications, a full-scale magnetically suspended vehicle would require robustness properties to be built into the controller directly. $\mathcal{H}_\infty$ and $\mu-$synthesis was thus considered as a suitable framework for multi-magnet controller design. The derivation of the $\mathcal{H}_\infty$ compensator is based on an optimisation procedure that minimises the worst-case gain, the ∞-norm, between unknown external disturbances entering the suspended system and a vector of penalty signals by selecting the feedback compensator. The optimisation nature of the controller derivation steps allows single and multi-magnet problems to be solved by following the same procedures.

For the $\mathcal{H}_\infty$ derivation, all disturbances acting on the suspended magnet, such as track irregularities, external force, payload disturbances and measurement noise are grouped together into one disturbance vector on the output (Fig. 6.1, page 88). The mixed sensitivity minimisation problem is then considered which aims to make the closed-loop system invariant to all disturbances by selecting a feedback compensator that minimises the sensitivity of the system. For robustness, an upper bound on the output of the controller (magnet current) was also considered (Fig. 6.3). To provide a basis for customisation of the $\mathcal{H}_\infty$ design and facilities of incorporating it into the DSP software, the algorithm for the solution of the $\mathcal{H}_\infty$ problem was fully derived using Lagrange multipliers and differential game

theories. The derivation steps result in a procedure which derives identical controllers in terms of performance as the algorithm in Matlab. State-feedback controllers using $\mathcal{H}_\infty$ weighted sensitivity minimisation were firstly derived and although these are not suitable for practical implementation, important design steps have been discussed. Comparison between simulation step responses show that the $\mathcal{H}_\infty$ state-feedback controller improved considerably the steady state response, overshoot and settling time (Figs. 6.9 and 6.10). In addition the $\mathcal{H}_\infty$ procedure provides a systematic way of describing suspension qualities by shaping the performance weights for the design. Based on these observations, the algorithm for $\mathcal{H}_\infty$ design is further extended to the output-feedback setting by incorporating an $\mathcal{H}_\infty-$optimal observer. Experimental results show that the weighted mixed sensitivity problem is suitable for Maglev control and the design parameters provide a valuable input for selecting desired suspension characteristics. The bandwidth of the closed-loop system can be suitably controlled as well as the upper bound on the sensitivity to the disturbances. In this respect a valuable mechanism can be derived for separating guidance disturbances from the system's bandwidth. Due to the integration characteristics of the loop-frequency response at low frequencies, the controllers give zero steady-state errors (Fig. 6.23). The mechanism proposed in this thesis based on the weighted sensitivity minimisation problem reduces considerably the overshoot and the response time compared to the simulation results presented in [30] and provides lower values for the $\infty-$norm on the sensitivity function compared to the response in [31]. The mechanism used for the digital implementation is based on a ZOH-transformation of the linearly-designed feedback compensator. The experimental work suggests that this approach is suitable for Maglev design. The sampling frequency was fixed at 1 kHz, which proved to be sufficient for the operational bandwidth.

Due to the nonlinear force-current and force-airgap relationships, changes in the operating conditions will modify the open-loop model used for the controller design. Although the $\mathcal{H}_\infty$ controller satisfies the performance criteria, analysis using the structured singular value μ has shown that ± 25 % variation in the typical operating point ($i_0 = 3A,\ z_0 = 4mm$ typicaly) and 200% variation in the suspended mass will lead to instability when using the $\mathcal{H}_\infty$ controller (Chapter 7). Using two methods for modelling uncertainty, the robustness analysis has shown that the closed-loop system with the $\mathcal{H}_\infty$ controller is more sensitive to changes in the operating conditions and the suspended mass and less sensitive to uncertainty in the electical parameters of the model (30% variation in R, L_0). Combining $\mathcal{H}_\infty$ and $\mu-$analysis provides a mechanism for embedding robust properties into the controller.

Using this new design tool, the μ-optimal controller, designed with the same performance requirements as the $\mathcal{H}_\infty$ compensator, provides a considerable increase in the robusness margin for the same uncertainty in the model (Fig. 7.19 versus Fig. 7.3). Simulation and experimental responses have shown that the suspension properties are considerably improved for a system subjected to additional mass disturbance.

A Maglev vehicle supported and guided by electromagnets acts as a free body in space unconstrained by a physical contact with its surroundings (Fig. 8.1). The requirement for the control system is to drive four or more magnets simultaneously and to keep the suspension modes (heave z, pitch θ and roll ϕ) in equilibrium. Controller synthesis based on optimisation provides a suitable basis for the derivation of the compensator with an appropriate cross-compensation structure to reduce coupling effects caused by the rigid body. Using a multivariable model for the vehicle and a set of performance criteria, this control problem has been solved using the $\mathcal{H}_\infty$ and $\mu-$synthesis tools and the weighted sensitivity optimisation criteria derived for the single-magnet case (Chapter 8). To improve the suspension qualities, a prefilter to specify the desired response in all three suspension modes is added to get over-damped transient responses (Fig. 8.15, page 192) and an acceleration level of maximum $0.4g$ for the heave response. The experimental work is carried out on a 88 kg vehicle developed in [21]. Since suspension forces in the experimental vehicle are actively controlled, Maglev controller design with guidance support is addressed in simulation only. Lateral guidance support in the experimental vehicle is provided by the inherent lateral stiffness of the suspension magnet (leakage flux). The multivariable controller designed using $\mu-$synthesis considerably improves the disturbance rejections properties as well as the transient response and the bandwidth of the system. Experimental results from the vehicle have shown that the multivariable controller improves the response to guidance induced disturbances (Fig. 8.8) and in contrast to the state-feedback controller it reduces the overshoot in the heave response to a minimum. $\mathcal{H}_\infty$ controllers for Maglev vehicle have been previously proposed in [31], but the design there has been simplified to a single loop design by neglecting the cross coupling. Therefore the design strategy proposed in this thesis considerably improves the response in the vehicle to disturbance rejection compared to [31]. Compared to the integrated and local vehicle control strategies presented in [1, 13], multivariable controller design with $\mu-$synthesis provides less overshoot in the response due to the integrated pre-filter. The experimental step-response to a 1mm simulated track step change has less overshoot and faster transient response compared to the force-feedback

controller presented in [21]. Responses to force disturbances are also successfully accommodated by the design (Fig. 8.24) without the necessity of an additional feedback loop from an estimator for the disturbance as proposed in [18](Fig. 11). For the controller-design process a trade off has to be made between the allowed uncertainty in the system, the closed-loop bandwidth, the sampling time magnet force saturation and operational stability. Increasing the uncertainty in the system typically require a relaxation the upper-bound requirements on the control actions and hence an increase in closed-loop bandwidth. The controller is then required to operate over a larger bandwidth which puts additional constraints on the sampling time. The increased number of state-variables in the multi-magnet controller tends to consume most of the available processing bandwidth. It was estimated that controlling a multivariable system with guidance support would require approximately 350-400 microseconds. Reducing the sampling time for wider operational range and higher closed-loop bandwidth uses up the available computation time-slot. For this application, the multi-processing facilities provided by the DSP hardware have to be used. In addition, an increase in operational bandwidth leads to exciting higher frequency modes in the vehicle body which are excluded from the modelling work. Without additional account for these, undesirable resonance effect are generated leading to increased acceleration levels. The multivariable controller is implemented on the DSP hardware in discrete state-space form. It has 14 state-variables, seven inputs and four outputs. It requires 345 DSP cycles and it takes 125 microseconds to execute. This considerably improves the rounding up errors and the phase delays in the computation in comparison to executing 28 compensators (needed for 7 input and 4 outputs).

The concepts of dissipativity, supply power and stored energy can be used to derive nonlinear $\mathcal{H}_\infty$ controllers using the nonlinear model of the suspension system directly without linearision (Chapter 9). The energy balance criteria are satisfied by solving a set of Hamiltonian-Jacobi-Isaacs inequalities to derive a nonlinear state- and output-feedback control laws. While the exact solution to this inequality is not readily available, an approximate solution involving Taylor series expansion is used to derive higher-order terms in the nonlinear controllers. The derivation process is performed analytically and a fully worked-out example for a single-magnet system is presented. The analysis of the control laws is performed on a single-magnet test rig which is equipped with a mechanism for guideway-induced disturbances. Experimental results over a large range of variation in the oscillating mechanism show that the nonlinear output-feedback controller improves the

bandwidth of the system and suppresses the guidance induced disturbances by minimising the energy of the disturbances. The attenuation rate with the nonlinear controller has been increased to 10 Hz and has been doubled in a comparison with the results presented in [16]. For the implementation, a nonlinear set of dynamic equations have to be solved to provide the estimations for the state-variables. Runge-Kutta method is implemented and run in real-time on the software as a part of the controller-derivation process. The nonlinear controller requires $400\mu s$ to execute on the DSP hardware. Nonlinear control for Maglev based on a coordinate transformation has been previously studied [25, 26, 27]. However, application of nonlinear $\mathcal{H}_\infty$ control for Maglev, as derived in this thesis is considered to have been presented for the first time [36].

10.2 Future research recommendations

A number of areas have been identified which could benefit from further research.

The control work described in this thesis has been derived on the basis of simplified single- and multi-magnet models. While this is sufficient for the controller-design work, a more detailed model is necessary for the simulation work to include unmodelled dynamics at high-frequencies, oscillation modes in the chassis, dynamic responses of the amplifier and transducers. In addition, the track-guidance interaction have to be included for the analysis of high-speed suspension characteristics which is difficult to reproduce in laboratory-scale experiments.

In the derivation of the $\mathcal{H}_\infty$ controllers it would be beneficial to employ cost optimisation objectives which include suspension qualities criteria, such as suspension stiffness and ride comfort. In addition, the flux leakage and eddy-current loses can be also accounted for in the electromagnetic suspension systems. Two possible approaches can be investigated in a further research work: (1) to develop a detailed model of the electromagnetic suspension system which includes flux leakage and to construct an adaptation scheme which is based on the suspension airgap in order to regulate the force to account for the leakage, or (b) to model the degradation in suspension forces due to the flux leakage using uncertainty models as described in Chapter 7 and to design a μ-optimal controller which accommodates a complex perturbation model for the uncertainty and provides robustness against it.

The nonlinear $\mathcal{H}_\infty$ controller is derived for the single-magnet model. It would be interesting to analyse the suspension qualities and the interaction of multi-magnet configurations controlled by a nonlinear multivariable controller. In addition, robustness in terms

of parameter perturbations is not accounted for in the proposed nonlinear design and it would therefore be beneficial to add robustness analysis and synthesis in the nonlinear $\mathcal{H}_\infty$ domain.

Appendix A

CVI environment for Maglev control

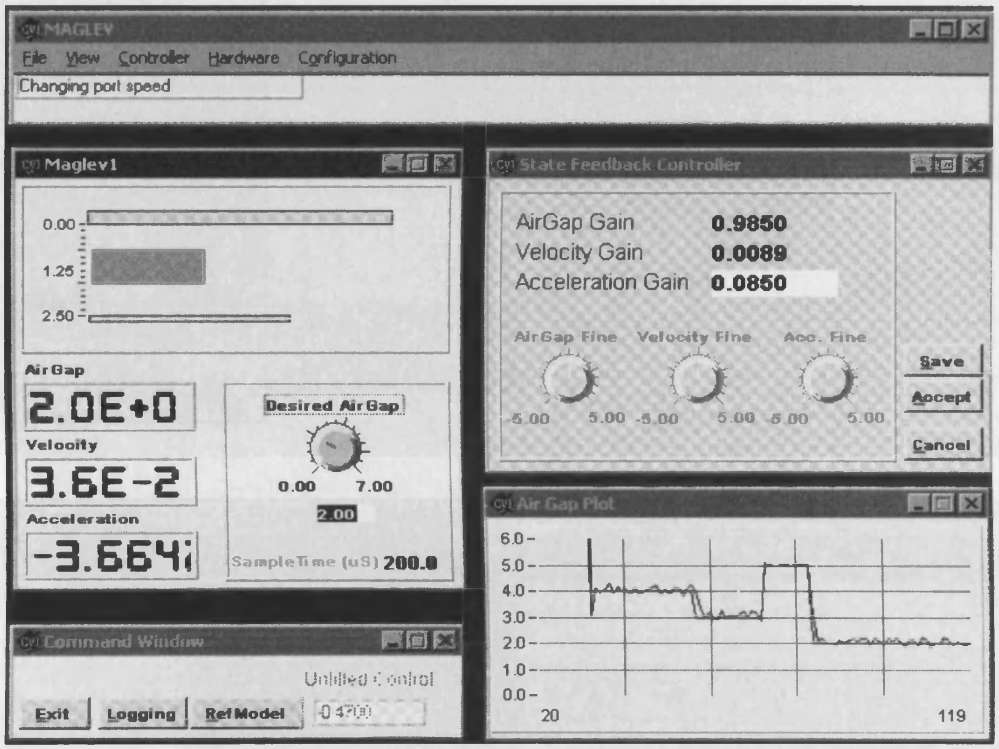

Figure A.1: The software application on the host working in Windows environment. This software communicates with the transputer-based and the DSP-based control hardware/software and facilitates monitoring and modifying different control techniques and parameters.
The top panel carries the main menu.
The left panel Maglev1 shows the suspended magnet on-line and the three state variables. From this panel the desired position may be modified in real-time.
The right panel shows a typical configuration screen related to a control technique. The state feedback screen is given as an example.
The bottom-right figure shows how a parameter may be monitored as a graph-plot in real-time. The figure shoes the airgap signal as an example.
The software is written in C language using the National Instruments LabWindows/CVI compiler.

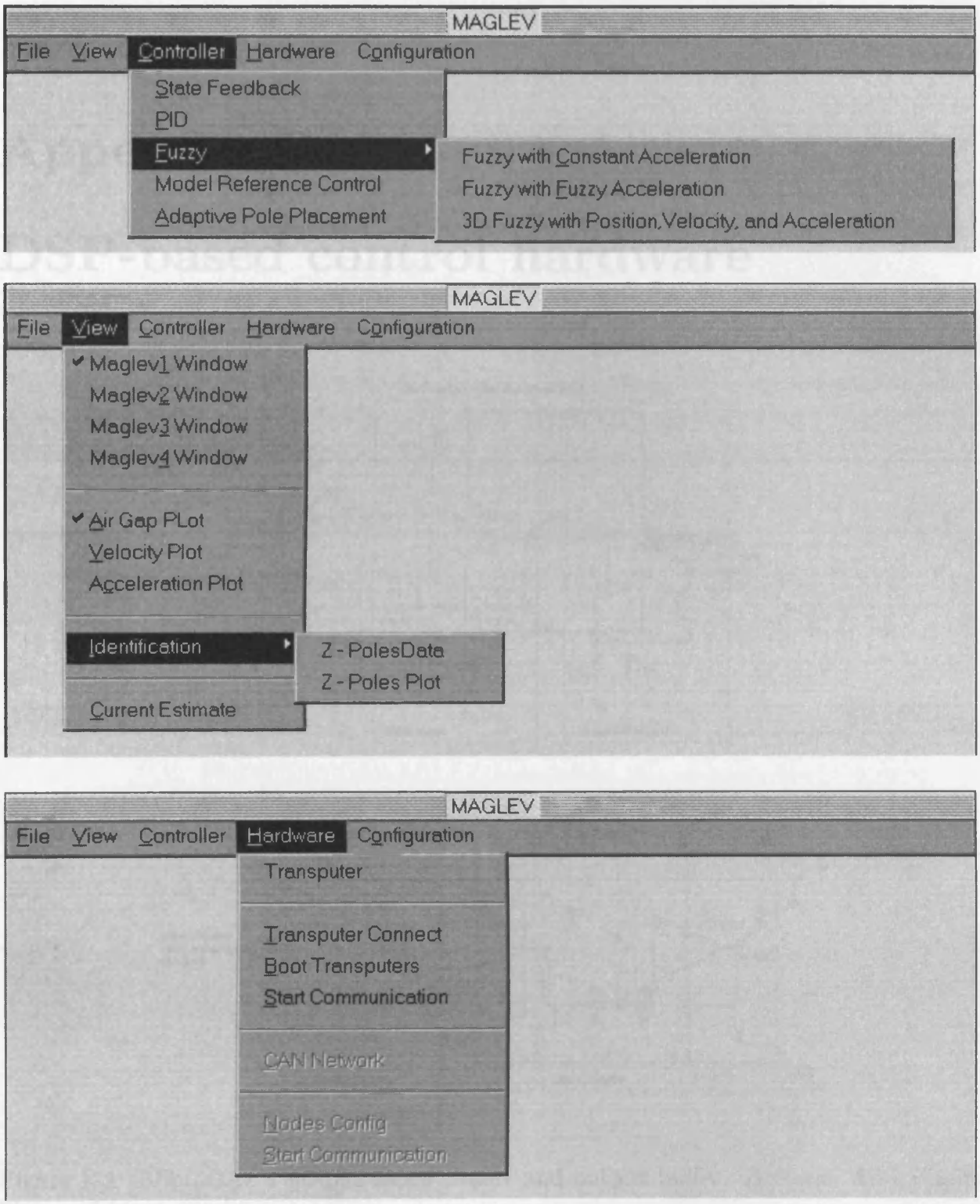

Figure A.2: The software application on the host working in Windows environment. This software communicates with the transputer-based and the DSP-based control hardware/software and facilitates monitoring and modifying different control techniques and parameters. On the top figure is shown the menu of the advanced control algorithms as described in Chapter 3. The next figure shows the menu of parameters that may be specified for plotting and/or monitoring. The last figure shows the menu, related to the control hardware.

Appendix B

DSP-based control hardware

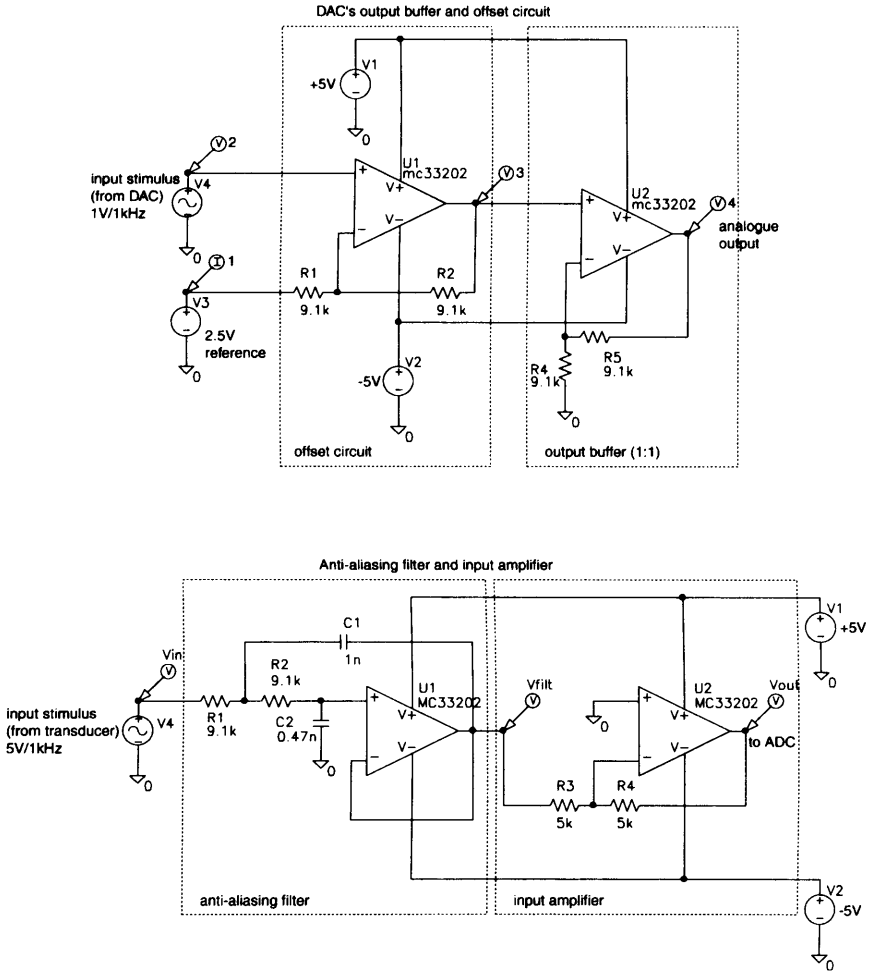

Figure B.1: Top: DAC's output offset circuit and output buffer. Bottom: Anti-aliasing filter and input amplifier.

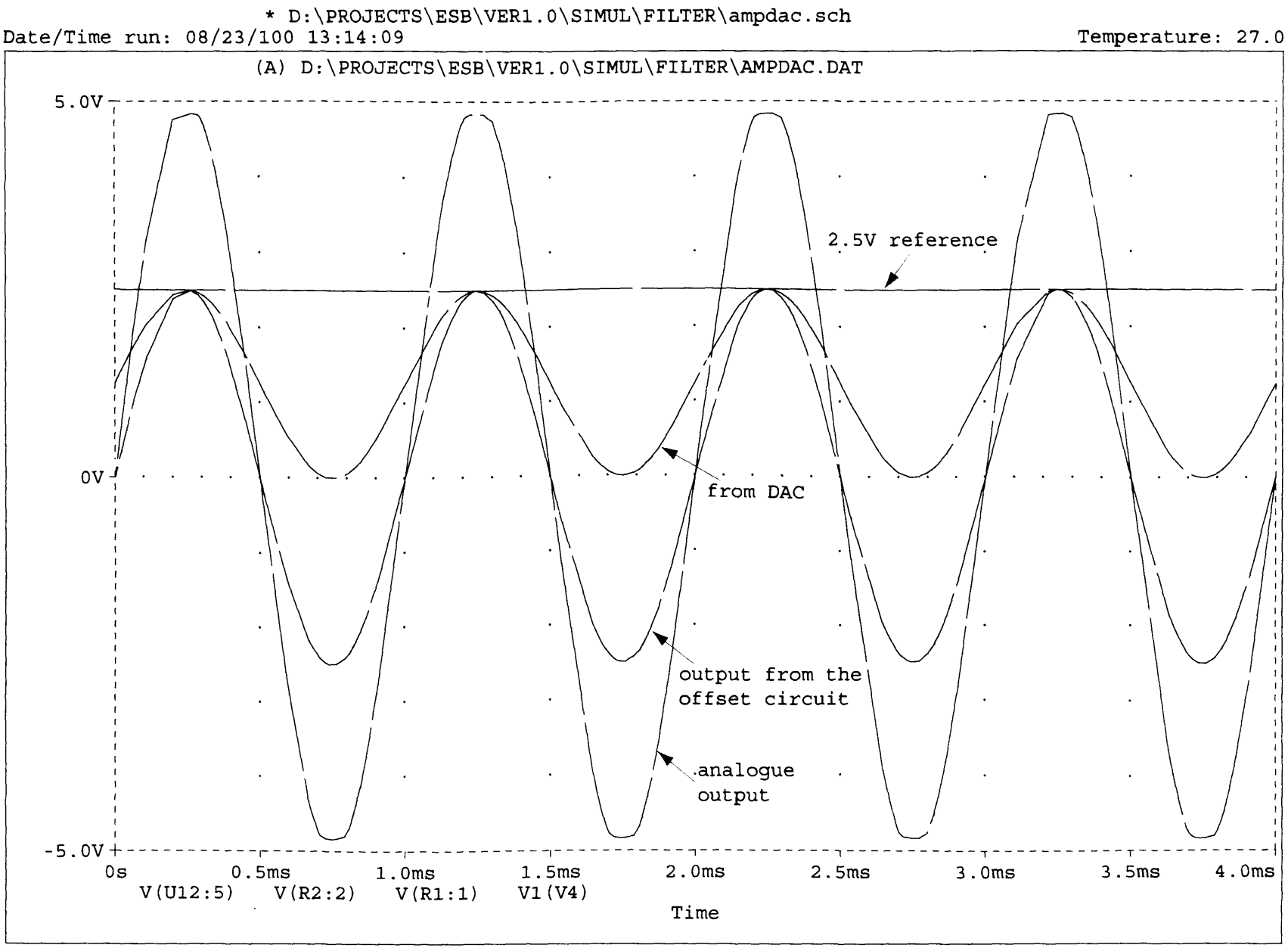

Figure B.2: DAC's output buffer and offset circuits.

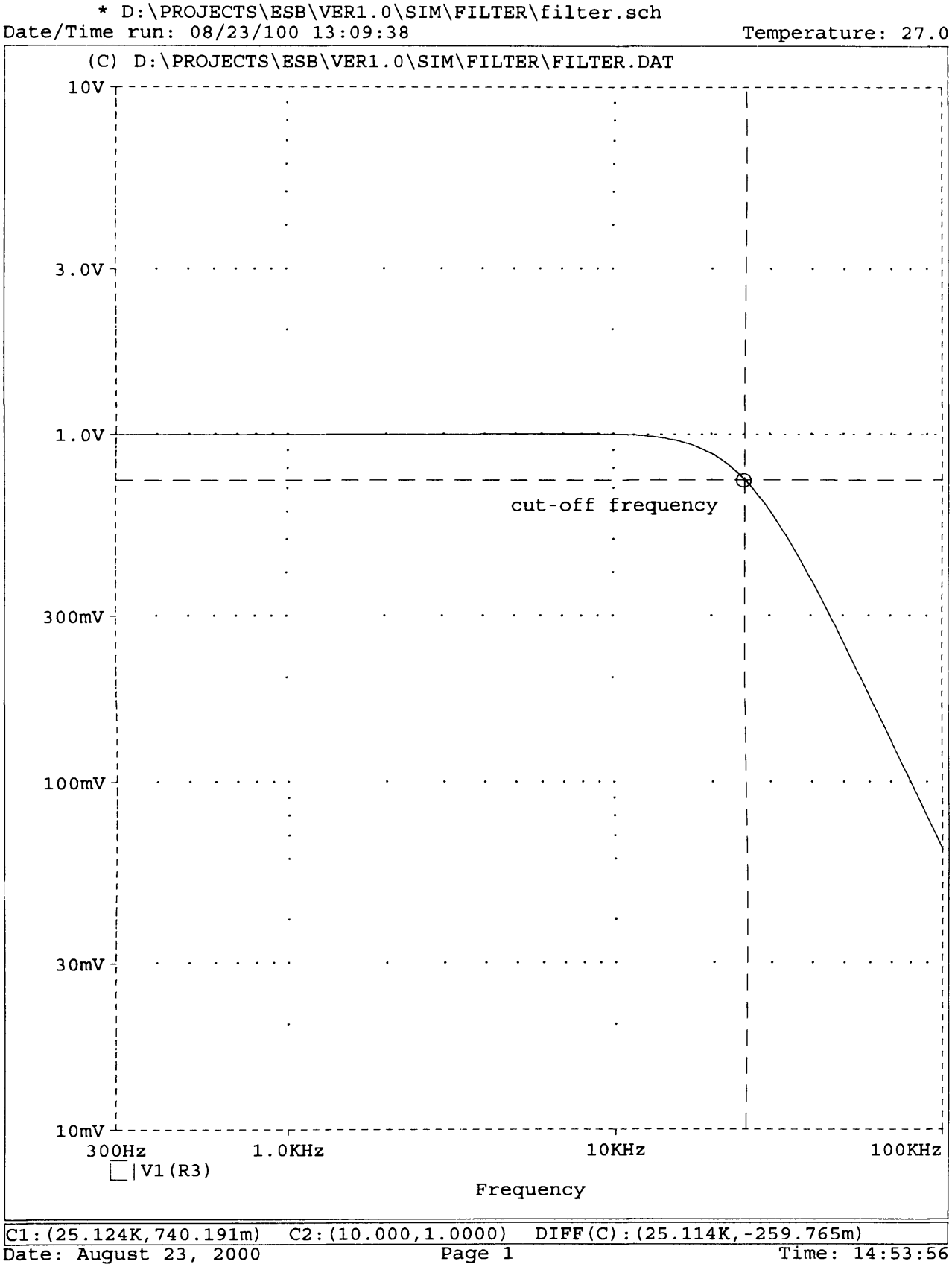

Figure B.3: Frequency response of the anti-aliasing filter. The circuit provides -2.6dB attenuation at 25kHz.

Processor	One ADSP-21062 Analog Devices SHARC processor 40MHz, 25ns instruction rate, 120MFLOPS, 40MIPS 32/40-bit floating point, 32-bit integer 2Mbits dual-ported on-chip SRAM memory, organised x32 or x48 six 40MB/s link ports, and two 40Mbit/s serial ports
Interface	One SHARCPACK standard interface
External Memory	4Mbit FLASH memory Up to 32Mbit SRAM zero wait state memory
Ethernet port	One 10Mbit/s Ethernet port 10Base-T unshielded twisted pair RJ45 interface
Link Ports	Four external link connectors Two are connected directly to the SHARC on the board Two are routed from the SHARCPAC module
Serial Ports	Four serial interfaces routed to the SHARCPAC connector
Analogue inputs	Eight 12-bit analogue inputs Maximum conversion rate 454 kHz four $\pm$5.0V input channels four 0-20mA input channels Eight independent anti-aliasing analogue filters (25KHz cut-off freq.) Four programmable gain amplifiers with 255 positions Four fixed gain amplifiers (1:1)
Analogue outputs	Four 12-bit analogue outputs 6μs settling time four $\pm$5.0V output channels Four fixed gain amplifiers (1:1)
Digital I/O	Eight programmable digital I/Os TTL input/output levels
Encoder inputs	Two 12-bit inputs for rotary encoders TTL input levels Direct interface to standard encoders
Programmable I/O	Gate-programmable digital I/Os (Lattice ispLSI1016-180 CPLD)
Debug Port	14-pin IDC header for IEEE JTAG 1149.1 boundary scan with extensions for in-circuit emulation Supports Analog Devices EZ-ICE emulator
Software support	Embedded kernel on board that supports TCP/IP and host booting Host interface tool for booting Support of the Analog Devices developing tools Matlab client/server module for direct interface to Matlab/Simulink
Power	650mA@5V typical (not including optional SHARCPAC module) optional 650mA@12V (not including optional SHARCPAC module)
Size	4.7"x6.4"

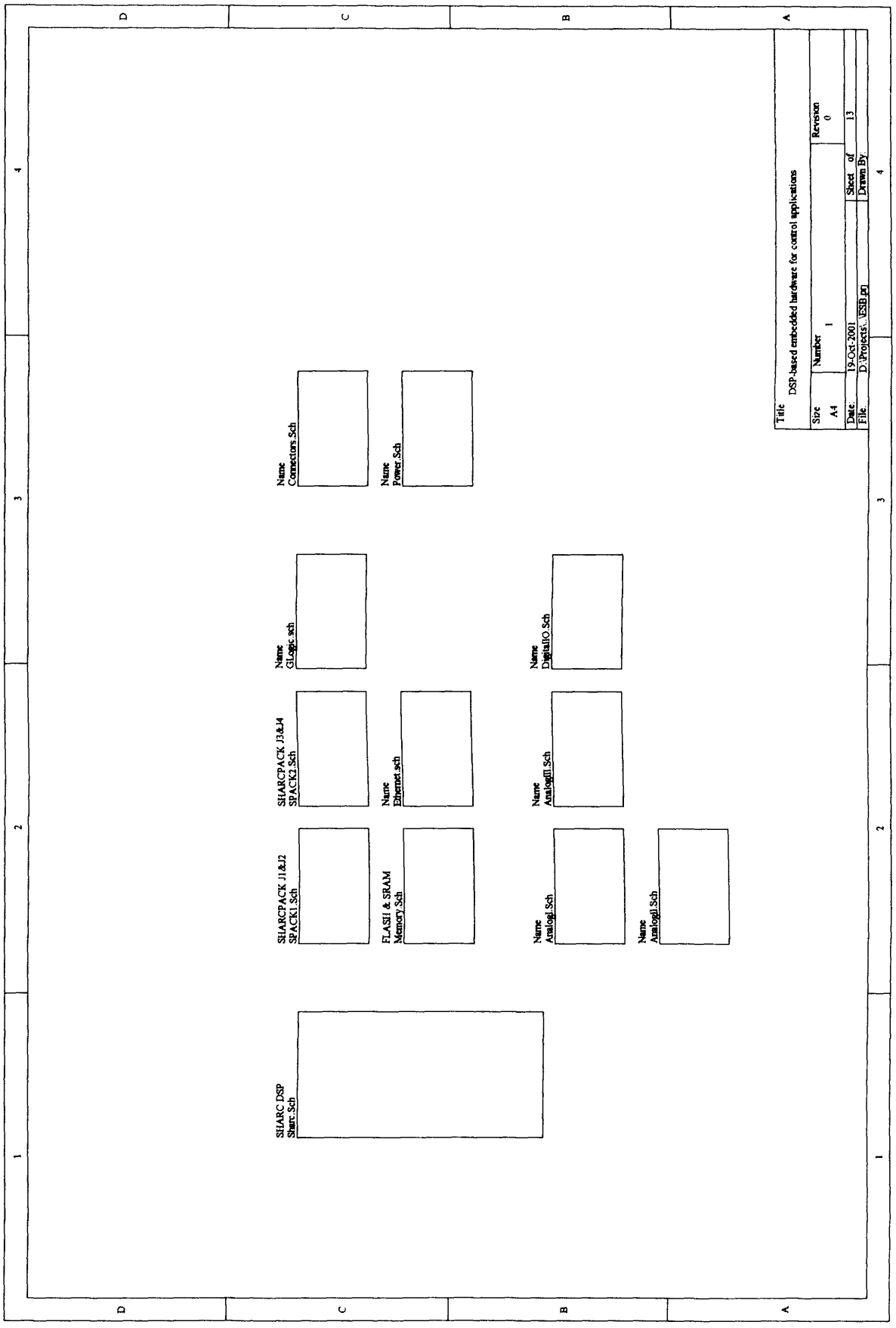

Figure B.4: Top-level schematics.

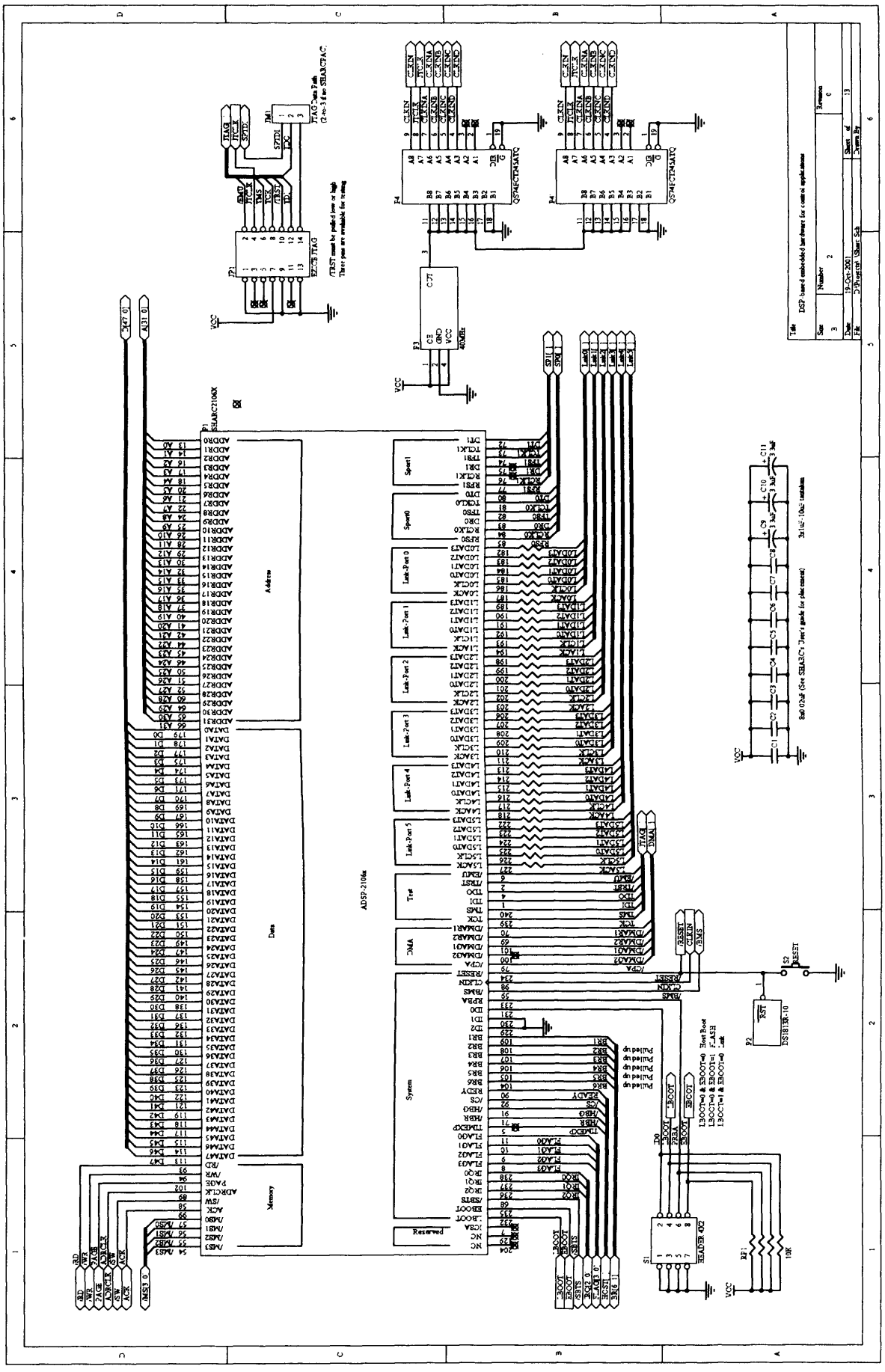

Figure B.5: SHARC DSP, Reset circuits, 40MHz clock and its buffers.

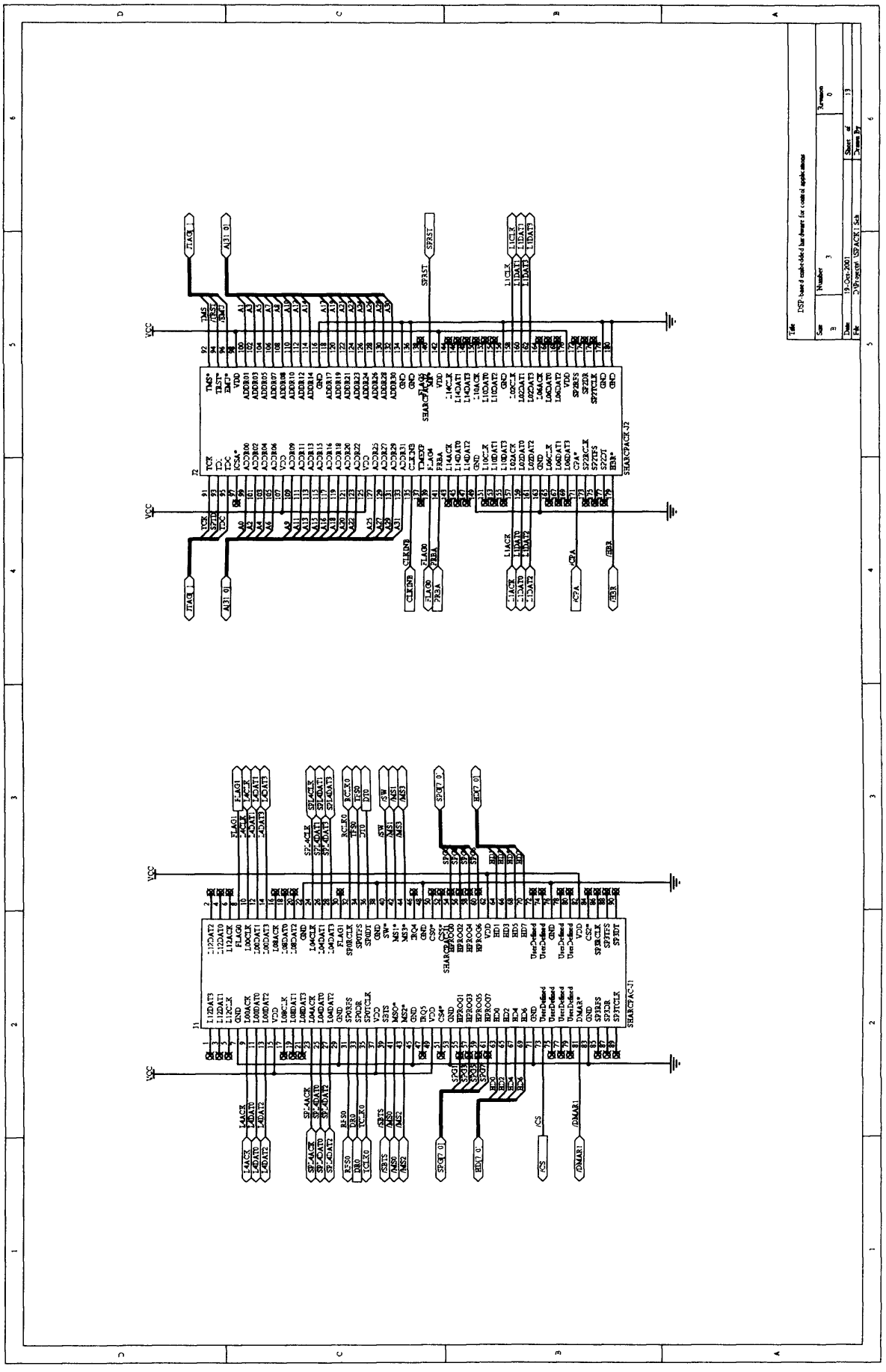

Figure B.6: SHARCPAC connectors J1 and J2.

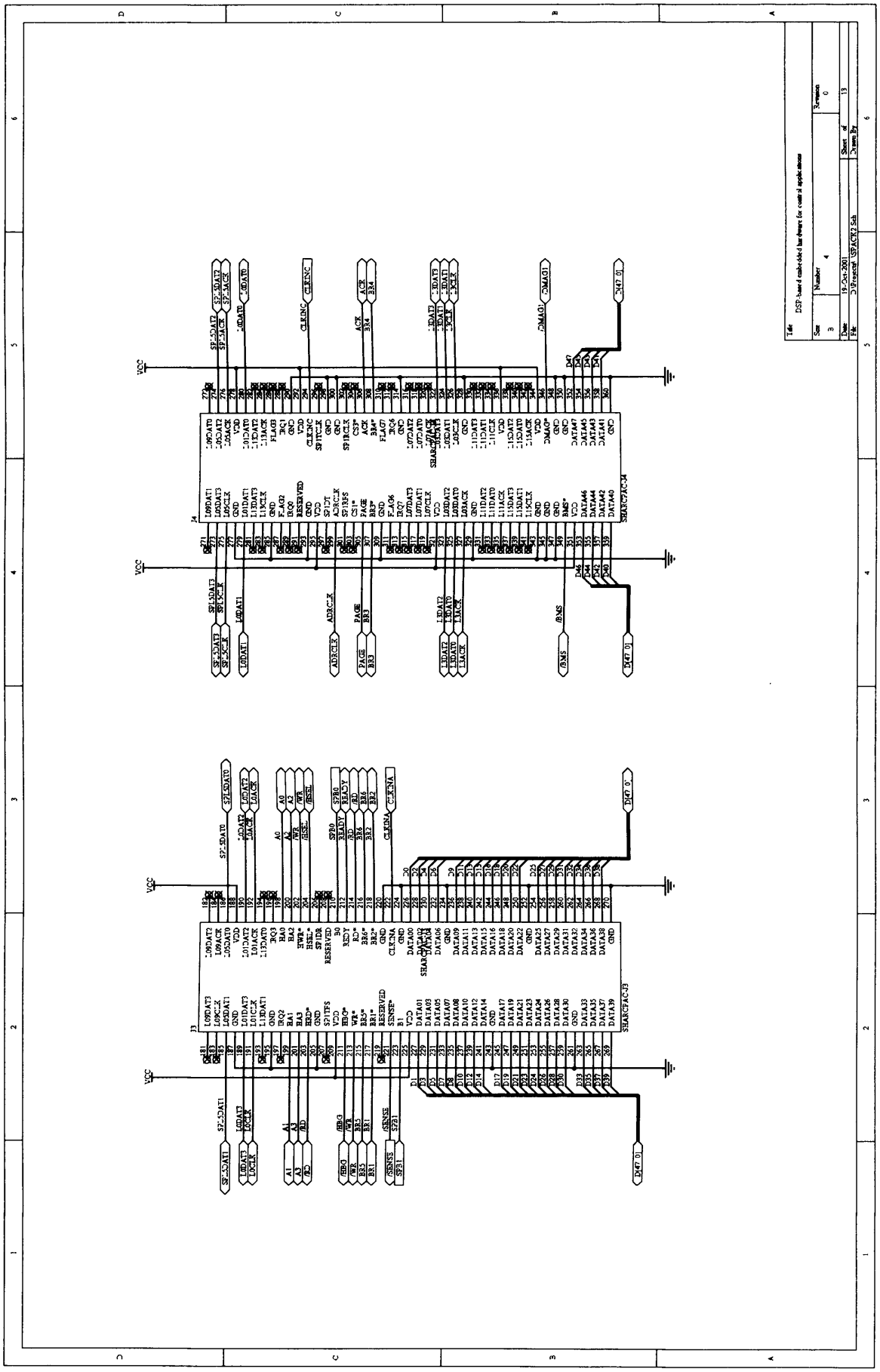

Figure B.7: SHARCPAC connectors J3 and J4.

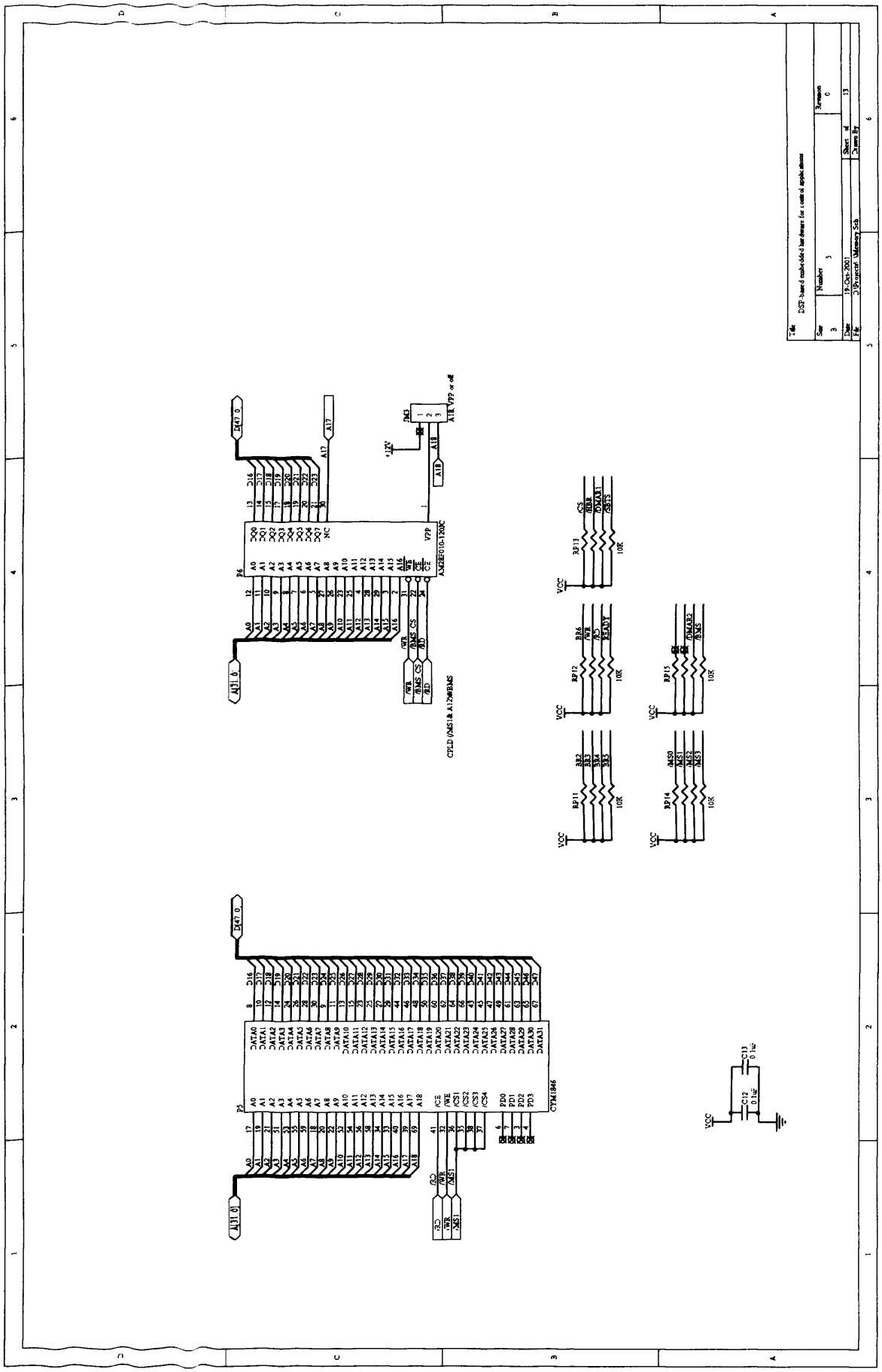

Figure B.8: SRAM memory and FLASH memory modules.

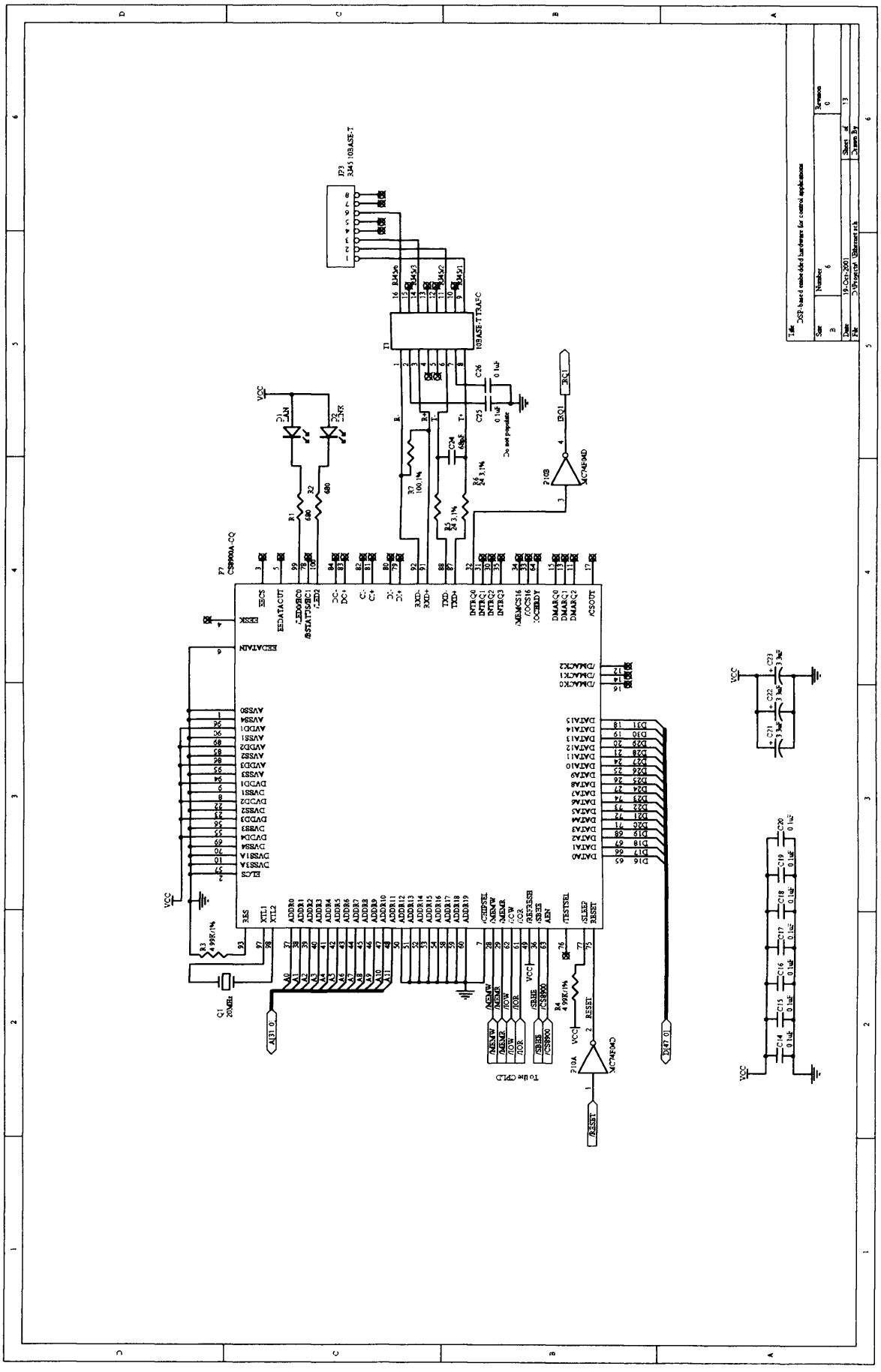

Figure B.9: Ethernet interface module.

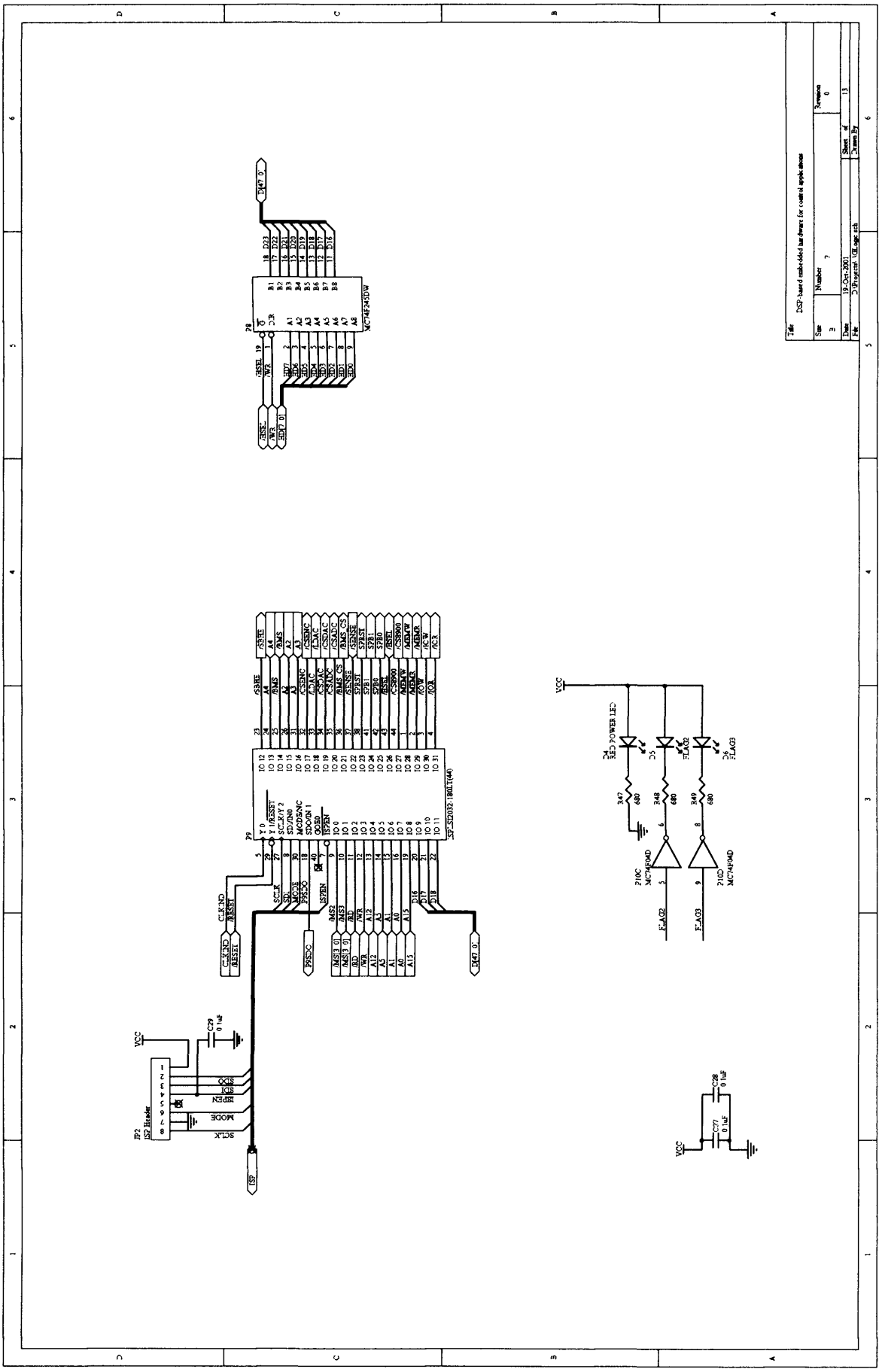

Figure B.10: Board control logic and LEDs.

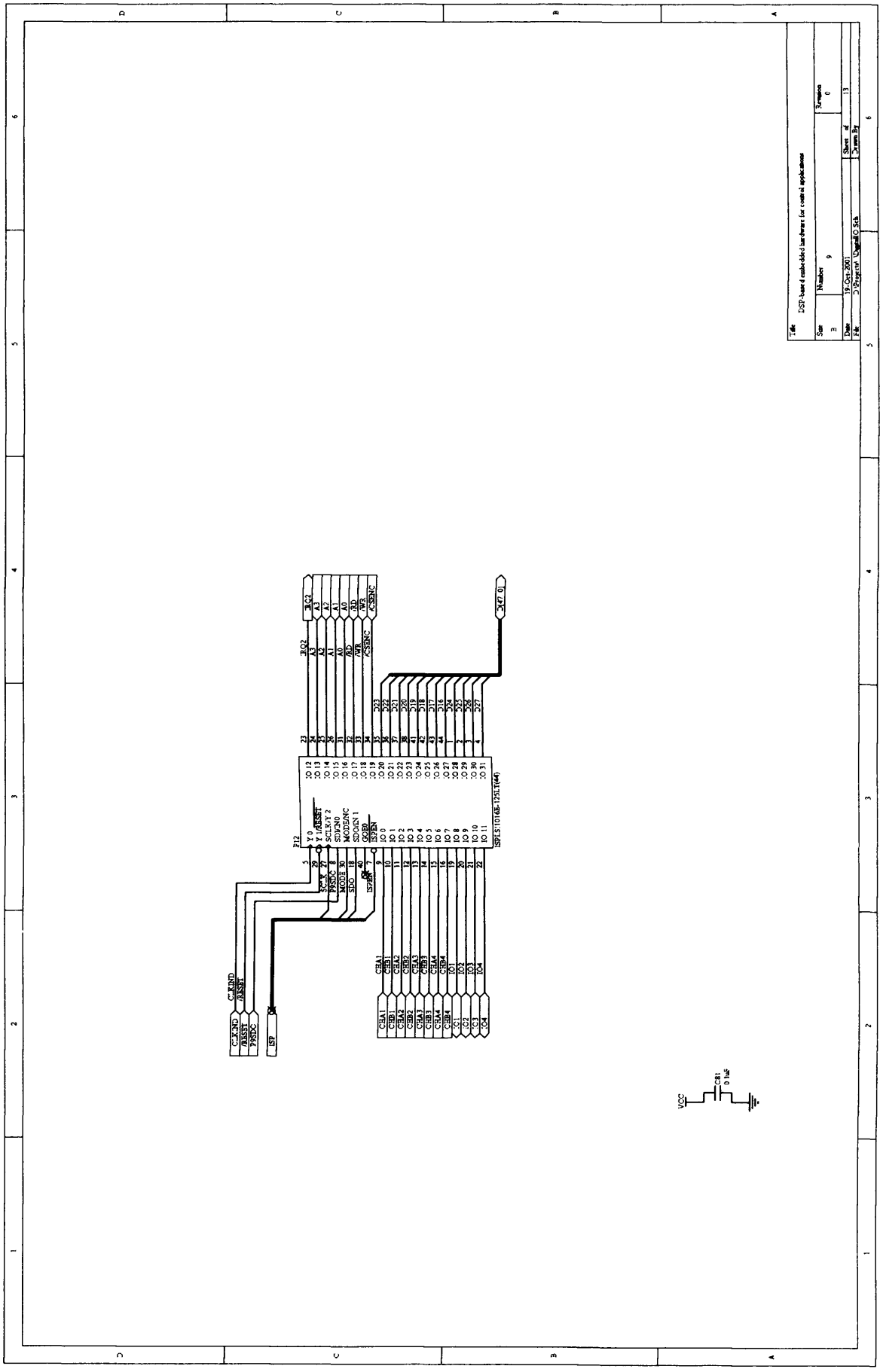

Figure B.11: Programmable digital I/O interface.

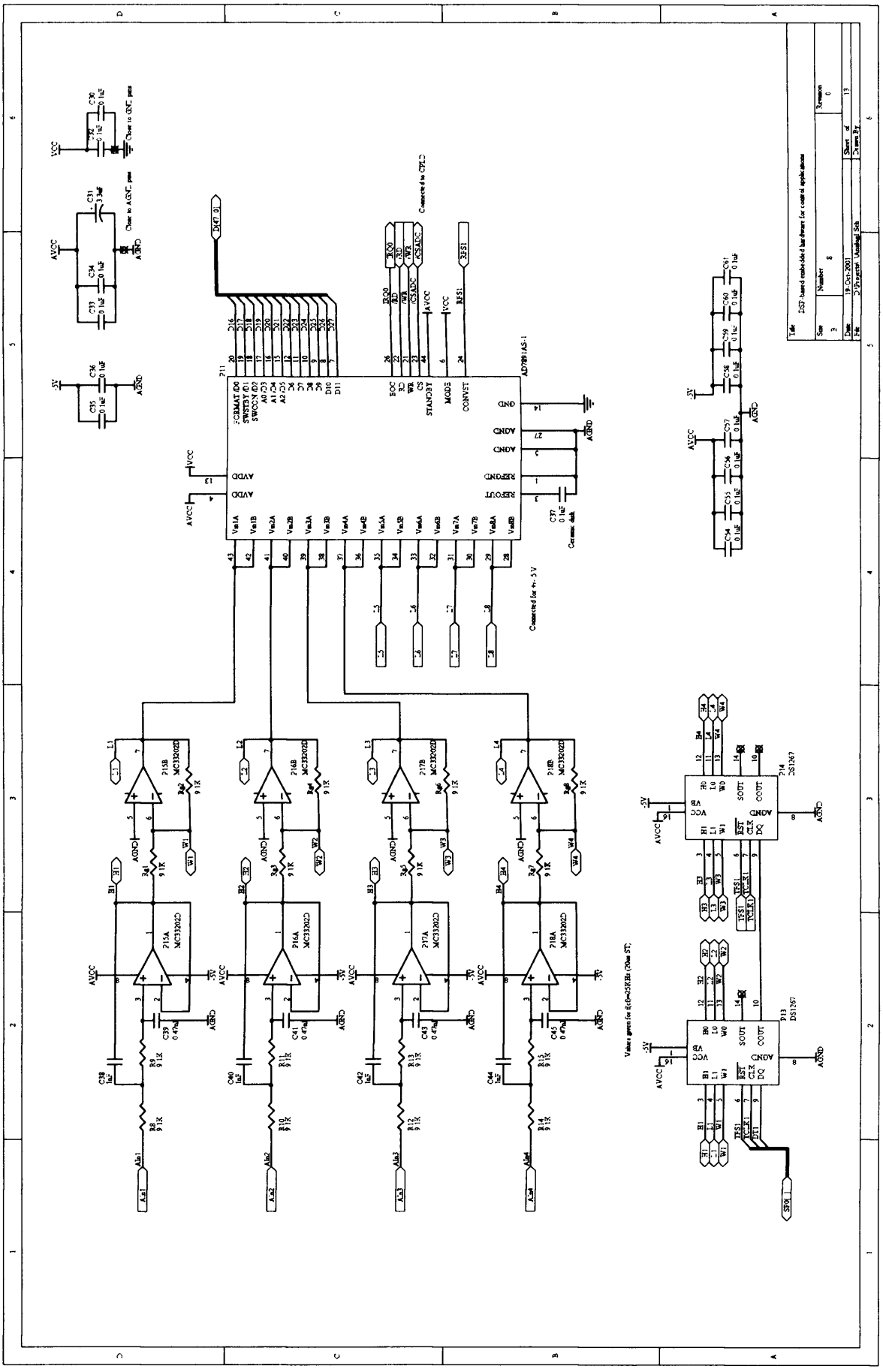

Figure B.12: ADC and four analogue inputs with programmable gain amplifiers and anti-aliasing filters.

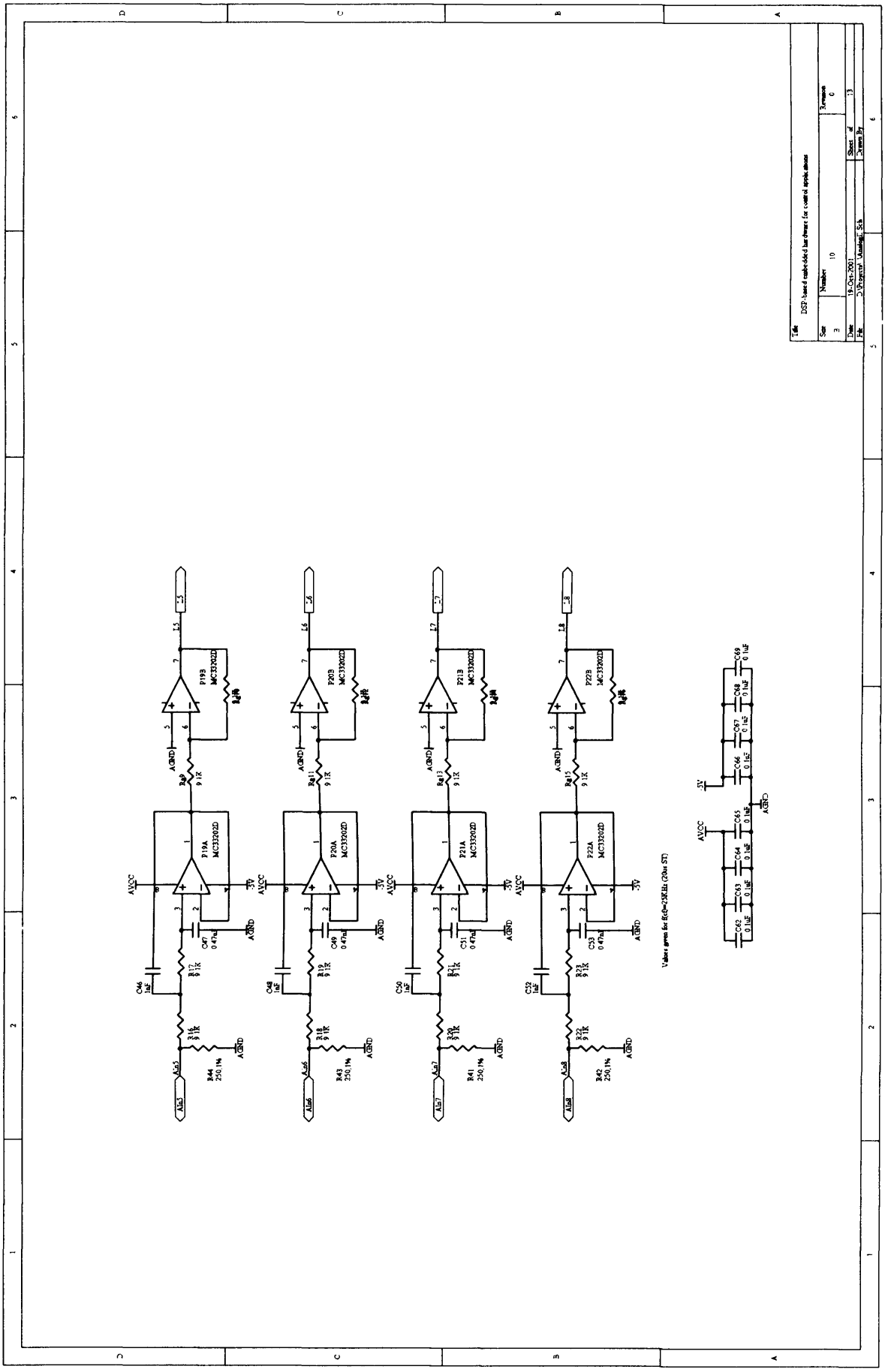

Figure B.13: Four analogue inputs with fixed gain amplifiers and anti-aliasing filters.

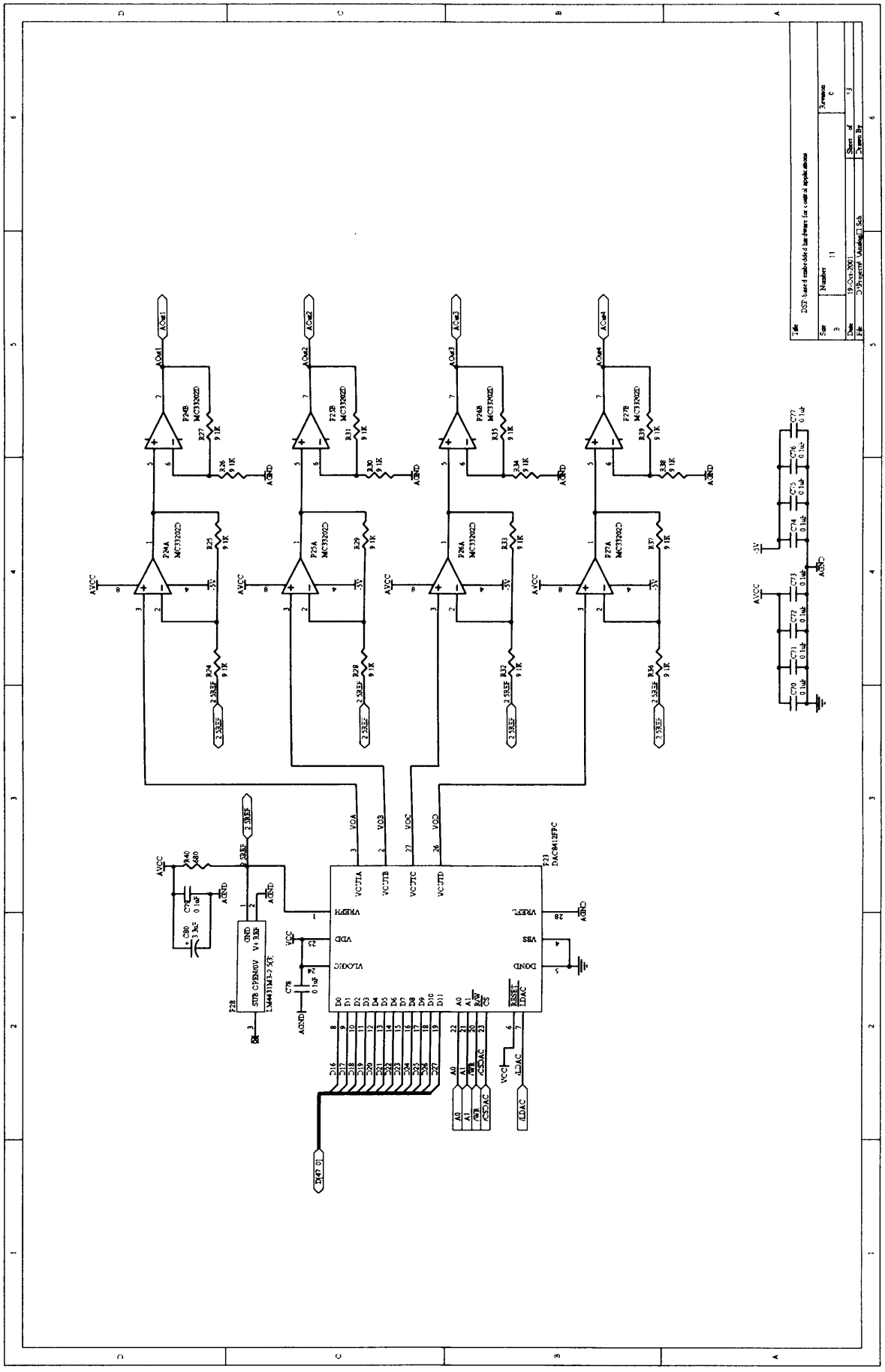

Figure B.14: The DAC and its output filters.

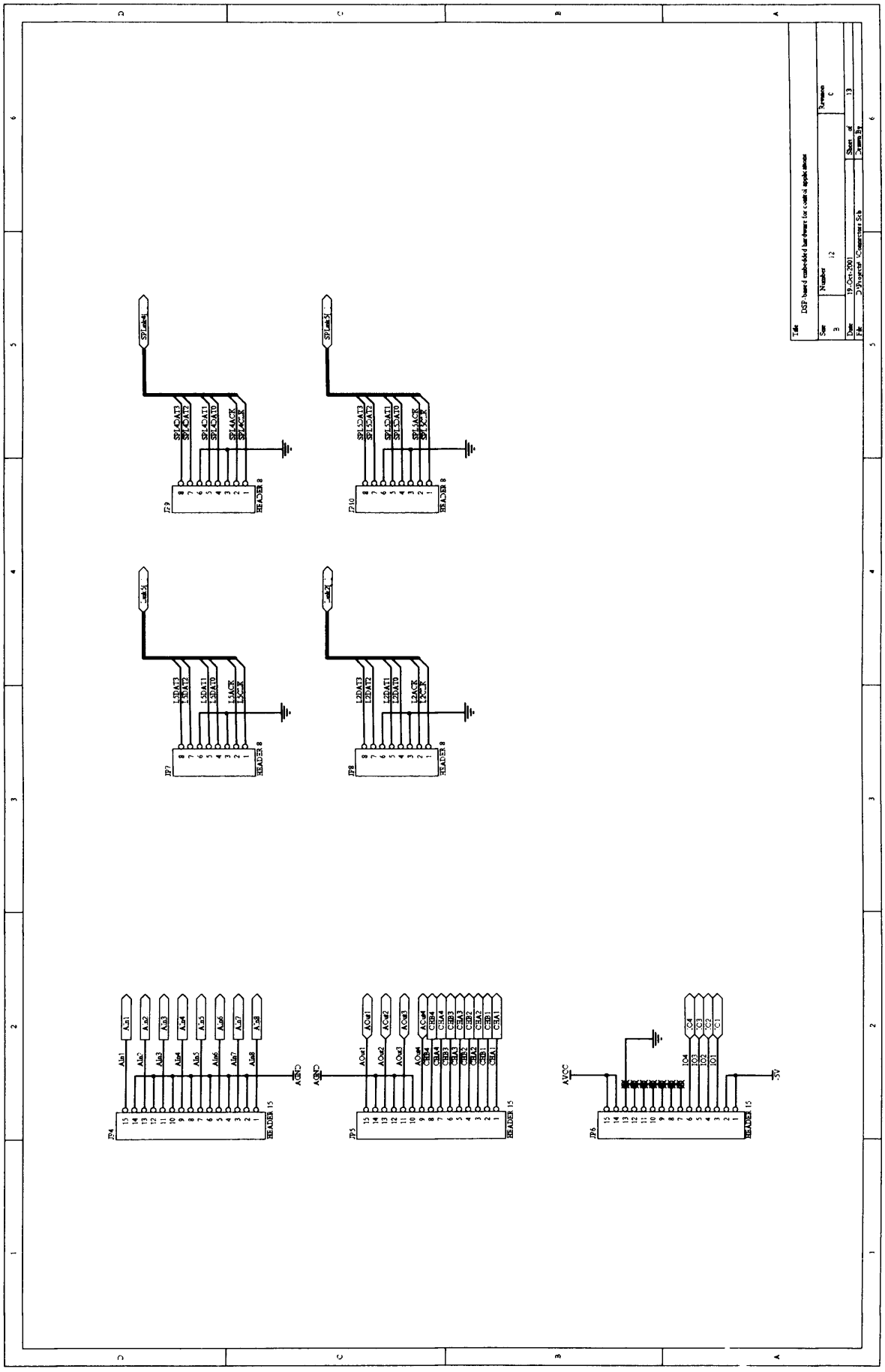

Figure B.15: Connectors: analogue I/O, digital I/O, and link ports for multiprocessing.

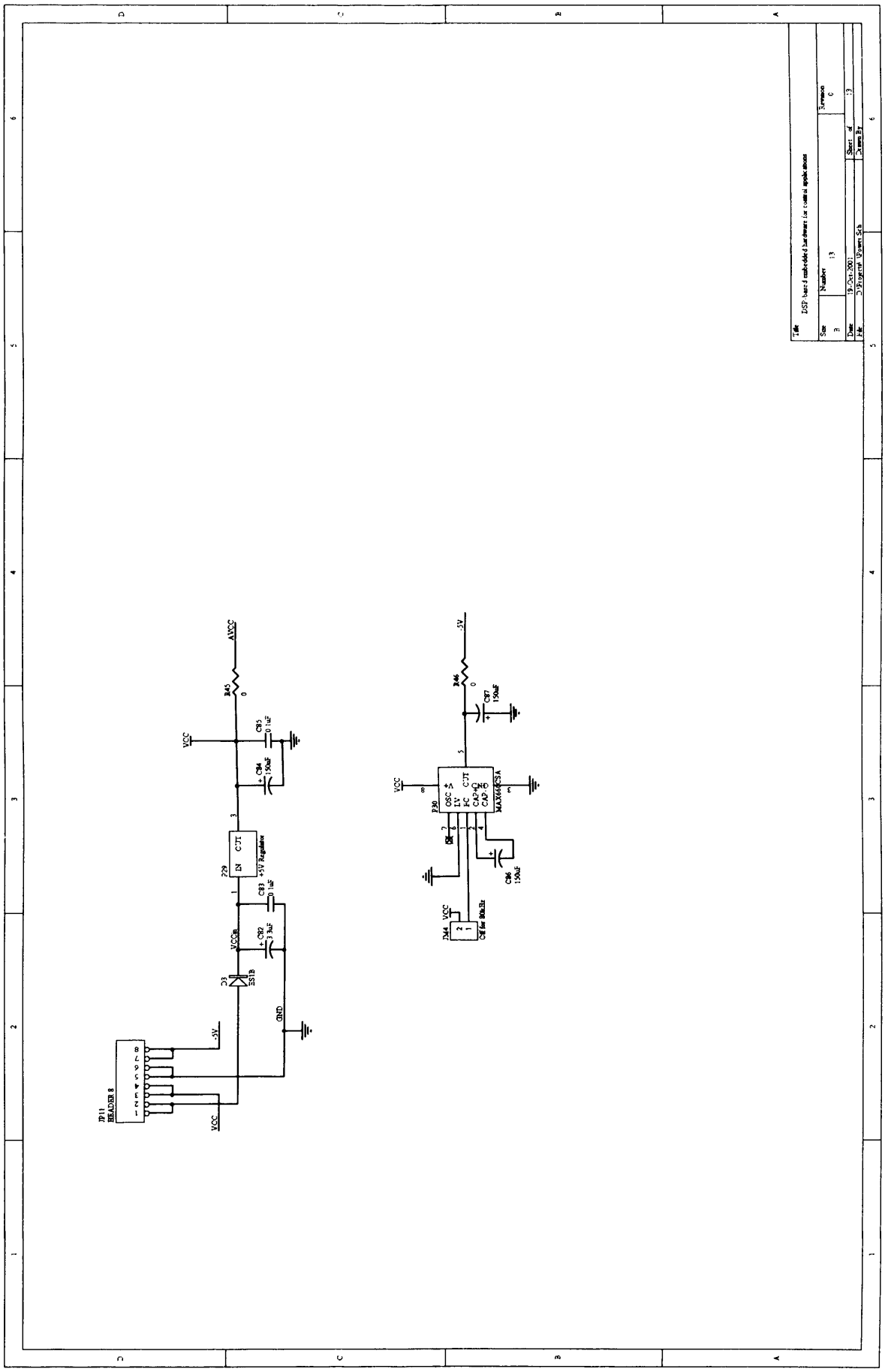

Figure B.16: Power supply and voltage inverter circuits.

Appendix C

Solutions to $\mathcal{H}_\infty$ control problems

Although the algorithm for deriving $\mathcal{H}_\infty$ controllers is readily available, an alternative analytical solution is developed using Lagrange multipliers methods and differential games theory [82, 81, 83]. Motivation for this work is its close analogies with the classical LQG solution. The mathematical derivations are fully described below. The algorithmic work is a summary of the analytical work in [80, 84, 85, 86, 87], which is further customised to suit the $\mathcal{H}_\infty$ optimisation problem.

C.1 State-feedback $\mathcal{H}_\infty$ optimisation problem

The state-feedback $\mathcal{H}_\infty$ problem requires the solution of the optimisation task in Eqn. 6.33 for K. This requires the construction of the state-space model of the open-loop model $P(s)$ (Fig. 6.4) from Eqn. 6.28 [y is not used for the state-feedback design and hence removed from the model]

$$\begin{aligned} \dot{x} &= Ax + B_1 w + B_2 u \\ q &= C_1 x + D_{12} u \end{aligned} \tag{C.1}$$

To simplify the derivations and without a loss of generality, D_{11} in Eqn. 6.28 is taken to be zero by selecting a strictly proper performance weight W (e.g. D_W=0 in Eqn. 6.27 and consequently $D_{11} = 0$). With reference to Eqn. C.1, the $\mathcal{H}_\infty$ design goal is to minimise the influence of the disturbance w on the penalty q by driving the control input $u = Kx$. This can be achieved by assigning an upper limit on the ∞-norm of the transfer function from w to q, i.e.

$$\|T_{qw}\|_\infty \leq \gamma$$

Since the ∞-norm is related to the energy of the input and the output signals (Eqn. 6.4), the above inequality can be rewritten to the following equivalent form

$$\|T_{qw}\|_\infty = \sup_w \frac{\|q\|_2}{\|w\|_2} \leq \gamma \tag{C.2}$$

where $\sup_w$ is the worst possible disturbance input w. Rearranging the right-hand-side of the above inequality to

$$\|q\|_2^2 - \gamma^2 \|w\|_2^2 \leq 0$$

provides a suitable basis for defining a cost function for the optimisation problem: Minimise

$$J(u, w) = \|q\|_2^2 - \gamma^2 \|w\|_2^2 \tag{C.3}$$

for the worst possible input w by finding a feedback controller K that drives u in Eqn. C.1. This optimisation problem is a two-player dynamic game problems [80, 81, 82, 83]. The first input (or player) w is driven by the nature and its goal is to maximise the cost function. The second input u is driven by the controller and its aim is to minimise the cost function for the worst possible w. This can be summarised as

$$J(u, w) = \inf_u \left\{ \sup_w \left(\|q\|_2^2 - \gamma^2 \|w\|_2^2 \right) \right\} \tag{C.4}$$

where inf and sup represent min and max, respectively, for a fixed interval of interest. Employing the definition of energy and substituting the 2-norm with its integral equivalent (see Eqn. 6.5), the above cost is rewritten to

$$J(u, w) = \int_0^{t_f} (q^T q - \gamma^2 w^T w) dt \tag{C.5}$$

Similar optimisation problems have been previously solved in the control literature (for example the LQR control problem [79, 80]). Defining $\hat{w}$ as the worst input w that maximises $J(u, w)$ and $\check{u}$ as the optimal u that minimises $J(u, w)$, the optimisation task is to find the saddle point in $J(u, w)$ such that

$$J(\check{u}, w) \leq J(\check{u}, \hat{w}) \leq J(u, \hat{w})$$

where w and u are arbitrary w and u.

Eqn. C.4 defines a constrained optimisation problem since q, w and u have to satisfy Eqn. C.1. To solve this, Lagrange multipliers can be used to transform the original optimisation problem to a higher-order, unconstrained problem [79, 80, 110, 91]. This requires transforming the original cost function to

$$J(u, w, p) = J(u, w) + pf(x)$$

where p is the Lagrange multiplier and $f(x) = 0$ is the constraint condition in Eqn. C.1. The solution to the above problem will give the optimal $\check{u}$ and $\hat{w}$, as well as p.

A: Deriving $\check{u}$ and $\hat{w}$

Employing the definition of Lagrange multipliers, the cost function in Eqn C.5 is converted to an unconstrained cost function by adding the constraint in Eqn. C.1

$$J(u,w,p) = \frac{1}{2}\int_0^{t_f} q^T q - \gamma^2 w^T w + 2p^T \underbrace{(Ax + B_1 w + B_2 u - \dot{x})}_{f(x)=0} dt \tag{C.6}$$

The factor of $\frac{1}{2}$ is included for convenience without changing the generality of the derivations. Substituting q in the definition above with its equivalent from Eqn. C.1, transforms $J(\cdot)$ to

$$\begin{aligned} J(u,w,p) = \tfrac{1}{2}\int_0^{t_f} \Big\{ &(C_1 x + D_{12}u)^T (C_1 x + D_{12}u) - \gamma^2 w^T w \\ &+ 2p^T (Ax + B_1 w + B_2 u - \dot{x}) \Big\} dt \end{aligned} \tag{C.7}$$

For convenience, the following Hamiltonian function [79, 80] is defined for the derivations

$$H(x,p,w,u) = \frac{1}{2}\left\{(C_1 x + D_{12}u)^T (C_1 x + D_{12}u) - \gamma^2 w^T w\right\} + p^T (Ax + B_1 w + B_2 u) \tag{C.8}$$

to simplify the notation of the performance cost in Eqn. C.7 to

$$J(u,w,p) = \int_0^{t_f} H(x,p,w,u) - p^T \dot{x}\, dt \tag{C.9}$$

Integrating $p^T \dot{x}$ by parts yields

$$\int_0^{t_f} p^T \dot{x} dt = p^T(t_f)x(0) - p^T(0)x(t_f) - \int_0^{t_f} \dot{p}^T x dt$$

Assuming that the initial condition $x(0)$ and the final condition $p(t_f)$ satisfy

$$p(t_f) = 0, \quad and \;\; x(0) = 0 \tag{C.10}$$

substituting the latter integral back in Eqn. C.9 transforms it to

$$J(u,w,p) = \int_0^{t_f} H(x,p,w,u) + \dot{p}^T x dt \tag{C.11}$$

The $\mathcal{H}_\infty$ minimisation task becomes determining $\hat{w}$ and $\check{u}$ that maximises and respectively minimise $J(u,w,p)$ in Eqn. C.11.

Deriving $\hat{w}$: Determining the worst estimation for the disturbance, $\hat{w}$, requires solving

$$\frac{\partial J(u,w,p)}{\partial w} = \frac{\partial}{\partial w}\int_0^{t_f} \left\{H(x,p,w,u) + \dot{p}^T x\right\} dt = 0$$

Since the limits of the integral are not functions of w, this differential equation is same as

$$\frac{\partial J(u,w,p)}{\partial w} = \frac{\partial}{\partial w}\left\{H(x,p,w,u) + \dot{p}^T x\right\} = \frac{\partial H(x,p,w,u)}{\partial w} = 0$$

Using the definition for the Hamiltonian function in Eqn. C.8, the optimal $\hat{w}$ is derived by solving

$$\left.\frac{\partial H(x,p,w,u)}{\partial w}\right|_{w=\hat{w}} = \left.-\gamma^2 w + B_1^T p\right|_{w=\hat{w}} = 0$$

This gives

$$\hat{w} = \gamma^{-2} B_1^T p \tag{C.12}$$

$\hat{w}$ maximises $J(u,w,p)$ since

$$\left.\frac{\partial^2 H(x,p,w,u)}{\partial w^2}\right|_{w=\hat{w}} = -\gamma^2 < 0$$

$\hat{w}$ in Equation C.12 is a function of the Lagrange multiplier p. the procedure for determining p, which is also called by some authors the co-state of the system [79], is given below on the page.

Deriving $\check{u}$: Determining the optimal control law $\check{u}$ requires differentiating the Hamiltonian function in terms of u

$$\left.\frac{\partial H(x,p,w,u)}{\partial u}\right|_{u=\check{u}} = \left.D_{12}^T D_{12} u + B_2^T p + D_{12}^T C_1 x\right|_{u=\check{u}} = 0$$

Solving this equation gives

$$\check{u} = -(D_{12}^T D_{12})^{-1}\left(B_2^T p + D_{12}^T C_1 x\right) \tag{C.13}$$

This function minimises $J(u,w,p)$ since $\partial^2 H(x,p,w,u)/\partial u^2 = 2 > 0$. The only unknown in the optimal state-feedback control law is p.

Deriving p: Determination of p requires differentiating the cost function in Eqn. C.11 in terms of x and p

$$\frac{\partial J(u,w,p)}{\partial x} = \frac{\partial H(x,p,w,u)}{\partial x} + \dot{p}^T = C_1^T C_1 x + C_1^T D_{12} u + A^T p + \dot{p}^T = 0$$

The differential equation for the co-state p becomes

$$\dot{p} = -\frac{\partial H(x,p,w,u)}{\partial x} = -C_1^T C_1 x - D_{12}^T C_1 u - A^T p$$

Similarly, differentiating $J(u,w,p)$ in terms of p gives

$$\frac{\partial J(u,w,p)}{\partial p} = Ax + B_1 w + B_2 u - \dot{x} = 0$$

The differential equation for x becomes

$$\dot{x} = \frac{\partial H(x,p,w,u)}{\partial p} = Ax + B_1 w + B_2 u$$

The validity of the latter equation can be easily checked by comparison with Eqn. C.1. To summarise, for a given Hamiltonian function $H(x,p,w,u)$, $\dot{x}$ and $\dot{p}$ are given as the solutions to [80, 79]

$$\begin{aligned} \dot{x} &= \frac{\partial H(x,p,w,u)}{\partial p} \\ \dot{p} &= -\frac{\partial H(x,p,w,u)}{\partial x} \end{aligned} \tag{C.14}$$

For the Hamiltonian function in Eqn. C.8, these solutions are

$$\begin{aligned} \dot{x} &= Ax + B_1 w + B_2 u \\ \dot{p} &= -C_1^T C_1 x - D_{12}^T C_1 u - A^T p \end{aligned} \tag{C.15}$$

To reduce the number of unknowns, u and w are substituted with their optimal values $\check{u}$ and $\hat{w}$ in Eqns. C.12 and C.13; this transforms $\dot{x}$ and $\dot{p}$ to

$$\begin{aligned} \dot{x} &= \left(A - B_2 V_1^{-1} D_{12}^T C_1\right) x + \left(\gamma^{-2} B_1 B_1^T - B_2 V_1^{-1} B_2^T\right) p \\ \dot{p} &= -\left(C_1^T C_1 - C_1^T D_{12} V_1^{-1} D_{12}^T C_1\right) x - \left(A - B_2 V_1^{-1} D_{12}^T C_1\right)^T p \end{aligned} \tag{C.16}$$

where $V_1 = (D_{12}^T D_{12})$. These equations can be grouped to one single state equation

$$\begin{bmatrix} \dot{x} \\ \dot{p} \end{bmatrix} = \left[\begin{array}{c|c} \left(A - B_2 V_1^{-1} D_{12}^T C_1\right) & \gamma^{-2} B_1 B_1^T - B_2 V_1^{-1} B_2^T \\ \hline -\left(C_1^T C_1 - C_1^T D_{12} V_1^{-1} D_{12}^T C_1\right) & \left(A - B_2 V_1^{-1} D_{12}^T C_1\right)^T \end{array}\right] \begin{bmatrix} x \\ p \end{bmatrix} \tag{C.17}$$

Finding the co-state p requires solving this unforced system of differential equations. Recalling from the state space theory that the solution to the unforced system $\dot{x} = Ax$ is given by its fundamental matrix, i.e. $x(t) = e^{At}x(0) = \Phi x$, the state and the co-state at the terminal moment t_f are given by

$$\begin{bmatrix} x(t_f) \\ p(t_f) \end{bmatrix} = \begin{bmatrix} \Phi_{11}(t_f - t) & \Phi_{12}(t_f - t) \\ \Phi_{21}(t_f - t) & \Phi_{22}(t_f - t) \end{bmatrix} \begin{bmatrix} x(t) \\ p(t) \end{bmatrix} \tag{C.18}$$

Since $p(t_f) = 0$, finding p requires solving

$$0 = \Phi_{21}(t_f - t)x + \Phi_{22}(t_f - t)p, \quad \text{or}$$

$$p = \Phi_{22}(t_f - t)^{-1}\Phi_{21}(t_f - t)x$$

The form of this equation suggests that p is a linear combination of the state variables x. This fact has been used by several authors and the solution to p can be found with the help of the *sweep* method [80, 110] which requires substituting p with

$$p = \mathbf{P}x \tag{C.19}$$

where $\mathbf{P}$ is the matrix of proportionality between the state x and the co-state p. The problem of determining p then becomes a problem of determining the matrix $\mathbf{P}$.

Determining the matrix of proportionality P: Finding $\mathbf{P}$ requires differentiating Eqn. C.19

$$\dot{p} = \dot{\mathbf{P}}x + \mathbf{P}\dot{x}$$

Substituting $\dot{p}$ and $\dot{x}$ with their equivalents in Eqn. C.16 and using the fact that $p = \mathbf{P}x$, the above equation is transformed to

$$\begin{aligned} &-\left(C_1^T C_1 - C_1^T D_{12} V_1^{-1} D_{12}^T C_1\right) x - \left(A - B_2 V_1^{-1} D_{12}^T C_1\right)^T \mathbf{P}x = \\ &\dot{\mathbf{P}}x + \mathbf{P}\left\{\left(A - B_2 V_1^{-1} D_{12}^T C_1\right) x + \left(\gamma^{-2} B_1 B_1^T - B_2 V_1^{-1} B_2^T\right) \mathbf{P}x\right\} \end{aligned}$$

Since this equation has to hold for all possible trajectories $x \neq 0$, x can be dropped from the above definition and the resultant equation transforms to a Riccati equation

$$\begin{aligned} &\mathbf{P}\left(A - B_2 V_1^{-1} D_{12}^T C_1\right) + \left(A - B_2 V_1^{-1} D_{12}^T C_1\right)^T \mathbf{P} - \\ &-\mathbf{P}\left(B_2 V_1^{-1} B_2^T - \gamma^{-2} B_1 B_1^T\right) \mathbf{P} + \left(C_1^T C_1 - C_1^T D_{12} V_1^{-1} D_{12}^T C_1\right) = 0 \end{aligned} \tag{C.20}$$

with the boundary condition $\mathbf{P}(t_f) = 0$. The solution to this equation is the unknown matrix $\mathbf{P}$. To solve this equation, one can substitute each element of $\mathbf{P}$ with $\mathbf{p}_{i,j}$ and then transform Eqn. C.20 to a linear system of equations with $\mathbf{p}_{i,j}$ unknowns. This approach, however, is tedious since it involves some analytical transformation and collecting terms. Riccati equations are typically solved numerically ([111] and the references therein). Once $\mathbf{P}$ is determined from Eqn. C.20, the optimal control signal $\breve{u}$ (Eqn. C.13) and the estimation of the worst disturbance $\hat{w}$ (Eqn. C.12) become

$$\begin{aligned} \breve{u} &= -V_1^{-1}\left(B_2^T \mathbf{P} + D_{12}^T C_1\right) x \\ \hat{w} &= \gamma^{-2} B_1^T \mathbf{P}x \end{aligned} \tag{C.21}$$

where $V_1 = (D_{12}^T D_{12})$. The optimal control law is a state feedback control law, since $\breve{u}$ is a linear combination of the state vector x. The spectrum of the Hamiltonian matrix in Eqn. C.16 is symmetrical with respect to the imaginary axis, i.e. it has n eigenvalues with Real(s) > 0 and n eigenvalues with Real(s) < 0. The Riccati equation in Eqn. C.20 has a solution $\mathbf{P}$ (and hence the feedback controller in Eqn. C.21 exists) as long as these eigenvalues are strictly real. The algorithm for deriving state-feedback $\mathcal{H}_\infty$ controllers is summarised in Section C.1.2.

C.1.1 Proof of results

To prove that $\hat{u}$ and $\breve{w}$ in Eqn. C.21 are the optimal solutions to the optimisation problem, these are substituted in the cost function $J(u, w)$ (Eqn. C.5) and its value is calculated.

The derivations in this section use the fact that since $p(t_f) = \mathbf{P}(t_f) = 0$ and $x(0) = 0$, the following function has a zero integral value

$$\int_0^{t_f} \frac{\partial x^T \mathbf{P} x}{\partial t} dt = x^T(t_f)\mathbf{P}(t_f)x(t_f) - x^T(0)\mathbf{P}(0)x(0) = 0$$

Furthermore, the following function is constructed

$$\frac{\partial x^T \mathbf{P} x}{\partial t} = \dot{x}^T \mathbf{P} x + x^T \mathbf{P} \dot{x}$$

Substituting $\dot{x}$ with its equivalent in Eqn. C.1, the above can be transformed to

$$\begin{array}{rcl} \frac{\partial x^T \mathbf{P} x}{\partial t} & = & (Ax + B_1 w + B_2 u)^T \mathbf{P} x + x^T \mathbf{P}(Ax + B_1 w + B_2 u) \\ & = & x^T(A^T\mathbf{P} + \mathbf{P}A)x + w^T B_1 \mathbf{P} x + x^T \mathbf{P} B_1^T w + u^T B_2 \mathbf{P} x + x^T \mathbf{P} B_2^T u \end{array} \tag{C.22}$$

Making use of the following equivalent transformations

$$\begin{aligned} w^T B_1 \mathbf{P} x + x^T \mathbf{P} B_1^T w &= -(w - B_1^T \mathbf{P} x)^T (w - B_1^T \mathbf{P} x) + w^T w + x^T \mathbf{P} B_1 B_1^T \mathbf{P} x \\ &= -\|w - B_1^T \mathbf{P} x\|^2 + \|w\|^2 + x^T \mathbf{P} B_1 B_1^T \mathbf{P} x \end{aligned}$$

and

$$\begin{aligned} u^T B_2 \mathbf{P} x + x^T \mathbf{P} B_2^T u &= (u + B_2^T \mathbf{P} x)^T (u + B_2^T \mathbf{P} x) - u^T u - x^T \mathbf{P} B_2 B_2^T \mathbf{P} x \\ &= \|u + B_2^T \mathbf{P} x\|^2 - \|u\|^2 - x^T \mathbf{P} B_2 B_2^T \mathbf{P} x \end{aligned}$$

the function in Eqn C.22 is further transformed to

$$\begin{array}{rcl} \frac{\partial x^T \mathbf{P} x}{\partial t} & = & x^T \left(A^T\mathbf{P} + \mathbf{P}A + \mathbf{P}(B_1 B_1^T - B_2 B_2^T)\mathbf{P} \right) x \\ & + & \|u + B_2^T \mathbf{P} x\|^2 - \|u\|^2 - \|w - B_1^T \mathbf{P} x\|^2 + \|w\|^2 \end{array} \tag{C.23}$$

To simplify this equation further, the Riccati equation in Eqn. C.20 is used to make the following substitutions

$$x^T \left(A^T\mathbf{P} + \mathbf{P}A + \mathbf{P}(B_1 B_1^T - B_2 B_2^T)\mathbf{P} \right) = \mathbf{P} B_2 D_{12}^T C_1 + (B_2 D_{12}^T C_1)^T \mathbf{P} - \left(C_1^T C_1 - C_1^T D_{12} D_{12}^T C_1 \right)$$

For better readability and without changing the generality of the solution, γ in Eqn. C.20 is considered to be $\gamma = 1$, and $V_1 = D_{12}^T D_{12}$ is considered to be $V_1 = I$ (this requires applying some equivalent transformations to the state-matrices [37]). Substituting the right-hand-side of this equation in Eqn. C.23, reduces the latter to

$$\begin{array}{rcl} \frac{\partial x^T \mathbf{P} x}{\partial t} & = & x^T \left(\mathbf{P} B_2 D_{12}^T C_1 + (B_2 D_{12}^T C_1)^T \mathbf{P} - \left(C_1^T C_1 - C_1^T D_{12} D_{12}^T C_1 \right) \right) x \\ & + & \|u + B_2^T \mathbf{P} x\|^2 - \|u\|^2 - \|w - B_1^T \mathbf{P} x\|^2 + \|w\|^2 \end{array} \tag{C.24}$$

With reference to the state-space representation in Eqn. C.1, $q^T q$ can be described as

$$q^T q = \|q\|^2 = (C_1 x + D_{12} u)^T (C_1 x + D_{12} u) = x^T C_1^T C_1 x + u^T D_{12}^T C_1 x + x^T C_1^T D_{12} u + u^T u$$

Making use of the following equivalent transformation

$$u^T D_{12}^T C_1 x + x^T C_1^T D_{12} u = \|u + D_{12}^T C_1 x\|^2 - \|u\|^2 - x^T C_1^T D_{12} D_{12}^T C_1 x$$

$\|q\|^2$ further reduces to

$$\|q\|^2 = x^T C_1^T C_1 x - x^T C_1^T D_{12} D_{12}^T C_1 x + \|u + D_{12}^T C_1 x\|^2$$

Substituting $-x^T(C_1^T C_1 - C_1^T D_{12} D_{12}^T C_1)x$ from this equation to Eqn. C.23 transforms the latter to

$$\begin{aligned} \frac{\partial x^T \mathbf{P} x}{\partial t} &= x^T \left(\mathbf{P} B_2 D_{12}^T C_1 + (B_2 D_{12}^T C_1)^T \mathbf{P}\right) x \\ &- \|q\|^2 + \|u + D_{12}^T C_1 x\|^2 + \|u + B_2^T \mathbf{P} x\|^2 - \|u\|^2 - \|w - B_1^T \mathbf{P} x\|^2 + \|w\|^2 \end{aligned} \tag{C.25}$$

Furthermore, the following equivalent transformation

$$\|u+D_{12}^T C_1 x\|^2+\|u+B_2^T \mathbf{P} x\|^2 = \|u+\left(B_2^T \mathbf{P} x + D_{12}^T C_1 x\right)\|^2+\|u\|^2-x^T C_1^T D_{12} B_2 \mathbf{P} x-x^T \mathbf{P} B_2 D_{12}^T C_1$$

is substituted the equation above to simplify Eqn. C.25 to

$$\frac{\partial x^T \mathbf{P} x}{\partial t} = \|u + \left(B_2^T \mathbf{P} x + D_{12}^T C_1 x\right)\|^2 - \|q\|^2 - \|w - B_1^T \mathbf{P} x\|^2 + \|w\|^2 \tag{C.26}$$

This equation is further integrated from 0 to t_f to get

$$\begin{aligned} \int_0^{t_f} \frac{\partial x^T \mathbf{P} x}{\partial t} dt &= \int_0^{t_f} \left\{ -\left(\|q\|^2 - \|w\|^2\right) - \|w - B_1^T \mathbf{P} x\|^2 + \|u + \left(B_2^T \mathbf{P} x + D_{12}^T C_1 x\right)\|^2 \right\} dt \\ &= -\left(\|q\|_2^2 - \|w\|_2^2\right) - \|w - B_1^T \mathbf{P} x\|_2^2 + \|u + \left(B_2^T \mathbf{P} x + D_{12}^T C_1 x\right)\|_2^2 \end{aligned} \tag{C.27}$$

Recalling the fact that the above integral has a zero value and that the cost of the optimisation problem is

$$\|q\|_2^2 - \|w\|_2^2 = J(q, w)$$

Eqn. C.27 simplifies to

$$0 = -J(u, w) + \|u + \left(B_2^T \mathbf{P} x + D_{12}^T C_1 x\right)\|_2^2 - \|w - B_1^T \mathbf{P} x\|_2^2 \tag{C.28}$$

which in turns implies that

$$J(u, w) = \|u + \underbrace{\left(B_2^T \mathbf{P} x + D_{12}^T C_1 x\right)}_{-\check{u}}\|_2^2 - \|w - \underbrace{B_1^T \mathbf{P} x}_{\hat{w}}\|_2^2 \tag{C.29}$$

Based on the above derivations the following conclusion can be made. If the control signal u and the disturbance w chose to use the design strategies $\check{u}$ and $\hat{w}$ in Eqn. C.21, the cost of the optimisation problem in Eqn. C.4 which turns to be same as the cost in Eqn. C.29 reduces to 0. This implies that any other control strategies u and w will make this cost larger and hence $\check{u}$ and $\hat{w}$ are the optimal solutions to the state-feedback control problem. Based on the mathematical derivations, the full algorithm for deriving state-feedback $\mathcal{H}_\infty$ controllers is presented below.

C.1.2 Algorithm for deriving state-feedback $\mathcal{H}_\infty$ control laws

Step 1: For a given open-loop system $G(s)$ and performance weights $W(s)$ and W_c, construct the state-space model of the generalised open-loop system in Fig. 6.4 using Eqn. 6.28.

Step 2: Use the state-space matrices to construct the following Riccati equation (Eqn. C.20); take γ to be a large number and $V_1 = D_{12}^T D_{12}$

$$\begin{aligned}&\mathbf{P}\left(A - B_2 V_1^{-1} D_{12}^T C_1\right) + \left(A - B_2 V_1^{-1} D_{12}^T C_1\right)^T \mathbf{P} - \\ &-\mathbf{P}\left(B_2 V_1^{-1} B_2^T - \gamma^{-2} B_1 B_1^T\right)\mathbf{P} + \left(C_1^T C_1 - C_1^T D_{12} V_1^{-1} D_{12}^T C_1\right) = 0\end{aligned}$$

Step 3: Solve this equation to determine $\mathbf{P}$, $\mathbf{P} > 0$ using a standard Riccati equation solver (for example *are* in Matlab). Use $\mathbf{P}$ to derive the $\mathcal{H}_\infty$ state-feedback gain K (Eqn. C.21) in Fig. 6.4

$$\breve{u} = Kx = -(D_{12}^T D_{12})^{-1}\left(B_2^T \mathbf{P} + D_{12}^T C_1\right) x \tag{C.30}$$

Use this control law $\breve{u}$ in Eqn. 6.28 to construct the closed-loop state-space matrices for the system in Fig. 6.4

$$\begin{aligned}\dot{x} &= Ax + B_1 w + B_2 \breve{u} = \underbrace{\left(A - B_2 V_1^{-1}\left(B_2^T \mathbf{P} + D_{12}^T C_1\right)\right)}_{A_{CL}} x + B_1 w = A_{CL} x + B_1 w \\ q &= C_1 x + D_{12} u = \underbrace{\left(C_1 - D_{12} V_1^{-1}\left(B_2^T \mathbf{P} + D_{12}^T C_1\right)\right)}_{C_{1CL}} x = C_{1CL} x \\ y &= C_2 x + D_{21} w\end{aligned} \tag{C.31}$$

Construct the closed-loop transfer function from the disturbance w to the penalty output q using the closed-loop state-space representation, i.e.

$$T_{qw} = C_{1CL}(sI - A_{CL})^{-1} B_1 = \left[\begin{array}{c|c} A_{CL} & B_1 \\ \hline C_{1CL} & 0 \end{array}\right] \tag{C.32}$$

Calculate the $\infty-$norm of this transfer function using the algorithm in Section 6.3. If the infinity norm is greater than one, reduce γ and continue from **Step 2**.

Step 4: If for a given value of γ the infinity norm of T_{qw} approaches its optimum value or the Riccati equation does not have a positively definite solution, stop the design loop. The state-feedback $\mathcal{H}_\infty$ controller is given in Eqn. C.30 where $\mathbf{P}$ is taken from the last design iteration.

C.2 Output-feedback $\mathcal{H}_\infty$ optimisation problem

The output-feedback design problem requires solving Eqn. 6.40 for K. In many control techniques, for example the Linear Quadratic Gaussian control (LQG) [79, 91, 88], the

output feedback controller is an interconnection of a state-observer (estimator) and a state-feedback controller. For design consistence this principle has been adopted here, and the proposed output-feedback $\mathcal{H}_\infty$ controller consists of an $\mathcal{H}_\infty$ state-estimator and a state-feedback $\mathcal{H}_\infty$ controller [37]. The problem of deriving the state-feedback controller was fully described in the Section C.1. The problem of deriving $\mathcal{H}_\infty$ estimators is the topic of this section.

The mathematical developments in the next section are organised as follows. Section C.2.1 develops an algorithm for deriving $\mathcal{H}_\infty$ state-estimators which can be used for a general-purpose estimation problems. This algorithm is extended in Section C.2.5 with the state-feedback controller to construct a design procedure for deriving output-feedback $\mathcal{H}_\infty$ controllers. A step by step algorithm for output-feedback $\mathcal{H}_\infty$ design is given in Section C.2.6.

C.2.1 Estimation problems using the $\mathcal{H}_\infty$ design criteria.

A typical estimation problem is shown in Fig. C.1 (a). The design goal is to find an auxiliary dynamic system called *an estimator or an observer* which uses the input u and output y to produce state estimations ($\bar{x}$) such that $\bar{x} \to x$ as $t \to \infty$. This problem has been solved by Kalman for cases when the power spectral density of the noise is known and the solution is the Kalman filter. In this section the task is to find the dynamics of the unknown observer

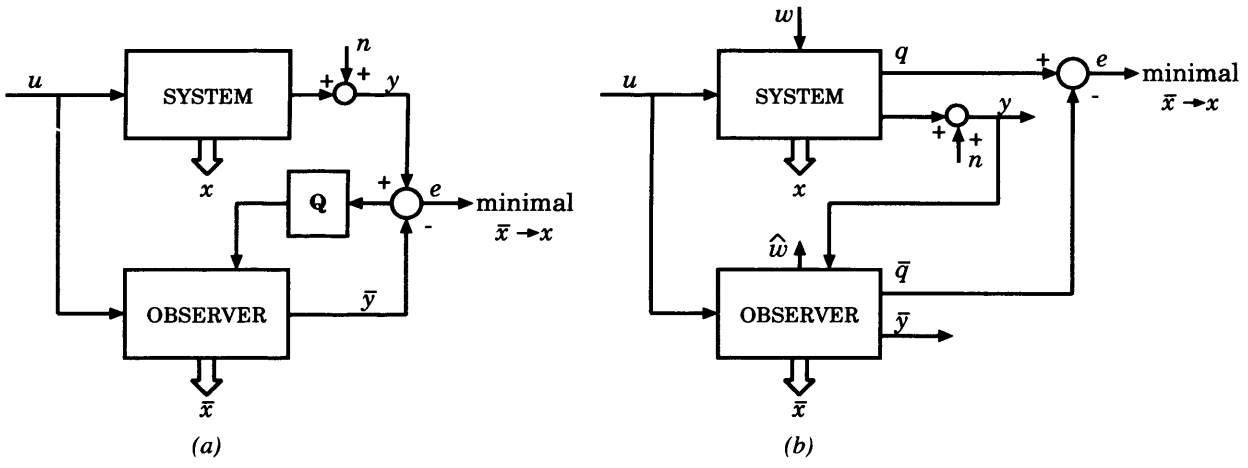

Figure C.1: (a) Kalman filter used as a state observer; Q is the output injection gain. (b) State observer using the $\mathcal{H}_\infty$ performance criterion.

in Fig. C.1(b) by minimising the error between the penalty output q and an estimation for

the penalty output $\bar{q}$, $e = q - \bar{q}$, for the worst possible noise w, i.e.

$$\max_{w,n} \frac{\|q - \bar{q}\|_2}{\|w\|_2 + \|n\|_2} < \gamma$$

This is an $\mathcal{H}_\infty$ design criterion, which is appropriate in applications with a significant uncertainty in the power spectral density of the noise [85, 72]. w is substituted with the worst possible disturbance $\hat{w}$ (Fig. C.1(b)) within the optimisation setting. At this early design stage, the structure of the observer in Fig. C.1 is unknown, and the penalty output from the observer is given below

$$\bar{q} = C_1 \bar{x}$$

where $\bar{x}$ is the observer's state vector. The design goal is to derive the dynamics of the the observer to provide $\bar{x}$ such that the difference between q and $\bar{q}$ is minimised for the worst possible disturbance input w [84, 85]. This is an $\mathcal{H}_\infty$ optimisation problem (see Eqn. C.2).

For the estimation problem, the state-space model in Eqn. 6.28 is used to describe the model of the SYSTEM in Fig. C.1(b)

$$\begin{aligned} \dot{x} &= Ax + B_1 w \\ q &= C_1 x \\ y &= C_2 x + D_{21} w + n \end{aligned} \tag{C.33}$$

Two changes to this model are made with reference to the original model in Eqn. 6.28 :

(a) In the equation for y, n has been added for derivation purposes to represent the measurement noise in the system (Fig. C.1(b)), and

(b) The known control input u has been removed from formulation to simplify the derivations. This does not change the generality of the derivations since using the superposition principle, u can be added to the estimator at the final design stage.

Based on the above two changes, the inputs to the system for the estimation problem are the noise components w and n. Substituting q with its equivalent in Eqn. C.33 and $\bar{q} = C_1 \bar{x}$, the following inequality is constructed [86, 87]

$$\max_{w,n} \frac{\|C_1(x - \bar{x})\|_2}{\|w\|_2 + \|n\|_2} < \gamma$$

This inequality provides a basis for the definition of the following cost function for the estimation problem (see Sec. C.1)

$$J(\bar{x}, w) = \gamma^{-2} \|C_1(x - \bar{x})\|_2^2 - \|w\|_2^2 - \|n\|_2^2 \tag{C.34}$$

With $n = y - C_2x - D_{21}w$, the integral form of this function is

$$J(\bar{x}, w) = \int_0^{t_f} \gamma^{-2}(x-\bar{x})^T C_1^T C_1(x-\bar{x}) - w^T w - (y-C_2x-D_{21}w)^T(y-C_2x-D_{21}w)dt \quad \text{(C.35)}$$

Similarly to the state-feedback problem, this optimisation problem has two players: the state vector $\bar{x}$ and the disturbance input w. The optimisation goal is formulated as finding a saddle point such that [84, 87, 89]

$$J(\check{\bar{x}}, w) \leq J(\check{\bar{x}}, \hat{w}) \leq J(\bar{x}, \hat{w})$$

where $\check{\bar{x}}$ minimises $J(\bar{x}, w)$, $\hat{w}$ maximises $J(\bar{x}, w)$, and $\bar{x}$ and w are arbitrary $\bar{x}$ and w. It has to be noted that the cost function defined in Eqn. C.35 is different from the cost function defined in Eqn. C.5. Therefore $\hat{w}$ derived here is different from $\hat{w}$ derived as a part of the state-feedback solution since these are the optimal results to two different optimisation problems. On another hand, w is the same disturbance signal for both problems with $\hat{w}$ being an estimate for the worst possible w. For the estimation problem, this duality does not play an important role. For the output-feedback controller, however, this duality leads to the violation of the separation principle. This is discussed in Section C.2.5.

Deriving the structure of the $\mathcal{H}_\infty$ estimator

To derive the structure of the unknown $\mathcal{H}_\infty$ estimator in Fig. C.1 (b), the cost function in Eqn. C.35 has to be solved. Since this is a constraint optimisation problem, Lagrange multipliers are used (see Section C.1) to transform the optimisation problem in Eqn. C.35 to a higher-order unconstrained problem defined by the following cost function

$$\begin{aligned} J(\bar{x}, w, \vartheta) = \; & \int_0^{t_f} \gamma^{-2}(x-\bar{x})^T C_1^T C_1(x-\bar{x}) - w^T w - (y-C_2x-D_{21}w)^T(y-C_2x-D_{21}w) \\ & + \vartheta^T(Ax + B_1 w - \dot{x})dt \end{aligned} \quad \text{(C.36)}$$

where ϑ is the Lagrange multiplier. To this problem, the following Hamiltonian function is assigned

$$\begin{aligned} H(x, \vartheta, \bar{x}, w) = \; & \tfrac{1}{2}\left\{(x-\bar{x})^T C_1^T C_1(x-\bar{x}) - \gamma^2 w^T w - \gamma^2(y-C_2x-D_{21}w)^T(y-C_2x-D_{21}w)\right\} \\ & + \vartheta^T(Ax + B_1 w) \end{aligned} \quad \text{(C.37)}$$

After applying integration by parts for $\int_0^{t_f} \vartheta^T \dot{x} dt = -\int_0^{t_f} \dot{\vartheta}^T x dt$ (see Sec. C.1), the latter function is rewritten to ($\vartheta(t_f) = 0$, $x(0) = 0$)

$$J(\bar{x}, w, \vartheta) = \int_0^{t_f} H(x, \vartheta, \bar{x}, w) + \dot{\vartheta}^T x dt \quad \text{(C.38)}$$

Since the disturbance w is unknown, the number of unknowns is reduced by estimating the worst-possible value $\check{w}$.

Determining $\hat{w}$: Finding $\hat{w}$ requires solving

$$\left.\frac{\partial H(x,\vartheta,\bar{x},w)}{\partial w}\right|_{w=\hat{w}} = 0$$

Differentiating $H(x,\vartheta,\bar{x},w)$ in Eqn C.37 in terms of w gives

$$\left.\frac{\partial H(x,\vartheta,\bar{x},w)}{\partial w}\right|_{w=\hat{w}} = -w + D_{21}^T y - D_{21}^T C_2 x - D_{21}^T D_{21} w + B_1^T \vartheta$$

Since $\partial^2 H(x,\vartheta,\bar{x},w)/\partial w^2 = -\gamma^2 < 0$, the above equation gives the following value

$$\hat{w} = V_2\left(B_1^T\vartheta + D_{21}^T y - D_{21}^T C_2 x\right) \tag{C.39}$$

where $V_2 = (1 + D_{21}^T D_{21})^{-1}$.

Constructing the augmented system: Similarly to determining p in the state-feedback problem, finding ϑ requires constructing the Hamiltonian matrix associated with the augmented system $[\dot{x},\ \dot{\vartheta}]$. Using Eqn. C.14, the dynamics of ϑ can be calculated from the Hamiltonian function as

$$\dot{\vartheta} = -\frac{\partial H(x,\vartheta,\bar{x},w)}{\partial x}$$

Differentiating $H(x,\vartheta,\bar{x},w)$ in Eqn C.37 in terms of x gives

$$\frac{\partial H(x,\vartheta,\bar{x},w)}{\partial x} = \gamma^{-2}C_1^T C_1 x - \gamma^{-2}C_1^T C_1 \bar{x} + C_2^T y - C_2^T C_2 x - C_2^T D_{21} w + A^T \vartheta$$

Substituting w with the estimation $\hat{w}$ that maximises H, after some rearrangement the above equation becomes

$$\begin{aligned}\dot{\vartheta} &= -\tfrac{\partial H(x,\vartheta,\bar{x},w)}{\partial x} \\ &= -(\gamma^{-2}C_1^T C_1 - C_2^T C_2 + C_2^T D_{21} V_2 D_{21}^T C_2)x - (A^T - C_2^T D_{21} V_2 B_1^T)\vartheta \\ &\quad +\gamma^{-2}C_1^T C_1 \bar{x} - C_2^T y + C_2^T D_{21} V_2 D_{21}^T y\end{aligned}$$

Similarly, $\dot{x}$ is derived below (Eqn. C.14)

$$\dot{x} = \frac{\partial H(x,\vartheta,\bar{x},w)}{\partial \vartheta} = Ax + B_1 w$$

Substituting w with $\hat{w}$, the dynamic equation for x becomes

$$\dot{x} = (A - B_1 V_2 D_{21}^T C_2)x + B_1 V_2 B_1^T \vartheta + B_1 V_2 D_{21}^T y$$

Finally, combining $\dot{x}$ and $\dot{\vartheta}$ to one single dynamic equation gives

$$\begin{aligned}\begin{bmatrix}\dot{x}\\ \dot{\vartheta}\end{bmatrix} &= \left[\begin{array}{c|c}(A - B_1 V_2 D_{21}^T C_2) & B_1 V_2 B_1^T \\ \hline -(\gamma^{-2}C_1^T C_1 - C_2^T C_2 + C_2^T D_{21} V_2 D_{21}^T C_2) & -(A - B_1 V_2 D_{21}^T C_2)\end{array}\right]\begin{bmatrix}x\\ \vartheta\end{bmatrix} \\ &\quad - \begin{bmatrix}-B_1 V_2 D_{21}^T \\ C_2^T - C_2^T D_{21} V_2 D_{21}^T\end{bmatrix} y + \begin{bmatrix}0\\ \gamma^{-2}C_1^T C_1\end{bmatrix}\bar{x}\end{aligned} \tag{C.40}$$

For better readability, in the subsequent derivations the above equation is represented in the following form

$$\begin{bmatrix} \dot{x} \\ \dot{\vartheta} \end{bmatrix} = \left[\begin{array}{c|c} \mathcal{A} & \mathcal{B} \\ \hline \mathcal{C} & -\mathcal{A}^T \end{array}\right] \begin{bmatrix} x \\ \vartheta \end{bmatrix} - \begin{bmatrix} \mathcal{E} \\ \mathcal{F} \end{bmatrix} y + \begin{bmatrix} 0 \\ \mathcal{G} \end{bmatrix} \bar{x} \tag{C.41}$$

To derive the structure of the unknown estimator $\bar{x}$, a new state variable $\tilde{x}$ is defined which satisfies the following equation [84, 86, 87, 80]

$$\tilde{x} = x - \mathbf{Q}\vartheta \tag{C.42}$$

where $\mathbf{Q}$ is an unknown matrix. This new variable $\tilde{x}$ represents the difference between the system's state x and a linear combination of ϑ, i.e. $\mathbf{Q}\vartheta$. To find the structure of $\tilde{x}$ and the unknown matrix $\mathbf{Q}$, Eqn. C.42 is differentiated to get

$$\dot{\tilde{x}} = \dot{x} - \dot{\mathbf{Q}}\vartheta - \mathbf{Q}\dot{\vartheta}$$

Substituting $\dot{x}$ and $\dot{\vartheta}$ with their equivalent in Eqn. C.41 yields to

$$\dot{\tilde{x}} = \mathcal{A}x + \mathcal{B}\vartheta - \mathcal{E}y - \dot{\mathbf{Q}}\vartheta - \mathbf{Q}[\mathcal{C}x - \mathcal{A}^T\vartheta - \mathcal{F}y + \mathcal{G}\bar{x}]$$

Substituting x in the above equation with $x = \tilde{x} + \mathbf{Q}\vartheta$ from Eqn. C.42 gives

$$\dot{\tilde{x}} = \mathcal{A}(\tilde{x} + \mathbf{Q}\vartheta) + \mathcal{B}\vartheta - \dot{\mathbf{Q}}\vartheta - \mathcal{E}y - \mathbf{Q}[\mathcal{C}(\tilde{x} + \mathbf{Q}\vartheta) - \mathcal{A}^T\vartheta - \mathcal{F}y + \mathcal{G}\bar{x}]$$

$$\dot{\tilde{x}} - \mathcal{A}\tilde{x} + \mathbf{Q}\mathcal{C}\tilde{x} + \mathcal{E}y - \mathbf{Q}\mathcal{F}y + \mathbf{Q}\mathcal{G}\bar{x} = -\dot{\mathbf{Q}}\vartheta + \mathcal{A}\mathbf{Q}\vartheta + \mathbf{Q}\mathcal{A}^T\vartheta - \mathbf{Q}\mathcal{C}\mathbf{Q}\vartheta + \mathcal{B}\vartheta$$

To satisfy Eqn. C.42, $\tilde{x}$ and $\mathbf{Q}$ have to satisfy the following two equations

$$\dot{\tilde{x}} = \mathcal{A}\tilde{x} - \mathbf{Q}\mathcal{A}\tilde{x} - \mathcal{E}y + \mathbf{Q}\mathcal{F}y - \mathbf{Q}\mathcal{G}\bar{x} \tag{C.43}$$

$$\dot{\mathbf{Q}}\vartheta = (\mathcal{A}\mathbf{Q} + \mathbf{Q}\mathcal{A}^T - \mathbf{Q}\mathcal{C}\mathbf{Q} + \mathcal{B})\vartheta \tag{C.44}$$

These two equations provide a basis for determining $\mathbf{Q}$ and the structure for $\tilde{x}$.

Determining Q: To determine $\mathbf{Q}$, Eqn. C.44 is used with $\mathcal{A}, \mathcal{B}$ and $\mathcal{C}$ substituted with their equivalents in Eqn. C.40. Since Eqn C.44 has to hold for all possible ϑ, the latter can be dropped from the expression and the resultant equation can be rewritten as a Riccati equation

$$\begin{aligned} \dot{\mathbf{Q}} &= (A - B_1V_2D_{21}^TC_2)\mathbf{Q} + \mathbf{Q}(A - B_1V_2D_{21}^TC_2)^T \\ &+ \mathbf{Q}\left(\gamma^{-2}C_1^TC_1 - C_2^TC_2 + C_2^TD_{21}V_2D_{21}^TC_2\right)\mathbf{Q} + B_1V_2B_1^T \end{aligned} \tag{C.45}$$

This Riccati equation can be solved for $\mathbf{Q}$.

Determining $\tilde{x}$: Substituting $\mathcal{A}$ to $\mathcal{F}$ in Eqn C.44 with their equivalents in Eqn C.40 gives the following structure for $\tilde{x}$

$$\begin{aligned}\dot{\tilde{x}} &= (A - B_1V_2D_{21}^TC_2)\tilde{x} + \mathbf{Q}\left(\gamma^{-2}C_1^TC_1 - C_2^TC_2 + C_2^TD_{21}V_2D_{21}^TC_2\right)\tilde{x} \\ &+B_1V_2D_{21}^Ty + \mathbf{Q}C_2^Ty - \mathbf{Q}C_2^TD_{21}V_2D_{21}^Ty - \gamma^{-2}\mathbf{Q}C_1^TC_1\bar{x}\end{aligned}$$

$$\begin{aligned}\dot{\tilde{x}} &= (A - B_1V_2D_{21}^TC_2)\tilde{x} - \mathbf{Q}C_2^T(1 - D_{21}V_2D_{21}^T)C_2\tilde{x} + B_1D_{21}^Ty \\ &+\mathbf{Q}C_2^T\left(1 - D_{21}V_2D_{21}^T\right)y - \gamma^{-2}\mathbf{Q}C_1^TC_1(\tilde{x} - \bar{x})\end{aligned}$$

$$\dot{\tilde{x}} = (A - B_1V_2D_{21}^TC_2)\tilde{x} + \mathbf{Q}C_2^T(1 - D_{21}V_2D_{21}^T)\{y - C_2\tilde{x}\} + B_1V_2D_{21}^Ty - \gamma^{-2}\mathbf{Q}C_1^TC_1(\tilde{x} - \bar{x}) \tag{C.46}$$

where $\mathbf{Q}$ is the solution to Eqn. C.45. Apart from the term $(\tilde{x} - \bar{x})$ all other terms in the above equations are known. To find the structure of the unknown observer $\bar{x}$, the subsequent derivations assume that [84, 86, 90]

$$\tilde{x} - \bar{x} = 0 \quad \rightarrow \quad \bar{x} = \tilde{x}$$

i.e. the optimal estimation is given with $\bar{x} = \tilde{x}$ in Eqn. C.46. With this assumption, Eqn. C.46 reduces to

$$\dot{\tilde{x}} = (A - B_1V_2D_{21}^TC_2)\tilde{x} + QC_2^T\left(1 - D_{21}V_2D_{21}^T\right)\{y - C_2\tilde{x}\} + B_1V_2D_{21}^Ty \tag{C.47}$$

This equation provides the structure of the unknown estimator in Fig. C.1(b) and hence it becomes the main result of this section. The output injection gain $\mathbf{Q}$ is the solution to Eqn. C.45. Based on this, the structure of the observer in Fig. C.1(b) is given below

$$\begin{aligned}\dot{\tilde{x}} &= (A - B_1V_2D_{21}^TC_2)\tilde{x} + QC_2^T\left(1 - D_{21}V_2D_{21}^T\right)\{y - C_2\tilde{x}\} + B_1V_2D_{21}^Ty \\ \bar{q} &= C_1\tilde{x} \\ \bar{y} &= C_2\tilde{x}\end{aligned}$$

Since the above $\mathcal{H}_\infty$ estimator is based on the assumption that $\bar{x} = \tilde{x}$, the next section shows that the value of the cost function in Eqn. C.34 is minimal when the estimator choses to use the structure in Eqn. C.47.

C.2.2 Value of the cost function in Eqn. C.34 when $\bar{x} = \tilde{x}$ in Eqn. C.47

To prove the assumption that Eqn. C.47 gives the optimal estimator that minimises the cost in Eqn. C.34, the estimation error is constructed as

$$e = x - \tilde{x}$$

Differentiating this equation on both sides and substituting: (a) $\dot{x}$ and y with their equivalents in Eqn. C.1 and (b) $\dot{\tilde{x}}$ with its equivalent in C.47 gives

$$\begin{aligned}\dot{e} &= \dot{x} - \dot{\tilde{x}} = \\ &= Ax + B_1 w - \left\{\left(A - B_1 D_{21}^T C_2 - \gamma^2 \mathbf{Q} C_2^T C_2\right)\tilde{x} + \left(\gamma^2 \mathbf{Q} C_2^T + B_1 D_{21}^T\right) y\right\} \\ &= Ax + B_1 w - \left\{\left(A - B_1 D_{21}^T C_2 - \gamma^2 \mathbf{Q} C_2^T C_2\right)\tilde{x} + \left(\gamma^2 \mathbf{Q} C_2^T + B_1 D_{21}^T\right)(C_2 x + D_{21} w + n)\right\}\end{aligned}$$

The simplify the subsequent derivations and for better readability, without a loss of generality D_{21} will be taken to be $D_{21} = 0$. With this assumption, after some suitable simplifications and the fact that $e = x - \tilde{x}$ the above equation simplifies to

$$\dot{e} = \left(A - \gamma^2 \mathbf{Q} C_2^T C_2\right) e + B_1 w - \gamma^2 \mathbf{Q} C_2^T n \tag{C.48}$$

Furthermore, the following quantity is constructed [84]

$$\frac{d(e^T \mathbf{Q}^{-1} e)}{dt} = \dot{e}^T \mathbf{Q}^{-1} e + e^T \mathbf{Q}^{-1} \dot{e} \tag{C.49}$$

Substituting $\dot{e}$ with its equivalent in Eqn. C.48, gives

$$\begin{aligned}\tfrac{d(e^T \mathbf{Q}^{-1} e)}{dt} &= \left\{\left(A - \gamma^2 \mathbf{Q} C_2^T C_2\right) e + B_1 w - \gamma^2 \mathbf{Q} C_2^T n\right\}^T \mathbf{Q}^{-1} e \\ &+ e^T \mathbf{Q}^{-1} \left\{\left(A - \gamma^2 \mathbf{Q} C_2^T C_2\right) e + B_1 w - \gamma^2 \mathbf{Q} C_2^T n\right\} \\ &= e^T A \mathbf{Q}^{-1} e - e^T C_2^T C_2 e + w^T B_1^T \mathbf{Q}^{-1} e - n^T C_2^T e \\ &+ e^T \mathbf{Q}^{-1} A e - e^T C_2^T C_2 e + e^T \mathbf{Q}^{-1} B_1 w - e^T C_2 n\end{aligned} \tag{C.50}$$

Using the fact that

$$\begin{aligned}w^T B_1^T \mathbf{Q}^{-1} e + e^T \mathbf{Q}^{-1} B_1 w &= -(w - B_1^T \mathbf{Q}^{-1} e)^T (w - B_1^T \mathbf{Q}^{-1} e) + w^T w + e^T \mathbf{Q}^{-1} B_1 B_1^T \mathbf{Q}^{-1} e \\ &= -\|w - B_1^T \mathbf{Q}^{-1} e\|^2 + \|w\|^2 + e^T \mathbf{Q}^{-1} B_1 B_1^T \mathbf{Q}^{-1} e\end{aligned}$$

and

$$\begin{aligned}n^T C_2^T e + e^T C_2 n &= (n + C_2 e)^T (n + C_2 e) - e^T C_2^T C_2 e - n^T n \\ &= \|n + C_2 e\|^2 - \|C_2 e\|^2 - \|n\|\|^2\end{aligned}$$

Eqn. C.50 reduces to

$$\begin{aligned}\tfrac{d(e^T \mathbf{Q}^{-1} e)}{dt} &= e^T A \mathbf{Q}^{-1} e + e^T \mathbf{Q}^{-1} A e - 2\|C_2 e\|^2 \\ &- \|w - B_1^T \mathbf{Q}^{-1} e\|^2 + \|w\|^2 + e^T \mathbf{Q}^{-1} B_1 B_1^T \mathbf{Q}^{-1} e \\ &- \|n + C_2 e\|^2 + \|C_2 e\|^2 + \|n\|\|^2 \\ &= e^T \left(A \mathbf{Q}^{-1} + \mathbf{Q}^{-1} A + \mathbf{Q}^{-1} B_1 B_1^T \mathbf{Q}^{-1}\right) e \\ &- \|C_2 e\|^2 - \|w - B_1^T \mathbf{Q}^{-1} e\|^2 - \|n + C_2 e\|^2 + \|w\|^2 + \|n\|\|^2\end{aligned}$$

To simplify this quantity further, Eqn. C.45 is multiplied by $\mathbf{Q}^{-1}$ from the left and right hand-sides to get

$$\begin{aligned}&\mathbf{Q}^{-1}\left\{A\mathbf{Q} + \mathbf{Q}A^T + \mathbf{Q}\left(C_1^T C_1 - \gamma^2 C_2^T C_2\right)\mathbf{Q} + \gamma^{-2} B_1 B_1^T\right\}\mathbf{Q}^{-1} = 0 \Leftrightarrow \\ &\mathbf{Q}^{-1} A + A^T \mathbf{Q}^{-1} + \mathbf{Q}^{-1}\gamma^{-2} B_1 B_1^T \mathbf{Q}^{-1} + C_1^T C_1 - \gamma^2 C_2^T C_2 = 0\end{aligned}$$

Substituting the left hand side of this equation in the equation above gives

$$\begin{aligned}\frac{d(e^T\mathbf{Q}^{-1}e)}{dt} &= e^T\left(-C_1^TC_1+\gamma^2C_2^TC_2\right)e-\|C_2e\|^2-\|w-B_1^T\mathbf{Q}^{-1}e\|^2-\|n+C_2e\|^2+\|w\|^2+\|r\\ &= -\|C_1e\|^2-\|w-B_1^T\mathbf{Q}^{-1}e\|^2-\|n+C_2e\|^2+\|w\|^2+\|n\|^2\end{aligned}$$

Since $\mathbf{Q}(t_f)=e(0)=0$, integrating Eqn. C.49 from 0 to t_f gives a zero quantity

$$\int_0^{t_f}\frac{d(e^T\mathbf{Q}^{-1}e)}{dt}=-\|C_1e\|_2^2-\|w-B_1^T\mathbf{Q}^{-1}e\|_2^2-\|n+C_2e\|_2^2+\|w\|_2^2+\|n\|_2^2=0$$

Consequently,

$$\|w\|_2^2+\|n\|_2^2=\|C_1e\|_2^2+\|w-B_1^T\mathbf{Q}^{-1}e\|_2^2+\|n+C_2e\|_2^2$$

Substituting $\|w\|_2^2+\|n\|_2^2$ from this equation in Eqn. C.34 reduces the cost of the estimation problem to

$$J(x,w)=\|C_1(x-\bar{x})\|_2^2-\|C_1e\|_2^2-\|w-B_1^T\mathbf{Q}^{-1}e\|_2^2-\|n+C_2e\|_2^2 \tag{C.51}$$

If the estimator $\bar{x}$ chooses to use the state-variable $\tilde{x}$ in Eqn C.47, then

$$\|C_1(x-\bar{x})\|_2^2-\|C_1e\|_2^2=\|C_1(x-\tilde{x})\|_2^2-\|C_1e\|_2^2=\|C_1e\|_2^2-\|C_1e\|_2^2=0$$

Using the fact that

$$\|n+C_2e\|_2^2=\|n+C_2(x-\tilde{x})\|_2^2=\|(n+C_2x)-C_2\tilde{x})\|_2^2=\|y-C_2\tilde{x}\|_2^2$$

the cost function to the estimation problem in Eqn. C.51 reduces to ($B_1^T\mathbf{Q}^{-1}e=B_1^T\mathbf{Q}^{-1}\mathbf{Q}\vartheta=B_1^T\vartheta$)

$$J(x,w)=-\|w-\underbrace{B_1^T\vartheta}_{\hat{w}}\|_2^2-\|y-\underbrace{C_2^T\tilde{x}}_{\bar{y}}\|_2^2 \tag{C.52}$$

To summarise, choosing the estimator to have the form in Eqn. C.47 reduces the cost for the optimisation problem to Eqn. C.52. This cost has is minimum when $\hat{w}=w$, $y=\bar{y}$, and $\bar{x}=\tilde{x}$. Any other estimator strategy $\bar{x}$ makes the cost larger and hence $\bar{x}=\tilde{x}$ is the optimal solution to the estimation problem.

C.2.3 Algorithm for deriving $\mathcal{H}_\infty$ state-estimators

The algorithm for deriving $\mathcal{H}_\infty$ state estimator is summarised below.

Step 1 Use the state-space representation of the system (e.g. Eqn. C.33) and a given large value for γ to construct the Riccati equation in Eqn. C.45 for the estimation problem. Solve this equation to find $\mathbf{Q}$.

Step 2 If the eigenvalues of the following Hamiltonian matrix associated with this Riccati equation

$$\left[\begin{array}{l|l} (A - B_1 V_2 D_{21}^T C_2)^T & B_1 V_2 B_1^T \\ \hline \left(\gamma^{-2} C_1^T C_1 - C_2^T C_2 + C_2^T D_{21} V_2 D_{21}^T C_2\right) & -(A - B_1 V_2 D_{21}^T C_2) \end{array}\right] \tag{C.53}$$

are away from the imaginary axes and $\mathbf{Q}$ is positively definite, reduce γ is reduced and the computation continues from step 1.

Step 3 When for a given value of γ one or more the eigenvalues become pure imaginary, stop the design loop. Use $\mathbf{Q}$ from the previous iteration to construct the following state-estimator

$$\begin{aligned} \dot{\tilde{x}} &= \underbrace{\left(A - B_1 V_2 D_{21}^T C_2 - \mathbf{Q} C_2^T \left(1 - D_{21} V_2 D_{21}^T\right) C_2\right)}_{A_{est}} \tilde{x} + \underbrace{\left(\mathbf{Q} C_2^T (1 - D_{21} V_2 D_{21}^T) + B_1 V_2 D_{21}^T\right)}_{B_{est}} y + B_2 u \\ \bar{q} &= C_1 \tilde{x} \\ \bar{y} &= C_2 \tilde{x} \end{aligned} \tag{C.54}$$

Step 4 End.

C.2.4 Design example: deriving $\mathcal{H}_\infty$ state estimator

For validation purposes, an $\mathcal{H}_\infty$ state estimator for the Maglev model is derived below using the above design steps. Since the open-loop Maglev model is unstable and hence inconvenient for estimation, the system is stabilised with the state-feedback controller from Chapter 2. The overall model is shown in Fig. C.2. The open-loop Maglev system is described using the state-space form in Eqn. 6.35, where A, B_2 and C_2 are given in Eqn. 6.35 (right-hand side), $C_1 = [1,\ 0,\ 0]$ and $B_1 = \left[\begin{array}{ccc} -1 & 0 & 0 \\ 1 & 0 & 0 \end{array}\right]^T$. Starting with $\gamma = 100$, after 18 iterations, γ saturated to 1.8 with the following positive definite solution to the Riccati equation in Eqn. C.45

$$\mathbf{Q} = \left[\begin{array}{rrr} 0.0026553 & -0.026054 & -12.557 \\ -0.026054 & 2.9965 & 0.033605 \\ -12.557 & 0.033598 & 64955 \end{array}\right]$$

This matrix and Eqn. C.54 are used to construct A_{est} and B_{est}; these are given below

$$A_{est} = \left[\begin{array}{rrr} -366.67 & 1 & 0 \\ 0.026054 & 0 & 1 \\ -3.4792 \times 10^9 & -3.0265 \times 10^7 & -6.7257 \times 10^5 \end{array}\right], \quad B_{est} = \left[\begin{array}{r} 0.0026553 \\ -0.026054 \\ -12.557 \end{array}\right]$$

Since the eigenvalues of A_{est} are negative, $\lambda(A_{est}) = [-6.7252 \times 10^5,\ -349.68,\ -61.984] < 0$, the estimator is stable. A step response in the desired airgap is applied to the system and the simulated output is shown in Fig. C.3. The output from the estimator overlaps almost

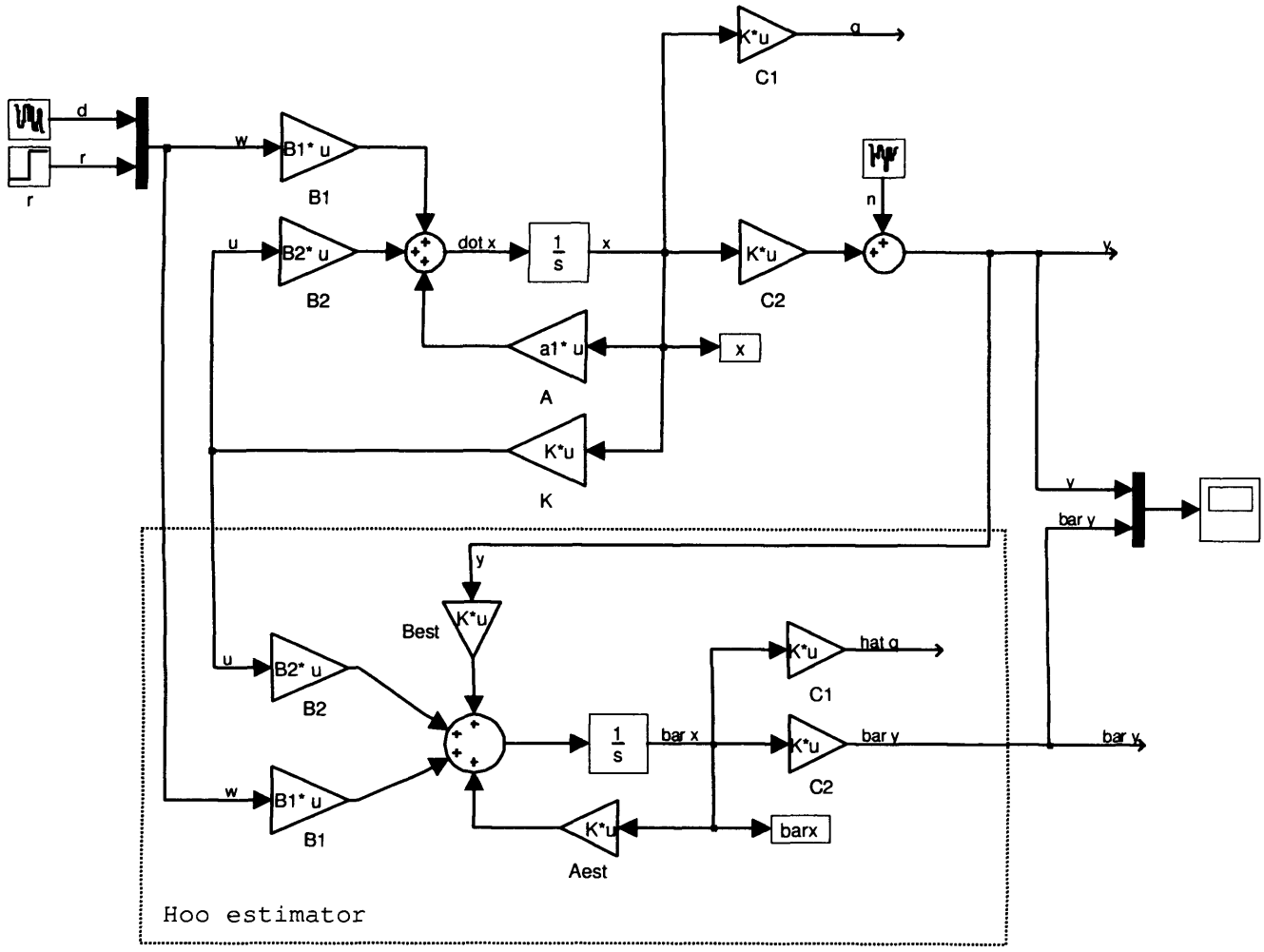

Figure C.2: Closed-loop Maglev system with an $\mathcal{H}_\infty$ state estimator. K is the state-feedback controller in Eqn. 2.17, 21.

completely with the output from the system. To investigate this further, the state variables of the system x are compared with the state variables of the estimator $\bar{x}$. Since these results are also very close, the difference between x and $\bar{x}$ is computed for plotting purposes. This is shown in Fig. C.4. The maximum error $x_3 - \bar{x}_3$ is $\approx 8 \times 10^{-3}$ for the acceleration

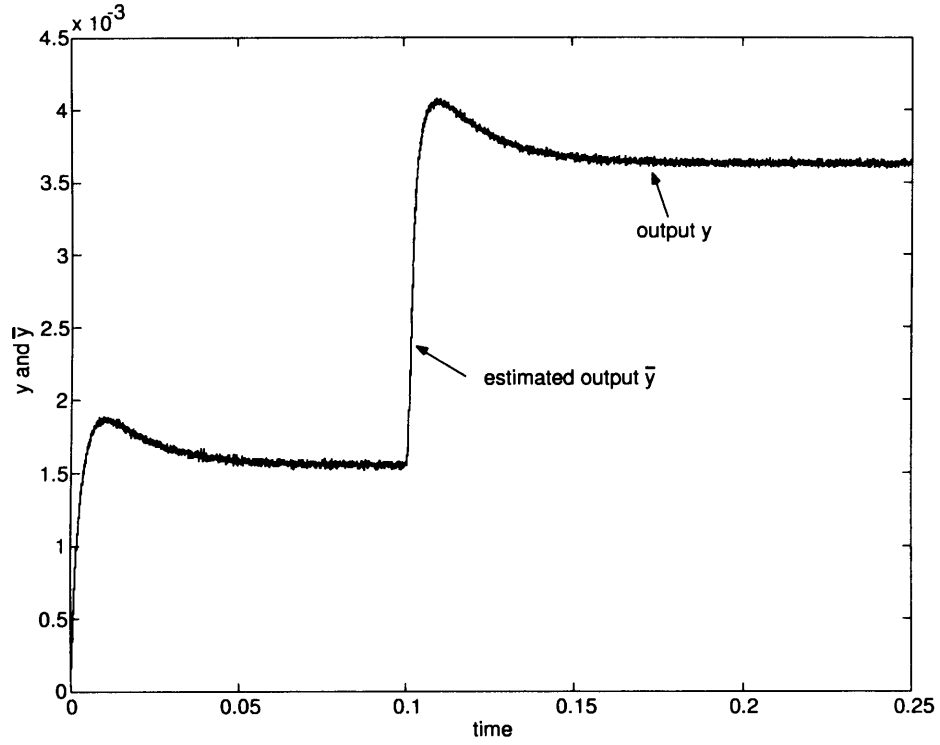

Figure C.3: Output with noise and estimated output.

signal while $x_1 - \bar{x}_1$ and $x_2 - \bar{x}_2$ are both below 1×10^{-5}. Therefore, the mathematical developments in Section C.2.1 derive observers with good estimation characteristics which can be used for the $\mathcal{H}_\infty$ output-feedback design.

C.2.5 Output-feedback $\mathcal{H}_\infty$ design

Classical output-feedback control techniques use separation principles to design the observer and the state-feedback controller independently (the *LQG* controller, for example, is a combination of a Kalman filter and a state-feedback controller [88]). A combination between the $\mathcal{H}_\infty$ estimator and the $\mathcal{H}_\infty$ state-feedback controller fails to provide separation properties since the disturbance signal w is derived independently in both designs (Eqns. C.21 and C.39) to estimate the worst case $\hat{w}$. This limitation can be overcome with some changes in the variables [37]. The $\mathcal{H}_\infty$ controller will be then derived by alternating between a state-feedback design and an estimator design until the optimal solution is found. This is described below.

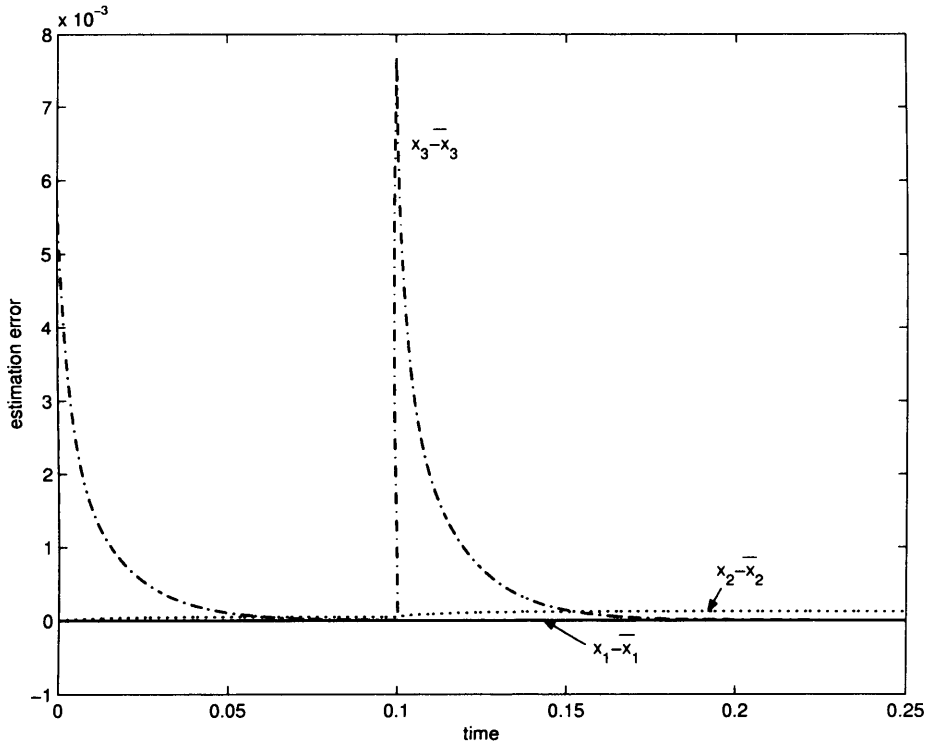

Figure C.4: Plot of the errors between the system's state variables and the estimated state variables, i.e. $x - \bar{x}$ for the transient responses in Fig. C.3.

The developments in Section C.2.2 suggest that the cost function in Eqn. C.3 can be equivalently transformed to

$$J(u,w) = \|q\|_2^2 - \gamma^2\|w\|_2^2 = \|u + \underbrace{V_1^{-1}\left(B_2^T\mathbf{P}x + D_{12}^T C_1 x\right)}_{-\check{u}}\|_2^2 - \|w - \underbrace{B_1^T\mathbf{P}x}_{\hat{w}}\|_2^2 \qquad \text{(C.55)}$$

where $\mathbf{P}$ is the solution to the Riccati equation in Eqn. C.20 for the state-feedback problem. Eqn. C.55 suggests that at every state-feedback design iteration q becomes approximately $u + \left(B_2^T\mathbf{P}x + D_{12}^T C_1 x\right)$ and w becomes approximately $(w - \gamma^{-2}B_1^T\mathbf{P}x)$. This observation motivates the definition of the following two new signals [37]

$$\begin{aligned}\bar{q} &= u - \check{u} = u + V_1^{-1}\left(B_2^T\mathbf{P}x + D_{12}^T C_1 x\right)\\ \bar{w} &= w - \hat{w} = w - \gamma^{-2}B_1^T\mathbf{P}x\end{aligned}$$

Since this is an equivalent transformation which does not change the value of the cost function, w and q in Eqn. C.33 can be substituted with $w = \bar{w} + \gamma^{-2}B_1^T\mathbf{P}x$ and $q = \bar{q} = u + V_1^{-1}\left(B_2^T\mathbf{P}x + D_{12}^T C_1 x\right)$. It can be proved that if $\|T_{\bar{q}\bar{w}}\| \leq \gamma$ then $\|T_{qw}\| \leq \gamma$ [37]. Using this result, the open-loop system (Eqn. C.33) used for the design of the $\mathcal{H}_\infty$ estimator can be modified as follows (note that $u = 0$ for the estimator design)

$$\begin{aligned}\dot{x} &= Ax + B_1 w = Ax + B_1(\bar{w} + \gamma^{-2}B_1^T\mathbf{P}x)\\ \bar{q} &= V_1^{-1}\left(B_2^T\mathbf{P} + D_{12}^T C_1\right)x\\ y &= C_2 x + D_{21}w = C_2 x + D_{21}(\bar{w} + \gamma^{-2}B_1^T\mathbf{P}x)\end{aligned}$$

This can be further rearranged to get the modified state and output equations

$$\begin{aligned} \dot{x} &= \underbrace{(A+\gamma^{-2}B_1B_1^T\mathbf{P})}_{A_M}x + B_1\bar{w} \\ \bar{q} &= \underbrace{V_1^{-1}\left(B_2^T\mathbf{P}+D_{12}^TC_1\right)}_{C_{1M}}x \\ y &= \underbrace{(C_2+\gamma^{-2}D_{21}B_1^T\mathbf{P})}_{C_{2M}}x + D_{21}\bar{w} \end{aligned} \tag{C.56}$$

which in a more compact form gives

$$\begin{aligned} \dot{x} &= A_Mx + B_1\bar{w} \\ \bar{q} &= C_{1M}x \\ y &= C_{2M}x + D_{21}\bar{w} \end{aligned} \tag{C.57}$$

To derive the estimator for the control problem, the algorithm requires using A_M, C_{1M} and C_{2M} in the process of deriving $\mathbf{Q}$. These results will be used to summarise the following algorithm for deriving output-feedback $\mathcal{H}_\infty$ controllers.

C.2.6 Algorithm for deriving output-feedback $\mathcal{H}_\infty$ controllers:

Step 1 For a given open-loop system $G(s)$ and performance weights $W(s)$ and W_c use Eqn. 6.28 to construct the state-space model of the mixed sensitivity $\mathcal{H}_\infty$ control problem in Fig. 6.3.

Step 2 Take γ to be a large number and construct the Riccati equation for the state-feedback controller in Eqn. C.20 ($V_1 = D_{12}^TD_{12}$)

$$\begin{aligned} &\mathbf{P}\left(A-B_2V_1^{-1}D_{12}^TC_1\right)+\left(A-B_2V_1^{-1}D_{12}^TC_1\right)^T\mathbf{P}- \\ &-\mathbf{P}\left(B_2V_1^{-1}B_2^T-\gamma^{-2}B_1B_1^T\right)\mathbf{P}+\left(C_1^TC_1-C_1^TD_{12}V_1^{-1}D_{12}^TC_1\right)=0 \end{aligned}$$

Solve this equation to determine $\mathbf{P}$, $\mathbf{P} > 0$.

Step 3 Use $\mathbf{P}$ to construct the following state-space matrices associated with the modified estimation problem in Eqn. C.56.

$$\begin{aligned} A_M &= (A+\gamma^{-2}B_1B_1^T\mathbf{P}) \\ C_{1M} &= V_1^{-1}\left(B_2^T\mathbf{P}+D_{12}^TC_1\right) \\ C_{2M} &= C_2+\gamma^{-2}D_{21}B_1^T\mathbf{P} \end{aligned}$$

Use these matrices to construct the Riccati equation for the estimator ($V_2 = (1 - D_{21}^TD_{21})^{-1}$)

$$\begin{aligned} &(A_M-B_1V_2D_{21}^TC_{2M})\mathbf{Q_M}+\mathbf{Q_M}(A-B_1V_2D_{21}^TC_{2M})^T \\ +\ &\mathbf{Q_M}\left(\gamma^{-2}C_{1M}^TC_{1M}-C_{2M}^TC_{2M}+C_{2M}^TD_{21}V_2D_{21}^TC_{2M}\right)\mathbf{Q_M}+B_1V_2B_1^T=0 \end{aligned} \tag{C.58}$$

Solve this equation to determine the output injection gain $\mathbf{Q_M}$, $\mathbf{Q_M} > 0$.

Step 3 Use this value for $\mathbf{Q_M}$ and the value for $\mathbf{P}$ (computed at Step 2) to construct the estimator-based output-feedback $\mathcal{H}_\infty$ controller which can be described in one of the following three equivalent forms:

(a) observer-based form

$$\begin{aligned} \dot{\tilde{x}} &= K_A\tilde{x} + K_B y \\ u &= K_C\tilde{x} \end{aligned} \tag{C.59}$$

where

$$\begin{aligned} K_A &= \left(A_M - B_2V_1^{-1}\left(B_2^T\mathbf{P}x + D_{12}^TC_1x\right) - B_1V_2D_{21}^TC_{2M}\right. \\ &\quad \left. -\mathbf{Q_M}\gamma^2C_{2M}^TC_{2M} + \mathbf{Q_M}C_{2M}^TD_{21}V_2D_{21}^TC_{2M}\right) \\ K_B &= \mathbf{Q_M}C_{2M}^T - \mathbf{Q_M}C_{2M}^TD_{21}V_2D_{21}^T + B_1V_2D_{21}^T \\ K_C &= -V_1^{-1}\left(B_2^T\mathbf{P} + D_{12}^TC_1\right) \end{aligned}$$

K_C is the state-feedback $\mathcal{H}_\infty$ controller (b) state-space form

$$K = \left[\begin{array}{c|c} K_A & K_B \\ \hline K_C & 0 \end{array}\right] \tag{C.60}$$

(c) transfer-function form

$$K = K_C \times (sI - K_A)^{-1} \times K_B \tag{C.61}$$

Step 4 Construct the closed-loop system in Fig. 6.3 by combining Eqn. 6.28 and Eqn. C.59. This is given below

$$\begin{aligned} \begin{bmatrix} \dot{x} \\ \dot{\tilde{x}} \end{bmatrix} &= \underbrace{\begin{bmatrix} A & B_2K_C \\ K_BC_2 & K_A \end{bmatrix}}_{A_{CL}} \begin{bmatrix} x \\ \tilde{x} \end{bmatrix} + \underbrace{\begin{bmatrix} B_1 \\ K_BD_{21} \end{bmatrix}}_{B_{CL}} w \\ q &= \underbrace{[C_1,\ D_{12}K_C]}_{C_{1CL}} \begin{bmatrix} x \\ \tilde{x} \end{bmatrix} \\ y &= \underbrace{[C_2,\ 0]}_{C_{2CL}} \begin{bmatrix} x \\ \tilde{x} \end{bmatrix} + D_{21}w \end{aligned} \tag{C.62}$$

where K_A, K_B, K_C are defined in Eqn. C.60.

Step 5 Use Eqn. C.62 to construct the closed-loop system from w to q for the mixed sensitivity problem.

$$T_{qw} = C_{1CL} \times (sI + A_{CL})^{-1} \times B_{CL} = \left[\begin{array}{c|c} A_{CL} & B_{CL} \\ \hline C_{1CL} & 0 \end{array}\right] \tag{C.63}$$

Compute the infinity norm of T_{qw}. IF for the current value for γ:

(a) Both Riccati equations have positively definite solutions $\mathbf{P}$ and $\mathbf{Q_M}$, and

(b) the norm $\|T_{qw}\|_\infty$ continues to decrease,

THEN reduce γ and continue the calculations from Step 2.

If for a given value for γ the infinity norm calculated in Step 5 reaches its minimum, stop the algorithm. The optimal output-feedback $\mathcal{H}_\infty$ controller is given in Eqns. C.59 to C.61.

It has been demonstrated in [37] that the state-feedback Riccati equation in Eqn. C.20 and the $\mathcal{H}_\infty$ estimator Riccati equation in Eqn. C.45 can be solved independently for $\mathbf{P}$ and $\mathbf{Q}$ [37] and the relationship between the solution $\mathbf{Q_M}$ in Eqn. C.58 and $\mathbf{Q}$ is given below [37, 112]

$$\mathbf{Q_M} = (I - \gamma^{-2}\mathbf{QP})^{-1}\mathbf{Q}$$

It has been established in Section 6.5.3, however, that the algorithm developed here produce identical to the algorithm in Matlab [37, 76] results.

Appendix D

Computing the structured singular value μ

At present, algorithms for the analytical computation of the structured singular value μ are not known. There exists, however, a numerical method that yields good results. From the fact that the matrix of perturbation Δ is structured along the main diagonal (Δ=diag(Δ_i)), for any diagonal matrix Δ, the following relationship can be written

$$D\Delta = \Delta D,$$

Using this and the transformation in Figure D.1 it follows that

$$\mu(M) = \mu(DMD^{-1}) \tag{D.1}$$

From the fact that $\mu(M) \leq \bar{\sigma}(M)$, from Equation D.1 it follows that [93]

$$\mu(M) \leq \bar{\sigma}(DMD^{-1}).$$

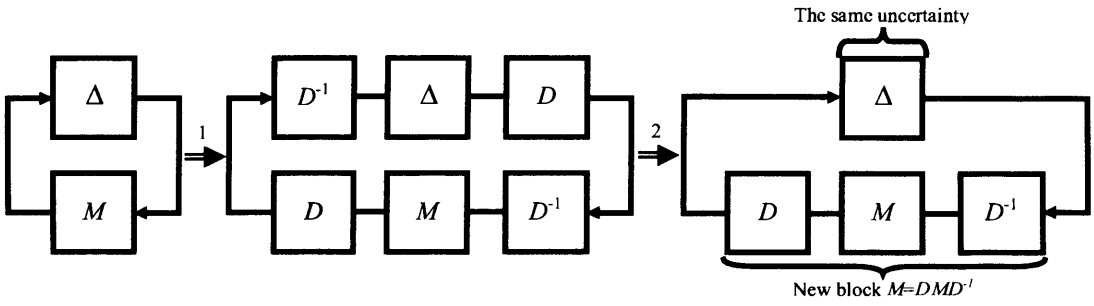

Figure D.1: Adding the D-structure to the general control configuration in Fig. 7.13.

This relation suggests that the upper bound of $\mu(M)$ can be determined by selecting the function D that minimises the maximum singular value of (DMD^{-1}) [74], i.e.

$$\mu(M) \leq \min_{D} \bar{\sigma}(DMD^{-1}) \tag{D.2}$$

Equation D.2 is a convex optimisation problem which finds D that minimises the largest singular value of (DMD^{-1}). It has been suggested in [113] that minimisation of the Frobenius norm $\|DMD^{-1}\|_F$ yields a very good approximation for the optimal D that minimises $\bar{\sigma}(DMD^{-1})$. A significant reduction in $\|DMD^{-1}\|_F$ will result in a significant reduction of $\bar{\sigma}(DMD^{-1})$. Therefore the matrix D that minimises $\|DMD^{-1}\|_F$ is usually a very good approximation of D that minimises $\bar{\sigma}(DMD^{-1})$.

A demonstrative algorithm that computes the upper bound on $\mu(M)$ is given below. Considering the complex matrix M

$$M = \begin{bmatrix} m_{11} & m_{12} \\ m_{21} & m_{22} \end{bmatrix},$$

and a scaling matrix D

$$D = \begin{bmatrix} d_1 & 0 \\ 0 & d_2 \end{bmatrix}.$$

DMD^{-1} is computed as below

$$DMD^{-1} = \begin{bmatrix} d_1 m_{11} d_1^{-1} & d_1 m_{12} d_2^{-1} \\ d_2 m_{21} d_1^{-1} & d_2 m_{22} d_2^{-1} \end{bmatrix}.$$

By definition the Frobenius norm of this matrix is

$$\left\|DMD^{-1}\right\|_{\mathrm{F}} = \sqrt{(d_1 m_{11} d_1^{-1})^2 + (d_1 m_{12} d_2^{-1})^2 + (d_2 m_{21} d_1^{-1})^2 + (d_2 m_{22} d_2^{-1})^2}$$

Without a loss of generality it can be assumed that d_2=1. Then the latter norm becomes

$$\left\|DMD^{-1}\right\|_{\mathrm{F}} = \sqrt{(d_1 m_{11} d_1^{-1})^2 + (d_1 m_{12})^2 + (m_{21} d_1^{-1})^2 + (m_{22})^2}$$

The optimisation problem is defined as finding this $d = d_1$, that minimises $\|DMD^{-1}\|_F$, or

$$\min_d J = \sqrt{(dm_{12})^2 + (m_{21} d^{-1})^2} \tag{D.3}$$

Let $\check{d}$ is the solution of Equation D.3, then the scaling matrix D becomes

$$D = \begin{bmatrix} \check{d} & 0 \\ 0 & 1 \end{bmatrix},$$

and the matrix DMD^{-1} is derived below

$$DMD^{-1} = \begin{bmatrix} m_{11} & \check{d}_1 m_{12} \\ m_{21} \check{d}^{-1} & m_{22} \end{bmatrix}.$$

Hence, the upper bound of the structured singular value is given by

$$\mu(M) \leq \bar{\sigma}(DMD^{-1}) = \bar{\sigma}\left(\begin{bmatrix} m_{11} & \check{d}_1 m_{12} \\ m_{21} \check{d}^{-1} & m_{22} \end{bmatrix}\right)$$

and equals the largest singular value of DMD^{-1}.

In the following section, a Matlab script is written that computes the structured singular value of M using the above numerical algorithm. The result is compared with the result from μ-Synthesis toolbox.

```
%*********************************************************************
% Computes the SSV of a 2x2 matrix M
%
%

M=[
   rand(1) rand(1); % generates the matrix M
   rand(1) rand(1)
  ];

d=0.1:0.01:5;       % the range of d

for i=1:length(d),
    Y(i)=sqrt((d(i)*M(3)        )^2 + ...
              (     M(2)*d(i)^-1)^2 ...
             );
end

plot(d,Y(1:i));     % plots the Frobenius norm as a function of d
miny=min(Y);        % finds the minimum of the norm

for i=1:length(d),  % determines which d produces this minimum
   if Y(i)==miny,
      Dmin=d(i);
   end
end

D=[
   Dmin 0;          % produces the scaling matrix D
   0    1
  ];

max(svd(D*M*D^-1)), % computes the maximum singular value of DMD-1
max(mu(M))          % compares to the result generated by Matlab
```

Appendix E

Robustness analysis

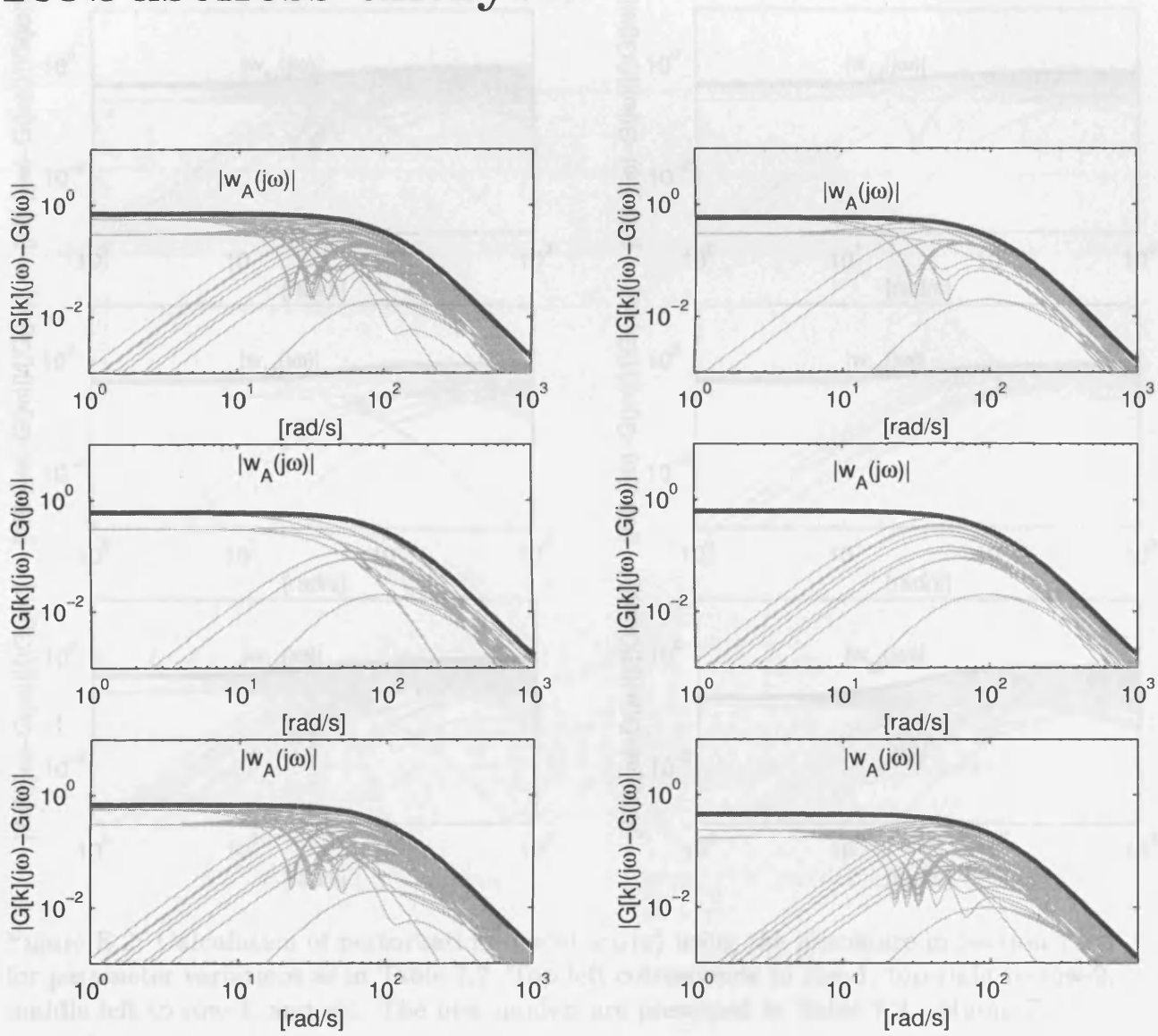

Figure E.1: Calculation of perturbation model $w_A(s)$ using the procedure in Section 7.2.3 for parameter variations as in Table 7.2. Top left corresponds to row-1, top-right to row-2, middle left to row-3, and etc. The new models are presented in Table 7.2, column-6.

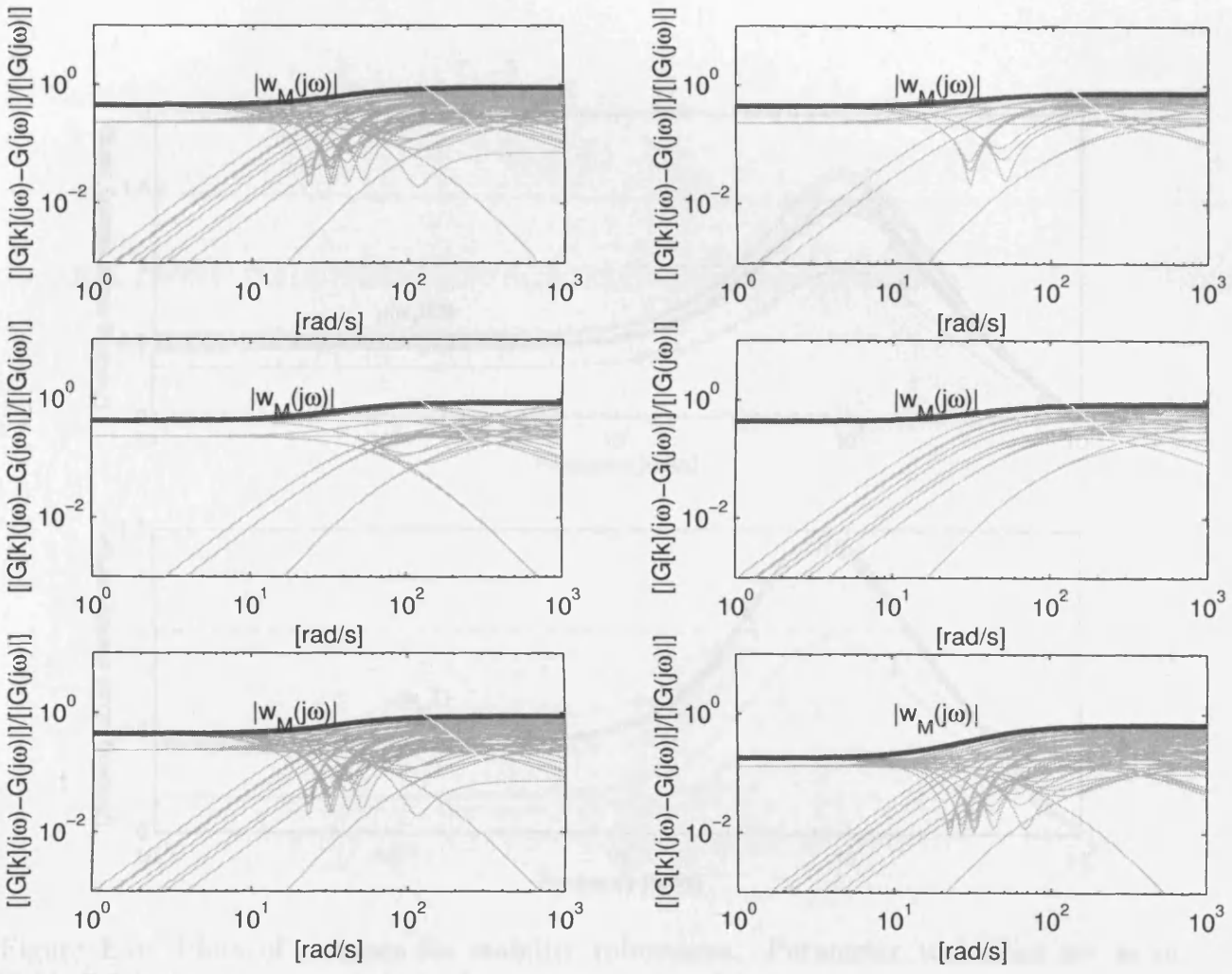

Figure E.2: Calculation of perturbation model $w_M(s)$ using the procedure in Section 7.2.3 for parameter variations as in Table 7.2. Top left corresponds to row-1, top-right to row-2, middle left to row-3, and etc. The new models are presented in Table 7.2, column-7.

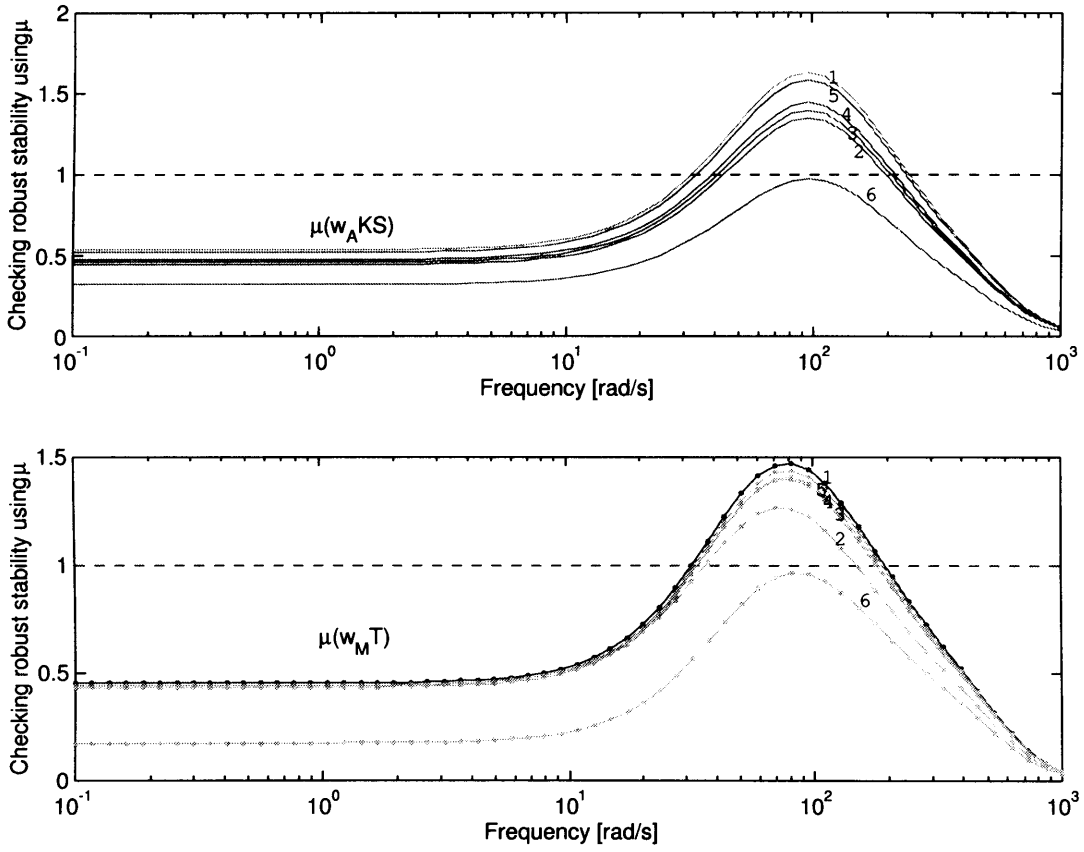

Figure E.3: Plots of μ-values for stability robustness. Parameter variations are as in Table 7.2 (indexes corresponds to the experiment numbers).

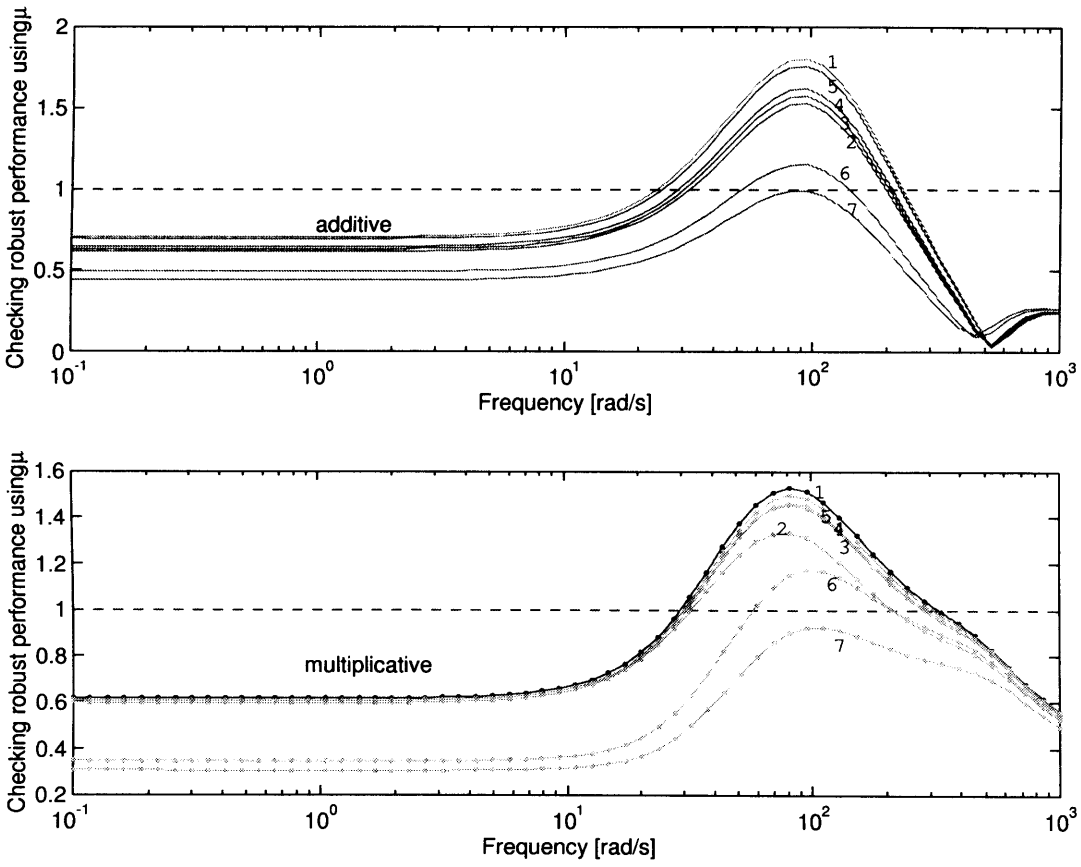

Figure E.4: Plots of μ-values for performance robustness. Parameter variations are as in Table 7.2 (indexes corresponds to the experiment numbers).

Appendix F

Multivariable controller design

F.1 Local control of Maglev vehicle using state-feedback

Local control of the electromagnetic suspension vehicle using state-feedback controllers for each corner is shown in Fig. F.1 [13]. The gains for each compensator are $kp = 2079.23$, $kv = 18.0$, $ka = 0.0423$. The open-loop model used for the analysis is taken from Section 8.2, page 168 with parameters in Table 8.1.

F.2 $\mathcal{H}_\infty$ design for multi-magnet systems

The initial multivariable design is based on the design process developed in Chapters 6. The controller-design task is based on optimisation of performance criteria (Section 6.4) and single- and multiple-input-output controllers are designed in the same framework. The design of the $\mathcal{H}_\infty$ controller is based on the block-diagram in Fig. 6.11, page 110, conveniently redrawn in Fig. F.2 for the multi-magnet design. The vector $\mathbf{r}$ consists of three reference signals: the reference heave, pitch and roll positions. These are subtracted from the heave, pitch and roll positions from the system (modelled in Eqn. 8.14 with state-space matrices given thereafter) and added to the vector of disturbance inputs $\mathbf{d}$. The unknown multivariable $\mathcal{H}_\infty$ feedback compensator $\mathbf{K}(s)$ which has to be designed has three inputs and four outputs (control voltages driving each of the magnet's current controllers). The performance specification of the system, as with the single-loop design, is specified by a performance function $\mathbf{W}$ with three inputs and three outputs. The same applies to the weight on the robustness performance $\mathbf{W_c}$. Since the performance requirements for all three channels (heave, roll and pitch) are required to be the same, $\mathbf{W}$ has the following

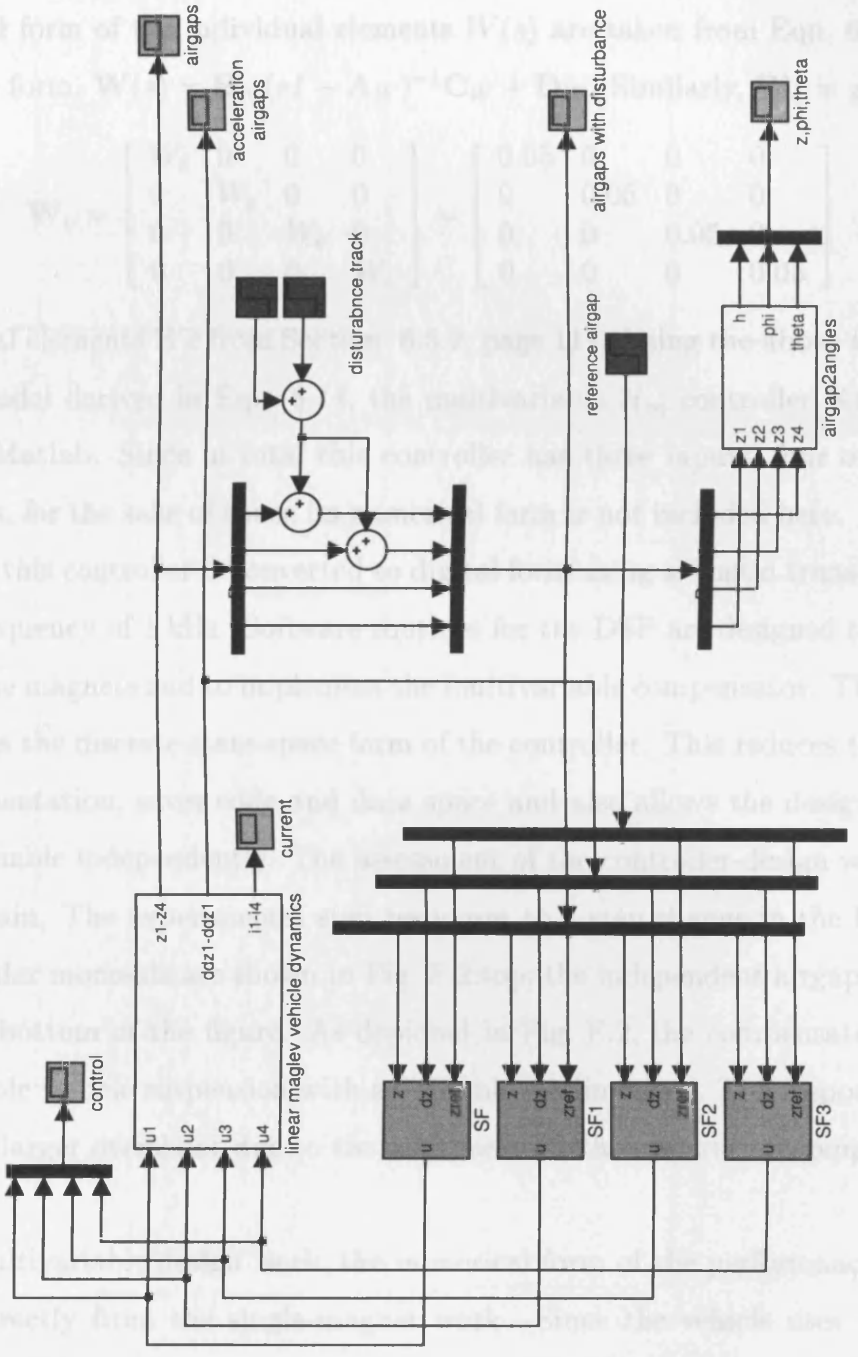

Figure F.1: Local vehicle control using four state-feedback compensators.

diagonal structure

$$\mathbf{W} = \begin{bmatrix} W(s) & 0 & 0 \\ 0 & W(s) & 0 \\ 0 & 0 & W(s) \end{bmatrix} = \begin{bmatrix} \frac{0.6667(s+60)}{(s+0.04)} & 0 & 0 \\ 0 & \frac{0.6667(s+60)}{(s+0.04)} & 0 \\ 0 & 0 & \frac{0.6667(s+60)}{(s+0.04)} \end{bmatrix}$$

The numerical form of the individual elements $W(s)$ are taken from Eqn. 6.43, page 115. In state-space form, $\mathbf{W}(s) = \mathbf{B}_W(sI - \mathbf{A}_W)^{-1}\mathbf{C}_W + \mathbf{D}_W$. Similarly, $\mathbf{W_c}$ is given below

$$\mathbf{W_c} = \begin{bmatrix} W_c & 0 & 0 & 0 \\ 0 & W_c & 0 & 0 \\ 0 & 0 & W_c & 0 \\ 0 & 0 & 0 & W_c \end{bmatrix} = \begin{bmatrix} 0.05 & 0 & 0 & 0 \\ 0 & 0.05 & 0 & 0 \\ 0 & 0 & 0.05 & 0 \\ 0 & 0 & 0 & 0.05 \end{bmatrix}$$

with individual elements Wc from Section. 6.5.2, page 111. Using the above two inputs and the vehicle model derived in Eqn. 8.14, the multivariable $\mathcal{H}_\infty$ controller $\mathbf{K}(s)$ in Fig. F.2 is derived in Matlab. Since in total this controller has three inputs, four outputs and 12 state-variables, for the sake of space its numerical form is not included here. For the experimental work, this controller is converted to digital form using a Tustin transformation and a sampling frequency of 1 kHz. Software routines for the DSP are designed to measure the inputs from the magnets and to implement the multivariable compensator. The DSP implementation uses the discrete state-space form of the controller. This reduces the complexity of the implementation, saves code and data space and also allows the designer to analyse each state-variable independently. The assessment of the controller-design work is done in the time-domain. The experimental step responses to a step change in the heave position at two particular moments are shown in Fig. F.2:top; the independent airgap responses are shown in the bottom of the figure. As depicted in Fig. F.2, the compensator manages to perform a stable vehicle suspension with acceptable settling time. The response at $t = 0.6$s has a slightly larger overshoot due to the additional earth acceleration component in that direction.

For the multivariable design work, the numerical form of the performance function $\mathbf{W}$ was copied directly from the single-magnet work. Since the vehicle uses magnets with different force-current characteristics, it is convenient to modify the design requirements by changing the performance function $\mathbf{W}$. Employing this, a new controller was designed to reduce the closed-loop overshot to 1.5 mm with settling time increased to 0.4 sec. For the sake of space these results are not presented here.

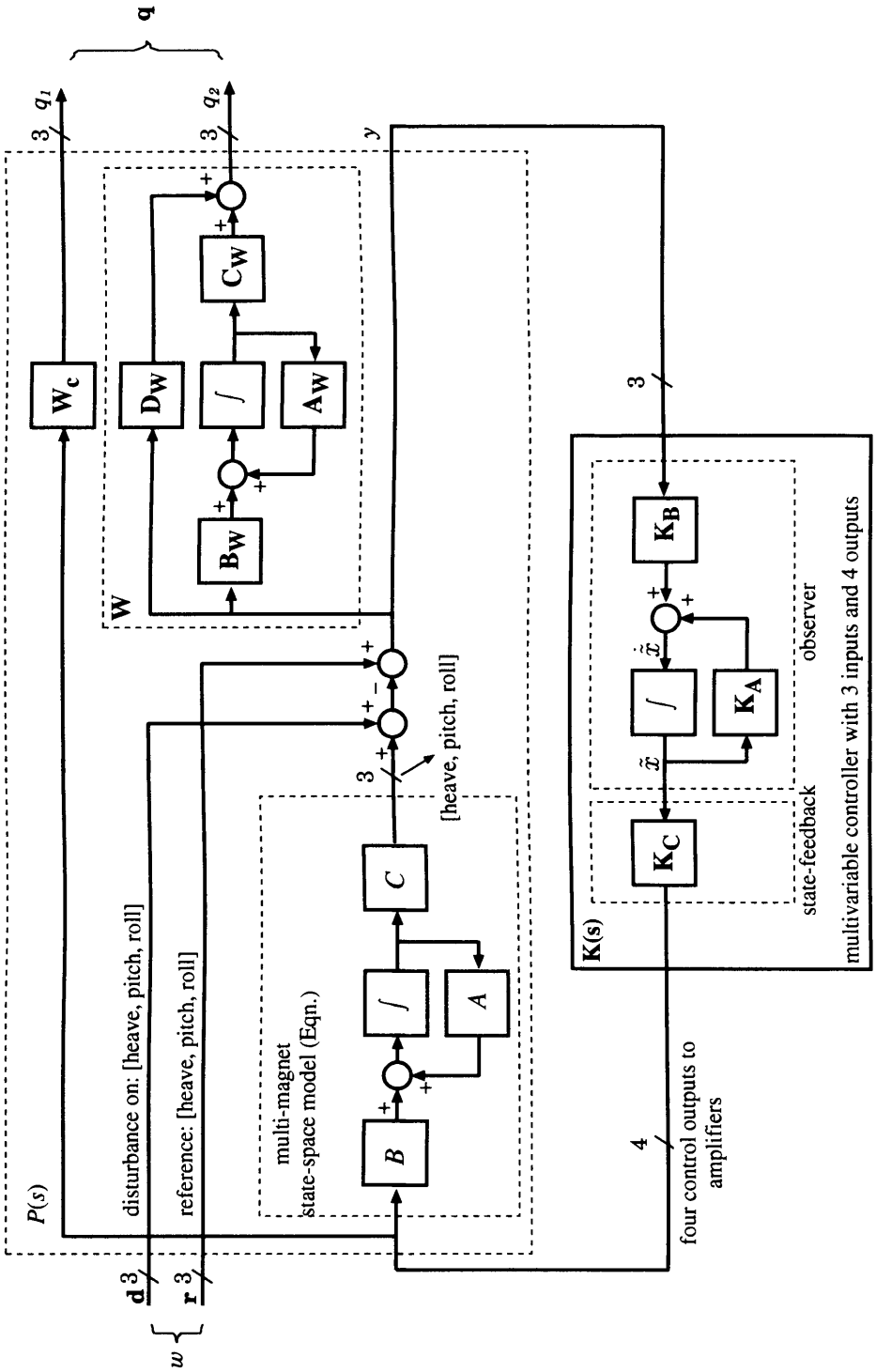

Figure F.2: $\mathcal{H}_\infty$ design for the multi-magnet systems.

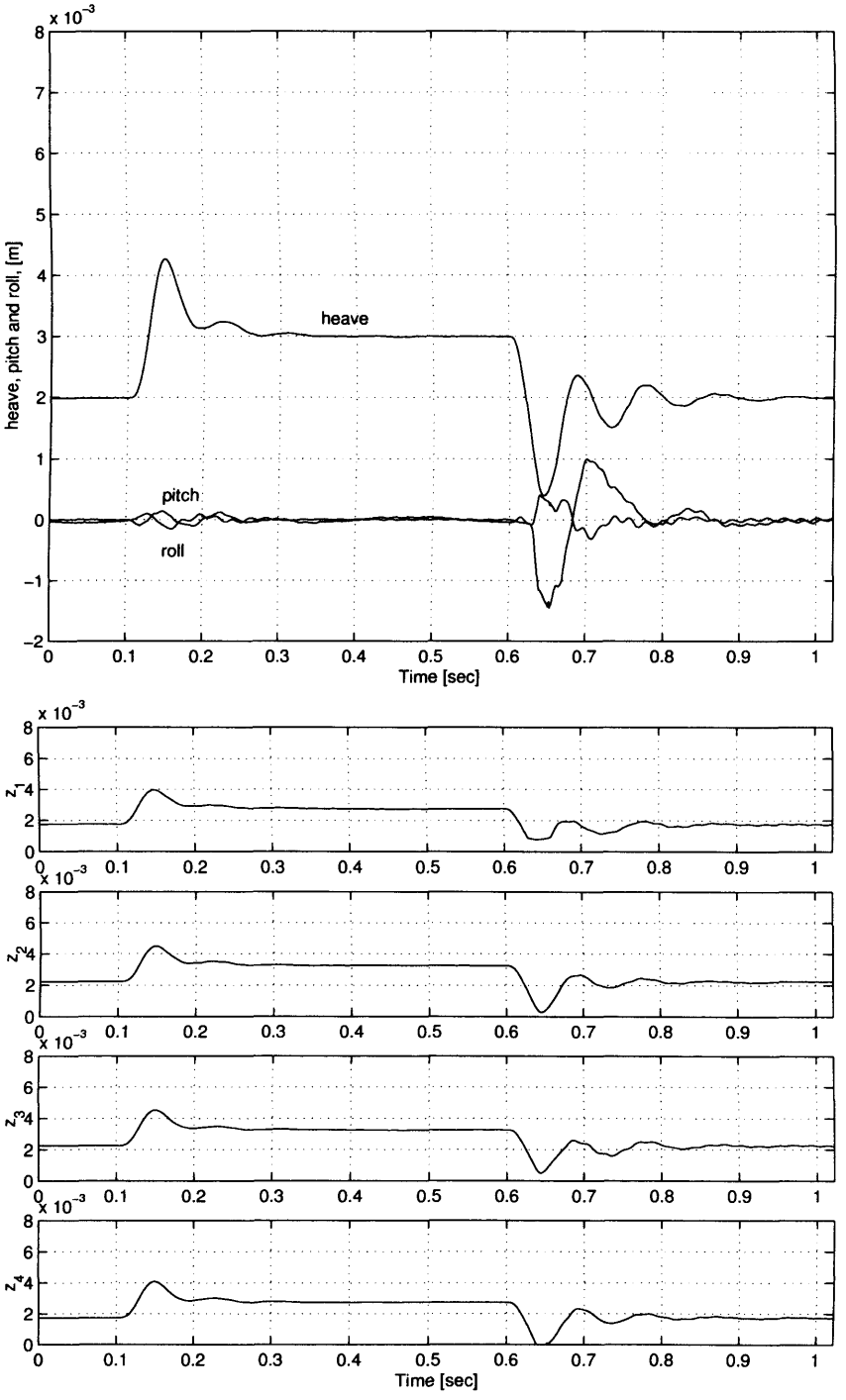

Figure F.3: Experimental step responses to a 1 mm reference heave change. Top: heave, roll and pitch responses; Bottom: independent airgap responses.

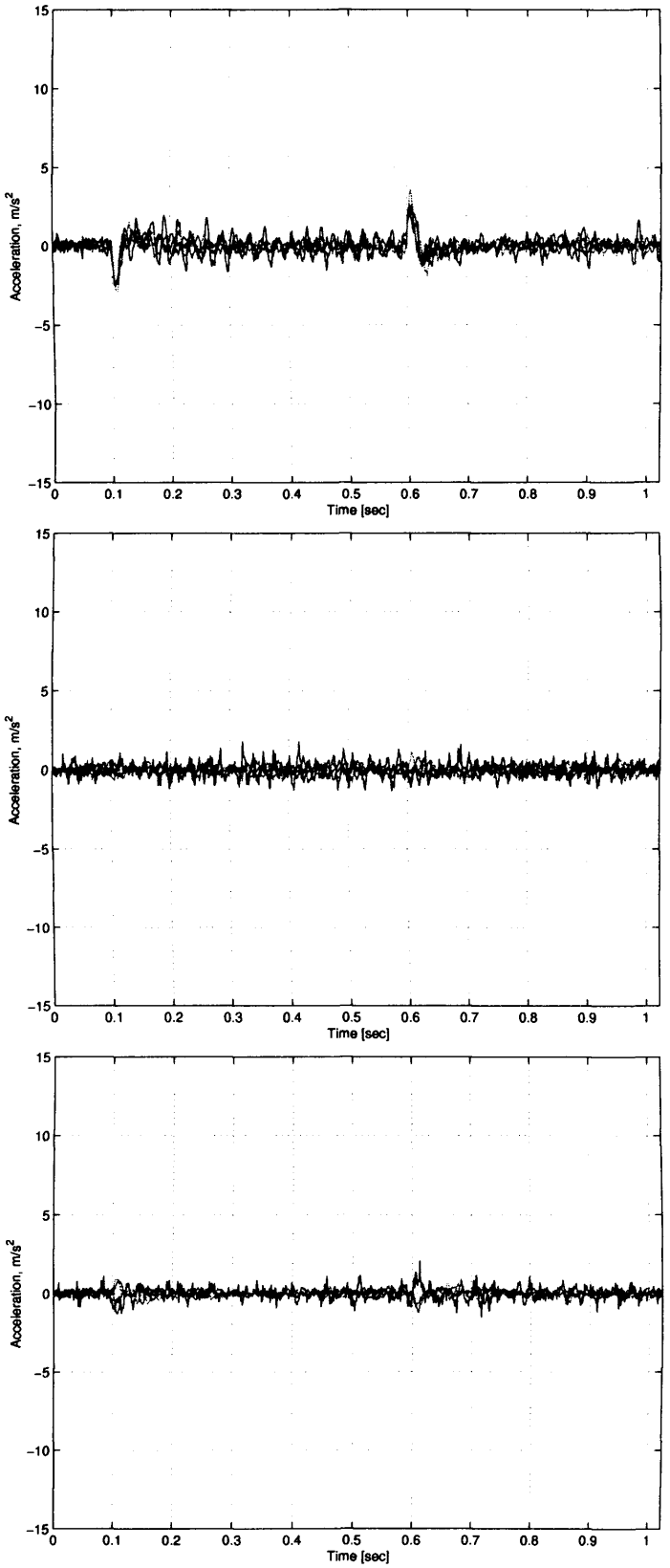

Figure F.4: Acceleration responses for: (top) 1mm step change in reference heave position; (middle) step change in reference roll position; (bottom) step change in reference pitch position;

F.3 Numerical form of the multivariable μ-controller

The multivariable controller derived in Section 8.4.1 is given below

$$\begin{bmatrix} u_1 \\ u_2 \\ u_3 \\ u_4 \end{bmatrix} = \left[\begin{array}{ccc|cccc} K_{r,1} & -K_{r,2} & K_{r,3} & K_{1,4} & K_{1,5} & K_{1,6} & K_{1,7} \\ K_{r,1} & K_{r,2} & K_{r,3} & K_{2,4} & K_{2,5} & K_{2,6} & K_{2,7} \\ K_{r,1} & -K_{r,2} & -K_{r,3} & K_{3,4} & K_{3,5} & K_{3,6} & K_{3,7} \\ K_{r,1} & K_{r,2} & -K_{r,3} & K_{4,4} & K_{4,5} & K_{4,6} & K_{4,7} \end{array}\right] = \left[\begin{array}{c} z \\ \phi \\ \theta \\ \hline z_1 \\ z_2 \\ z_3 \\ z_4 \end{array}\right] \tag{F.1}$$

The individual numerical forms of the compensator are included below. For the presentation, these are included after cancelling closely located poles and zeros. The simulation and the experimental work, however, uses the full form of the controller as given in the following page.

$$K_{r,1} = \frac{0.015353(s-3.598e5)(s+73.18)(s+3.554)(s^2+346.5s+7.026e4)}{(s+1.644e4)(s+3.615)(s+0.02)(s^2+691s+1.684e5)}$$

$$K_{r,2} = \frac{0.011979(s-1737)(s+28.75)(s^2-25.23s+9.814e4)}{(s+496.3)(s+0.02)(s^2+489.7s+1.586e5)}$$

$$K_{r,3} = \frac{0.0030971(s-7529)(s+80.09)(s+3.316)(s^2+308.1s+9.553e4)}{(s+634.9)(s+3.521)(s+0.02)(s^2+475.4s+1.693e5)}$$

$$K_{1,4} = \frac{-0.0042752(s+1.9e7)(s+1045)(s+555.9)(s+210.4)(s+53.09)(s+6.136)(s^2+673.4s+1.957e5)(s^2+482.9s+1.646e5)}{(s+1.644e4)(s+634.9)(s+496.3)(s+0.0201)(s^2+691s+1.684e5)(s^2+489.7s+1.586e5)(s^2+475.4s+1.693e5)}$$

$$K_{1,5} = \frac{0.012183(s-6.388e6)(s+736.5)(s+381.9)(s+274.8)(s+42.33)(s+9.515)(s^2+432.5s+1.249e5)(s^2+523.9s+1.993e5)}{(s+1.644e4)(s+634.9)(s+496.3)(s+0.02011)(s^2+691s+1.684e5)(s^2+489.7s+1.586e5)(s^2+475.4s+1.693e5)}$$

$$K_{1,6} = \frac{-0.0087673(s+8.878e6)(s+183.3)(s+51.59)(s+8.352)(s^2+1122s+3.302e5)(s^2+563.6s+1.719e5)(s^2+407.2s+1.666e5)}{(s+1.644e4)(s+634.9)(s+496.3)(s+0.0201)(s^2+691s+1.684e5)(s^2+489.7s+1.586e5)(s^2+475.4s+1.693e5)}$$

$$K_{1,7} = \frac{0.0076895(s-9.676e6)(s+584.4)(s+158.1)(s+96.13)(s-273.7)(s-4.466)(s^2+609.2s+1.08e5)(s^2+480.5s+1.637e5)}{(s+1.644e4)(s+634.9)(s+496.3)(s+0.02009)(s^2+691s+1.684e5)(s^2+489.7s+1.586e5)(s^2+475.4s+1.693e5)}$$

$$K_{2,4} = \frac{0.012183(s-6.388e6)(s+736.5)(s+381.9)(s+274.8)(s+42.33)(s+9.514)(s^2+432.5s+1.249e5)(s^2+523.9s+1.993e5)}{(s+1.644e4)(s+634.9)(s+496.3)(s+0.0201)(s^2+691s+1.684e5)(s^2+489.7s+1.586e5)(s^2+475.4s+1.693e5)}$$

$$K_{2,5} = \frac{-0.0042752(s+1.9e7)(s+1045)(s+555.9)(s+210.4)(s+53.09)(s+6.136)(s^2+673.4s+1.957e5)(s^2+482.9s+1.646e5)}{(s+1.644e4)(s+634.9)(s+496.3)(s+0.02011)(s^2+691s+1.684e5)(s^2+489.7s+1.586e5)(s^2+475.4s+1.693e5)}$$

$$K_{2,6} = \frac{0.0076895(s-9.676e6)(s+584.4)(s+158.1)(s+96.13)(s-273.7)(s-4.466)(s^2+609.2s+1.08e5)(s^2+480.5s+1.637e5)}{(s+1.644e4)(s+634.9)(s+496.3)(s+0.0201)(s^2+691s+1.684e5)(s^2+489.7s+1.586e5)(s^2+475.4s+1.693e5)}$$

$$K_{2,7} = \frac{-0.0087673(s+8.878e6)(s+183.3)(s+51.59)(s+8.352)(s^2+1122s+3.302e5)(s^2+563.6s+1.719e5)(s^2+407.2s+1.666e5)}{(s+1.644e4)(s+634.9)(s+496.3)(s+0.02009)(s^2+691s+1.684e5)(s^2+489.7s+1.586e5)(s^2+475.4s+1.693e5)}$$

$$K_{3,4} = \frac{-0.0087672(s+8.878e6)(s+183.3)(s+51.59)(s+8.352)(s^2+1122s+3.302e5)(s^2+563.6s+1.719e5)(s^2+407.2s+1.666e5)}{(s+1.644e4)(s+634.9)(s+496.3)(s+0.02009)(s^2+691s+1.684e5)(s^2+489.7s+1.586e5)(s^2+475.4s+1.693e5)}$$

$$K_{3,5} = \frac{0.0076894(s-9.676e6)(s+584.4)(s+158.1)(s+96.13)(s-273.7)(s-4.466)(s^2+609.2s+1.08e5)(s^2+480.5s+1.637e5)}{(s+1.644e4)(s+634.9)(s+496.3)(s+0.0201)(s^2+691s+1.684e5)(s^2+489.7s+1.586e5)(s^2+475.4s+1.693e5)}$$

$$K_{3,6} = \frac{-0.0042753(s+1.9e7)(s+1045)(s+555.9)(s+210.4)(s+53.09)(s+6.136)(s^2+673.4s+1.957e5)(s^2+482.9s+1.646e5)}{(s+1.644e4)(s+634.9)(s+496.3)(s+0.02011)(s^2+691s+1.684e5)(s^2+489.7s+1.586e5)(s^2+475.4s+1.693e5)}$$

$$K_{3,7} = \frac{0.012183(s-6.388e6)(s+736.5)(s+381.9)(s+274.8)(s+42.33)(s+9.514)(s^2+432.5s+1.249e5)(s^2+523.9s+1.993e5)}{(s+1.644e4)(s+634.9)(s+496.3)(s+0.0201)(s^2+691s+1.684e5)(s^2+489.7s+1.586e5)(s^2+475.4s+1.693e5)}$$

$$K_{4,4} = \frac{0.0076896(s-9.676e6)(s+584.4)(s+158.1)(s+96.13)(s-273.7)(s-4.466)(s^2+609.2s+1.08e5)(s^2+480.5s+1.637e5)}{(s+1.644e4)(s+634.9)(s+496.3)(s+0.02009)(s^2+691s+1.684e5)(s^2+489.7s+1.586e5)(s^2+475.4s+1.693e5)}$$

$$K_{4,5} = \frac{-0.0087674(s+8.878e6)(s+183.3)(s+51.59)(s+8.352)(s^2+1122s+3.302e5)(s^2+563.6s+1.719e5)(s^2+407.2s+1.666e5)}{(s+1.644e4)(s+634.9)(s+496.3)(s+0.0201)(s^2+691s+1.684e5)(s^2+489.7s+1.586e5)(s^2+475.4s+1.693e5)}$$

$$K_{4,6} = \frac{0.012183(s-6.388e6)(s+736.5)(s+381.9)(s+274.8)(s+42.33)(s+9.515)(s^2+432.5s+1.249e5)(s^2+523.9s+1.993e5)}{(s+1.644e4)(s+634.9)(s+496.3)(s+0.02011)(s^2+691s+1.684e5)(s^2+489.7s+1.586e5)(s^2+475.4s+1.693e5)}$$

$$K_{4,7} = \frac{-0.0042751(s+1.9e7)(s+1045)(s+555.9)(s+210.4)(s+53.09)(s+6.136)(s^2+673.4s+1.957e5)(s^2+482.9s+1.646e5)}{(s+1.644e4)(s+634.9)(s+496.3)(s+0.0201)(s^2+691s+1.684e5)(s^2+489.7s+1.586e5)(s^2+475.4s+1.693e5)}$$

In state-space form the above controller used for the simulation work in Fig. 8.13, page 188 has the following representation:

A: Continuous s-domain

$$\mathbf{K} = C_K(sI - A_K)^{-1}B_K + D_K$$

B: Discrete z-domain

$$\mathbf{K} = dC_K(zI - dA_K)^{-1}dB_K + dD_K$$

The individual numerical terms of the above matrices are given below. dA_K, dB_K, dC_K and dD_K are used for the DSP work.

$$A_K = \begin{bmatrix}
-2.0071 \times 10^{-002} & -3.3489 \times 10^{-012} & 8.7461 \times 10^{-013} & 1.2924 \times 10^{-002} & 4.6703 \times 10^{+000} & -6.7412 \times 10^{-011} & 7.7883 \times 10^{-010} & -5.0661 \times 10^{-009} & -1.8161 \times 10^{-009} \\
-1.1320 \times 10^{-013} & -2.0265 \times 10^{-002} & 4.2356 \times 10^{-012} & -7.6044 \times 10^{-010} & 8.7637 \times 10^{-010} & -1.4289 \times 10^{+000} & 9.4004 \times 10^{-003} & -7.8331 \times 10^{-008} & 1.1376 \times 10^{-007} \\
4.5539 \times 10^{-013} & 4.2251 \times 10^{-012} & -2.0356 \times 10^{-002} & -3.7109 \times 10^{-010} & 5.4460 \times 10^{-009} & -8.4246 \times 10^{-008} & 3.5452 \times 10^{-007} & 1.5069 \times 10^{+000} & 1.3105 \times 10^{-002} \\
5.0802 \times 10^{-003} & -6.0523 \times 10^{-010} & -8.2456 \times 10^{-010} & -1.2452 \times 10^{-001} & -2.6929 \times 10^{+003} & -2.4378 \times 10^{-007} & -1.9336 \times 10^{-008} & 1.4026 \times 10^{-007} & 4.6267 \times 10^{-008} \\
2.1882 \times 10^{+000} & 1.5864 \times 10^{-009} & 1.7192 \times 10^{-008} & 2.6749 \times 10^{+003} & -1.6746 \times 10^{+004} & -1.2139 \times 10^{-006} & -4.5538 \times 10^{-006} & 2.7046 \times 10^{-005} & 1.7870 \times 10^{-005} \\
-2.2885 \times 10^{-011} & -1.1035 \times 10^{+000} & -8.3563 \times 10^{-008} & -2.8629 \times 10^{-007} & 2.5932 \times 10^{-006} & -7.1125 \times 10^{+002} & 5.1769 \times 10^{+002} & -8.3625 \times 10^{-005} & 4.5549 \times 10^{-005} \\
2.8321 \times 10^{-010} & -9.0346 \times 10^{-003} & 3.2768 \times 10^{-007} & 1.3998 \times 10^{-008} & -2.0193 \times 10^{-006} & -5.1738 \times 10^{+002} & -2.7499 \times 10^{-002} & -1.4185 \times 10^{-004} & -7.5711 \times 10^{-005} \\
-4.1070 \times 10^{-009} & -8.0836 \times 10^{-008} & 1.3955 \times 10^{+000} & 2.9371 \times 10^{-007} & 1.2433 \times 10^{-005} & 8.0998 \times 10^{-005} & -1.7117 \times 10^{-004} & -6.7218 \times 10^{+002} & -4.9916 \times 10^{+002} \\
1.8888 \times 10^{-010} & 9.0539 \times 10^{-008} & -1.2768 \times 10^{-002} & -2.1764 \times 10^{-008} & -1.0471 \times 10^{-005} & 7.2345 \times 10^{-005} & 7.5682 \times 10^{-005} & 4.9911 \times 10^{+002} & -4.3853 \times 10^{-002} \\
-1.1667 \times 10^{-001} & 8.3093 \times 10^{-010} & -1.0376 \times 10^{-008} & -2.9836 \times 10^{+000} & 1.4756 \times 10^{+003} & 8.1972 \times 10^{-007} & 3.2828 \times 10^{-007} & 5.5179 \times 10^{-006} & 4.2009 \times 10^{-007} \\
-2.1170 \times 10^{-010} & -2.5292 \times 10^{-001} & -9.3010 \times 10^{-009} & -8.5465 \times 10^{-008} & 2.0236 \times 10^{-006} & -2.8372 \times 10^{+002} & -1.9853 \times 10^{+000} & -8.1539 \times 10^{-006} & 2.4390 \times 10^{-005} \\
1.4179 \times 10^{-009} & 1.2892 \times 10^{-008} & -2.9044 \times 10^{-001} & -5.2645 \times 10^{-008} & -1.3724 \times 10^{-005} & -3.7398 \times 10^{-006} & 5.5738 \times 10^{-005} & 2.4136 \times 10^{+002} & -2.3243 \times 10^{+000} \\
2.6593 \times 10^{-003} & -9.7685 \times 10^{-012} & 9.9318 \times 10^{-011} & -9.7003 \times 10^{-002} & 1.7759 \times 10^{+001} & -2.3357 \times 10^{-008} & 4.4031 \times 10^{-009} & -1.4153 \times 10^{-007} & 2.9756 \times 10^{-009} \\
-3.1104 \times 10^{-012} & -1.6787 \times 10^{-003} & 2.1234 \times 10^{-010} & -1.9838 \times 10^{-009} & 1.5807 \times 10^{-008} & -6.8891 \times 10^{+000} & -2.6683 \times 10^{-002} & -4.2769 \times 10^{-007} & 5.9468 \times 10^{-007}
\end{bmatrix}$$

$$\begin{bmatrix}
-2.2843 \times 10^{-001} & -2.0628 \times 10^{-011} & 1.2143 \times 10^{-009} & -5.0863 \times 10^{-003} & 2.0281 \times 10^{-011} \\
6.6529 \times 10^{-010} & -3.1700 \times 10^{-001} & 1.1854 \times 10^{-008} & -6.5083 \times 10^{-011} & -9.6517 \times 10^{-003} \\
-8.3135 \times 10^{-009} & -1.0006 \times 10^{-008} & -3.0438 \times 10^{-001} & 8.8660 \times 10^{-011} & -2.7930 \times 10^{-010} \\
4.6719 \times 10^{+000} & -7.9460 \times 10^{-008} & -5.6625 \times 10^{-008} & 9.7829 \times 10^{-002} & -2.9078 \times 10^{-009} \\
1.4767 \times 10^{+003} & -2.0868 \times 10^{-008} & -7.4851 \times 10^{-006} & 3.6106 \times 10^{+001} & -1.4697 \times 10^{-007} \\
5.2201 \times 10^{-007} & -2.8378 \times 10^{+002} & -2.4078 \times 10^{-006} & -6.1900 \times 10^{-008} & -9.2907 \times 10^{+000} \\
4.7191 \times 10^{-007} & 2.0961 \times 10^{+000} & 5.5813 \times 10^{-005} & 1.2436 \times 10^{-008} & 5.8734 \times 10^{-002} \\
2.4496 \times 10^{-006} & -8.2684 \times 10^{-006} & 2.4201 \times 10^{+002} & -1.5458 \times 10^{-007} & -2.9160 \times 10^{-007} \\
-1.3492 \times 10^{-006} & 2.3859 \times 10^{-005} & 2.3285 \times 10^{+000} & -2.9974 \times 10^{-008} & 7.8569 \times 10^{-007} \\
-3.8814 \times 10^{+002} & 7.5488 \times 10^{-007} & -2.4565 \times 10^{-006} & -1.6918 \times 10^{+001} & 9.2235 \times 10^{-008} \\
-9.4587 \times 10^{-008} & -3.9816 \times 10^{+002} & 8.6745 \times 10^{-006} & -1.5669 \times 10^{-007} & -2.2878 \times 10^{+001} \\
-3.5198 \times 10^{-007} & 1.7782 \times 10^{-006} & -3.1374 \times 10^{+002} & 3.6724 \times 10^{-007} & 3.1935 \times 10^{-007} \\
-7.1971 \times 10^{+000} & -4.5281 \times 10^{-008} & 4.0049 \times 10^{-007} & -3.9313 \times 10^{+000} & 7.3613 \times 10^{-010} \\
1.5970 \times 10^{-008} & -1.5794 \times 10^{+001} & 7.8021 \times 10^{-007} & -1.4349 \times 10^{-008} & -4.4353 \times 10^{+000}
\end{bmatrix}$$

$$B_K = \begin{bmatrix}
4.2505 \times 10^{+000} & 7.3712 \times 10^{-009} & -8.1192 \times 10^{-010} & 1.0667 \times 10^{+000} & 1.0667 \times 10^{+000} & 1.0667 \times 10^{+000} & 1.0667 \times 10^{+000} \\
6.4014 \times 10^{-010} & 4.7811 \times 10^{-008} & 1.3992 \times 10^{+000} & 8.8141 \times 10^{-001} & 8.8141 \times 10^{-001} & -8.8141 \times 10^{-001} & -8.8141 \times 10^{-001} \\
7.5366 \times 10^{-009} & -7.4565 \times 10^{-001} & 7.2107 \times 10^{-008} & 9.3882 \times 10^{-001} & -9.3882 \times 10^{-001} & 9.3882 \times 10^{-001} & -9.3882 \times 10^{-001} \\
-1.1926 \times 10^{+000} & 7.4769 \times 10^{-010} & 3.7463 \times 10^{-010} & 4.8825 \times 10^{-001} & 4.8825 \times 10^{-001} & 4.8825 \times 10^{-001} & 4.8825 \times 10^{-001} \\
-2.0598 \times 10^{+001} & 3.6983 \times 10^{-008} & 2.3892 \times 10^{-009} & -2.7860 \times 10^{+002} & -2.7860 \times 10^{+002} & -2.7860 \times 10^{+002} & -2.7860 \times 10^{+002} \\
6.9350 \times 10^{-009} & -1.6597 \times 10^{-008} & 4.9291 \times 10^{-001} & 4.0821 \times 10^{+001} & 4.0821 \times 10^{+001} & -4.0821 \times 10^{+001} & -4.0821 \times 10^{+001} \\
-2.4913 \times 10^{-009} & 1.3460 \times 10^{-007} & 1.8706 \times 10^{-001} & 2.3372 \times 10^{-001} & 2.3373 \times 10^{-001} & -2.3373 \times 10^{-001} & -2.3372 \times 10^{-001} \\
1.3115 \times 10^{-008} & 5.9608 \times 10^{-001} & -6.3922 \times 10^{-008} & -3.8948 \times 10^{+001} & 3.8948 \times 10^{+001} & -3.8948 \times 10^{+001} & 3.8948 \times 10^{+001} \\
-4.0769 \times 10^{-009} & -8.7310 \times 10^{-002} & -4.7514 \times 10^{-008} & 3.0813 \times 10^{-001} & -3.0813 \times 10^{-001} & 3.0813 \times 10^{-001} & -3.0813 \times 10^{-001} \\
1.9567 \times 10^{+000} & -3.0293 \times 10^{-008} & -1.6237 \times 10^{-009} & 1.3508 \times 10^{+001} & 1.3508 \times 10^{+001} & 1.3508 \times 10^{+001} & 1.3508 \times 10^{+001} \\
1.5885 \times 10^{-008} & 6.8208 \times 10^{-009} & 4.5354 \times 10^{-001} & 8.8205 \times 10^{+000} & 8.8205 \times 10^{+000} & -8.8205 \times 10^{+000} & -8.8205 \times 10^{+000} \\
-6.4654 \times 10^{-009} & -1.1399 \times 10^{+000} & 6.5707 \times 10^{-008} & 7.5573 \times 10^{+000} & -7.5573 \times 10^{+000} & 7.5573 \times 10^{+000} & -7.5573 \times 10^{+000} \\
-5.1197 \times 10^{-001} & -7.4713 \times 10^{-009} & -6.0498 \times 10^{-010} & 1.5889 \times 10^{-001} & 1.5889 \times 10^{-001} & 1.5889 \times 10^{-001} & 1.5889 \times 10^{-001} \\
3.2044 \times 10^{-010} & -1.0835 \times 10^{-008} & -3.5535 \times 10^{-001} & 2.0062 \times 10^{-001} & 2.0062 \times 10^{-001} & -2.0062 \times 10^{-001} & -2.0062 \times 10^{-001}
\end{bmatrix}$$

$$C_K = \begin{bmatrix}
-2.3779 \times 10^{+000} & -1.1253 \times 10^{+000} & -1.0101 \times 10^{+000} & 7.7067 \times 10^{-001} & 2.7879 \times 10^{+002} & -4.0822 \times 10^{+001} & 2.5175 \times 10^{-001} & 3.8949 \times 10^{+001} & 3.1121 \times 10^{-001} \\
-2.3779 \times 10^{+000} & -1.1253 \times 10^{+000} & 1.0101 \times 10^{+000} & 7.7067 \times 10^{-001} & 2.7879 \times 10^{+002} & -4.0822 \times 10^{+001} & 2.5174 \times 10^{-001} & -3.8949 \times 10^{+001} & -3.1120 \times 10^{-001} \\
-2.3779 \times 10^{+000} & 1.1253 \times 10^{+000} & -1.0101 \times 10^{+000} & 7.7067 \times 10^{-001} & 2.7879 \times 10^{+002} & 4.0822 \times 10^{+001} & -2.5174 \times 10^{-001} & 3.8949 \times 10^{+001} & 3.1120 \times 10^{-001} \\
-2.3779 \times 10^{+000} & 1.1253 \times 10^{+000} & 1.0101 \times 10^{+000} & 7.7067 \times 10^{-001} & 2.7879 \times 10^{+002} & 4.0822 \times 10^{+001} & -2.5175 \times 10^{-001} & -3.8949 \times 10^{+001} & -3.1121 \times 10^{-001}
\end{bmatrix}$$

$$\begin{bmatrix}
-1.3543 \times 10^{+001} & -8.8234 \times 10^{+000} & -7.5788 \times 10^{+000} & -3.0129 \times 10^{-001} & -2.6799 \times 10^{-001} \\
-1.3543 \times 10^{+001} & -8.8234 \times 10^{+000} & 7.5788 \times 10^{+000} & -3.0129 \times 10^{-001} & -2.6799 \times 10^{-001} \\
-1.3543 \times 10^{+001} & 8.8234 \times 10^{+000} & -7.5787 \times 10^{+000} & -3.0129 \times 10^{-001} & 2.6799 \times 10^{-001} \\
-1.3543 \times 10^{+001} & 8.8234 \times 10^{+000} & 7.5787 \times 10^{+000} & -3.0129 \times 10^{-001} & 2.6799 \times 10^{-001}
\end{bmatrix}$$

$$D_K = \begin{bmatrix}
1.5353 \times 10^{-002} & -1.1979 \times 10^{-002} & 3.0971 \times 10^{-003} & -4.2752 \times 10^{-003} & 1.2183 \times 10^{-002} & -8.7673 \times 10^{-003} & 7.6895 \times 10^{-003} \\
1.5353 \times 10^{-002} & 1.1979 \times 10^{-002} & 3.0971 \times 10^{-003} & 1.2183 \times 10^{-002} & -4.2752 \times 10^{-003} & 7.6895 \times 10^{-003} & -8.7673 \times 10^{-003} \\
1.5353 \times 10^{-002} & -1.1979 \times 10^{-002} & -3.0971 \times 10^{-003} & -8.7672 \times 10^{-003} & 7.6894 \times 10^{-003} & -4.2753 \times 10^{-003} & 1.2183 \times 10^{-002} \\
1.5353 \times 10^{-002} & 1.1979 \times 10^{-002} & -3.0971 \times 10^{-003} & 7.6896 \times 10^{-003} & -8.7674 \times 10^{-003} & 1.2183 \times 10^{-002} & -4.2751 \times 10^{-003}
\end{bmatrix}$$

$$dA_K = \begin{bmatrix} 9.9998 \times 10^{-001} & -3.0356 \times 10^{-015} & 4.5827 \times 10^{-015} & 5.7592 \times 10^{-004} & 4.2106 \times 10^{-004} & -2.2538 \times 10^{-013} & -2.3227 \times 10^{-013} & 9.4279 \times 10^{-013} & 1.7392 \times 10^{-012} \\ -6.7143 \times 10^{-017} & 9.9998 \times 10^{-001} & 7.7224 \times 10^{-015} & -5.2243 \times 10^{-013} & 6.8770 \times 10^{-014} & -9.9149 \times 10^{-004} & -2.4709 \times 10^{-004} & 4.6740 \times 10^{-012} & 9.7561 \times 10^{-011} \\ -4.9419 \times 10^{-016} & -7.6222 \times 10^{-015} & 9.9998 \times 10^{-001} & 1.1111 \times 10^{-012} & 9.8044 \times 10^{-013} & -7.9936 \times 10^{-011} & 2.2871 \times 10^{-010} & 1.0669 \times 10^{-003} & -2.5299 \times 10^{-004} \\ -2.6159 \times 10^{-004} & -6.6538 \times 10^{-013} & -4.2223 \times 10^{-012} & 6.6435 \times 10^{-001} & -2.5105 \times 10^{-001} & -1.6775 \times 10^{-010} & 4.8724 \times 10^{-010} & -2.9900 \times 10^{-009} & -1.4910 \times 10^{-009} \\ 1.9810 \times 10^{-004} & 1.1705 \times 10^{-013} & 2.5742 \times 10^{-012} & 2.4947 \times 10^{-001} & -8.1333 \times 10^{-001} & 4.0817 \times 10^{-012} & -4.0737 \times 10^{-010} & 2.3071 \times 10^{-009} & 1.1227 \times 10^{-009} \\ 2.1383 \times 10^{-013} & -7.6537 \times 10^{-004} & -3.8892 \times 10^{-011} & 3.6553 \times 10^{-011} & 1.7285 \times 10^{-010} & 4.2262 \times 10^{-001} & 3.6840 \times 10^{-001} & -5.7739 \times 10^{-008} & 3.0812 \times 10^{-008} \\ 3.1944 \times 10^{-014} & 1.8883 \times 10^{-004} & 2.5473 \times 10^{-010} & -2.1364 \times 10^{-010} & -2.0749 \times 10^{-010} & -3.6819 \times 10^{-001} & 9.0462 \times 10^{-001} & -9.6862 \times 10^{-008} & -5.5800 \times 10^{-008} \\ -1.9208 \times 10^{-012} & -1.0289 \times 10^{-010} & 9.8739 \times 10^{-004} & 1.5526 \times 10^{-009} & 1.0051 \times 10^{-009} & 5.7430 \times 10^{-008} & -1.1807 \times 10^{-007} & 4.4320 \times 10^{-001} & -3.6036 \times 10^{-001} \\ -1.3418 \times 10^{-012} & 4.2891 \times 10^{-011} & 2.3346 \times 10^{-004} & -1.0409 \times 10^{-009} & -8.0290 \times 10^{-010} & 4.9847 \times 10^{-008} & 5.5431 \times 10^{-008} & 3.6033 \times 10^{-001} & 9.0998 \times 10^{-001} \\ 2.4999 \times 10^{-005} & 4.9424 \times 10^{-013} & -4.6190 \times 10^{-012} & 1.5205 \times 10^{-001} & 1.1564 \times 10^{-001} & 3.8730 \times 10^{-010} & 1.2166 \times 10^{-010} & 4.6732 \times 10^{-009} & 2.3937 \times 10^{-010} \\ -2.6641 \times 10^{-014} & -1.2055 \times 10^{-004} & -4.8873 \times 10^{-012} & 1.4094 \times 10^{-010} & 1.4153 \times 10^{-010} & -1.6797 \times 10^{-001} & -4.5152 \times 10^{-002} & 6.2119 \times 10^{-009} & 1.6904 \times 10^{-008} \\ -1.4566 \times 10^{-013} & 6.0615 \times 10^{-012} & -1.4829 \times 10^{-004} & -1.3775 \times 10^{-009} & -1.0133 \times 10^{-009} & -5.3579 \times 10^{-009} & 3.2879 \times 10^{-008} & 1.5019 \times 10^{-001} & -3.9510 \times 10^{-002} \\ 4.3326 \times 10^{-006} & 1.6057 \times 10^{-015} & 3.9703 \times 10^{-014} & 1.5842 \times 10^{-003} & 1.2511 \times 10^{-003} & -1.4943 \times 10^{-011} & -3.1599 \times 10^{-012} & -6.7572 \times 10^{-011} & 2.9554 \times 10^{-011} \\ -1.6396 \times 10^{-015} & 1.9029 \times 10^{-006} & 1.8152 \times 10^{-013} & 2.8687 \times 10^{-013} & 9.2648 \times 10^{-013} & -3.5611 \times 10^{-003} & -9.3576 \times 10^{-004} & 8.2129 \times 10^{-012} & 3.8982 \times 10^{-010} \end{bmatrix}$$

$$\begin{bmatrix} 7.0187 \times 10^{-005} & 8.6228 \times 10^{-015} & -3.0044 \times 10^{-013} & 1.9458 \times 10^{-006} & -7.3011 \times 10^{-015} \\ 3.3899 \times 10^{-013} & -1.4723 \times 10^{-004} & 5.3520 \times 10^{-012} & -2.5973 \times 10^{-014} & -3.3613 \times 10^{-006} \\ -5.0943 \times 10^{-012} & -4.9926 \times 10^{-012} & -1.5177 \times 10^{-004} & 4.2886 \times 10^{-014} & -1.2303 \times 10^{-013} \\ -1.5198 \times 10^{-001} & -8.0534 \times 10^{-011} & 6.1801 \times 10^{-010} & -3.1591 \times 10^{-003} & 1.0709 \times 10^{-011} \\ 1.1591 \times 10^{-001} & 2.5770 \times 10^{-011} & -4.9019 \times 10^{-010} & 2.3969 \times 10^{-003} & -9.0388 \times 10^{-012} \\ 4.9743 \times 10^{-010} & -1.6799 \times 10^{-001} & 7.6653 \times 10^{-010} & -2.9572 \times 10^{-011} & -4.6657 \times 10^{-003} \\ 1.6533 \times 10^{-010} & 4.5226 \times 10^{-002} & 3.6309 \times 10^{-008} & 1.4503 \times 10^{-011} & 1.2462 \times 10^{-003} \\ 2.2865 \times 10^{-009} & -1.5346 \times 10^{-008} & 1.5059 \times 10^{-001} & -7.9457 \times 10^{-011} & -4.2171 \times 10^{-010} \\ -1.2136 \times 10^{-009} & 1.1937 \times 10^{-008} & 3.9611 \times 10^{-002} & -5.3376 \times 10^{-011} & 3.3690 \times 10^{-010} \\ 7.4679 \times 10^{-001} & 4.9789 \times 10^{-010} & -1.7456 \times 10^{-009} & -1.2656 \times 10^{-002} & 6.4201 \times 10^{-011} \\ -2.4447 \times 10^{-011} & 6.8790 \times 10^{-001} & 6.0743 \times 10^{-009} & -1.2417 \times 10^{-010} & -1.8488 \times 10^{-002} \\ -7.1088 \times 10^{-010} & 1.0437 \times 10^{-009} & 7.4447 \times 10^{-001} & 2.9638 \times 10^{-010} & 2.5448 \times 10^{-010} \\ -5.2390 \times 10^{-003} & -3.7643 \times 10^{-011} & 3.3996 \times 10^{-010} & 9.9614 \times 10^{-001} & 8.9680 \times 10^{-013} \\ 1.3500 \times 10^{-011} & -1.2723 \times 10^{-002} & 6.0766 \times 10^{-010} & -1.3289 \times 10^{-011} & 9.9574 \times 10^{-001} \end{bmatrix}$$

$$dB_K = \begin{bmatrix} 4.2458 \times 10^{+000} & 7.3784 \times 10^{-009} & -8.1143 \times 10^{-010} & 1.0086 \times 10^{+000} & 1.0086 \times 10^{+000} & 1.0086 \times 10^{+000} & 1.0086 \times 10^{+000} \\ 6.3577 \times 10^{-010} & 4.7796 \times 10^{-008} & 1.3989 \times 10^{+000} & 8.6049 \times 10^{-001} & 8.6049 \times 10^{-001} & -8.6049 \times 10^{-001} & -8.6049 \times 10^{-001} \\ 7.5288 \times 10^{-009} & -7.4523 \times 10^{-001} & 7.2074 \times 10^{-008} & 9.1742 \times 10^{-001} & -9.1742 \times 10^{-001} & 9.1742 \times 10^{-001} & -9.1742 \times 10^{-001} \\ 1.4447 \times 10^{+000} & -2.8841 \times 10^{-009} & 1.1989 \times 10^{-010} & 3.4352 \times 10^{+001} & 3.4352 \times 10^{+001} & 3.4352 \times 10^{+001} & 3.4352 \times 10^{+001} \\ -1.9580 \times 10^{+000} & 2.6982 \times 10^{-009} & 1.4525 \times 10^{-010} & -2.5159 \times 10^{+001} & -2.5159 \times 10^{+001} & -2.5159 \times 10^{+001} & -2.5159 \times 10^{+001} \\ 1.8315 \times 10^{-009} & -6.5550 \times 10^{-009} & 3.4727 \times 10^{-001} & 2.8338 \times 10^{+001} & 2.8338 \times 10^{+001} & -2.8338 \times 10^{+001} & -2.8338 \times 10^{+001} \\ -8.6728 \times 10^{-010} & 8.4162 \times 10^{-008} & 9.7566 \times 10^{-002} & -7.0928 \times 10^{+000} & -7.0928 \times 10^{+000} & 7.0928 \times 10^{+000} & 7.0928 \times 10^{+000} \\ 6.9189 \times 10^{-010} & 3.5966 \times 10^{-001} & -3.2948 \times 10^{-008} & -2.7591 \times 10^{+001} & 2.7591 \times 10^{+001} & -2.7591 \times 10^{+001} & 2.7591 \times 10^{+001} \\ 6.0554 \times 10^{-009} & 1.3485 \times 10^{-003} & -3.5435 \times 10^{-008} & -6.5730 \times 10^{+000} & 6.5730 \times 10^{+000} & -6.5730 \times 10^{+000} & 6.5730 \times 10^{+000} \\ 4.3060 \times 10^{-001} & -2.1836 \times 10^{-008} & -1.0390 \times 10^{-009} & -4.2757 \times 10^{+000} & -4.2757 \times 10^{+000} & -4.2757 \times 10^{+000} & -4.2757 \times 10^{+000} \\ 1.1343 \times 10^{-008} & 1.8621 \times 10^{-009} & 3.4035 \times 10^{-001} & 4.0085 \times 10^{+000} & 4.0085 \times 10^{+000} & -4.0085 \times 10^{+000} & -4.0085 \times 10^{+000} \\ 5.9106 \times 10^{-009} & -9.4772 \times 10^{-001} & 5.5396 \times 10^{-008} & 3.6609 \times 10^{+000} & -3.6609 \times 10^{+000} & 3.6609 \times 10^{+000} & -3.6609 \times 10^{+000} \\ -5.2993 \times 10^{-001} & -7.5690 \times 10^{-009} & -6.1044 \times 10^{-010} & -5.0690 \times 10^{-002} & -5.0693 \times 10^{-002} & -5.0693 \times 10^{-002} & -5.0690 \times 10^{-002} \\ 2.1441 \times 10^{-010} & -1.1250 \times 10^{-008} & -3.5844 \times 10^{-001} & 7.1287 \times 10^{-002} & 7.1290 \times 10^{-002} & -7.1287 \times 10^{-002} & -7.1290 \times 10^{-002} \end{bmatrix}$$

$$dC_K = \begin{bmatrix} -2.3506 \times 10^{-003} & -1.1091 \times 10^{-003} & -9.9030 \times 10^{-004} & 3.4385 \times 10^{-002} & 2.5140 \times 10^{-002} & -2.8342 \times 10^{-002} & -7.0803 \times 10^{-003} & 2.7592 \times 10^{-002} & -6.5708 \times 10^{-003} \\ -2.3506 \times 10^{-003} & -1.1091 \times 10^{-003} & 9.9030 \times 10^{-004} & 3.4385 \times 10^{-002} & 2.5140 \times 10^{-002} & -2.8342 \times 10^{-002} & -7.0803 \times 10^{-003} & -2.7592 \times 10^{-002} & 6.5708 \times 10^{-003} \\ -2.3506 \times 10^{-003} & 1.1091 \times 10^{-003} & -9.9030 \times 10^{-004} & 3.4385 \times 10^{-002} & 2.5140 \times 10^{-002} & 2.8342 \times 10^{-002} & 7.0803 \times 10^{-003} & 2.7592 \times 10^{-002} & -6.5708 \times 10^{-003} \\ -2.3506 \times 10^{-003} & 1.1091 \times 10^{-003} & 9.9030 \times 10^{-004} & 3.4385 \times 10^{-002} & 2.5140 \times 10^{-002} & 2.8342 \times 10^{-002} & 7.0803 \times 10^{-003} & -2.7592 \times 10^{-002} & 6.5708 \times 10^{-003} \end{bmatrix}$$

$$\begin{bmatrix} 4.2710 \times 10^{-003} & -4.0101 \times 10^{-003} & -3.6715 \times 10^{-003} & 1.1790 \times 10^{-004} & -9.0459 \times 10^{-005} \\ 4.2710 \times 10^{-003} & -4.0101 \times 10^{-003} & 3.6715 \times 10^{-003} & 1.1790 \times 10^{-004} & -9.0459 \times 10^{-005} \\ 4.2710 \times 10^{-003} & 4.0101 \times 10^{-003} & -3.6715 \times 10^{-003} & 1.1790 \times 10^{-004} & 9.0459 \times 10^{-005} \\ 4.2710 \times 10^{-003} & 4.0101 \times 10^{-003} & 3.6715 \times 10^{-003} & 1.1790 \times 10^{-004} & 9.0459 \times 10^{-005} \end{bmatrix}$$

$$dD_K = \begin{bmatrix} -2.6491 \times 10^{-001} & -1.0069 \times 10^{-003} & -6.2194 \times 10^{-003} & -4.6205 \times 10^{+000} & -3.4987 \times 10^{+000} & -3.4300 \times 10^{+000} & -2.3082 \times 10^{+000} \\ -2.6491 \times 10^{-001} & 1.0069 \times 10^{-003} & -6.2194 \times 10^{-003} & -3.4987 \times 10^{+000} & -4.6205 \times 10^{+000} & -2.3082 \times 10^{+000} & -3.4300 \times 10^{+000} \\ -2.6491 \times 10^{-001} & -1.0069 \times 10^{-003} & 6.2194 \times 10^{-003} & -3.4300 \times 10^{+000} & -2.3082 \times 10^{+000} & -4.6205 \times 10^{+000} & -3.4987 \times 10^{+000} \\ -2.6491 \times 10^{-001} & 1.0069 \times 10^{-003} & 6.2194 \times 10^{-003} & -2.3082 \times 10^{+000} & -3.4300 \times 10^{+000} & -3.4987 \times 10^{+000} & -4.6205 \times 10^{+000} \end{bmatrix}$$

Appendix G

Matlab programs for deriving nonlinear $\mathcal{H}_\infty$ state-feedback and output-feedback controllers

```
% Nonlinear state-feedback Hoo controller for Maglev
% used for the derivations in Chapter 9
clear all

syms F Z A B C D R Ham P syms x v f Res m gamma tmp tmp1 res K IC vs
V Vx syms As Vs3 Lc i j V3 Vx3 V2 index f2 f2Vx2 xl c Veq syms Vind
k;

syms x1 x2 x3 v1 v2 syms c1 c2 c3 c4 c5 c6 c7 c8 c9 c10

x=[x1 x2 x3];

 disp('Nonlinear Hoo controller for MAGLEV');
 disp('-----------------------------------');
 disp('');

% parameters of the maglev system
f   =5.04424e-5;      % f = uo*N^2*A/2
Res =1.1;             % magnet's coil resistance
m   =1.8;             % mass of thge magnet

% energy limit
gamma   =1;          % gamma

% Initial conditions
IC = [4e-3,0,3.13,0,5];

% Dynamics of the system
F = [   x2      -1/(2*m)*f*x3^2/x1^2+1/m*v1
-x1*Res/f*x3+1/x1*x3*x2+x1/f*v2*1.0  ];

Z = [   1*x1,   1*x2,   1*x3,   0.12*v2  ];

% Section A
% Computing the jacobians
```

```
A = subs(jacobian(F,[x1 x2 x3]),{x1 x2 x3 v1
v2},{IC(1),IC(2),IC(3),IC(4),IC(5)}); B = subs(jacobian(F,[v1
v2])      ,{x1 x2 x3 v1 v2},{IC(1),IC(2),IC(3),IC(4),IC(5)}); C =
subs(jacobian(Z,[x1 x2 x3]),{x1 x2 x3 v1
v2},{IC(1),IC(2),IC(3),IC(4),IC(5)}); D = subs(jacobian(Z,[v1
v2])      ,{x1 x2 x3 v1 v2},{IC(1),IC(2),IC(3),IC(4),IC(5)});


% R matrix
R = D'*D - [gamma^2,0;0,0];

% Hamiltonian system
Ham = [
     A,          -(B*R^-1*B') ;
        -C'*C,  -A'
        ];

% Riccati equation state-feedback
result = are(double(A),double(-(B*R^-1*B')),double(-C'*C));

% P matrix
P   = - result;

% first-order state-feedback controller
K   = R^-1*B'*P;
vs  = -K*[x1;x2;x3];

disp('------------------------------------------------------------');
disp(' First order Hoo controller:'); K1 = double(-K(2,:))
disp('------------------------------------------------------------');

V   = [x1 x2 x3]*P*[x1; x2; x3];
Vx  = jacobian(V,[x1 x2 x3]);

% First order closed-loop system A*
As = (A-B*K); As =    As*[x1;x2;x3];

% storage function V2
V2=[x1^2, x1*x2, x1*x3, x2^2, x2*x3, x3^2];

% storage function V3
V3=[x1^3, x1^2*x2, x1^2*x3, x1*x2^2, x1*x2*x3, x1*x3^2, x2^3,
x2^2*x3, x2*x3^2, x3^3];

% Expanding in series,

tmp(1) = mtaylor(F(1),[x1 x2 x3],[IC(1) IC(2) IC(3)]);
tmp(2) = mtaylor(F(2),[x1 x2 x3],[IC(1) IC(2) IC(3)]);
tmp(3) = mtaylor(F(3),[x1 x2 x3],[IC(1) IC(2) IC(3)]);

f2(1) = subs(tmp(1) - subs(tmp(1),{x1 x2 x3},{0 0 0}),{v1 v2},{0 0});
f2(2) = subs(tmp(2) - subs(tmp(2),{x1 x2 x3},{0 0 0}),{v1 v2},{0 0});
```

```
f2(3) = subs(tmp(3) - subs(tmp(3),{x1 x2 x3},{0 0 0}),{v1 v2},{0 0});

%AsVx3=-f2Vx2

% right-hand side
f2Vx2 = (Vx*[f2(1);f2(2);f2(3)]);

% left-hand side
c = [c1;c2;c3;c4;c5;c6;c7;c8;c9;c10];
Vx3 = jacobian(V3*c,[x1 x2 x3]);

% solution for the unknown storage function
Veq = simplify(Vx3*As + f2Vx2);

disp('Arranging the coefficients');
disp('-------------------------------------------------------');
disp('');

% arrange the coefficients
srtcoef;

disp('Solving the system of equations');
disp('-------------------------------------------------------');
disp('');

% Solving the system of ten equations with ten unknowns (ck)
S = solve(Sveq(1),Sveq(2),Sveq(3),Sveq(4),Sveq(5),Sveq(6),Sveq(7),Sveq(8),
Sveq(9),Sveq(10));
% coefficients from the resultant staructure
clear C;
    for i = 1:10,
    tmps = sprintf('c%d',i);
      C(i) = double(getfield(S,tmps));
    end

% Computes the second order controller
V = V + V3*C'; Vx = jacobian(V,[x1 x2 x3]); vs = -0.5*R^-1* (B'*Vx');
K = expand(vs(2));

% Get the coefficients from the symbolic solution
getcoef;

disp('-------------------------------------------------------');
disp(' Nonlinear state-feedback Hoo controller:'); K2
disp('-------------------------------------------------------');


% Nonlinear output-feedback Hoo controller for Maglev
% used for the derivations in Chapter 9

clear all

syms        F Z A B C D R Ham P ...
            x v f Res m gamma tmp tmp1 res K IC vs V Vx ...
```

```
            As Vs3 Lc i j V3 Vx3 V2 index f2 f2Vx2 xl c Veq ...
            Vind k C1 C2 B1 D11 D21 w u Y X Ae Qe ...
            n m1 m2 p1 p2 us ws Xs Zs Hs ...
            D11t D21t R1 R1i DRD DRDi eyem1 ...
            hs Be Ce Q ys y wh wss Ys G W Wx;


syms x1 x2 x3 v1 v2 v3 u1 syms w1 w2

x = [x1 x2 x3]; v = [v1 v2 v3];

disp('Nonlinear output-feedback Hoo controller for MAGLEV');
disp('-------------------------------------------------');
disp('');

% parameters of maglev system
f   =5.04424e-5;     % f = uo*N^2*A/2
Res =1.1;          % magnet's coil resistance
m   =1.8;            % mass of thge magnet

gamma   =1;         % gamma

% Initial conditions
IC = [4.0,0,3.3,  0,0,1] ;

w(1) = v(1); w(2) = v(2); u1 = v(3);

% System's dynamics
X = [   x2, ...
   -1/(2*m)*f*x3^2/x1^2+1/m*v1, ...
   -x1*Res/(f)*x3+1/(x1)*x3*x2+x1/(f)*v3 ];

% System's dynamics
Z = [1*x(1),0.2*v3 ];
% System's dynamics
Y = [x(1)+1*v2];

% linear state-space system

A = subs(jacobian(X,[x1 x2 x3]),{x1 x2 x3 v1 v2
v3},{IC(1),IC(2),IC(3),IC(4),IC(5),IC(6)}); B = subs(jacobian(X,[v1
v2 v3]),{x1 x2 x3 v1 v2 v3},{IC(1),IC(2),IC(3),IC(4),IC(5),IC(6)});
C = subs(jacobian(Z,[x1 x2 x3]),{x1 x2 x3 v1 v2
v3},{IC(1),IC(2),IC(3),IC(4),IC(5),IC(6)}); D = subs(jacobian(Z,[v1
v2 v3]),{x1 x2 x3 v1 v2 v3},{IC(1),IC(2),IC(3),IC(4),IC(5),IC(6)});

C2  = subs(jacobian(Y,[x1 x2 x3]),{x1 x2 x3 v1 v2
v3},{IC(1),IC(2),IC(3),IC(4),IC(5),IC(6)}); B1  =
subs(jacobian(X,[w(1) w(2)]),{x1 x2 x3 v1 v2
v3},{IC(1),IC(2),IC(3),IC(4),IC(5),IC(6)}); D11 =
subs(jacobian(Z,[w(1) w(2)]),{x1 x2 x3 v1 v2
v3},{IC(1),IC(2),IC(3),IC(4),IC(5),IC(6)}); D21 =
subs(jacobian(Y,[w(1) w(2)]),{x1 x2 x3 v1 v2
```

```
v3},{IC(1),IC(2),IC(3),IC(4),IC(5),IC(6)});

C1   = C; D11t= D11'; D21t= D21';

% R matrix
R = (D'*D - [gamma^2 0 0;0 gamma^2 0;0 0 0]);

% Riccati equation
Ae  = (A - B*R^-1*D'*C1); Qe  = (C1'*C1 - C1'*D*R^-1*D'*C1);
result = -are(double(Ae),double(-(B*R^-1*B')),double(-Qe));

% P matrix
P   = result;

% first-order state-feedback controller
F  = R^-1*B'*P + D'*C1; vs = -F*[x1;x2;x3];

disp(' First-order Hoo controller:'); pretty(vs(3)); double(-F(3,:))
disp(' ------------------------------------------------------------');

% storage function V=xTPx
V   = [x1 x2 x3]*P*[x1; x2; x3];
% it's gradient
Vx  = jacobian(V,[x1 x2 x3]);

% Closed loop matrix A*
As =    A-B*F; As =    As*[x1;x2;x3];

ws = [vs(1),vs(2)]; us = vs(3);

Xs = subs(X ,{v1 v2 v3},{vs(1),vs(2),vs(3)}); Zs = subs(Z ,{v1 v2
v3},{vs(1),vs(2),vs(3)});

% Hamiltonian function
Hs = (Vx*Xs' + Zs*Zs' - gamma^2*ws*ws');

% Riccati equation, to find W and Wx

R1   = D11t*D11 - gamma^2 * eye(2,2);
DRD  = D21*R1^-1*D21t; DRDi = DRD^-1;

hs   = 0.5*subs(Hs ,{x1 x2 x3},{IC(1),IC(2),IC(3)});

Ae  = (A - (B1*R1^-1*(D11t*C1+ (D21t*DRDi*(C2 - (D21*R1i*D11t*C1))))));
Be  = (B1*(-R1^-1 + (R1^-1*D21t*DRDi*D21*R1i))*B1');
Ce  = (C2 - D21*R1^-1*D11t*C1)'*DRDi*(C2 - D21*R1^-1*D11t*C1) - ...
       (C1'* D11* R1^-1* D11t*C1) + (C1'*C1) - eye(3,3)*hs;

result = -are(double(Ae'),double(Ce),double(-Be));

% what, ystar, and wstarstar.
Q  = result^-1; ys = (-2 * (DRDi*(C2 - (D21*R1^-1*(D11t*C1+
B1'*Q)))*[x1;x2;x3])); wh = (-R1^-1 * ((D11t*C1*[x1;x2;x3]) +
```

```
(B1'*Q*[x1;x2;x3])- 0.5*D21t * y)); wss = subs(wh ,{y},{ys});

Ys    = subs(Y,{v1 v2},{ws(1) ws(2)});

% Compute Q(x)
G = -((Q - P)^-1*(C2 - (D21*R1i*(D11t*C1+B1'*Q)))'*DRDi);

% Compute W and Wx
W = ([x1 x2 x3]*Q*[x1;x2;x3]); Wx = jacobian(W,[x1 x2 x3]);

% nonlinear observer
Sys=expand([Xs(1);Xs(2);Xs(3)] + G * (y - Ys));

disp('------------------------------------------------------------');
disp('Nonlinear Hoo observer'); disp('State1=');
%pretty(Sys(1));
disp('State2=');pretty(Sys(2)); disp('State3=');pretty(Sys(3));
disp(' ------------------------------------------------------------');



%function Sveq = srtcoef(Veq,c,x)
% sort the identical terms in x

clear sveq i j pat RES coef Sveq;

debug = 0;

if(0), tsteq, end

Veq=collect(Veq,c);
sVeq = char(Veq);

j = 1;
p = 1;
 while j<=200,
   for i=1:length(sVeq)
      if ( (sVeq(i) == '+' | sVeq(i) == '-') & i > 1)
        break;
       else
       sveq(j,i) = sVeq(i);
      end %if
   end %for i
   sVeq = sVeq(i:length(sVeq));
   j = j+1;
end %while

pat(1,:) = {'x1*x2*x3' 'x1*x3*x2' 'x2*x1*x3' 'x2*x3*x1' 'x3*x2*x1' 'x3*x1*x2'};
pat(2,:) = {'x1^2*x2' 'x2*x1^2' '' '' '' ''};
pat(3,:) = {'x1^2*x3' 'x3*x1^2' '' '' '' ''};
pat(4,:) = {'x2^2*x1' 'x1*x2^2' '' '' '' ''};
pat(5,:) = {'x2^2*x3' 'x3*x2^2' '' '' '' ''};
pat(6,:) = {'x3^2*x1' 'x1*x3^2' '' '' '' ''};
pat(7,:) = {'x3^2*x2' 'x2*x3^2' '' '' '' ''};
```

```
pat(8,:)  = {'x1*x2' 'x2*x1' '' '' '' ''};
pat(9,:)  = {'x1*x3' 'x3*x1' '' '' '' ''};
pat(10,:) = {'x2*x3' 'x3*x2' '' '' '' ''};
pat(11,:) = {'x1^2' '' '' '' '' ''};
pat(12,:) = {'x2^2' '' '' '' '' ''};
pat(13,:) = {'x3^2' '' '' '' '' ''};
pat(14,:) = {'x1^3' '' '' '' '' ''};
pat(15,:) = {'x2^3' '' '' '' '' ''};
pat(16,:) = {'x3^3' '' '' '' '' ''};
pat(17,:) = {'x1' '' '' '' '' ''};
pat(18,:) = {'x2' '' '' '' '' ''};
pat(19,:) = {'x3' '' '' '' '' ''};

   for j=1:19
    tmpc = '';

      for k = 1:6,
          for i=1:length(sveq(:,1))

            % move all c-coefficients at the end of expresion
              where   =  findstr(sveq(i,:),'c');
              ends    =  length(sveq(i,:));

              if( (where+3) < length(sveq(i,:))  )
                 if( sveq(i,where+2)=='*' )
                    tmps = sveq(i,where-1:where+1);
                    sveq(i,where-1:ends-3)=sveq(i,where+2:ends);
                    sveq(i,ends-2:ends)=tmps;
                 elseif( sveq(i,where+3)=='*' )
                    tmps = sveq(i,where-1:where+2);
                    sveq(i,where-1:ends-4)=sveq(i,where+3:ends);
                    sveq(i,ends-3:ends)=tmps;
                 end
              end

            where =  findstr(sveq(i,:),char(pat(j,k)) );
            if( ~isempty(where) )

if(debug)
              disp('-------------------------');
              sveq(i,:),
end;

              if(where>2)
                 sveq(i,where-1:where-1+length(char(pat(j,k)))) = blanks(1);
              else
                 sveq(i,where:where-1+length(char(pat(j,k)))) = blanks(1);
                      sveq(i,where+0:where+1)='1 ';
                 sveq(i,where+2:where+length(char(pat(j,k))));
                 %                sveq(i,where+length(char(pat(j,k)))) = '';
              end

              tmpc = strcat(tmpc,sveq(i,:));
```

```
            end %if
         end %i
   end %k

   k = 1;
   len = length(tmpc);
   %clear empty spaces
   for i=1:len
      if (isspace(tmpc(i))),

         where =  findstr(tmpc,'*');

         tmpc(i:length(tmpc(where(k):length(tmpc)))+i-1)=tmpc(where(k):length(tmpc));
         tmpc(length(tmpc(where(k):length(tmpc)))+i:len)=
                     blanks(length(tmpc(length(tmpc(where(k):length(tmpc)))+i:len)));
         if( isempty(findstr(tmpc(where(k):length(tmpc)),'*')) )
            break;
         end %if
         k = k+1;

      end
   end

 % Remove coefficients without terms in 'c'
   where =  findstr(tmpc,'c');
   if(~isempty(where)),
      Sveq(p) = sym(tmpc(1:where(k)+5));
      p = p+1;
   end


 end %j
% get the numerical form of the coefficients of the state-feedback

clear sveq sK K2 k sK;

k=collect(K,x);
sK = char(k);
j = 1;i = 1;

while j<10,
   for i=1:length(sK)
      if ((sK(i) == '+' | sK(i) == '-') & i > 1)
        break;
       else
       sveq(j,i) = sK(i);
      end %if
   end %for i
   sK = sK(i:length(sK));
   j = j+1;
end %while
```

```
for i=1:length(sveq(:,1))
   where   =  findstr(sveq(i,:),'*');
   K2(i) = double(sym(sveq(i,1:where-1)));
end

% customised second-order Taylor expansion of F around x0
function f = mtaylor(F,x,x0)

Df = jacobian(F,x) ;
DDf= jacobian(Df,x);

f = subs(F,{x(1) x(2) x(3)},{x0(1),x0(2),x0(3)}) + ...
    subs(   Df(1),{x(1) x(2) x(3)},{x0(1),x0(2),x0(3)})*(x(1)-x0(1)) + ...
     subs(   Df(2),{x(1) x(2) x(3)},{x0(1),x0(2),x0(3)})*(x(2)-x0(2)) + ...
    subs(   Df(3),{x(1) x(2) x(3)},{x0(1),x0(2),x0(3)})*(x(3)-x0(3)) + ...
1/2*subs(DDf(1,1),{x(1) x(2) x(3)},{x0(1),x0(2),x0(3)})*(x(1)-x0(1))^2 + ...
    subs(DDf(1,2),{x(1) x(2) x(3)},{x0(1),x0(2),x0(3)})*(x(1)-x0(1))*(x(2)-x0(2)) + .
    subs(DDf(1,3),{x(1) x(2) x(3)},{x0(1),x0(2),x0(3)})*(x(1)-x0(1))*(x(3)-x0(3)) + .
1/2*subs(DDf(2,2),{x(1) x(2) x(3)},{x0(1),x0(2),x0(3)})*(x(2)-x0(2))^2 + ...
    subs(DDf(2,3),{x(1) x(2) x(3)},{x0(1),x0(2),x0(3)})*(x(2)-x0(2))*(x(3)-x0(3)) + .
1/2*subs(DDf(3,3),{x(1) x(2) x(3)},{x0(1),x0(2),x0(3)})*(x(3)-x0(3))^2 ;
```

Bibliography

[1] P.K. Sinha. *Electromagnetic Suspension, Dynamics & Control.* Peter Peregrinus Ltd., London, UK, 1987.

[2] B.V. Jayawant. Review lecture: Electromagnetic suspension and levitation techniques. *Proc. Royal Society of London*, 416:pp. 245–320, 1988.

[3] SKF Magnetic Bearings. Skf magnetic bearings: Products and applications. *http://www.skf.com*, 2003.

[4] Transrapid International. Maglev technology – technical reports. *http://www.transrapid.de*, 2004.

[5] Japanese Railway Technical Research Institute. Technical reports. *http://www.rtri.or.jp*, 2004.

[6] V. Nenadovic and E.E. Riches. Maglev at Birmingham Airport: from system concept to successful operation. *GEC Review*, 1 (1):pp. 3–17, 1985.

[7] IEEE Spectrum. Record run. *IEEE Spectrum*, vol. 4(1):pp. 24–25, 2003.

[8] New Scientist. First passenger maglev train set for lift-off. *NewScientist*, vol. 2(4):pp. 268–280, 2002.

[9] Transrapid International Press Release. The Shanghai-Pudon airport highspeed link. *Press Release*, Hanover, April, 2001.

[10] P. Holmer. Faster than a speeding bullet train. *IEEE Spectrum*, vol. 40(8):pp. 30–34, 2003.

[11] P.K. Sinha. *Magnetic levitation.* McGraw-Hill Encyclopedia of Science and Technology, New York, 2001.

[12] The Economist. The new age of the train: A better way to fly. *The Economist, London*, pages pp. 23–25, 1998.

[13] P.K. Sinha and B.V. Jayawant. Analytical and design aspects of magnetically suspended vehicles. *Automatica*, vol. 15:pp. 539–552, 1979.

[14] B.V. Jayawant and J. C. West. Electromagnetic control apparatus. *British patent*, 1165704, 1965.

[15] B.V. Jayawant, P.K. Sinha, A. R. Wheeler, and R. J. Whorlow. Development of 1-ton magnetically suspended vehicle using controlled d.c. electromagnets. *Proc. IEE*, vol. 123:pp. 941–948, 1976.

[16] B.V. Jayawant and P.K. Sinha. Low-speed vehicle dynamics and ride quality using controlled d.c. electromagnets. *Automatica*, vol. 13:pp. 605–610, 1977.

[17] E. Gottzein and B. Lange. Magnetic suspension control systems for the MBB high speed train. *Automatica*, 11:pp. 271–284, 1975.

[18] E. Gottzein, K.H. Brock, E. Schneider, and J. Pfefferl. Control aspects of a tracked magnetic levitation high speed test vehicle. *Automatica*, 13:pp. 205–223, 1977.

[19] P.K. Sinha, G. Pech, and H.A. Abbassi. Digital control of an electromagnetic suspension system using the tms-32020 signal processor. *Automatica*, vol. 27:pp. 1051–1054, 1991.

[20] J. F. Whidborne. Ems control system design for a maglev vehicle – a critical system. *Automatica*, vol. 29:pp. 1345–1349, 1993.

[21] N.S. McLagan. *Control of electromagnetic vehicle suspension.* PhD Thesis, Reading University, Reading University, UK, 1992.

[22] M. Fujita, T. Namerikawa, F. Matsumura, and K. Uchida. μ-synthesis of an electromagnetic suspension system. *IEEE Transactions on Automatic Control*, vol. 40:pp. 530–536, 1995.

[23] T. Namerikawa and M. Fujita. Modelling and robustness analysis of a magnetic suspension system considering structured uncertainty. *"IEEE Proc. of the 36th Conference on Decision and Control"*, pages pp. 2559–2564, 1997.

[24] C.J. Macleod R.M. Goodall. Frequency-shaping lq control of maglev suspension systems for optimal performance with deterministic and stochastic inputs. *IEE Proceedings on Control Theory Applications*, vol. 143(1):pp. 25–30, 1996.

[25] B.C. Fabien. Observer-based feedback linearising control of an electromagnetic suspension. *Journal of Dynamics Systems, Measurements and Control*, vol. 118:pp. 615–619, 1996.

[26] S-J. Joo and J.H. Seo. Design and analysis of the nonlinear feedback linearizing control for an electromagnetic suspension system. *IEEE Transactions on Control Systems Technology*, vol. 5(1):pp. 135–144, 1997.

[27] D.L. Trumper, S.M. Olson, and P.K. Subrahmanyan. Linearizing control of magnetic suspension systems. *IEEE Transactions on Control Systems Technology*, vol. 5(4):pp. 427–438, 1997.

[28] Zi-Jiang Yang and M. Minashima. Robust nonlinear control of a feedback linearizable voltage-controlled magnetic levitation system. *Transaction IEE Japan*, vol. 121-C:pp. 1203–1211, 2001.

[29] Zi-Jiang Yang and M. Minashima. Adaptive robust nonlinear control of a magnetic levitation system. *Automatica*, vol. 37:pp. 1125–1131, 2001.

[30] N.V. Dakev, J.F. Whidborne, A.J. Chipperfield, and P.J. Fleming. Evolutionary $\langle_\infty$ design of an electromagnetic suspension control system for a maglev vehicle. *Proc. Instn. Mech. Engers.*, vol. 211:pp. 345–355, 1997.

[31] A. Bittar and R.M. Sales. $\mathcal{H}_2$ and $\mathcal{H}_\infty$ control for maglev vehicles. *IEEE Control Systems Magazine*, vol. 18:pp. 18–25, 1998.

[32] S.-H. Lee and J.-T. Lim. Switching control of $\mathcal{H}_\infty$ gain scheduled controllers in uncertain nonlinear systems. *Automatica*, vol. 36:pp. 1067–1074, 2000.

[33] W. A. Jacobs. Magnetic launch assist – NASA's vision for the future. *IEEE Transactions on Magnetics*, vol. 37(1):pp. 55–57, 2001.

[34] University of Sussex. Engineers develop revolutionary rocket launching system. *University of Sussex Media Release*, 1998.

[35] P.K. Sinha and A.N. Pechev. Model reference adaptive control of a maglev system with stable maximum descent criterion. *Automatica*, 35:pp. 1457–1465, 1999.

[36] P.K. Sinha and A.N. Pechev. Nonlinear $\mathcal{H}_\infty$ controllers for electromagnetic suspension systems. *IEEE Transactions on Automatic Control*, Vol. 49(4):pp. 563–568, 2004.

[37] P. Khargonekar J.C. Doyle, K. Glover and B. Francis. State-space solutions to standard $\mathcal{H}_2$ and $\mathcal{H}_\infty$ control problems. *IEEE Transactions on Automatic Control*, 34:pp. 831–847, 1989.

[38] G. F. Franklin, J.D. Powell, and A.E. Naeini. *Feedback control of dynamic systems.* Addison-Wesley, 1994.

[39] Inmos Limited and SGS-Thomson. *The Transputer Databook.* Inmos Limited and SGS-Thomson, 1992.

[40] Inmos Limited and SGS-Thomson. *The Transputer Databook.* Inmos Limited and SGS-Thomson, 1992.

[41] National Instruments. *Lab/Windows CVI User's manual.* National Instruments, 1998.

[42] P.Katz. *Digital control using Microprocessors.* Prentice Hall International, London, UK, 1981.

[43] K.J.Astrom and B.Wittenmark. *Computer controlled systems–theory and design.* Prentice Hall Inc., Englewood Cliffs, NJ 07632, US, 1984.

[44] Analog Devices Inc. *ADSP-2106x SHARC User's Manual.* Analog Devices Inc., P.O.Box 9106, Norwood, MA 02062-9106, USA, 1997.

[45] Analog Devices Inc. *ADSP-2106x SHARC DSP Microcomputer Family.* Analog Devices Inc., P.O.Box 9106, Norwood, MA 02062-9106, USA, 1996.

[46] Analog Devices Inc. *EZ-KIT Lite Reference Manual.* Analog Devices Inc., P.O.Box 9106, Norwood, MA 02062-9106, USA, 1997.

[47] Lattice Semiconductor Corp. *ispLSI-1016 In-System Programmable High Density PLD.* Lattice Semiconductor Corp., 5555 Northeast Moore Ct., Hillsboro, Oregon 97124, U.S.A., 1999.

[48] Analog Devices Inc. *LC^2MOS 8-Channel, 12-Bit High Speed Data Acquisition System.* Analog Devices Inc., P.O.Box 9106, Norwood, MA 02062-9106, USA, 1998.

[49] Analog Devices Inc. *Microprocessor compatible 12-bit D/A converter.* Analog Devices Inc., P.O.Box 9106, Norwood, MA 02062-9106, USA, 1994.

[50] L.A. Zadeh. Outline of a new approach to the analysis of complex systems and decision processes. *IEEE Transactions on Systems, Man, and Cybernetics*, Vol. 3(1):28–44, 1974.

[51] E.H. Mamdani and B.R Gaines. *Fuzzy reasoning and its applications.* Academic Press, New York, 1981.

[52] K.M. Passino and S.Yurkovich. *Fuzzy control.* Addison-Wesley., 2725 Sand Hill Road, Menlo Park, California 94025, USA, 1998.

[53] Bart Kosko. *Neural networks and fuzzy systems.* Prentice Hall International, Inc., Englewood Cliffs, N.J. 07632, USA, 1992.

[54] D.Driankov, H. Hellendoorn, and M. Reinfrank. *An introduction to Fuzzy Control.* Springer-Verlag, 1993.

[55] C.J. Harris, C.G. Moore, and M. Brown. *Intelligent control – aspects of fuzzy logic and neural nets.* Singapore: World Scientific, 1993.

[56] Analog Devices Inc. *Quad, 12-Bit DAC Voltage Output with Readback.* Analog Devices Inc., P.O.Box 9106, Norwood, MA 02062-9106, USA, 1996.

[57] Motorola Inc. *Three terminal positive fixed voltage regulators.* Motorola Inc., P.O. Box 20912; Phoenix, Arizona 85036, USA, 1996.

[58] Advanced Micro Devices Inc. *Am29F040B 4 Megabit (512 K x 8-Bit) CMOS 5.0 Volt-only, Uniform Sector Flash Memory.* Advanced Micro Devices, Inc., 1999.

[59] Cirrus Logic Inc. *CS8900A Product Data Sheet.* Cirrus Logic Inc., P.O. Box 17847, Austin, Texas 78760, USA, 1999.

[60] Cirrus Logic Inc. *Crystal LAN CS8900A Ethernet controller Technical reference manual.* Cirrus Logic Inc., P.O. Box 17847, Austin, Texas 78760, USA, 1999.

[61] Lattice Semiconductor Corp. *ispLSI-2032 In-System Programmable High Density PLD.* Lattice Semiconductor Corp., 5555 Northeast Moore Ct., Hillsboro, Oregon 97124, U.S.A., 1999.

[62] Analog Devices Inc. and BittWare Research Systems Inc. *SHARCPAC Module Specification, Rev. 1.2 - 02/22/96.* BittWare Research Systems, Inc., 33 N Main St. Concord, NH 03301, USA, 1996.

[63] Tim Williams. *EMC for product designers.* Oxford:Newnes, UK, 1992.

[64] Tim Williams. *The circuit designer's companion.* Oxford : Butterworth Heinemann, UK, 1991.

[65] IEEE. *IEEE Std 610.12-1990, IEEE Standard Glossary of Software Engineering Terminology.* IEEE, 1990.

[66] University of Southern California Information Sciences Institute. *Internet Protocol, DARPA internet program, protocol specification.* Information Sciences Institute, University of Southern California, 4676 Admiralty Way, Marina del Rey, California 90291, USA, 1981.

[67] University of Southern California Information Sciences Institute. *Transmission Control Protocol, DARPA internet program, protocol specification.* Information Sciences Institute, University of Southern California, 4676 Admiralty Way, Marina del Rey, California 90291, USA, 1981.

[68] Robert M. Metcalfe and David R. Boggs. Ethernet: Distributed packet switching for local computer networks. *Communications of the ACM*, Vol. 19:pp. 395 – 404, 1976.

[69] Analog Devices Inc. *C Tools Manual.* Analog Devices Inc., P.O.Box 9106, Norwood, MA 02062-9106, USA, 1996.

[70] Analog Devices Inc. *C Run Time Library Manual.* Analog Devices Inc., P.O.Box 9106, Norwood, MA 02062-9106, USA, 1996.

[71] Analog Devices Inc. *Assembler tools and Simulator Manual.* Analog Devices Inc., P.O.Box 9106, Norwood, MA 02062-9106, USA, 1996.

[72] G.Zames. Feedback and optimal sensitivity: Model reference transformations, multiplicative seminorms, and approximate inverses. *IEEE Transactions on Automatic Control*, AC-26, 2:pp. 301–320, 1981.

[73] Kemin Zhou with J.Doyle and K. Glover. *Robust and optimal control.* Prentice Hall, New Jersey, USA, 1996.

[74] Bruce A. Francis. *A course in $\mathcal{H}_\infty$ Control Theory.* Springer-Verlag, Berlin, Germany, 1987.

[75] P. Gahinet and P. Apkarian. A linear matrix inequality approach to $\mathcal{H}_\infty$ control. *"Int. Journal of Robust and Nonlinear Control"*, pages pp. 421–448, 1994.

[76] G.Balas J.Doyle K.Glover A.Packard and R.Smith. *μ-Analysis and Synthesis Toolbox.* The MathWorks, Inc., USA, 1998.

[77] J. Eaton. *High-level language for numerical computation.* http://www.che.wisc.edu/octave, 2003.

[78] INRIA and ENPC. *Scientific software package for numerical computation.* http://www-rocq.inria.fr/scilab, 2003.

[79] M. Athans and P. Falb. *Optimal Control. An introduction to the Theory and Its Applications.* McGraw-Hill Book Company, 1966.

[80] A.E. Bryson Jr. and Yu-Chi Ho. *Applied Optimal Control.* Hemisphere Publishing Corporation, 1975.

[81] T.Basar and G.J.Olsder. *Dynamic Noncooperative Game Theory.* Academic Press, 1982.

[82] Y.C. Ho, A.E. Bryson Jr., and S. Baron. Differential games and optimal pursuit-evasion strategies. *"IEEE Transaction on Automatic Control"*, AC-10, 4:pp. 385–389, 1965.

[83] T.Basar and P.Bernhard. *$\mathcal{H}_\infty$ optimal control and Related Minmax design problems, A Dynamic Game Approach.* Birkhauser, 1995.

[84] I. Yaesh and U. Shaked. Game theory approach to finite-time horizon optimal estimation. *"IEEE Transaction on Automatic Control"*, Vol.38, 6:pp. 957–963, 1993.

[85] K.M. Nagpal and P.P. Khargonekar. Filtering and smoothing in an $\mathcal{H}_\infty$ setting. *"IEEE Transaction on Automatic Control"*, Vol.36, 2:pp. 152–166, 1991.

[86] I.Yaesh and U. Shaked. Game theory approach to optimal linear state estimation and its relation to the minimum $\mathcal{H}_\infty$-norm estimation. *"IEEE Transaction on Automatic Control"*, Vol.37, 6:pp. 828–831, 1992.

[87] I.Rhee and J.L. Speyer. A game theoretic approach to a finite-time disturbance attenuation problem. *"IEEE Transaction on Automatic Control"*, Vol.36, 9:pp. 1021–1032, 1991.

[88] J.M. Maciejowski. *Multivariable Feedback Design.* Addison Wesley Longman Lim., Edinburgh Gate, Essex CM20 2JE, England, 1989.

[89] U. Shaked and C.E. de Souza. Continuous-time tracking problem in an $\mathcal{H}_\infty$ setting: A game theory approach. *"IEEE Transaction on Automatic Control"*, Vol.40, 5:pp. 841–852, 1995.

[90] I.Yaesh and U. Shaked. $\mathcal{H}_\infty$-minimum error state estimation of linear stationary processes. *"IEEE Transaction on Automatic Control"*, Vol.35, 5:pp. 554–558, 1990.

[91] D.S. Bernstein and W.M. Haddad. LQG control with an $\mathcal{H}_\infty$ performance bound: A Riccati equation approach. *"IEEE Transaction on Automatic Control"*, AC-13, 5:pp. 496–503, 1968.

[92] J.C. Doyle. Analysis of feedback systems with structured uncertainties. *Proc. Inst. Electr. Eng.*, 129:pp. 242–250, 1982.

[93] A. Packard and J.C. Doyle. The complex structured singular value. *Automatica*, 29:71–109, 1993.

[94] J.C. Doyle. Synthesis of robust controllers and filters. *Proc. IEEE Conf. Decision Contr.*, 1983.

[95] Inc. The MathWorks. *Matlab, the language of technical computing.* The MathWorks, Inc., USA, 1999.

[96] J.L. Merlam. *Engineering Mechanics: Statics and Dynamics.* Chichester Wlley, New York, 1980.

[97] D.C. Youla and J.J. Bongiorno Jr. A feedback theory of two-degree-of-freedom optimal winer-hopf design. *IEEE Transactions on Automatic Control*, vol. AC-30(7):pp. 652–665, 1985.

[98] A.J. van der Schaft. $\mathcal{L}_2$-gain analysis of nonlinear systems and nonlinear state feedback $\mathcal{H}_\infty$ control. *IEEE Transactions on Automatic Control,*, 6:pp. 770–784, 1992.

[99] Jan C. Willems. Dissipative dynamical systems part i: General theory. *Arch. Rational Mech. Anal.,*, 22:pp. 321–351, 1972.

[100] D.Hill and P.Moylan. The stability of nonlinear dissipative systems. *IEEE Transactions on Automatic Control*, pages pp. 708–711, 1976.

[101] A.Isidori and A.Astolfi. Disturbance attenuation and $\mathcal{H}_\infty$-control via measurement feedback in nonlinear systems. *IEEE Transactions on Automatic Control,*, 37:pp. 1283–1293, 1992.

[102] A.Isidori and Wei Kang. $\mathcal{H}_\infty$ control via measurement feedback for general nonlinear systems. *IEEE Transactions on Automatic Control,*, 40:pp. 466–472, 1995.

[103] J.Ball and J.Helton. Viscosity solutions of hamilton-jacobi equations arising in nonlinear $\mathcal{H}_\infty$ control. *Journal of Mathematical Systems, Estimation, and Control,*, 6:pp. 1–22, 1996.

[104] J.Ball, J.Helton, and M.Walker. $\mathcal{H}_\infty$ control for nonlinear systems with output feedback. *IEEE Transactions on Automatic Control,*, 4:pp. 546–559, 1993.

[105] A.Isidori and Wei Kang. $\mathcal{H}_\infty$ control via measurement feedback for general nonlinear systems. *IEEE Transactions on Automatic Control*, vol. 40:pp. 466–472, 1995.

[106] A.Isidori and A.Astolfi. Disturbance attenuation and $\mathcal{H}_\infty$-control via measurement feedback in nonlinear systems. *IEEE Transactions on Automatic Control*, vol. 37:pp. 1283–1293, 1992.

[107] E.G. Al'brekht. On the optimal stabilization of nonlinear systems. *J. Appl. Math. Mech.*, vol. 25:pp. 1254–1266, 1962.

[108] D.L. Lukes. Optimal regulation of nonlinear dynamical systems. *SIAM Journal of Control,*, 7:pp. 75–100, 1969.

[109] P. Tsiotras, M. Corless, and M. Rotea. An $\mathcal{L}_2$ disturbance attenuation solution to the nonlinear benchmark problem. *International Journal of Robust and Nonlinear Control*, vol. 8:pp. 311–330, 1998.

[110] R.K. Mehra and A.E. Bryson Jr. Linear smoothing using measurements containing correlated noise with an application to inertial navigation. *"IEEE Transaction on Automatic Control"*, AC-13, 5:pp. 496–503, 1968.

[111] P. Benner, A.J. Laub, and V. Mehrmann. Benchmarks for the numerical solution of algebraic riccati equations. *IEEE Control Systems Magazine*, vol. 17:pp. 18–28, 1997.

[112] D.J.N.Limebeer, B.D.O.Anderson, P.O. Khargonekar, and M.Green. A game theoretic approach to $\mathcal{H}_\infty$ control for time varying systems. *"SIAM Journal on Control and Optimization"*, Vol.30:pp. 262–283, 1992.

[113] M. Morari and E. Zafiriou. *Robust Process Control.* Printece Hall, 1989.

Appendix H

Journal publications

PERGAMON

Automatica 35 (1999) 1457–1465

www.elsevier.com/locate/automatica

Technical Communique

Model reference adaptive control of a maglev system with stable maximum descent criterion[1]

P.K. Sinha*, A.N. Pechev

Department of Engineering, University of Reading, Whiteknights, P.O. Box-225, Reading, RG6 6AY,:UK

Received 21 August 1998; received in final form 3 February 1999

Abstract

This paper develops a model-reference adaptive controller (MRC) design framework for magnetically suspended vehicles (maglev) using the criterion of stable maximum descent. The adaptation algorithm is constrained to reduce the airgap error between the reference model and the actual system. The explicit relationship between the parameters of the performance criterion (function of the airgap error and its derivative) and the state feedback adaptation rule is derived for a single degree-of-freedom suspension system. Experimental results from a small representative test-rig are presented to illustrate the effectiveness of the proposed non-linear controller in the presence of variations in pay-load (suspended mass), disturbance force and airgap set-point. Hardware aspects of the transputer and DSP-based real-time controller are briefly discussed to highlight some of the practical issues related to digital implementation of the airgap adaptive control law.

Keywords: Magnetic suspension; Maglev; Transportation; Electromagnetic suspension; Adaptive control; Model-reference adaptive control; Real-time control; Transputers; Digital signal processors

1. Introduction

Interest in the development of magnetically levitated (maglev) vehicle technology continues to grow world wide. The environmental, commercial and technological attractiveness of maglev is likely to be enhanced in the new millennium with the completion of the high-speed maglev link between Hamburg and Berlin in Germany (The Economist, 1998). Improvements in materials and control technology (hardware and software) are expected to be important in maglev's evolution. Until recently, the stabilising controllers for the electromagnetic (attraction type) maglev systems have been based on variations of model-based state feedback control laws (Sinha, 1987). This paper presents a new basis for model-reference adaptive controller of a single-degree-of-freedom maglev system based on the theoretical concept developed earlier (Sinha and Hulme, 1983). While expert knowledge of suspension dynamics is still required, by removing the need for a priori knowledge of the non-linear force characteristics of the suspension magnet, the adaptive controller generates a control law capable of providing an acceptable degree of disturbance stability with enhanced stiffness. A full account of the design framework and a selection of transputer and DSP-based experimental results from a single-magnet suspension system are presented in the paper to provide a basis for further work for multi-magnet maglev vehicles.

2. Modelling and design preliminaries

For the electromagnetic suspension (EMS) system shown in Fig. 1a, if the reaction surface (= guideway for moving magnets) is considered to be sufficiently rigid, $z(t)$ may be taken as the absolute position [= airgap or clearance] of the suspended magnet with $\ddot{z}(t)$ being its absolute vertical acceleration at any instance of time t. With these assumptions, the dynamics of the suspension system is described by (Sinha, 1987)

$$\frac{di(t)}{dt} = \left[\frac{i(t)}{z(t)}\right]\frac{dz(t)}{dt} - \frac{R}{\Gamma}i(t)z(t) + \frac{1}{\Gamma}z(t)v(t), \tag{1a}$$

$$m\frac{d^2z(t)}{dt^2} = -\frac{\Gamma}{2}\left[\frac{i(t)}{z(t)}\right]^2 + f_d(t) + mg, \tag{1b}$$

* Corresponding author. E-mail: p.k.sinha@reading.ac.uk.

[1] This paper was not presented at any IFAC meeting. The paper was recommended for publication in revised form by Editor Peter Dorato.

0005-1098/99/$ - see front matter
PII: S0005-1098(99)00040-0

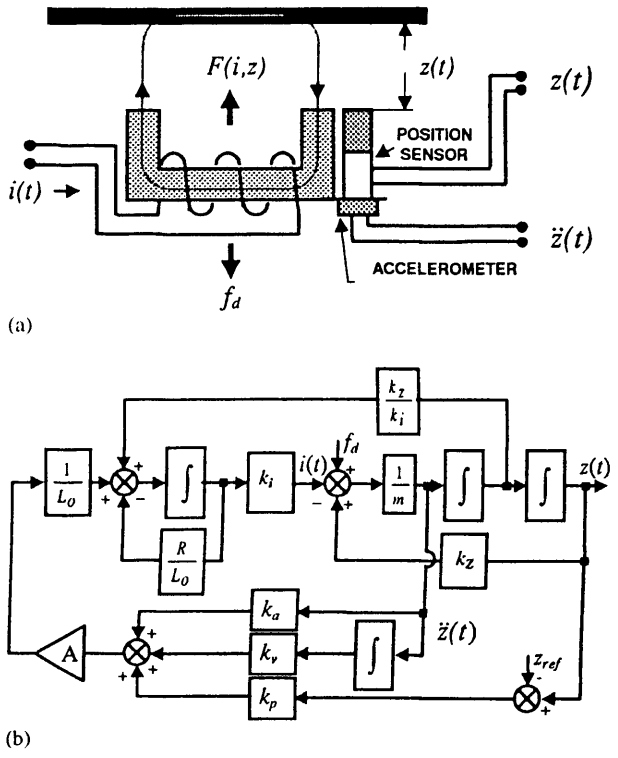

Fig. 1. Maglev system configuration; (a) sensor and guideway locations, (b) linearised model with linear state feedback controller.

where $\Gamma = \mu_0 \bar{n}^2 A_P/2$ is a characteristic feature of the suspension magnet, with $\bar{n}$ as the number of turns in the magnet winding and A_P as the pole face area; R is the total resistance of the electrical circuit (output resistance of the voltage to current amplifier plus the magnet winding resistance), $f_d(t)$ is the vertical disturbance force, mg is the total weight of the suspended object, and $v(t)$ is the input voltage to the magnet amplifier. The now-classical method of designing stabilising controller for the system is based on a small perturbation linear model around a specified nominal operating point (i_0,z_0). The corresponding linear model being described by

$$\frac{d\Delta i(t)}{dt} = \left[\frac{i_0}{z_0}\right]\frac{d\Delta z(t)}{dt} - \left[\frac{R_0}{L_0}\right]\Delta i(t) + \left[\frac{1}{L_0}\right]\Delta v(t), \quad (2a)$$

$$m\frac{d^2\Delta z(t)}{dt} = \left.\frac{\partial F(i,z)}{\partial z}\right|_{(i_0,z_0)}\Delta z(t) - \left.\frac{\partial F(i,z)}{\partial i}\right|_{(i_0,z_0)}\Delta i(t) + \Delta f_d(t)$$

$$= k_z\Delta z(t) - k_i\Delta i(t) + \Delta f_d(t), \quad (2b)$$

where

$$k_z = \Gamma i_0^2/z_0^3;\ k_i = \Gamma i_0/z_0^2;\ L_0 = \Gamma/z_0;\ k_i^2 = k_z L_0,$$

and $mg = \Gamma/2[i_0/z_0]^2$.

Table 1
Parameters of the magnet and the linear state feedback controller for the experimental system used here

Parameter	Value	Parameter	Value
k_z (N/m)	50,000	R (Ω)	7.0
k_i (N/A)	38.0	m (kg)	5.0
z_0 (mm)	5.2	k_p	20,833
L_0 (mH)	33.0	k_v	250.0
i_0 (A)	1.8	k_a	4.0

A wide range of controllers for suspension stability and ride control has been developed using Eq. (2) as the base-line model (Fig. 1b) and a linear state feedback control law of the form in Eq. (3) (Sinha, 1987):

$$\Delta v(t) = k_a\Delta\ddot{z}(t) + k_v\Delta\dot{z}(t) + k_p[z(t) - z_{\text{ref}}]. \quad (3)$$

The key feature in the design of linear controllers is the choice of the nominal operating point (i_0,z_0) such that the parameters k_i, k_z, and L_0 are constant over the whole of the operating ranges of current and airgap (Table 1 gives the key system parameters for the experimental system used here). This is usually achieved by choosing the nominal operating point on the linear part of the magnet's force–current and force–airgap characteristics. Extensive theoretical and experimental maglev results indicate that feedback of at least position and velocity signals are required for stability and damping, and the addition of acceleration feedback (a) yields a stiffer suspension by increasing the range of permissible k_p, (b) extends bandwidth to give greater stability margin, and (c) provides a better basis to control vertical acceleration levels (ride quality) (Sinha, 1987). While the success of the linear controller has been demonstrated through the design and operation of numerous laboratory prototypes and full-scale vehicles, the constraints of small perturbations on the suspension model (constant k_i and k_z) imply that the airgap has to be very tightly controlled with magnets operating on the lower end of their magnetising characteristics ($B - H$ curves), typically with flux densities around 0.5 T and 10–12 mm airgaps, with a corresponding reduction in magnet's lift force to weight ratio. Although a theoretical basis of an adaptive controller concept was developed some years ago (Sinha and Hulme, 1983) to overcome some of these operational constraints, with advances in digital processing devices it is now becoming a realistic engineering proposition to implement real-time adaptation laws for maglev systems.

3. Model following adaptation

The general configuration of the overall control environment is shown in Fig. 2, where the reference model is derived from off-line identification of the closed-loop

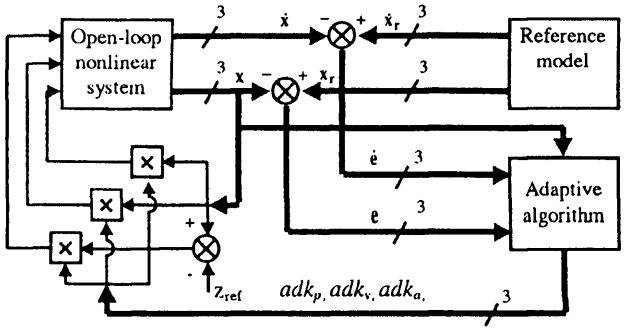

Fig. 2. Configuration of the model-reference controller set-up. Reference model in the experimental results presented here has the structure as shown in Fig. 1b.

suspension system operating at its nominal airgap and current levels. This is considered to be a realistic basis for adaptive control as (a) magnets are designed to offer optimum performance (lift to weight ratio) over a preferred range of airgaps and currents, and (b) the operating airgap (set-point) of the system is normally set at a prescribed value to meet various (somewhat conflicting) requirements, including magnet efficiency, passenger ride comfort, and probability of contact between the moving magnet and the guideway (Sinha, 1987). Furthermore, due to variations introduced during the magnets' manufacturing process and system component tolerances, analytical modelling of a magnet is likely to have limited scope. In contrast, implementation of a fully automated identification of the system while suspended at its nominal airgap with rated payload may be treated as a routine operation within the manufacturing/assembly process.

Using standard notations and terminology (Sinha, 1984), the airgap error dynamics of the system may be expressed by an nth-order state equation of the form (Sinha and Humle, 1983)

$$\begin{aligned}\dot{\mathbf{e}}(t) &= \dot{\mathbf{x}}_r(t) - \dot{\mathbf{x}}_p(t) = [\mathbf{A}_r\mathbf{x}_r(t) + \mathbf{b}_r v(t) + \mathbf{d}_r(t)] \\ &\quad - [\mathbf{A}_p\mathbf{x}_p(t) + \mathbf{b}_p v(t) + \mathbf{d}_p(t)] \\ &= \mathbf{A}_r\mathbf{e}(t) + \mathbf{G}\mathbf{x}_p(t) + \mathbf{d}(t),\end{aligned}$$

where

$$\mathbf{G} = \mathbf{A}_r - \mathbf{A}_p, \quad \mathbf{d}(t) = \mathbf{d}_r(t) - \mathbf{d}_p(t),$$

$$\mathbf{e}(t) = \mathbf{x}_r(t) - \mathbf{x}_p(t). \tag{4}$$

The state variables are defined as: $[x_1, x_2, x_3]^T = [z(t), \dot{z}(t), \ddot{z}(t)]^T$ with appropriate subscript **p** for process (actual system) and **r** for reference model, respectively. For notational convenience, the subscript **p** is dropped in subsequent derivations. The disturbance term $\mathbf{d}_r(t)$ in the reference model may be removed in a first analysis without any loss of generality. In the conventional scheme of adaptation, the control law is usually derived by asymptotic stability assumption of the reduced unforced system

$$\dot{\mathbf{e}}(t) = \mathbf{A}_r\mathbf{e}(t)$$

by using a Lyapunov function of the form $\mathbf{V}(\mathbf{e},t) = \mathbf{e}^T(t)\mathbf{P}\mathbf{e}(t)$ with **P** chosen by solving $\mathbf{A}_r\mathbf{P} + \mathbf{P}\mathbf{A}_r = -\mathbf{Q}$, **Q** typically being taken to be an identity matrix of appropriate dimension. The associated design stages are well established in adaptive control theory, e.g. for pole placement (Sinha, 1984; Porter, 1969). While there is some flexibility in the choice of the performance function for this form of adaptive control, for maglev system the state error as well as its derivative need to be included to exert a greater degree of control over stability and damping of the overall closed-loop system. In an earlier theoretical work, a performance criterion of the type $J(\mathbf{e},t) = \| \mathbf{E}_1\mathbf{e}(t) + \mathbf{E}_2\dot{\mathbf{e}}(t)\|^2$ was used to develop a conceptual framework for state feedback adaptation (Sinha and Humle, 1983). While this was successfully applied to simulation models, more recent work, with emphasis on experimental implementation, indicates that a choice of cost function of the form (**P** and **Q** being n-square matrices):

$$J(\mathbf{e}) = \mathbf{e}^T\mathbf{P}\mathbf{e} + \dot{\mathbf{e}}^T\mathbf{Q}\dot{\mathbf{e}}, \quad \text{notation } t \text{ for time is dropped for convenience} \tag{5}$$

offers significant improvement in transient response. In addition, as the airgap error and vertical velocity have dominant effects on stiffness and suspension stability, such a criterion offers a flexible framework for the choice of the controller parameters (Gottzein and Lange, 1975; Jayawant and Sinha, 1977).

4. Method of stable maximum descent

If α is an arbitrary parameter in **A** (which is to be controlled), then for a given performance criterion $J(..)$, the conventional method of steepest descent rule to adjust α is given by (Sinha, 1984)

$$\frac{d\alpha}{dt} = -c\frac{\partial J(\mathbf{e})}{\partial \alpha}, \quad c > 0.$$

However, a more detailed analysis of the concept of maximum descent indicates that a more effective version of the above adaptation rule is to use maximum stable descent giving (Sinha and Humle, 1983; Sinha, 1984; Donaldson, 1961)

$$\frac{d\alpha}{dt} = +\gamma\frac{\partial J(\mathbf{e})}{\partial \alpha}, \quad \gamma > 0, \tag{6}$$

where $\mathbf{A} = \{a(\alpha)\}_{i,j}$ with α being the parameter to be adapted in any (i,j) element of **A**. The dynamic adjustment of α relies on the sensitivity of J to the elements of **A** (Donaldson, 1961). Similarly the adjustment for the

parameter δ in disturbance $\mathbf{d}(t)$ may be derived as (Sinha and Humle, 1983)

$$\frac{\mathrm{d}\delta}{\mathrm{d}t} = +\beta\frac{\partial J(\mathbf{e})}{\partial\delta}, \quad \beta > 0. \tag{7}$$

In general, for any n-error vector, the first derivative of the performance criterion in Eq. (5) with respect to the controller parameters α is

$$\frac{\partial J(\mathbf{e})}{\partial\alpha} = \frac{\partial(\mathbf{e}^{\mathrm{T}}\mathbf{P}\mathbf{e} + \dot{\mathbf{e}}^{\mathrm{T}}\mathbf{Q}\dot{\mathbf{e}})}{\partial\alpha} = \mathbf{e}^{\mathrm{T}}\mathbf{M}\frac{\partial\mathbf{e}}{\partial\alpha} + \dot{\mathbf{e}}^{\mathrm{T}}\mathbf{N}\frac{\partial\dot{\mathbf{e}}}{\partial\alpha}, \tag{8a}$$

where $\mathbf{P}$, $\mathbf{Q}$, $\mathbf{M}$, $\mathbf{N}$ are n-square matrixes related by $\mathbf{M} = \mathbf{P} + \mathbf{P}^{\mathrm{T}}$ and $\mathbf{N} = \mathbf{Q} + \mathbf{Q}^{\mathrm{T}}$. Combination of Eqs. (4), (8a) and (8b) gives

$$\begin{aligned}\frac{\partial J(\mathbf{e})}{\partial\alpha} &= \mathbf{e}^{\mathrm{T}}\mathbf{M}\frac{\partial\mathbf{e}}{\partial\alpha} + \dot{\mathbf{e}}^{\mathrm{T}}\mathbf{N}\left(\mathbf{A}_{\mathrm{r}}\frac{\partial\mathbf{e}}{\partial\alpha} + \frac{\partial\mathbf{G}}{\partial\alpha}\mathbf{x}\right)\\ &= \mathbf{e}^{\mathrm{T}}\mathbf{M}\frac{\partial\mathbf{e}}{\partial\alpha} + \dot{\mathbf{e}}^{\mathrm{T}}\mathbf{N}\mathbf{A}_{\mathrm{r}}\frac{\partial\mathbf{e}}{\partial\alpha} + \dot{\mathbf{e}}^{\mathrm{T}}\mathbf{N}\frac{\partial\mathbf{G}}{\partial\alpha}\mathbf{x}.\end{aligned} \tag{8b}$$

By choosing $\mathbf{M}$ and $\mathbf{N}$ in the form $\mathbf{M} = \mathbf{W}\dot{\mathbf{e}}\mathbf{I}_{\mathrm{r}}\mathbf{A}_{\mathrm{r}}$ and $\mathbf{N} = -\mathbf{W}\mathbf{e}\mathbf{I}_{\mathrm{r}}$, the gradient optimisation equation becomes

$$\frac{\mathrm{d}\alpha}{\mathrm{d}t} = \gamma\frac{\partial J(\mathbf{e})}{\partial\alpha} = -\gamma\dot{\mathbf{e}}^{\mathrm{T}}\mathbf{W}\mathbf{e}\mathbf{I}_{\mathrm{r}}\frac{\partial\mathbf{G}}{\partial\alpha}\mathbf{x}, \tag{9a}$$

where $\mathbf{I}_{\mathrm{r}} = [1\,1\,1]$ and $\mathbf{W}$ is a diagonal normalisation matrix (chosen to make $\mathbf{N}$ symmetric). $\mathbf{W}$ is derived from the maximum amplitudes of the errors in the adaptation channels. For the single-degree-of-freedom suspension system, α assumes three adaptive gains adk_p, adk_v, and adk_a, and $\mathbf{W}$ (with an additional scaling parameter w) being given by

$$\mathbf{W} = \begin{bmatrix} w\dfrac{1}{\max(e_1)} & 0 & 0 \\ 0 & w\dfrac{\max(e_1)}{\max(e_2)} & 0 \\ 0 & 0 & w\dfrac{\max(e_1)}{\max(e_3)} \end{bmatrix}. \tag{9b}$$

Substitution of the values of $\mathbf{G}$ from Eq. (4) and its partial derivatives with respect to the three feedback gains k_p, k_v, and k_a in Eqs. (9a) and (9b) generates the following three first-order differential equations for adaptive feedback gains:

$$\begin{aligned}\frac{\mathrm{d}}{\mathrm{d}t}(adk_p) &= -\gamma\dot{\mathbf{e}}^{\mathrm{T}}\mathbf{W}\mathbf{e}\frac{g_p}{L_o}x_1,\\ \frac{\mathrm{d}}{\mathrm{d}t}(adk_v) &= -\gamma\dot{\mathbf{e}}^{\mathrm{T}}\mathbf{W}\mathbf{e}\frac{g_v}{L_o}x_2,\\ \frac{\mathrm{d}}{\mathrm{d}t}(adk_a) &= -\gamma\dot{\mathbf{e}}^{\mathrm{T}}\mathbf{W}\mathbf{e}\left(\frac{g_a k_z}{mL_o}x_1 - \frac{g_a k_i}{mL_o}x_3\right),\end{aligned} \tag{10}$$

where g_p, g_v and g_a are the gains of the corresponding sensors (voltage/physical unit). Integration of Eq. (10), with the initial values set at their respective linear state feedback gains, produces the adaptive gains required to minimise the performance criterion in Eq. (5).

5. Hardware set-up

To implement the control laws derived above, a 5 kg one-degree-of-freedom suspension system, schematically shown in Fig. 1a was set up. Operational details of the control components are given in Sinha (1987) and Sinha and Jayawant (1979). Initially the adaptation algorithm in Eq. (10) was implemented on a network of three transputers (Fig. 3a), this has now been ported on to Analog Devices' SHARC digital signal processor using a proprietary interface and control board within a PC/Windows environment (Fig. 3b). In the transputer hardware, data transfer amongst the three networked transputers is performed by Inmos serial links at 20 Mb/s (Sinha and McLagam, 1993). The data transfer loading between the interface processor (T-225) and other two processors, and the execution times for the various tasks on all three processors were such that the adaptation control required a sampling time ranging from 370 to 430 μs (400 μs was observed to be an average value). Because of the periodic time sharing between high and low priority tasks within any given transputer, execution time is likely to vary, depending on the overall loading of the individual transputers (processors) in a network. This, along with the event-driven nature of data transfer architecture of the transputer (rather than interrupt sources as in DSPs), creates variations between two consecutive sampling intervals. The proprietary DSP hardware consists of one 32-bit AD21061-40MHz processor communicating with interface components memory mapped on the processor's address space. There are three main tasks in the implementation of the adaptive algorithm in Fig. 2: data acquisition and low-level processing to read the position and acceleration signals, solution of a set of three first-order differential equations to generate three reference model state variables, and the derivation of three adaptive state feedback gains. The last task includes the derivation of the two error vectors [$\mathbf{e}(t)$ and $\dot{\mathbf{e}}(t)$], composition of the adaptive rules as per Eq. (10) with user specified values of w and γ, and the multiplication of the three feedback signals with their adaptive gains (Fig. 2).

6. Experimental results

From operational viewpoints, a maglev system should ideally possess infinite suspension stiffness, that is the airgap error should be zero for any changes in operating

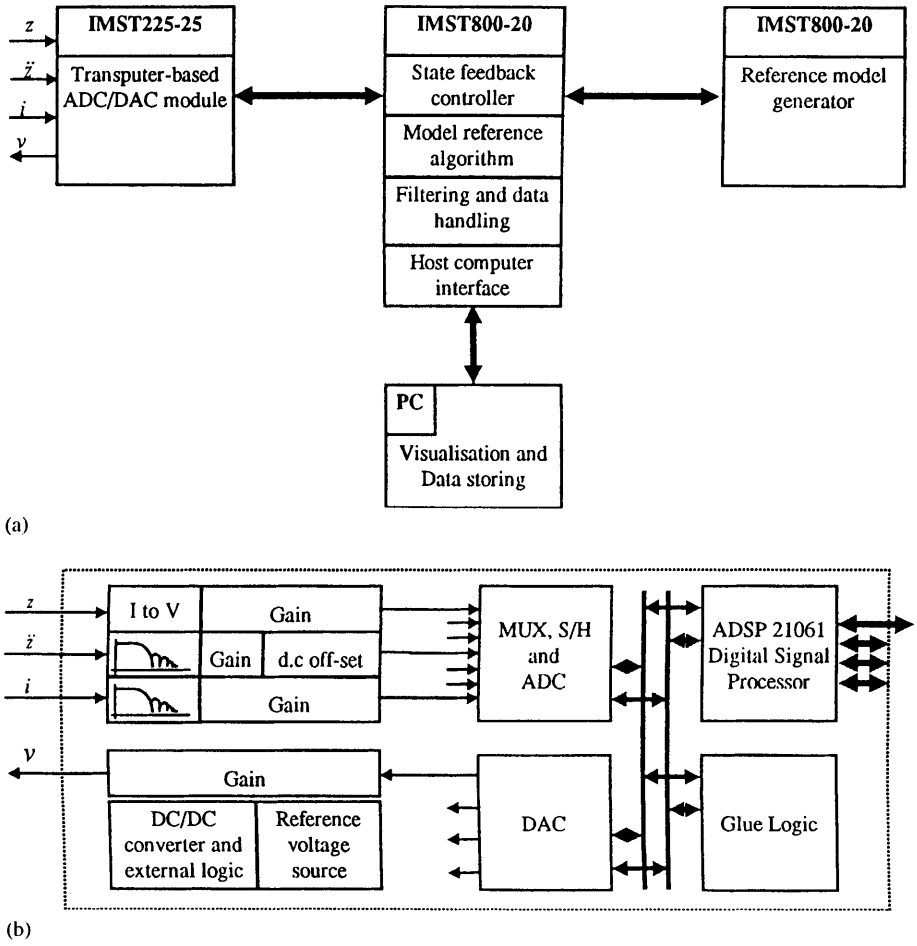

Fig. 3. Transputer and DSP-based system configurations. (a) Task distribution for transputer implementation of Fig. 2. The transputer hardware employed here forms part of a 100 kg multimagnet test vehicle designed and built in 1988 (Sinha and McLagan, 1993). (b) Interface details for the proprietary DSP board. This hardware is now being extended to work with networked DSP devices for adaptive control of multimagnet vehicles.

conditions or any external disturbance. For example, a change in suspended mass will induce a change in the model, consequently with a non-adaptive controller the steady-state error in airgap will change from its nominal design value. Although a maglev system is designed with a rated suspended mass at the nominal operating point, changes in passenger loading (in full-scale vehicles) are to be expected. Any significant change in suspension stiffness will be manifested in the form of a changed airgap (above or below the set-point), with the possibility that the suspension magnet may be moved from its ideal linear design range to the non-linear parts of its magnetising curve. The effectiveness of the proposed adaptive controller in reducing the static position error, and hence significantly improved suspension stiffness, is highlighted by the responses due to step input of mass in Fig. 4.

Disturbance force acting in line with the suspension axis adds an additional input to the system; this in turn will change the operating airgap according to the dynamics within the open-loop system in Fig. 1a. In linear controllers, the state feedback gains are chosen to assure stability with a notional force disturbance at the expense of a change in steady-state error in the airgap. Another factor that has a destabilising effect on the suspension system is the reduction in suspension (lift) force due to eddy-current effects of a moving magnet. This reduction in lift force has been found to be somewhere between a linear and an exponential form with much of the reduction being in the range 10–50 m/s, depending on magnet and guideway geometry (Sinha, 1987). Although this reduction in effective lift force is taken into account in the design process, a precise a priori description of the linear velocity profile is not available. The adaptive controller again was able to return the airgap to its nominal value for step changes in disturbance force as shown in Fig. 5. As indicated earlier with its enhanced processing power (80 MFLOPS as opposed to 4.3 MFLOPS for the transputer), the SHARC-DSP was able to run with a much lower sampling interval. For comparison,

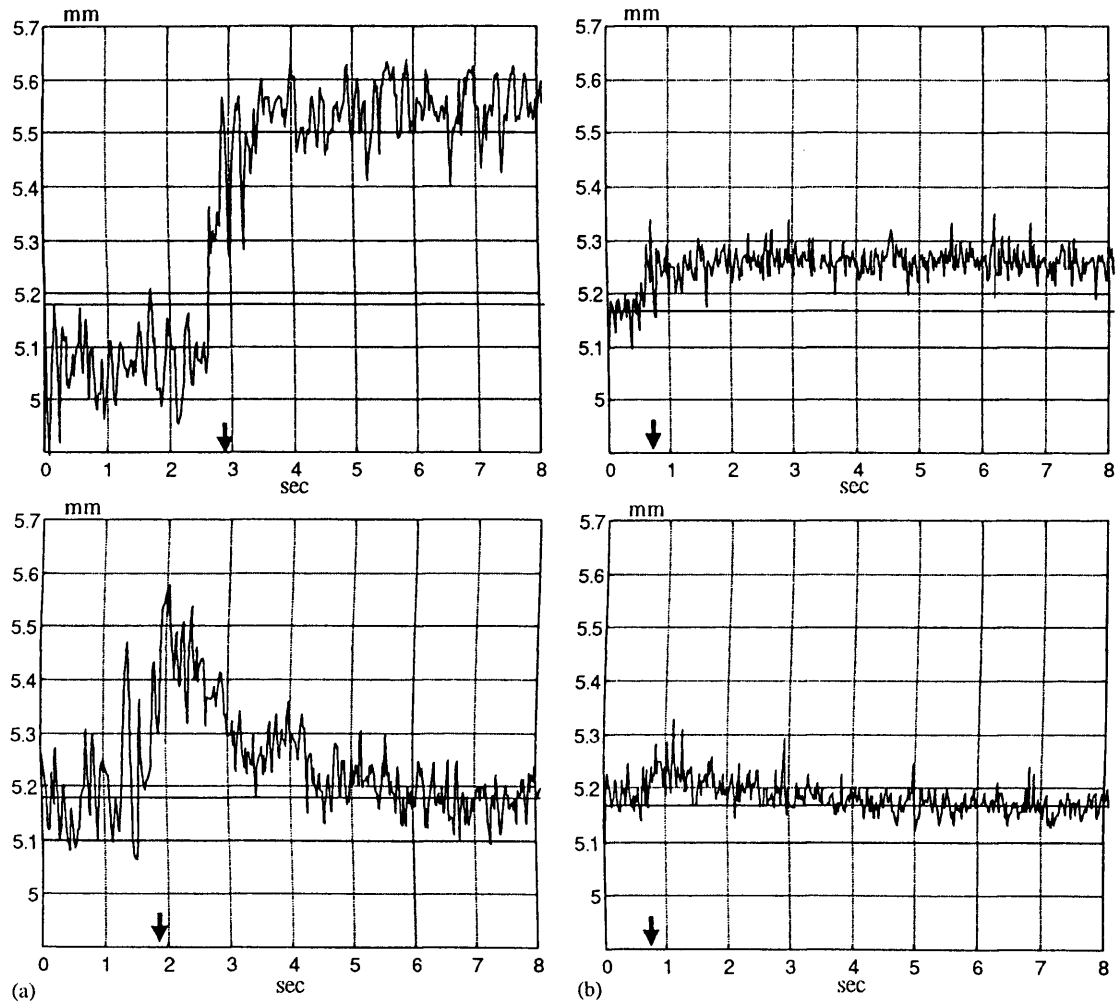

Fig. 4. Transient responses of airgap due to a step change of 5 kg mass (100% mass change) with 400 μs sampling time (nominal operating point set at 5.2 mm and 1.8 A). (a) Transputer-based system. Top: non-adaptive system (linear state feedback control law). Bottom: adaptive system. (b) DSP-based system. Top: non-adaptive system. Bottom: adaptive system.

responses from the transputer-based and DSP-based controllers are included; the DSP system being capable of producing improved transient response at a half the sampling time with twice the disturbance input (Fig. 5b, bottom).

Thus, while the set-point for the airgap in a maglev system is not changed during a particular run, pay-load and force disturbances or linear motion are likely to change the actual airgap which in some cases may drive the magnets away from their nominal operating points. These highlight the desirability of an adaptive airgap control law rather than a linear controller; the latter being only able to compensate for operational changes and disturbances by adjusting the steady-state error in airgap.

Several comments regarding the choice of the design parameters are in order. The three elements in **W** correspond to the scaling factors for the widely differing sensor signals to bring Eq. (10) to within a uniform range. In the experimental results presented here, normalisation was performed with reference to the airgap signal. Any of the other two signals may be used, but the choice of airgap is preferred as the amplitude of the feedback gain in this channel has the highest numerical value (in the order of 20,000). The weight w offered a further choice in scaling; it was chosen to be unity in all responses presented here. The scalar parameter γ is then chosen to control the integration rate: smaller value corresponding to slower adaptation and larger value faster adaptation without reaching the saturation limits associated with the DAC. Although the values of γ and the elements of **W** collectively ensure that the three adaptive gains remain within the bounds of the interface hardware, use of two param eters provides some additional flexibility in the selection of the initial feedback gains. While the elements of **W** are related to the calibration parameters of the sensors and

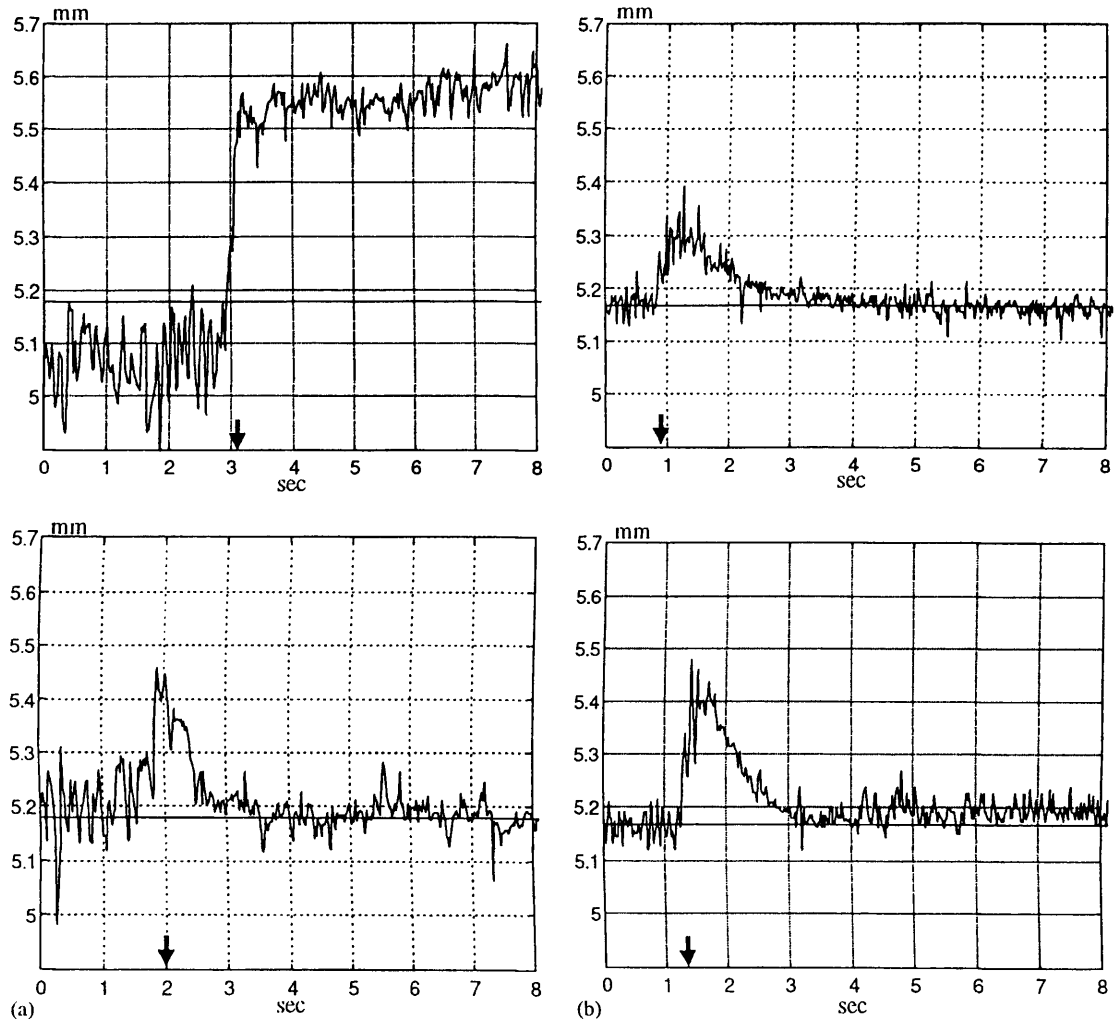

Fig. 5. Transient responses of airgap due to a step change of force (nominal operating point as in Fig. 4). (a) 50 N step force disturbance, transputer-based controller with 400 μs sampling time. Top: linear state feedback controller (non-adaptive), bottom: adaptive controller. (b) DSP-based adaptive controller. Top: adaptation with 400 μs sampling time for 50 N step force disturbance. Bottom: adaptation with 200 μs sampling time for 100 N step force disturbance.

hence not adjustable, the value of γ may be set at the design stage to control adaptation rate. This is demonstrated in Fig. 6 for step disturbances of mass and force with the DSP-based controller.

7. Concluding comments

Numerous studies related to the stability of model-reference adaptive systems have been undertaken in the late 1960s and throughout the 1970s. Since convergence of the augmented error vector in Eq. (4) is the basis for the derivation of the adaptation algorithm, a necessary condition for closed-loop stability is satisfied (Narendra and Valavrin, 1978). In addition, by suitable choice of the design parameters, boundedness of the three adaptive gains may be assured, leading to stability on a piecewise linear basis. As the adaptation algorithm gets implemented, the three state feedback gains in the adaptive loop move from their nominal (initial) values towards their new values to drive (asymptotically) all three elements in the error vector to zero. Since suspension dynamics is driven by force balance [Eq. 1(b)], the vertical acceleration signal is most sensitive to external disturbances. For this reason, the acceleration feedback gain (adk_a) has been observed to be most responsive during adaptation, typically changing from 25% to as much as 250% of its initial value during experiments which produced Fig. 6. The other two gains have been relatively less responsive; adk_v remaining within $\pm$ 25% of its initial value, and adk_p varying by only around $\pm$ 5%. This boundedness of the three adaptive gains provides an experimental verification for the asymptotic stability of the overall system. Further work to derive

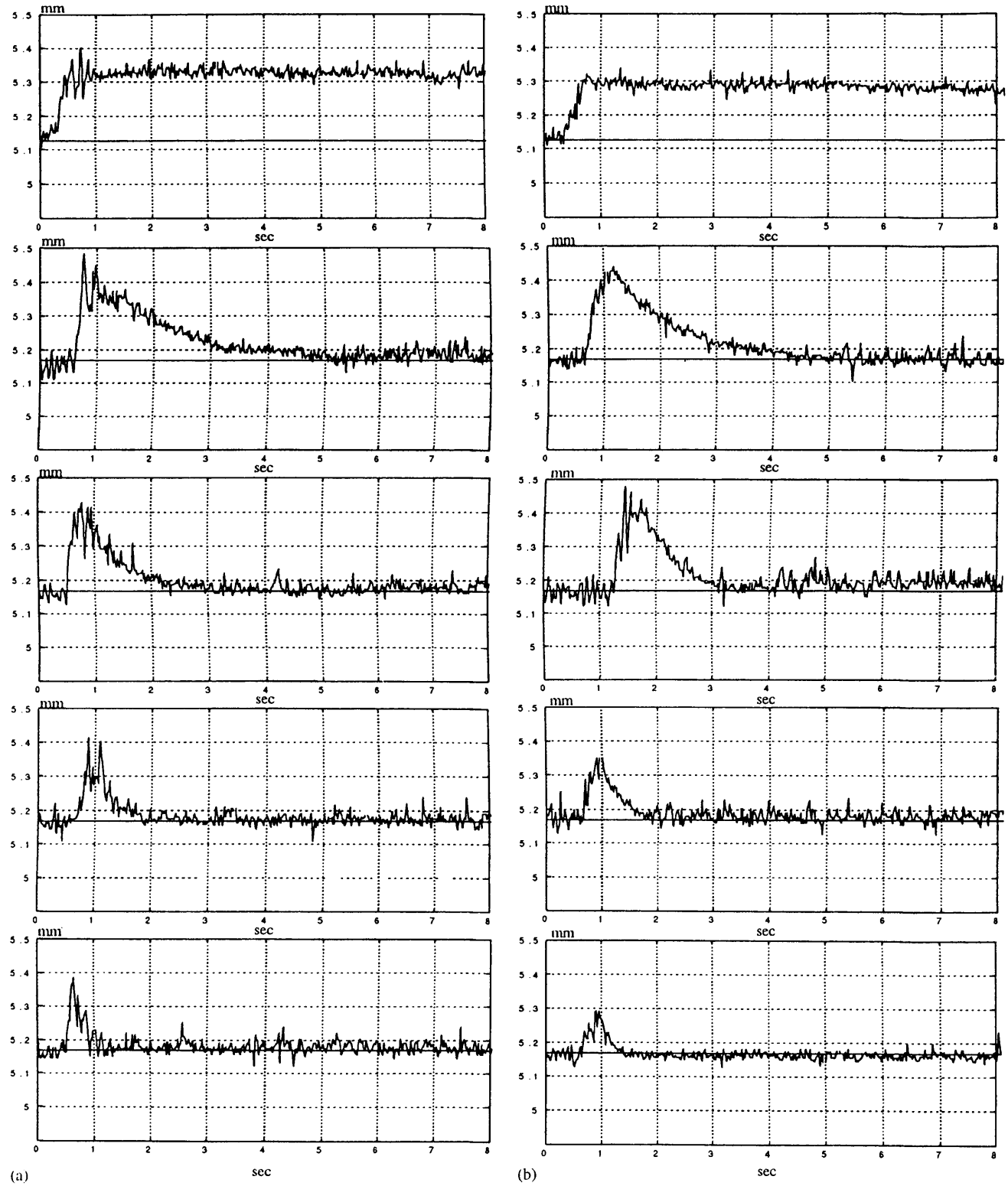

Fig. 6. Transient responses of airgap with DSP-based controller for four different values of γ. Top: state feedback controller without any adaptation, then top-down adaptive loop where the values of γ are: 19.25, 38.5, 77.0 and 144.0. Nominal operating parameters are as in Fig. 4. (a) Step change of 10 kg mass and (b) step change of 100 N force. Sampling time was set at 200 μs for all experiments.

an analytical framework for stability assessment with non-linear force–distance–current characteristics is in progress.

Several factors may influence the choice of the reference model, including the range of airgap to be adapted. Such a requirement, while appearing to be contradictory

to the very concept of adaptation, is essential as the amount of energy available for adaptation is physically limited by the magnet lift force rating, available power supply (forcing voltage and current rating (Sinha, 1987)) and the bandwidth of the control signal. In the experimental results presented above, the reference model corresponds to the suspended mass of 5 kg with a 10 cm laminated U-core magnet; the operating airgap was set at 5.2 mm requiring a current of around 1.8 (Sinha, 1987). These values and their corresponding linear state feedback gains have been used here to set the reference model (Table 1). Consequently, the adaptation rule brings the airgap of the suspended magnet to that of the reference model for any variations in the operating conditions as shown in Figs. 4–6. Such adaptation in airgap is achieved by varying the magnet current along the non-linear force–airgap characteristics of the magnet. Thus, in conceptual form, the algorithm is capable of maintaining adaptation as long as the power amplifier is able to generate the required current within the practical operating constraints (saturation limits of sensors and magnetic flux as well as the thermal limits of the magnet and its windings). Several modifications in the choice of the reference model may be made. For example, a non-linear model or a family of pre-stored linear models may be used to provide a particular ride quality or stability properties, subject to the condition that the integration interval within the reference model is compatible with the sampling time of the adaptation routine. Some of the practical aspects of these are being investigated and a mechanism to relate the airgap adaptation algorithm in Eq. (10) to real-time parameter estimation of the suspended system (e.g. attraction force and suspended mass) is being formulated.

References

The Economist (London) (1998). The new age of the train: A better way to fly (pp. 23–25).

Sinha, P. K. (1987). *Electromagnetic suspension: Dynamics and control.* London: IEE. ISBN-0-86341-063-4.

Sinha, P. K., & Hulme, A. J. (1983). Simulation and control of a non-linear electromagnetic suspension system. In: J. Burger, & Y. Jarny (Eds.), *Simulation in engineering sciences.* Amsterdam: Elsevier (pp. 257–262).

Sinha, P. K. (1984). *Multivariable control: An introduction.* New York: Marcel Dekker.

Porter, B. (1969). *Synthesis of dynamical systems.* London; Thomas Nelson.

Gottzein, E., & Lange, B. (1975). Magnetic suspension control system for the MBB high-speed train, *Automatica, 11*, 271–284.

Jayawant, B. V., & Sinha, P. K. (1977). Low-speed vehicle dynamics and ride quality using controlled d.c. electromagnets. *ibid, 13*, 605–610.

Donaldson, D. D. (1961). *The theory and stability of a model referenced parameter tracking technique for automatic control systems.* Ph.D Thesis, University of California.

Sinha, P. K., & Jayawant, B. V. (1979). Analytical and design aspects of magnetically suspended vehicles. *Automatica, 15*. 539–552.

Sinha, P. K., & McLagan, N. S. (1993). Transputer control of nonlinear multivariable systems. In: R. Grebe, J. Hektor, S. C. Hinton, M. R. Jane, & P. H. Welch (Eds.), *Transputer applications and systems* (pp. 169–182). Amsterdam; IOS Press.

Narendra, K. S., & Valavani, L. S. (1978). Stable adaptive controller design-direct control, *IEEE Transactions of Automatic Control, AC-23*, 570–583.

Technical Notes and Correspondence

Nonlinear H_∞ Controllers for Electromagnetic Suspension Systems

P. K. Sinha and A. N. Pechev

***Abstract*—This note presents a unified framework to derive nonlinear H_∞ state and output feedback controllers for magnetically levitated (Maglev) vehicles with controlled dc electromagnets, referred to as electromagnetic suspension systems. The theoretical exposition, based on the Taylor series expansion solution to the Hamilton–Jacobi–Isaacs inequality, is followed by an assessment of some of the practical issues in realizing the nonlinear controllers with a digital signal processor and embedded hardware. A select set of experimental results from a single-degree-of-freedom suspension system is included to highlight the effectiveness of the proposed nonlinear state- and output-feedback H_∞ controllers to suppress guideway-induced disturbances.**

***Index Terms*—H_∞ controllers, digital signal processors, electromagnetic suspension systems, embedded control, Maglev, magnetic levitation, nonlinear systems.**

I. Introduction

With the construction of the Shanghai city-Pudon international airport link in the Peoples Republic of China and the Hamburg–Berlin intercity route in Germany, magnetic levitation (Maglev) using electromagnetic suspension technology has come of age [1], [2]. The electromagnetic suspension (EMS) provides noncontacting suspension by means of dc electromagnets in conjunction with a position regulator using position (= airgap), velocity and acceleration feedback. Linear control theories have provided much of the benchmark design procedures for numerous full-scale vehicles in large test facilities [3]. However, due to constraints of linearization, the resulting time- and frequency-domain controllers have restricted capability to cope with significant changes in the suspended load (payload and disturbance force) or large variations in the guideway profile. An adaptive controller to compensate for payload variations and external force disturbances has been presented earlier [4]. This note develops a unified account for the derivation of nonlinear H_∞ state and output feedback controllers to attenuate the effects of guideway-induced oscillations on suspension stability of the EMS system.

II. Nonlinear Model of the EMS System

A schematic of a single-degree-of-freedom suspension system with a controlled dc electromagnet is shown in Fig. 1. The vehicle module, with its suspension magnet and payload (total mass m), travels under the fixed reaction surface (track or guideway); the linear propulsion motor is not shown in this illustration. Using the notations given in Fig. 1, the vertical dynamics is described by [3]

$$\begin{aligned} m\frac{d^2z(t)}{dt^2} &= -F(i,z,t)+f_d+mg \\ &= -\frac{\mu_0 N^2 a_m}{4}\left[\frac{i(t)}{z(t)}\right]^2+f_d+mg \\ \frac{di(t)}{dt} &= \frac{i(t)}{z(t)}\frac{dz(t)}{dt}-\frac{2}{\mu_0 N^2 a_m}z(t)(\mathrm{R}_m i(t)-u(t)). \end{aligned} \tag{1}$$

Defining a state vector $x(t)=[z(t)\quad \dot{z}(t)\quad i(t)]^T\in\Re^n$, $n=3$ and an external disturbance vector $w(t)=[w_1(t)\quad w_2(t)]^T,\in\Re^l$, $l=2$, (1) yields the following nonlinear state-space model of the open-loop suspension system:

$$\begin{aligned} \begin{bmatrix}\dot{x}_1(t)\\ \dot{x}_2(t)\\ \dot{x}_3(t)\end{bmatrix} &= \begin{bmatrix} x_2(t) \\ -\left(\frac{\mu_0 N^2 a_m}{4m}\right)\left[\frac{x_3(t)}{x_1(t)}\right]^2 \\ \frac{-2\mathrm{R}_m}{\mu_0 N^2 a_m}x_1(t)x_3(t)+\frac{x_2(t)x_3(t)}{x_1(t)}\end{bmatrix} \\ &\quad+\begin{bmatrix}0 & 0\\ \frac{1}{m}\alpha_1 & 0\\ 0 & 0\end{bmatrix}\begin{bmatrix}w_1(t)\\ w_2(t)\end{bmatrix}+\begin{bmatrix}0\\ 0\\ \frac{2}{\mu_0 N^2 a_m}x_1(t)\end{bmatrix}u(t) \\ \dot{x}(t) &= A(x(t))+B_1(x(t))w(t)+B_2(x(t))u(t) \end{aligned} \tag{2a}$$

$$\begin{aligned} y(t) &= [1\quad 0\quad 0]\begin{bmatrix}x_1(t)\\ x_2(t)\\ x_3(t)\end{bmatrix}+[0\quad \alpha_2]\begin{bmatrix}w_1(t)\\ w_2(t)\end{bmatrix} \\ &= C_2x(t)+D_{21}w(t) \end{aligned} \tag{2b}$$

with α_1 and α_2 as gains of the two disturbance inputs: $w_1(t)$ [= force disturbance, f_d] and $w_2(t)$ [= track or guide way disturbance, $z_{\mathrm{track}}(t)$]. While a predefined stability margin around a nominal operating point (i_0, z_0) is readily provided by a linear state feedback control law of the form (z_{ref} = reference airgap)

$$u(t)=k_p\{x_1(t)-z_{\mathrm{ref}}\}+k_v x_2(t)+k_a x_3(t) \tag{3}$$

where k_p influences the steady-state error and hence stiffness, k_v controls suspension damping and k_a overall stability margin, linear controllers have limited ability to suppress guideway-induced disturbances. The track oscillating mechanism in the experimental rig shown in Fig. 1 has specifically been added to emulate vertical movement of the guideway as the vehicle travels along. The analytical derivations presented in this note demonstrate that the H_∞ control methodology offers a convenient design framework to deal with the effects of such external disturbances with respect to a user-defined penalty vector $q(t)\in\Re^{n+1}$ (Fig. 2)

$$\begin{aligned} q(t) &= \begin{bmatrix}q_1\\ q_2\\ q_3\\ q_4\end{bmatrix}=\begin{bmatrix}\beta_1 & 0 & 0\\ 0 & \beta_2 & 0\\ 0 & 0 & \beta_3\\ 0 & 0 & 0\end{bmatrix}\begin{bmatrix}x_1\\ x_2\\ x_3\end{bmatrix}+\begin{bmatrix}0\\ 0\\ 0\\ W_u\end{bmatrix}u \\ &= C_1x+D_{12}u \end{aligned} \tag{4}$$

where W_u is a weight on the control signal and $C_1\in\Re^{(n+1)\times n}$ is a scaling matrix chosen to define the relative influence of the state variable in the construction of the penalty vector. The objective of the non-

Manuscript received April 18, 2002; revised December 16, 2002. Recommended by Associate Editor K. M. Grigoriadis. Equipment and software support from Analog Devices and financial support from Jupelier Technology during this basic research project are gratefully acknowledged.

P. K. Sinha is with the Department of Engineering, The University of Reading, Reading RG6 6AY, U.K. (e-mail: p.k.sinha@rdg.ac.uk).

A. N. Pechev is with the Cardiff School of Engineering, Cardiff University, Cardiff CF24 0YF, U.K.

Digital Object Identifier 10.1109/TAC.2003.822865

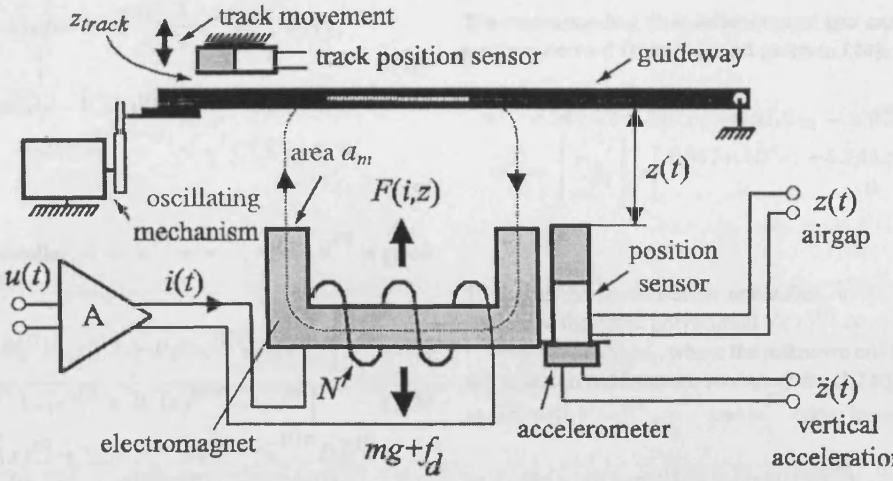

Fig. 1. Magnet-guideway configuration of the experimental system used in this note. Guideway disturbance is introduced by the oscillating mechanism on the top left corner. Notations: m = mass; f_d = force disturbance; g = gravitational acceleration; N = number of turns in the magnet winding; a_m = magnet pole face area; R_m = magnet winding resistance.

linear design procedure developed here is to identify a class of feedback controllers that satisfies the $\mathcal{L}_2$-gain inequality [5]

$$\int_0^T \|q(t)\|^2 dt \le \gamma^2 \int_0^T \|w(t)\|^2 dt, \qquad 0 \le \gamma \le 1 \tag{5}$$

by keeping the energy of the penalty vector $q(t)$ bounded and smaller than the energy of the disturbance input $w(t)$. Because of this bounded energy notion, the concepts of *dissipativity* and *storage function* [6], [7] are adopted here. It has been established that the equilibrium point of a dissipative dynamical system is stable if for $x(t)|_{t=0} = 0$, there exists a nonnegative smooth storage function $V(x(t))$ that satisfies the Hamilton–Jacobi–Isaacs (HJI) inequality [8], [9]

$$V_x(x)^T [A(x) + B_1(x)w + B_2(x)u] + [C_1 x + D_{12}u]^T [C_1 x + D_{12}u] - \gamma^2 w^T w \le 0 \tag{6}$$

(where $V_x(x) = \partial V(x(t))/\partial x(t)$; for notational simplicity, time (t) is dropped in subsequent derivations). In subsequent derivations, the whole left-hand side of the HJI inequality is denoted as the Hamiltonian function $H[x, V_x(x), w, u]$. The premise of the proposed algorithm is that any feedback control law that satisfies the HJI inequality will yield a stable closed-loop system; i.e., the closed-loop system is locally dissipative with respect to its supply rate. As local dissipativity also implies the existence of storage function, the H_∞ design in this context may be recast as the problem of deriving a class of control laws and their corresponding storage functions which satisfy (6)

III. Nonlinear H_∞ State Feedback

The general configuration of the closed-loop system is shown in Fig. 2, where the unknown disturbance inputs w_1 and w_2 are force and track disturbances with the penalty vector q being defined in (4).

As the design criterion is to find $u(x)$ that satisfies the HJI inequality, the analytical derivations are focussed on finding a saddle point in the Hamiltonian function such that

$$H\left[x, V_x(x), w, \breve{u}\right] \le H\left[x, V_x(x), \hat{w}, \breve{u}\right] \le H\left[x, V_x(x), \hat{w}, u\right] \tag{7}$$

with $\hat{w}$ as the worst disturbance input that maximizes $H(\bullet)$ and $\breve{u}$ as the control input that minimizes $H(\bullet)$. With $D = D_{12}^T D_{12}$ and $C_1^T D_{12} = 0$ for the Maglev model, these are given by [5], [8], [9]

$$\hat{w} = \hat{w}\{x, V_x(x)\} = \frac{1}{2}\gamma^{-2} B_1(x)^T V_x(x)$$
$$\breve{u} = \breve{u}\{x, V_x(x)\} = -\frac{1}{2} D^{-1} B_2(x)^T V_x(x). \tag{8a}$$

To compute the unknown storage function $V(x(t))$ that satisfies the above saddle point condition, (8a) is substituted into (6) to give the following HJI inequality:

$$H_*[x, V_x(x)] = V_x(x)^T A(x) - \breve{u}^T D\,\breve{u} + x^T C_1^T C_1 x + \gamma^2 \hat{w}^T \hat{w} \le 0. \tag{8b}$$

In the absence of an analytical solution, (8b) is transformed into an infinite sum inequality by Taylor series (originally proposed in [10]) with the k^{th} power term as

$$V_x(x)^{[2]T} A(x)^{[k]} + \cdots + V_x(x)^{[k+1]T} A x^{[1]} - \breve{u}^{[1]T} D \breve{u}^{[k]} - \cdots - \breve{u}^{[k]T} D \breve{u}^{[1]} + x^T C_1^T C_1 x + \gamma^2 \left\{ \hat{w}^{[1]T} \hat{w}^{[k]} + \cdots + \hat{w}^{[k]T} \hat{w}^{[1]} \right\} \le 0 \tag{9}$$

where $Ax^{[1]}, A(x)^{[2]}, \ldots A(x)^{[k]}$ are the first, second, $\ldots, k^{th}$ terms in the Taylor series expansion of $A(x)$ in (2a). Application of the same power series expansion to (8a) gives the following generic relationships for the worst disturbance vector and the input control signal for any kth order term

$$\hat{w}^{[k]} = \frac{1}{2}\gamma^{-2} \left\{ B_1^{[1]T} V_x(x)^{[k+1]} + \cdots + B_1(x)^{[k]T} V_x(x)^{[2]} \right\}$$
$$\breve{u}^{[k]} = -\frac{1}{2} D^{-1} \left\{ B_2^{[1]T} V_x(x)^{[k+1]} + \cdots + B_2(x)^{[k]T} V_x(x)^{[2]} \right\} \tag{10}$$

where $B_1^{[j]}, B_2^{[j]}$ and $V_x(x)^{[j+1]}, j = 1, \ldots k$, are the Taylor series expansion of the system in (1) and the storage function $V(x)$. The generic properties of these power series provide a mechanism to build up higher order controllers cumulatively, as given as follows for first- and second-order controllers.

a) **First-order controller**, $\breve{u} = \breve{u}^{[1]}$, with $\breve{u}^{[1]}$ given with $k = 1$ in (10)

$$\text{control input} \rightarrow \breve{u}^{[1]} = -\frac{1}{2} D^{-1} B_2^{[1]T} V_x(x)^{[2]} \tag{11a}$$

$$\text{worst disturbance vector} \rightarrow \widehat{w}^{[1]} = \frac{1}{2}\gamma^{-2} B_1^{[1]T} V_x(x)^{[2]} \tag{11b}$$

$$\text{HJI inequality} \rightarrow V_x(x)^{[2]T} A x^{[1]} - 2\breve{u}^{[1]T} D \breve{u}^{[1]} + 2\gamma^2 \widehat{w}^{[1]T} \widehat{w}^{[1]} + x^T C_1^T C_1 x \leq 0. \tag{11c}$$

b) **Second-order controller,** $\breve{u} = \breve{u}^{[1]} + \breve{u}^{[2]}$, where $\breve{u}^{[2]}$ is given with $k = 2$ in (10)

$$\breve{u}^{[2]} = -\frac{1}{2} D^{-1} \left[B_2^{[1]} V_x(x)^{[3]} + B_2(x)^{[2]T} V_x(x)^{[2]} \right] \tag{12a}$$

$$\widehat{w}^{[2]} = \frac{1}{2}\gamma^{-2} \left[B_1^{[1]T} V_x(x)^{[3]} + B_1(x)^{[2]T} V_x(x)^{[2]} \right] \tag{12b}$$

$$V_x(x)^{[2]T} A(x)^{[2]} + V_x(x)^{[3]T} A x^{[1]} - \breve{u}^{[1]T} D \breve{u}^{[2]} - \breve{u}^{[2]T} D \breve{u}^{[1]} + \gamma^2 \left\{ \widehat{w}^{[1]T} \widehat{w}^{[2]} + \widehat{w}^{[2]T} \widehat{w}^{[1]} \right\} \leq 0. \tag{12c}$$

A. Numerical Results

To derive the above nonlinear H_∞ state-feedback controllers, the Taylor-series-expansions for the Maglev system in (2) is derived as in (13a) for a nominal operating point $z_0 = 4.0 \times 10^{-3}$ m, $i_0 = 3.13$ A with $N = 280, m = 1.5\,\text{kg}, a_m = 1.024 \times 10^{-2}\,\text{m}^2$ and $\text{R}_m = 1.1\,\Omega$

$$A(x) = Ax^{[1]} + A(x)^{[2]} = \begin{bmatrix} 0 & 1 & 0 \\ \left(\frac{\mu_0 N^2 a_m}{2m}\right)\frac{i_0^2}{z_0^3} & 0 & -\left(\frac{\mu_0 N^2 a_m}{2m}\right)\frac{i_0}{z_0^2} \\ \left(\frac{-2\text{R}_m}{\mu_0 N^2 a_m} - \frac{\dot{z}_0}{z_0^2}\right) i_0 & \frac{i_0}{z_0} & \left(\frac{-2\text{R}_m}{\mu_0 N^2 a_m} + \frac{\dot{z}_0}{z_0}\right) \end{bmatrix} \begin{bmatrix} x_1 \\ x_2 \\ x_3 \end{bmatrix} + \begin{bmatrix} 0 \\ -\frac{\mu_0 N^2 a_m}{4m}\left\{\frac{3i_0^2}{z_0^4} x_1^2 + \frac{1}{z_0^2} x_3^2 - \frac{4i_0}{z_0^3} x_1 x_3\right\} \\ -\frac{i_0}{z_0^2} x_1 x_2 + \left(\frac{-2\text{R}_m}{\mu_0 N^2 a_m} - \frac{\dot{z}_0}{z_0^2}\right) x_1 x_3 + \frac{1}{z_0} x_2 x_3 + \frac{\dot{z}_0 i_0}{z_0^3} x_1^2 \end{bmatrix}$$

$$B_1(x) = B_1^{[1]} + B_1(x)^{[2]} = \begin{bmatrix} 0 & 0 \\ \frac{1}{m}\alpha_1 & 0 \\ 0 & 0 \end{bmatrix} + 0;$$

$$B_2(x) = B_2^{[1]} + B_2(x)^{[2]} = \begin{bmatrix} 0 \\ 0 \\ \frac{2}{\mu_0 N^2 a_m} z_0 \end{bmatrix} + \begin{bmatrix} 0 \\ 0 \\ \frac{2}{\mu_0 N^2 a_m} [x_1 - z_0] \end{bmatrix};$$

$$D = D_{12}^T D_{12} = W_u^2. \tag{13a}$$

It can be shown that for a dissipative system to be stable, the storage function has the characteristic features of a Lyapunov function with a strong local minimum at the equilibrium point [6]. To derive $\breve{u}^{[1]}$, $V(x)^{[2]}$ is taken as the quadratic function $V(x)^{[2]} = x^T P x$, with $P > 0$ being unknown, the HJI inequality in (11c) then holds good if P satisfies the Riccati equation in (13b)

$$H_{1*} = A^{[1]T} P + P A^{[1]} + P\left(\gamma^{-2} B_1^{[1]} B_1^{[1]T} - B_2^{[1]} D^{-1} B_2^{[1]T}\right) P + C_1^T C_1 = 0. \tag{13b}$$

Assigning the values $\alpha_1 = \alpha_2 = 1, \beta = I_3, W_u = 0.12$ and $\gamma = 1$ in the series expansion matrices shown previously, a solution of (13) (using Matlab algebraic Riccati equation routine) gives

$$P = \begin{bmatrix} 5.5198 \times 10^4 & 6.3994 \times 10^2 & -4.7601 \\ 6.3994 \times 10^2 & 7.5823 & -5.2934 \times 10^{-2} \\ -4.7601 & -5.2934 \times 10^{-2} & 1.0844 \times 10^{-3} \end{bmatrix}.$$

The corresponding first-order control law and the disturbance signals are then derived from (11) and given in (14).

$$\breve{u}^{[1]} = 262.13 \times 10^2 x_1 + 291.5 x_2 - 5.972 x_3 \tag{14a}$$

$$\widehat{w}^{[1]} = \begin{bmatrix} \widehat{w}_1^{[1]} \\ \widehat{w}_2^{[2]} \end{bmatrix} = \begin{bmatrix} 4.647 \times 10^4 x_1 + 5.534 x_2 - 3.822 \times 10^{-2} x_3 \\ 0 \end{bmatrix}. \tag{14b}$$

To derive the second-order controller, $\breve{u} = \breve{u}^{[1]} + \breve{u}^{[2]}$, $V(x)^{[3]}$ is defined as the cubic polynomial $V(x)^{[3]} = c_1 x_1^3 + c_2 x_1^2 x_2 + c_3 x_1^2 x_3 + \cdots + c_9 x_2 x_3^2 + c_{10} x_3^3$, where the unknown coefficients $\{c_i\}, i = 1..10$, are to be derived from the second-order HJI equation in (12c), rewritten as (15) with $V(x)^{[2]}$, $\breve{u}^{[1]}$ and $\widehat{w}^{[1]}$ taken from the first-order controller

$$V_x(x)^{[3]}\left(Ax^{[1]} + B_1^{[1]T}\widehat{w}^{[1]} + B_2^{[1]T}\breve{u}^{[1]}\right) x + V_x(x)^{[2]}\left(A(x)^{[2]} + B_1(x)^{[2]T}\widehat{w}^{[1]} + B_2(x)^{[2]T}\breve{u}^{[1]}\right) = 0. \tag{15}$$

Equating terms in (15) with equal powers leads to a set of ten equations. Solution of these equations using the Gauss–Seidel elimination method gives the values for the unknown coefficients $\{c_i\}, i = 1, \ldots, 10$ and hence the unknown storage function $V(x)^{[3]}$. With the parameters given earlier, the second-order controller in (11a) and (12a) becomes

$$\begin{aligned} \breve{u}(x) &= \{\breve{u}^{[1]}\} + \{\breve{u}^{[2]}\} \\ &= \{262.13 \times 10^2 x_1 + 291.5 x_2 - 5.972 x_3\} \\ &\quad - \{483.88 \times 10^3 x_1^2 - 574.38 \times 10^2 x_1 x_2 - 4392.37 x_1 x_3 \\ &\quad - 194.32 x_2^2 - 31.80 x_2 x_3 + 0.403 x_3^2\}. \end{aligned} \tag{16}$$

This second-order controller has been implemented on the experimental single-degree-of-freedom system; the controller's performance in attenuating track disturbance is discussed in Section VI.

IV. Nonlinear H_∞ Output Feedback

Although all state variables are available for feedback in a Maglev vehicle suspension system, results Section III are extended to output feedback for two reasons: a) use of H_∞ controllers to other applications, such as magnetic bearings which usually employ only position sensors; and b) provide a basis for further work related to sensor fault accommodation [11]. The output feedback control law derived here uses a state estimator in conjunction with the same state-feedback control law in (16). For uniformity in the design procedure, the nonlinear state estimator [(17)] is derived using the concept of local dissipation described earlier [9].

$$\begin{aligned} \dot{\tilde{x}} &= A(\tilde{x}) + B_1(\tilde{x}) w + B_2(\tilde{x}) u + Q(\tilde{x})(y - \tilde{y}) \\ \tilde{y} &= C_2 \tilde{x} + D_{21} w \end{aligned} \tag{17}$$

where $\tilde{x}$ is the estimator state vector and $\tilde{y}$ is the estimator output. In general, the unknown *output gain* $Q(\tilde{x})$ has a nonlinear structure; an approximate solution maybe derived by using the same procedure based on Taylor series expansions as in Section IV. The corresponding first-order solution for $Q^{[1]}$ is then derived as [9]

$$(R - P) Q^{[1]} = \left(D_{21} D_{21}^T\right)^{-1} \left(D_{21} B_1^{[1]T} R + \gamma^2 C_2^T\right) \tag{18a}$$

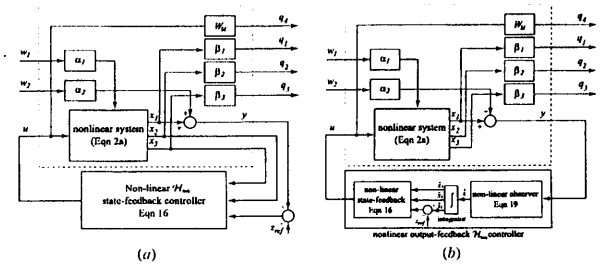

(a) (b)

Fig. 2. (a) State-feedback and (b) output-feedback control configurations.

where P defines the storage function $V(x)$[2] as computed in the state feedback controller derivation and R is the solution of the following Riccati equation:

$$\begin{aligned}&\left(A^{[1]} - B_1^{[1]}D_{21}^T\left(D_{21}D_{21}^T\right)^{-1}C_2\right)^T R\\&+ R\left(A^{[1]} - B_1^{[1]}D_{21}^T\left(D_{21}D_{21}^T\right)^{-1}C_2\right)\\&+ R\left(\gamma^{-2}B_1^{[1]}B_1^{[1]T} - B_1^{[1]}D_{21}^T\left(D_{21}D_{21}^T\right)^{-1}D_{21}B_1^{[1]T}\right)R\\&+ C_1^TC_1 - \gamma^2C_2^T\left(D_{21}D_{21}^T\right)^{-1}C_2 - H_{1*} = 0 \qquad (18b)\end{aligned}$$

with H_{1*} as defined on the left-hand side of (13b). For the Maglev system with parameters in Fig. 1 and the value of P as computed in Section III.A, the solutions for R and $Q^{[1]}$ are derived as

$$R = \begin{bmatrix} 9.6628\times10^{11} & -2.8380\times10^{7} & -9.3912\times10^{8}\\ -2.8379\times10^{7} & 2.4514\times10^{4} & -1.2372\times10^{5}\\ -9.3912\times10^{8} & -1.2372\times10^{5} & 2.4921\times10^{6}\end{bmatrix}$$

and

$$Q^{[1]} = \begin{bmatrix} 8.1733\times10^{3}\\ 33.401\times10^{6}\\ 47.382\times10^{5}\end{bmatrix}$$

with the corresponding state estimator given by (19), as shown at the bottom of the page. Solution of these nonlinear equations gives the estimated state variables $\tilde{x}_1$, $\tilde{x}_2$ and $\tilde{x}_3$ which are then used in (16) to implement the output feedback controller using the configuration in Fig. 2(b); performance of the resulting controller is discussed in Section VI.

V. Control Hardware

As part of a hardware design project for commercial Maglev vehicles and magnetic bearings, an Analog Devices Sharc 21 062 DSP-based embedded controller hardware has been manufactured by the authors and their industrial collaborators [12]. It integrates Ethernet/TCP/IP communication facilities and software functions for real-time communication with Matlab/SIMULINK environment. The sampling time has been chosen to be 1 ms for compatibility with the typical inductance values of the windings of suspension magnets and the cut-off frequency of the anti-aliasing filter set at 25 kHz [= (1/2) of per-channel sampling rate of ADC]. The main tasks performed in each sample are: data capture and conversion (including integration of the acceleration signal to generate velocity), execution of the control law, outputting of the control signal and storing data for offline analysis (the embedded hardware offers up to 4 Mbytes of onboard RAM). Each sample is interrupt-driven from the internal timer of the DSP. The software written in C/assembler for SHARC DSP's offers facilities to serve host-based Matlab visualization. The analogue processing tasks consume 5% to 8% of the sampling time and the nonlinear state-feedback ((16)) a further 5%–40%, the remainder being used to serve the host.

To implement an output-feedback controller (state estimator + state-feedback controller) on an embedded hardware, the classical linear control would require a transformation from the continuous time-domain to a discrete time-domain. Because of the nonlinear nature of the observer [(19)], this procedure is inapplicable. The scheme adopted here to overcome this limitation is to include a Runge–Kutta solver within the control loop. In doing so at every sample, the software on the DSP reads the most recent output of the system and multiplies it by the output injection gain $Q^{[1]}$. The set of first-order differential equations in (19) is then integrated by a dedicated Runge-Kutta-4 integration routine. For satisfactory convergence of this integration process, experience suggested that around 50 steps, each of length $h = 10^{-5}$, are typically required for reasonable estimation of the state vector $\tilde{x}_{50} = [\tilde{x}_1 \quad \tilde{x}_2 \quad \tilde{x}_3]_{50}^T$. At the end of the 50th step, final values of these three state variables are taken as the input to the nonlinear state-feedback controller ((16)). The full collection of software tasks for nonlinear output-feedback control takes around 400 μs per cycle; the remaining 600 μs of the sampling time is available to serve the host.

VI. Experimental Results

The oscillating mechanism in Fig. 1 is capable to introducing step change as well as periodic motion of the guideway. The vertical profile of the guideway is measured by a noncontacting position sensor mounted on a fixed datum. Fig. 3 shows responses of the suspension system with a step change in the guideway position (z_{track}) and a step change in the reference airgap (z_{ref}) for three types of controllers: linear state-feedback, second order nonlinear state-feedback and the nonlinear output-feedback. The first-order nonlinear state-feedback control law in (14a) was also implemented, but as the corresponding step responses almost overlapped with those with the linear state-feedback control law in (3), they are not included. The responses in Fig. 3 indicate that the new nonlinear controllers improve the overall settling time almost by a factor of two, compared with the conventional linear state feedback controller. The reduction in overshoots in Fig. 3 (curve-3) indicates that, within the definitions of linear systems, peak amplitude in the sensitivity function will remain below the 0-dB boundary. To study this further, a series of experiments was carried out with sinusoidal variations in the guideway position. At each run, the system is suspended at a fixed z_{ref}, the track is oscillated and the airgap and the guideway positions recorded. Fourier analysis is then performed on these data to determine the fundamental frequency of the guideway profile and the attenuation rate of the airgap error ($z_{\text{ref}} - z$). Initially, these experiments were performed with a linear state-feedback controller ((3)); the corresponding response for the highest frequency is shown in Fig. 4 (top, with attenuation rates as given). These experiments were repeated over the whole of the

$$\begin{bmatrix}\dot{\tilde{x}}_1\\ \dot{\tilde{x}}_2\\ \dot{\tilde{x}}_3\end{bmatrix} = \begin{bmatrix}-8173.3\tilde{x}_1 + \tilde{x}_2 + 8173.3y\\ -33.4\times10^{6}\tilde{x}_1 + 7.99\tilde{x}_2 + 159\times10^{-3}\tilde{x}_3 + 0.168\times10^{-4}\frac{\tilde{x}_3^2}{\tilde{x}_1^2} + 33.4\times10^{6}y\\ -4738.2\times10^{3}\tilde{x}_1 + 0.7508\times10^{7}\tilde{x}_1\tilde{x}_2 - 151.461\times10^{7}\tilde{x}_1\tilde{x}_3 + 0.5406\times10^{9}\tilde{x}_1^2 + \frac{\tilde{x}_2\tilde{x}_3}{\tilde{x}_1} + 47.382\times10^{5}y\end{bmatrix}. \qquad (19)$$

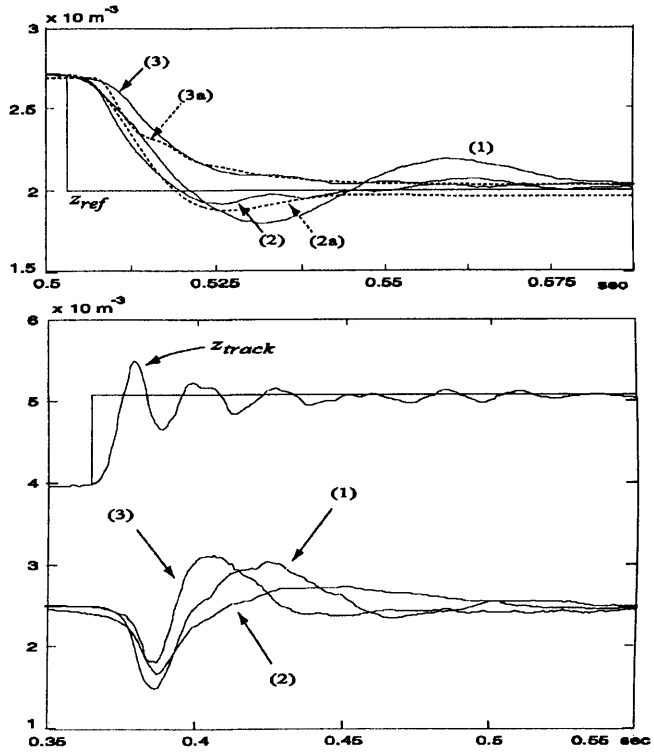

Fig. 3. Experimental and simulation transient responses. Top: step change in airgap reference $z_{\rm ref}$ from 2.75 mm to 2.0 mm with clamped guideway. (1) Linear state-feedback controller (3) with $k_p = 207.923$, $k_v = 1.5$ and $k_n = 0.004\,24$. (2) Experimental responses with nonlinear state-feedback controller (16) and (2a) the corresponding simulation response. (3) Experimental response with nonlinear output-feedback controller (16) and (19) and (3a) the corresponding simulation response. Nominal operating conditions for all controllers are $i_0 = 3.13$ A and $z_0 = 4.0$ mm. Bottom: Experimental responses due to a step change in guideway position ($z_{\rm ref}$ kept constant at 2.5 mm) with controller parameters as above.

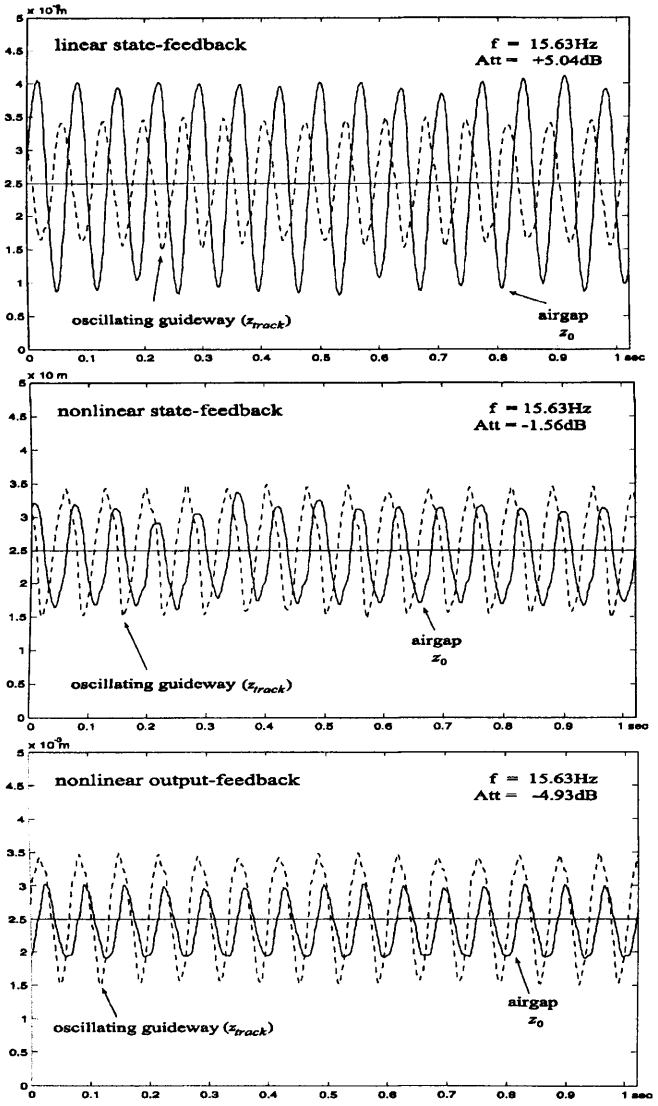

Fig. 4. Experimental responses with sinusoidally oscillating track. Top: linear state-feedback controller (3); middle: nonlinear second-order state-feedback controller (16); bottom: nonlinear output-feedback H_∞ controller (16) and (19).

frequency range for which the system maintained a stable suspension and the corresponding sensitivity function (curve-1) is plotted in Fig. 5; bandwidth of the closed-loop system with linear state feedback controller was observed to be around 9.5 Hz with the peak value of its sensitivity function being 6 dB. Consequently, disturbances with frequencies $\approx$ 15 Hz will be amplified nearly by a factor of two, leading to an unacceptable operation (airgap error rising up to two times the guideway variation). Although there was insignificant difference between the step responses of the linear state feedback and the nonlinear first-order state feedback controllers, the latter was seen to have a narrower bandwidth but a lower peak (curve-2 in Fig. 5). The above sequence of operations was also performed with the nonlinear second-order state-feedback controller and the nonlinear output-feedback controller over the same range of frequencies. The corresponding responses for 15.63 Hz are shown in Fig. 4 (middle and bottom). The respective experimentally derived frequency responses are marked as curves 3 and 4 in Fig. 5. To provide a basis for comparison with theoretical results, frequency responses with nonlinear state feedback and output feedback controllers from simulation studies have been included in Fig. 5 (dotted lines). These, along with the simulated step response in Fig. 3, underline the overall effectiveness of the proposed control architecture.

Two specific observations may be made from the shapes of the sensitivity function (Fig. 5): a) bandwidth is increased, giving increased attenuation in the low-frequency range; and b) the increase in energy on the output remains bounded by $\gamma = 1$ and hence the inequality in (5) is satisfied. Consequently, at low frequencies (< 10 Hz) the magnet will follow the guideway profile satisfactorily and at higher frequencies it would still remain below the amplitude of the guideway movement (measured from its datum line). As the permissible peak variation in the guideway is closely related to the mean operating airgap, this implies that the second order state-feedback and the output-feedback nonlinear H_∞ controllers are capable of maintaining a stable suspension over a wider frequency range than their linear counterpart.

VII. Conclusion

While the linear state feedback controllers have successfully been used over the years, the new experimental results presented here demonstrate the viability of using more computationally demanding nonlinear controllers for stabilization and control of electromagnetic suspension systems. The superiority of the second-order state feedback and the output feedback controllers in tracking a moving guideway with improved disturbance rejection properties has been illustrated. While both nonlinear controllers improve suspension characteristics, the output feedback controller (which subsumes a nonlinear state estimator) has been observed to provide significant improvement over

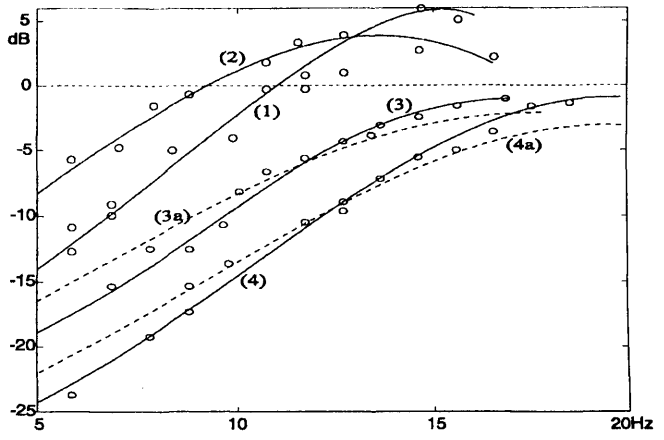

Fig. 5. Experimental and simulation sensitivity functions of the closed-loop system. (1) Linear state-feedback controller (3), (2) first-order nonlinear state-feedback controller (14a), (3) second order nonlinear state-feedback controller (16) and (4) nonlinear output-feedback controller (16) and (19). (3a) and (4a) represent the simulation responses corresponding to (3) and (4). The value of W_u puts a penalty on the control signal; small values of W_u lead to faster transient response and, hence, wider bandwidth. In all responses contained in this note γ and $W_u = 0.12$.

the now-classical linear state feedback controllers. The concept of linear H_∞ [13] has been used for Maglev control [14], [15] earlier, however, direct application of nonlinear H_∞ to deal with track disturbance in an EMS system is considered to be novel.

Although several issues require careful assessment for the real-time implementation of these nonlinear H_∞ controllers derived here, extensive range of experimental work carried out by the authors indicate that, providing a reasonable care is taken in specifying the physical parameters of the suspension magnet, the analytically derived control laws, for a given set of α, β, γ and W_u, may directly be used in assessing the performance of laboratory-scale demonstration systems. A key difference between the nonlinear state and the output feedback controllers is the execution time of the control algorithms ((16) and (19)): 50 μs for the former and 400 μs for the latter (within a sampling interval of 1 ms). In multimagnet vehicles this may impose some operational constraints. To overcome this, the embedded DSP hardware described in Section V provides communication protocols between local control loops for individual magnets and supervisory control functions to coordinate the distribution of suspension force. The dynamics of these mechanically coupled magnets on suspension stability and tracking properties are currently under investigation.

REFERENCES

[1] *The Economist: "The New Age of the Train: A Better Way to Fly"*, The Economist, London, U.K., 1998, pp. 23–25.
[2] *The Shanghai-Pudon Airport Highspeed Link*, Transrapid International, Berlin, Germany, 2001.
[3] P. K. Sinha, *Electromagnetic Suspension: Dynamics & Control*. London, U.K.: Peter Peregrinus, 1987.
[4] P. K. Sinha and A. N. Pechev, "Model reference adaptive control of a Maglev system with stable maximum descent criterion," *Automatica*, vol. 35, pp. 1457–1465, 1999.
[5] A. J. van der Schaft, "L_2-gain analysis of nonlinear systems and nonlinear state feedback H_∞ control," in *IEEE Trans. Automat. Contr.*, vol. 37, June 1992, pp. 770–784.
[6] J. G. Willems, "Dissipative dynamical systems Part I: General theory," *Arch. Rational Mech. Anal.*, vol. 22, pp. 321–351, 1972.
[7] D. Hill and P. Moylan, "The stability of nonlinear dissipative systems," *IEEE Trans. Automat. Contr.*, vol. AC-21, pp. 708–711, June 1976.
[8] J. A. Ball, J. Helton, and M. L. Walker, "H_∞ control for nonlinear systems with output feedback," *IEEE Trans. Automat. Contr.*, vol. 38, pp. 546–559, May 1993.
[9] A. Isidori and W. Kang, "H_∞ control via measurement feedback for general nonlinear systems," *IEEE Trans. Automat. Contr.*, vol. 40, pp. 466–472, Mar. 1995.
[10] E. G. Al'brekht, "On the optimal stabilization of nonlinear systems," *J. Appl. Math. Mech.*, vol. 25, pp. 1254–1266, 1962.
[11] P. K. Sinha, F. B. Zhou, and R. S. Kutiyal, "Fault detection in electromagnetic suspension systems with state estimation methods," *IEEE Trans. Magn.*, vol. 29, pp. 2971–2973, Dec. 1993.
[12] *"Sharc DSP Board for Embedded Control" Data Sheet*, Jupelier Technology, Hamm, Germany, 2000.
[13] J. C. Doyle, K. Glover, P. Khargonekar, and B. Francis, "State-space solutions to standard H_2 and H_∞ control problems," *IEEE Trans. Automat. Contr.*, vol. 34, pp. 831–847, Aug. 1989.
[14] A. Bittar and R. M. Sales, "H_2 and H_∞-control for maglev vehicles," *IEEE Control Syst. Mag.*, vol. 18, pp. 18–25, Jan. 1998.
[15] M. Fujita, T. Namerikawa, F. Matsumura, and K. Uchida, "μ-synthesis of an electromagnetic suspension system," *IEEE Trans. Automat. Contr.*, vol. 40, pp. 530–536, Apr. 1995.

Robust Stability and Stabilization of Discrete Singular Systems: An Equivalent Characterization

Shengyuan Xu and James Lam

***Abstract*—This note deals with the problems of robust stability and stabilization for uncertain discrete-time singular systems. The parameter uncertainties are assumed to be time-invariant and norm-bounded appearing in both the state and input matrices. A new necessary and sufficient condition for a discrete-time singular system to be regular, causal and stable is proposed in terms of a strict linear matrix inequality (LMI). Based on this, the concepts of generalized quadratic stability and generalized quadratic stabilization for uncertain discrete-time singular systems are introduced. Necessary and sufficient conditions for generalized quadratic stability and generalized quadratic stabilization are obtained in terms of a strict LMI and a set of matrix inequalities, respectively. With these conditions, the problems of robust stability and robust stabilization are solved. An explicit expression of a desired state feedback controller is also given, which involves no matrix decomposition. Finally, an illustrative example is provided to demonstrate the applicability of the proposed approach.**

***Index Terms*—Discrete-time systems, linear matrix inequality (LMI), parameter uncertainty, robust stability, robust stabilization, singular systems.**

I. INTRODUCTION

The problems of robust stability analysis and robust stabilization of linear state-space systems with parameter uncertainties have received much attention in the past decades [3], [23]. A great number of results on these topics have appeared in the literature. Among the different approaches dealing with these problems, the methods based on the concepts of *quadratic stability* and *quadratic stabilizability* have

Manuscript received March 28, 2003; revised July 17, 2003. Recommended by Associate Editor P. A. Iglesias. This work was supported in part by RGC HKU 7103/01P, the Foundation for the Author of National Excellent Doctoral Dissertation of China under Grant 200240, and the National Science Foundation under Grants 60304001 and 60074007.

S. Xu is with the Department of Automation, Nanjing University of Science and Technology, Nanjing 210094, P. R. China.
J. Lam is with the Department of Mechanical Engineering, University of Hong Kong, Hong Kong.

Digital Object Identifier 10.1109/TAC.2003.822854